Resilience of power grids and other supply networks: structural stability, cascading failures and optimal topologies

Inaugural-Dissertation

zur

Erlangung des Doktorgrades

der Mathematisch-Naturwissenschaftlichen Fakultät

der Universität zu Köln

vorgelegt von

Franz Nikolas Kaiser

aus Köln

Berichterstatter:	*JProf. Dr. Dirk Witthaut*
	Prof. Dr. David Gross
	Prof. Dr. Bert Zwart
Vorsitzende der Prüfungskomission:	*Prof. Dr. Berenike Maier*

Tag der mündlichen Prüfung: 15. September 2021

Abstract

The consequences of the climate crisis are already present and can be expected to become more severe in the future. To mitigate long-term consequences, a major part of the world's countries has committed to limit the temperature rise via the Paris Agreement in the year 2015. To achieve this goal, the energy production needs to decarbonise, which results in fundamental changes in many societal aspects. In particular, the electrical power production is shifting from fossil fuels to renewable energy sources to limit greenhouse gas emissions.

The electrical power transmission grid plays a crucial role in this transformation. Notably, the storage and long-distance transport of electrical power becomes increasingly important, since variable renewable energy sources (VRES) are subjected to external factors such as weather conditions and their power production is therefore regionally and temporally diverse. As a result, the transmission grid experiences higher loadings and bottlenecks appear. In a highly-loaded grid, a single transmission line or generator outage can trigger overloads on other components via flow rerouting. These may in turn trigger additional rerouting and overloads, until, finally, parts of the grid become disconnected. Such cascading failures can result in large-scale power blackouts, which bear enormous risks, as almost all infrastructures and economic activities depend on a reliable supply of electric power. Thus, it is essential to understand how networks react to local failures, how flow is rerouted after failures and how cascades emerge and spread in different power transmission grids to ensure a stable power grid operation.

In this thesis, I examine how the network topology shapes the resilience of power grids and other supply networks. First, I analyse how flow is rerouted after the failure of a single or a few links and derive mathematically rigorous results on the decay of flow changes with different network-based distance measures. Furthermore, I demonstrate that the impact of single link failures follows a universal statistics throughout different topologies and introduce a stochastic model for cascading failures that incorporates crucial aspects of flow redistribution. Based on this improved understanding of link failures, I propose network modifications that attenuate or completely suppress the impact of link failures in parts of the network and thereby significantly reduce the risk of cascading failures. In a next step, I compare the topological characteristics of different kinds of supply networks to analyse how the trade-off between efficiency and resilience determines the structure of optimal supply networks. Finally, I examine what shapes the risk of incurring large scale cascading failures in a realistic power system model to assess the effects of the energy transition in Europe.

Zusammenfassung

Die Folgen der Klimakrise sind global bereits für viele Menschen spürbar und werden sich in Zukunft voraussichtlich noch deutlich verschärfen. Um die langfristigen Folgen abzumindern, hat sich ein Großteil der Staaten der Welt im Pariser Klimaabkommen im Jahr 2015 auf eine Begrenzung des Temperaturanstiegs verständigt. Die dafür erforderliche Dekarbonisierung in der Energieerzeugung erfordert grundlegende Veränderungen in vielen gesellschaftlichen Bereichen. Zentral für eine erfolgreiche Reduktion des Ausstoßes klimawirksamer Gase ist eine Abkehr von fossilen Brennstoffen bei der Stromerzeugung und eine Umstellung letzterer auf erneuerbare Energiequellen.

Für ein Gelingen der Transformation spielt das Übertragungsnetz eine zentrale Rolle. Die Erzeugung fluktuierender erneuerbarer Energien hängt von Wetterbedingungen und anderen äußeren Faktoren ab und kann daher regional und zeitlich sehr unterschiedlich ausfallen. Deshalb gewinnt neben der Speicherung von Energie die Übertragung über große Distanzen zunehmend an Bedeutung. Dies führt zu Engpässen im Stromnetz und trägt insgesamt zu dessen höherer Auslastung bei. In stark ausgelasteten Netzen kann der Ausfall einer einzelnen Leitung oder eines Generators durch Verlagerung der Lastflüsse zur Überlastung anderer Leitungen führen. Diese werden dann ebenfalls abgeschaltet, was eine weitere Verlagerung hervorruft, bis schließlich Teile des Netzes nicht mehr miteinander verbunden sind. Derartige kaskadierende Ausfälle können zu großflächigen Stromausfällen führen. Da fast die gesamte Infrastruktur und ökonomische Aktivität von einer verlässlichen Stromversorgung abhängt, sind Stromausfälle mit großen Risiken verbunden. Um eine stabile Stromversorgung zu gewährleisten, ist es daher zentral, zu verstehen, wie Netzwerke auf lokale Störungen reagieren, wie Flüsse sich nach Ausfällen verlagern und wie kaskadierende Ausfälle sich in verschiedenen Stromnetzen ausbreiten.

In dieser Arbeit untersuche ich, inwiefern die Netzwerktopologie von Stromnetzen und anderen Versorgungsnetzwerken ihre Resilienz prägt. Zunächst analysiere ich die Verlagerung der Flüsse nach Ausfall einer oder mehrerer Leitungen im Detail und leite mathematisch rigorose Ergebnisse für die Bedeutung verschiedener netzwerkbasierter Distanzmaße zur Verminderung der Flüsse her. Weiterhin zeige ich, dass die Auswirkung eines einzelnen Leitungsausfalls in verschiedenen Topologien einer universellen Verteilung folgt. Hieraus leite ich ein stochastisches Modell für kaskadierende Ausfälle ab, welches den zentralen Mechanismus der Verlagerung von Flüssen nach Ausfällen berücksichtigt. Ein besseres Verständnis der Verlagerung von Flüssen nach Leitungsausfällen ermöglicht mir, Anpassungen an der Netzwerktopologie herzuleiten, welche zu einer starken Verminderung oder einer kompletten Aufhebung der Leistungsflussänderungen in ganzen Regionen führen und somit das Risiko kaskadierender Ausfälle stark reduzieren. In einem nächsten Schritt analysiere und vergleiche ich die topologischen Charakteristika verschiedener Arten von Versorgungsnetzwerken, um darzulegen, wie äußere Faktoren die Struktur optimaler Netzwerke prägen und beeinflussen. Abschließend untersuche ich in einem realistischen Energiesystemmodell, welche Faktoren gefährliche kaskadierende Leitungsausfälle begünstigen, um die Ausiwrkungen der Energiewende in Europa zu analysieren.

Acknowledgements

First of all, I'd like to gratefully thank my supervisor, Dirk Witthaut, for the support in terms of ideas, discussions and advice, both on the scientific and the personal level. Furthermore, I'd like to thank Professor David Gross and Professor Bert Zwart for the time spent to review my thesis and for joining my thesis defence committee and Professor Berenike Maier for heading the committee. In addition to that, I want to thank all members of the research group for the discussions, the helpful inputs and their time to read and comment on my manuscripts and this thesis. Finally, I want to thank my family for their support throughout the years in completing this work.

Contents

1. Introduction

1.1. Why research on power grids is important: climate change and the energy transition

In the Paris Agreement, most of the world's countries have committed to "holding the increase in the global average temperature to well below 2 °C above pre-industrial levels" [11]. In order to reach this target, a rapid transformation in many aspects of modern society is necessary, as stated by the Intergovernmental Panel on Climate Change (IPCC) in the summary for policymakers [12]:

> "Pathways limiting global warming to 1.5 °C with no or limited overshoot would require rapid and far-reaching transitions in energy, land, urban and infrastructure (including transport and buildings), and industrial systems (high confidence). These systems transitions are unprecedented in terms of scale, but not necessarily in terms of speed, and imply deep emissions reductions in all sectors, a wide portfolio of mitigation options and a significant upscaling of investments in those options (medium confidence)."

As a result, many of the world's countries have implemented policies and committed to net-zero emission targets which are, however, currently believed to be non-sufficient to limit global warming to or below 2 °C [13–15].

For now, we focus on the transformation in the European Union and in particular its member state Germany. In Germany, the 'Federal Climate Protection Act' establishes emission reduction goals on a national level to fulfil the pledges given in the Paris Agreement [16]. By 2030, Germany plans to reduce its greenhouse gas emissions by 55% as compared to 1990, reaching net-zero emissions by 2050. In Figure 1.1, I show the annual emissions in million carbon dioxide equivalents since 1990 based on data provided by the German Environment Agency ("Umweltbundesamt") [17]. As we can see, around 35% of the emissions can be directly attributed to the energy industry. Furthermore, there is a growing effort for electrification in other sectors as a means to reduce carbon emissions, ranging from the transport sector via electric vehicles to industry [18–20] which altogether account for much more than half of the emissions on average. For this reason, a decarbonisation of the electricity sector is one of the crucial ingredients to achieve the short- and long-term emission reduction goals.

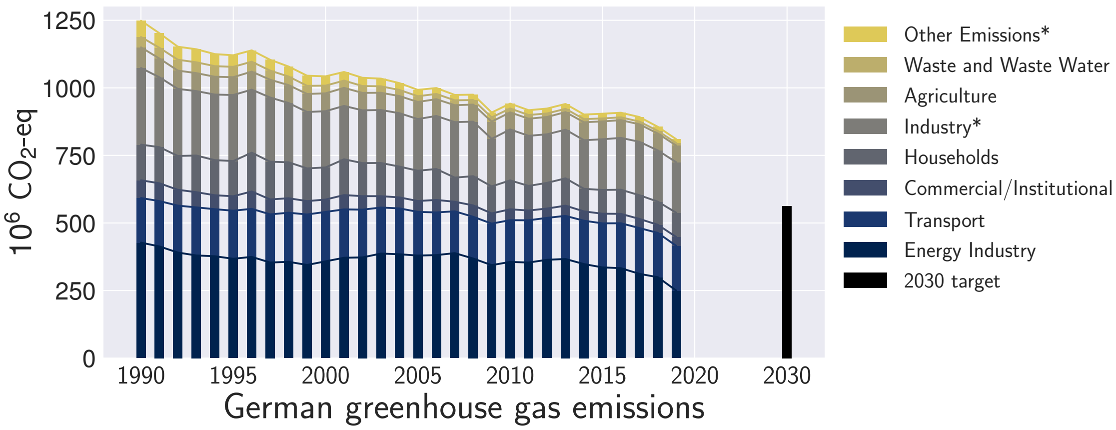

Figure 1.1.: German greenhouse gas emissions in million carbon dioxide equivalents (CO_2-eq) by sector in the years 1990-2019 and governmental emission reduction target for the year 2030. A large share of Germany's greenhouse gas emissions results from the production of electrical power by the energy industry (very dark blue) while showing a strong decrease in recent years. Taking into account the fact that there is a growing electrification also in other sectors such as the transport sector (dark blue) or industry (grey), a major part of the emissions is directly related to electricity production. Data provided by the German Environment Agency (Ref. [17]) and Figure self-designed. See Ref. [17] for further information on how the data is calculated.

Throughout this thesis, I will focus on the electricity sector and in particular the electricity grid. As a result of the emission reduction goals, today's energy system will need to transform from a fossil-fuel based energy production to a production based on renewable energy sources, which has far-reaching consequences for the power transmission grid [21–23]. At present, the vast majority of electricity on a global scale is being produced by burning fossil fuels at centralised locations [24]. Typically, power production based on these conventional carriers can be scheduled ahead and, for some power plants, changed momentarily if needed. In contrast to that, highly-renewable power production will rely on a decentralised energy production and cannot easily be planned ahead or increased spontaneously due to the dependency of variable renewable energy (VRE) sources on weather conditions. Extending today's transmission grid is essential to compensate for this regional variability of VRE and to account for the fact that the decentralised production tends to increase the geographical distance between locations of generation and consumption of electrical power [23, 25–27]. Thus, the power transmission grid will likely play a more important role in future electric power systems [24]. For this reason, it is crucial to understand how the future electricity grid can be operated reliably.

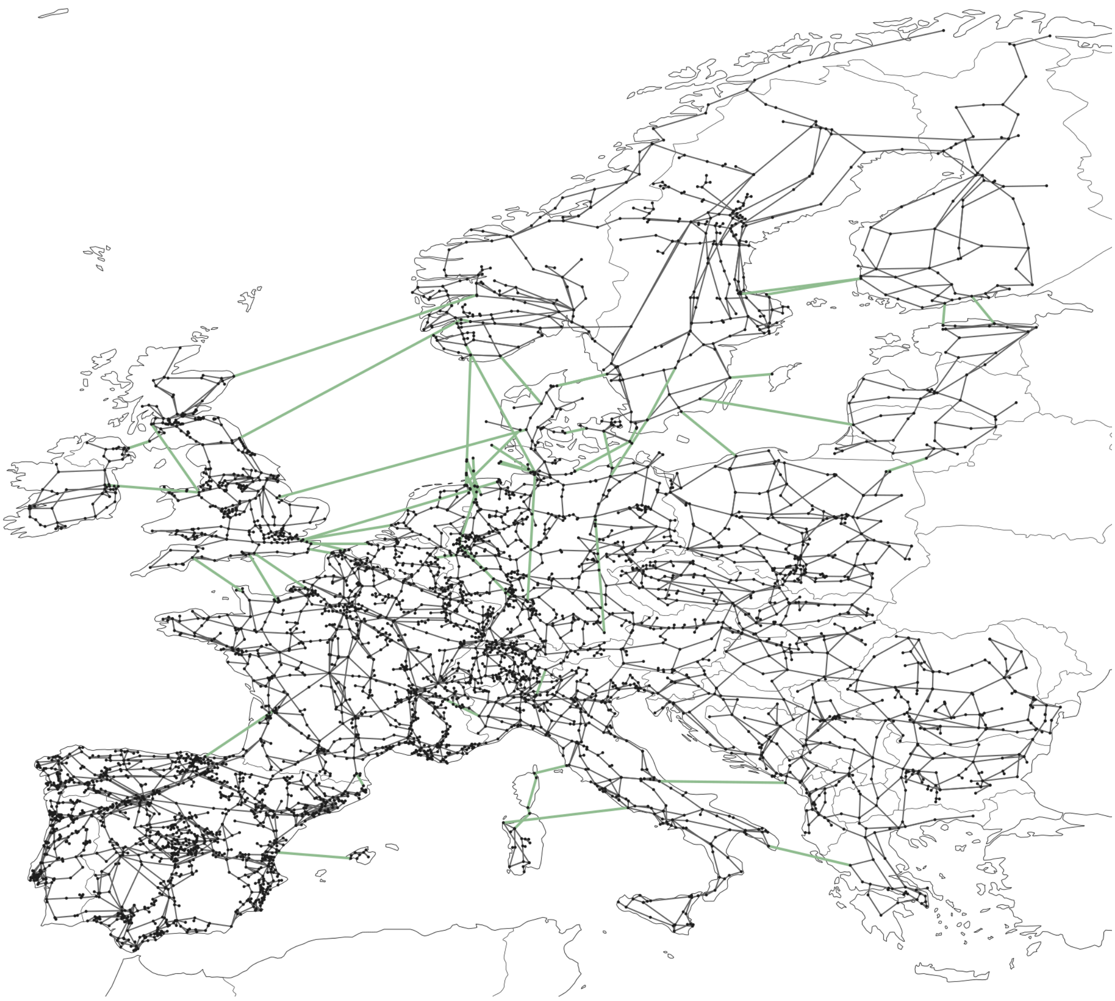

Figure 1.2.: Power grids as graphs. European power grid at the high-voltage transmission level covering transmission lines with voltage levels 220kV, 300kV and 380kV based on the open energy system model PyPSA-Eur [28] with the network topology fully available online [29]. The network consists of nodes (black circles) that represent buses to which consumers, generators or storages are connected directly or via lower-voltage distribution grids. Pairs of nodes are joint by edges (black and green lines) that connect pairs of buses and correspond to transmission lines or transformers. Here, I present the power grid at the transmission level that consists of high-voltage alternating current (HVAC) lines (black) and high-voltage direct current (HVDC) lines (green).

1.2. Power grids and complex networks research

As we have seen, a decarbonisation of the power system is key to achieve emission reduction goals and prevent climate change. We will now turn to the question of how to model the energy system to assess important issues of stability and efficiency that arise during the energy transition. In Figure 1.2, I present the European power grid at the transmission level. As clearly visible, the power grid is highly interconnected: high-voltage alternating current (black) and direct current (green) transmission lines transport power over large distances and connect buses (black circles) to which consumers or producers of electrical power are connected either directly or via distribution grids. Using the language of graph theory, we may interpret the buses as nodes and the lines as edges that together form a graph.

This graph-theoretical perspective on power grids turns out to be fruitful in many regards. Firstly, it allows applying methods from algebraic graph theory to power system analysis [30, 31]. In algebraic graph theory, the interdependence of nodes and edges is incorporated into matrices, which allows describing the network topology of power grids compactly while making them more easily accessible from a theoretical point of view. Furthermore, it establishes a link between power systems research and network science as well as networked dynamical systems analysis and has thus attracted growing interest from the physics and network science community [32–36].

Dynamical system models of power grids incorporate the topological aspects as well as the dynamics, i.e. the time-dependent behaviour, of individual generators and loads attached to the graph's nodes. Purely topological analyses of power grid network structures on the other hand allow comparing different grid structures to each other using tools from network science [37]. In particular, the topological analysis has led to the development of synthetic models of power grids that correspond to real-world power grids in terms of different topological indicators [34, 38–41]. Finally, the purely topological perspective on power grids allows comparing them to other types of supply networks or spatially embedded networks in general [42].

1.3. Power system stability

Given the meshed structure of power transmission grids discussed in the last section, one can imagine the effort it takes to keep a system of this dimension and complexity running stably. At present, the majority of electrical power in Europe is being produced by synchronous generators that generate power in the form of alternating current via rotating masses [43]. Remarkably, the generators in large geographical regions, called synchronous regions, rotate synchronously with the grid's nominal frequency ω_0 in the absence of major disturbances. The largest such region in the European power system spans mainland Europe from Portugal to Turkey, excluding Scandinavia and the Baltics. Within this region, buses are mostly connected via AC transmission lines, i.e. power is mainly being transferred via alternating currents with the grid frequency of oscillations of $\omega_0 = 50\mathrm{Hz}$.

Deviations of the grid frequency from its reference value ω_0 can have severe consequences, which is why it is one of the central indicators of power system stability [43]. As a consequence, the transmission system operators in Europe are obliged to have control schemes in place to keep the grid frequency close to its nominal value of $\omega_0 = 50\mathrm{Hz}$. The schemes are based on the time and magnitude the grid frequency deviates from its nominal value and aim to keep the power system stable [44]. There is a direct connection between the grid frequency and the synchronous generators connected to the power grid: In the first seconds immediately following an increase or decrease in the power being consumed in the grid, the grid frequency responds by a decrease or increase, respectively, which is governed by the inertia constants of the generators [45, 46]. The physical mechanism behind this behaviour is the following: If there is an overproduction of energy, the energy not being consumed is transformed into kinetic energy and, as a result, the synchronous generators start rotating faster than the nominal frequency.

One of the biggest threats to power system stability is given by cascading outages [47, 48]. A cascading outage is typically triggered by the failure of a single transmission line or generator, whose failure leads to a rerouting of power flows in the network. This rerouting mechanism typically increases the power flows on other transmission lines, which may become overloaded and undergo an emergency shutdown. Again, power flow from the lines being shut down is rerouted in the network, which may trigger additional overloads and so forth. As a result of this cascading failure, parts of the power grid can become disconnected. In these so-called system splits, there typically is a significant mismatch between power being produced and consumed in each of the disconnected parts of the grid, resulting in a sharp increase or decrease in the grid frequency as discussed in the last paragraph. This whole process may happen within seconds as recent examples demonstrate [47, 49–51]. For this reason, transmission system operators are left with only very few options to limit the impact of large scale failures that result from the cascade once the entire process is triggered. This is why different security measures are in place to prevent cascades from happening in the first place. One such measure is the so-called ‘N-1 criterion’ by which the TSOs are obliged to operate the grid only such that the failure of any transmission or generation element will not trigger any additional failures [44, 52].

As a next step, we will turn to potential impacts of the energy transition on this aspect of power system stability. Economic analyses have compared different pathways towards a fully renewable power systems in Europe to identify cost-optimal transformation scenarios. Some studies come to the conclusion that the cheapest transformation of Europe’s power system can be achieved by building renewable energy sources at favourable, decentralised locations distributed along the continent, which increases the need for electric power transmission. As a result, the analyses conclude that transmission capacities between these locations and between different countries have to be increased significantly [22, 23, 26, 53]. Thus, cost-optimal highly-renewable power grids likely require transmission expansion. Until transmission expansion is completed, an increase in renewable energy sources can result in higher transmission line utilisation and in some cases in network congestion [54, 55] where renewables need to be curtailed to avoid levels of line loading that would threaten stability. Note that the curtailment is also assumed to be caused by the design of the electricity market [56, 57]. As a result, the risk for cascading failures increases due to larger amounts of flows being redistributed after line failures.

1.4. Cascading outages as a major threat to power system stability

As we have seen, cascading power outages present the major threat to power system stability [47]. In a cascading outage, the failure of a single or only a few transmission or generation elements causes additional failures, which then lead to a sequence of failures that propagate non-locally through the power grid [47, 58]. Cascading power outages can leave millions of households without electricity as recent examples in Europe or the U.S. have demonstrated [49, 50, 59, 60]. To illustrate the mechanisms involved in a cascading

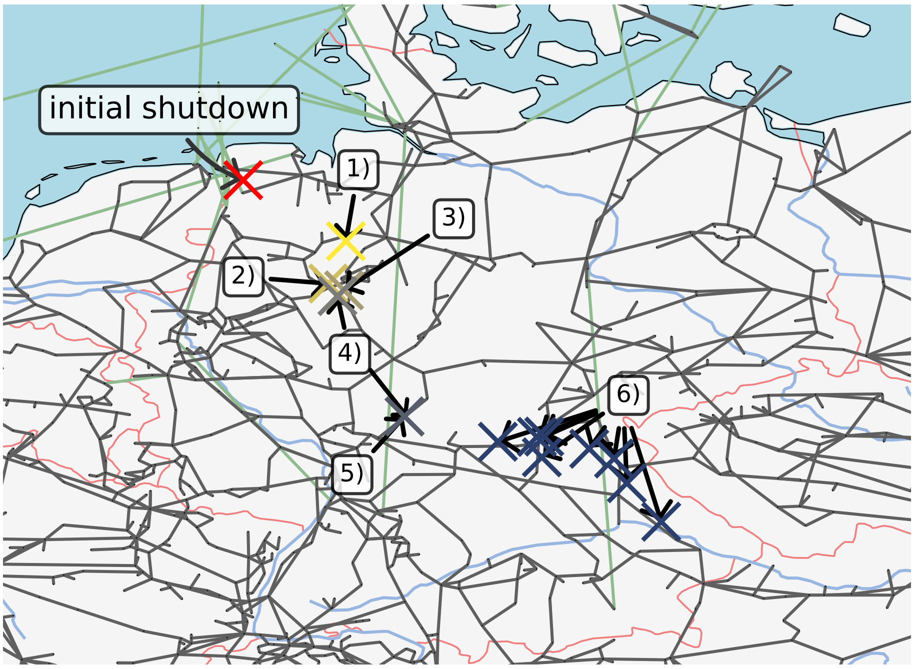

Figure 1.3.: Cascading failures of transmission lines in the German transmission grid (black and green lines) during the power outage in Europe in 2006. Initially, a transmission line over the river Ems near the city of Oldenburg was shut down for the passage of a ship (red cross). This shutdown caused a power flow rerouting through other transmission lines, which became overloaded. As a result, a sequence of transmission line failures occurred (numbers, crosses coloured from light yellow to dark blue) until finally, the European grid was split into multiple disconnected parts (see Figure 1.4). Crosses represent approximate locations of the failure events. The sequence of events was obtained from the report on the split by the UCTE [49, Appendix 3] provided by its successor organisation, the ENTSO-E and network data is based on PyPSA-EUR [28, 29] showing today's grid.

outage, I now turn to the European blackout of 2006 and discuss it in detail based on a report by the union for the co-ordination of transmission of electricity (UCTE) [49]. The propagation of the cascading outage through the German grid is shown in Figure 1.3.

The outage took place on November 4, 2006 and resulted in a disruption of electricity supply for more than 15 million household. Let us first look at the situation in the power grid before the outage happened. Initially, the transmission lines connecting Germany to the Netherlands and the corresponding East-West connections within Germany were carrying large power flows due to cross-border trading and significant wind power generation in Northern Germany. Around 10 pm, a transmission line in North-Western Germany on top of the river Ems near the city of Oldenburg was shut down for the passage of a ship (Figure 1.3, red cross). Shortly afterwards, the transmission system operator (TSO) of the region decided to perform a small change in the power grid network topology by coupling two buses at Landesbergen substation near the city of Hanover such that all connecting transmission lines shared the same bus after the coupling. As a result, the transmission line connecting the Landesbergen substation to the one in Wehrendorf near the city of Osnabrück, which also carried significant power flows in East-West direction, tripped and was shut down. The shutdown of the transmission lines resulted in a rerouting of the power flows initially carried by the lines to other East-West connections which then became overloaded and resulted in further shutdowns in a sequence of events until, within seconds, more than 20 transmission lines all over Europe tripped, and the European transmission system was divided into three isolated regions.

Such events, where different regions that are otherwise connected and operated synchronously become disconnected, are referred to as system splits. In the immediate after-

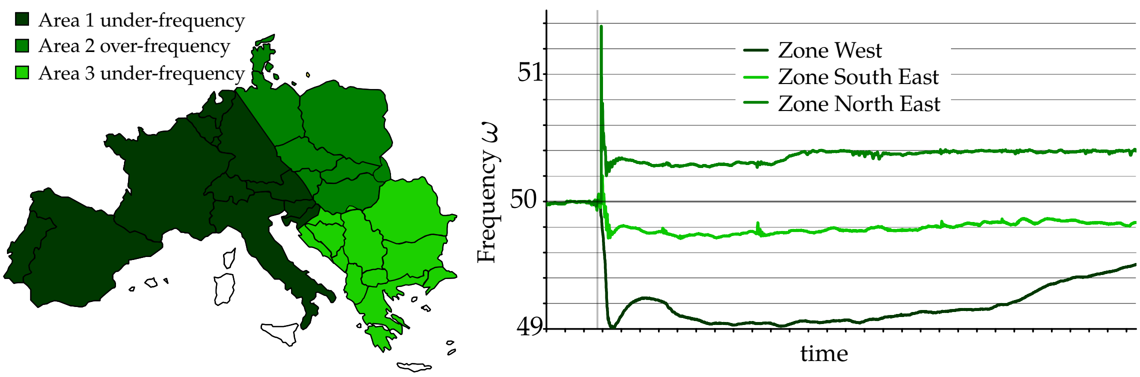

Figure 1.4.: Cascading outage in the European power system in 2006. As a result of the outage, the power system is split into three individual components that are no longer connected to each other (shades of green, left). Significant deviations from the system's nominal frequency $\omega_0 = 50$Hz occur in the three isolated components in response to the system split (right). Figure adapted and recombined from the report on the split by the UCTE [49] provided by its successor organisation, the ENTSO-E.

math, there may be a significant imbalance between load and generation in each of the separated components due to the lack or surplus of power that is otherwise imported or exported. This imbalance results in a frequency deviation from the nominal frequency of $\omega_0 = 50$Hz whose rate of change is determined by the magnitude of the imbalance and the inertia of the remaining generators in each component. Figure 1.4 shows the three disconnected regions in Europe after the system split in 2006 (left) and the corresponding frequency deviation over time (right). In the region experiencing an under-frequency (dark green), which ranges from parts of Germany to Spain and Italy, the power system could only be protected from a complete collapse by performing significant load shedding, i.e. cutting electricity supply to customers. This underlines the severity of cascading outages and demonstrates the importance to understand and prevent such events.

1.5. Scope of this thesis: resilience in linear flow networks

In this thesis, I analyse what shapes a power grid's resilience against perturbations – from small failures to large scale cascades. I focus on the network structure as the central characteristic of large scale power systems to understand which factors determine a grid's structural stability. To this end, I analyse how flow is rerouted after failures in relationship to the network topology. The linear approximation of power flows which is the main approach used in this thesis allows to unveil a direct connection between network structure and flow rerouting such that small- and large scale failures may be understood by focusing on the network topology.

The aim of this thesis is thus to understand on a very fundamental level which network structures make a given network more resilient to failures and which ones make it particularly vulnerable. Throughout this thesis, I will discuss and try to answer the following questions: How do failures spread in different kinds of power grids and supply networks? Is there a common trait that underlies all or most real-world networks, i.e. do they share a common optimal design – and how are such traits related to network resilience? Does vulnerability with respect to single link failures determine vulnerability in terms of cascading failures? And finally: How can we design networks in such a way that dangerous cascades and system splits are identified and prevented?

Since this thesis heavily relies on linear flow networks, I will briefly discuss why this focus is advantageous for its scope in the following paragraph. Firstly, it largely increases the generality of the results obtained and derived here. Linear flow models are not restricted to linearised power flow models, but may be used to describe – among others – resistor networks [31, 61], hydraulic networks [62] or leaf venation networks [63, 64]. Thus, findings obtained for linear flow networks find a broad applicability. As a result, there is a large body of historical literature about linear flow networks that dates back to early works by Kirchhoff in 1847 [65] which we can profit from. Secondly, the linear treatment is more accessible and allows even for rigorous results, as we will see in the following. Flow redistribution after transmission element failures is determined purely by the network topology in linear flow networks. Thus, the flow redistribution patterns leading to cascading failures may be understood mainly by analysing the network topology. Finally, with regard to the applicability to power flow studies, in most cases linear flow networks capture the relevant aspects well, in particular when looking at power flow rerouting and cascading failures [66–69]. For this reason, they have been successfully applied to better understand how cascading power outages emerge [70].

1.5.1. Structure of the thesis and publications

The thesis is structured as follows: In Chapter 2, I present three publications that lay the foundation for understanding the impact of link failures in linear flow networks. First, we explored the effect of a single link failure and the subsequent flow rerouting in Ref. [1] (Section 2.1). We then extended the analysis to the interplay of two simultaneous failures in Ref. [2] (Section 2.2). Finally, we found universal properties of flow rerouting throughout different network topologies that we then exploited to come up with a probabilistic flow redistribution model for cascading failures in Ref. [3] (Section 2.3).

In the next chapter, we turn to strategies counteracting cascading failures by analysing network structures that limit the effect of link failures. In Ref. [4], we proved the existence of a subgraph that completely suppresses the impact of link failures between subgraphs that it connects (Section 3.1). We then extended on this result and suggested further containment strategies based on a fundamental lemma on the importance of specific path for flow rerouting in Ref. [5] (Section 3.2).

As a next step, we turn to another fundamental aspect of network structure and consider optimal network design in Chapter 4. In Ref. [6], we analysed a class of networks whose structure provide resilience in an optimal way and minimise the dissipated energy with a particular focus on the formation of loops (Section 4.1). In Ref. [7], we considered a novel type of community structure and showed that these communities result from a trade-off between resilience and costs in optimal supply networks and power grid models (Section 4.2).

Finally, we move on to the topic of realistic cascading failures resulting in system splits, as discussed in detail in the last section. In the last, unpublished manuscript, we considered different transmission expansion scenarios and different levels of renewable energy sources in the European power system and analysed and classified cascading outages resulting in system splits to reveal which factors favour particularly dangerous splits.

In addition to the aforementioned publications, I contributed to several other manuscripts while working on my thesis that are, however, not part of the thesis: I contributed to Ref. [8] where we studied multistability in power grid models, Ref. [9] where we used our results on failure spreading in linear flow networks to shield specific solutions in coupled oscillator models and Ref. [10] where we analysed specific states in coupled oscillator networks.

2. Foundations of link failures and linear flow networks

In the first three publications, we discuss the fundamentals of flow rerouting after the failure of a single or few transmission lines. This scenario is of utmost importance for the understanding of power grid stability, as most large-scale blackouts can be traced back to the outage of a single transmission element [47]. In Section 2.1, we review the mathematical description of link failures, outline a connection to classical electrostatics and analyse the spatial distribution of flow rerouting with a focus on the role of different measures of distance. In Section 2.2, we extend the analysis to the case of several simultaneously failing links, with a focus on the different manifestations and the strengths of collective effects. Section 2.3 complements these 'microscopic' results by a statistical analysis of flow distribution factors, revealing universal properties throughout different power grid topologies.

In regular networks where each node has the same amount of neighbours, for example in square grids, flow rerouting turns out to be well-described by an analogy to electrostatics: The failure of a single link induces a dipole-like pattern of flow changes. Here, I contributed to the publication by analysing additional regular networks such as triangular grids and hexagonal grids and deriving simple scaling laws of flow changes with distance. To study which of these analyses translates to more realistic networks, I extended the analysis to sparse grids where an increasing share of links was removed from the regular networks. Furthermore, I contributed by deriving parts of the theoretical results on the relationship between flow rerouting and network topology. Finally, I contributed to writing the manuscript and designing some of the figures.

Even though the analysis of link failures relies on *linear* flow networks, the simultaneous failure of multiple links results in collective effects that cause flow patterns different from the linear superposition of the two individual failures. In the second publication, we focus on these collective effects: We demonstrate that two simultaneous link failures can amplify or attenuate each other depending on the network topology. The latter effect provides an effective strategy to contain damages caused by a single failure since the additional, intentional removal of another link can actually increase the system performance – this is known as Braess' paradox [71]. But in which cases do these effects dominate, and when is it sufficient to consider the failure of each link separately in a linear superposition? To answer this question, we introduce a simple predictor that is based on the network topology and performs very well in forecasting whether two links interact strongly collectively and prove that it is a lower bound for the actual interactions. Here, I contributed by writing a large part of the paper, deriving parts of the theoretical results and designing half of the figures.

Now we shift perspective from an individual link failure to the statistics of all possible single link failures in an entire network. Since the redistribution factor describing single link failures is based purely on the network topology, the statistics of these factors is a characteristic of a given network's resilience. In the third publication, we compare this statistics for different synthetic, random and test case grids. We find a universal statistics of redistribution factors that displays a large similarity throughout different networks. This finding offers an explanation for the scale-free nature of outage sizes observed in empirical data, as we demonstrate by introducing a stochastic load redistribution model that incorporates the universal redistribution statistics. Here, I contributed by performing all numerical simulations and analyses, designing all figures and writing most of the paper.

2.1. A) Non-local impact of link failures in linear flow networks

[1] Strake, J., Kaiser, F., Basiri, F., Ronellenfitsch, H. & Witthaut, D. Non-local impact of link failures in linear flow networks. *New Journal of Physics* **21,** 053009. doi:10.1088/1367-2630/ab13ba (2019).

New Journal of Physics
The open access journal at the forefront of physics

Deutsche Physikalische Gesellschaft DPG
IOP Institute of Physics

Published in partnership with: Deutsche Physikalische Gesellschaft and the Institute of Physics

CrossMark

OPEN ACCESS

RECEIVED
3 December 2018

REVISED
11 March 2019

ACCEPTED FOR PUBLICATION
27 March 2019

PUBLISHED
6 May 2019

PAPER

Non-local impact of link failures in linear flow networks

Julius Strake[1,2,4], Franz Kaiser[1,2,4], Farnaz Basiri[1], Henrik Ronellenfitsch[3] and Dirk Witthaut[1,2,5]

[1] Forschungszentrum Jülich, Institute for Energy and Climate Research—Systems Analysis and Technology Evaluation (IEK-STE), D-52428 Jülich, Germany
[2] University of Cologne, Institute for Theoretical Physics, D-50937 Köln, Germany
[3] Department of Mathematics, Massachusetts Institute of Technology, Cambridge, MA 02139, United States of America
[4] JS and FK contributed equally to this work.
[5] Author to whom any correspondence should be addressed.

E-mail: f.kaiser@fz-juelich.de and d.witthaut@fz-juelich.de

Keywords: complex networks, network flows, power grids, link failure

Abstract

The failure of a single link can degrade the operation of a supply network up to the point of complete collapse. Yet, the interplay between network topology and locality of the response to such damage is poorly understood. Here, we study how topology affects the redistribution of flow after the failure of a single link in linear flow networks with a special focus on power grids. In particular, we analyze the decay of flow changes with distance after a link failure and map it to the field of an electrical dipole for lattice-like networks. The corresponding inverse-square law is shown to hold for all regular tilings. For sparse networks, a long-range response is found instead. In the case of more realistic topologies, we introduce a rerouting distance, which captures the decay of flow changes better than the traditional geodesic distance. Finally, we are able to derive rigorous bounds on the strength of the decay for arbitrary topologies that we verify through extensive numerical simulations. Our results show that it is possible to forecast flow rerouting after link failures to a large extent based on purely topological measures and that these effects generally decay with distance from the failing link. They might be used to predict links prone to failure in supply networks such as power grids and thus help to construct grids providing a more robust and reliable power supply.

1. Introduction

The robust operation of supply networks is essential for the function of complex systems across scales and disciplines. Almost all of our technical and economical infrastructure depends on the reliable operation of the electric power grid [1, 2]. Biological organisms distribute water and nutrients via their vascular networks, for instance in plant leaves [3], the human and animal circulatory system [4], or in protoplasmic veins of certain slime molds [5]. Huge amounts of money and assets are exchanged through a complex financial network [6]. Structural damages to such networks can have catastrophic consequences such as a stroke, a power outage or a major economic crisis.

In power grids, large scale outages are typically triggered by the failure of a single transmission or generation element [7–11]. The outages in the United States in 2003, Italy in 2003 and Western Europe in 2006 are very well documented and provide a detailed insight into the dynamics of a large scale network failure [12–14]. Each outage was triggered by the loss of a transmission line during a period of high grid load. Subsequently, the power flows were rerouted, causing secondary overloads and eventually a cascade of failures. In these three examples, the cascades propagated mostly locally—overloads took place in the proximity of previous failures. However, this is not necessarily the case during power outages (see, e.g. [15]), raising the question of how networks flows are rerouted after failures [16–23].

In biological distribution networks, robustness against link failure is a critical prerequisite that guards against potentially life-threatening events such as stroke [24] or embolism [25, 26], but also to function efficiently in the presence of fluctuations [3, 27, 28]. Thus, biological networks are often (but not in all cases, such as in the penetrating arterioles of the cortical vasculature [29]) endowed with highly resilient, redundant topologies that optimize rerouting of flow in case of link failure to the network [28] and are generated through adaptive developmental mechanisms [30]. For the understanding of such life-threatening conditions it is therefore crucial to investigate the behavior of the vascular network in the case of failure.

To understand the vulnerability of networks, we here provide a detailed analysis of the impact of link failures in linear flow networks. We focus on how the network topology determines the overall network response as well as the spatial flow rerouting. We consider linear supply network models, where the flow between two adjacent nodes is proportional to the difference of the nodal potential, pressure or voltage phase angle. Linear models are applied to hydraulic networks [31], vascular networks of plants and animals [28, 32–35], economic input–output networks [36] as well as electric power grids [37–42]. The linearity allows to obtain several rigorous bounds for flow rerouting in general network topologies and to solve special cases fully analytically.

The paper is structured as follows; first, we formally introduce linear flow networks in section 2 and present a framework for studying line outages in such networks in section 3. Afterwards, we establish a mathematical analogy of flow rerouting after line outages and electric dipole fields on square grids in the continuum limit in section 4. We then derive rigorous bounds on the strength of this effective dipole to describe how the flow is rerouted on arbitrary network topologies in section 5. Finally, we establish a new distance measure on networks, the rerouting distance, which is able to predict the flow redistribution much better than the ordinary geodesic distance in section 6. Furthermore, we study the effect of network sparsity on the dipole pattern of flow redistribution and quantify this scaling with distance from the failing link in the same section.

2. Linear flow networks

Consider a network consisting of N nodes (vertices) that are connected to each other via lines (edges) denoted by $(m,\ n)$ for a line going from node m to node n. We assume the network to be globally connected, otherwise consider each connected component of the network separately. Assign a potential or phase angle $\theta_m \in \mathbb{R}$ to each node m in the network. Then we assume the flow $F_{m\to n}$ between nodes m and n connected via line $(m,\ n)$ to be *linear* in the potential drop along the line

$$F_{m\to n} = b_{mn}(\theta_m - \theta_n). \tag{1}$$

Here, $b_{mn} = b_{nm}$ is the transmission capacity assigned to the line $(m,\ n)$ that describes its ability to carry flow. This equation may for example be used to describe hydraulic networks [31, 43] or vascular networks of plants [28], where the θ_n denotes the pressure at some node n and the capacity b_{mn} scales with the diameter of a pipe or vein. Our main focus will be its application to electric power engineering, where this linear approximation of the power flow equations is referred to as the DC approximation [38–40]. In this case, $F_{m\to n}$ refers to the flow of real power along a transmission line $(m,\ n)$, θ_n is the voltage phase angle at node n and b_{mn} is proportional to the line's susceptance. For the sake of consistency, we refer to the θ_n as 'potentials' throughout this paper. Since only phase differences are involved in the flow calculation, these potentials are only defined up to a constant phase shift. Typically, an arbitray node is selected where the potential is set to zero, $\theta_n = 0$.

In addition to that, we assume that Kirchhoff's current law holds at the nodes of the network which states that the inflows and outflows at any node m balance

$$\sum_{n=1}^{N} F_{m\to n} = P_m, \tag{2}$$

where the right-hand side denotes the inflow ($P_m > 0$) or outflow ($P_m < 0$) at node m, commonly called the 'power injection' in power engineering. Equations (1) and (2) describe the state and the flow of the network up to a constant phase shift as described above once the line parameters b_{mn} and the injections P_m are given.

These equations may be conveniently written using a vectorial notation. Define the vector $\boldsymbol{\theta} = (\theta_1,\ldots,\ \theta_N)^\top \in \mathbb{R}^N$ of the nodal potentials or voltage phase angles and the vector $\boldsymbol{P} = (P_1,\ldots,\ P_N)^\top \in \mathbb{R}^N$ of nodal injections. Here and in the following sections, the superscript '$\top$' denotes the transpose of a vector or matrix. We further label all lines in the grid by $\ell = 1,\ldots,\ L$ and summarize all line flows in a vector $\boldsymbol{F} = (F_1,\ldots,\ F_L)^\top \in \mathbb{R}^L$. Equation (1) may then be rewritten as

$$\boldsymbol{F} = \boldsymbol{B}_d \boldsymbol{K}^\top \boldsymbol{\theta}, \tag{3}$$

where $\boldsymbol{B}_d \in \mathbb{R}^{L\times L}$ is a diagonal matrix containing the capacities b_ℓ of all edges. Furthermore, we defined the node-edge incidence matrix $\boldsymbol{K} \in \mathbb{R}^{N\times L}$. To define this matrix in an undirected graph, one typically fixes an arbitrary orientation of the graph's edges such that its components read

$$K_{n,\ell} = \begin{cases} 1 & \text{if line } \ell \text{ starts at node } n, \\ -1 & \text{if line } \ell \text{ ends at node } n, \\ 0 & \text{otherwise.} \end{cases} \tag{4}$$

The node-edge incidence matrix also relates the injections to the flows incident at a node. More specifically, Kirchhoff's current law (2) may be rewritten as follows

$$\boldsymbol{P} = \boldsymbol{K}\boldsymbol{F} = \boldsymbol{K}\boldsymbol{B}_d\boldsymbol{K}^\top\boldsymbol{\theta} = \boldsymbol{B}\boldsymbol{\theta}. \tag{5}$$

Here, we defined the matrix $\boldsymbol{B} = \boldsymbol{K}\boldsymbol{B}_d\boldsymbol{K}^\top \in \mathbb{R}^{N\times N}$ commonly referred to as the nodal susceptance matrix in power engineering. Mathematically, $\boldsymbol{B}$ is a weighted Laplacian matrix [44, 45] with components

$$B_{mn} = \begin{cases} \sum_{\ell\in\Lambda_m} b_\ell & \text{if } m = n; \\ -b_\ell & \text{if } m \text{ is connected to } n \text{ by } \ell. \end{cases}$$

Here, Λ_m is the set of lines which are incident to m.

3. Algebraic description and analysis of line outages

An important question in network security analysis is how the flows in the network change if a line fails. Denoting by F_ℓ the initial flow of the failing line $\ell \triangleq (r, s)$, the flow change ΔF_e at a transmission line $e \triangleq (m, n)$ is written as

$$\Delta F_e = \mathrm{LODF}_{e,\ell}\, F_\ell. \tag{6}$$

Adopting the language of power system security analysis [37, 38], we call the factor of proportionality the line outage distribution factor (LODF). In the following, we present two alternative derivations as well as a physical interpretation of the linear flow rerouting problem.

3.1. Self-consistent derivation of LODFs

To derive an explicit expression for the LODFs one generally starts with a related problem. Consider an increase of the real power injection at node r and a corresponding decrease at node s by the amount ΔP. The new vector of real power injections is then given by

$$\hat{\boldsymbol{P}} = \boldsymbol{P} + \Delta P\, \boldsymbol{\nu}_{rs}, \tag{7}$$

where the components of $\boldsymbol{\nu}_{rs} \in \mathbb{R}^N$ are $+1$ at position r, -1 at position s and zero otherwise. Here and in the following, we use a hat to indicate the state of the network after a line outage or a similar change of the topology. The change of the real power injections causes the following change in the real power flow

$$\Delta F_{mn} = \underbrace{b_{mn}\boldsymbol{\nu}_{mn}^\top \boldsymbol{B}^\dagger \boldsymbol{\nu}_{rs}}_{=:\mathrm{PTDF}_{(m,n),r,s}}\Delta P. \tag{8}$$

Here, $\boldsymbol{B}^\dagger$ denotes the Moore–Penrose pseudo-inverse of the Laplacian matrix $\boldsymbol{B}$ and the factor of proportionality is referred to as the power transfer distribution factor (PTDF).

The LODFs can be expressed by PTDFs in the following way [38]. To consistently model the outage of line (r, s), one assumes that the line is disconnected from the grid by circuit breakers and that some fictitious real power ΔP is injected at node s and taken out at node r. The entire flow over the line (r, s) after the opening thus equals the fictitious injections $\hat{F}_{rs} = \Delta P$. Using PTDFs, we also know that

$$\hat{F}_{rs} = F_{rs} + \mathrm{PTDF}_{(r,s),r,s}\, \Delta P.$$

Substituting $\hat{F}_{rs} = \Delta P$, solving for ΔP and inserting equation (8) yields

$$\mathrm{LODF}_{(mn),(rs)} = \frac{\mathrm{PTDF}_{(m,n),r,s}}{1 - \mathrm{PTDF}_{(r,s),r,s}}. \tag{9}$$

For consistency, one usually defines the LODF for the failing line as follows: $\mathrm{LODF}_{(rs),(rs)} = -1$. In addition to that, we exclude cases where the failing line is a bridge, i.e. a line whose removal disconnects the graph, from our analysis in the following sections.

3.2. Algebraic derivation of LODFs

The LODFs can also be obtained in a purely algebraic way without any self-consistency argument [46]. As the line $\ell \triangleq (r, s)$ fails, the nodal susceptance matrix of the network changes as

$$\boldsymbol{B} \to \hat{\boldsymbol{B}} = \boldsymbol{B} + \Delta\boldsymbol{B}, \text{ where } \Delta\boldsymbol{B} = B_{rs}\boldsymbol{\nu}_{rs}\boldsymbol{\nu}_{rs}^\top, \tag{10}$$

which causes a change of the nodal potentials or voltage phase angles respectively,

$$\boldsymbol{\theta} \to \hat{\boldsymbol{\theta}} = \boldsymbol{\theta} + \boldsymbol{\psi}. \tag{11}$$

Equation (5) for the perturbed grid now reads

$$(\boldsymbol{B} + \Delta\boldsymbol{B})(\boldsymbol{\theta} + \boldsymbol{\psi}) = \boldsymbol{P}. \tag{12}$$

Subtracting equation (5) for the unperturbed grid, we see that the change of the voltage angles is given by

$$\boldsymbol{\psi} = -(\boldsymbol{B} + \Delta\boldsymbol{B})^{\dagger}\Delta\boldsymbol{B}\,\boldsymbol{\theta} = (\boldsymbol{B} + \Delta\boldsymbol{B})^{\dagger}\,\boldsymbol{\nu}_{rs}F_{rs}. \tag{13}$$

The change of flows after the outage of line $(r,\ s)$ and thus the LODFs are calculated from the change of the voltage angles which yields

$$\begin{aligned}\Delta F_{mn} &= b_{mn}(\psi_m - \psi_n) = b_{mn}\boldsymbol{\nu}_{mn}^{\top}\boldsymbol{\psi}\\ &= b_{mn}\boldsymbol{\nu}_{mn}^{\top}(\boldsymbol{B} + \Delta\boldsymbol{B})^{\dagger}\boldsymbol{\nu}_{rs}F_{rs}.\end{aligned} \tag{14}$$

In principle, we could now use these equations to calculate the flow changes and the LODFs. However, this would require to invert the matrix $\hat{\boldsymbol{B}} = \boldsymbol{B} + \Delta\boldsymbol{B}$ separately for every possible line $(r,\ s)$ in the grid, which is impractical. Nevertheless, we can simplify the expression using the Woodbury matrix identity,

$$(\boldsymbol{B} + B_{rs}\boldsymbol{\nu}_{rs}\boldsymbol{\nu}_{rs}^{\top})^{\dagger} = \boldsymbol{B}^{\dagger} - \boldsymbol{B}^{\dagger}\boldsymbol{\nu}_{rs}(B_{rs}^{\dagger} + \boldsymbol{\nu}_{rs}^{\top}\boldsymbol{\nu}_{rs})^{\dagger}\boldsymbol{\nu}_{rs}^{\top}\boldsymbol{B}^{\dagger}.$$

Thus we obtain

$$(\boldsymbol{B} + B_{rs}\boldsymbol{\nu}_{rs}\boldsymbol{\nu}_{rs}^{\top})^{\dagger}\boldsymbol{\nu}_{rs} = (1 + B_{rs}\boldsymbol{\nu}_{rs}^{\top}\boldsymbol{B}^{\dagger}\boldsymbol{\nu}_{rs})^{-1}\,\boldsymbol{B}^{\dagger}\boldsymbol{\nu}_{rs}, \tag{15}$$

such that the flow change (14) reads

$$\Delta F_{mn} = \frac{b_{mn}\boldsymbol{\nu}_{mn}^{\top}\boldsymbol{B}^{\dagger}\boldsymbol{\nu}_{rs}}{1 - b_{rs}\boldsymbol{\nu}_{rs}^{\top}\boldsymbol{B}^{\dagger}\boldsymbol{\nu}_{rs}} \times F_{rs}\,, \tag{16}$$

which is identical to equation (9) obtained using the standard approach.

3.3. Electrostatic interpretation

A deeper physical insight into the network flow rerouting problem is obtained by the analogy to discrete electrostatics. Equation (13) can be rearranged into a linear set of equations for the change of the nodal potentials

$$\hat{\boldsymbol{B}}\boldsymbol{\psi} = F_{rs}\boldsymbol{\nu}_{rs}. \tag{17}$$

Here, $\hat{\boldsymbol{B}}$ is the Laplacian of the grid after the failure, i.e. the grid where line $(r,\ s)$ has been removed. Alternatively, we can formulate the equation in terms of the original network topology, substituting equation (15) into equation (13). This yields the linear set of equations

$$\boldsymbol{B}\boldsymbol{\psi} = \boldsymbol{q} \tag{18}$$

with the dipole source

$$\boldsymbol{q} = (1 - b_{rs}\boldsymbol{\nu}_{rs}^{\top}\boldsymbol{B}^{\dagger}\boldsymbol{\nu}_{rs})^{-1}F_{rs}\boldsymbol{\nu}_{sr}. \tag{19}$$

As noted before, $\boldsymbol{B}$ and $\hat{\boldsymbol{B}}$ are Laplacian matrices and the right-hand side of both equations (18) and (17) are non-zero only at positions r and s with opposite sign. Hence, these equations are *discrete Poisson equations* with a dipole source and $\boldsymbol{\psi}$ is a dipole potential, see [47, ch 15] for a detailed analysis of this equation. The main complexity of the line outage problem thus arises from the network topology encoded in the Laplacian $\boldsymbol{B}$, which can be highly irregular.

The two equations (18) and (17) yield the same potential $\boldsymbol{\psi}$, but are formulated on different topologies—either on the original network topology or the topology after the outage. To compare the impact of different failures it is beneficial to use the original topology, such that only the dipole inhomogeneity differs—not the electrostatic problem itself. Then, the strength of the dipole depends on the network topology via the prefactor $(1 - b_{rs}\boldsymbol{\nu}_{rs}^{\top}\boldsymbol{B}^{\dagger}\boldsymbol{\nu}_{rs})^{-1}$.

Using the analogy to electrostatics we can solve the flow rerouting problem for regular network topologies (section 4) and provide some general rigorous results (section 6.1). To understand flow rerouting in networks with complex topologies, we thus have to account for the spatial spreading pattern described by $\boldsymbol{B}^{\dagger}$ (see section 6.3) as well as the dipole strength, which quantifies the gross response of the grid (see section 5).

4. Failures in regular networks and the continuum limit

To obtain a first insight into the spatial aspects of flow rerouting, we consider an elementary example admitting a solution in the continuum limit. Consider a regular square lattice embedded in a plane as depicted in figure 1 and studied in a slightly different form in [48]. All nodes are labeled by their positions $\boldsymbol{r} = (x,\ y)^{\top}$ in this

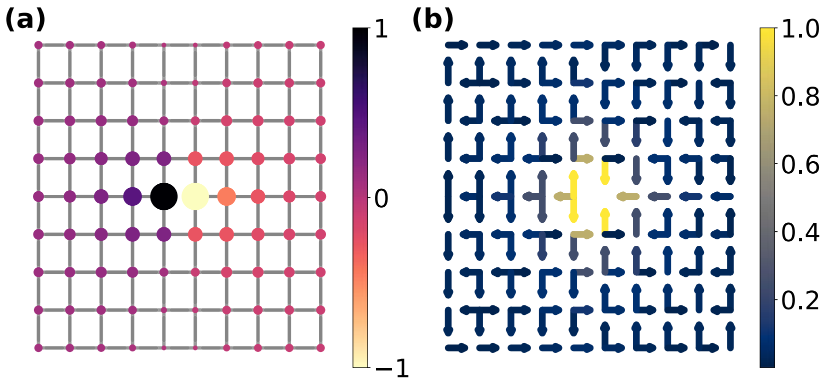

Figure 1. Impact of a link failure in a homogeneous square lattice. (a) Normalized change of the nodal potentials ψ_n, which are the nodal phase angles when referring to power grids, for a network with uniform edge weights for a single failing link located in the center of the network. The size of the nodes as well as the colorcode represent the strength of the change in potential. The change is strongest close to the failing link and decays with distance. (b) Normalized change of the link flows ΔF_{mn} for the same topology. Arrows and color represent direction and strength of flow changes, respectively. The pattern corresponds to the one produced by an electrostatic dipole in two dimensions.

two-dimensional embedding and the lattice spacing is denoted as h. We introduce continuous functions ψ and b such that $\psi(x, y)$ is the potential of the node at (x, y) and $b(x + h/2, y)$ is the weight of the link connecting the two nodes at (x, y) and $(x + h, y)$. The left-hand side of the Poisson equation (18) evaluated at position (x, y) reads

$$\begin{aligned}(\boldsymbol{B}\psi)(x, y) &= b(x + h/2, y)[\psi(x, y) - \psi(x + h, y)] + b(x - h/2, y)[\psi(x, y) - \psi(x - h, y)] \\ &\quad + b(x, y + h/2)[\psi(x, y) - \psi(x, y + h)] + b(x, y - h/2)[\psi(x, y) - \psi(x, y - h)] \\ &= -h^2\nabla\cdot(b(x, y)\nabla\psi) + \mathcal{O}(h^3). \end{aligned} \tag{20}$$

Here, we made use of the fact that the components of the gradient $\nabla\psi = (\partial_x\psi, \partial_y\psi)^\top$ may be expressed as

$$\frac{\partial\psi(x, y)}{\partial x} = \lim_{h\to 0}\frac{\psi(x + h, y) - \psi(x, y)}{h},$$

but did not take the limit yet. The derivative with respect to y may be calculated analogously.

Before we proceed to the right-hand side, we remark that the flow changes $\Delta \boldsymbol{F}$ according to equation (14) are given by

$$\begin{aligned}\Delta F_{mn} \equiv \quad & h\Delta \boldsymbol{F}_x(x + h/2, y) = b(x + h/2, y)(\psi(x + h, y) - \psi(x, y)), \\ & h\Delta \boldsymbol{F}_y(x, y + h/2) = b(x, y + h/2)(\psi(x, y + h) - \psi(x, y)),\end{aligned}$$

where (m, n) denotes the link where the flow changes are monitored which is either oriented parallel to the x-axis, thus considering $\Delta \boldsymbol{F}_x$ or the y-axis, thus considering $\Delta \boldsymbol{F}_y$. If we divide by h and take the continuum limit $h \to 0$ the overall continuous flow changes read thus

$$\Delta \boldsymbol{F}(x, y) = b(x, y)\nabla\psi(x, y). \tag{21}$$

Note that the expression $\Delta \boldsymbol{F}$ refers to the change in flow due to the link failure here and should not be confused with the continuous Laplace operator.

The right-hand side of the discrete Poisson equation (18) may be calculated similarly noting that only two nodes contribute with opposite signs. Let us assume that the failing link is parallel to the x-axis connecting nodes r and s located at $\boldsymbol{r}_r = (x_r, y_r)^\top$ and $\boldsymbol{r}_s = (x_s, y_s)^\top = (x_r + h, y_r)^\top$. The discrete version of the right-hand side reads

$$\boldsymbol{q} = \frac{F_{rs}}{1 - b_{rs}\boldsymbol{\nu}_{rs}^\top \boldsymbol{B}^\dagger \boldsymbol{\nu}_{rs}}\boldsymbol{\nu}_{rs}.$$

We will now derive the continuum version of this equation. First, the flow on the failing link before the outage F_{rs} may be calculated as

$$\begin{aligned}F_{rs} &\equiv b(x_r + h/2, y_r)(\theta(x_r + h, y_r) - \theta(x_r, y_r)) \\ &= hb(x_r, y_r)\frac{\partial\theta}{\partial x} + \mathcal{O}(h^2) \\ &= h\boldsymbol{F}_x(x_r, y_r) + \mathcal{O}(h^2),\end{aligned}$$

where $\boldsymbol{F}(x, y) = b(x, y)\boldsymbol{\nabla}\theta(x, y)$ is the continuum flow before the outage. Second, the vector $\boldsymbol{\nu}_{rs}$ can be formally interpreted in terms of the two-dimensional delta function $\delta(x, y)$ and reads for the given link failure

$$\begin{aligned}\boldsymbol{\nu}_{rs} &\equiv \delta(x - x_r + h, y - y_r) - \delta(x - x_r, y - y_r)\\ &= h\frac{\partial\delta(x - x_r, y - y_r)}{\partial x} + \mathcal{O}(h^2).\end{aligned}$$

Finally, let us assume that a continuum version of the Green's function $\boldsymbol{B}^\dagger$ exists. Then the denominator may be calculated as

$$\begin{aligned}b_{rs}\boldsymbol{\nu}_{rs}^\top\boldsymbol{B}^\dagger\boldsymbol{\nu}_{rs} &\equiv h^2 b(x_r + h/2, y_r)\left(\int \partial_y\delta(x - x_r, y - y_r) b^\dagger(x, y)\partial_x\delta(x - x_r, y - y_r)\mathrm{d}x\,\mathrm{d}y\right)\\ &= h^2 b(x_r, y_r)\frac{\partial^2 b^\dagger(x_r, y_r)}{\partial x\partial y} + \mathcal{O}(h^3),\end{aligned}$$

where $b^\dagger(x, y)$ is the aforementioned continuum version.

Thus, in total we obtain after expanding the entire right-hand side to lowest order in the continuum limit

$$q(x, y) = h^2\boldsymbol{F}(x_r, y_r)^\top\boldsymbol{\nabla}\delta(x - x_r, y - y_r) + \mathcal{O}(h^3). \tag{22}$$

Here, $\boldsymbol{F}(x_r, y_r)$ is assumed to be parallel to the dipole axis, i.e. the direction of the link failure, which is either the x- or the y-direction for the given setting.

We can now formally divide left-hand side (20) and right-hand side (22) by h^2 and take the limit $h \to 0$ to obtain the final continuum limit of the Poisson equation,

$$\nabla\cdot(b(x, y)\nabla\psi) = -\boldsymbol{q}^\top\nabla\delta(x - x_r, y - y_r), \tag{23}$$

where the source term is $\boldsymbol{q}(x_r, y_r) = \boldsymbol{F}(x_r, y_r)$, the unperturbed current field. We note that we obtain the same continuum limit regardless of whether we use equation (17) or (18) to do the expansions. Thus, the non-locality that is encoded in equation (18) is lost in the continuum formulation.

If the link weights are homogeneous, $b(x, y) = b$, and the failing link is assumed to be located at the origin $(x_r, y_r) = (0, 0)$ the solution is given by the well-known two-dimensional dipole field

$$\psi(\boldsymbol{r}) = \frac{\boldsymbol{q}\cdot\boldsymbol{r}}{||\boldsymbol{r}||^2}, \tag{24}$$

$$\Delta\boldsymbol{F}(\boldsymbol{r}) = b\cdot\left(\frac{\boldsymbol{q}}{||\boldsymbol{r}||^2} - 2\boldsymbol{r}\frac{\boldsymbol{q}\cdot\boldsymbol{r}}{||\boldsymbol{r}||^4}\right). \tag{25}$$

We thus obtain a fully analytic solution in the continuum limit. This solution reveals that the impact of link failures decays algebraically in homogeneous lattices. We consider this decay along two different axes. Assume the dipole to be located at the origin in x-direction, such that $\boldsymbol{q} = (\varepsilon, 0)^\top$ where $\varepsilon \ll 1$ is some small real number. First, consider the decay in x-direction where $\boldsymbol{r} = (x, 0)^\top$. In this case, we obtain for the decay of the potential and the flow changes

$$\begin{aligned}\psi((x, 0)^\top) &= \frac{\varepsilon\cdot x}{x^2} \propto \frac{1}{x},\\ \Delta\boldsymbol{F}((x, 0)^\top) &= b\left(\frac{\varepsilon}{x^2} - 2x\frac{\varepsilon x}{x^4}, 0\right)^\top = -b\left(\frac{\varepsilon}{x^2}, 0\right)^\top.\end{aligned}$$

This decay in the flow changes may also be observed in the discrete version of equation (22) and is shown in figure 2(a), for a line failure in a discrete square grid. Along the same lines, we may quantify the decay in y-direction where $\boldsymbol{r} = (\varepsilon, y)^\top$ for the same dipole orientation. In this case, we obtain

$$\begin{aligned}\psi((\varepsilon, y)^\top) &= \frac{\varepsilon^2}{y^2} \propto \frac{1}{y^2}\\ \Delta\boldsymbol{F}((\varepsilon, y)^\top) &\approx b\left(\frac{\varepsilon}{y^2}, -2\frac{\varepsilon^2}{|y|^3}\right)^\top.\end{aligned}$$

Here, we assumed the position vector to be dominated by its y-component, $\varepsilon \ll y$ such that $||\boldsymbol{r}|| \approx |y|$. In total, we observe a y^{-3}-scaling in the flow changes in y-direction perpendicular to the dipole source and a y^{-2}-scaling in y-direction parallel to the dipole source, see figures 2(a)–(c).

5. Rigorous bounds on the dipole strength

We now turn to realistic networks with irregular topologies. The change in the nodal potentials or voltage phase angles ψ_n and flows $\Delta F_{m\to n}$ is determined by the discrete Poisson equation (18). We first consider the right-hand side of this equation, the dipole strength, which describes the gross response of the network flows to the outage. This response is proportional to the initial flow of the failing edge F_{rs} and the factor

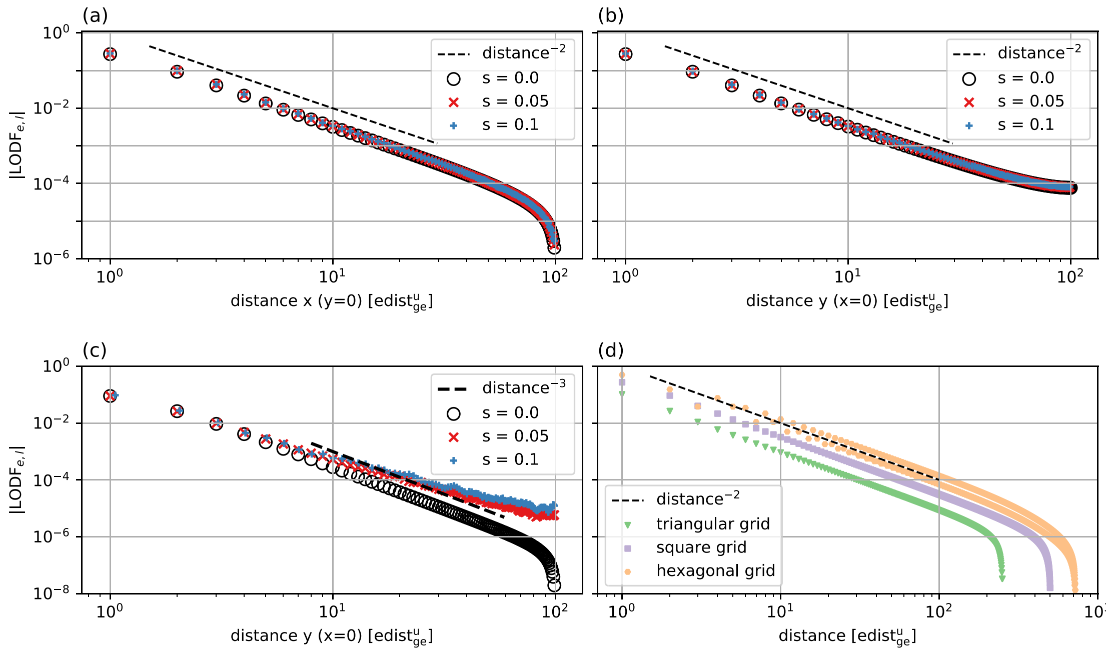

Figure 2. Scaling of LODFs versus geodesic distance to failing edge for different unweighted topologies and different levels of sparsity. (a)–(c) LODFs are evaluated in different directions from the link failure and averaged over 100 realizations of square lattices from which a fraction of $s = 0$ (black circles), $s = 0.05$ (red crosses) and $s = 0.1$ (blue plusses) links was removed randomly. The failing edge is assumed to be located in x-direction at the center of a square grid of size 201×202, see figure 1. LODFs are calculated for (a) links along the x-direction (between $(x, 0)$ and $(x + 1, 0)$), (b) links along the y-direction parallel to failing link (between $(0, y)$ and $(1, y)$) and (c) links along the y-direction perpendicular to the failing link (between $(0, y)$ and $(0, y + 1)$). The dist^{-2} (a), (b) and dist^{-3} (c) scaling agrees with the dipole scaling predicted using equation (25) as indicated by black lines. The levels of sparsity considered here do not show any effect on the scaling when considering directions parallel to the dipole axis (a), (b), but the scaling becomes more long-ranged with increasing sparsity in direction perpendicular to this axis (c). (d) The dist^{-2} scaling is not unique to square grids (purple squares, size 1000×1000) but may also be observed for the two other regular tilings, namely the hexagonal grid (orange hexagons, 150×150 hexagons) and the triangular grid (green triangles, size 1001×500). LODFs were again computed along the shortest path in x-direction for links oriented parallel to the dipole. The branching for the hexagonal grid is due to the fact that the path in x-direction is non-unique and non-straight here, such that one of the shortest paths was chosen arbitrarily. Deviations from the scaling occur for large distances due to finite-size effects.

$$(1 - b_{rs}\boldsymbol{\nu}_{rs}^{\top}\boldsymbol{B}^{\dagger}\boldsymbol{\nu}_{rs})^{-1} =: (1 - \eta(r, s))^{-1}. \tag{26}$$

The factor $1 - \eta(r, s)$ describes the non-locality of the network response to a local perturbation at link (r, s). To see this, consider a grid where the real power ΔP is injected and withdrawn at the terminal nodes of the link (r, s). The direct flow over the link is given by

$$F_{r\to s} = b_{rs}\boldsymbol{\nu}_{rs}^{\top}\boldsymbol{B}^{\dagger}\boldsymbol{\nu}_{rs}\,\Delta P = \eta(r, s)\Delta P, \tag{27}$$

whereas the total flow is just given by ΔP. The factor $\eta(r, s)$ thus measures the fraction of the flow which is transmitted directly and $1 - \eta(r, s)$ is the fraction transmitted non-locally via other pathways. Hence, $1 - \eta(r, s)$ can also be seen as a measure of redundancy. A high non-local flow indicates that there are strong alternative routes from r to s in addition to the direct link (r, s). If no alternative path exists, the flow must be routed completely via the direct link such that $1 - \eta(r, s) = 0$.

We conclude that the properties of alternative and direct paths are decisive for the understanding of flow rerouting. Before we proceed, we thus review the formal definition of a path in graph theory.

Definition 1. A path from vertex r to vertex s is defined as an ordered set of vertices

$$(v_0 = r, v_1, v_2, \ldots, v_k = s), \tag{28}$$

where two subsequent vertices must be connected by an edge and no vertex is visited twice. Two paths are called independent if they share no common edge. The unweighted length of such a path is defined as the number of steps k, while the weighted path length is given by the sum of the edge weights along the path, $\sum_{j=1}^{k} w_{v_{j-1}v_j}$. In this work, the edge weights are given by the inverse susceptances $w_{ij} = 1/b_{ij}$. The (weighted or unweighted) geodesic or shortest path distance of two vertices r and s is defined as the (weighted or unweighted) length of the shortest path from r to s.

The interpretation as a redundancy measure directly relates the factor $1 - \eta(r, s)$ to the topology of the network. A first rough estimate can be obtained from the topological connectivity $\lambda_T(r, s)$, which is defined as

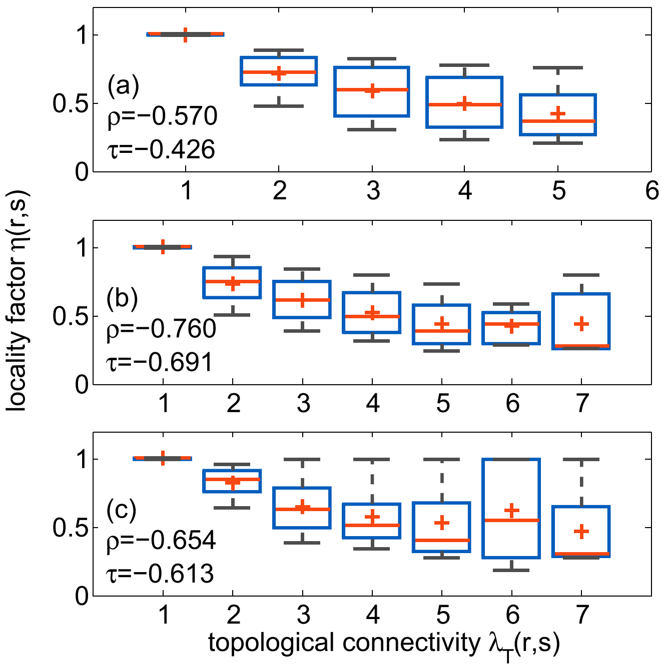

Figure 3. The locality factor $\eta(r, s)$ generally decreases with the topological connectivity $\lambda_T(r, s)$. Values of $\eta(r, s)$ for all links (r, s) with given value of $\lambda_T(r, s)$ are shown in a box-whisker-plot: the cross gives the mean, the read line the median, the box the 25%/75% quantiles and the and the grey horizontal line the 9%/91% quantiles. Results are shown for three standard test grids: (a) 'case118', (b) 'case1354pegase', (c) 'case2383wp'[49]. The values of Pearson's correlation coefficient ρ and Kendall's rank correlation coefficient τ are given for each test grid.

the number of independent paths from node r to node s. A comparison for several test grids in figure 3 shows that $\eta(r, s)$ decreases with $\lambda_T(r, s)$ on average as expected, but that there is a large heterogeneity between the links.

To obtain a better topological estimate for the locality factor we need to take into account the heterogeneity of the link weights. The topological connectivity $\lambda_T(r, s)$ counts the minimum number of edges which have to be removed to disconnect the nodes r and s. We can define a weighted analog $\lambda_F(r, s)$ as the *minimum capacity* which has to be removed to disconnect the nodes r and s. This is a classical problem in graph theory, where it is referred to as the *minimum cut* [50]. We will now elaborate this quantity in a definition. An (r, s)-*cut* can be defined as follows. Let $r \in S \subset V$ and $s \in V\backslash S$ be two vertices taken from the two disjoint sets. The (r, s)-cut is defined as the set of edges $\delta(S) = \{(u, v) \in E \mid u \in S, v \in V\backslash S \text{ or } v \in S, u \in V\backslash S\}$ connecting the two disjoint vertex-sets. The set of edges $\delta^+(S) = \{(u, v) \in E \mid u \in S, v \in V\backslash S\}$ is referred to as the *forward edges* of the cut. The capacity C of a cut $\delta(S)$ and the corresponding minimum capacity $\lambda_F(r, s)$ between r and s are then given by

$$\begin{aligned} C(\delta(S)) &= \sum_{(i,j)\in\delta^+(S)} b_{ij}, \\ \lambda_F(r, s) &= \min_{\{S\subset V \mid r\in S, s\in V\backslash S\}} C(\delta(S)). \end{aligned}$$

By virtue of the max-flow-min-cut theorem [51], $\lambda_F(r, s)$ is equivalent to the maximum flow which can be transmitted from r to s respecting link capacity limits:

$$\begin{aligned} &\lambda_F(r, s) = \max_{\boldsymbol{F}} \sum_{n=1}^{N} F_{r\to n} \\ &\text{such that } |F_{mn}| \leqslant b_{mn} \ \forall \text{ edges } (m, n) \\ &\text{and } \sum_{n=1}^{N} F_{mn} = 0 \ \forall \ m \neq r, s. \end{aligned} \tag{29}$$

Numerous efficient algorithms exist to calculate this maximum flow without performing the optimization explicitly [51]. The ratio $b_{rs}/\lambda_F(r, s)$ then gives the ratio of direct flow to total flow from r to s and thus provides an adequate topology-based estimate for the locality factor $\eta(r, s)$. Indeed, we can prove that it provides a rigorous lower bound.

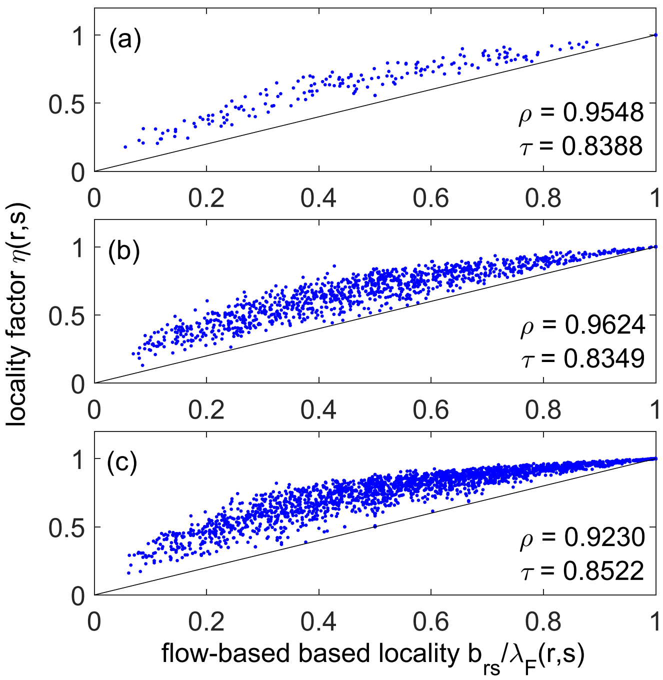

Figure 4. The locality factor $\eta(r, s)$ is estimated by the topology based measure $b_{rs}/\lambda_F(r, s)$ with high quality. Results are shown for three standard test grids: (a) 'case118', (b) 'case1354pegase', (c) 'case2383wp'[49]. The values of Pearson's correlation coefficient ρ and Kendall's rank correlation coefficient τ are given for each test grid. The black line is the lower bound given by proposition 1.

Proposition 1. *The algebraic locality factor* $\eta(r, s)$ *is bounded by*

$$\frac{b_{rs}}{\lambda_F(r, s)} \leqslant \eta(r, s) \leqslant 1. \tag{30}$$

A proof is given in appendix A. Numerical simulations for several test grids reported in figure 4 reveal that the topological estimate not only provides a lower bound, but a high-quality estimate for the algebraic locality factor. The Pearson correlation coefficient ρ between $\eta(r, s)$ and $b_{rs}/\lambda_F(r, s)$ exceeds 0.92 for the three grids under consideration.

We arrive at the conclusion that the dipole strength given by $F_{rs}(1 - \eta(r, s))^{-1}$ generally decreases with the redundancy measures $\lambda_T(r, s)$ and $\lambda_F(r, s)$.

An upper limit for the locality factor $\eta(r, s)$ can be obtained from an elementary topological distance measure. We consider the weighted geodesic distance of the two nodes r and s after the failure of the direct link (r, s), which we denote by $\mathrm{dist}_1^{\mathrm{w}}(r, s)$. The superscript w stands for weighted distance, the subscript 1 for the distance measured in the graph after removal of the link (r, s). We then have the following upper bound.

Proposition 2. *The algebraic locality factor* $\eta(r, s)$ *is bounded from above by*

$$\eta(r, s) \leqslant \left[1 + \frac{1}{b_{rs} \times \mathrm{dist}_1^{\mathrm{w}}(r, s)}\right]^{-1}. \tag{31}$$

A proof is given in appendix B. Numerical simulations for several test grids reported in figure 5 reveal that the estimate in terms of the shortest path length not only provides an upper bound, but a high quality estimate for the algebraic locality factor. The Pearson correlation coefficient ρ exceeds 0.94 for the three grids under consideration.

We further note that the factor $\boldsymbol{\nu}_{rs}^\top \boldsymbol{B}^\dagger \boldsymbol{\nu}_{rs}$ can also be interpreted as a distance measure—the resistance distance [52, 53]. We come back to the quantification of distances in flow networks later in section 6.3.

6. Spatial distribution of flow rerouting

We now turn to the spatial aspects of flow rerouting in general network topologies. We first discuss some rigorous results, showing how the network topology determines the rerouting flows. Then, we return to the

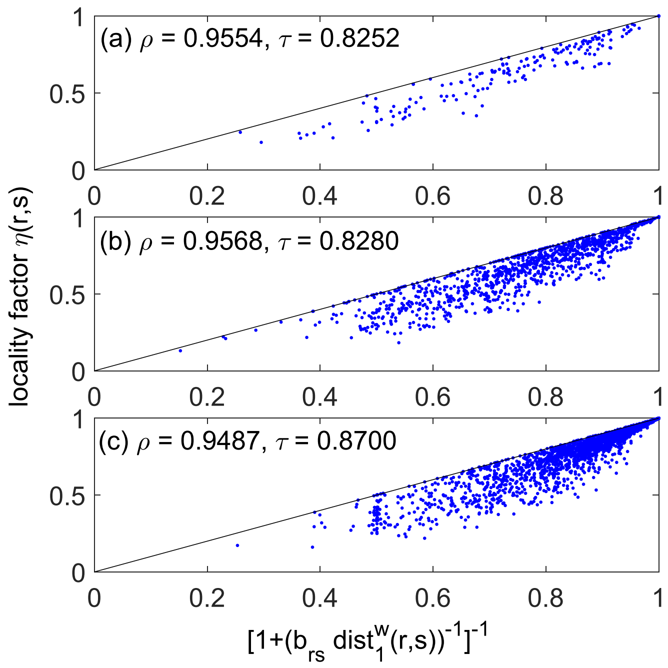

Figure 5. An upper bound for the locality factor $\eta(r, s)$ is found in terms of the length of the shortest alternative path from r to s, assigning to each link (m, n) a weight b_{mn}^{-1}. The black line is the lower bound given by proposition 2 and the blue dots give results for all links in three standard test grids: (a) 'case118', (b) 'case1354pegase', (c) 'case2383wp'[49]. High values of Pearson's correlation coefficient ρ and Kendall's rank correlation coefficient τ show that the expression in proposition 2 provides a good estimate for the locality factor $\eta(r, s)$, not only a lower bound.

regular tilings and study the effect of increasing sparsity in these topologies on the dipole scaling. Finally, we suggest a new measure of distance for flow rerouting and examine its performance on realistic network topologies taken from power grids.

6.1. Rigorous results

To start off, we first present a lemma due to Shapiro [54], relating the flow changes after a link failure in an unweighted graph solely to the topology of the underlying network.

Lemma 1. *Consider an unweighted network with a unit dipole source along the edge (r, s), i.e. a unit inflow at node* r *and unit outflow at node* s. *Then the flow along any other edge (m, n) is given by*

$$F_{m\to n} = \frac{\mathcal{N}(r, m \to n, s) - \mathcal{N}(r, n \to m, s)}{\mathcal{N}},$$

where $\mathcal{N}(r, m \to n, s)$ is the number of spanning trees that contain a path from r *to* s *of the form $r, \ldots, m, n, \ldots, s$ and $\mathcal{N}$ is the total number of spanning trees of the graph.*

This lemma exactly gives the LODFs in terms of purely topological properties—the number of spanning trees containing certain paths. A generalization of this theorem to weighted graphs was recently presented in [55].

However, counting spanning trees is typically a difficult task such that these results are of limited use for practical applications. Nevertheless, they reveal the importance of certain paths through networks which we will analyze numerically in more detail below. Before we turn to this issue, we derive some weaker, but more easily applicable rigorous results.

We expect that the flow changes ΔF_{mn} decay with distance as for the case of the square lattice analyzed in section 4. Can we establish some rigorous results on the decay with distance for arbitrary networks? Consider the outage of a single edge and assume that the network remains connected afterwards. We label the failing link as (r, s) such that $F_{r\to s} > 0$ w.l.o.g. We first consider the change of the nodal potential or voltage phase angle ψ_n and its decay with distance to the failing link (r, s). More specifically, we define the maximum and minimum values of ψ_n attained at a given distance:

$$u_d = \max_{n, \mathrm{dist}_0^u(n,r)=d} \psi_n$$
$$\ell_d = \min_{n, \mathrm{dist}_0^u(n,s)=d} \psi_n.$$

Here, $\mathrm{dist}_0^u(n, r)$ denotes the geodesic distance between two nodes n and r in the initial unweighted graph (indicated by the superscript u for unweighted and subscript 0 for the initial pre-contingency network). We then find the following result.

Proposition 3. *Consider the failure of a single link (r, s) with $F_{r\to s} > 0$ in a flow network. Then the maximum (minimum) value of the potential change ψ_n decreases (increases) monotonically with the distance to nodes* r *and* s*, respectively:*

$$u_d \leqslant u_{d-1}, \quad 1 \leqslant d \leqslant d_{\max}.$$
$$\ell_d \geqslant \ell_{d-1}, \quad 1 \leqslant d \leqslant d_{\max}.$$

A proof is given in appendix C. We thus find that potential changes generally decrease with the distance in magnitude and so do the flow changes.Furthermore, we can exploit the analogy to electrostatics to gain an insight into the scaling of flow changes with distance. As the flows are determined by a discrete Poisson equation, a discrete version of Gauss' theorem follows immediately. We note that we formulate this result in terms of the original network topology, see equation (18).

Lemma 2. *Consider the failure of a single link (r, s) in a flow network and denote by* V *the set of vertices in the network. For every decomposition of the network $V = V_1 + V_2$ with $r \in V_1$ and $s \in V_2$ we have*

$$\sum_{m\in V_1, n\in V_2} \Delta F_{m\to n} = F_{rs}\,(1 - \eta(r, s))^{-1}\,. \tag{32}$$

That is, for each decomposition the total flow between the two parts V_1 *and* V_2 *equals the dipole strength.*

This lemma supports the intuitive expectation that on average flow changes decay with distance in meshed networks: choose V_1 to include all nodes which are closer to r than to s and have a distance to r smaller than a given value

$$V_1 = \{n \in V | \mathrm{dist}_0^u(r, n) \leqslant d;\ \mathrm{dist}_0^u(r, n) \leqslant \mathrm{dist}_0^u(s, n)\}.$$

With increasing value of d the number of nodes in V_1 increases and typically the number of edges between V_1 and V_2 increases, too. The total flow over these links remains constant according to lemma 2, such that the average flow will generally decrease. The exact scaling of the number of edges between V_1 and V_2 of course depends on the topology of the network.

One can furthermore show that a sufficient connectivity is needed for perturbations to spread. Generally, flow can be rerouted via an edge (m, n) only if it can enter and leave the link via two independent paths. One can thus prove the following statement [55, 56].

Proposition 4. *The line outage distribution factor $\mathrm{LODF}_{e,\ell}$ between two edges $e = (m, n)$ and $\ell = (r, s)$ vanishes if there are less than two independent paths between the vertex sets $\{r, s\}$ and $\{m, n\}$.*

6.2. Impact of network topology

Now that we derived rigorous results on the scaling of LODFs, we want to study the influence of network connectivity on the scaling in more detail.

To do so, we first compare the scaling obtained for the square grid to the one in the other two regular tilings of two-dimensional space, namely the hexagonal grid and the triangular grid. In perfect realizations of these grids, each node has a degree of $\mathrm{deg}_{\mathrm{hex}} = 3$ and $\mathrm{deg}_{\mathrm{tri}} = 6$, respectively, whereas the degree for the square grid reads $\mathrm{deg}_{\mathrm{sg}} = 4$. In figure 2(d), the LODFs are evaluated for these three topologies with increasing geodesic distance from the failing edge located again in the center of the networks between the nodes at $(x_r, y_r) = (0, 0)$ and $(x_s, y_s) = (1, 0)$. The quadratic scaling with the geodesic distance in x-direction $||x||^{-2}$ (black, dotted line) is preserved for all three topologies, i.e. the triangular grid (green triangles, bottom), the square grid (red squares, center) and the hexagonal grid (blue hexagons, top). The grids used here were of size 1000×1000 and 1001×500 nodes for the square grid and the triangular grid, respectively, and 150×150 hexagons for the hexagonal grid.

Thus, the quadratic scaling is robust throughout different regular networks. However, real networks are in general not regular. For this reason, we proceed by studying the effect of increasing sparsity in these regular tilings. Define the sparsity $\xi \in [0, 1] \subset \mathbb{R}$ as the *fraction of edges removed from the original graph*. We make use

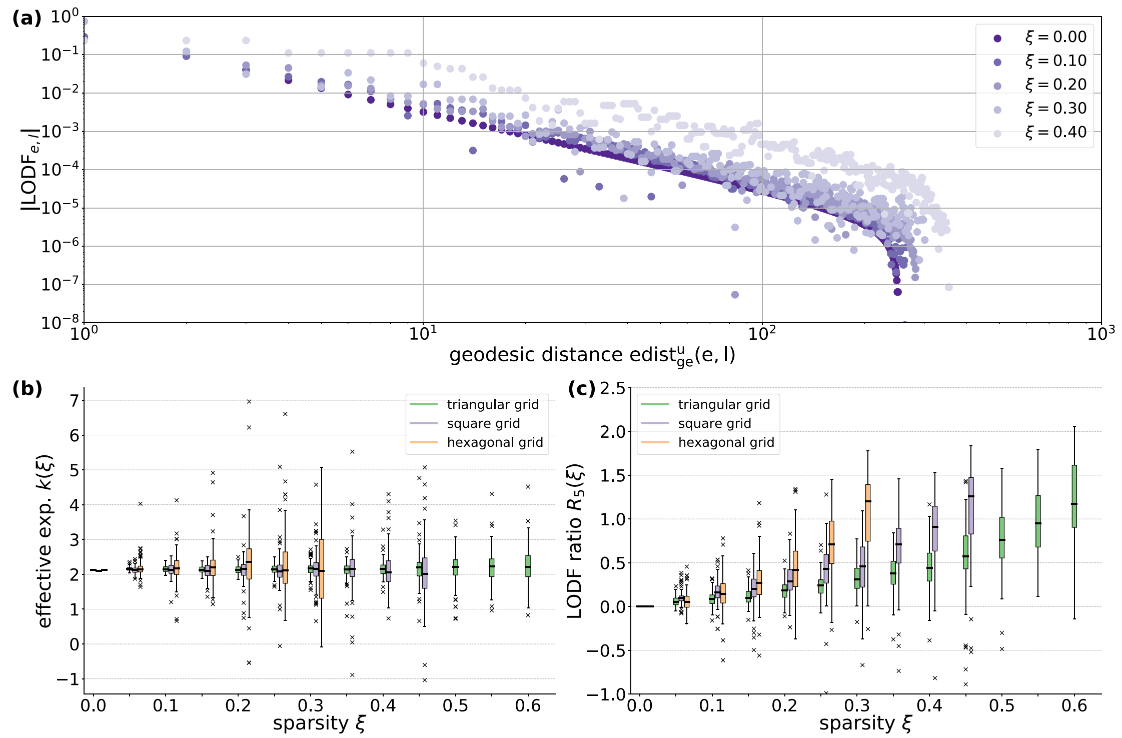

Figure 6. Increasing sparsity leads to more long-ranged effects of link failures in regular grids. (a) Exemplary scaling of LODFs in a square grid of size 500 $\times$ 500 with increasing sparsity (colors from dark to light purple), now achieved through the removal of edges not contained in an arbitrary spanning tree. (b) Whereas the effective exponent shows no change and thus still obeys approximately the inverse-square law for all topologies, (c) the logarithmic ratio between LODFs with and without sparsity at a certain distance increases on average with increasing sparsitiy. Boxplots are shown for 100 realizations of the hexagonal grid (left, orange), square grid (purple, center) and triangular grid (green, left) choosing a random spanning tree as the basis for edge removal for each realization and value of sparsity.

of two different methods to achieve increasing sparsity. Our first method is a completely random removal of edges in the graph followed by measuring the LODFs along a specified path. If an edge along the path does no longer exist, we simply skip the edge. The results obtained from this method are shown in figures 2(a)–(c). There is no change visible in the scaling of LODFs, except for the direction perpendicular to the dipole in panel (c). In particular, only small values of sparsity ξ can be studied using this method, since a random removal of edges may easily result in disconnected graphs. For this reason, we make use of another method.

For the second method, we first construct an arbitrary spanning tree of the network after removal of the failing edge. Then, we subsequently remove random edges from the graph that are not part of the tree until a fraction ξ of its original edges is removed from the graph. This way, we make sure that the whole graph stays connected at all times. We continue by constructing the shortest path from the failing edge $((0,\ 0),\ (1,\ 0))$ to the node located at $(x_{\max},\ 0)$ and quantify the LODFs along this path. Note that using this method to make a graph sparser, we need to take into account the graph-specific maximal sparsity $\xi_{\max,G}$, i.e. the fraction of edges whose removal would disconnect the graph. Assuming the initial tree to be minimal, this fraction may be calculated as $\xi_{\max,\mathrm{hex}} = 1/3$, $\xi_{\max,\mathrm{sg}} = 1/2$ and $\xi_{\max,\mathrm{tri}} = 2/3$ for the hexagonal grid, square grid and triangular grid, respectively.

Using this procedure, we can quantify the scaling of LODFs in grids with increasing sparsity. The direct assessment of a scaling exponent is difficult for sparser graphs due to the large spread in LODF values, see figure 6(a). This is why we construct a different measure to quantify this scaling. We consider the *effective exponent* $k(\xi)$, where ξ is the graph's sparsity, and assume a scaling of the form

$$|\mathrm{LODF}(r,\ \xi)| \propto r^{-k(\xi)}$$

in some region of the geodesic distance $r = \|\boldsymbol{r}\|$ from the link failure. This effective exponent is calculated as follows

$$k(\xi) = -\log_5\left(\frac{\sum_{r\in[5\times 10^1 - w, 5\times 10^1 + w]}|\mathrm{LODF}(r,\ \xi)|}{\sum_{r\in[10^1 - w, 10^1 + w]}|\mathrm{LODF}(r,\ \xi)|}\right),$$

where $w \in \mathbb{N}$ is a window specifying the range to average over in order to smooth the LODF values considered. We chose a window size of $w = 2$ when calculating the effective exponent in practice which we found to result in a good compromise between smoothing and completely removing the trend. However, we did not observe a strong effect of the window size on the results. In addition to that, we chose to compare the LODFs at values centered around $r = 10^1$ and $r = 5 \times 10^1$ when calculating the effective exponent since using this range allows us to capture only the intermediate range of the curve. For larger distances from the failing link, finite size effects prevent the assessment of the exponent whereas for smaller distances, the LODF does not yet decay when considering high values of sparsity due to a lack of alternative paths, as may also be observed in figure 6(a). For a perfect inverse square law $|\mathrm{LODF}| \propto \|\boldsymbol{r}\|^{-2}$ and a vanishing window $w = 0$, this parameter yields $k = -\log_5(5^{-2}) = 2$ as required. In figure 6(b), it can be observed that this effective exponent stays approximately constant at $k \approx 2$ over different values of sparsity and the three different topologies considered, where results for each value of sparsity were obtained using 100 random realizations of edge removals and with the same grid sizes as stated previously.

To further quantify the effect of increasing sparsity in regular networks, we make use of another measure which we refer to as the LODF *ratio* $R_w(\xi)$. It is simply calculated as the logarithmic ratio between the LODFs with and without sparsity, again averaged over a fixed window of distances

$$R_w(\xi) = \log_{10}\left(\frac{\sum_{r\in[10^1-w,10^1+w]}|\mathrm{LODF}(r,\ \xi)|}{\sum_{r\in[10^1-w,10^1+w]}|\mathrm{LODF}(r,\ \xi=0)|}\right).$$

Note that we evaluate this parameter at a distance of 10^1 but we found the parameter to yield similar values for all distances considered. A parameter of $R_w(\xi) = 1$ then represents a tenfold increase in the LODFs as compared to the network without any edges removed. In figure 6(c), this parameter is shown for the different topologies and sparsities. Here, a window size of $w = 5$ was used. An increase with increasing sparsity is clearly visible. In particular, the LODFs increase on average more than tenfold close to the highest possible values of sparsity.

In total, we observe that the scaling exponent derived from the dipole analogy in section 5 holds for the regular networks even when removing a large fraction of their edges. On the other hand, the LODF values at a certain distance from the failing link show an increase with increasing sparsity, such that the actual effect of a link failure can be up to tenfold stronger than for the corresponding regular grid with no links removed. Thus, the overall effect of a link failure is more long-ranged in a sparser network, although no change in the effective exponent can be observed.

6.3. Scaling with distance

The impact of a link failure generally decays with distance. While the definition of distance is straightforward in regular lattices, different measures are meaningful in networks with complex topologies. The geodesic distance of two links follows from definition 1 for two vertices

$$\mathrm{edist}^{\mathrm{w}}_{\mathrm{ge}}[(r,\ s),\ (m,\ n)] = \min_{v_1\in\{r,s\},v_2\in\{m,n\}} \mathrm{dist}^{\mathrm{w}}_0(v_1,\ v_2) + \frac{w_{rs} + w_{mn}}{2}.$$

Here, $w_{rs} = 1/b_{rs}$ is the edge weight assigned to the edge $(r,\ s)$. When considering the unweighted analog, the edge distance is defined analogously setting all edge weights to one. The additional term $\frac{w_{rs}+w_{mn}}{2}$ ensures that neighboring edges have non-zero distance, e.g. unity distance $\mathrm{edist}^{\mathrm{u}}_{\mathrm{ge}} = 1$ in the unweighted case. However, this distance is a bad indicator for flow rerouting in real-world irregular topologies. An example shown in figure 8 demonstrates that this simple distance is only weakly correlated with the magnitude of the LODFs for a real-world power grid test case.

Instead, we need a distance measure based on flow rerouting. If a link $(r,\ s)$ fails, the flow must be rerouted through other pathways, as described by the electrical lemma 1. However, it is not feasible to take into account all spanning trees which govern the flow rerouting. In order to still be able to estimate the impact on another link $(m,\ n)$, we will thus consider a path from r to s that crosses this link. The main difference to the ordinary graph theoretical distance is that we have to take into account a path *back and forth*. We are thus led to the following definition.

Definition 2. A rerouting path from vertex r to vertex s via the edge $(m,\ n)$ is a path

$$(v_0 = r,\ v_1,\ldots,v_i = m,\ v_{i+1} = n,\ v_{i+2},\ldots,v_k = s) \tag{33}$$

or

$$(v_0 = r,\ v_1,\ldots,v_i = n,\ v_{i+1} = m,\ v_{i+2},\ldots,v_k = s), \tag{34}$$

where no vertex is visited twice. The rerouting distance between two edges $(r,\ s)$ and $(m,\ n)$ denoted by $\mathrm{edist}^{\mathrm{u/w}}_{\mathrm{re}}[(r,\ s),\ (m,\ n)]$ is the length of the shortest rerouting path from r to s via $(m,\ n)$ plus the length of edge

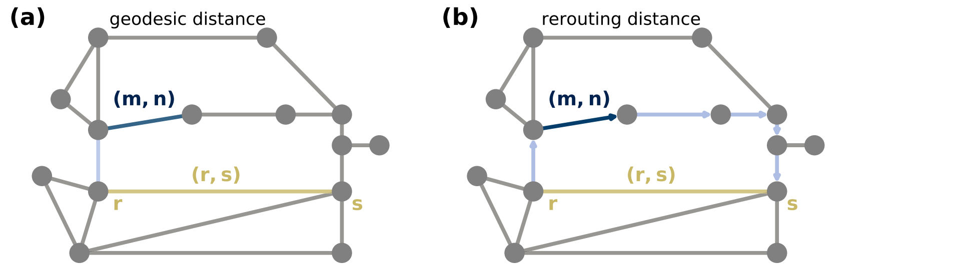

Figure 7. Illustration of two different distance measures between two links $(r,\ s)$ and $(m,\ n)$ (coloured in yellow and dark blue). (a) The common geodesic or shortest-path distance (indicated by lines coloured in light blue). (b) The rerouting distance is defined as the length of the shortest path from r to s crossing the link $(m,\ n)$ and is indicated by thick arrows and lines colored in light blue. The sample network in this figure is based on the topology of the IEEE 14-bus test grid [57].

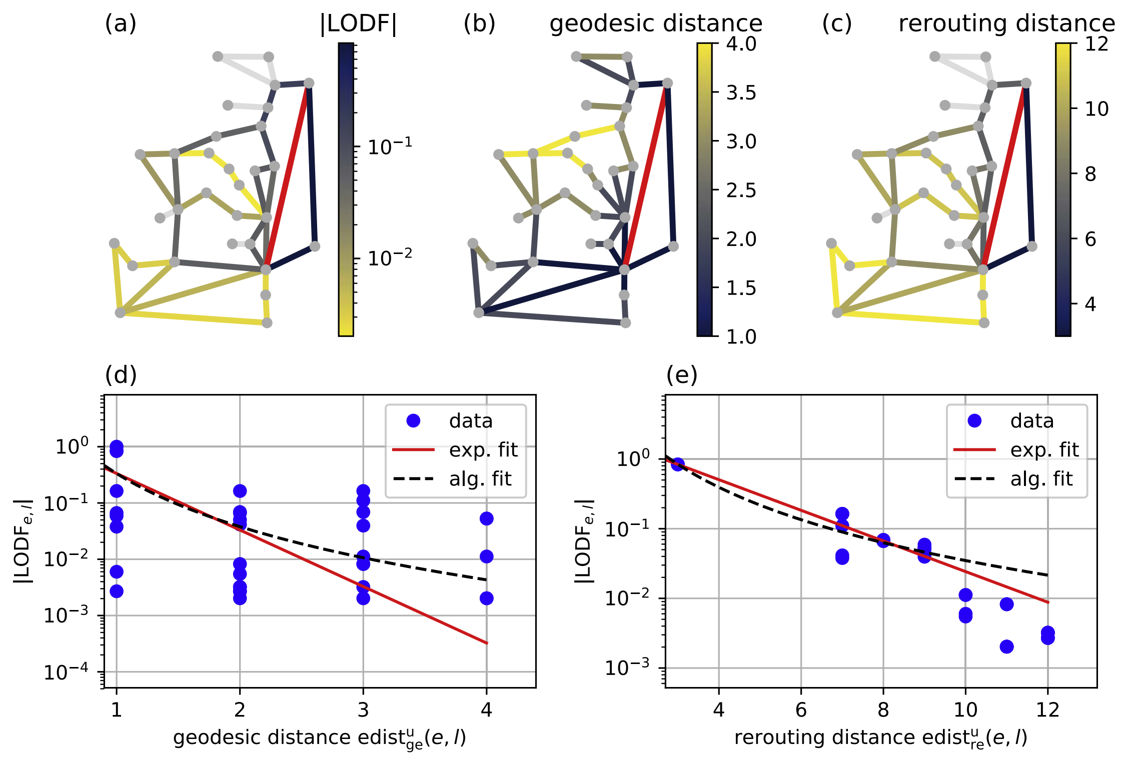

Figure 8. Line outage distribution factors (LODFs) in comparison to the unweighted geodesic and rerouting distances. (a) Magnitude of the LODFs in the IEEE 30-bus test grid 'case30' [57]. The failing link l is marked in red. (b) The geodesic distance to the failing link $\mathrm{edist}^{\mathrm{u}}_{\mathrm{ge}}$. (c) The rerouting distance to the failing link $\mathrm{edist}^{\mathrm{u}}_{\mathrm{re}}$. (d), (e) LODFs versus geodesic and rerouting distance (blue dots) including an exponential (red solid line) and an algebraic (black dashed line) least-squares fit to the data. Due to the low number of data points, a clear decision whether the correlation is algebraic or exponential is not possible.

$(r,\ s)$. Equivalently, it is the length of the shortest cycle crossing both edges $(r,\ s)$ and $(m,\ n)$. If no such path exists, the rerouting distance is defined to be ∞.

The definition of a rerouting path is illustrated in figure 7. Again, we consider a weighted and an unweighted version of this distance indicated by the superscript w and u, respectively. We note that the length of the edge $(r,\ s)$ is included in order to make the distance measure symmetric. In appendix D, we show explicitly that this definition satisfies the axioms of a metric and discuss how to compute the shortest rerouting path.

An example of rerouting distances in comparison to the LODFs is shown in figure 8 for a small test grid. We observe a much better correlation in comparison to the ordinary geodesic distance defined above. The limitation of geodesic distances becomes especially clear for situations described by proposition 4. If exactly one independent path exists between two links, the rerouting distance is ∞, while the geodesic distance is finite. Hence, the latter fails to explain why the LODF between the two links vanishes.

To further investigate the importance of distance, we simulate all possible link failures in four test grids of different size. For every failing link $(r,\ s)$ we evaluate the geodesic distance as well the rerouting distance to all

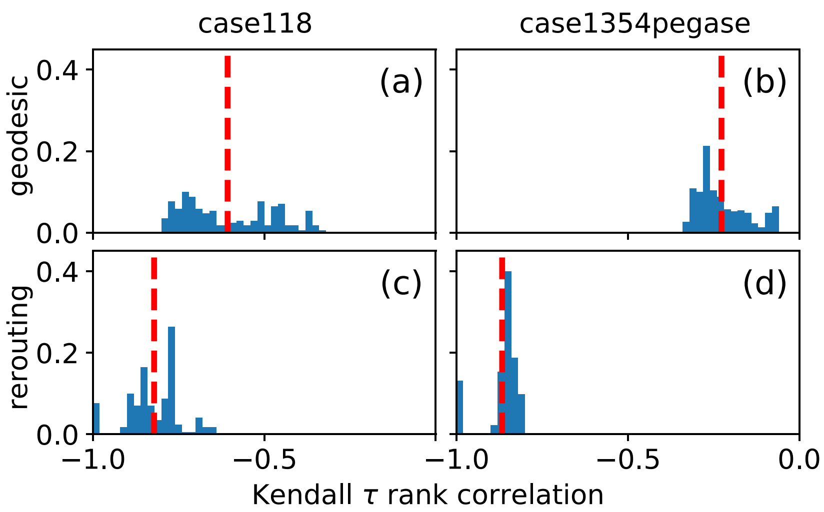

Figure 9. ((a), (b), top) Normalized histograms of the Kendall τ rank correlation for the magnitude of LODF and unweighted geodesic distance and ((c), (d), bottom) |LODF| and unweighted rerouting distance between two links in the IEEE test cases 118 (a), (c) and 1354pegase (b), (d). Vertical red lines show the average of the distribution of tau values (see table 1). The stronger correlation of the rerouting distance with the LODFs as compared to the geodesic distance is clearly visible.

Table 1. Average of the Kendall τ rank correlation values for magnitude of LODF versus different distance measures. The four different IEEE test cases consistently show a higher degree of correlation between rerouting distances and LODF than between geodesic distances and LODF in both weighted and unweighted cases, while the unweighted rerouting distance slightly outperforms the weighted one. For examplary distributions of the τ values see figure 9.

test grid	Rank correlation τ for |LODF| versus distance			
	Geodesic distance		Rerouting distance	
	unw.	weighted	unw.	weighted
case30	−0.4027	−0.4015	−0.8528	−0.8440
case118	−0.6069	−0.5233	−0.8211	−0.7920
case1354pegase	−0.2269	−0.1341	−0.8664	−0.8438
case2383wp	−0.3604	−0.2318	−0.7213	−0.6066

other links in the grid. To quantify to which extend the distance predicts the magnitude of the LODFs, we then calculate the Kendall rank correlation coefficient τ [58]. This coefficient is used on ordinal data and assumes values in the interval $[-1,\ 1]$. A value of (minus) one indicates perfect (anti)correlation, whereas a zero value implies no correlation between the data. Table 1 shows the results, averaging over all trigger links $(r,\ s)$ in the respective grid discarding bridges. The rank correlation is negative as LODFs generally decay with distance. The magnitude of the rank correlation is significantly higher for the rerouting distance. In particular for the test grid 'case1354pegase' we see that the ordinary geodesic distance has a very limited predictive power for the LODFs ($|\tau| < 0.25$), while the rerouting distance is strongly correlated to the magnitude of the LODFs ($|\tau| > 0.83$). Figure 9 illustrates this discrepancy in the distribution of τ values for the different distance measures for the test grids 'case118' and 'case1354pegase'. We are thus led to the conclusion that geodesic distances are of limited interest when considering the impact of link failures and should be replaced by other measures such as rerouting distances. Notably, we observe no major difference when comparing weighted and unweighted distances.

7. Conclusion

Link failures represent major threats to the operation of complex supply networks across disciplines. In this article, we examined the impact of such failures in terms of the induced flow changes, which are commonly described by LODFs. We provide mathematically rigorous results and extensive numerical simulations with a focus on the gross network response (i.e. the dipole strength), the scaling of flow changes with distance and the role of network topology. These quantities are crucial to understand the global robustness of supply networks as each failure can trigger a cascade of secondary failures with potentially catastrophic consequences.

First, we demonstrated rigorously that the flow changes created by a single failure in a square lattice correspond to the field of an electromagnetic dipole. Hence the effects of a failure decay with the distance following an inverse-square law. The dipole analogy developed here allows for an analytical expression describing the spreading of link failures. Although this treatment is rigorously valid only in the continuum limit, we showed that the observed scaling extends to the other regular tilings of two-dimensional space even after removing a fraction of links. Thus, we conclude that the scaling may be expected to hold also for realistic topologies.

Increasing the sparsity of a network promotes more long-ranged effects up to the point where two links are only related by one independent pathway. Then, a rerouting between the two links becomes impossible and a failure of one link does not affect the other. However, this also implies a lack of redundancy such that a link failure can have catastrophic consequences locally. Our results thus suggest that sparsity promotes non-local responses to line failures. This is of potential relevance to the understanding of cascading failures, where previous outages increase sparsity, and deserves further study.

In real-world irregular networks, the gross response of a failure depends on the loading of the link as well as the local network structure. Rigorous upper and lower bounds were given for the dipole strength relating it to the redundancy of the failing link. Furthermore, the common notion of a geodesic graph distance is of limited use to predict flow rerouting. We thus introduced a *rerouting distance* which we showed to be much more meaningful to predict the impact of failures.

Whereas the classical analysis of link failures relies heavily on simulation results, our results provide heuristic methods and rigorous bounds which allow for an analytical insight into the relationship between the structure of a network and its robustness towards link failures. In particular for large networks where simulations are difficult, our results allow for an *a priori* analysis of link failures and might also be used to identify critical links, for instance in terms of the locality factor which quantifies the response of a network to a single failure. This type of analysis is aided by the general results on decay of maximal flow changes with geodesic and rerouting distances. We expect that these results fit the better, the more heterogeneous or disordered a network is. Previous studies [59] have shown that a strong heterogeneity of link parameters leads to a concentration of flows along the shortest path. In this limit, flow rerouting should be fully dominated by the shortest rerouting path.

We expect our results to be applicable far beyond power grids since the linearized treatment extends to other phenomena such as hydraulic or biological networks. The rerouting distance along with the bounds on the locality factor may greatly simplify the study of link failures in all kinds of supply networks and makes them more accessible. We expect our results on the scaling of LODFs for networks with increasing sparsity along with this distance measure to help identifying critical parts and paths and improving the overall robustness of supply networks.

Acknowledgments

We gratefully acknowledge support from the German Federal Ministry of Education and Research (BMBF grant no. 03SF0472) and the Helmholtz Association (via the joint initiative 'Energy System 2050—a contribution of the research field energy' and the grant no. VH-NG-1025 to D.W.).

Appendix A. Proof of proposition 1

Proof. By definition, $\eta(r, s)$ is given by the flow $F_{rs}/\Delta P$ when the power ΔP is injected at node r and withdrawn at node s, while there is no injection at any other node,

$$\begin{aligned} \sum\nolimits_n F_{r\to n} &= \sum\nolimits_n F_{n\to s} = \Delta P, \\ \sum\nolimits_n F_{m\to n} &= 0 \quad \forall\ m \neq r, s, \end{aligned} \tag{A.1}$$

such that

$$\eta(r, s) = \frac{F_{r\to s}}{\sum_n F_{r\to n}}. \tag{A.2}$$

For the sake of simplicity, we choose ΔP such that $\theta_r - \theta_s = 1$ w.l.o.g. Then, the inverse of $\eta(r, s)$ may be calculated using the basic relation $F_{r\to s} = b_{rs}(\theta_r - \theta_s)$ as

$$\frac{b_{rs}}{\eta(r,\ s)} = \sum\nolimits_n F_{rn}. \tag{A.3}$$

We can now use that the potential drop over all other links in the network is smaller than for the link $(r,\ s)$

$$|\theta_m - \theta_n| \leqslant \theta_r - \theta_s, \tag{A.4}$$

see proposition 3. If $\theta_r - \theta_s = 1$ we thus know that

$$|F_{mn}| = |b_{mn}(\theta_m - \theta_n)| \leqslant b_{mn}. \tag{A.5}$$

We thus obtain

$$\frac{b_{rs}}{\eta(r,\ s)} = \sum\nolimits_n F_{rn} \tag{A.6}$$

$$\begin{aligned}
&\text{such that } \theta_r - \theta_s = 1,\\
&F_{mn} = b_{mn}(\theta_m - \theta_n),\\
&|F_{mn}| \leqslant b_{mn}\ \forall \text{ edges } (m,\ n),\\
&\sum_{n=1}^{N} F_{mn} = 0\ \forall\ m \neq r,\ s.
\end{aligned} \tag{A.7}$$

Comparing to the expression (29) for $\lambda_F(r,\ s)$ we see that two additional constraints have to be satisfied. Additional constraints can only decrease the flow-value with respect to the maximum in equation (29) such that we have

$$\frac{b_{rs}}{\eta(r,\ s)} \leqslant \lambda_F(r,\ s) \Rightarrow \eta(r,\ s) \geqslant \frac{b_{rs}}{\lambda_F(r,\ s)}. \tag{A.8}$$

□

Appendix B. Proof of proposition 2

Proof. Consider first a reduced network consisting only of the link $(r,\ s)$ and the shortest alternative path between the two nodes, which we denote as $(j_1 = r,\ j_2,\ j_3,\cdots,\ j_n = s)$. Fixing the nodal potentials such that $\theta_r - \theta_s = 1$ as in A, the direct flow over the link $(r,\ s)$ is given by

$$F'_{r\to s} = b_{rs}, \tag{B.1}$$

whereas the indirect flow over the shortest alternative path is given by

$$\begin{aligned}
F'_{r\to j_2} = F'_{j_2\to j_3} &= \cdots = F'_{j_{n-1}\to j_n}\\
&= [b^{-1}_{j_1,j_2} + b^{-1}_{j_2,j_3} + \cdots + b^{-1}_{j_{n-1},j_n}]^{-1}\\
&= \frac{1}{\mathrm{dist}_1^{\mathrm{w}}(r,\ s)}.
\end{aligned} \tag{B.2}$$

Now consider the initial network, to which all edges have been reintroduced, where we keep the same difference in nodal potentials $\theta_r - \theta_s = 1$ which might require a different power injection ΔP. The direct flow thus remains the same while the total flow can only increase because new alternative paths may be present such that

$$\sum_n F_{r\to n} \geqslant F'_{r\to s} + F'_{r\to j_2} = b_{rs} + \frac{1}{\mathrm{dist}_1^{\mathrm{w}}(r,\ s)}. \tag{B.3}$$

Thus we obtain (see equation (A.2))

$$\eta(r,\ s) = \frac{F_{r\to s}}{\sum_n F_{r\to n}} \leqslant \left[1 + \frac{1}{b_{rs}\times \mathrm{dist}_1^{\mathrm{w}}(r,\ s)}\right]^{-1}. \tag{B.4}$$

□

Appendix C. Proof of proposition 3

In this appendix we first give the proof for proposition 3 and then show when the decay becomes strictly monotonous.

Proof. The proof is carried out by induction starting from $d = d_{\max}$. We only give the proof for the maximum, the proof for the minimum proceeds in an analogous way. We assume that the network is large enough such that $d_{\max} \geqslant 2$, otherwise the statement is trivial anyway.

(1) Base case $d = d_{\max}$: Consider the node n of the network for which $\mathrm{dist}(n, r) = d_{\max}$ and ψ_n assumes its maximum $\psi_n = u_{d_{\max}}$. By assumption we have $\mathrm{dist}(n, r) \geqslant 2$ such that the node n cannot be adjacent to the perturbed edge such that $q_n = 0$. The n-th component of equation (18) yields

$$\begin{aligned} B_{nn}\psi_n &= -\sum_{m\neq n} B_{nm}\psi_m \\ &= -\sum_{m\neq n,\mathrm{dist}(m,r)=d_{\max}} B_{nm}\psi_m - \sum_{m\neq n,\mathrm{dist}(m,r)=d_{\max}-1} B_{nm}\psi_m. \end{aligned}$$

We define the abbreviations

$$\mathcal{B}_d = -\sum_{m\neq n,\mathrm{dist}(m,r)=d} B_{nm} \tag{C.1}$$

and use some important properties of the matrix $\boldsymbol{B}$:

$$\begin{aligned} B_{nm} &\leqslant 0 \text{ for } n \neq m \quad \Rightarrow \quad B_d \geqslant 0, \\ B_{nn} &\geqslant B_{d_{\max}} + B_{d_{\max}-1}. \end{aligned} \tag{C.2}$$

We can furthermore bound the values of ψ_m in equation (C) by $u_{d_{\max}}$ or $u_{d_{\max}-1}$, respectively, such that we obtain

$$u_{d_{\max}} = \psi_n \leqslant \frac{\mathcal{B}_{d_{\max}} u_{d_{\max}} + \mathcal{B}_{d_{\max}-1} u_{d_{\max}-1}}{\mathcal{B}_{d_{\max}} + \mathcal{B}_{d_{\max}-1}} \Rightarrow u_{d_{\max}} \leqslant u_{d_{\max}-1}. \tag{C.3}$$

(2) Inductive step $d \to d - 1$: We consider the node n of the network with $\mathrm{dist}(n, r) = d$ and $\psi_n = u_d$. Starting from equation (18) and using the same estimates as above, we obtain

$$u_d = \psi_n = \frac{q_n - \sum_{m\neq n} B_{nm}\psi_m}{B_{nn}} \leqslant \frac{\mathcal{B}_{d-1}u_{d-1} + \mathcal{B}_d u_d + \mathcal{B}_{d+1}u_{d+1}}{\mathcal{B}_{d-1} + \mathcal{B}_d + \mathcal{B}_{d+1}}. \tag{C.4}$$

Note that the inhomogeneity $q_n \leqslant 0$ for all nodes except for $n = r$. With the induction hypothesis $u_{d+1} \leqslant u_d$ this yields

$$u_d \leqslant \frac{B_{d-1}u_{d-1} + (B_d + B_{d+1})u_d}{B_{d-1} + B_d + B_{d+1}} \Rightarrow u_d \leqslant u_{d-1}, \tag{C.5}$$

which completes the proof.

□

Appendix D. Rerouting distance

The rerouting distance introduced in definition 2 is a proper distance measure in the sense that it satisfies the axioms of a metric as shown in the following lemma. It can be calculated by mapping it to the two-edge disjoint shortest path problem, which can be solved by Suurballe's algorithm [60]. The mapping is provided by the lemma 4.

Lemma 3. *Consider an undirected graph with non-negative (all-equal) edge weights. Then the rerouting distance* $\mathrm{edist}_{\mathrm{re}}^{\mathrm{w/u}}[(r, s), (m, n)]$ *of two edges* (r, s) *and* (m, n) *satisfies the following properties.*

(i) Positive definiteness:

$$\mathrm{edist}_{\mathrm{re}}^{\mathrm{w/u}}[(r, s), (m, n)] \geqslant 0.$$

(ii) Symmetry:

$$\mathrm{edist}_{\mathrm{re}}^{\mathrm{w/u}}[(r, s), (m, n)] = \mathrm{edist}_{\mathrm{re}}^{\mathrm{w/u}}[(m, n), (r, s)].$$

(iii) Triangular inequality:

$$\mathrm{edist}_{\mathrm{re}}^{\mathrm{w/u}}[(a,\ b),\ (r,\ s)] \leqslant \mathrm{edist}_{\mathrm{re}}^{\mathrm{w/u}}[(a,\ b),\ (m,\ n)] + \mathrm{edist}_{\mathrm{re}}^{\mathrm{w/u}}[(m,\ n),\ (r,\ s)],$$

both in the weighted and unweighted case.

Proof.

(1) Positive definiteness: as long as all edge weights are non-negative, all paths lengths and hence also the rerouting distances are non-negative.

(2) Symmetry: suppose

$$(v_0 = r,\ v_1,\ldots,v_i = m,\ v_{i+1} = n,\ldots v_k = s) \tag{D.1}$$

is the shortest rerouting path from r to s via $(m,\ n)$. Then

$$(v_{i+1} = n,\ v_{i+2},\ldots,v_k = s,\ v_0 = r,\ v_1,\ldots,\ v_i = m) \tag{D.2}$$

is also a rerouting path from n to m via $(r,\ s)$. One can then show that this must be the shortest such rerouting path via contradiction. So suppose that another path from n to m via $(r,\ s)$,

$$(u_{j+1} = n,\ u_{j+2},\ldots u_\ell = s,\ u_0 = r,\ u_1,\ldots,\ u_j = m), \tag{D.3}$$

is shorter. Then the path

$$(v_0 = r,\ v_1,\ldots,v_i = m,\ v_{i+1} = n,\ldots v_\ell = s) \tag{D.4}$$

is a rerouting path from r to s via $(m,\ n)$ and it is shorter than than the one defined in equation (D.1). This contradicts our initial assumption such that the path defined in equation (D.1) is the shortest rerouting path from n to m via $(r,\ s)$ and we obtain

$$\mathrm{edist}_{\mathrm{re}}^{\mathrm{w/u}}[(r,\ s),\ (m,\ n)] = \mathrm{edist}_{\mathrm{re}}^{\mathrm{w/u}}[(m,\ n),\ (r,\ s)]. \tag{D.5}$$

(3) Triangle inequality: let the paths

$$p_1 = (v_0 = a,\ v_1,\ldots,v_i = m,\ v_{i+1} = n,\ldots v_\ell = b),$$
$$p_2 = (u_0 = m,\ u_1,\ldots,u_j = r,\ u_{j+1} = s,\ldots u_\ell = n)$$

be the shortest rerouting paths from a to b via edge $(m,\ n)$ and from m to n via $(r,\ s)$, respectively. Here, we assume the paths to be oriented as $v_i = m$, $v_{i+1} = n$ and $u_i = r$, $u_{i+1} = s$, but the proof is the same if the order of these vertices in the path is reversed. In addition to that, we assume the two distances on the right-hand side of the inequality to be finite, otherwise the proof is trivial. We can extend the path p_2 to become a cycle by adding the edge $(n,\ m)$ to the end of the path

$$c_2 = (u_0 = m,\ldots,\ u_i = r,\ u_{i+1} = s,\ldots u_\ell = n,\ u_{\ell+1} = m).$$

Now we can explicitly construct a rerouting path from a to b via $(r,\ s)$. Let $u_j \equiv v_p$ be the first vertex that appears in both p_1 and c_2 and let $u_k \equiv v_q$ the last such vertex. In this case, one of the following paths is a rerouting path from a to b via $(r,\ s)$

$$p_3 = (u_0 = a,\ u_1,\ldots,\ u_j = v_p,\ v_{p+1},\ldots,v_{q-1},\ u_k = v_q,\ldots u_\ell = b)$$
$$\text{or } p_4 = (u_0 = a,\ u_1,\ldots,\ u_j = v_p,\ v_{p-1},\ldots,v_{q+1},\ u_k = v_q,\ldots u_\ell = b).$$

Assume without loss of generality that p_3 is a rerouting path from a to b via $(r,\ s)$. In this case, we obtain

$$\begin{aligned}
\mathrm{edist}_{\mathrm{re}}^{\mathrm{w/u}}[(a,\ b),\ (r,\ s)] &\leqslant \mathrm{length}((a,\ b)) + \mathrm{length}(p_3)\\
&\leqslant \mathrm{length}((a,\ b)) + \mathrm{length}(p_1) + \mathrm{length}(c_2)\\
&= \mathrm{length}((a,\ b)) + \mathrm{length}(p_1) + \mathrm{length}((m,\ n)) + \mathrm{length}(p_2)\\
&= \mathrm{edist}_{\mathrm{re}}^{\mathrm{w/u}}[(a,\ b),\ (m,\ n)] + \mathrm{edist}_{\mathrm{re}}^{\mathrm{w/u}}[(m,\ n),\ (r,\ s)].
\end{aligned}$$

Note that again the length of a path is the sum of the edge weights of all edges in the path when considering a weighted graph.

□

Lemma 4. *The shortest rerouting path form* r *to* s *via edge* (m, n) *is given by the union of the edge* (m, n) *and the two edge*-independent *paths* $r \to m$ *and* $n \to s$ *or* $r \to n$ *and* $m \to s$ *which minimize the total path length.*

Proof. Assume that we have found a solution to the two-disjoint shortest path problem, i.e. we have found two edge-independent paths

$$(v_0 = r, v_1, \ldots, v_i = m) \text{ and } (u_0 = s, u_1 \ldots u_j = s), \tag{D.6}$$

which minimize the total path length. By assumption the two paths are edge-independent such that

$$(v_0 = r, v_1, \ldots, v_i = m, u_0 = s, u_1 \ldots u_j = s) \tag{D.7}$$

is a valid rerouting path. Now it remains to show that this path is indeed the shortest possible. So assume the contrary, i.e. that there exists a path

$$(w_0 = r, w_1, \ldots, w_i = m, w_{i+1} = n, \ldots w_k = s) \tag{D.8}$$

which is shorter than (D.7). But then the two paths

$$(w_0 = r, w_1, \ldots, w_i = m) \tag{D.9}$$

$$(w_{i+1} = n, w_{i+2} \ldots w_k = s) \tag{D.10}$$

are edge independent and have a shorter total path length than the two paths D.6. Contradiction. □

ORCID iDs

Franz Kaiser https://orcid.org/0000-0002-7089-2249
Dirk Witthaut https://orcid.org/0000-0002-3623-5341

References

[1] Marris E 2008 *Nature* **454** 570
[2] van der Vleuten E and Lagendijk V 2010 *Energy Policy* **38** 2042
[3] Sack L and Scoffoni C 2013 *New Phytologist* **198** 983–1000
[4] Pittman R N 2011 The circulatory system and oxygen transport *Regulation of Tissue Oxygenation* (San Rafael, CA: Morgan & Claypool)
[5] Tero A, Takagi S, Saigusa T, Ito K, Bebber D P, Fricker M D, Yumiki K, Kobayashi R and Nakagaki T 2010 *Science* **327** 439–42
[6] Schweitzer F, Fagiolo G, Sornette D, Vega-Redondo F, Vespignani A and White D R 2009 *Science* **325** 422–5
[7] Pourbeik P, Kundur P and Taylor C 2006 *IEEE Power Energy Mag.* **4** 22–9
[8] Yang Y, Nishikawa T and Motter A E 2017 *Science* **358** eaan3184
[9] Rohden M, Jung D, Tamrakar S and Kettemann S 2016 *Phys. Rev.* E **94** 032209
[10] Witthaut D, Rohden M, Zhang X, Hallerberg S and Timme M 2016 *Phys. Rev. Lett.* **116** 138701
[11] Schäfer B, Witthaut D, Timme M and Latora V 2018 *Nat. Commun.* **9** 1975
[12] US-Canada Power System Outage Task Force 2004 Final report on the august 14, 2003 blackout in the united states and Canada: causes and recommendations https://energy.gov/sites/prod/files/oeprod/DocumentsandMedia/BlackoutFinal-Web.pdf
[13] Andersson G *et al* 2005 *IEEE Trans. Power Syst.* **20** 1922–8
[14] Union for the Coordination of Transmission of Electricity 2007 Final report on the system disturbance on 4 November 2006 https://entsoe.eu/fileadmin/user_upload/_library/publications/ce/otherreports/Final-Report-20070130.pdf
[15] Venkatasubramanian V and Li Y 2004 *Bulk Power System Dynamics and Control-VI (Cortina d'Ampezzo, Italy, August 22–27)*
[16] Dobson I, Carreras B A, Newman D E and Reynolds-Barredo J M 2016 *IEEE Trans. Power Syst.* **31** 4831–41
[17] Hines P D, Dobson I and Rezaei P 2017 *IEEE Trans. Power Syst.* **32** 958–67
[18] Labavic D, Suciu R, Meyer-Ortmanns H and Kettemann S 2014 *Eur. Phys. J. Spec. Top.* **223** 2517–25
[19] Jung D and Kettemann S 2016 *Phys. Rev.* E **94** 012307
[20] Kettemann S 2016 *Phys. Rev.* E **94** 062311
[21] Witthaut D and Timme M 2015 *Phys. Rev.* E **92** 032809
[22] Witthaut D and Timme M 2013 *Eur. Phys. J.* B **86** 377
[23] Tyloo M, Pagnier L and Jacquod P 2018 arXiv:1810.09694
[24] Schaffer C B, Friedman B, Nishimura N, Schroeder L F, Tsai P S, Ebner F F, Lyden P D and Kleinfeld D 2006 *PLoS Biology* **4** e22
[25] Roth-Nebelsick A, Uhl D, Mosbrugger V and Kerp H 2001 *Ann. Bot.* **87** 553–66
[26] Sack L, Dietrich E M, Streeter C M, Sanchez-Gomez D and Holbrook N M 2008 *Proc. Natl Acad. Sci. USA* **105** 1567–72
[27] Nesti T, Zocca A and Zwart B 2018 *Phys. Rev. Lett.* **120** 258301
[28] Katifori E, Szöllősi G J and Magnasco M O 2010 *Phys. Rev. Lett.* **104** 048704
[29] Shih A Y, Blinder P, Tsai P S, Friedman B, Stanley G, Lyden P D and Kleinfeld D 2013 *Nat. Neurosci.* **16** 55–63
[30] Ronellenfitsch H and Katifori E 2017 arXiv:1707.03074
[31] Hwang N and Houghtalen R 1996 *Fundamentals of Hydraulic Engineering Systems* (Upper Saddle River, NJ: Prentice-Hall)
[32] Hu D and Cai D 2013 *Phys. Rev. Lett.* **111** 138701
[33] Corson F 2010 *Phys. Rev. Lett.* **104** 048703
[34] Ronellenfitsch H and Katifori E 2016 *Phys. Rev. Lett.* **117** 138301
[35] Gavrilchenko T and Katifori E 2019 *Phys. Rev.* E **99** 012321
[36] Miller R E and Blair P D 2009 *Input–Output Analysis: Foundations and Extensions* (Cambridge: Cambridge University Press)
[37] Grainger J J and Stevenson W D Jr 1994 *Power System Analysis* (New York: McGraw-Hill)
[38] Wood A J, Wollenberg B F and Sheblé G B 2014 *Power Generation, Operation and Control* (New York: Wiley)

[39] Purchala K, Meeus L, Dommelen D V and Belmans R 2005 Usefulness of dc power flow for active power flow analysis *IEEE Power Eng. Soc. Gen. Meeting* **1** 454–9
[40] Van Hertem D, Verboomen J, Purchala K, Belmans R and Kling W 2006 Usefulness of dc power flow for active power flow analysis with flow controlling devices *The 8th IEEE Int. Conf. on AC and DC Power Transmission* pp 58–62
[41] Hörsch J, Ronellenfitsch H, Witthaut D and Brown T 2018 *Electr. Power Syst. Res.* **158** 126–35
[42] Manik D, Rohden M, Ronellenfitsch H, Zhang X, Hallerberg S, Witthaut D and Timme M 2017 *Phys. Rev.* E **95** 012319
[43] Díaz S, González J and Mínguez R 2016 *J. Water Resour. Plan. Manage.* **142** 04015071
[44] Newman M E J 2010 *Networks-An Introduction* (Oxford: Oxford University Press)
[45] Merris R 1994 *Linear Algebr. Appl.* **197–198** 143–76
[46] Guo J, Fu Y, Li Z and Shahidehpour M 2009 *IEEE Trans. Power Syst.* **24** 1633–4
[47] Biggs N 1997 *Bull. London Math. Soc.* **29** 641–82
[48] Cserti J, Dávid G and Piróth A 2002 *Am. J. Phys.* **70** 153–9
[49] Zimmerman R D, Murillo-Sanchez C E and Thomas R J 2011 *IEEE Trans. Power Syst.* **26** 12
[50] Diestel R 2010 *Graph Theory* (New York: Springer)
[51] Ahuja R K, Magnanti T L and Orlin J B 1993 *Network Flows: Theory, Algorithms, and Applications* (Englewood Cliffs, NJ : Prentice-Hall)
[52] Klein D and Randic M 1993 *J. Math. Chem.* **12** 81
[53] Xiao W and Gutman I 2003 *Theor. Chem. Acc.* **110** 284–9
[54] Shapiro L W 1987 *Mathematics Magazine* **60** 36–8
[55] Guo L, Liang C and Low S H 2017 Monotonicity properties and spectral characterization of power redistribution in cascading failures *2017 55th Annual Allerton Conf. on Communication, Control, and Computing* pp 918–25
[56] Ronellenfitsch H, Manik D, Hörsch J, Brown T and Witthaut D 2017 *IEEE Trans. Power Syst.* **32** 4060–8
[57] Zimmerman R D, Murillo-Sánchez C E and Thomas R J 2011 MATPOWER: steady-state operations, planning and analysis tools for power systems research and education *IEEE Trans. Power Systems* **26** 12–9
[58] Kendall M G 1948 *Rank Correlation Methods* (Oxford: Griffin)
[59] Wu Z, López E, Buldyrev S V, Braunstein L A, Havlin S and Stanley H E 2005 *Phys. Rev.* E **71** 045101
[60] Suurballe J W and Tarjan R E 1984 *Networks* **14** 325–36

2.2. B) Collective effects of link failures in linear flow networks

[2] Kaiser, F., Strake, J. & Witthaut, D. Collective effects of link failures in linear flow networks. *New Journal of Physics* **22,** 013053. doi:10.1088/1367-2630/ab6793 (2020).

IOP Publishing New J. Phys. 22 (2020) 013053 https://doi.org/10.1088/1367-2630/ab6793

New Journal of Physics
The open access journal at the forefront of physics

Deutsche Physikalische Gesellschaft DPG
IOP Institute of Physics
Published in partnership with: Deutsche Physikalische Gesellschaft and the Institute of Physics

RECEIVED
2 October 2019

REVISED
23 December 2019

ACCEPTED FOR PUBLICATION
3 January 2020

PUBLISHED
30 January 2020

PAPER

Collective effects of link failures in linear flow networks

Franz Kaiser[1,2,3], Julius Strake[1,2,3] and Dirk Witthaut[1,2]

1 Forschungszentrum Jülich, Institute for Energy and Climate Research—Systems Analysis and Technology Evaluation (IEK-STE), D-52428, Jülich, Germany
2 University of Cologne, Institute for Theoretical Physics, D-50937, Köln, Germany
3 FK and JS contributed equally to this work.

E-mail: f.kaiser@fz-juelich.de and d.witthaut@fz-juelich.de

Keywords: complex networks, network flows, power grids, link failure

Abstract

The reliable operation of supply networks is crucial for the proper functioning of many systems, ranging from biological organisms such as the human blood transport system or plant leaves to man-made systems such as power grids or gas pipelines. Whereas the failure of single transportation links has been analysed thoroughly, the understanding of multiple failures is becoming increasingly important to prevent large scale damages. In this publication, we examine the collective nature of the simultaneous failure of several transportation links. In particular, we focus on the difference between single link failures and the collective failure of several links. We demonstrate that collective effects can amplify or attenuate the impacts of multiple link failures—and even lead to a reversal of flows on certain links. A simple classifier is introduced to predict the overall strength of collective effects that we demonstrate to be generally stronger if the failing links are close to each other. Finally, we establish an analogy between link failures in supply networks and dipole fields in discrete electrostatics by showing that multiple failures may be treated as superpositions of multiple electrical dipoles for lattice-like networks. Our results show that the simultaneous failure of multiple links may lead to unexpected effects that cannot be easily described using the theoretical framework for single link failures.

1. Introduction

The failure of links can impede the operation of supply networks leading to potentially critical events [1–3]. Cascading failures in power grids can cause power outages affecting millions of households [4–7], and embolism in humans and plants may result in strokes [8, 9] or leaf death [10]. Such events are typically caused by the failure of one or few transportation links [5].

In this article, we analyse the impacts of multiple link failures in linear flow networks. We focus on electric power grid operation while the mathematical results apply to a variety of networks. In case of the power grid, cascades triggered by a single failure are in most cases prevented by the transmission grid operators. This is typically achieved by running the grid $N-1$ secure which means that a single failing transmission or generation element does not prevent stable operation of the power grid [11]. However, grid operators are now encouraged to also take specific dangerous $N-2$ contingencies into account [12] due to an increased vulnerability of the grid. For instance, an increased risk of extreme weather events caused by climate change raises the risk of several transmission elements failing, thus leading to power outages [13]. More specifically, an increase in correlation between transmission line outages, e.g. through more extreme weather events, was recently associated with an increased risk of cascading outages, raising the relative contribution of multiple link failures to such cascades [14]. In addition to that, future power systems with a high share of renewable energy sources will have to transport power over long distances using long transmission lines, thus also increasing the risk of dependent link failures.

Many computational approaches towards studying and classifying $N-2$ outages have been developed in order to identify contingencies that result in additional overloads [15–18]. Nevertheless, such outages still lack a fundamental theoretical understanding. Basic mathematical tools have been developed extending the concept of

Line Outage Distribution Factors (LODFs) originally used for single link contingencies [11] to include multiple link failures thereby allowing for a mathematical description of these contingencies [19–21]. These tools demonstrate that the nature of multiple outages may be fundamentally different from the outage of single lines, thus making a direct transfer of understanding and intuition developed for single link failures [22] difficult. In particular, multiple outages can enhance or attenuate each other in a counterintuitive manner. Which topologies drive such phenomena and which ones prevent them from happening is at present not fully understood.

In this article we analyse the collective nature of $N-2$ failures in linear flow networks, which describe different systems including AC power grids in the linear approximation [11]. We demonstrate that two simultaneous failures can cause a disturbance that strongly differs from the sum of the disturbances induced by individual failures; they can amplify or attenuate the flow changes in a grid. In addition to that, we introduce a predictor which allows us to understand under which circumstances these collective effects play an important role and when they can be neglected. We then apply the predictor to different test grids and reveal its performance in forecasting collective effects for multiple link failures quantitatively, outperforming also distance measures proven to be good predictors in the case of single link failures. Finally, we extend on previous work [22] that successfully established an analogy between flow rerouting after single link failures and the fields of electromagnetic dipoles in regular grids by demonstrating that flows after multiple link failures may be treated as a superposition of multiple individual dipole fields in such grids in the continuum limit.

2. Link failures in linear flow networks

2.1. Fundamentals of linear flow networks

Linear flow networks describe the operation of various types of systems including AC power grids [11, 23, 24], DC electric circuits [25–27], hydraulic networks [28, 29], and vascular networks of plants [30]. In such networks, the flow $F_{m\to n}\in\mathbb{R}$ over a link (m, n) is assumed to be linear in the potential or pressure drop along this link,

$$F_{m\to n} = b_{mn}(\theta_m - \theta_n). \tag{1}$$

In this article, we focus on applications to AC power grids, where $F_{m\to n}$ is the real power flow, $\theta_n\in\mathbb{R}$ is the voltage phase angle at node n and $b_{mn}\in\mathbb{R}$ is proportional to the link's susceptance. We assume that the susceptance is independent of the direction of the link, $b_{mn}=b_{nm}$, and that it vanishes if no link (m, n) exists. In this context, the linear description is commonly referred to as the DC approximation due to its formal equivalence with DC resistor networks [11, 23, 24]. This approximation is typically good for transmission grids with weak link loading, see [23] for details. In hydraulic or vascular networks, θ_n denotes the pressure at node n while the transmission capacity b_{mn} depends on the geometry of a pipe or vein [28–30]. The flows are subject to the continuity equation which means that at each node of the grid the sum of the network flows must equal the inflow to the grid;

$$\sum_{n=1}^{N} F_{m\to n} = P_m. \tag{2}$$

The inflow P_m is positive if a current, power, or fluid is injected to the node and negative if it is withdrawn from the node. In the following, we assume these in- and outflows to be balanced, $\sum_{i=1}^{N}P_i = 0$.

Equations (1) and (2) fully describe the state and the flow of the network—up to a constant phase shift applied to all voltage phase angles—once the link parameters b_{mn} and the injections P_m are given. We introduce a compact vectorial notation summarising the nodal potentials or voltage phase angles in the vector $\boldsymbol{\theta}=(\theta_1,\ \ldots,\ \theta_N)^\top\in\mathbb{R}^N$ and the nodal injections in the vector $\boldsymbol{P}=(P_1,\ \ldots,\ P_N)^\top\in\mathbb{R}^N$. Here and in the following sections, the superscript '$\top$' denotes the transpose of a vector or matrix. We further label all lines in the grid by $l=1,\ \ldots,\ M$ and fix an orientation for each link. Summarising all link flows in the vector $\boldsymbol{F}=(F_1,\ \ldots,\ F_M)^\top\in\mathbb{R}^M$, equation (1) reads as

$$\boldsymbol{F} = \boldsymbol{B}_d\boldsymbol{I}^\top\boldsymbol{\theta},$$

with the diagonal matrix of link strengths $\boldsymbol{B}_d=\mathrm{diag}(b_1, b_2,\ \ldots,\ b_M)\in\mathbb{R}^{M\times M}$. Furthermore, we made use of the node-edge incidence matrix $\boldsymbol{I}\in\mathbb{R}^{N\times M}$ commonly used in graph theory. It establishes a correspondence between the nodes in the graph and the edges connecting them and has the components [31]

$$I_{n,\ell} = \begin{cases} 1 & \text{if link } \ell \text{ starts at node } n,\\ -1 & \text{if link } \ell \text{ ends at node } n,\\ 0 & \text{otherwise.}\end{cases}$$

In the following, we use this matrix to assign an (arbitrary) orientation to each link in the network such that $F_{m\to n}=-F_{n\to m}$. Using the node-edge incidence matrix we can further rewrite the continuity equation (2) in the compact form

$$\boldsymbol{P} = \boldsymbol{IF} = \boldsymbol{IB}_d\boldsymbol{I}^\top\boldsymbol{\theta} = \boldsymbol{B\theta}. \tag{3}$$

The matrix $\boldsymbol{B} = \boldsymbol{IB}_d\boldsymbol{I}^\top \in \mathbb{R}^{N\times N}$ is commonly referred to as the nodal susceptance matrix in power engineering. Mathematically, $\boldsymbol{B}$ is a weighted Laplacian matrix [31, 32] with components

$$B_{mn} = \begin{cases} \sum_{s=1}^{N} b_{ns} & \text{if} \quad m = n; \\ -b_{mn} & \quad\quad m \neq n. \end{cases} \tag{4}$$

For a connected network, this matrix has one zero eigenvalue $\lambda_1 = 0$ with eigenvector $\boldsymbol{v}_1 = \boldsymbol{1}$ such that $\boldsymbol{B} \cdot \boldsymbol{v}_1 = \boldsymbol{0}$. For this reason, it is not invertible. However, the matrix inverse appears naturally in many different contexts involving the spreading of failures in networks. To be able to nevertheless study these processes, one typically considers the Moore–Penrose pseudoinverse $\boldsymbol{B}^\dagger$ which has properties similar to the actual inverse, see e.g. [33, 34] for details. We are now ready to extend the notation to cover link failures as well.

2.2. Single and double link failures

Assume that a single link k in the network fails, thus losing its ability to carry any flow. Since the network after the failure is still subject to the continuity equation (2), the failure will cause the flows on other links to change to account for the remaining necessary transport. Assume that the new flows are given as $\boldsymbol{F}^{[k]} = \boldsymbol{F}^{(0)} + \Delta\boldsymbol{F}$, where $\Delta\boldsymbol{F}$ is the vector of flow changes and $\boldsymbol{F}^{(0)}$ is the preoutage flow. In general, we will use the superscript $^{(0)}$, i.e. round brackets, to indicate a flow before an outage and the superscript $^{[k]}$, i.e. square brackets, to indicate a flow after the failure of link k. Then the new vector fulfils the continuity equation (3),

$$\boldsymbol{P} = \boldsymbol{IF}^{[k]}.$$

In power engineering, the changes of flows are typically captured in a matrix of LODFs whose element $L_{l,k}$ describes the flow changes monitored on a link l after another link k fails. Suppose that $F_k^{(0)}$ is the flow on link k before the outage. Then the LODF is defined by its elements [11]

$$L_{l,k} := \frac{\Delta F_l}{F_k^{(0)}}. \tag{5}$$

For consistency, the effect of an outage of a line k onto itself is typically defined as $L_{k,k} = -1$. Importantly, the LODF may be expressed in purely algebraic form using the (pseudo-) inverse of the graph Laplacian $\boldsymbol{B}$ [11],

$$L_{l,k} = b_l \frac{\boldsymbol{d}_l^\top \boldsymbol{B}^\dagger \boldsymbol{d}_k}{1 - b_k \boldsymbol{d}_k^\top \boldsymbol{B}^\dagger \boldsymbol{d}_k}. \tag{6}$$

Here, we abbreviate the line susceptance $b_{l_1 l_2}$ of a link $l = (l_1, l_2)$ by b_l. Furthermore, we defined a vector $\boldsymbol{d}_k \in \mathbb{Z}^N$ that characterises a link $k = (r, s)$ and has the entries $+1$ at position r, -1 at position s and zero otherwise. Using the standard basis vectors in $\mathbb{R}^N$, this vector may be written as $\boldsymbol{d}_k = \boldsymbol{e}_r - \boldsymbol{e}_s$. In power engineering, the expression in the numerator is also referred to as the Power Transfer Distribution Factor (PTDF) [11]. A PTDF between links l and k is calculated as

$$\mathrm{PTDF}_{l,k} = b_l \boldsymbol{d}_l^\top \boldsymbol{B}^\dagger \boldsymbol{d}_k$$

and describes the flow changes on link l upon a power transfer from one end of link k to the other one. PTDFs are typically defined for power injections and withdrawals at arbitrary nodes in the network [11]. In the context of link failures, however, it is useful to restrict them to power injection and withdrawal taking place at the two ends of a link. For this reason, power injection vectors $\boldsymbol{d}_k$ have to correspond to the columns of the incidence matrix in our setup such that $\boldsymbol{d}_k = \boldsymbol{I} \cdot \boldsymbol{e}_k$, where $\boldsymbol{e}_k \in \mathbb{R}^M$ is again the standard basis vector.

On the other hand, the link failure may also be described on the nodal level. If we collect all changes in voltage phase angles after the failure of link k in the vector $\boldsymbol{\psi} = \boldsymbol{\theta}^{[k]} - \boldsymbol{\theta}$, denoting phase angles after the failure by $\boldsymbol{\theta}^{[k]}$, a Poisson-like equation describing the outage in terms of the phase differences may be derived [22],

$$\boldsymbol{B}^{[k]}\boldsymbol{\psi} = F_k^{(0)}\boldsymbol{d}_k. \tag{7}$$

Here, $\boldsymbol{B}^{[k]}$ is the Laplacian of the network after removal of link k and $F_k^{(0)}$ is the pre-outage flow on link k. This equation was studied in the past in different settings [35, 22, 36, 33]. The failure of single links is thus comparably well understood [22, 37, 38], whereas the simultaneous failure of multiple links was not yet studied to the same extend on a theoretical level.

For this reason, we now turn to the case of multiple link failures and derive an expression for the flow changes on the remaining lines in the grid. We will focus on the case of two outages for now, but extend the results to more than two outages in section 4. Naively, we could just superpose the flow changes caused by the two individual outages as described by equation (5). Assuming that two arbitrary links o and k fail, this naive approach yields the following expression for the flow changes on link l,

$$\Delta F_l^{\text{naive}} = L_{l,k} F_k^{(0)} + L_{l,o} F_o^{(0)}. \tag{8}$$

However, this approach neglects the effect of the outage of link k on link o and vice versa. To arrive at the correct formula, we need to consider this interaction as follows; the outage of link o changes the flow on link k by

$$\tilde{F}_k = F_k^{(0)} + L_{k,o} \tilde{F}_o,$$

where we denote by $\tilde{F}_k$ the effective flow on link k as a result of the simultaneous failure of o and k. Note that this is not the actual flow on link k, but rather an effective quantity used for calculation here since link k fails and thus carries no flow after the outage. An analogous expression holds for the effect of the outage of link k on link o. Inserting these corrected flows into equation (8), we arrive at the following result for the flow changes on link l [17],

$$\Delta F_l^{[o,k]} = L_{l,k} \tilde{F}_k + L_{l,o} \tilde{F}_o.$$

Here, the superscript $^{[o,k]}$ is used to indicate the flow or flow changes on a link after the failure of both links o and k. Finally, expanding this expression results in the following equation encoding the collective flow changes in a compact form,

$$\Delta F_l^{[o,k]} = (L_{l,o}, L_{l,k}) \begin{pmatrix} 1 & -L_{o,k} \\ -L_{k,o} & 1 \end{pmatrix}^{-1} \begin{pmatrix} F_o^{(0)} \\ F_k^{(0)} \end{pmatrix}. \tag{9}$$

The resulting expression for $\Delta F_l^{[o,k]}$ is different from the simple linear combination (8) due to the interaction of the two failing lines o and k, which is encoded in the matrix in the centre. More precisely, the collective effects are governed by the LODFs of the interacting lines $L_{o,k}$ and $L_{k,o}$ forming the off-diagonal elements of the matrix. The inverse matrix in this formula may be calculated as

$$\begin{pmatrix} 1 & -L_{o,k} \\ -L_{k,o} & 1 \end{pmatrix}^{-1} = \frac{1}{1 - L_{o,k} L_{k,o}} \begin{pmatrix} 1 & L_{o,k} \\ L_{k,o} & 1 \end{pmatrix}.$$

Thus, the flow changes on a link l are given by

$$\Delta F_l^{[o,k]} = \mathcal{L}(k, o) \cdot (L_{l,k} F_k^{(0)} + L_{l,o} F_o^{(0)} + L_{l,k} L_{k,o} F_o^{(0)} + L_{l,o} L_{o,k} F_k^{(0)}),$$

where $\mathcal{L}(k, o) = \mathcal{L}(o, k) := \frac{1}{1 - L_{k,o} L_{o,k}}$ is a symmetric prefactor.

The equation describing flow changes after the failure of two links thus differs from a naive overlay of the two individual outages. In the following sections, we will demonstrate in which cases these collective effects resulting from the interaction of both outages are important and in which cases they may be neglected.

2.3. Elementary examples

In this section, we elucidate different elementary examples that describe possible interactions between the individual outages and allow us to understand the role played by collective effects in more detail.

2.3.1. Amplifying single outages

To start with, we present a case where the naive superposition of two individual outages underestimates the collective effects such that

$$|\Delta F_l^{[o,k]}| \gg |\Delta F_l^{\text{naive}}|$$

for some link l. An elementary example of a network where this is happening is shown in figure 1 where the topology is given by a network consisting of $N = 9$ nodes and $M = 12$ links connecting them in a square grid. This initial setup is shown in panel a. Panels b and c illustrate the flows on each link (numbers on links) after the failure of two different individual links (coloured red). The bold number indicates the link with maximal flow for the given setup. Each single outage leads to a maximal flow on the top right link of $|F_{\max}| = 0.57$ and $|F_{\max}| = 0.625$ after the failure shown in panels b and c, respectively. Naively, we would thus expect the failure of both links to lead to a flow of

$$|F_{\max}^{\text{naive}}| \approx 0.125 + 0.07 + 0.5 = 0.72$$

by simply superposing the two individual outages. The actual outage of both links, however, results in a much larger flow on the link that reads as

$$|F_{\max}| = 1.0.$$

Whereas the two individual outages separately lead to a moderate increase in flow on the most heavily loaded link, their interaction results in a larger flow potentially reaching the link limit. If the flow on all links was limited to, say, $F_{\text{limit}} = 0.9$, the naive superposition would thus predict no overload caused by the two link failures, whereas in fact, the link loaded maximally in panel d breaks down in this case. This example demonstrates that

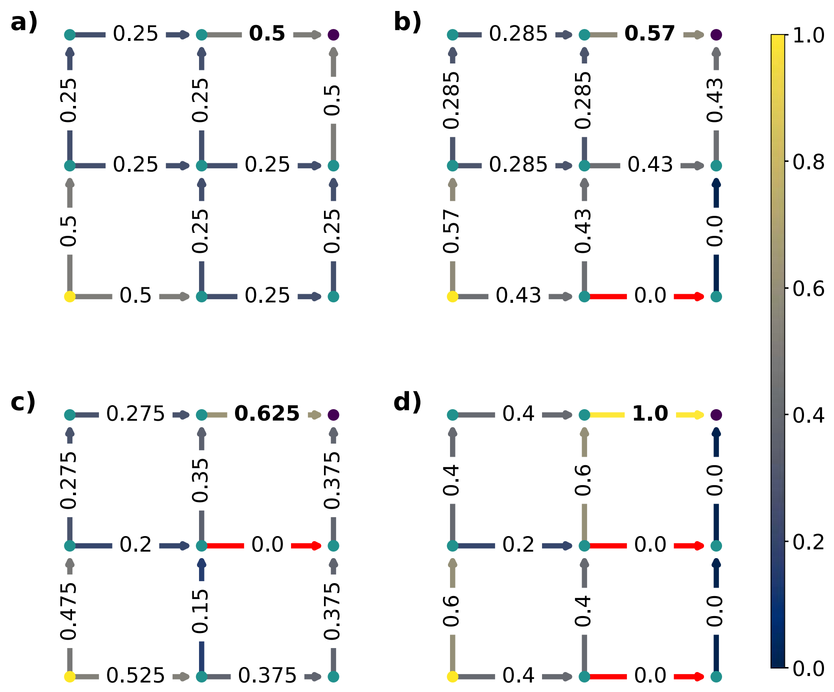

Figure 1. Collective effects can amplify the flow changes after the failure of two links, thus increasing maximum link loading. The node in the lower left corner (yellow) is assumed to be a producer of one unit of power and the node in the upper right corner (purple) a consumer of the same amount. All links have a capacity of $b = 1$ and the numbers on the edges indicate the absolute value of the flow carried by the respective link. In addition to that, the colour code ranging from dark blue (no loading) to bright yellow (maximal loading) indicates the loading of the links. Bold face numbers indicate the link with the highest loading. The single link failures lead to an increase of the flow on the upper right link by (b) 0.07 $(0.5 \to 0.57)$ and (c) 0.125 $(0.5 \to 0.625)$. If both links fail, the flows increases by (d) $0.5 > 0.07 + 0.125$. Thus, the naive superposition underestimates the flow on the maximally loaded link in this case.

the results predicted by the theory of single link failures may differ drastically from the correct calculation that takes into account the collective effects.

2.3.2. Effect of individual outages exceeding simultaneous outage

In addition to the effect presented in the last section, it may also happen that an additional outage is beneficial for the most heavily loaded link. A minimal example is shown in figure 2. In this setup, we have a unit inflow of power at the centre left node (coloured yellow), $P = +1$, and a unit outflow at the bottom right node (coloured purple), $P = -1$, whereas all other nodes neither consume nor create power, $P = 0$. The initial setup is shown in panel a, where again (absolute) flows are indicated as numbers on the edges as well as colour coded. Panels b and c show the network after the single outage of two different links (coloured red). The edge with the highest absolute flow is indicated by a bold face number in both cases. In panel b, we have $|F_{\max,\mathrm{b}}| = 0.6$ whereas for panel c the maximum flow reads as $|F_{\max,\mathrm{c}}| = 0.52$. The situation after the simultaneous outage of both links is shown in panel d. The edge with maximum flow now carries an absolute flow of $|F_{\max,\mathrm{d}}| = 0.5$, i.e. the collective effects attenuate the flow on the edge with the highest flow compared to each individual outage. This effect can be seen as a realisation of Braess' paradox [39–42] since the outage of an additional link is beneficial in terms of the maximum absolute flow in the network for each individual outage. Hence, cascades of failures may in some situations be prevented by the intentional removal of a second, carefully chosen link after a first link failure threatens stability [1, 43].

2.3.3. Sign inversion through double outages

In this section, we discuss a highly surprising phenomenon that appears in the case of multiple interacting outages: the collective effects may dominate in such a way that purely collective effects can cancel (as shown in the previous section) or even overcompensate the direct effects of individual link failures such that the flow changes resulting from the failure of both links have a different sign compared to the flow changes after each of the individual failures.

To study this in more detail, we will use the following notation in this section. Suppose that links o and k fail and flow changes are monitored on link l. Then we denote by $\Delta F_l^{[o]}$ or $\Delta F_l^{[k]}$ the flow changes on link l when link o or k fail, respectively. For the simultaneous outage of both links o and k, we denote by $\Delta F_l^{[o,k]}$ the actual flow

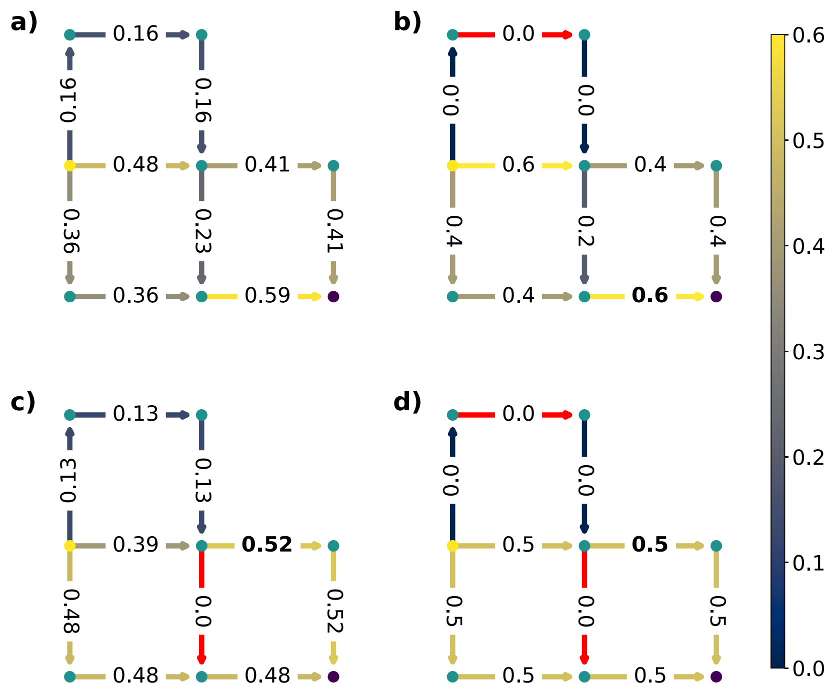

Figure 2. Collective effects can attenuate flow changes after the failure of two links, thus making the contingency less severe. Colour code of edges indicates the absolute flow on the link going from dark blue for no flow to bright yellow for links with maximum flow. The numbers on the links also represent the flow with the arrows pointing in the direction of positive flow. (a) Initial flow setup if there is a unit inflow at the yellow node on the left and a unit outflow at the purple node on the bottom right. (b) Flow setup after the failure of the top horizontal link (red). (c) Flow setup after the failure of the central, vertical link (red). (d) Flow setup after the failure of both links. While the maximum flow after a single outage is given by (b) $|F_{\max}| = 0.6$ and (c) $|F_{\max}| = 0.52$, the simultaneous outage of both links lead to a smaller maximum flow (d) $|F_{\max}| = 0.5$. Thus, in both cases of individual failures, the failure of an additional link would be beneficial in terms of the maximal absolute flow in the network. This is a realisation of *Braess' paradox*.

change on link l. With this notation at hand, we will construct examples where flow changes caused by individual link failures $\Delta F_l^{[o]}$ and $\Delta F_l^{[k]}$ have the same sign, but the collective flow change $\Delta F_l^{[o,k]}$ has the opposite sign.

A small example of a network where such a situation occurs is shown in figure 3. In the initial setup, there is a small flow $F_l = 0.5$ on link l (a, bold face number). For the failure of two individual links o and k shown in panels b and c, respectively (red links), the flow on this link is amplified showing positive flow changes in both situations, $\Delta F_l^{[o]} = 0.3$ and $\Delta F_l^{[k]} = 0.1$, respectively. However, if both links fail simultaneously, the overall flow change has the opposite sign, $\Delta F_l^{[o,k]} = -0.7$, thus even inverting the direction of the flow $F_l = -0.2$ with respect to both, the individual setup and the situation after the failure of each individual link.

In the next paragraph, we explain this surprising phenomenon on a theoretical level in more detail. For simplicity, let us assume the flow changes due to the individual outages to be positive and the flow change in the case of a simultaneous outage to be negative,

$$\Delta F_l^{[o,k]} < 0, \qquad \Delta F_l^{[k]} > 0, \qquad \Delta F_l^{[o]} > 0. \tag{10}$$

Plugging in equation (9), we can cast these three conditions into the following form based on LODFs,

$$\begin{aligned}
&(1)\ L_{l,o}L_{o,k}F_k^{(0)} + L_{l,k}L_{k,o}F_o^{(0)} < -(L_{l,k}F_k^{(0)} + L_{l,o}F_o^{(0)}),\\
&(2)\ L_{l,k}F_k^{(0)} > 0 \quad \text{and}\\
&(3)\ L_{l,o}F_o^{(0)} > 0.
\end{aligned}$$

We can assume that both the initial flows on the failing links and the LODFs between the failing links and the reference link are positive, $F_o^{(0)}, F_k^{(0)}, L_{l,o}, L_{l,k} > 0$, without loss of generality–this can always be accomplished by redefining the orientation of one or both of the initial flows. Then the right-hand side of condition (1) is negative. Hence, the condition can only be satisfied if the left-hand side is negative as well, which requires that the mutual LODFs are both negative, $L_{o,k}, L_{k,o} < 0$ because they always have the same sign (see appendix A). Note that we do not consider cases where both of the LODFs $L_{k,o}$ and $L_{o,k}$ are equal to (minus) one, thus keeping $\mathcal{L}(o, k)$ finite. For notational convenience, let us now introduce positive constants α and β defined by the following quotients;

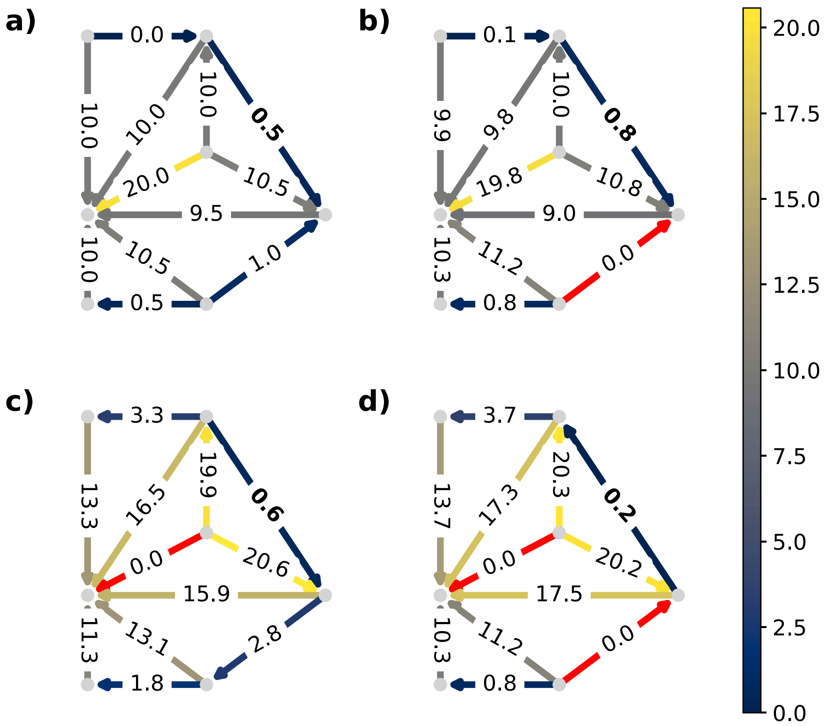

Figure 3. Collective effects can lead to a complete reversal of the flow changes compared to individual outages. Colour coded links represent the magnitude of flow ranging from blue for no flow to yellow for maximal flow. Red indicates failing links and arrows denote the direction of flow. Note that this does not necessarily correspond to link orientation. Line susceptances are homogeneously set to $b = 1$. (a) Initial flow setup with $F_k^{(0)} = 20 \gg F_o^{(0)} = 1$. (b), (c) Flow setup after individual failure of two links (o and k respectively, marked red). In both cases, the flow on the top right link (l, bold font) is larger than in the unperturbed grid; $\Delta F_l^{[o]} \approx 0.3$, $\Delta F_l^{[k]} \approx 0.1$. (d) Flow setup after simultaneous failure of both links. The flow on the top right link is smaller than in the unperturbed grid. In fact, not only does the flow change reverse sign, the total flow direction is reversed, too; $\Delta F_l^{[o,k]} \approx -0.7 < -F_l^{(0)} \approx -0.5$.

$$\alpha(o, k) = F_k^{(0)}/F_o^{(0)} > 0 \quad \text{and} \quad \beta(l, o, k) = L_{l,k}/L_{l,o} > 0.$$

We thus incorporated the whole dependency on the link monitoring the flow changes l into the purely topological constant β, whereas any dependency on the flows, i.e. the specific power injections, is incorporated into α. Dividing the first condition (1) by its right-hand-side, we arrive at the following inequality

$$\frac{\alpha(o, k)|L_{o,k}| + \beta(l, o, k)|L_{k,o}|}{1 + \alpha(o, k)\beta(l, o, k)} > 1. \tag{11}$$

This inequality can only be fulfilled if there is a strong degree of heterogeneity between α and β, i.e. the ratio of initial flows on links k and o differs strongly from the ratio of their LODFs with respect to link l. Furthermore, the mutual LODFs $L_{o,k}$ and $L_{k,o}$ need to be both large in magnitude in order to reduce the size of the denominator compared to the numerator. We will see in the next sections that strong mutual LODFs also imply strong collective effects caused by the simultaneous failure of links k and o.

Condition (11) can be simplified drastically if $\alpha \gg \beta$ which may be realised e.g. through a very small initial flow on link o compared to link k, such that $|F_o^{(0)}| \ll |F_k^{(0)}|$. The above inequality then reduces to

$$\frac{\alpha(o, k)|L_{o,k}| + \beta(l, o, k)|L_{k,o}|}{1 + \alpha(o, k)\beta(l, o, k)} \approx \frac{|L_{o,k}|}{\beta(l, o, k)}, \Rightarrow L_{l,o}|L_{o,k}| > L_{l,k}.$$

We will now demonstrate how to design a network where this inequality is satisfied. The construction works as follows; we design a network topology where two links o and k influence each other heavily (measured in terms of LODFs) while a third link l is influenced very differently by each of the links. Formally, $L_{o,k}$ and $L_{k,o}$ both need to be comparatively large while $L_{l,o}$ and $L_{l,k}$ should be very different in size, thus leading to a small value of β. To observe flow sign reversal, we choose the power injections $\boldsymbol{P}$ in such a way that the flow on link k is much larger than the one on link o, which results in $\alpha \gg \beta$. Furthermore, our choice of power injections also needs to make sure that flow changes on link l are positive $\Delta F_l^{[o]} > 0$. The resulting network fulfils the three conditions on the flow changes given in the inequalities (10).

Indeed, we can find networks where the inequalities are fulfilled as shown in figure 3. The parameters in this case are given by $\alpha(o, k) = 20$, $\beta(l, o, k) \approx 0.03$, $L_{o,k} \approx -0.19$ and $L_{k,o} \approx -0.23$. Inequality (11) then holds and reads as

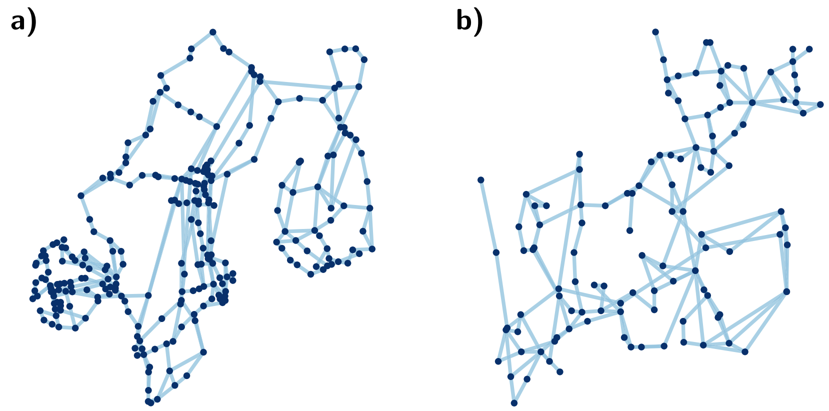

Figure 4. Two different network topologies are used to demonstrate the performance of the predictor for collective effects. (a) Topology of the Scandinavian power grid extracted from an aggregated version of the PyPSA-eur model [44] after the removal of dead ends. The resulting topology has 260 nodes and 361 edges. (b) Topology of the IEEE test case 118 designed for testing power flow algorithms [45]. The topology has 118 nodes and 179 edges.

$$\frac{20 \cdot 0.19 + 0.03 \cdot 0.23}{1 + 20 \cdot 0.03} = 2.38 > 1.$$

As discussed previously, the mutual LODFs $L_{o,k}$ and $L_{k,o}$ are both relatively large in this case. This is indicative of strong collective interactions as illustrated in the following sections. The purely collective effects not only overshadow the individual outages' effects on link l, indeed they reverse the total flow over the link.

3. Collective effects in complex networks

As shown above, the impact of a double link failure is not given by the simple sum of the individual outages' effects, but strong collective effects may be present. Based on the intuition developed in the last section, we will introduce a quantifier in the following section that may be used to identify in which situations collective effects need to be taken into account and in which situations they may be neglected, thus being able to rely on results obtained for single link failures. We will test this predictor on different test grids, mainly on the ones shown in figure 4; the Scandinavian power grid extracted from the software package PyPSA-eur [44] (panel a) and the IEEE test case 118 [45] (panel b).

3.1. Quantifying the strength of collective effects

To understand the purely collective effects of a simultaneous outage of two given links o and k, we first calculate the difference between the real flow changes in case of an outage of both links $\Delta F^{[o,k]}$ and the naive prediction in terms of the sum of individual flow changes ΔF^{naive}. The difference calculated according to equations (8) and (9) reads as

$$\Delta F_l^{[o,k]} - \Delta F_l^{\text{naive}} = \mathcal{L}(o,\, k)((L_{l,o} + L_{l,k}L_{k,o})L_{o,k},\, (L_{l,k} + L_{l,o}L_{o,k})L_{k,o})^{\top} \begin{pmatrix} F_k^{(0)} \\ F_o^{(0)} \end{pmatrix}.$$

The overall prefactor $\mathcal{L}(o,\, k)$ is one if the product $L_{o,k}L_{k,o}$ is zero and tends to infinity as the product approaches one. In order to write this expression more compactly, we introduce the matrix Ξ: $\mathbb{R}^2 \to \mathbb{R}^M$ which has the row vectors

$$\begin{aligned} \Xi_l &= \mathcal{L}(o,\, k)[(L_{l,o} + L_{l,k}L_{k,o})L_{o,k},\, (L_{l,k} + L_{l,o}L_{o,k})L_{k,o}] \\ &=: \mathcal{L}(o,\, k)[\Xi_l^{(1)},\, \Xi_l^{(2)}]. \end{aligned}$$

This matrix includes the topological properties of the rerouting problem and ignores the initial flows $F_o^{(0)}$ and $F_k^{(0)}$, which are determined by the specific power injections that may be time-dependent. The approach thus allows to quantify the impact of collective effects purely based on the network topology. However, this comes at the price of potentially missing situations with very unusual flow patterns in which the approach presented here might not be valid any more to predict collective effects. To get an overall measure of the purely collective part of the failure of two specific links o and k, we define a single collectivity parameter $\xi(o, k)$ by taking the ℓ^2-norm $\|\cdot\|_2$ of the matrix Ξ,

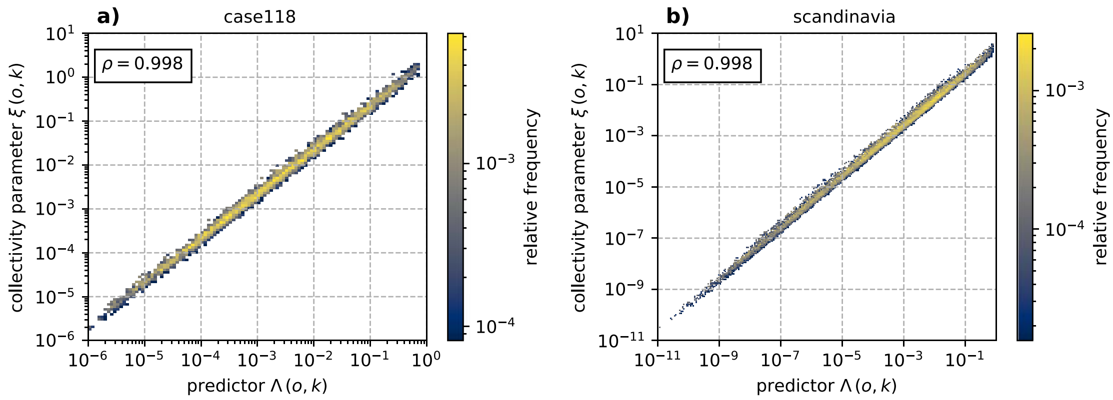

Figure 5. The predictor $\Lambda(o, k)$ performs very well in forecasting the collectivity parameter $\xi(o, k)$ for a link failure of two links o and k. In both the IEEE test grid 'case118' (a) and the Scandinavian grid (b) the relationship between collectivity parameter $\xi(o, k)$ (ordinate) and predictor $\Lambda(o, k)$ (abscissa) appears to be linear when plotted on a log–log scale. The slope of the curve indicates a linear relationship on the normal scale as well. This implies a strong correlation between the two quantities as implied also by a very large Pearson correlation coefficient of $\rho = 0.998$ in both cases indicating a linear relationship. The histograms' colour code indicates the relative frequency of data points in the given bin. Double logarithmic plots were used to showcase the consistency of the scaling over many orders of magnitude. Note that binning was also done on a double logarithmic basis, leading to much smaller bins for lower values of Λ and ξ.

$$\xi(o, k) := \mathcal{L}(o, k)\left(\sum_{l=1}^{M}[(\Xi_l^{(1)})^2 + (\Xi_l^{(2)})^2]\right)^{1/2}. \tag{12}$$

The collectivity parameter thus quantifies the overall collective effects in the whole network to be expected if links o and k fail and indicates whether links o and k interact strongly or not. Since interpreting the collectivity parameter ξ in this form is rather cumbersome and we are looking for an easily accessible criterion that tells us which pairs of links interact strongly, we further reduce this expression by making a few approximations. Since the LODFs are bounded by one, $-1 \leqslant L_{a,b} \leqslant 1$ for all links a, b, and are typically much smaller than one, in the order of $\mathcal{O}(10^{-3})$, we expect terms of third order in LODFs to be negligible against terms of second order such that we can on average neglect the former ones. In doing so, we arrive at the following approximation for the collectivity parameter,

$$\begin{aligned}\xi(o, k) &\approx \mathcal{L}(o, k)\left(\sum_{l=1}^{M}[(L_{l,o}L_{o,k})^2 + (L_{l,k}L_{k,o})^2]\right)^{1/2}\\ &= \mathcal{L}(o, k)\left((L_{o,k})^2\sum_{l=1}^{M}(L_{l,o})^2 + (L_{k,o})^2\sum_{l=1}^{M}(L_{l,k})^2\right)^{1/2}.\end{aligned}$$

Furthermore, we can make the following observation allowing us to further simplify the expression: summing over all links l in a large network, $L_{l,o}$ and $L_{l,k}$ will vary a lot and may thus essentially be treated as random variables. We therefore expect the collectivity parameter $\xi(o, k)$ to be predicted by the two non-varying quantities $L_{o,k}$ and $L_{k,o}$ characterising the interaction between the two failing links. Since LODFs are in general non-symmetric (see appendix A), both $L_{o,k}$ and $L_{k,o}$ need to be incorporated to successfully predict the collectivity parameter $\xi(o, k)$. In addition to that, we expect the prefactor $\mathcal{L}(o, k) = (1 - L_{o,k}L_{k,o})^{-1}$ to be well approximated by one in general, $\mathcal{L}(o, k) \approx 1$ since (absolute) LODFs are typically small.

Based on these considerations, we introduce a parameter that predicts the overall strength of collective effects ξ and is defined as follows,

$$\Lambda(o, k) := \sqrt{L_{o,k}L_{k,o}}. \tag{13}$$

This predictor takes into account the relative effect of the failing links o and k on one another: it is the geometric mean of the mutual LODFs between the two failing links. It is not only a good predictor for the collectivity parameter $\xi(o, k)$, but can also be shown to bound it from below as summarised in the following theorem.

Theorem 1. *Consider a connected network where two links o and k with non-vanishing mutual LODFs $L_{o,k}, L_{k,o} \neq 0$ fail. Then the collectivity parameter $\xi(o, k)$ as defined in equation (12) is bounded from below by the predictor $\Lambda(o, k) = \sqrt{L_{o,k}L_{k,o}}$*

$$\xi(o, k) \geqslant \Lambda(o, k).$$

A proof is given in appendix C. Figure 5 illustrates the performance of the predictor in forecasting collective effects for the IEEE test case 118 (panel a) and the Scandinavian power grid (panel b) when averaging over all possible trigger links. The predictor $\Lambda(o, k)$ (abscissa) has a Pearson correlation coefficient with the collectivity

Table 1. Pearson correlation ρ between predictor $\Lambda(o, k)$ and collectivity parameter $\xi(o, k)$ in the case of a double outage of links o and k for all possible pairs of inks o and k and different test grids. Values are given for a number of test grids, namely IEEE 'case30', 'case118' and 'pegase1354' [45, 46] as well as the Scandinavian grid, the German grid, [47, 48] a periodic square grid with 20×20 nodes and another one with a share of $s = 0.45$ of its links removed, and different norms used to calculate the collectivity parameter $\xi(o, k)$. While $\xi(o, k)$ is predicted very well for all norms, the 2-norm consistently yields the best results, albeit by a small margin.

	Pearson correlation ρ $\Lambda(o, k)$ versus $\xi(o, k)$			
test grid	1-norm	2-norm	10-norm	∞-norm
case30	0.959	0.98	0.951	0.946
case118	0.947	0.984	0.972	0.97
pegase1354	0.933	0.974	0.967	0.966
Square grid	0.994	0.999	0.995	0.992
Sparse square grid	0.946	0.968	0.981	0.976
Scandinavia	0.909	0.964	0.968	0.967
Germany	0.869	0.951	0.927	0.921

parameter ξ (ordinate) of $\rho = 0.998$ for both grids, thus indicating a linear relationship between the two quantities.

The predictor performs equally well if we replace the Euclidean ℓ^2-norm in the definition of the collectivity parameter ξ in equation (12) by other ℓ^p-norms Norms with $p > 2$ are dominated more by large values compared to norms with $p < 2$, therefore we also tested the $p = 10$-norm and even up to the $p = \infty$-norm, which simply takes the maximum value. The predictor performs very well in forecasting collective effects also for other test grids and norms as summarised in table 1. For all norms and all grids tested, we observe a very strong correlation between predictor and collectivity parameter, exceeding $\rho = 0.9$ in most cases. We discuss the predictor and the different norms used to calculate it in more detail in appendix B.

To summarise, we find that two links show the strongest collective interaction if their mutual LODF values are large, thus implying that a failure of one link has a strong effect on the flow going over the other one and vice versa.

3.2. Impact of network distance

Distance is known to play an important role for failure spreading in power grids and other types of linear flow networks [22, 49, 37, 50]. In this section, we will examine if it may also be used to successfully predict collective effects in multiple link failures. Typically, distances in networks are measured between two nodes with the most prominent distance measure being the geodesic distance. It is given by the sum of the lengths or weights of all edges along a shortest path between the respective nodes,

$$\mathrm{dist}_0^{\mathrm{u/w}}(v_1, v_2) = \min_{\text{paths } p(v_1,v_2)} \sum_{e\in p} \ell_e,$$

where the superscript 'u' or 'w' denotes the unweighted or weighted distance, the subscript '0' describes the distance in the initial graph before any kind of outage, v_1 and v_2 are the nodes whose distance is calculated, $p(v_1, v_2)$ is a path from v_1 to v_2 and ℓ_e is the length or weight of edge e, which is set to unity when calculating unweighted distances. For our purposes, we use the inverse link strength as the length, $l_e = 1/b_e$. Additionally, one can define the geodesic distance between edges as the smallest possible distance between the nodes incident to the corresponding edges plus half of each edge's length,

$$\mathrm{edist}_{\mathrm{ge}}^{\mathrm{u/w}}[(r, s), (m, n)] = \min_{v_1\in\{r,s\}, v_2\in\{m,n\}} \mathrm{dist}_0^{\mathrm{u/w}}(v_1, v_2) + \frac{\ell_{(r,s)} + \ell_{(m,n)}}{2}. \tag{14}$$

Here the subscript 'ge' denotes the geodesic distance while (r, s) and (m, n) are the respective edges given by the nodes they are incident in. As we demonstrated in a recent publication [22], this distance measure does not capture essential aspects of the flow rerouting after a link failure. Instead, we proposed the rerouting distance

$$\mathrm{edist}_{\mathrm{re}}^{u/w}[(r, s), (m, n)],$$

given by the length of the shortest cycle crossing both edges (r, s) and (m, n). If no such cycle exists, the rerouting distance is defined to be ∞. This distance measure is strongly correlated with the magnitude of the LODFs as shown in [22].

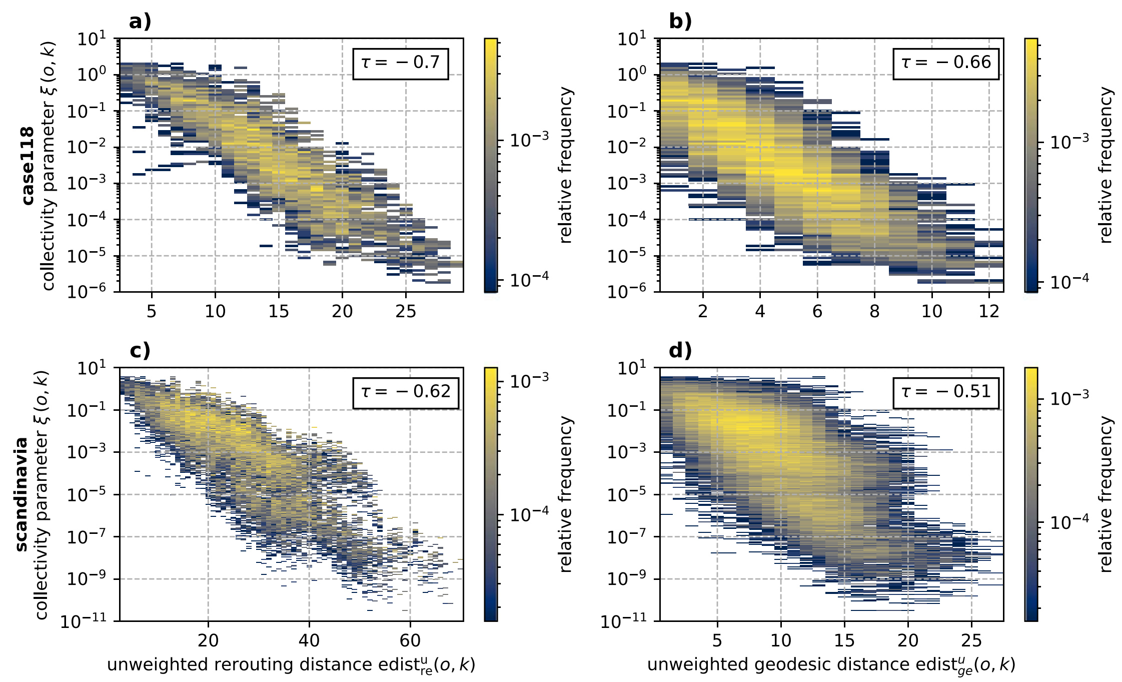

Figure 6. Distance performs moderately in predicting the overall collective effects of a double link failure of two links o and k. In both the IEEE test grid 'case118' (a), (b) and the Scandinavian grid (c), (d) the collectivity parameter $\xi(o, k)$ is plotted against the unweighted rerouting distance $\mathrm{edist}^{u}_{re}(o, k)$ (a), (c) and unweighted geodesic distance $\mathrm{edist}^{u}_{ge}(o, k)$ (b), (d), respectively. The Kendall rank correlation τ is given in all cases. Although there is a clear trend towards smaller collectivity parameters for larger distances, the correlation is much smaller than for the predictor $\Lambda(o, k)$, thus indicating that effects other than distance play an important role for collective effects as well. The histograms' colour code indicates the relative frequency of data points in the given bin. Logarithmic plots were used to resolve more details for very small values of the collectivity parameter. Note that binning was also done on a logarithmic basis, leading to much smaller bins for lower values of ξ.

Figure 6 shows the scaling of ξ with distance between the failing links for a failure of two links. Here, we use the Kendall rank correlation τ to quantify the degree of general non-linear correlation between the two quantities. The rerouting distance performs slightly better in predicting the collectivity parameter ξ than the geodesic distance, where the former has a rank correlation of $\tau = -0.7$ and $\tau = -0.62$ with ξ and the latter a correlation of $\tau = -0.66$ and $\tau = -0.51$ in the test grid 'case118' and the Scandinavian grid, respectively. Thus both distance measures perform moderately in predicting the collectivity parameter although not nearly as well as the predictor introduced in the last section. Still, the distance seems to be an important factor in determining the simultaneous outages' effects–but contrary to the case of a single outage [22], other factors play an important role, too. We may thus deduce that links that are closer to each other in both, the rerouting distance and the simple edge distance tend to have a stronger collective response. This behaviour is expected given that the predictor performing best is given by the product of the mutual LODFs between the two failing links and the rerouting distance is known to be a good predictor for the LODF [22].

3.3. Impact of community structures

Besides the effect of distance on failure spreading analysed in the last section, community structure is also known to play an important role. We analyse this effect exemplarily for the Scandinavian grid whose community structure we present in figure 7(a). The communities are determined using spectral graph partitioning [51–53] based on the sign of the eigenvector $\boldsymbol{v}_2$ of the Laplacian matrix corresponding to the second smallest eigenvalue λ_2, also referred to as Fiedler eigenvalue [31]. The affiliation of a node to one of the two communities is encoded in red and blue colouring representing the value of the eigenvector at the respective node, such that two nodes belong to the same community if they have the same colour. As shown in figure 7(b), we evaluate ξ for the case were both trigger links are located in the same community (right, green boxplots) and different communities (left, blue boxplots). Overall, we observe that community structure plays an important role for the overall strength of collective effects; if both links, are located in the same community, the collectivity parameter is on average three orders of magnitude larger evaluated in terms of the respective median.

Community structure affects ξ directly and indirectly through the distance, because the distance between two links tends to be higher if they are in different communities. To account for this effect, we also present the collectivity parameter ξ in dependence of the rerouting distance (c, cf equation (14)) and the geodesic distance (d). We consistently observe a stronger collectivity parameter for both distance measures when the trigger links

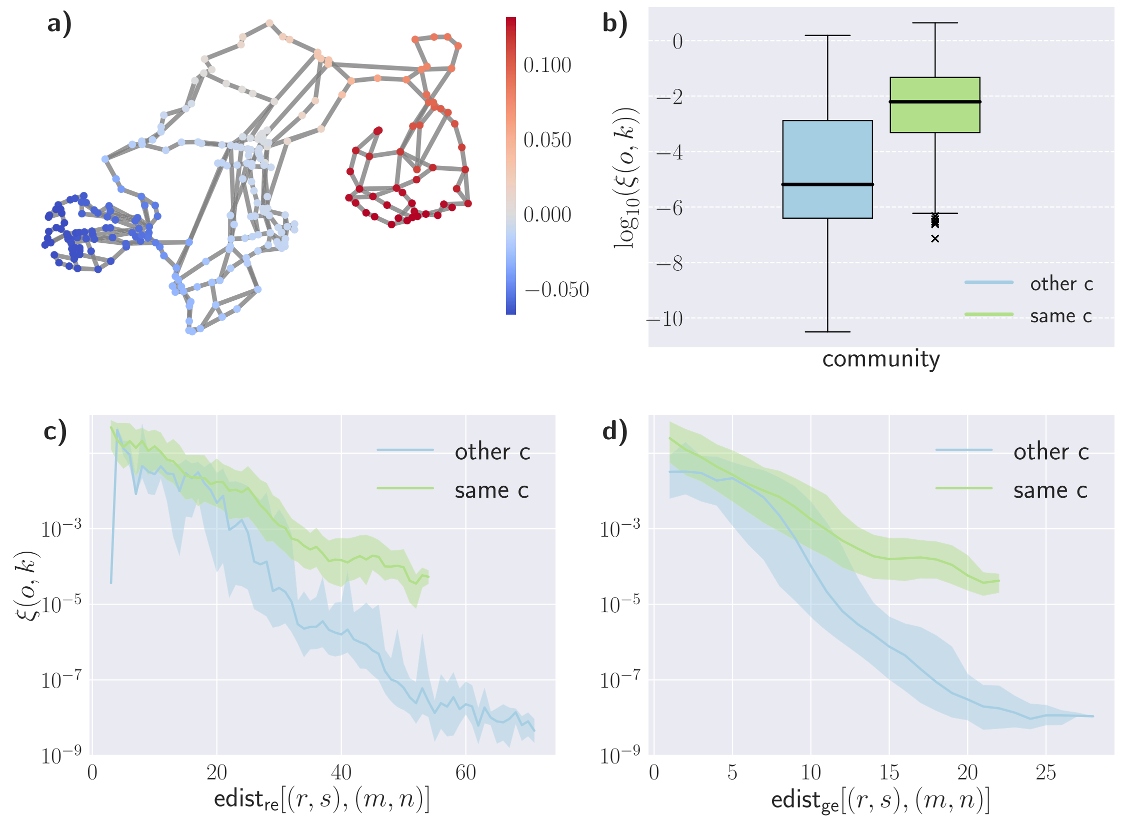

Figure 7. Location of the two trigger links in the same community increases the collectivity parameter ξ. (a) Fiedler vector colour coded from blue (negative values) to red (positive value) reveals community structure in the Scandinavian grid. (b) Logarithmic collectivity parameter ξ (boxplots) evaluated for two failing links located in the same (left, blue) and in different communities (right, green) for the Scandinavian power grid shown in panel (a). Collective effects are stronger if the two links are located in the same community. The whiskers cover all data points that fall outside of the quantiles by at most 150% of the inter-quantile range, while crosses show the remaining outliers [54]. (c), (d) Collectivity parameter ξ consistently yields stronger values for two trigger links in the same community (green, top) compared to two trigger links contained in different communities (blue, bottom) when plotted against (c) the rerouting distance and (d) the geodesic distance. Lines indicate median values whereas shading represents 0.75 and 0.25 quantiles. For all plots, links with collectivity parameter almost zero ($\xi < 10^{-12}$) were excluded from the analysis.

are contained in the same communitiy (green, upper curve) compared to the case of trigger links contained in different communities (blue, lower curve). We thus conclude that community structure also determines if two links interact strongly collectively.

4. Extension to arbitrary link failures

Now that we analysed the simultaneous failure of two links in detail, we will extend the theoretical framework to more than two links failing. To this end, we will derive a formula that describes this type of contingencies on a nodal level and perform a continuum limit that is valid for infinitely large regular grids.

4.1. Derivation of generalized LODFs

Now consider the simultaneous outage of K links $\{l_1, \ldots, l_K\}$ with $K < M$. Then we define the projection matrix from the space of all links onto the subset of failing links $\boldsymbol{\mathcal{P}}$: $\mathbb{R}^M \to \mathbb{R}^K$ via

$$\mathcal{P}_{kl} = \delta_{l,l_k},$$

where δ_{l,l_k} denotes the Kronecker delta. Consequently, let $\boldsymbol{D}$: $\mathbb{R}^K \to \mathbb{R}^N$ be the projection of the node-edge-incidence matrix $\boldsymbol{I}$: $\mathbb{R}^M \to \mathbb{R}^N$ onto the subset of failing links which reads as

$$D_{nk} = (\boldsymbol{I}\boldsymbol{\mathcal{P}}^\top)_{nk} = I_{n,l_k}, \text{ for } k \in \{1, 2, \ldots, K\}.$$

With this definition the columns of this matrix are the vectors $\boldsymbol{d}_{l_k}$ introduced in the definition of the LODF, as per equation (6). As a reminder, they are defined by their entries being $+1$ at the node corresponding to the start of the respective failing link, -1 at the node corresponding to the end of the failing link and 0 otherwise. Furthermore, we define the projected branch reactance matrix $\boldsymbol{B}_{\mathrm{out}}$: $\mathbb{R}^K \to \mathbb{R}^K$ by

$$\boldsymbol{B}_{\rm out} = \boldsymbol{\mathcal{P}}\boldsymbol{B}_{\rm d}\boldsymbol{\mathcal{P}}^\top = {\rm diag}(b_{l_1}, b_{l_2}, \ldots, b_{l_K}).$$

Using this matrix, we can also project the vector of all initial flows onto the failing links defined by

$$\boldsymbol{F}_{\rm out}^{(0)} = \boldsymbol{\mathcal{P}}\boldsymbol{F}^{(0)} = \boldsymbol{B}_{\rm out}\boldsymbol{D}^\top\boldsymbol{\theta} = (F_{l_1}^{(0)}\ F_{l_2}^{(0)}\ \cdots\ F_{l_K}^{(0)})^\top.$$

The failure of multiple links may be regarded as a perturbation to the graph Laplacian $\boldsymbol{B}$ in the same way as for a single link, see [22],

$$\hat{\boldsymbol{B}} = \boldsymbol{B} + \Delta\boldsymbol{B},$$

where $\hat{\boldsymbol{B}}$ is the graph Laplacian after the failure of the K links. The corresponding perturbation matrix $\Delta\boldsymbol{B}$ may then also be expressed using the projected node-edge-incidence matrix as

$$\Delta\boldsymbol{B} = -\boldsymbol{D}\boldsymbol{B}_{\rm out}\boldsymbol{D}^\top. \tag{15}$$

In addition to that, the failure causes the nodal potentials to change,

$$\hat{\boldsymbol{\theta}} = \boldsymbol{\theta} + \boldsymbol{\psi},$$

where $\boldsymbol{\psi}$ is a vector of the changes in angles. Using the continuity equation (3) in the new grid,

$$\boldsymbol{P} = (\boldsymbol{B} + \Delta\boldsymbol{B})(\boldsymbol{\theta} + \boldsymbol{\psi}),$$

subtracting from it the current balance for the old grid, and applying the Moore–Penrose-pseudoinverse to the resulting equation, the change in potential is calculated as

$$\boldsymbol{\psi} = -(\boldsymbol{B} + \Delta\boldsymbol{B})^\dagger\Delta\boldsymbol{B}\boldsymbol{\theta}. \tag{16}$$

We can simplify this expression by making use of the Woodbury matrix identity [55] and arrive at the final result,

$$\boldsymbol{\psi} = \boldsymbol{B}^\dagger\boldsymbol{D}(\mathbf{1}_K - \mathfrak{P})^{-1}\boldsymbol{F}_{\rm out}^{(0)}. \tag{17}$$

Here, we defined a projection of the PTDF matrix onto the subset of failing links $\mathfrak{P}\colon \mathbb{R}^K \to \mathbb{R}^K$ given by

$$\mathfrak{P} \coloneqq \boldsymbol{B}_{\rm out}\boldsymbol{D}^\top\boldsymbol{B}^\dagger\boldsymbol{D} = \boldsymbol{\mathcal{P}}\ \textbf{PTDF}\ \boldsymbol{\mathcal{P}}^\top.$$

The change in phase angles may then be used to calculate the flow changes by making use of equation (1). The vector of flow changes reads as

$$\Delta\boldsymbol{F} = \boldsymbol{B}_{\rm d}\boldsymbol{I}^\top\boldsymbol{B}^\dagger\boldsymbol{D}(\mathbf{1}_K - \mathfrak{P})^{-1}\boldsymbol{F}_{\rm out}^{(0)}. \tag{18}$$

In principle, we may now make use of equation (18) to calculate the flow changes after an arbitrary number of simultaneous contingencies. The immediate insight into the structure of the contingency problem from this equation is, however, limited. We will thus try to gain more insight into the interplay of multiple outages by rearranging the equation.

Starting with equation (17) expressing the change of voltage phase angles after the failure $\boldsymbol{\psi}$, we can derive the following Poisson-like equation similar to the case of a single link failure as presented in equation (7)

$$\boldsymbol{B}\boldsymbol{\psi} = \boldsymbol{D}\boldsymbol{F}^{(K)}, \tag{19}$$

where we defined the vector of flows weighted by the dipole source terms

$$\boldsymbol{F}^{(K)} \coloneqq (\mathbf{1}_K - \mathfrak{P})^{-1}\boldsymbol{F}_{\rm out}^{(0)}.$$

We may thus rewrite equation (19) for the change in nodal potentials as follows, making the correspondence to the Poisson equation more apparent;

$$\boldsymbol{B}\boldsymbol{\psi} = \sum_{k=1}^{K}\boldsymbol{q}_k, \tag{20}$$

with the dipole sources

$$\boldsymbol{q}_k = \boldsymbol{d}_k F_k^{(K)}$$

and the $\boldsymbol{d}_k$ being the rows of $\boldsymbol{D}$, see also section 2.2. In addition to this expression, we can derive an analogous equation for the graph $\hat{G}$ from which all the failing links have been removed. Simply plugging equation (15) into equation (16), we arrive at the following equation

$$\hat{\boldsymbol{B}}\boldsymbol{\psi} = \boldsymbol{D}\boldsymbol{F}_{\rm out}^{(0)}.$$

We are thus left with a *discrete Poisson equation* with potential $\boldsymbol{\psi}$, which is analogous to the result obtained in our previous work [22], sections 3 and 4 for a single failing link. Instead of a single dipole source this equation is governed by K dipole sources. However, this equation differs from the naive approach obtained by simply superposing single dipole sources. To see this, consider the case of $K = 2$ link failures. As we have seen in the previous section 3, collective effects play an important role in the interaction of the two links. In this case, a simple superposition of two dipoles results in the equation

$$\boldsymbol{B}\psi^{\text{naive}} = \boldsymbol{q}_1^{\text{naive}} + \boldsymbol{q}_2^{\text{naive}},$$

where we defined the dipole sources resulting from the naive approach

$$\boldsymbol{q}_1^{\text{naive}} = \boldsymbol{d}_1(1 - \mathfrak{P}_{11})^{-1}F_{\text{out},1}^{(0)},$$
$$\boldsymbol{q}_2^{\text{naive}} = \boldsymbol{d}_2(1 - \mathfrak{P}_{22})^{-1}F_{\text{out},2}^{(0)}.$$

On the other hand, using the exact approach in equation (20), the actual dipole sources read as

$$\boldsymbol{q}_1 = \boldsymbol{d}_1([(\boldsymbol{1}_2 - \mathfrak{P})^{-1}]_{11}F_{\text{out},1}^{(0)} + [(\boldsymbol{1}_2 - \mathfrak{P})^{-1}]_{12}F_{\text{out},2}^{(0)}),$$
$$\boldsymbol{q}_2 = \boldsymbol{d}_2([(\boldsymbol{1}_2 - \mathfrak{P})^{-1}]_{21}F_{\text{out},1}^{(0)} + (\boldsymbol{1}_2 - \mathfrak{P})^{-1}]_{22}F_{\text{out},2}^{(0)}).$$

The naive approach thus underestimates the interaction between the two dipole sources encoded in the matrix inverse $(\boldsymbol{1}_2 - \mathfrak{P})^{-1}$, as discussed in detail in section 3. In the following paragraph, we will demonstrate, however, that this collective effect can be neglected in the continuum limit, thus making the naive superposition approach exact in that case.

4.2. Continuum limit for regular square lattice

We will now demonstrate how one may derive an exact formula for the potential changes after an arbitrary number of link failures for the setup of an infinite square lattice extending on our previous work [22]. Consider the elementary example of a regular square lattice embedded in the plane $\mathbb{R}^2$. Label all nodes by their positions $\boldsymbol{r} = (x, y)$ and let the lattice spacing be denoted by h. Now introduce continuous functions ψ and b such that $\psi(x, y)$ is the potential of the node at (x, y) and $b(x + h/2, y)$ is the weight of the link connecting the two nodes at (x, y) and $(x + h, y)$ and analogously for two nodes connected in y-direction.

For a small lattice spacing $h \to 0$ and an infinitely large grid, the left-hand side of the Poisson equation (20) evaluated at position (x, y) can be written in a continuum version as [22]

$$(\boldsymbol{B}\psi)(x, y) = -h^2\boldsymbol{\nabla}(b(x, y)\boldsymbol{\nabla}\psi) + \mathcal{O}(h^3). \tag{21}$$

Then, the flow changes according to equation (18) are given by

$$\Delta\boldsymbol{F}(x, y) = b(x, y)\boldsymbol{\nabla}\psi(x, y),$$

where $\Delta\boldsymbol{F}$ refers to the change in flow due to the link failures here and should not be confused with the continuous Laplace operator.

The right-hand side of the Poisson equation (20) may be calculated similarly noting that at most $2K$ nodes contribute when K links fail. Let any failing link $l_k \in \{l_1, l_2, \ldots, l_K\}$ connect the nodes s_k and t_k with positions (x_{s_k}, y_{s_k}) and (x_{t_k}, y_{t_k}) respectively. The discrete version of a single addend on the right-hand side reads:

$$\boldsymbol{q}_k = [(\boldsymbol{1}_K - \mathfrak{P})^{-1}\boldsymbol{F}_{\text{out}}^{(0)}]_k\boldsymbol{d}_k$$
$$= \boldsymbol{d}_k\textstyle\sum_{i=1}^{K}[(\boldsymbol{1}_K - \mathfrak{P})^{-1}]_{ki}F_{\text{out},i}^{(0)}.$$

We will now show how this equation may be interpreted in the continuum version. First, the flow on a failing link before the outage $F_{l_i}^{(0)}$ may be calculated as

$$F_{l_i}^{(0)} \;\hat{=}\; h\boldsymbol{F}^{(0)}(x_{s_i}, y_{s_i}) + \mathcal{O}(h^2),$$

where $\boldsymbol{F}^{(0)}(x_{s_i}, y_{s_i}) = b(x_{s_i}, y_{s_i})\boldsymbol{\nabla}\theta(x_{s_i}, y_{s_i})$ is the continuum version of the flow before the outage. Second, the vector $\boldsymbol{d}_k$ can be formally interpreted in terms of the two-dimensional delta function $\delta(x, y)$ and reads for a link l_k oriented in x-direction

$$\boldsymbol{d}_k \;\hat{=}\; h\partial_x\delta(x - x_{s_k}, y - y_{s_k}) + \mathcal{O}(h^2).$$

For links oriented in y-direction, we simply replace ∂_x by ∂_y. Finally, in order to calculate the continuum version of the inverse matrix elements $[(\boldsymbol{1}_K - \mathfrak{P})^{-1}]_{ki}$ for two arbitrarily chosen links l_k and l_i, assume without loss of generality that both links are oriented in x-direction and that a continuum version $b^\dagger$ of the Green's function $\boldsymbol{B}^\dagger$ exists. Then, the elements of the projected PTDF matrix may be calculated as

$$\begin{aligned}\mathfrak{P}_{ki} &= b_k\boldsymbol{d}_k^\top\boldsymbol{B}^\dagger\boldsymbol{d}_i\\ &\hat{=} h^2 b(x_{s_k}, y_{s_k})\int\partial_y\delta(x - x_{s_k}, y - y_{s_k})b^\dagger(x, y)\partial_x\delta(x - x_{s_i}, y - y_{s_i})\mathrm{d}x\mathrm{d}y\\ &= \delta_{ki}\left[h^2 b(x_{s_k}, y_{s_k})\frac{\partial^2 b^\dagger(x_{s_k}, y_{s_k})}{\partial x\partial y} + \mathcal{O}(h^3)\right].\end{aligned}$$

All off-diagonal entries are zero due to the delta functions' different arguments. Importantly, this observation is independent of the orientation of the two links under consideration. The inverted matrix is thus diagonal and can be calculated as

$$[(\mathbf{1}_K - \mathfrak{P})^{-1}]_{ki} \triangleq (1 - \mathfrak{P}_{ki})^{-1} = (1 - \mathcal{O}(h^2))^{-1}.$$

In total, we obtain after expanding the entire expression to lowest order in the continuum limit

$$q_k(x, y) = h^2 \boldsymbol{F}^{(0)}(x_{s_i}, y_{s_i})^\top \boldsymbol{\nabla}\delta(x - x_{s_k}, y - y_{s_k}) + \mathcal{O}(h^3). \tag{22}$$

We can now formally divide the left-hand side (21) and the right-hand side (22) by h^2 and take the limit $h \to 0$ to obtain the final continuum limit of the Poisson equation,

$$\boldsymbol{\nabla}(b(x, y)\boldsymbol{\nabla}\psi) = -\sum_{k=1}^{M} \boldsymbol{q}_k^\top \boldsymbol{\nabla}\delta(x - x_{s_k}, y - y_{s_k}), \tag{23}$$

where the source terms are $\boldsymbol{q}_k(x_{s_k}, y_{s_k}) = \boldsymbol{F}^{(0)}(x_{s_k}, y_{s_k})$, the unperturbed current field.

If the link weights are homogeneous, $b(x, y) = b$, the solution is given by the superposition of K two-dimensional dipole fields

$$\psi(\boldsymbol{r}) = \sum_{k=1}^{K} \frac{\boldsymbol{q}_k(\boldsymbol{r} - \boldsymbol{r}_k)}{||\boldsymbol{r} - \boldsymbol{r}_k||^2}, \tag{24}$$

$$\Delta\boldsymbol{F}(\boldsymbol{r}) = b \cdot \sum_{k=1}^{K} \left(\frac{\boldsymbol{q}_k}{||\boldsymbol{r} - \boldsymbol{r}_k||^2} - 2(\boldsymbol{r} - \boldsymbol{r}_k)\frac{\boldsymbol{q}_k \cdot (\boldsymbol{r} - \boldsymbol{r}_k)}{||\boldsymbol{r} - \boldsymbol{r}_k||^4} \right). \tag{25}$$

We thus obtain a fully analytic solution in the continuum limit. This solution reveals that in homogeneous lattices the effects of multiple outages are given by the superposition of single outages.

5. Conclusion and outlook

In this article, we have shown that multiple link failures can lead to fundamentally different impacts than expected from a naive superposition of single link failures. We have also established a parameter, namely the predictor $\Lambda(o, k)$, quantifying in which cases these effects have to be taken into account. In addition to that, we have extended on previous work demonstrating that multiple link failures correspond to the overlay of correspondingly many single dipoles in infinitely large regular grids, thus allowing for a description similar to single link failures in this case. However, the strength of the effective dipoles is strongly determined by the collective effects, i.e. the interplay of the failing links. Our results demonstrate that further understanding of multiple link failures is an important task for the development and security of future power systems, thus helping to understand in which cases additional link shutdowns can help or counteract overall system security.

We have presented several elementary examples which demonstrate the counterintuitive behaviour of collective effects in some particular cases. Furthermore, we have shown that additional outages can be beneficial for the overall grid loading, thus presenting another occurence of Braess' paradox in power grids. In addition to that, we have shown that collective effects may lead to a sign inversion of flow direction compared to the individual failure of each single link. Both phenomena are potentially of high relevance when operating power grids as they might help to resolve situations where a single link fails or a redispatch occurs. However, further work should be dedicated to understanding and predicting these particular collective effects on a more fundamental theoretical basis.

The predictor for collective flow changes introduced in this manuscript allows for an easier understanding of when collective effects become considerably important. Mostly, collective effects are small, they only become relevant in cases where both failing links have a strong effect on one another. This is for example the case if the links are in close proximity or if they are both bottlenecks. Conversely, this implies that the intuition developed for single link failures may in many cases also be applied to study multiple link failures if the possibility of collective effects is kept in mind.

Distance between the two failing links seems to play an important role for the overall collective effects. Previous work has addressed the role of distance in flow changes for single link failures where in particular the rerouting distance was shown to be a decisive measure in predicting the flow changes [22]. In predicting collective effects, the rerouting distance between the failing links still seems to be an important quantity but not to the same degree as it is important for single link failures. In the future, it would be interesting to extend the rerouting distance to more than two links which could potentially also predict collective effects better.

Further work should address the role particular flow patterns play in more detail. In the approach used here, we abstracted from individual flow patterns and focused on topological aspects. This should be a good approximation for many cases, in particular when dealing with large power grids. However, there might be cases in which specific lines are nearly always more heavily loaded than other ones which should imply a more important contribution of such lines to collective effects.

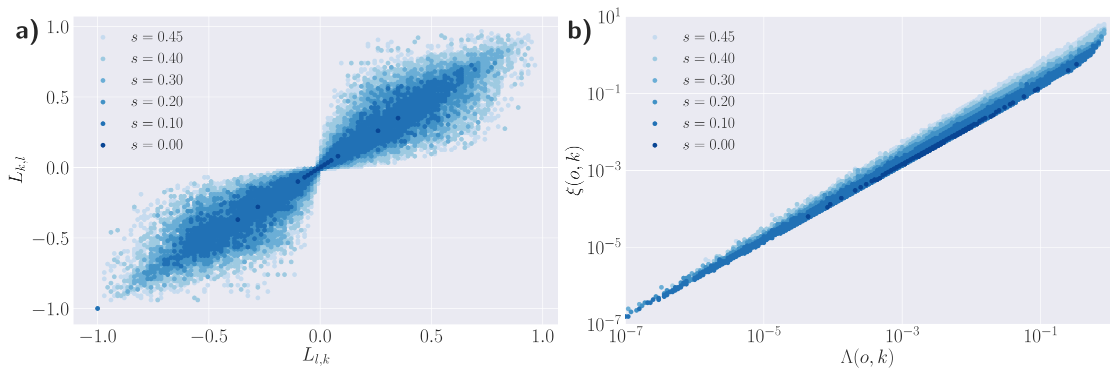

Figure A1. With increasing degree of sparsity s in square grids, the LODFs become less symmetric. (a) Whereas we observe fully symmetric LODFs in a periodic square grid without any edges removed $s = 0$, removing edges increases the degree of asymmetry continuously up to $s = 0.45$. This is due to the fact that the entries of the inverse Laplacian $\boldsymbol{B}^{\dagger}$ become increasingly heterogeneous with more edges removed. (b) The degree of asymmetry in LODFs induced by increased sparsity in periodic square grids also influences the performance of the predictor for collective effects $\Lambda(o, k)$; it performs almost perfectly for a periodic square grid with no links removed and homogeneous edge weights, where also LODFs are perfectly symmetric. With increasing degree of sparsity, the performance reduces slightly, see also table 1. For very high values of the predictor, the prefactor $\mathcal{L}(o,\ k)$ dominates leading to the change from a linear scaling to a nonlinear scaling for these values.

Acknowledgments

We gratefully acknowledge support from the German Federal Ministry of Education and Research (BMBF grant no. 03EK3055B) and the Helmholtz Association (via the joint initiative 'Energy System 2050—a contribution of the research field energy' and the grant no. VH-NG-1025 to D W).

Appendix A. Symmetry of LODFs

The LODFs according to equation (6) are given by

$$L_{l,k} = b_l \frac{\boldsymbol{d}_l^{\top} \boldsymbol{B}^{\dagger} \boldsymbol{d}_k}{1 - b_k \boldsymbol{d}_k^{\top} \boldsymbol{B}^{\dagger} \boldsymbol{d}_k}.$$

In this section, we will study the symmetry of this matrix in terms of interchanging the role of the failing link k and the link l on which flow changes are monitored. This symmetry describes the extend to which the flow change on one link l due to another, failing link k corresponds to the opposite flow change on link k if link l fails instead and thus provides a measure of symmetry for the whole network. In particular, we analyse how the matrix becomes asymmetric with an increasing degree of asymmetry in the links surrounding the monitored, and failing link. This explains why both LODFs are important for predicting the strength of collective effects in the predictor (13).

If we assume homogeneous edge weights for the time being such that $\boldsymbol{B}_d = b \cdot \mathbf{1}$, we notice that the numerator in equation (6) is symmetric with respect to interchanging l and k. This numerator is also referred to as PTDF in power engineering [11]. The symmetry can be seen by taking the matrix transpose of the expression

$$(\boldsymbol{d}_l^{\top} \boldsymbol{B}^{\dagger} \boldsymbol{d}_k)^{\top} = \boldsymbol{d}_k^{\top} (\boldsymbol{B}^{\dagger})^{\top} \boldsymbol{d}_l = \boldsymbol{d}_k^{\top} \boldsymbol{B}^{\dagger} \boldsymbol{d}_l.$$

On the other hand, the denominator is non-symmetric even in the case that line susceptances are uniform, as it reads as $1 - b \cdot \boldsymbol{d}_k^{\top} \boldsymbol{B}^{\dagger} \boldsymbol{d}_k$ for $L_{l,k}$ and $1 - b \cdot \boldsymbol{d}_l^{\top} \boldsymbol{B}^{\dagger} \boldsymbol{d}_l$ for $L_{k,l}$ thus encoding the importance of the link that fails. The LODFs are only completely symmetric if both links have not only the same weights, but also the same topological structure around them. This is for example the case for the periodic square grid, see figure A1, dark blue dots corresponding to $s = 0$ in the legend. We analysed this expression in detail in our previous publication [22] and showed that it can be predicted using the minimum cut that disconnects the two vertices k_1 and k_2. In the case of uniformly distributed line susceptances, this expression simply reduces to the well-studied resistance distance [56, 57]. Thus, the asymmetry in LODFs is encoded in both, the asymmetry in connectivity in the network, i.e. the variance in the node degree, and the asymmetry in the line susceptances.

In addition to the observation made before, we can notice that the mutual LODFs $L_{l,k}$ and $L_{k,l}$ will always have the same sign. This is due to the fact that as discussed above, the numerator is the same for both expressions. On the other hand, the denominator is always positive or equal to zero

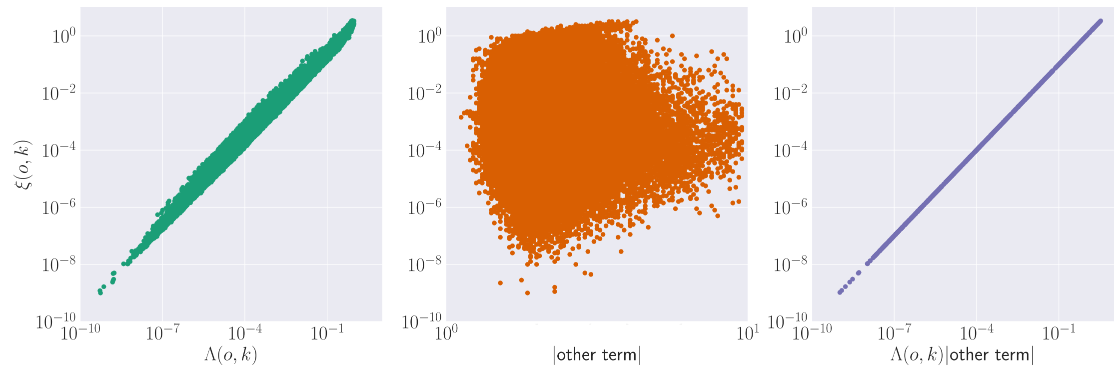

Figure B1. (a) The predictor $\Lambda(o, k)$ performs well predicting the collectivity parameter ξ for the test case 'pegase1354' [46]. Predictor and collectivity parameter are plotted on a log–log-scale. (b) The remaining term does not show any visible correlation with the collectivity parameter ξ. (c) The product of both terms exactly reproduces the collectivity parameter ξ as expected.

$$1 - b_k \boldsymbol{d}_k^\top \boldsymbol{B}^\dagger \boldsymbol{d}_k \geqslant 0.$$

Whereas this is not obvious from the above expression, it follows from the definition of the PTDFs given by $b_k \boldsymbol{d}_k^\top \boldsymbol{B}^\dagger \boldsymbol{d}_k = \mathrm{PTDF}_{k,k} \in [-1,\ 1]$ [11]. Therefore we may conclude that mutual LODFs always have the same sign.

In figure A1, we demonstrate how asymmetry in LODFs arises with an increasing degree in inhomogeneity in the nodal degrees for a periodic square lattice from which we randomly remove a fraction s of its total number of links according to the procedure described in [22]. In this figure, we plot $L_{l,k}$ against $L_{k,l}$ for all possible combinations of links l and k. Starting at $s = 0$ for a perfect periodic square lattice with 50×50 nodes, the LODF is perfectly symmetric (dark blue dots). With increasing degree of sparsity $s \in \{0.1, 0.2, 0.3, 0.4, 0.45\}$ (dots from dark blue to light blue), we observe an increasing spread of the LODFs indicating an increasing degree of asymmetry in the LODFs.

Appendix B. A predictor for collective effects

To support the choice of the predictor for collective effects, consider figures B1(a) and (b). We show the predictor $\Lambda(o, k)$ and the remaining term, referred to as 'other term' in the figure, for all possible combinations of trigger links for the test case 'pegase1354' [46]. The remaining term is constructed by factoring out the predictor $\Lambda(o, k)$ defined in equation (13) from the expression for the collectivity parameter $\xi(o, k)$ given in equation (12) and assuming both LODFs $L_{k,o}$ and $L_{o,k}$ to be non-zero,

$$\xi(o,\ k) = \Lambda(o,\ k)\cdot \mathcal{L}(o,\ k)\left(\sum_{l=1}^{M}\left(L_{l,o}\mathrm{sign}(L_{o,k})\sqrt{\frac{L_{o,k}}{L_{k,o}}} + L_{l,k}\sqrt{L_{k,o}L_{o,k}}\right)^2 + \left(L_{l,k}\mathrm{sign}(L_{k,o})\sqrt{\frac{L_{k,o}}{L_{o,k}}} + L_{l,o}\sqrt{L_{k,o}L_{o,k}}\right)^2\right)^{1/2}.$$

Applying the approximations discussed in section 3 to this equation, this expression reduces to the following equation,

$$\xi(o,\ k) \approx \Lambda(o,\ k)\left(\frac{L_{o,k}}{L_{k,o}}\sum_{l=1}^{M}(L_{l,o})^2 + \frac{L_{k,o}}{L_{o,k}}\sum_{l=1}^{M}(L_{l,k})^2\right)^{1/2}.$$

Based on this expression, we discuss certain limiting cases which explain the performance of the predictor. Assume that $L_{o,k}$ is very small keeping $L_{k,o}$ constant and much larger than $L_{o,k}$. In this case, the expression is dominated by $\xi(o,\ k) \approx |L_{k,o}|(\sum_{l=1}^{M}(L_{l,k})^2)^{1/2}$ which is predicted well by $L_{k,o}$. Performing the same approximation for small values of $L_{k,o}$ keeping $L_{o,k}$ constant and large, the expression is well predicted by $L_{o,k}$. For this reason, we need to keep both values in order to predict the overall collective effects. On the other hand, one can easily check that the approximation is equally valid if both LODFs are of the same order.

Importantly, considering an arbitrary ℓ^p-norm instead, the conclusions differ only slightly. An ℓ^p norm $||\boldsymbol{x}||_p$ of an arbitrary vector $\boldsymbol{x} \in \mathbb{R}^N$ is defined as

$$\|\boldsymbol{x}\|_p = \left(\sum_{i=1}^{N}|x_i|^p\right)^{1/p}.$$

For the predictor, we then have

$$\xi_p(o, k) = \Lambda(o, k)\cdot\mathcal{L}(o, k)\left(\sum_{l=1}^{M}\left|L_{l,o}\mathrm{sign}(L_{o,k})\sqrt{\frac{L_{o,k}}{L_{k,o}}} + L_{l,k}\sqrt{L_{k,o}L_{o,k}}\right|^p\right.$$
$$\left. + \left|L_{l,k}\mathrm{sign}(L_{k,o})\sqrt{\frac{L_{k,o}}{L_{o,k}}} + L_{l,o}\sqrt{L_{k,o}L_{o,k}}\right|^p\right)^{1/p}.$$

Therefore, the general expression to be considered does not change fundamentally when calculating the ℓ^p norm instead.

Appendix C. Proof of theorem 1

Proof. The collectivity parameter defined by equation (12) reads as

$$\xi(o, k) = \mathcal{L}(o, k)\left[\sum_{l=1}^{M}((L_{l,o} + L_{l,k}L_{k,o})L_{o,k})^2 + ((L_{l,k} + L_{l,o}L_{o,k})L_{k,o})^2\right]^{1/2}.$$

We will demonstrate that $\xi(o, k)$ is bounded from below by $\Lambda(o, k)$. First, since all addends in the sum are greater than zero, neglecting any or all of them will not increase the expression's value. We can thus choose the addends with $l = o$ and $l = k$. The expression then reads as

$$\begin{aligned}\xi(o, k) &= \mathcal{L}(o, k)\left[\sum_{l=1}^{M}((L_{l,o} + L_{l,k}L_{k,o})L_{o,k})^2 + ((L_{l,k} + L_{l,o}L_{o,k})L_{k,o})^2\right]^{1/2}\\ &\geqslant \mathcal{L}(o, k)[((L_{o,o} + L_{o,k}L_{k,o})L_{o,k})^2 + ((L_{k,k} + L_{k,o}L_{o,k})L_{k,o})^2]^{1/2}\\ &\overset{!}{\geqslant} \Lambda(o, k).\end{aligned}$$

Now we can make use of the fact that $L_{o,o} = L_{k,k} = -1$. In order to show that this expression is bounded from below by $\Lambda(o, k)$, we can square both sides of the inequality since all expressions considered here are positive. This yields

$$\begin{aligned}\xi(o, k)^2 &\geqslant \mathcal{L}(o, k)^2[((L_{o,k}L_{k,o} - 1)L_{o,k})^2 + ((L_{k,o}L_{o,k} - 1)L_{k,o})^2]\\ &= \mathcal{L}(o, k)^2\frac{1}{\mathcal{L}(o, k)^2}(L_{o,k}^2 + L_{k,o}^2)\\ &= (L_{o,k}^2 + L_{k,o}^2) \geqslant \Lambda(o, k)^2.\end{aligned}$$

The last inequality follows from the following considerations

$$\begin{aligned}&(L_{o,k} - L_{k,o})^2 + L_{o,k}L_{k,o} > 0\\ \Leftrightarrow\ &L_{o,k}^2 + L_{k,o}^2 - L_{o,k}L_{k,o} > 0\\ &\Leftrightarrow L_{o,k}^2 + L_{k,o}^2 > L_{o,k}L_{k,o} = \Lambda(o, k)^2,\end{aligned}$$

which completes the proof. For $L_{o,k}, L_{k,o} \neq 0$, the inequality is strict. □

Note that the proof makes use of the fact that $L_{o,o} = -1$ for all links o, but we expect the statement to hold even without this assumption.

ORCID iDs

Franz Kaiser https://orcid.org/0000-0002-7089-2249
Julius Strake https://orcid.org/0000-0002-1683-0397
Dirk Witthaut https://orcid.org/0000-0002-3623-5341

References

[1] Motter A E 2004 *Phys. Rev. Lett.* **93** 098701
[2] Crucitti P, Latora V and Marchiori M 2004 *Phys. Rev.* E **69** 045104
[3] Albert R, Jeong H and Barabási A L 2000 *Nature* **406** 378–82
[4] Atputharajah A and Saha T K 2009 Power system blackouts—literature review *2009 Int. Conf. on Industrial and Information Systems (ICIIS)* pp 460–5

[5] Pourbeik P, Kundur P and Taylor C 2006 *IEEE Power Energy Mag.* **4** 22–9
[6] Yang Y, Nishikawa T and Motter A E 2017 *Science* **358** eaan3184
[7] Schäfer B, Witthaut D, Timme M and Latora V 2018 *Nat. Commun.* **9** 1975
[8] Shih A Y, Blinder P, Tsai P S, Friedman B, Stanley G, Lyden P D and Kleinfeld D 2013 *Nat. Neurosci.* **16** 55–63
[9] Schaffer C B, Friedman B, Nishimura N, Schroeder L F, Tsai P S, Ebner F F, Lyden P D and Kleinfeld D 2006 *PLoS Biol.* **4** e22
[10] Brodribb T J, Bienaimé D and Marmottant P 2016 *Proc. Natl Acad. Sci.* **113** 4865–9
[11] Wood A J, Wollenberg B F and Sheblé G B 2014 *Power Generation, Operation and Control* (New York: Wiley)
[12] North American Electric Reliability Corporation 2007 Top-0042: Transmission operations https://nerc.com/files/TOP-004-2.pdf
[13] Campbell R J 2012 Weather-related power outages and electric system resiliency Congressional Research Service https://fas.org/sgp/crs/misc/R42696.pdf
[14] Clarfeld L A, Hines P D H, Hernandez E M and Eppstein M J 2019 arXiv:1901.03304 [physics]
[15] Turitsyn K S and Kaplunovich P A 2013 Fast algorithm for n-2 contingency problem *2013 46th Hawaii Int. Conf. on System Sciences* pp 2161–6
[16] Kaplunovich P A and Turitsyn K S 2013 Fast selection of n-2 contingencies for online security assessment *2013 IEEE Power Energy Society General Meeting* pp 1–5
[17] Davis C M and Overbye T J 2011 *IEEE Trans. Power Syst.* **26** 1294–301
[18] Weckesser T and Cutsem T V 2018 Identifying plausible harmful n-k contingencies: A practical approach based on dynamic simulations *2018 Power Systems Computation Conf. (PSCC)* pp 1–8
[19] Guler T, Gross G and Liu M 2007 *IEEE Trans. Power Syst.* **22** 879–81
[20] Guo J, Fu Y, Li Z and Shahidehpour M 2009 *IEEE Trans. Power Syst.* **24** 1633–4
[21] Soltan S and Zussman G 2016 Quantifying the effect of k-line failures in power grids *2016 IEEE Power and Energy Society General Meeting (PESGM)* pp 1–5
[22] Strake J, Kaiser F, Basiri F, Ronellenfitsch H and Witthaut D 2019 *New J. Phys.* **21** 053009
[23] Purchala K, Meeus L, Dommelen D V and Belmans R 2005 Usefulness of dc power flow for active power flow analysis *IEEE Power Engineering Society General Meeting* vol 1, pp 454–9
[24] Van Hertem D, Verboomen J, Purchala K, Belmans R and Kling W 2006 Usefulness of dc power flow for active power flow analysis with flow controlling devices *The 8th IEEE Int. Conf. on AC and DC Power Transmission* pp 58–62
[25] Bollobás B 1998 *Modern Graph Theory* (*Graduate Texts in Mathematics* vol 184) (Berlin: Springer)
[26] Dörfler F, Simpson-Porco J W and Bullo F 2018 *Proc. IEEE* **106** 977–1005
[27] Kirchhoff G 1847 *Ann. Phys.* **148** 497–508
[28] Hwang N and Houghtalen R 1996 *Fundamentals of Hydraulic Engineering Systems* (Upper Saddle River, NJ: Prentice Hall)
[29] Díaz S, González J and Mínguez R 2016 *J. Water Resour. Plann. Manage.* **142** 04015071
[30] Katifori E, Szöllősi G J and Magnasco M O 2010 *Phys. Rev. Lett.* **104** 048704
[31] Newman M E J 2010 *Networks—An Introduction* (Oxford: Oxford University Press)
[32] Merris R 1994 *Linear Algebr. Appl.* **197–198** 143–76
[33] Van Mieghem P, Devriendt K and Cetinay H 2017 *Phys. Rev.* E **96** 032311
[34] Moore E H 1920 *Bull. Am. Math. Soc.* **26** 394–5
[35] Biggs N 1997 *Bull. London Math. Soc.* **29** 641–82
[36] Ronellenfitsch H, Manik D, Hörsch J, Brown T and Witthaut D 2017 *IEEE Trans. Power Syst.* **32** 4060–8
[37] Labavic D, Suciu R, Meyer-Ortmanns H and Kettemann S 2014 *Eur. Phys. J. Spec. Top.* **223** 2517–25
[38] Witthaut D, Rohden M, Zhang X, Hallerberg S and Timme M 2016 *Phys. Rev. Lett.* **116** 138701
[39] Braess D 1969 *Unternehmensforschung Oper. Res.* **12** 258–68
[40] Witthaut D and Timme M 2012 *New J. Phys.* **14** 083036
[41] Witthaut D and Timme M 2013 *Eur. Phys. J.* B **86** 377
[42] Tchuisseu E B T, Gomila D, Colet P, Witthaut D, Timme M and Schäfer B 2018 *New J. Phys.* **20** 083005
[43] Witthaut D and Timme M 2015 *Phys. Rev.* E **92** 032809
[44] Hörsch J, Hofmann F, Schlachtberger D and Brown T 2018 *Energy Strategy Rev.* **22** 207–15
[45] Zimmerman R D, Murillo-Sanchez C E and Thomas R J 2011 *IEEE Trans. Power Syst.* **26** 12
[46] Josz C, Fliscounakis S, Maeght J and Panciatici P 2016 arXiv:1603.01533 [math]
[47] Meyer-Huebner N, Suriyah M R, Leibfried T, Slednev V, Bertsch V, Fichtner W, Gerstner P, Schick M and Heuveline V 2015 Time constrained optimal power flow calculations on the german power grid *Int. ETG Congress 2015; Die Energiewende—Blueprints for the New Energy Age* pp 1–7
[48] Mahmood M, Meyer-Huebner N, Sunyah M and Leibfried T 2016 Load flow analysis of the german high voltage transmission grid in the year 2023 *2016 5th Int. Conf. on Informatics, Electronics and Vision (ICIEV)* pp 129–32
[49] Kettemann S 2016 *Phys. Rev.* E **94** 062311
[50] Jung D and Kettemann S 2016 *Phys. Rev.* E **94** 012307
[51] Radicchi F, Castellano C, Cecconi F, Loreto V and Parisi D 2004 *Proc. Natl Acad. Sci.* **101** 2658–63
[52] Newman M E J 2006 *Proc. Natl Acad. Sci.* **103** 8577–82
[53] Newman M E J 2012 *Nat. Phys.* **8** 25–31
[54] Dekking F M, Kraaikamp C, Lopuhaä H P and Meester L E 2005 *A Modern Introduction to Probability and Statistics: Understanding Why and How* (Berlin: Springer)
[55] Woodbury M A 1950 *Memorandum Rep.* **42** 106
[56] Klein D and Randic M 1993 *J. Math. Chem.* **12** 81
[57] Xiao W and Gutman I 2003 *Theor. Chem. Acc.* **110** 284–9

2.3. C) Universal statistics of redistribution factors and large scale cascades in power grids

[3] Kaiser, F. & Witthaut, D. Universal Statistics of Redistribution Factors and Large Scale Cascades in Power Grids. *IEEE Access* **9,** 67364–67378. doi:10.1109/ACCESS.2021.3076892 (2021).

IEEE Access
Multidisciplinary ⋮ Rapid Review ⋮ Open Access Journal

Received April 20, 2021, accepted April 28, 2021, date of publication April 30, 2021, date of current version May 12, 2021.

Digital Object Identifier 10.1109/ACCESS.2021.3076892

Universal Statistics of Redistribution Factors and Large Scale Cascades in Power Grids

FRANZ KAISER AND DIRK WITTHAUT
Forschungszentrum Jülich, Institute for Energy and Climate Research–Systems Analysis and Technology Evaluation (IEK-STE), 52428 Jülich, Germany
Institute for Theoretical Physics, University of Cologne, 50937 Köln, Germany

Corresponding author: Franz Kaiser (f.kaiser@fz-juelich.de)

This work was supported in part by the German Federal Ministry of Education and Research [Bundesministerium für Bildung und Forschung (BMBF)] under Grant 03EK3055B, and in part by the Helmholtz Association through the joint initiative Energy System 2050–A Contribution of the Research Field Energy and through the Grant VH-NG-1025.

ABSTRACT Cascades of failures are among the biggest threats to supply networks such as power grids: An initially failing element may trigger the failure of other elements, thereby eventually causing the entire network to collapse. Here, we analyse the statistics of Line Outage Distribution Factors (LODFs), which describe the rerouting of electric power flows after a line failure. In particular, we demonstrate that absolute LODFs are approximately log-normally distributed throughout network topologies. We then illustrate that this log-normal distribution of redistribution factors results in a heavy tailed distribution of outage sizes in a simplified, stochastic cascade model over a certain range of parameters. This cascade model extends previous stochastic cascade models by adding more realistic redistribution mechanisms as well as including more realistic initial trigger events. Our results demonstrate that the statistics of redistribution factors is a fundamental trait throughout different networks and presents a possible explanation for the vast occurrence of heavy tailed distributions in real-world reanalyses of power outage sizes.

INDEX TERMS Transmission lines, network theory (graphs), graph theory, cascading failures, transmission line outages, power grids.

I. INTRODUCTION

In our daily lives, we depend on a reliable supply with electrical power. Large scale power outages can have a catastrophic impact on society, economy and other infrastructure networks as recent examples demonstrate [1], [2]. Remarkably, empirical reanalyses of historic power grid blackouts have revealed the scale-free nature of outage sizes: large scale outages are not rare, but the size of outage sizes decays algebraically [3], [4]. The reason for this scaling is still not fully understood, but different possible explanations have been put forward [5]–[8].

Blackouts are in most cases initiated by the failure of a single or only very few transmission or generation elements which cause the failure of other elements and so forth – eventually leading to a cascade of failures where a large part of the system breaks down [9]. A single step in a cascade is essentially governed by two variables: The initial flows in the network and the flow rerouting in the network after a failure. The latter may be compactly summarised in terms of the Line Outage Distribution Factors (LODFs) which arise from a linearisation of power flows and relate the initial flows to the flow changes after a failure [10]. Remarkably, LODFs are a purely topological property of a network, i.e. they do not depend on the power injections. Thus, a key indicator of a given network's resilience is their distribution. Previous work on spatial aspects of flow rerouting has mainly focused on a microscopic perspective on link failures, studying different properties of individual failures such as the distribution of flow changes after line outages [11] with a particular focus on the decay with distance [12]–[16]. Here, we adopt a statistical perspective on the distribution of LODFs for an entire network which yields a structural indicator of a complex network's resilience with respect to perturbations.

The access to real-world power grid data such as network topologies is limited due to the sensitive nature of the information – power grids are considered to be a critical infrastructure. However, recent efforts increase the availability of openly available power grid datasets that typically rely on OpenStreetMap [17]–[19]. Different synthetic power grids that are based on real-world grids have been designed for power flow studies [20]–[24]. In addition to that, different algorithms have been developed to generate synthetic networks that display the main topological properties of real

The associate editor coordinating the review of this manuscript and approving it for publication was Giambattista Gruosso.

world power grids [25]–[29]. Besides, several studies have addressed the statistical properties of real world transmission grids and the corresponding transmission lines [30].

In this article, we analyse the distributions of LODFs for various real-world and synthetic grids systematically. To the best of our knowledge, this is the first systematic analysis of the distribution of LODFs for different real-world and synthetic transmission grids. In fact, the distribution of LODFs is purely based on the network topology and may thus be considered as a network observable, similarly to the degree distribution or betweenness measures that have been considered in previous analyses of power grids [26], [31], [32].

II. LINEAR FLOW NETWORKS AND LINE OUTAGE DISTRIBUTION FACTORS

In most cases, cascades of failures are well-described by a linearised approach to the power flow equations known as the DC approximation. Here, we briefly review the mathematical aspects and the derivation of LODFS using a more general language that applies to power grids as well as to other types of networks to facilitate a translation of our results.

A. THEORY OF LINEAR FLOW NETWORKS

Consider a linear flow network on a simple, connected graph $G(E, V)$ with $\mathcal{M} = |E|$ edges and $\mathcal{N} = |V|$ vertices. Assume that each edge $\ell = (j, k)$ in the graph is assigned a weight $b_\ell \in \mathbb{R}$ and each node has a potential $\vartheta_n \in \mathbb{R}, n \in \{1, \ldots, \mathcal{N}\}$. In a linear flow network, the flow $F_\ell \in \mathbb{R}, \ell \in \{1, \ldots, \mathcal{M}\}$, on an edge $\ell = (j, k)$ connecting nodes $j, k \in V$ scales linearly with the potential drop along the line such that [14]

$$F_\ell = b_\ell \cdot (\vartheta_j - \vartheta_k). \tag{1}$$

Next, we assign an orientation to each edge $\ell = (j, k)$ in the graph and say that the edge is oriented from node j to node k such that $F_\ell > 0$ is a flow from node j to node k and a negative sign indicates a flow in the opposite direction. This setup applies for example to power transmission grids [14], [34], where F_ℓ is the flow of real power on a transmission line ℓ, ϑ_n denotes the nodal voltage phase angle and b_ℓ is the line susceptance. This corresponds to the so-called 'DC approximation' of AC power flows that typically offers a good description of the power flows if lines are lossless and not too heavily loaded [34]. An equivalent description is also used for hydraulic and vascular networks [35], where F_ℓ is the flow of water or nutrients, ϑ_n is the local pressure and b_ℓ the edge's capacity.

Now assume that each node m has an in- or outflow p_m. Then the edge flows are related to the inflows by Kirchhoff's current law

$$p_m = \sum_{\ell \in \Gamma(m)} F_\ell. \tag{2}$$

Here, $\Gamma(m) \subset E(G)$ is the set of all edges connected to vertex m with each edge sorted according to its orientation. Combining Eqs. (1) and (2), we arrive at the following set of equations

$$p_m = \sum_{\ell \in \Gamma(m)} b_\ell \cdot (\vartheta_m - \vartheta_k), \tag{3}$$

where the sum runs again over all edges $\ell = (m, k)$ whose start point or terminal end is node m. As a next step, we can define the graph Laplacian $\boldsymbol{L} \in \mathbb{R}^{\mathcal{N} \times \mathcal{N}}$ that encodes the topology of the graph in a compact form and is defined by its entries as follows [36]

$$L_{jk} = \begin{cases} -b_\ell & \text{if } \ell = (j, k) \in E(G) \\ \sum_{m \in \Gamma(j)} b_m & \text{if } j = k \\ 0 & \text{otherwise.} \end{cases} \tag{4}$$

We will see in the following that this matrix is crucial to describe link failures in linear flow networks. To write the above set of equations more compactly, we define a vector of potentials $\boldsymbol{\vartheta} = (\vartheta_1, \ldots, \vartheta_\mathcal{N})^\top \in \mathbb{R}^N$ and a vector of in- and outflows $\boldsymbol{p} = (p_1, \ldots, p_\mathcal{N})^\top \in \mathbb{R}^N$ to write Equation (3) compactly [14], [37]

$$\boldsymbol{L}\boldsymbol{\vartheta} = \boldsymbol{p}. \tag{5}$$

The nodal potentials are thus subject to a Poisson-type equations. To solve for the vector of potentials, this equation needs to be inverted. However, the Laplacian always has a vanishing eigenvalue $\lambda_1 = 0$ and is thus not invertible. This problem is typically overcome by making use of the matrix's *Moore-Penrose pseudoinverse* $\boldsymbol{L}^\dagger$ which has properties similar to the actual matrix inverse [38], [39].

B. SINGLE LINK FAILURES IN LINEAR FLOW NETWORKS

Assume that a single link e fails that carries the initial flow $F_e^{(0)}$. Then the flow change ΔF_ℓ on another link ℓ can be calculated as follows [10], [14]

$$\Delta F_\ell = \mathrm{LODF}_{\ell,e} F_e^{(0)}.$$

The factor $\mathrm{LODF}_{\ell,e}$ connecting the initial flows and the flow changes is known as *Line Outage Distribution Factor* (LODF) and measures the change in flow on a link ℓ when a link e fails. Thus, the flow F_ℓ on a link ℓ after the failure may be calculated as

$$F_\ell = F_\ell^{(0)} + \Delta F_\ell = F_\ell^{(0)} + \mathrm{LODF}_{\ell,e} F_e^{(0)}. \tag{6}$$

Summarising the LODF for all possible failing links e and all possible monitoring links ℓ, we can define an LODF matrix, $\mathrm{LODF} \in \mathbb{R}^{\mathcal{M} \times \mathcal{M}}$. Its entries may then be expressed in a purely topological manner [10], [14]

$$\mathrm{LODF}_{\ell,e} = b_\ell \frac{\boldsymbol{q}_\ell^t \boldsymbol{L}^\dagger \boldsymbol{q}_e}{1 - b_\ell \boldsymbol{q}_e^t \boldsymbol{L}^\dagger \boldsymbol{q}_e}. \tag{7}$$

Here, $e = (r, s) \in E(G)$ is an edge, $\boldsymbol{q}_e \in \mathbb{R}^\mathcal{N}$ is a vector with entry one at position r and entry minus one at position s and t denotes the transposed vector. The LODF assumes values between minus one and one, $\mathrm{LODF}_{\ell,e} \in [-1, 1]$, i.e. only the amount of flow that was present initially may be redistributed. The diagonal elements are typically set to minus one for consistency, i.e. $\mathrm{LODF}_{\ell,\ell} = -1, \forall \ell \in E(G)$. Furthermore, there are several cases where the LODF vanishes, for example if two parts of the network are only connected via a bridge [14], [40] or via a network isolator [37], [41].

III. LOGARITHMIC LODFs ARE APPROXIMATELY NORMALLY DISTRIBUTED

In this section, we analyse the distribution of LODFs for real-world and synthetic power grids in detail. We use the term distribution synonymous to the probability density function here and in the following. Since the absolute LODFs are bounded by unity, they may be naturally studied on a logarithmic scale. For this analysis, we neglect the cases where the LODF vanishes since these are typically rare in large networks. We also do not consider the diagonal elements $\mathrm{LODF}_{\ell,\ell} = -1$. The distribution of LODFs is mainly governed by two factors: Firstly, the distribution of edge weights b which we denote by P_B in the following. Secondly, it is governed the distribution of entries of the Laplacian matrix's Moore-Penrose pseudoinverse $\boldsymbol{L}^\dagger$ which we denote by $P_{L^\dagger}$. Importantly, the former distribution is in some sense incorporated into the latter one since the off-diagonal elements of the Laplacian matrix are again (summed) elements from the distribution of weights P_B.

The study of the elements of random matrices has led to the development of random matrix theory. Typically, the distribution of these elements is analysed using its eigenvalues [42]. On the other hand, research has addressed the spectra of complex networks as encoded in the graph's adjacency matrix or its Laplacian matrix [43]–[45]. The Moore-Penrose pseudoinverse $\boldsymbol{L}^\dagger$ - as the actual inverse - has eigenvalues inverse to the eigenvalues of the Laplacian $\boldsymbol{L}$ except for the zero eigenvalue. Thus, diagonalizing both matrices using the eigenvalues $\lambda_1 = 0, \lambda_2, \ldots \lambda_\mathcal{N}$ ordered by magnitude and corresponding eigenvectors $\vec{v}_1 = \vec{1}/\sqrt{\mathcal{N}}, \vec{v}_2, \ldots, \vec{v}_\mathcal{N}$ of the Laplacian matrix, we may write [39]

$$\boldsymbol{L} = (\vec{v}_1, \vec{v}_2, \ldots, \vec{v}_\mathcal{N}) \begin{pmatrix} 0 & 0 & \ldots & 0 \\ 0 & \lambda_2 & \ldots & 0 \\ \ldots & \ldots & \ldots & \ldots \\ \ldots & \ldots & \ldots & \lambda_\mathcal{N} \end{pmatrix} \begin{pmatrix} \vec{v}_1^\top \\ \vec{v}_2^\top \\ \ldots \\ \vec{v}_\mathcal{N}^\top \end{pmatrix}$$

$$\Rightarrow \boldsymbol{L}^\dagger = (\vec{v}_1, \vec{v}_2, \ldots, \vec{v}_\mathcal{N}) \begin{pmatrix} 0 & 0 & \ldots & 0 \\ 0 & \lambda_2^{-1} & \ldots & 0 \\ \ldots & \ldots & \ldots & \ldots \\ \ldots & \ldots & \ldots & \lambda_\mathcal{N}^{-1} \end{pmatrix} \begin{pmatrix} \vec{v}_1^\top \\ \vec{v}_2^\top \\ \ldots \\ \vec{v}_\mathcal{N}^\top \end{pmatrix}.$$

Understanding the spectrum of the graph Laplacian and thus the topology of the underlying graph is key to understanding the spectrum of the pseudo-inverse $\boldsymbol{L}^\dagger$ and thus the distribution of LODFs. In addition to that, the Laplacian eigenvalues determine the dynamical properties of power grids [46].

A. DISTRIBUTION OF LINE SUSCEPTANCES

In this section, we analyse the distribution of transmission line susceptances P_B. It has been demonstrated that the distribution of line reactances x_e follows approximately an exponential distribution $P_x(x_e) = \lambda e^{-\lambda x_e}$ by making use of the Kullback-Leibler divergence [30]. The DC approximation of the power flow is based on the assumption that transmission lines are purely inductive [34]. In this case, the line reactance and susceptance are related by $b_e \approx -x_e^{-1}$, i.e. we can obtain the distribution of line susceptances by taking the inverse distribution of the distribution of line reactances P_x. We will make use of this fact to compare the distribution of LODFs in networks with unit line susceptances and suceptances following an inverse exponential distribution.

B. DISTRIBUTION OF INITIAL LINE LOADINGS

Here, we consider the distribution of line flows as it appears in a dispatch of the open energy system model 'PyPSA-EUR' which models the European energy system [33]. To this end, we evaluate the absolute flow $|F_i^{(0)}|$ on a line i and divide it by the maximal flow $F_i^{\max}$ on the line to evaluate the relative loading

$$L_i^{(0)} = \frac{|F_i^{(0)}|}{F_i^{\max}}. \tag{8}$$

We then examine the statistics of relative loadings for a dispatch spanning an entire year in hourly resolution. The network has 4428 lines and 3037 nodes and, as a result, there is a detailed statistics of relative loadings. For the given dataset, the flow on a line is limited to 80% of the maximal flow to incorporate a security constraint.

We find that the relative loadings are approximately exponentially distributed, i.e. they are described by the probability density function $P_L(L^{(0)}) = \lambda e^{-\lambda L^{(0)}}$ (see Figure 1). The maximum likelihood estimator for an exponential distribution is calculated as

$$\hat{\lambda} = \langle L^{(0)} \rangle^{-1}, \tag{9}$$

where $\langle \cdot \rangle$ denotes the average. For the empirical distribution of line loadings in 'PyPSA-EUR', we observe an estimate of $\hat{\lambda} \approx 5$ with small monthly variations.

C. DISTRIBUTION OF LODFS

To preprocess the data for evaluating the logarithmic distribution, we first create the set of all pairs of edges for which the LODF has non-zero entries

$$\mathcal{L} = \{\ell, k \in E(G) | \mathrm{LODF}_{\ell,e} \neq 0 \wedge \ell \neq k\}.$$

In Figure 2, we present the distribution of LODFs for two different topologies: The MATPOWER test case '2736sp' that represents the Polish power grid during peak conditions in summer of 2004 [21] (top row) and a 100×100 square grid with unit line susceptances (bottom row). Whereas the distribution of logarithmic LODFs closely corresponds to a log-normal distribution (a,d) with significantly stronger tails in both cases (b,e), the distribution of Laplacian eigenvalues differs greatly for the two topologies (c,f). Thus, there is a surprising similarity between the distribution of LODFs for vastly different topologies. Here, Gaussian fits are based

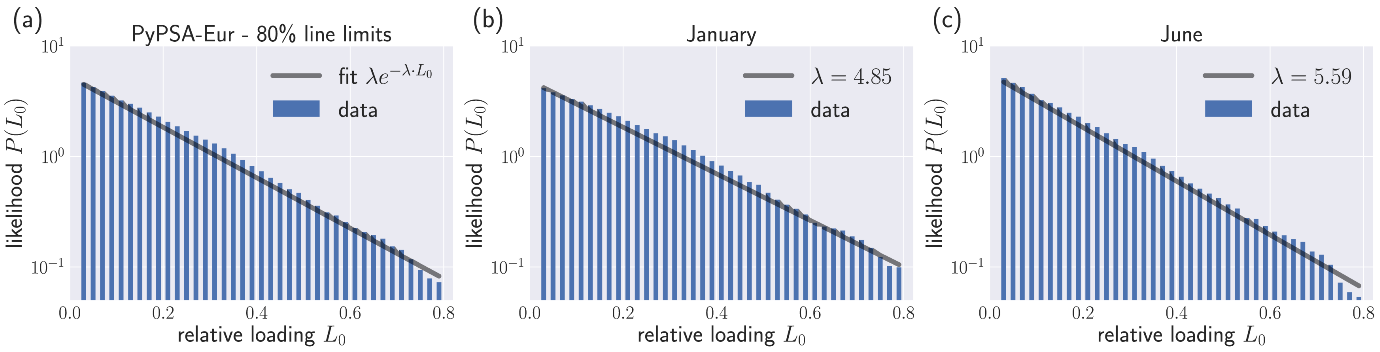

FIGURE 1. Distribution of absolute line loadings in a high-resolution energy system model. (a) We evaluate the magnitude of the relative line loadings $L^{(0)}$ over a year of demand and generation patterns in hourly resolution occurring in the European energy system model 'PyPSA-EUR' [33] described in table 1. The dispatch is calculated via an optimal power flow algorithm including a security margin, $|L_i^{(0)}| \leq L^{\text{thresh}} = 0.8$, as a proxy for $N-1$ security (cf. Eq. (17)). The probability density function is well approximated by an exponential distribution with parameter $\hat{\lambda} \approx 5.26$ estimated using the maximum likelihood estimator in Eq. (9). (b,c) The given dataset contains a weak seasonal effect, displaying slightly higher relative loading in winter months (b) than in summer months (c) that result in a steeper exponent of the distribution of relative loadings in the latter case.

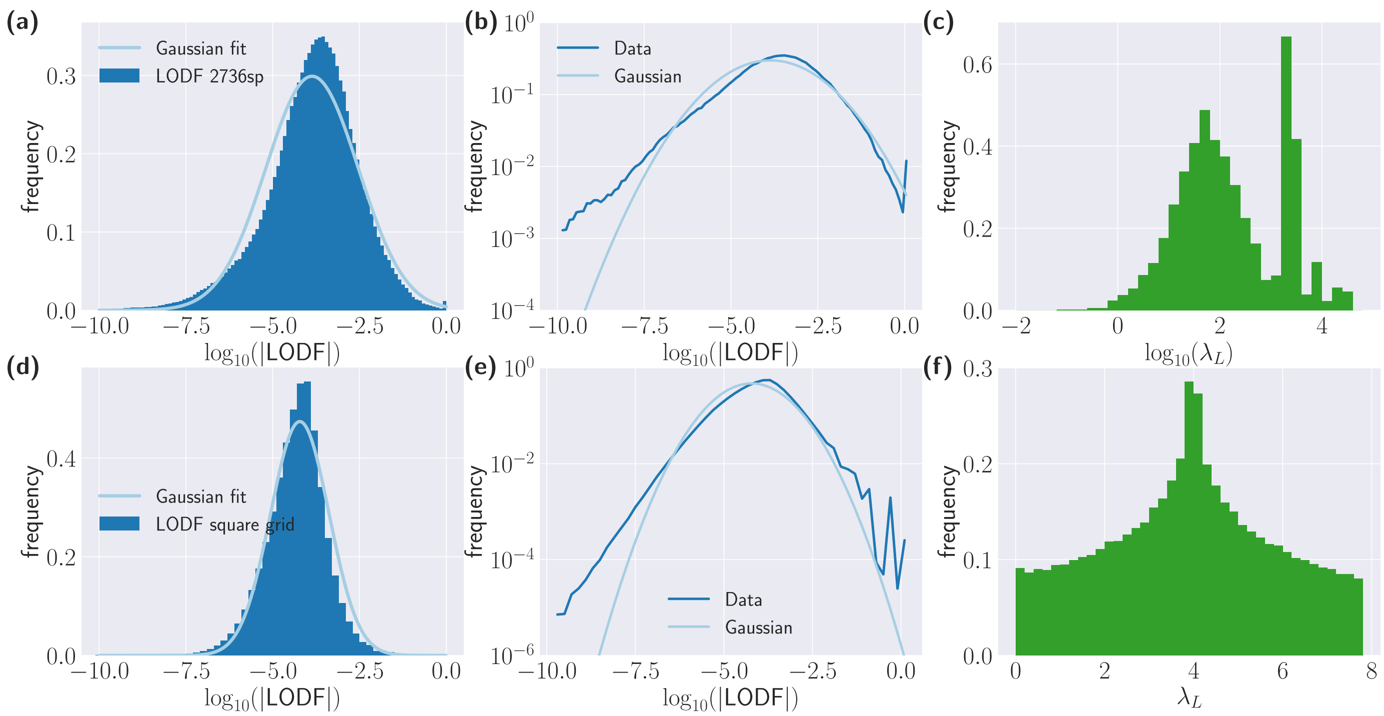

FIGURE 2. The distribution of absolute LODFs is approximately log-normal for both real-world and artificial network structure. We analyse the distribution of LODFs and Laplacian eigenvalues for (a-c) the real-world power grid '2736sp' that corresponds to the Polish power grid during summer peak 2004 with edge weights representing the link susceptance and (d-f) a regular square lattice of size 100 × 100 with unit edge weights. (a,d) The distribution of LODFs (dark blue histogram) follows approximately a log-normal distribution (light blue) except for the tails at low values for both the '2736sp' grid (a) and the square grid (d). (b,e) The heavy tails (dark blue) – as compared to the Gaussian distribution (light blue) – become clearly visible when analysing the distributions on a log-log scale. (c,f) Even though the distributions of LODFs have a similar shape for both networks, the spectra of the Graph Laplacian differ significantly between the two topologies. For the real-world grid, the distribution is clearly bimodal and spreads over 4 orders of magnitude – note the logarithmic x-scale. In contrast, for the regular lattice, the distribution differs considerably and spans only 1 order of magnitude. Thus, although both quantities are purely topological, the similarity in the log-normal distribution of LODFs cannot easily be understood in terms of the Laplacian spectrum alone.

on the maximum likelihood estimates of the mean μ_{LN} and variance σ^2_{LN} for a log-normal distribution which are given by [47]

$$\hat{\mu}_{\text{LN}} = \frac{\sum_{i=1}^{N} \log(X_i)}{N}, \tag{10}$$

$$\hat{\sigma}^2_{\text{LN}} = \frac{\sum_{i=1}^{N} \left(\log(X_i) - \hat{\mu}_{\text{LN}}\right)^2}{N}, \tag{11}$$

where X_i are the realizations of the random variable "X" under consideration.

To further examine the characteristics of the distribution of LODFs, we systematically evaluate different moments of the underlying distribution for different grids [48]. First, we calculate the mean of the absolute logarithmic LODFs

$$\mu = \frac{1}{|\mathcal{L}|} \sum_{\ell,k \in \mathcal{L}} \log(|\text{LODF}_{\ell,e}|). \tag{12}$$

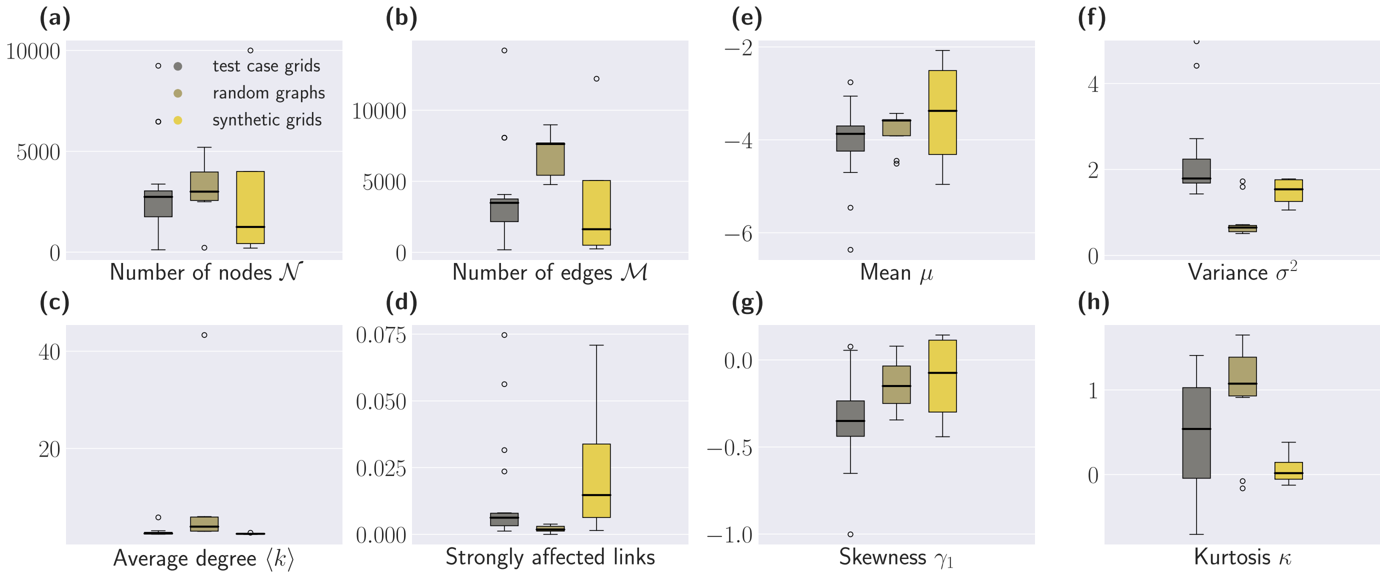

FIGURE 3. **Statistical properties of the logarithmic LODF distribution and the network structure for synthetic grids, real world grids and random graphs. We analyse 11 random graphs, 4 synthetic grids and 20 test case grids that are inspired or correspond to real world grids (see tables 1 and 2 for details). (a,b,c) Attributes of the network topologies underlying the grids: The topological attributes span a wide range in terms of their number of nodes $\mathcal{N}$, their number of edges $\mathcal{M}$ and their average degree $\langle k \rangle$. (c,d,g,h) We analyse the first, second, third and fourth moment (see sec. III) of different real-world, random and synthetic grids (see tables 1 and 2). Although the grids are of different sizes (d) and different connectivities (g,h), the statistical properties are similar: the (logarithmic) mean lies approximately at $\mu \approx -4$, the variance around $\sigma^2 \approx 2$ except for the random grids which are much more regular, the skewness γ_1 is slightly negative and the excess kurtosis κ positive for almost all grids, indicating that large deviations are more likely than for Gaussian distributions. Test cases are taken from Refs. [20]–[24], [33] (see table 1 for details).**

Second, we calculate the variance σ^2

$$\sigma^2 = \frac{1}{|\mathcal{L}|} \sum_{\ell,k\in\mathcal{L}} (\log(|\mathrm{LODF}_{\ell,e}|) - \mu)^2. \qquad (13)$$

To specifically compare the distributions to log-normal distributions, we also calculate the normalized third and fourth moment, namely the skewness γ_1

$$\gamma_1 = \frac{1}{|\mathcal{L}|} \sum_{\ell,k\in\mathcal{L}} \left(\frac{\log(|\mathrm{LODF}_{\ell,e}|) - \mu}{\sigma} \right)^3, \qquad (14)$$

and the excess kurtosis

$$\kappa = \frac{1}{|\mathcal{L}|} \sum_{\ell,k\in\mathcal{L}} \left(\frac{\log(|\mathrm{LODF}_{\ell,e}|) - \mu}{\sigma} \right)^4 - 3. \qquad (15)$$

The skewness vanishes for a Gaussian distribution due to its symmetry. The excess kurtosis measures the deviation from a kurtosis of three observed for the Gaussian distribution and indicates if rare events happen more ($\kappa > 0$) or less ($\kappa < 0$) frequently than for a Gaussian distribution [49].

Finally, we make use of another indicator that is related to the upper tail of the distribution of LODFs and gives a measure of a grid's vulnerability: We calculate the relative number of LODFs exceeding a threshold of 0.1

$$\frac{\left|\{\ell, k \in \mathcal{L} \,|\, |\mathrm{LODF}_{\ell,e}| > 0.1\}\right|}{\mathcal{M}(\mathcal{M}-1)}, \qquad (16)$$

and refer to this measure as the 'strongly affected links'. The measure may be interpreted as the probability that the failure of a randomly chosen link results in the increase of the flow on another randomly chosen link by more than 10% of the flow carried initially by the failing link.

We analyse these properties of the distribution of logarithmic LODFs for different power grids in Figure 3(e-h). In particular, we consider test case grids that are based on power system test cases and synthetic grids that are created using a synthetic power grid algorithm (see Table 1 in the Appendix). To get a better statistics and benchmark the results, we also consider random graphs that are generated either from regular grids or random network models (see Table 2 in the Appendix).

All grids are similar in terms of their average degree $\langle k \rangle$ except for the random graphs that – in some cases – display a much higher number of edges which results in larger average degrees (see panels (a-c)). The mean of the logarithmic absolute LODFs is $\overline{\mu} = -3.91$ for all grids tested and the variance is $\overline{\sigma^2} = 1.73$, except for the random graphs where a much lower value of a variance close to unity may be observed. This is likely due to the fact that the random graphs considered here are in most cases very regular in terms of the graph degree and thus much more homogeneous than realistic power grids. The skewness is negative for almost all distributions tested with a mean skewness of $\overline{\gamma_1} = -0.26$ evaluated over all grids, indicating distributions with a peak located at values larger than the mean value. For the excess kurtosis, we observe almost exclusively values larger than zero, in most cases exceeding unity, with a mean of $\overline{\kappa} = 0.60$. This indicates that almost all LODF distributions have heavier tails than a log-normal distribution. In terms of the network vulnerability as measured by the strongly affected links, we observe a mean of $9.5 \cdot 10^{-3}$ with the synthetic grid models displaying a much higher vulnerability with a mean of $2.5 \cdot 10^{-2}$. Thus, we conclude that the distribution of LODFs displays a high degree of similarity for different power grids and synthetic networks. In Figures 7,8,9 and 10 in the Appendix, we show the actual statistics of LODFs for 24 test case grids and synthetic grids, for which aggregated statistical properties are summarized in Figure 3.

IV. APPLICATION: A CASCADE MODEL WITH LOG-NORMAL LOAD REDISTRIBUTION

Based on our finding that LODFs are log-normally distributed over a wide range of topologies, we will now discuss a simple probabilistic cascade model that incorporates this effect. To this end, we will study a modification of the 'CASCADE' model due to Dobson *et al.* [7], [8].

A. THE CASCADE MODEL AND A POSSIBLE EXTENSION

Consider a simple network consisting of N components. Initially, each component j is assumed to have a load $L_j^{(0)}$ that is smaller than its maximal load $L_j^{\max}$. If a component exceeds its maximal load, the component breaks down and a redistribution mechanism is triggered that distributes the load to the other components in the network. These may in turn trigger further breakdowns, resulting in a cascade of breakdowns that eventually stops if the network has broken down entirely or if no further overloads occur.

In the original setup by Dobson *et al.*, the initial loads $L^{(0)}$ are drawn from a uniform distribution, i.e. $L^{(0)} \in \mathcal{U}(L^{\min}, L^{\text{thresh}})$ where $L^{\min}$ is the minimum loading in the distribution and $L^{\text{thresh}} \leq L^{\max}$ is the threshold loading, potentially incorporating a security margin to the maximal loading $L^{\max}$. Redistribution after failures is incorporated by increasing the load on all components in the network by a constant addend D_1. Furthermore, the cascade of failures is triggered by an initial shock that increases the load on all components by an added D_0. Thus, the loading on a component i in a network after the failure of M components is calculated as

$$L_i^{(1)} = L_i^{(0)} + D_0 + MD_1.$$

Choosing critical values of these parameters that depend on the system size N, Dobson *et al.* demonstrate that this model yields a power law of the number of components failing – in close correspondence with power laws of blackout sizes observed empirically in historic power blackout sizes [3].

Inspired by the redistribution of real power flow after line failures in power transmission grids as described in Eq. (6), we suggest extending this mechanism as follows:

1. Security margin and distribution of line loadings: Typically, real-world power grids are operated using the $N-1$ security criterion which means that upon the failure of any transmission or generation element, no other line becomes overloaded. This is approximately taken into account in the model by a security margin

$$L^{\text{thresh}} = c \cdot L^{\max} \tag{17}$$

which limits the maximal initial loading to a share $c \in [0, 1]$ of the maximal $L^{\max}$. In the following, we simply set $L^{\max} = 1$ for all components such that our model emulates relative loading of components.

We then consider either a uniform distribution of component loadings as in the original 'CASCADE' model such $L^{(0)} \in \mathcal{U}(-L^{\text{thresh}}, L^{\text{thresh}})$, or an exponential distribution that we have found empirically in a large-scale energy system model (see Sec. III-B). In the latter case, we initially draw all loadings from an exponential distribution $P_L(L^{(0)}) = \lambda e^{-\lambda L^{(0)}}$ with $\lambda \approx 5$. If the initial loading on an element i exceeds the threshold value, we simply reset it with the threshold value $L_i^{(0)} := L^{\text{thresh}}$.

2. Redistribution after failures: Inspired by our findings on log-normally distributed LODFs, we adopt a redistribution scheme after failures in the spirit of the redistribution of real power flow on transmission lines as introduced in Eq. (6). Assume that the component k with initial load $L_k^{(0)}$ fails. We suggest updating the load on another component i by

$$L_i^{(1)} = L_i^{(0)} + (-1)^m \mathfrak{L} L_k^{(0)}, \quad \forall i \neq k \in \{1, \ldots, N\}. \tag{18}$$

Here, $\mathfrak{L} \in \text{Lognormal}(\mu, \sigma)$ is drawn from a log-normal distribution with mean μ and standard deviation σ and m assumes the values one or zero with equal probability to model the randomly chosen sign. This update rule thus corresponds to a probabilistic version of the update rule (6) if we insert the relative loadings (see Eq. (8)) and assume that all lines have the same maximal loading. Thus, our model adopts the redistribution scheme observed in power transmission grids in the DC approximation and takes into account the fact

Algorithm 1 Stochastic cascade model

```
% Randomly choose initial trigger element k ∈ {1, ..., N} and add it to set of failing components C
C ← k
repeat
  has_overloads ← 0
  % Redistribute load from all failed components:
  for all remaining components do
    % Update ∀i ∈ {1, ..., N}, i ∉ C:
    L_i ← L_i + Σ_{k∈C} (−1)^m 𝔏 L_k,   .
    % Reset set of current failures and remove failed components
    C ← {}
    if |L_i| > L^max then
      Add i to set of current failures C
      has_overloads ← 1
    end if
  end for
until has_overloads = 0
```

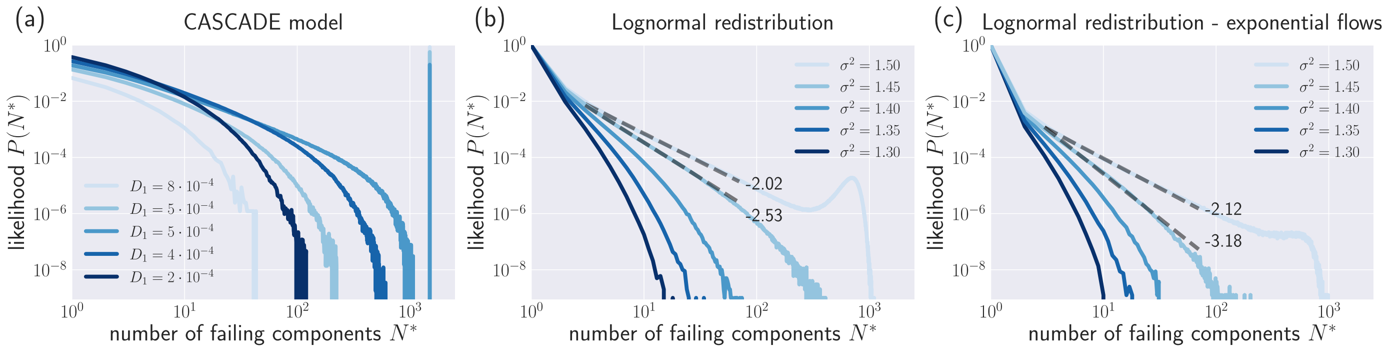

FIGURE 4. Distribution of outage sizes for different random redistribution models. We show the likelihood $P(N^*)$ of an outage of size N^* for (a) the CASCADE model, (b) the log-normal redistribution model with uniform initial loads and (c) with exponentially distributed initial loads. The effective parameters in the CASCADE model are chosen to be consistent to the parameters in the other models or their averages, respectively (see Eq. (19)). Colour code (from dark blue to light blue) represents increasing values of redistribution constant D_1 for the CASCADE model (a) and variance of the Gaussian distribution of logarithmic redistribution factors σ^2 for the other models (b,c). While the CASCADE model displays an abrupt transition point at which either less or all components in the system fail, the transition is smoother for the suggested models. Note the peak in the histogram at the system size $N = 1500$ for the CASCADE model (a), which indicates that the entire system fails with a high likelihood. The system considered here has $N = 1500$ elements for all panels, the mean of the distribution is set to $\mu = -5$ for panels (b) and (c) and parameters for CASCADE model are calculated using the parameters shown in b) and Eqs. (19) and (20). Grey dotted lines represent least-square fits of linear functions on the intermediate range of failure sizes performed on the log-log scales for the two top curves along with the resulting scaling exponent. The range of parameters is chosen such that it agrees with typical values found in statistics of LODFs in test case and synthetic grids (see Table 1).

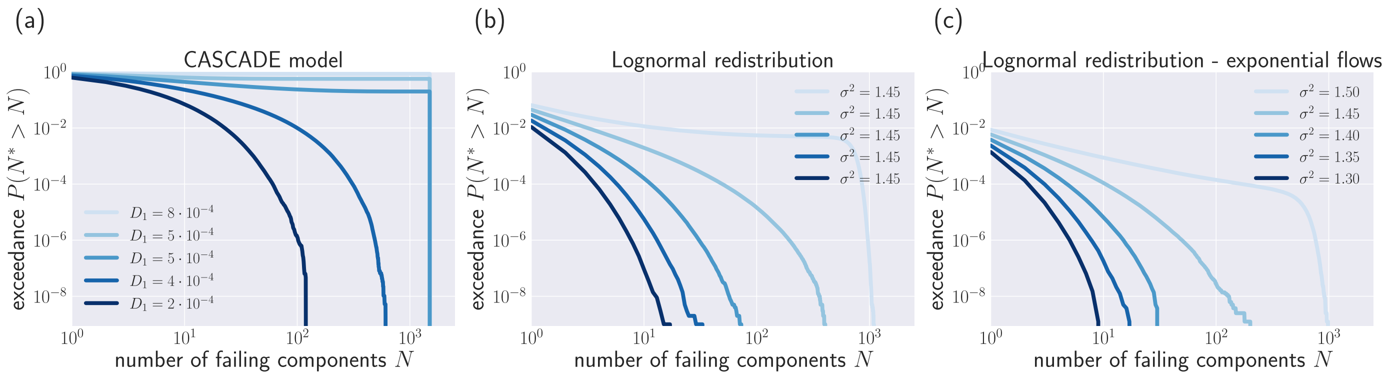

FIGURE 5. Distribution of outage sizes for different random redistribution models. We show the exceedance $P(N^* > N)$ which is the likelihood that an outage will result in the failure of N or more elements. The distributions shown here are the same as in Figure 4.

that LODFs are log-normally distributed throughout different topologies.

3. Initial trigger event: In contrast to the 'CASCADE' model, we assume that the initial event triggering the cascade of failures is the failure of a single element as well, i.e. the cascade is triggered by the same mechanism that makes it propagate. This corresponds to the mechanism for cascading failures in real power transmission grid, where large scale cascades are often triggered by a single link failure that triggers other link failures and so forth [9], [14], [15].

We summarise this cascade model in the Algorithm 1.

The proposed model thus incorporates crucial aspects of flow rerouting and cascading failures in power flow models while remaining entirely probabilistic and, in this regard, extending previous models. Similar to the 'CASCADE' model, this has the advantage that there is no need to consider a particular grid topology and allows approaching the statistics of cascading failures purely from a probabilistic viewpoint. Thus, the model fills a gap between realistic, but non-probabilistic models and purely probabilistic models that are ruled by less realistic redistribution schemes [4], [50]–[52].

B. HEAVY TAILS OCCUR OVER WIDE RANGE OF PARAMETERS

Outage sizes in empirical data have been demonstrated to have heavy tails [53]. Different explanations for this scaling law have been put forward, ranging from an interpretation of the power system being in a critical state [4], [7] to relating the power law to power laws in city size distributions [5]. A recent analysis of the probability distribution of the number of customers affected per outage in the U.S. has found a load dependency of the scaling exponent with typical values ranging from -2.1 to -2.8 [54]. Here, we demonstrate that power laws of outage sizes occur over a wide range of parameters in our extended CASCADE model. Our model incorporates essential properties of failure cascade in linear flow models while being entirely probabilistic.

TABLE 1. Distribution of topological parameters and moments of the logarithmic LODF distribution for 24 different test grids. We refer to the 20 first grids as 'test case grids' since they are mostly based on power system cases except for the two grids taken from PyPSA-Eur and to the latter four as 'synthetic grids'. Test grids are either taken from the publicly available test case archive of MATPOWER [20]–[22] or taken from the University of Washington power systems test case archive [24]. The Scandinavian grid data and the central European topology where extracted from the open energy system model PyPSA-Eur [33] which are based on the publicly available network data by the transparency platform of the European Network of Transmission System Operators (ENTSO-E). 'case_ACTIVSg' are synthetic power grids inspired by real-world North American power grids [23].

Test case	Mean μ	Variance σ^2	Skewness γ_1	Kurtosis κ	Number of nodes $\mathcal{N}$	Number of edges $\mathcal{M}$	Average degree $\langle k \rangle$
IEEE case118	-2.762	1.698	-0.090	-0.707	118	179	3.034
case145	-3.481	2.631	-1.002	1.407	145	422	5.821
IEEE case300	-3.060	2.069	-0.401	-0.040	300	409	2.727
case1354pegase	-3.544	1.431	0.012	0.042	1354	1710	2.526
case1888rte	-3.680	1.689	-0.330	0.604	1888	2308	2.445
case1951rte	-3.737	1.791	-0.412	0.827	1951	2375	2.435
case2383wp	-3.816	1.584	-0.324	1.072	2383	2886	2.422
case2737sop	-3.875	1.810	-0.651	1.329	2737	3497	2.555
case2746wop	-3.868	1.790	-0.651	1.398	2746	3505	2.553
case2848rte	-4.081	1.894	-0.157	0.215	2848	3442	2.417
case2868rte	-4.157	2.110	-0.429	1.012	2868	3471	2.421
case2869pegase	-5.461	4.982	-0.466	-0.200	2869	3968	2.766
case3012wp	-3.841	1.574	-0.261	0.882	3012	3566	2.368
case3120sp	-3.893	1.668	-0.293	0.827	3120	3684	2.362
case3375wp	-3.907	1.627	-0.382	1.196	3374	4068	2.411
case6468rte	-4.702	1.713	0.055	0.474	6468	8065	2.494
case6470rte	-4.691	1.689	0.076	0.459	6470	8066	2.493
case9241pegase	-6.366	5.117	-0.306	-0.410	9241	14207	3.075
Scandinavia_PyPSA	-3.709	4.412	-0.623	-0.310	272	373	2.743
Central_Europe_PyPSA	-4.502	2.717	-0.371	-0.057	2440	3494	2.864
case_ACTIVSg200	-2.077	1.057	-0.441	0.065	200	245	2.450
case_ACTIVSg500	-2.653	1.323	-0.252	-0.032	500	584	2.336
case_ACTIVSg2000	-4.100	1.754	0.143	-0.126	2000	2667	2.667
case_ACTIVSg10k	-4.958	1.780	0.104	0.382	10000	12217	2.443

TABLE 2. Distribution of topological parameters and moments of the logarithmic LODF distribution for different regular and random graphs. Link weights were either set to unity or calculated based on the inverse parameters of an exponential distribution with $\lambda = 0.02$. To produce the Voronoi lattics, we distributed 2000 points randomly in the unit square $[0, 1] \times [0, 1]$ and calculated their Voronoi tessellation. For the Erdős–Rényi (ER) random graph we used a connection probability of $p = 0.2$.

Test case	Mean μ	Variance σ^2	Skewness γ_1	Kurtosis κ	Number of nodes $\mathcal{N}$	Number of edges $\mathcal{M}$	Average degree $\langle k \rangle$
ER graph - unweighted	-3.819	0.565	-0.335	0.911	220	4766	43.327
Square grid - unweighted	-3.584	0.663	-0.170	0.947	2500	4900	3.920
Square grid - weighted	-3.582	0.715	-0.150	0.978	2500	4900	3.920
Triangular grid - unweighted	-4.451	1.595	-0.344	-0.164	2626	7625	5.807
Triangular grid - weighted	-4.514	1.725	-0.330	-0.078	2626	7625	5.807
Delaunay lattice - unweighted	-3.909	0.509	0.071	1.649	3000	8974	5.983
Delaunay lattice - weighted	-3.914	0.515	0.079	1.594	3000	8975	5.983
Voronoi lattice - weighted	-3.469	0.649	-0.062	1.074	3973	5947	2.994
Voronoi lattice - unweighted	-3.431	0.540	-0.008	1.491	3976	5953	2.994
Hexagonal grid - unweighted	-3.558	0.601	-0.126	1.284	5200	7699	2.961
Hexagonal grid - weighted	-3.575	0.681	-0.162	1.135	5200	7699	2.961

To be able to compare the proposed model to the CASCADE model, we choose the redistribution parameter D_1 in the CASCADE model as the expected value of the product probability distribution between initial loadings $L^{(0)}$ and redistribution factors $\mathfrak{L}$, such that

$$D_1 := E\left(|\mathfrak{L} \cdot L^{(0)}|\right). \tag{19}$$

If a large number of components fails, we thus have the formal equivalence in the update equations

$$L_i^{(1)} = L_i^{(0)} + \sum_{k=1}^{M} |\mathfrak{L} \cdot L_k^{(0)}| \approx L_i^{(0)} + MD_1.$$

Furthermore, we choose the initial trigger parameter D_0 to be equal to the initial security margin to which we add a small value

$$D_0 := (L^{\max} - L^{\text{thresh}}) + E\left(|\mathfrak{L} \cdot L^{(0)}|\right), \tag{20}$$

since below this value, the initial trigger event cannot result in a cascade and this value simulates a behaviour close to criticality, where power-laws of cascade sizes have been observed.

In Figure 4, we compare the resulting cascade sizes obtained for a large number of simulations of the model with the parameters indicated. We analyse the likelihood $P(N^*)$ that a given number of components N^* fails, calculated over 10^8–10^9 realisations of the initial conditions and randomly chosen trigger elements. We consider (a) the CASCADE model, (b) the stochastic load redistribution model suggested at the beginning of this section IV with uniform initial

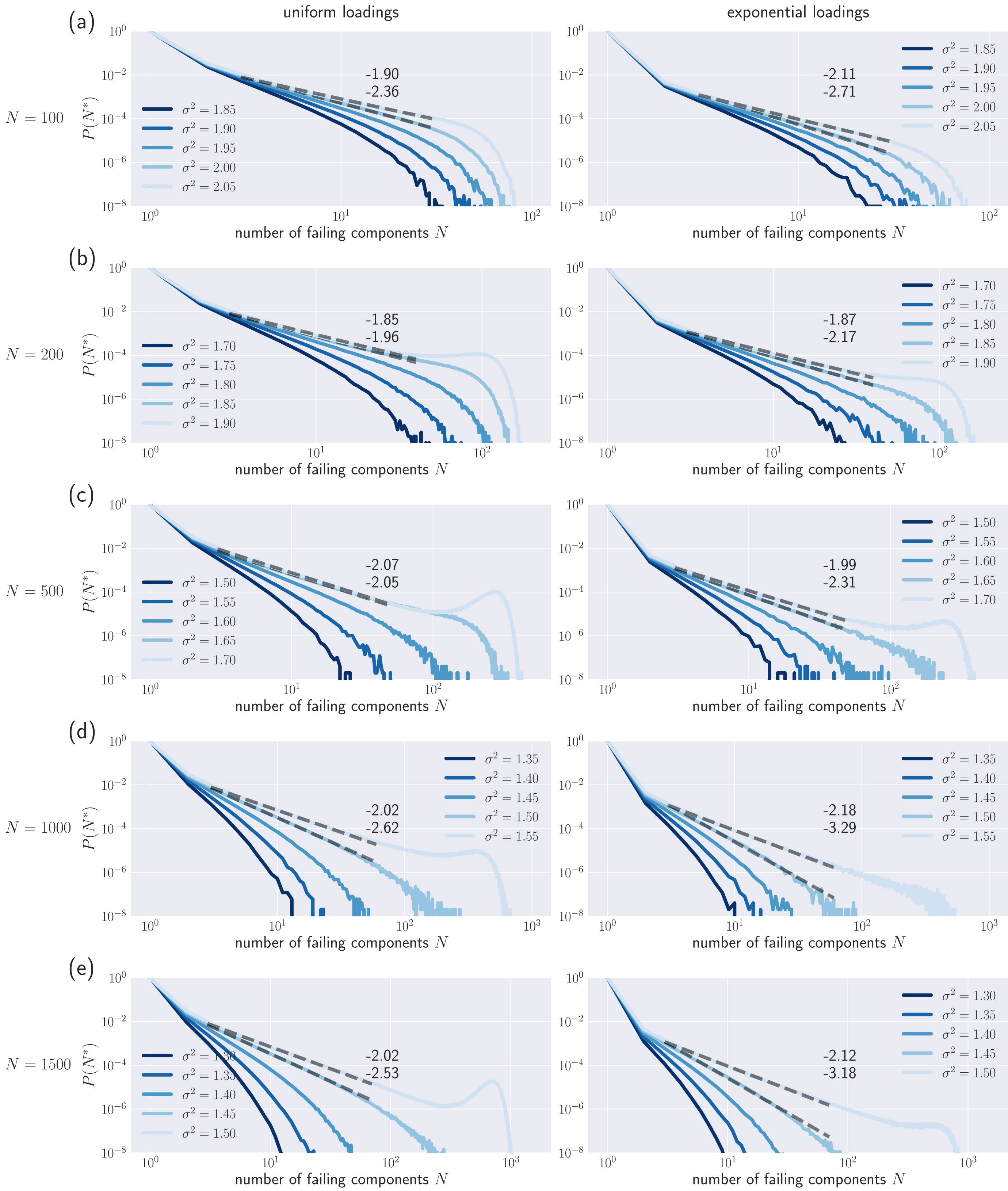

FIGURE 6. **Distribution of outage sizes in the stochastic load redistribution model for systems of different sizes. We compare the likelihood $P(N^*)$ of an outage of size N^* for systems with initial element loadings drawn uniformly (left) and exponentially (right) for systems with different number of elements (a-e). We fix the mean of redistribution factors to $\mu = -5$ and choose the range of variances σ^2 for each system size such that power laws of outage sizes occur. The range of parameters considered here matches typical values found in redistribution factors for synthetic and test case grids (see Table 1).**

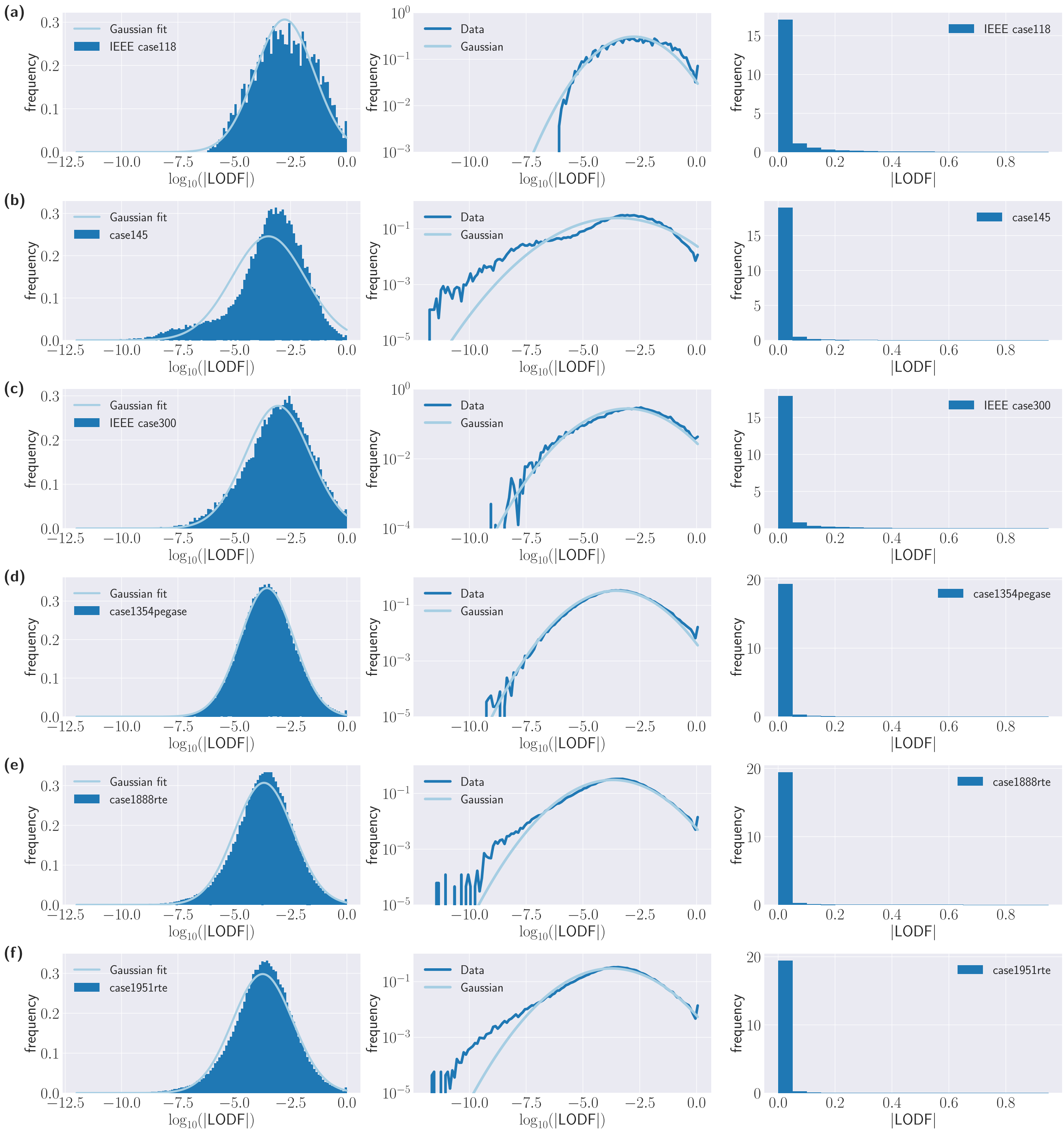

FIGURE 7. Distribution of absolute LODFs for the first six test grids listed in table 1. We plot the frequency of occurence of logarithmic absolute LODFs and a Gaussian fit (see sec. III) with a linear y-scale (left) and a logarithmic y-scale (center). In most cases, the frequency of occurence of logarithmic absolute LODFs is well-approximated by the Gaussian fit. Furthermore, we plot the frequency of occurrence of absolute LODFs (right).

loadings and (c) with exponential initial loadings. Typical values for the log-normal statistics of redistribution factors used in the stochastic load redistribution model are extracted from the parameters obtained for test case and synthetic grids listed in Table 1 and discussed in section III-C: We choose a mean of $\mu = -5$ which is in the typical range of $\mu \in [-3, -6]$ observed for the logarithmic mean and a variance of $\sigma^2 \in [1.3, 1.5]$ which also matches the typical range of $\sigma^2 \in [1, 3]$ observed for actual grid datasets. In Figure 6 in the Appendix, we analyse the sensitivity of these results for varying system sizes and varying variance σ^2 chosen in the critical range. Note that values differing from the critical range will result in either only a small share of the components or the entire system failing due to a limited system size. Furthermore, we fix the security margin on the relative loading to $c = 0.7$. Note that this "70%-rule" is

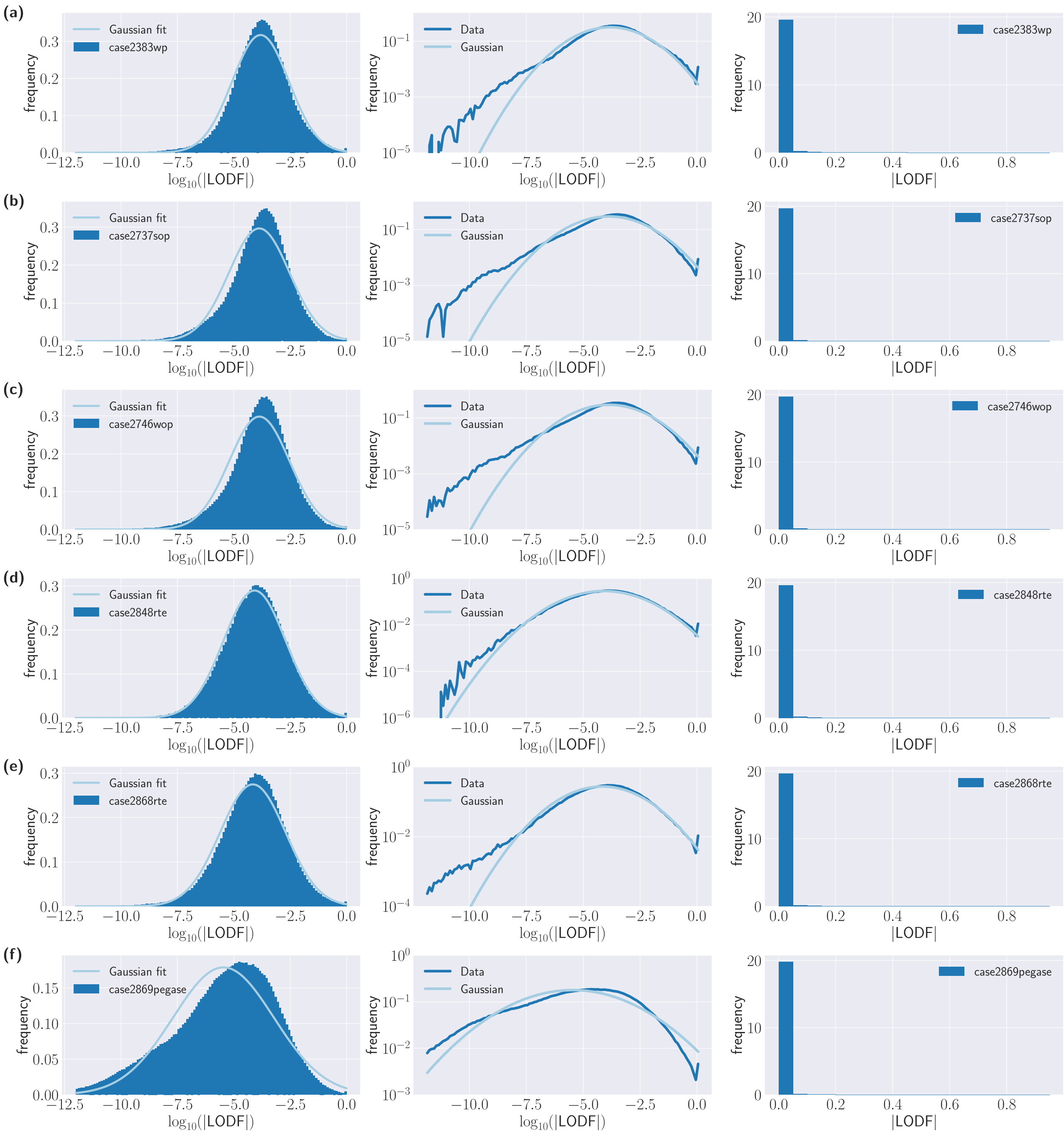

FIGURE 8. Distribution of absolute LODFs for the sixth up to the twelfth test grids listed in table 1. We plot the frequency of occurence of logarithmic absolute LODFs and a Gaussian fit (see sec. III) with a linear y-scale (left) and a logarithmic y-scale (center). In most cases, the frequency of occurence of logarithmic absolute LODFs is well-approximated by the Gaussian fit. Furthermore, we plot the frequency of occurrence of absolute LODFs (right).

a common way to ensure approximate $N-1$ security also when operating and modelling real-world power transmission grids [55]–[57].[1]

[1] Note that in the dataset shown in Figure 1 the security margin is set to $L^{\text{thresh}} = 0.8$, i.e. 80% of the maximal loading. We make use of this dataset to estimate the scaling exponent since flows are not strongly affected by the threshold in this case which would otherwise result in a peak at $L^{(0)} = 0.7$ as an indication of positive shadow prices, i.e. a possible economic optimum with higher line flows [58]. Thus, we estimate the exponent from this distribution to be able to use the entire range of loadings for estimation of the scaling exponent.

Whereas the CASCADE model (a) displays a rather abrupt transition point for which either fewer components or the entire system fail, the curves are smoother for all parameters in the models suggested here. In particular, the curves in the suggested models are more flat for all parameters under consideration indicating a power law over a wider range of parameters. Thus, we conclude that our model can reproduce essential features observed in the CASCADE model while presenting power laws over a wide range of parameters. For the critical cases where power laws occur, we find that the

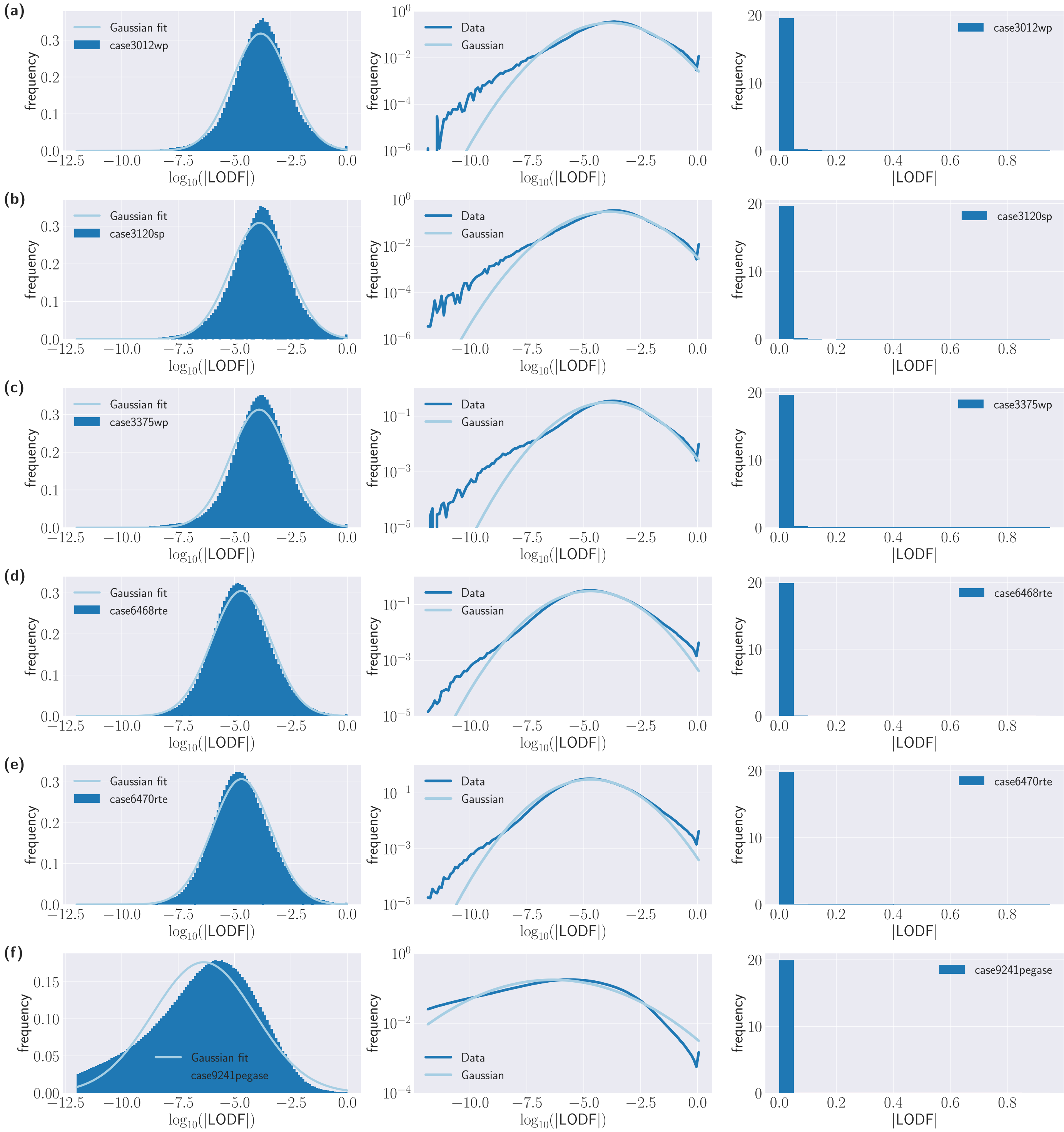

FIGURE 9. **Distribution of absolute LODFs for the twelfth up to the eighteenth test grids listed in table 1. We plot the frequency of occurence of logarithmic absolute LODFs and a Gaussian fit (see sec. III) with a linear y-scale (left) and a logarithmic y-scale (center). In most cases, the frequency of occurence of logarithmic absolute LODFs is well-approximated by the Gaussian fit. Furthermore, we plot the frequency of occurrence of absolute LODFs (right).**

scaling exponents (dotted lines, Figure 4) matches the scaling exponents found in empirical data with values in the range of -2 to -3. To confirm this result, we also analyse the likelihood of exceedance $P(N^* > N)$, which is the likelihood that the outage size exceeds N elements, for the same distributions of outage sizes in Figure 5 in the Appendix and analyse the scaling of the probability of outage sizes for systems with different number of elements in Figure 6 in the Appendix.

V. DISCUSSION AND CONCLUSION

In this manuscript, we analysed the distribution of Line Outage Distribution Factors for different real-world- and

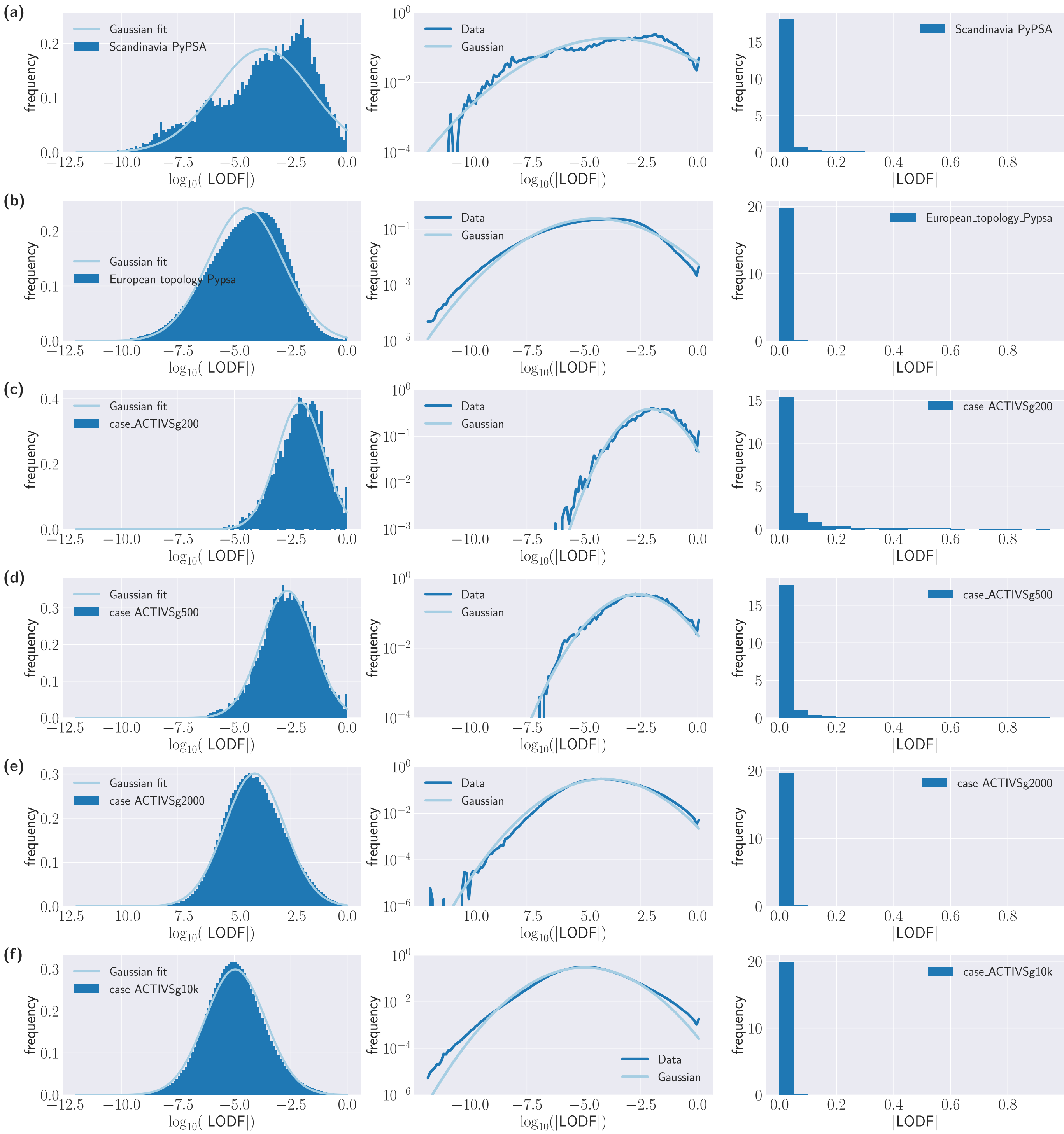

FIGURE 10. Distribution of absolute LODFs for the final six test grids listed in table 1. We plot the frequency of occurence of logarithmic absolute LODFs and a Gaussian fit (see sec. III) with a linear y-scale (left) and a logarithmic y-scale (center). In most cases, the frequency of occurence of logarithmic absolute LODFs is well-approximated by the Gaussian fit. Furthermore, we plot the frequency of occurrence of absolute LODFs (right).

synthetic grids. In particular, we analysed how this distribution changes throughout different synthetic and real-world topologies: We found that the distribution of the magnitude of LODFs is approximately log-normal, but additionally shows heavy tails throughout the topologies analysed here. We made use of this finding to introduce a stochastic load redistribution model for cascading failures that incorporates essential mechanisms of link failures in linear flow models – such as the aforementioned log-normal distribution of redistribution factors. The model, as a result of the log-normal distribution of LODFs, offers a potential explanation for the widespread occurrence of power laws in empirical data of power outage sizes.

In contrast to microscopic studies that analyse the impact of individual failures, our approach is a macroscopic one, focusing on the statistics of redistribution factors.

This approach has been demonstrated to be fruitful in many regards. On the one hand, it allows shifting the focus from the small-scale network structure to the vulnerability of a network as a whole. The distribution may thus be used to characterise network resilience, and potentially come up with a single index for an entire network – similar to the relative number of ''strongly affected links'' suggested here. Furthermore, this distribution could be used to evaluate whether a given synthetic network topology corresponds to realistic power grid topology in terms of network resilience. Our results demonstrate that there is a strong correspondence between the distributions of LODFs for vastly different topologies and even random graphs. Although the calculation of LODFs is based purely on the network topology via the pseudoinverse of the graph Laplacian, we could not find a simple theoretical explanation for this universal scaling.

On the other hand, a focus on the statistics of LODFs rather than individual values allows studying cascade models that feature more realistic flow redistribution. These models remain entirely probabilistic and thus do not require any assumptions about network topology. In this manuscript, we laid a first foundation by proposing such a cascade model that we study numerically. However, in principle, the a priori knowledge of the statistics of loadings and redistribution will also allow estimating cascade statistics analytically. This could help to shed further light on empirical observation of cascade sizes in real-world outages.

The stochastic load redistribution model for cascading failures introduced here focuses on the number of the failing components as an indicator for the severity of blackout sizes. This is due to the fact that the statistics of LODFs can be most easily and most directly related to the failure of individual components and thus outage sizes. Nevertheless, a number of other indicators has been proposed that aim to classify the severity of blackouts such as the number of customers affected, the unserved power or the value of lost load to name but a few [5], [7], [59], [60]. However, in order to extend our model with one or several other indicators, we would have to tune additional parameters to estimate e.g. the statistics of power consumption, which is why we leave this question open for future studies.

APPENDIX
TABLE OF POWER GRID TEST CASES

See Table 1 and 2.

APPENDIX
ADDITIONAL FIGURES

See Figure (5)–(10).

ACKNOWLEDGMENT

The authors would like to thank Tom Brown for providing the power grid data and dispatch of the European power system and Jonas Wassmer and Philipp Böttcher for helpful comments.

REFERENCES

[1] K. Everhart and G. Molnar. (2021). *International Energy Agency*. Accessed: Mar. 1, 2021. [Online]. Available: https://www.iea.org/commentaries/severe-power-cuts-in-texas-highlight-energy-security-risks-related-to-extreme-weather-events

[2] Union for the Coordination of Transmission of Electricity. (2007). *Final Report on the System Disturbance on 4 November 2006*. Accessed: Mar. 1, 2021. [Online]. Available: https://www.entsoe.eu/fileadmin/user_upload/_library/publications/ce/otherreports/Final-Report-20070130.pdf

[3] P. Hines, K. Balasubramaniam, and E. C. Sanchez, ''Cascading failures in power grids,'' *IEEE Potentials*, vol. 28, no. 5, pp. 24–30, Sep. 2009.

[4] B. A. Carreras, D. E. Newman, I. Dobson, and A. B. Poole, ''Evidence for self-organized criticality in a time series of electric power system blackouts,'' *IEEE Trans. Circuits Syst. I, Reg. Papers*, vol. 51, no. 9, pp. 1733–1740, Sep. 2004.

[5] T. Nesti, F. Sloothaak, and B. Zwart, ''Emergence of scale-free blackout sizes in power grids,'' *Phys. Rev. Lett.*, vol. 125, no. 5, Jul. 2020, Art. no. 058301.

[6] J. Lehmann and J. Bernasconi, ''Stochastic load-redistribution model for cascading failure propagation,'' *Phys. Rev. E*, vol. 81, no. 3, Mar. 2010, Art. no. 031129.

[7] I. Dobson, B. A. Carreras, V. E. Lynch, and D. E. Newman, ''Complex systems analysis of series of blackouts: Cascading failure, critical points, and self-organization,'' *Chaos, Interdiscipl. J. Nonlinear Sci.*, vol. 17, no. 2, Jun. 2007, Art. no. 026103.

[8] I. Dobson, B. A. Carreras, and D. E. Newman, ''A loading-dependent model of probabilistic cascading failure,'' *Probab. Eng. Inf. Sci.*, vol. 19, no. 1, pp. 15–32, Jan. 2005.

[9] P. Pourbeik, P. S. Kundur, and C. W. Taylor, ''The anatomy of a power grid blackout–root causes and dynamics of recent major blackouts,'' *IEEE Power Energy Mag.*, vol. 4, no. 5, pp. 22–29, Sep. 2006.

[10] A. J. Wood, B. F. Wollenberg, and G. B. Sheblé, *Power Generation, Operation and Control*. New York, NY, USA: Wiley, 2014.

[11] H. Cetinay, F. A. Kuipers, and P. Van Mieghem, ''A topological investigation of power flow,'' *IEEE Syst. J.*, vol. 12, no. 3, pp. 2524–2532, Sep. 2018.

[12] S. Kettemann, ''Delocalization of disturbances and the stability of AC electricity grids,'' *Phys. Rev. E*, vol. 94, no. 6, Dec. 2016, Art. no. 062311.

[13] D. Labavić, R. Suciu, H. Meyer-Ortmanns, and S. Kettemann, ''Long-range response to transmission line disturbances in DC electricity grids,'' *Eur. Phys. J. Special Topics*, vol. 223, no. 12, pp. 2517–2525, Oct. 2014.

[14] J. Strake, F. Kaiser, F. Basiri, H. Ronellenfitsch, and D. Witthaut, ''Non-local impact of link failures in linear flow networks,'' *New J. Phys.*, vol. 21, no. 5, May 2019, Art. no. 053009.

[15] F. Kaiser, J. Strake, and D. Witthaut, ''Collective effects of link failures in linear flow networks,'' *New J. Phys.*, vol. 22, no. 1, Jan. 2020, Art. no. 013053.

[16] J. Lehmann and J. Bernasconi, ''Current redistribution in resistor networks: Fat-tail statistics in regular and small-world networks,'' *Phys. Rev. E*, vol. 95, no. 3, Mar. 2017, Art. no. 032310.

[17] W. Medjroubi, U. P. Müller, M. Scharf, C. Matke, and D. Kleinhans, ''Open data in power grid modelling: New approaches towards transparent grid models,'' *Energy Rep.*, vol. 3, pp. 14–21, Nov. 2017.

[18] F. Wiese, I. Schlecht, W.-D. Bunke, C. Gerbaulet, L. Hirth, M. Jahn, F. Kunz, C. Lorenz, J. Mühlenpfordt, J. Reimann, and W.-P. Schill, ''Open power system data—Frictionless data for electricity system modelling,'' *Appl. Energy*, vol. 236, pp. 401–409, Feb. 2019.

[19] J. Bennett, *OpenStreetMap*. Birmingham, U.K.: Packt, 2010.

[20] C. Josz, S. Fliscounakis, J. Maeght, and P. Panciatici, ''AC power flow data in MATPOWER and QCQP format: ITesla, RTE snapshots, and PEGASE,'' 2016, *arXiv:1603.01533*. [Online]. Available: http://arxiv.org/abs/1603.01533

[21] R. D. Zimmerman, C. E. Murillo-Sanchez, and R. J. Thomas, ''Matpower: Steady-state operations, planning and analysis tools for power systems research and education,'' *IEEE Trans. Power Syst.*, vol. 26, no. 1, pp. 12–19, Feb. 2011.

[22] S. Fliscounakis, P. Panciatici, F. Capitanescu, and L. Wehenkel, ''Contingency ranking with respect to overloads in very large power systems taking into account uncertainty, preventive, and corrective actions,'' *IEEE Trans. Power Syst.*, vol. 28, no. 4, pp. 4909–4917, Nov. 2013.

[23] A. B. Birchfield, T. Xu, K. M. Gegner, K. S. Shetye, and T. J. Overbye, ''Grid structural characteristics as validation criteria for synthetic networks,'' *IEEE Trans. Power Syst.*, vol. 32, no. 4, pp. 3258–3265, Jul. 2017.

[24] R. D. Christie. (1999). *Power Systems Test Case Archive*. Accessed: Mar. 1, 2021. [Online]. Available: http://www.ee.washington.edu/research/pstca/
[25] S. Soltan and G. Zussman, "Generation of synthetic spatially embedded power grid networks," in *Proc. IEEE Power Energy Soc. Gen. Meeting (PESGM)*, Jul. 2016, pp. 1–5.
[26] P. Schultz, J. Heitzig, and J. Kurths, "A random growth model for power grids and other spatially embedded infrastructure networks," *Eur. Phys. J. Special Topics*, vol. 223, no. 12, pp. 2593–2610, Oct. 2014.
[27] Z. Wang, A. Scaglione, and R. J. Thomas, "Generating statistically correct random topologies for testing smart grid communication and control networks," *IEEE Trans. Smart Grid*, vol. 1, no. 1, pp. 28–39, Jun. 2010.
[28] R. Espejo, S. Lumbreras, and A. Ramos, "A complex-network approach to the generation of synthetic power transmission networks," *IEEE Syst. J.*, vol. 13, no. 3, pp. 3050–3058, Sep. 2019.
[29] Z. Wang, R. J. Thomas, and A. Scaglione, "Generating random topology power grids," in *Proc. 41st Annu. Hawaii Int. Conf. Syst. Sci. (HICSS)*, Waikoloa, HI, USA, Jan. 2008, p. 183.
[30] M. H. Athari and Z. Wang, "Statistically characterizing the electrical parameters of the grid transformers and transmission lines," 2017, p. 7, *arXiv:1706.02754*. [Online]. Available: http://arxiv.org/abs/1706.02754
[31] E. Bompard, D. Wu, and F. Xue, "The concept of betweenness in the analysis of power grid vulnerability," in *Proc. Complex. Eng.*, Feb. 2010, pp. 52–54.
[32] B. Liu, Z. Li, X. Chen, Y. Huang, and X. Liu, "Recognition and vulnerability analysis of key nodes in power grid based on complex network centrality," *IEEE Trans. Circuits Syst. II, Exp. Briefs*, vol. 65, no. 3, pp. 346–350, Mar. 2018.
[33] J. Hörsch, F. Hofmann, D. Schlachtberger, and T. Brown, "PyPSA-Eur: An open optimisation model of the European transmission system," *Energy Strategy Rev.*, vol. 22, pp. 207–215, Nov. 2018.
[34] K. Purchala, L. Meeus, D. V. Dommelen, and R. Belmans, "Usefulness of DC power flow for active power flow analysis," in *Proc. IEEE Power Eng. Soc. Gen. Meeting*, vol. 1, Jun. 2005, pp. 454–459.
[35] E. Katifori, G. J. Szöllősi, and M. O. Magnasco, "Damage and fluctuations induce loops in optimal transport networks," *Phys. Rev. Lett.*, vol. 104, no. 4, Jan. 2010, Art. no. 048704.
[36] M. E. J. Newman, *Networks: An Introduction*. London, U.K.: Oxford Univ. Press, 2010.
[37] F. Kaiser, V. Latora, and D. Witthaut, "Inhibiting failure spreading in complex networks," 2020, *arXiv:2009.02910*. [Online]. Available: http://arxiv.org/abs/2009.02910
[38] P. Van Mieghem, K. Devriendt, and H. Cetinay, "Pseudoinverse of the Laplacian and best spreader node in a network," *Phys. Rev. E*, vol. 96, no. 3, 2017, Art. no. 032311.
[39] F. Dörfler, J. W. Simpson-Porco, and F. Bullo, "Electrical networks and algebraic graph theory: Models, properties, and applications," *Proc. IEEE*, vol. 106, no. 5, pp. 977–1005, May 2018.
[40] H. Ronellenfitsch, D. Manik, J. Hörsch, T. Brown, and D. Witthaut, "Dual theory of transmission line outages," *IEEE Trans. Power Syst.*, vol. 32, no. 5, pp. 4060–4068, Sep. 2017.
[41] F. Kaiser and D. Witthaut, "Topological theory of resilience and failure spreading in flow networks," Sep. 2020, *arXiv:2009.10349*. [Online]. Available: http://arxiv.org/abs/2009.10349
[42] G. W. Anderson, A. Guionnet, and O. Zeitouni, *An Introduction to Random Matrices* (Cambridge Studies in Advanced Mathematics). Cambridge, U.K.: Cambridge Univ. Press, 2009.
[43] S. N. Dorogovtsev, A. V. Goltsev, J. F. F. Mendes, and A. N. Samukhin, "Spectra of complex networks," *Phys. Rev. E*, vol. 68, no. 4, Oct. 2003, Art. no. 046109.
[44] P. N. McGraw and M. Menzinger, "Laplacian spectra as a diagnostic tool for network structure and dynamics," *Phys. Rev. E*, vol. 77, no. 3, Mar. 2008, Art. no. 031102.
[45] P. Van Mieghem, *Graph Spectra for Complex Networks*. Cambridge, U.K.: Cambridge Univ. Press, 2010.
[46] M. Rohden, A. Sorge, M. Timme, and D. Witthaut, "Self-organized synchronization in decentralized power grids," *Phys. Rev. Lett.*, vol. 109, no. 6, Aug. 2012, Art. no. 064101.
[47] E. Limpert, W. A. Stahel, and M. Abbt, "Log-normal distributions across the sciences: Keys and clues," *BioScience*, vol. 51, no. 5, p. 341, 2001.
[48] D. Zwillinger and S. Kokoska, *CRC Standard Probability and Statistics Tables and Formulae*. Boca Raton, FL, USA: CRC Press, Dec. 1999.
[49] P. H. Westfall, "Kurtosis as peakedness, 1905–2014.R.I.P," *Amer. Statistician*, vol. 68, no. 3, pp. 191–195, Jul. 2014.
[50] B. A. Carreras, V. E. Lynch, I. Dobson, and D. E. Newman, "Complex dynamics of blackouts in power transmission systems," *Chaos, Interdiscipl. J. Nonlinear Sci.*, vol. 14, no. 3, p. 11, 2004.
[51] S. Mei, F. He, X. Zhang, S. Wu, and G. Wang, "An improved OPA model and blackout risk assessment," *IEEE Trans. Power Syst.*, vol. 24, no. 2, pp. 814–823, May 2009.
[52] P. Hines, E. Cotilla-Sanchez, and S. Blumsack, "Do topological models provide good information about electricity infrastructure vulnerability?" *Chaos, Interdiscipl. J. Nonlinear Sci.*, vol. 20, no. 3, Sep. 2010, Art. no. 033122.
[53] B. A. Carreras, D. E. Newman, and I. Dobson, "North American blackout time series statistics and implications for blackout risk," *IEEE Trans. Power Syst.*, vol. 31, no. 6, pp. 4406–4414, Nov. 2016.
[54] S. Biswas and L. Goehring, "Load dependence of power outage statistics," *Europhys. Lett.*, vol. 126, no. 4, p. 44002, Jun. 2019.
[55] D. P. Schlachtberger, T. Brown, S. Schramm, and M. Greiner, "The benefits of cooperation in a highly renewable European electricity network," *Energy*, vol. 134, pp. 469–481, Sep. 2017. [Online]. Available: http://arxiv.org/abs/1704.05492
[56] M. Gathmann. (2019). *World's First Dynamic Control Center in Germany Automates Load Balancing and Outage Prevention*. Accessed: Mar. 1, 2021. [Online]. Available: https://new.siemens.com/global/en/company/stories/infrastructure/2019/ dynamic-power-grid.html
[57] T. Brown, P. Schierhorn, E. Tröster, and T. Ackermann, "Optimising the European transmission system for 77% renewable electricity by 2030," *IET Renew. Power Gener.*, vol. 10, no. 1, pp. 3–9, Jan. 2016.
[58] M. Frysztacki and T. Brown, "Modeling curtailment in germany: How spatial resolution impacts line congestion," in *Proc. 17th Int. Conf. Eur. Energy Market (EEM)*, Sep. 2020, pp. 1–7.
[59] T. Schröder and W. Kuckshinrichs, "Value of lost load: An efficient economic indicator for power supply security? A literature review," *Frontiers Energy Res.*, vol. 3, p. 55, Dec. 2015.
[60] B. Johnson, V. Chalishazar, E. Cotilla-Sanchez, and T. K. A. Brekken, "A Monte Carlo methodology for earthquake impact analysis on the electrical grid," *Electr. Power Syst. Res.*, vol. 184, Jul. 2020, Art. no. 106332.

FRANZ KAISER received the B.Sc. degree in physics from the University of Göttingen, Germany, in 2015, and the M.Sc. degree in physics from the University of Göttingen and with the Max Planck Institute for Dynamics and Self-Organization, Göttingen, in 2018. He is currently pursuing the Ph.D. degree in physics with the Forschungszentrum Jülich and the University of Cologne, Germany.

DIRK WITTHAUT received the M.Sc. and Ph.D. degrees in physics from the Technical University of Kaiserslautern, Kaiserslautern, Germany, in 2004 and 2007, respectively. He worked as a Postdoctoral Researcher with the Niels Bohr Institute, Copenhagen, Denmark, and the Max Planck Institute for Dynamics and Self-Organization, Gottingen, Germany. He has been a Guest Lecturer with the Kigali Institute of Science and Technology, Rwanda. Since 2014, he has been leading a Research Group with the Forschungszentrum Jülich, Germany. He is currently an Assistant Professor with the University of Cologne.

3. Reducing the impact of link failures: topology and symmetry

As we have analysed in the last chapter, link failures are among the biggest threats to the stability of supply networks. For this reason, strategies to limit their impact and prevent cascading outages are of great importance. An intuitive strategy to limit the impact of failures is given by reducing the connectivity between the part of the network where the failure happened and another part that shall be protected against the impact of the failure, in some cases even disconnecting parts of the network [72, 73]. However, as discussed in detail in the introduction, future power transmission systems require more long-range transport and thus more connectivity. In our publications, we overcome this problem by introducing *network isolators* – subgraphs that connect different parts of the network and completely inhibit failure spreading between these parts. Network isolators may be realised at an arbitrary degree of connectivity and completely suppress flow changes as a result of link failures while letting power flows pass. Thus, they help to design reliable future power systems by allowing for more connectivity and increasing security at the same time.

In the first publication, we introduce the concept of network isolators by rigorously proving that network isolators have the desired effect: They completely suppress any flow changes in the shielded parts in linear flow networks. We then discuss different possible applications of network isolators and their robustness with respect to small modifications in the isolator topology and their ability to suppress cascade propagation. Here, I contributed most of the text, designed all figures and performed all numerical simulations (see author contribution statement in the manuscript).

The second publication builds upon the first one. Here, we develop a novel understanding of failure spreading in linear flow networks by analysing the importance played by certain paths. To this end, we trace back the problem of flow rerouting to spanning trees in the network, making use of a formula already introduced by Kirchhoff in the context of resistor networks [65]. We then exploit this formulation of flow rerouting to analyse why certain graph structures attenuate failure spreading. In particular, we come up with a different perspective on network isolators: They introduce symmetry into the spanning trees that govern flow rerouting, making these trees balance each other and thus completely suppressing flow changes. Here, I wrote most of the text, designed all figures and performed all simulations.

3.1. D) Network isolators inhibit failure spreading in complex networks

[4] Kaiser, F., Latora, V. & Witthaut, D. Network isolators inhibit failure spreading in complex networks. *Nature Communications* **12,** 3143. doi:10.1038/s41467-021-23292-9 (2021).

nature COMMUNICATIONS

ARTICLE

https://doi.org/10.1038/s41467-021-23292-9 OPEN

Network isolators inhibit failure spreading in complex networks

Franz Kaiser [1,2], Vito Latora [3,4,5,6] & Dirk Witthaut [1,2]✉

In our daily lives, we rely on the proper functioning of supply networks, from power grids to water transmission systems. A single failure in these critical infrastructures can lead to a complete collapse through a cascading failure mechanism. Counteracting strategies are thus heavily sought after. In this article, we introduce a general framework to analyse the spreading of failures in complex networks and demostrate that not only decreasing but also increasing the connectivity of the network can be an effective method to contain damages. We rigorously prove the existence of certain subgraphs, called network isolators, that can completely inhibit any failure spreading, and we show how to create such isolators in synthetic and real-world networks. The addition of selected links can thus prevent large scale outages as demonstrated for power transmission grids.

[1] Forschungszentrum Jülich, Institute for Energy and Climate Research (IEK-STE), Jülich, Germany. [2] Institute for Theoretical Physics, University of Cologne, Köln, Germany. [3] School of Mathematical Sciences, Queen Mary University of London, London, UK. [4] Dipartimento di Fisica ed Astronomia, Università di Catania and INFN, Catania, Italy. [5] The Alan Turing Institute, The British Library, London, UK. [6] Complexity Science Hub Vienna, Vienna, Austria. ✉email: d.witthaut@fz-juelich.de

Complex networked systems are subject to external perturbations, damages or attacks with potentially catastrophic consequences[1,2]. The loss of even a single edge can cause a blackout in a power grid[3,4], the dieback of a biological network[5], or the collapse of an entire ecological network[6]. It is thus essential to understand how the structure of a network determines its response to perturbations and its global resilience[7–11]. Here, we propose a general framework to model the redistribution of flows in a complex network that follows a small and local failure, and we suggest novel and more efficient strategies to improve network resilience. Our findings reveal that propagation of damages can be better limited by adding selected links instead of removing links and can turn very useful to construct more robust networks or to improve existing ones.

The division of a network into weakly coupled parts provides the most intuitive method to inhibit the spreading of failures, thus improving system resilience[12–15]. An example is shown in Fig. 1a for an elementary supply network with two weakly connected modules. The response to an edge failure is strong locally, but it is reduced in the other module of the network which has only few links connecting to the part where the failure happened. A similar effect is observed in a real-world case: the Scandinavian power grid in Fig. 1d. The study of community structures in both natural and man-made systems is an integral part of network science: a variety of methods has been developed to define and identify the weakly connected modules of a network[16–18], and the important role of community structures in network dynamics is today well recognised.

Limiting connectivity for the sake of additional security is, however, not always desirable. For instance, microgrid concepts and intentional islanding are heavily discussed in energy systems research[19,20], but the overall demand for electric power transmission actually increases[21,22]. Other methods to contain perturbations or damages in complex networks are thus needed. Indeed, an exceptionally strong interconnectivity between two modules can also suppress failure spreading as shown in Fig. 1b, e. Notably, a strong interconnectivity can be realised in different ways. In the random network example in Fig. 1b, a high number of links connects a subset of nodes of the two modules. In real vascular networks of leaves the suppression of failure spreading occurs naturally because the central vein between the left and right parts has an exceptionally large weight (Fig. 1e, cf. also[23]).

Remarkably, failure spreading can be completely stopped by certain subgraphs which we refer to as *network isolators* in the following, an example being shown in Fig. 1c. The failure of an edge in the right part of the network does not affect the flows in the left part at all. Real world networks can be made perfectly resistant to failure propagation by the ad-hoc addition of few links to create network isolators, as demonstrated for the Scandinavian power grid in Fig. 1f consisting of three weakly coupled modules. The suppression of failure spreading is readily generalised to networks with more than two modules.

Results

A model for supply networks. Our results are based on a general framework that allows a theoretical analysis of the interplay of network connectivity and robustness in the context of supply or transportation networks. Consider a simple graph G with edge set E and vertex set V consisting of $L=|E|$ edges and $N=|V|$ vertices. Many such systems can in fact be modelled by linear flow networks where the flow over an edge $e=(i,j)\in E(G)$ depends linearly on the gradient of a potential function across the edge,

$$F_{i\to j}=A_{ij}\cdot(\vartheta_i-\vartheta_j). \tag{1}$$

In particular, this description applies to power transmission grids[2,24–26], where F is the real power flow, ϑ_i denotes the nodal voltage phase angle and A_{ij} is given by the line susceptance. Nonlinear effects in electric power grids will be discussed below. Furthermore, the description (1) applies to hydraulic and vascular networks[27,28], where F is the flow of water or nutrients, ϑ_i is the local pressure and A_{ij} the edge's weight. Equivalent problems arise in the linearisation of general diffusively coupled networks of dynamical systems around an equilibrium or limit cycle[29]. We discuss these and other applications of linear flow models in detail in Supplementary Note 1.

Now assume that there are sources and sinks attached to the nodes in the network $P_i\in\mathbb{R}$, $i\in V(G)$ where $P_i>0$ represents a

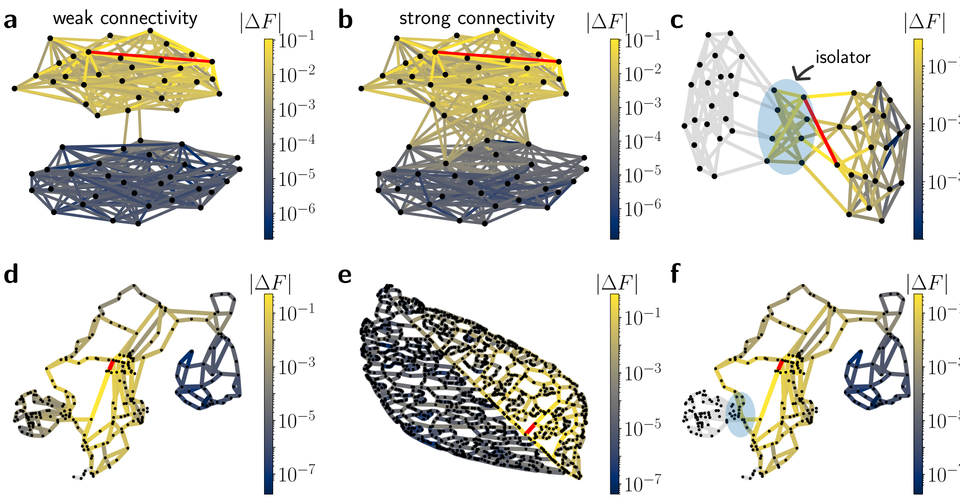

Fig. 1 Different network structures inhibit the spreading of failures in complex networks. We simulate the impact of a single failing link (red) for different network structures; resulting flow changes are colour coded. **a**, **b** Both a weak and a strong interconnectivity can suppress the spreading of failures between two modules of a complex network. **c** Failure spreading is prevented completely by a network isolator (blue shading); flow changes on the grey links are exactly zero. **d** The Scandinavian power grid consists of three weakly connected modules, which suppresses failure spreading between the modules[44]. **e** The vascular network of a *Bursera hollickii* leaf contains a strong central vein[47], which suppresses failure spreading between the two sides of the leaf. **f** Same as in (**d**) but with the addition of two links (blue shading) to create a network isolator. See Methods and caption of Fig. 2 for further information on the graphs used here.

source and $P_i < 0$ a sink. Then the flows at each node have to balance with the sources and sinks

$$P_i = \sum_{j=1}^{N} F_{i\to j} \qquad \forall i \in V(G). \tag{2}$$

This equation is known as continuity equation or *Kirchhoff's current law*. If the sources and sinks P_i are given, Eqs. (2) and (1) completely determine the potentials in the network (up to a constant shift to all potentials). In a power grid, the sources and sinks are the power injections or withdrawals as a result of power production or consumption, respectively. When looking at the stable, operational fixed point of a power grid they are balanced such that

$$\sum_{i=1}^{N} P_i = 0, \tag{3}$$

we therefore assume this to hold in the following sections.

For further use, we introduce a compact vectorised notation, defining the vector of injections $\vec{P} = (P_1, \ldots, P_N)^\top$ and the vector of potentials $\vec{\vartheta} = (\vartheta_1, \ldots, \vartheta_N)^\top$, where the superscript $\top$ denotes the transpose. The coupling coefficients $A_{ij} = A_{ji}$ are summarised in the weighted adjacency matrix $\boldsymbol{A} \in \mathbb{R}^{N\times N}$. Furthermore, we define the diagonal matrix $\boldsymbol{D} \in \mathbb{R}^{N\times N}$ with entries $D_{ii} = \sum_j A_{ij}$ as well as the weighted graph Laplacian[30]

$$\boldsymbol{L} = \boldsymbol{D} - \boldsymbol{A}. \tag{4}$$

Kirchhoff's equations then assume the compact form

$$\boldsymbol{L}\vec{\vartheta} = \vec{P}. \tag{5}$$

Notably, the Laplacian matrix is also useful to infer the large scale connectivity and the community structure of a given network[31].

Modelling link failures. The impact of a damage in linear flow networks can be calculated analytically. Assume that an edge $\ell = (r, s)$ fails, and summarise the response at all nodes $i = 1, \ldots, N$ in terms of the vector of changes in nodal potentials $\Delta\vec{\vartheta} = (\Delta\vartheta_1, \ldots, \Delta\vartheta_N)^\top$. The response can be calculated by subtracting Eq. (5) for the new and the old network which yields after some manipulations (Ref. [25], Supplementary Note 2)

$$\boldsymbol{L}\,\Delta\vec{\vartheta} = q_\ell \vec{\nu}_\ell, \tag{6}$$

where $\vec{\nu}_\ell$ is a vector with $+1$ at position r and -1 at position s, and $q_\ell = 1 - A_{rs}\vec{\nu}_\ell^\top \boldsymbol{L}^{-1}\vec{\nu}_\ell$ is a source strength[25]. We thus find that the response of a network to failures is essentially determined by the Laplacian $\boldsymbol{L}$.

To quantify the effect of connectivity on failure spreading, we have studied the impact of different failures in a variety of synthetic networks as well as in several real-world networks. For a given initial failure of an edge ℓ, we compute the flow changes

$$\Delta F_{i\to j} = A_{ij}\cdot(\Delta\vartheta_i - \Delta\vartheta_j) \tag{7}$$

for all edges $e = (i, j)$ in a given subgraph G' of the network. Furthermore, we must take into account that the impact of a failure generally decreases with distance[25,32,33]. As an overall measure of the impact of a failure we thus consider the expression $\langle|\Delta F_{i\to j}|\rangle_d^{(i,j)\in G'}$, which gives the magnitude of flow changes averaged over all edges $(i, j) \in G'$ at a given distance d to the edge ℓ (see Methods for details on the notion of distance used here). The prime question is now whether the impact differs substantially between the communities or moduli of a network. Here, we assume that the moduli or communities are known for the network under consideration and thus do not address the question how to determine them. We thus plot the ratio

$$R(\ell, d) = \frac{\langle|\Delta F_{i\to j}|\rangle_d^{(i,j)\in \mathrm{O}}}{\langle|\Delta F_{i\to j}|\rangle_d^{(i,j)\in \mathrm{S}}}. \tag{8}$$

between the module of the network $G' = \mathrm{O}$ without initial failures and the module $G' = \mathrm{S}$ containing the failing edge ℓ. If this ratio approaches or reaches zero, this is indicative of a very strong suppression of failure spreading into the other part of the network.

The impact of network connectivity on failure spreading. To study how the impact of failure spreading depends on the network structure, we considered synthetic graphs obtained by connecting two Erdős–Rényi (ER) random graphs to each other at preselected, randomly chosen vertices with a tunable probability $\mu \in [0, 1]$[34] (see Methods). The resulting graphs have a connectivity structure ranging from two weakly connected communities for low values of μ shown in Fig. 1a to strongly connected parts shown in panel b. In the limit $\mu = 1$, the two modules are connected via a complete bipartite graph as shown in Fig. 1c. This is a possible realisation of a *network isolator*, since it completely suppresses flow changes. We will explain the concept of *network isolators* and provide a rigorous definition in the next section.

The corresponding adjacency matrices clearly indicate the connectivity structure, revealing the strong or weak coupling between the two modules of the networks (Fig. 2a, b, d). Remarkably, evaluating the quantity $R(\ell)$, obtained by averaging the ratio over flow changes $R(\ell, d)$ over all distances d for a specific trigger link ℓ, for a varying connectivity structure tuned by μ, we find that the spreading of failures is largely suppressed for both weak and strong connectivity between the two modules as shown in Fig. 2c. Note that this finding is not limited to the interconnectivity of two modules, but can be readily generalised to three—or more—modules as we demonstrate in Supplementary Fig. 3. Distance plays a minor role for the ratio of flow changes $R(\ell, d)$ as illustrated in Supplementary Fig. 2.

Network isolators inhibit failure spreading. Network symmetries are known to play an important role for the dynamics and synchronisability of a network[35–37]. Network isolators as a specific connectivity structure completely inhibit the spreading of failures from one network module to another. They manifest also as particular, symmetric patterns in the region of the adjacency matrix describing the connectivity between the two parts of the network as we have seen in Fig. 2d. To see this, we make use of Eq. (4) to rewrite the Laplacian matrix $\boldsymbol{L}$ of the entire network as follows

$$\boldsymbol{L} = \begin{pmatrix} \boldsymbol{L}_1 + \boldsymbol{D}_1 & -\boldsymbol{A}_{12} \\ -\boldsymbol{A}_{12}^\top & \boldsymbol{L}_2 + \boldsymbol{D}_2 \end{pmatrix} \tag{9}$$

Here, $\boldsymbol{L}_1$ and $\boldsymbol{L}_2$ are the Laplacian matrices of the two parts of the network which consist of N_1 and N_2 nodes, $\boldsymbol{A}_{12} \in \mathbb{R}^{N_1\times N_2}$ is the region of the weighted adjacency matrix encoding the connectivity between the two parts of the network and $\boldsymbol{D}_1$ and $\boldsymbol{D}_2$ are the degree matrices of these mutual connections, i.e. the matrices containing the nodes' weighted degrees on the diagonals. Then network isolators are characterised by the following theorem.

Theorem 1 Consider a linear flow network composed of two modules 1,2 and let $\mathbf{A}_{12}$ denote the weighted adjacency matrix of the mutual connections as described in Eq. (9). An edge failure in one module does not affect the flows in the other module if rank $(\mathbf{A}_{12}) = 1$. For unweighted networks this criterion is fulfilled if

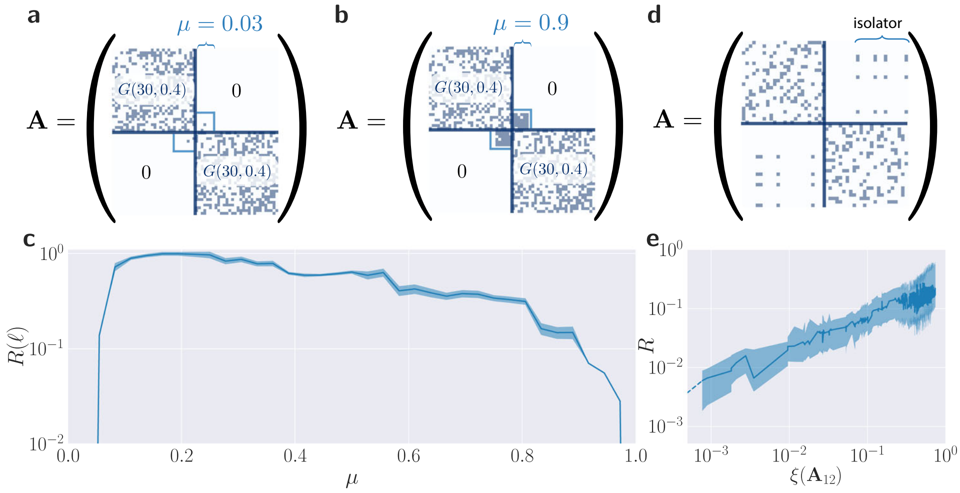

Fig. 2 Effectiveness and robustness of shielding network structures. a, **b** Adjacency matrices for the graphs shown in Fig. 1a, b. Two random graphs $G(30,0.4)$ are inter-connected via a fraction $c = 0.2$ of their nodes chosen at random, and links are added with probability μ, interpolating between weak (**a**) or strong (**b**) interconnectivity (see Methods for details). **c** The average ratio of flow changes $R(\ell)$ in the two components (Eq. (8)) is strongly suppressed for both high and low interconnectivity μ. The blue line represents the median value over all distances and the shaded region indicates the 0.25- and 0.75-quantiles. **d** Adjacency matrix for the six-regular graph shown in Fig. 1c and containing a network isolator. Note that all nodes in the graph including those in the network isolator have degree equal to six, which allows us to exclude any potential impact of heterogeneity in the degree on failure spreading in this case. **e** The ratio of flow changes R, now averaged over all possible trigger links ℓ and distances d, vanishes for a network isolator described by the condition $\xi(\mathbf{A}_{12}) = 0$ and increases algebraically with the coherence parameter ξ (cf. Eq. (10)) when perturbed (see Methods for details on the simulation). Again, median and 0.25- and 0.75-quantiles are shown resulting from averaging over all distances and then trigger links.

$\mathbf{A}_{12}$ describes a complete bipartite graph. The subgraph connecting the two modules is referred to as a *network isolator*.

A proof can be found in Supplementary Note 3. Note that, while network isolators prevent failure spreading, we found that they do not influence network controllability as we illustrate in Supplementary Note 4 and Supplementary Fig. 8.

Since most real world examples of networks do not contain perfect network isolators, we have studied the robustness of a network isolator against modifications of the topology. Starting from a unit rank matrix, we perturb the adjacency matrix $\mathbf{A}_{12}$ iteratively (see Methods for details). The deviation of the perturbed matrix $\mathbf{A}_{12}$ from a unit rank matrix is then quantified using its coherence statistics defined as[38],

$$\xi(\mathbf{A}_{12}) = 1 - \min_{i,j} \frac{\langle \vec{a}_i, \vec{a}_j \rangle}{\| \vec{a}_i \| \| \vec{a}_j \|}, \tag{10}$$

where $\vec{a}_i, i = 1, \ldots, m$ are the matrix columns. Note that the latter expression $\cos(\angle \vec{a}_i, \vec{a}_j) = \frac{\langle \vec{a}_i, \vec{a}_j \rangle}{\| \vec{a}_i \| \| \vec{a}_j \|}$ may also be interpreted via the angle between two matrix columns, $\vec{a}_i$ and thus $\xi(\mathbf{A}_{12})$ approaches a value of unity if all columns are parallel. The performance of the isolator is then measured by calculating the ratio of flow changes R, which is obtained from $R(\ell, d)$ by averaging over all possible trigger links and distances. A perfect isolator is characterised by $\xi(\mathbf{A}_{12}) = 0$ and enables a complete containment of failure spreading such that $R = 0$. For perturbed isolators, we find that R increases approximately algebraically with $\xi(\mathbf{A}_{12})$, see Fig. 2e and Supplementary Fig. 5. Hence, the isolation effect persists for small perturbations, albeit with reduced efficiency. Note also that network isolators are not limited to two connected modules, but can be readily generalised to the interconnectivity of three—or more—modules that are mutually shielded against failures as we demonstrate in Supplementary Fig. 4. Finally, we illustrate that network isolators do not increase the vulnerability of a network in case a link located in the isolator fails in Supplementary Fig. 6.

Constructing network isolators in real-world graphs. Network isolators are not limited to the particular situation shown in Fig. 1. In Fig. 3a–c, we identify several subgraphs that allow to easily introduce network isolators into existing topologies. For subgraphs with a prior low connectivity, as measured by a small vertex cut (Fig. 3a) or a small edge cut (Fig. 3b, c), network isolators may be introduced with small network modifications—by adding (a,b) or removing and adding (c) selected links with weights adjusted such that Theorem 1 is fulfilled. For a given graph these recipes may thus be applied as follows: (1) Identify modules of the graph that are weakly connected to one another as measured by a low vertex cut or edge cut of the vertices or edges connecting them. (2) Depending on the target—e.g. whether building new edges or vertices is costly or, on the other hand, a minimum connectivity between the modules is required after the modification—identify the optimal strategy to achieve a complete bipartite connectivity between the modules by adding or removing vertices and edges. Here, the recipes shown in the Figure may be applied directly if the prior connectivity has the indicated edge or vertex cuts. (3) Tune the edge weights such that $\mathrm{rank}(\mathbf{A}_{12}) = 1$ is achieved, i.e. a network isolator is realised.

We illustrate each of the strategies in real-world power grids. We consider the British grid (d), the Scandinavian power grid (e) and the Central European power grid (f) and add a network isolator to each of the networks by making use of the strategies shown in panels a–c. We then simulate the failure of a single link to illustrate that network isolators suppress failure spreading in each situation. Thus, network isolators can be used to make various real-world power grids more resilient to failures. In a Supplementary Fig. 7, we compare the situation with the isolator to the situation before constructing the isolator for each of the networks.

Network isolators suppress cascade propagation. Perfect network isolators can be easily constructed to improve the resilience of complex networked systems. As a practical example we show an application to electric power grids, where large scale blackouts

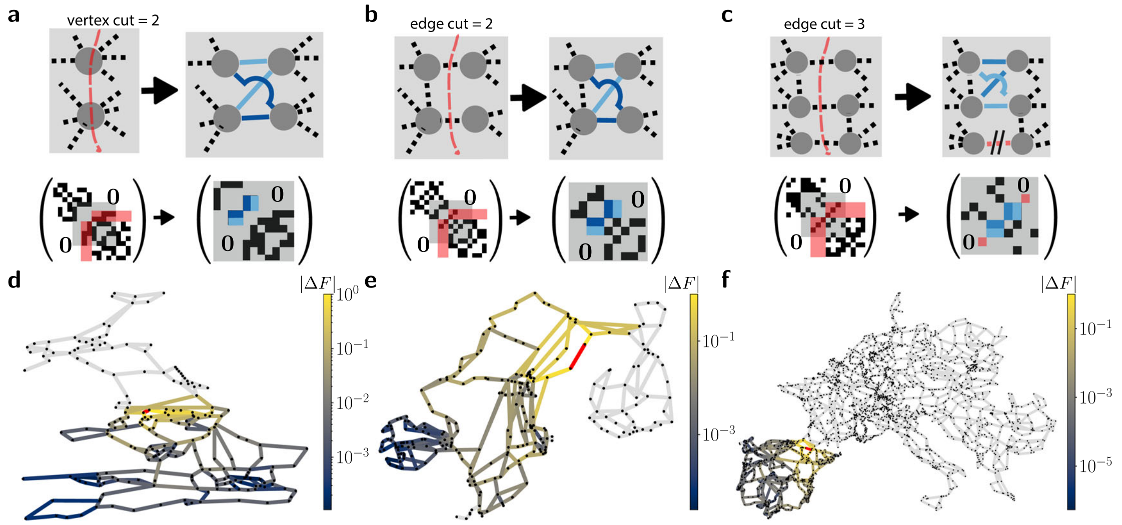

Fig. 3 Different ways of constructing isolators in real-world power grids. a–c Alternative methods of creating an isolator in a given network. We show the network structure before (top left) and after (top right) the addition of a network isolator, as well as corresponding adjacency matrices (bottom) with the different shades of blue representing the weight A_{ij} of the respective edge. A lower prior connectivity simplifies the creation of isolators as measured by the vertex cut (**a**) or edge cut (**b**, **c**) which is visible in the adjacency matrix (entries colored red). The creation of network isolators results in characteristic patterns in the adjacency matrix in terms of the capacities of the isolator edges (shades of blue). **d–f** Realisation of network isolators in real-world power grids. We construct network isolators in the British power grid (**d**), the Scandinavian power grid (**e**) and the Central European power grid (**f**) using the recipes illustrated in (**a–c**). For each power grid, we colour code the flow changes after the failure of a single link carrying a unit flow (red). In each case, the network isolator inhibits flow changes, i.e. $\Delta F = 0$, (light grey) in the part of the network that is shielded by the isolator.

are typically triggered by the outage of a single transmission element which leads to a cascade of failures[3,39]. We demonstrate the impact of network isolators against cascading failures in the case of the Scandinavian grid.

In the original grid layout, the modules are weakly connected, thus failure spreading between these modules is reduced—but it is possible. A failure in one area can spread to other areas and cause a global cascade of failures, as demonstrated in Fig. 4a, b for a cascade emerging in Western Norway. This spreading may in principle be prevented by decoupling different areas of the grid, but this is highly undesired. In fact, future energy systems will require more connectivity, not less, to transmit an increasing amount of renewable electric power[21,22]. In contrast, building a network isolator can completely inhibit failure spreading at increased connectivity. A perfect isolator can be realised with moderate effort by reconstructing two substations in Norway, such that they effectively form two nodes each. The new nodes must be linked by internal connections and one additional two-circuit overhead line, whose parameters are optimised such that the condition $\mathrm{rank}(\mathbf{A}_{12}) = 1$ is satisfied (Fig. 4c). A simulation for such an optimised grid layout shows that the spreading of the cascade is completely suppressed (Fig. 4d). The network remains connected and load shedding is no longer necessary as a containment strategy[2,3]. To demonstrate that network isolators effectively suppress cascade propagation for different networks and initial failure patterns, we evaluate the statistics of cascade sizes in networks with and without network isolators (see Supplementary Fig. 9). To analyse how the relatively localised flow changes involved here lead to a non-local cascade, individual steps of the cascade are shown in Supplementary Fig. 12.

Network isolators beyond linear flow networks. The concept of network isolators has been established for linear flow networks, but can be extended in two ways. (1) We can rigorously prove that network isolators determine the response to structural damages for a class of non-linear networked dynamical systems with diffusive coupling. More precisely, the isolator effect is still rigorously valid if the dynamics of a node i depends on the state of the other nodes x_j only through the term $f_i(\sum_j L_{ij} x_j)$, where $\boldsymbol{L}$ is the Laplacian and the function f_i satisfies $f_i(0) = 0$, but is arbitrary otherwise (see Supplementary Note 3, Corollary 2). (2) For many non-linear systems of practical importance, the impact of failures or perturbations is well described by a linearisation around an equilibrium or limit cycle (see ref. [29]) for which an approximate isolation can be achieved (see Supplementary Note 3, subsection 4).

To systematically analyse how non-linearity affects failure spreading through network isolators we first consider a natural extension of the linear flows in Eq. (1), replacing the linear coupling by its sinusoidal counterpart

$$\tilde{F}_{i\to j} = A_{ij} \cdot \sin(\vartheta_i - \vartheta_j), \tag{11}$$

which yields the well-known Kuramoto model[40,41]. If phase differences between neighbouring vertices are small, one can expand the sine function as $\sin(\vartheta_i - \vartheta_j) = (\vartheta_i - \vartheta_j) + \mathcal{O}((\vartheta_i - \vartheta_j)^3)$ (see Supplementary Note 1). Hence, our previous result remain valid to linear order, whereas a higher degree of non-linearity may gradually weaken the effects. In particular, the effectiveness of a network isolator depends on the relative load of the edges $|\tilde{F}_{i\to j}|/A_{ij}$. We study this numerically by increasing the injections P_i at all nodes proportionally, thus increasing the relative edge loads and the importance of the non-linearity of the sine function.

We then analyse the non-linear flow changes $\Delta\tilde{F}(\ell)$ after the failure of a single link for different degrees of non-linearity in Fig. 5a, b (light to dark lines). To systematically evaluate the degree of non-linearity, we analyse the maximal absolute non-linear flow $|\tilde{F}|_{\max}$ in the entire network. Due to the sinusoidal character of the coupling (see Eq. (11)) and since edge weights are set to unity for the Figure, a relative loading close to unity indicates a highly non-linear system. As expected, the flow changes decrease with distance independently of the non-linearity. However, even for the strongest degree of non-linearity considered here, flow changes in the module shielded by the isolator are still

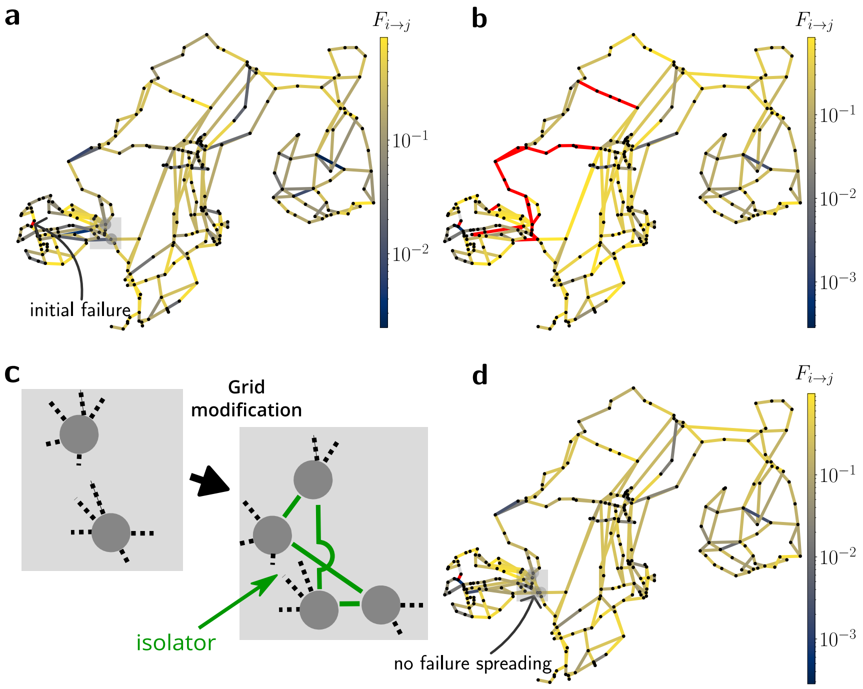

Fig. 4 Network isolators can contain cascading failures in power grids. a Line loading (colour code) on the Scandinavian grid in units relative to maximal loading before the initial failure of a single line (coloured red). **b** The initial failure results in a cascade of overloads (red coloured lines) until the grid disconnects into several parts. **c** Magnification of the grid structure in Eastern Norway (grey box, **a**). A small modification of the grid enables the construction of a network isolator: adopting the recipe presented in Fig. 3a, we select two nodes (left) that are further split up into two separate nodes each which are mutually connected via a network isolator by adding four edges (right, green). Note that the removal of these two nodes would disconnect the network into two separate parts, i.e. they form a vertex cut of size two. **d** Introducing the network isolator completely suppresses the spreading of failures from Western Norway to the rest of the grid thus inhibiting the cascade observed in (**b**). The first two steps of this cascade are shown in Supplementary Fig. 12.

several orders of magnitude lower than at the same distance in the module containing the trigger link. We confirm this result by evaluating the non-linear version of the flow ratio (8) for different graphs, network conditions and degrees of non-linearity in Supplementary Fig. 10. Furthermore, we demonstrate that introducing a network isolator may slightly improve the system's resilience against dynamically induced failures due to transient overloads in Supplementary Fig. 11.

We now study the robustness of this effect in several regards and elucidate possible ways to designing robust network isolators for non-linear systems. The condition $\text{rank}(\mathbf{A}_{12}) = 1$ allows for different possible realisations of network isolators in terms of the edge weights. In linear flow networks, all these realisations are equally efficient: They completely suppress flow changes in the module shielded by the network isolator by virtue of Theorem 1. But which combination of edge weights provides the strongest isolating effect in weakly non-linear systems?

To examine this question systematically we consider a simple but non-trivial realisation of a network isolator where two nodes in one module are connected to two nodes in the other module (see e.g. Fig. 3a, right). The isolator is thus formed by four edges, and we fix the overall possible available edge weight to build the network isolator to a constant value $\mathfrak{A} \in \mathbb{R}$. Hence, the weights of the four edges in the isolator have to satisfy two conditions,

$$a_1 + a_2 + a_3 + a_4 = \mathfrak{A} \quad \text{and} \quad a_1a_4 - a_2a_3 = 0,$$

leaving two degrees of freedom to optimise the isolator performance (see Methods for details). In Fig. 5c we examine the network isolator's performance measured by the averaged, non-linear flow changes in the module shielded by the isolator for all possible failing links in the other module for a weakly non-linear system with flows described by Eq. (11). On the other hand, we analyse the worst-case available $N-1$ weight, i.e. the overall edge weight connecting the two modules if the edge in the network isolator with the largest weight fails. We find that network isolators with strongly heterogeneous edge weights a_1 and a_2 inhibit failure spreading the most in the weakly non-linear system under consideration. However, the uniform choice $a_i = \mathfrak{A}/4, i \in \{1, 2, 3, 4\}$ yields the highest the available $N-1$ weight, while still inhibiting failure spreading relatively strongly. Note that other choices to estimate the impact of removing a single link in the network isolator, e.g. the size of the cascade caused by the failure of the link in the isolator or the reduction in shielding provided by the isolator after the failure might come to a different conclusion which choice of weights yields the "best" network isolator.

We now further extend the results on non-linear systems by considering the full load flow equations that describe power flows in power grids with line losses. The results of the numerical simulations are reported in Fig. 6: First, we consider the impact of a single failing line for a realistic dispatch and realistic line weights in the British power grid without any modification, where flows are now evaluated based on the full non-linear AC load flow[42]. For a given vertex $i \in V(G)$ they are calculated as (Supplementary Note 1, Eq.(8))

$$\begin{aligned} P_i &= \sum_{k=1}^{N} |V_i||V_k|(G_{ik}\cos(\vartheta_i - \vartheta_k) + B_{ik}\sin(\vartheta_i - \vartheta_k)), \\ Q_i &= \sum_{k=1}^{N} |V_i||V_k|(G_{ik}\sin(\vartheta_i - \vartheta_k) - B_{ik}\cos(\vartheta_i - \vartheta_k)). \end{aligned} \tag{12}$$

Note that this set of equations again reduces to the linear flow

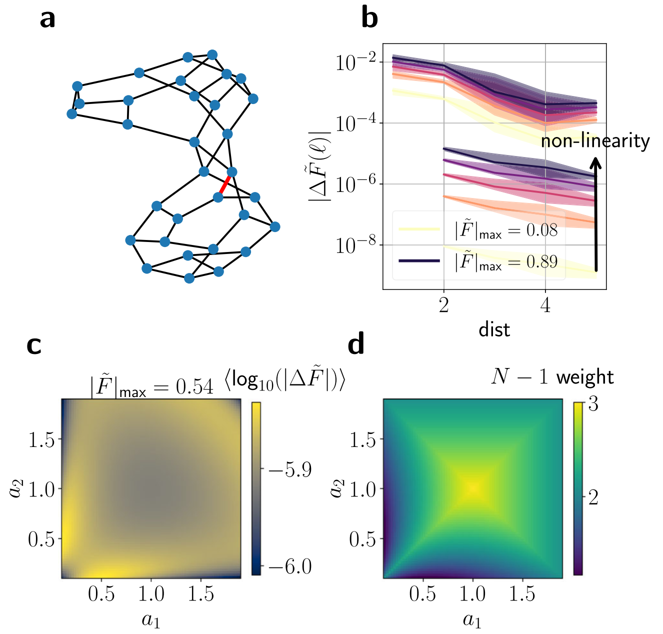

Fig. 5 Robust design of network isolators in the Kuramoto model. a To study the effect of non-linearity on network isolators, we simulate the failure of a single link (red) in a network consisting of two modules that are connected via a network isolator. **b** We consider the median absolute non-linear flow changes $|\Delta\tilde{F}(\ell)|$ (Eq. (11)) on a link ℓ after the removal of the link shown in (**a**). We analyse the effect of edge distance to the failing link (*x*-axis) and increasing degree of non-linearity (colour code from light to dark). We compare the flow changes in the lower module that contains the failing link (curves on the upper left) and the isolated module (curves on the lower right) by averaging the flow changes over all links in the given module at a fixed distance. As expected, flow changes in the upper module are lowest for a weakly non-linear system (bright line) and increase with the non-linearity, but a strong isolation effect persists even for a high degree of non-linearity (dark purple line). Shaded region indicates the 0.25- and 0.75-quantiles evaluated over the given distance. **c** We fix the overall available edge weight of the four edges forming the isolator to $\sum_i a_i = 4$ and systematically scan over the remaining degrees of freedom, measuring the isolator performance in terms of the mean logarithmic flow changes $\langle \log_{10}(|\Delta\tilde{F}|)\rangle$ for a fixed degree of (intermediate) non-linearity. We observe that a heterogeneous isolator where the weights differ strongly provides the best shielding. **d** We evaluate the available worst-case $N-1$ weight, i.e. the overall edge weight connecting the two modules after the failure of a single link in the isolator, for the same set of edge weights as in (**c**). Here, isolators with homogeneous weights perform best. Edge weights of all non-isolator edges are set to unity, $A_{ij} = 1, \forall (i,j) \in E(G)$ in all panels.

model in Eqs. (2) and (1) in the so-called DC approximation (see Supplementary Note 1). As a result, failures spread to both the Northern part of the power grid and the Southern part equally (panel a). After introducing a network isolator by adding two links, flow changes are completely suppressed in the linear approximation of power flows (panel b), but also significantly reduced when calculating the flow changes based on the full non-linear AC power flow: Comparing the non-linearly calculated flow changes in the initial scenario and the scenario with the isolator, we observe an ~100-fold reduction at all distances to the failing link in the module shielded by the network isolator (panel d). Thus we conclude that isolators also suppress failure spreading in non-linear models.

Discussion

In conclusion, connectivity determines the resilience of complex networks in manifold ways. As expected, a division of a network into weakly coupled modules suppresses the spreading of failures from one module to the others. Remarkably, we have found that a strong interconnectivity can equally well suppress the spreading in both flow networks and in networks of non-linear dynamical systems. We have demonstrated that an even stronger effect can be obtained by certain subgraphs called isolators, which completely inhibit the spreading of failures in linear systems.

We then showed that isolators can be easily created in a network to mitigate cascading failures, for instance in electric power grids, while enabling an arbitrary degree of connectivity between the different parts of the network. These results widen our perspective on the large scale organisation of complex networks in general, showing that very diverse structural patterns can exist that isolate functional units and improve network resilience.

Furthermore, our results show that algebraic properties of networks can have striking effects on their function and robustness—depending on the type of flow model. Similar effects are not present in simple models where flows are rerouted along the shortest paths only[4,9], but they can become essential in physical supply network models where various paths contribute and interact in a non-trivial way.

Methods

Creating graphs with strong or weak inter-module connectivity. We introduce a model to create ensembles of graphs consisting of two subgraphs with weak or strong interconnectvity similar to the approach in ref. [43], see Figs. 1 and 2. We start with two disconnected Erdős–Rényi random graphs $G_1(N_1, p_1)$ and $G_2(N_2, p_2)$, where N denotes the number of nodes in the graph and p the probability that two randomly chosen nodes are connected by an edge[34]. Then we randomly choose $n_1 = [c \cdot N_1]$ nodes $v = \{v_1, \ldots, v_{n_1}\}$ in G_1 and $n_2 = [c \cdot N_2]$ nodes $w = \{w_1, \ldots, w_{n_2}\}$ in G_2. Here, $c \in [0, 1] \subset \mathbb{R}$ is a constant representing the share of nodes connecting

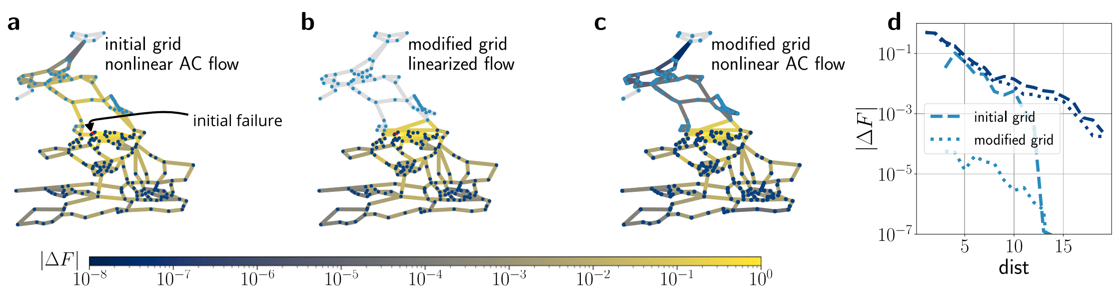

Fig. 6 Network isolators suppress failure spreading in full non-linear AC load flow. a An initially failing link with unit flow (red) in the British power grid results in changes of real power flow (colour code) throughout the whole network, as obtained by computing a non-linear full AC power flow[44]. **b**, **c** After introducing a network isolator based on the strategy presented in panel (**a** of Fig. 3), failure spreading is perfectly inhibited in the linear power flow approximation, and still significantly reduced in the non-linear full AC load flow. **d** We compare the median absolute flow changes, calculated using the non-linear load flow (Eq. (12)), after the failure of the link in the initial grid (dashed lines, **a**) and the modified grid (dotted lines, **c**). Whereas the flow changes in the lower module of the power grid (dark blue nodes) stay approximately the same after the grid modification (dark blue lines), they are significantly reduced in the grid's upper module (light blue nodes) that is shielded by the network isolator (light blue lines).

to the other subgraph and $[\cdot]$ denotes the nearest integer. Out of all possible edges $e = \{(v_1, w_1), \ldots, (v_{n_1}, w_1), \ldots, (v_{n_1}, w_{n_2})\}$ between the two sets of nodes v and w, we randomly add a share of $\mu \in [0, 1]$. The parameter μ controls the connectivity of the two subgraphs G_1 and G_2: They remain disconnected for $\mu = 0$ and they are connected via a complete bipartite graph for for $\mu = 1$. For $c = 1$ and $\mu = p_1 = p_2$ we recover a single Erdős–Rényi random graph with $N = N_1 + N_2$ nodes. Note that this procedure is in principal not limited to ER random graphs. We apply it to study other types of graphs as shown in Supplementary Fig. 1.

Calculating the distance between edges. The notion of distance used throughout the manuscript is the unweighted edge distance. This notion of distance measures the length of the shortest path between two edges $\ell = (r, s)$ and $e = (m, n)$ and is defined as follows[25]

$$\mathrm{dist}(\ell, e) = \min_{v_1 \in \{r,s\}, v_2 \in \{m,n\}} \mathrm{d}(v_1, v_2) + 1, \tag{13}$$

where $\mathrm{d}(v_1, v_2)$ is the unweighted shortest-path or geodesic distance between nodes v_1 and v_2 and the addition of unity ensures that neighbouring edge have a non-vanishing distance.

Perturbing network isolators. The robustness of network isolators to structural perturbations is analysed as follows. Let $G = (E, V)$ be a graph whose nodes are split into two subsets V_1 and V_2 consisting of N_1 and N_2 nodes, respectively. Furthermore, let $\mathbf{A}_{12}$ be the $N_1 \times N_2$ weighted adjacency matrix that encodes the mutual connections between the two parts as described in Theorem 1. Without loss of generality we can order the nodes of the network in such a way that the matrix has the structure

$$\mathbf{A}_{12} = \begin{pmatrix} \vec{a}_1 & \cdots & \vec{a}_m & \vec{0} & \cdots & \vec{0} \\ \vec{0} & \cdots & \vec{0} & \vec{0} & \cdots & \vec{0} \end{pmatrix}, \tag{14}$$

where we assume that n nodes of the first subset are connected to m nodes of the other subset and thus $\vec{a}_1, \ldots, \vec{a}_m \in \mathbb{R}^n$. According to Theorem 1, a perfect network isolator is found if $\mathrm{rank}(\mathbf{A}_{12}) = 1$, i.e. if all vectors $\vec{a}_1, \ldots, \vec{a}_m$ are linearly dependent.

To investigate the robustness of network isolators, we start from a unit rank matrix $\mathrm{rank}\,(\mathbf{A}_{12}) = 1$ and perturb it iteratively. In each step we choose one of the vectors $\vec{a}_i, i = 1, \ldots, m$ at random and perturb it according to $\vec{a}\,'_i = \vec{a}_i + \vec{e}\, \| \vec{a}_i \|$. The elements of the perturbation vector $\vec{e}$ are chosen uniformly at random from the interval $[-\beta, \beta]$, where β is a small parameter, here $\beta = 0.05$.

The deviation of the perturbed matrix $\mathbf{A}_{12}$ from a unit rank matrix is quantified using its coherence statistics[38], Eq. (10),

$$\xi(\mathbf{A}_{12}) = 1 - \min_{i,j} \frac{\langle \vec{a}_i, \vec{a}_j \rangle}{\| \vec{a}_i \| \| \vec{a}_j \|},$$

where $\langle \cdot, \cdot \rangle$ denotes the standard scalar product on $\mathbb{R}^n$ and $\|\cdot\|$ denotes the ℓ^2-norm. For a matrix $\mathbf{A}_{12}$ of unit rank we have $\xi(\mathbf{A}_{12}) = 0$ as all vectors are linearly dependent. For vectors deviating from linear dependence, the measure increases until it reaches its maximum value if two vectors are orthogonal with $\xi(\mathbf{A}_{12}) = 1$.

To create Fig. 2e, we repeated this process 1000 times starting from the perfect isolator shown in panel c. Edge weights were randomly chosen from a normal distribution $\mathcal{N}(10, 1)$ with mean $\mu = 10$ and variance $\sigma^2 = 1$ except for the isolator. The network isolator consists of four nodes in the left subgraph that are completely connected to four nodes in the other subgraph (see Fig. 1c). We select groups of four edges that are connected to a single node in one subgraph and to all four nodes in the other subgraph to have the same weight such that initially rank $(\mathbf{A}_{12}) = 1$. For each perturbed network, we evaluate $\xi(\mathbf{A}_{12})$ and the ratio of flow changes R according to Eq. (3) averaged over all possible trigger links ℓ and distances d. For a perfect isolator, this ratio vanishes due to a vanishing numerator.

Power grid data and cascade model. Power grid data has been extracted from the open European energy system model PyPSA-Eur, which is fully available online[44]. The model includes the topology as well as the susceptance b_ℓ and the line rating $F_{i\to j}^{\max}$ for each high voltage transmission line in Europe. We consider the Scandinavian synchronous grid spanning Norway, Sweden, Finland and parts of Denmark. This grid is coupled to other synchronous grids (central European grid, British grid and Baltic grid) only via high voltage DC transmission lines. Power flow on these lines are actively controlled and can thus be considered constant, thus leading to constant real power injections at the coupling nodes. The Scandinavian grid has 269 nodes and 370 edges, counting multiple-circuit lines only once.

Cascading failures are simulated for fixed power injections P_i for each node corresponding to an economic dispatch for the entire PyPSA-Eur model that includes a security margin given by the constraint $|F_{i\to j}| \le 0.8 \cdot F_{i\to j}^{\max}$. The cascade is triggered by the failure of a single line (r, s) which is effectively removed from the grid. The simulation then proceeds step-wise; In each step, we first calculate the nodal phase angles ϑ_i and real power flows $F_{i\to j}$ for all nodes and lines, respectively, by solving the continuity equation $P_i = \sum_j F_{i\to j}$ with $F_{i\to j} = A_{ij}(\vartheta_i - \vartheta_j)$. Then we check for overloads: Any line (i, j) with $|F_{i\to j}| > F_{i\to j}^{\max}$ undergoes an emergency shutdown and is removed from the grid. The simulations are stopped when no further overload occurs or when the grid is disconnected.

Note that this mechanism for cascading failures is different from the cascading failure mechanism typically analysed in node capacity load models (see e.g. refs. [45,46]). The redistribution of nodal loads or flows after failures in such models is typically based on the neighbourhood of nodes, on shortest path betweenness measures or on other 'intelligent' redistribution schemes whereas the redistribution of flows after failures in linear flow networks or power grids studied using AC load flow analysis are given by the physical laws governing electrical networks. Furthermore, in most cases nodes—not edges—are assumed to fail, which is not the typical case in real power grids.

Processing leaf data. The leaf venation network is based on a microscopic recording of a leaf of the species *Bursera hollickii* provided by the authors of ref. [47]. Edge weights A_{ij} are assumed to scale with the radius r_{ij} of the corresponding vein (i, j) as $A_{ij} \propto r_{ij}^4$ according to the Hagen–Poisseuille law, see ref. [28] for a detailed discussion. We used the radius in pixel scanned at a resolution of 6400 dpi.

Parametrising network isolators with four edges. Consider a network isolator that connects two vertices from one module with two vertices in the other module and consists of four edges in total (see Fig. 3a, right). Denote the weights of the four edges by a_1, a_2, a_3, a_4 and assume that we fix the overall available weight to build the network isolator. Including the rank conditions, the edge weights have to satisfy two constraints,

$$\sum_{\ell=1}^{4} a_\ell = \mathfrak{A} = 4$$

$$\mathrm{rank}\left(\begin{pmatrix} a_1 & a_2 \\ a_3 & a_4 \end{pmatrix} \right) = 1 \Rightarrow a_1 \cdot a_4 = a_2 \cdot a_3,$$

thus leaving two degrees of freedom. We can then solve this set of equations for two variables and treat the remaining ones, a_3, a_4, as parameters that are varied independently:

$$a_1 = a_3 \frac{(\mathfrak{A} - a_4 - a_3)}{a_3 + a_4}, \quad a_2 = a_4 \frac{(\mathfrak{A} - a_4 - a_3)}{a_3 + a_4}.$$

For the simulations shown in Fig. 5c, d. we have set $\mathfrak{A} = 4$.

Varying the degree of non-linearity. To vary the degree of non-linearity systematically in Fig. 5, we first randomly assign 25% of the nodes to be identical sources and the remaining ones to be identical sinks and choose their value such that Eq. (3) is fulfilled. We then calculate the non-linear flows by combining Eq. (2) with the non-linear flows (Eq. (11)). For sources, we set $P_i = 0.09$ (bright line) initially and then systematically increase (decrease) the injections at all sources (sinks) by the factors 3.5, 6.0, 8.5, 11 (lines from light to dark) up until a maximum value of $P_i = 0.99$ is reached (black line) which corresponds to a maximum flow in the network of $|\tilde{F}|_{\max} = 0.89$.

Data availability

The topology of the Scandinavian power grid, the Central European power grid and the British power grid have been extracted from the open European energy system model PyPSA-Eur[44], which is fully available online at https://doi.org/10.5281/zenodo.3886532. Leaf data was provided by the authors of ref. [47] and is available from the respective authors upon reasonable request.

Code availability

Computer code will be made available at https://github.com/FNKaiser/Inhibiting_Failure_Spreading upon publication.

Received: 26 October 2020; Accepted: 19 April 2021;
Published online: 25 May 2021

References

1. Albert, R., Jeong, H. & Barabási, A.-L. Error and attack tolerance of complex networks. *Nature* **406**, 378–382 (2000).
2. Yang, Y., Nishikawa, T. & Motter, A. E. Small vulnerable sets determine large network cascades in power grids. *Science* **358**, eaan3184 (2017).
3. Pourbeik, P., Kundur, P. & Taylor, C. The anatomy of a power grid blackout - root causes and dynamics of recent major blackouts. *IEEE Power Energy Mag.* **4**, 22–29 (2006).

4. Witthaut, D., Rohden, M., Zhang, X., Hallerberg, S. & Timme, M. Critical links and nonlocal rerouting in complex supply networks. *Phys. Rev. Lett.* **116**, 138701 (2016).
5. Sack, L., Dietrich, E. M., Streeter, C. M., Sanchez-Gomez, D. & Holbrook, N. M. Leaf palmate venation and vascular redundancy confer tolerance of hydraulic disruption. *Proc. Natl Acad. Sci.* **105**, 1567–1572 (2008).
6. Dunne, J. A. & Williams, R. J. Cascading extinctions and community collapse in model food webs. *Philos. Transact. Royal Soc. B: Biol. Sci.* **364**, 1711–1723 (2009).
7. Strogatz, S. H. Exploring complex networks. *Nature* **410**, 268 (2001).
8. Sahasrabudhe, S. & Motter, A. E. Rescuing ecosystems from extinction cascades through compensatory perturbations. *Nat. Commun.* **2**, 170 (2011).
9. Motter, A. E. Cascade Control and Defense in Complex Networks. *Phys. Rev. Lett.* **93**, 098701 (2004).
10. D'Souza, R. M. Curtailing cascading failures. *Science* **358**, 860–861 (2017).
11. Lin, Y., Burghardt, K., Rohden, M., Noël, P.-A. & D'Souza, R. M. Self-organization of dragon king failures. *Phys. Rev. E* **98**, 022127 (2018).
12. Stouffer, D. B. & Bascompte, J. Compartmentalization increases food-web persistence. *Proc. Natl Acad. Sci.* **108**, 3648–3652 (2011).
13. Gilarranz, L. J., Rayfield, B., Liñán-Cembrano, G., Bascompte, J. & Gonzalez, A. Effects of network modularity on the spread of perturbation impact in experimental metapopulations. *Science* **357**, 199–201 (2017).
14. Hens, C., Harush, U., Haber, S., Cohen, R. & Barzel, B. Spatiotemporal signal propagation in complex networks. *Nat. Phys.* **15**, 403 (2019).
15. Brummitt, C. D., D'Souza, R. M. & Leicht, E. A. Suppressing cascades of load in interdependent networks. *Proc. Natl Acad. Sci.* **109**, E680–E689 (2012).
16. Radicchi, F., Castellano, C., Cecconi, F., Loreto, V. & Parisi, D. Defining and identifying communities in networks. *Proc. Natl Acad. Sci.* **101**, 2658–2663 (2004).
17. Girvan, M. & Newman, M. E. J. Community structure in social and biological networks. *Proc. Natl Acad. Sci.* **99**, 7821–7826 (2002).
18. Newman, M. E. J. Communities, modules and large-scale structure in networks. *Nat. Phys.* **8**, 25–31 (2012).
19. Lasseter, R. H. Microgrids. In *2002 IEEE Power Engineering Society Winter Meeting. Conference Proceedings (Cat. No. 02CH37309)*, vol. 1, 305–308 (IEEE, 2002).
20. Mureddu, M., Caldarelli, G., Damiano, A., Scala, A. & Meyer-Ortmanns, H. Islanding the power grid on the transmission level: less connections for more security. *Sci. Rep.* **6**, 34797 (2016).
21. Schlachtberger, D. P., Brown, T., Schramm, S. & Greiner, M. The benefits of cooperation in a highly renewable european electricity network. *Energy* **134**, 469–481 (2017).
22. Tröndle, T., Lilliestam, J., Marelli, S. & Pfenninger, S. Trade-offs between geographic scale, cost, and infrastructure requirements for fully renewable electricity in europe. *Joule* **4**, 1929–1948 (2020).
23. Gavrilchenko, T. & Katifori, E. Resilience in hierarchical fluid flow networks. *Phys. Rev. E* **99**, 012321 (2019).
24. Purchala, K., Meeus, L., Dommelen, D. V. & Belmans, R. Usefulness of dc power flow for active power flow analysis. In *IEEE Power Engineering Society General Meeting*, Vol. 1, 454–459 (IEEE, 2005).
25. Strake, J., Kaiser, F., Basiri, F., Ronellenfitsch, H. & Witthaut, D. Non-local impact of link failures in linear flow networks. *N J. Phys.* **21**, 053009 (2019).
26. Stott, B., Jardim, J. & Alsac, O. DC Power Flow Revisited. *IEEE Transact. Power Syst.* **24**, 1290–1300 (2009).
27. Katifori, E., Szöllősi, G. J. & Magnasco, M. O. Damage and fluctuations induce loops in optimal transport networks. *Phys. Rev. Lett.* **104**, 048704 (2010).
28. Coomes, D. A., Heathcote, S., Godfrey, E. R., Shepherd, J. J. & Sack, L. Scaling of xylem vessels and veins within the leaves of oak species. *Biol. Lett.* **4**, 302–306 (2008).
29. Manik, D. et al. Network susceptibilities: theory and applications. *Phys. Rev. E* **95**, 012319 (2017).
30. Newman, M. E. J. *Networks: An introduction* (Oxford University Press, 2010).
31. Fortunato, S. Community detection in graphs. *Phys. Rep.* **486**, 75–174 (2010).
32. Kaiser, F., Strake, J. & Witthaut, D. Collective effects of link failures in linear flow networks. *N J. Phys.* **22**, 013053 (2020).
33. Kettemann, S. Delocalization of disturbances and the stability of ac electricity grids. *Phys. Rev. E* **94**, 062311 (2015).
34. Erdős, P. On the evolution of random graphs. *Publ. Math. Inst. Hungarian Acad. Sci.* **5**, 17–61 (1960).
35. Pecora, L. M., Sorrentino, F., Hagerstrom, A. M., Murphy, T. E. & Roy, R. Cluster synchronization and isolated desynchronization in complex networks with symmetries. *Nat. Commun.* **5**, 1–8 (2014).
36. Sorrentino, F., Pecora, L. M., Hagerstrom, A. M., Murphy, T. E. & Roy, R. Complete characterization of the stability of cluster synchronization in complex dynamical networks. *Sci. Adv.* **2**, e1501737 (2016).
37. Nicosia, V., Valencia, M., Chavez, M., Díaz-Guilera, A. & Latora, V. Remote Synchronization Reveals Network Symmetries and Functional Modules. *Phys. Rev. Lett.* **110**, 174102 (2013).
38. Tropp, J. A. & Wright, S. J. Computational methods for sparse solution of linear inverse problems. *Proc. IEEE* **98**, 948–958 (2010).
39. Schäfer, B., Witthaut, D., Timme, M. & Latora, V. Dynamically induced cascading failures in power grids. *Nat. Commun.* **9**, 1975 (2018).
40. Dörfler, F. & Bullo, F. Synchronization in complex networks of phase oscillators: a survey. *Automatica* **50**, 1539–1564 (2014).
41. Rodrigues, F. A., Peron, T. K. D., Ji, P. & Kurths, J. The kuramoto model in complex networks. *Phys. Rep.* **610**, 1–98 (2016).
42. Wood, A. J., Wollenberg, B. F. & Sheblé, G. B. *Power Generation, Operation and Control*. (John Wiley & Sons, 2014).
43. Nematzadeh, A., Ferrara, E., Flammini, A. & Ahn, Y.-Y. Optimal Network Modularity for Information Diffusion. *Phys. Rev. Lett.* **113**, 8 (2014).
44. Hörsch, J., Hofmann, F., Schlachtberger, D. & Brown, T. PyPSA-eur: an open optimisation model of the european transmission system. *Energy Strategy Rev.* **22**, 207–215 (2018).
45. Motter, A. E. & Lai, Y.-C. Cascade-based attacks on complex networks. *Phys. Rev. E* **66**, 065102 (2002).
46. Crucitti, P., Latora, V. & Marchiori, M. Model for cascading failures in complex networks. *Phys. Rev. E* **69**, 045104 (2004).
47. Ronellenfitsch, H., Lasser, J., Daly, D. C. & Katifori, E. Topological Phenotypes Constitute a New Dimension in the Phenotypic Space of Leaf Venation Networks. *PLOS Comput. Biol.* **11**, e1004680 (2015).

Acknowledgements

We thank Tom Brown and Jonas Hörsch for help with the processing of power grid data, Eleni Katifori and Henrik Ronellenfitsch for providing the leaf data and Raissa D'Souza and Jürgen Kurths for valuable discussions. We gratefully acknowledge support from the Federal Ministry of Education and Research (BMBF grant no. 03EK3055B D.W.), the Helmholtz Association (via the joint initiative "Energy System 2050—a Contribution of the Research Field Energy" and grant no. VH-NG-1025 to D.W.). V.L.'s work was funded by the Leverhulme Trust Research Fellowship CREATE.

Author contributions

D.W. conceived research and acquired funding. F.K., V.L. and D.W. designed research. F.K. carried out all numerical simulations, evaluated the results and designed all figures. All authors contributed to discussing the results and writing the paper.

Funding

Open Access funding enabled and organized by Projekt DEAL.

Competing interests

The authors declare no competing interests.

Additional information

Supplementary information The online version contains supplementary material available at https://doi.org/10.1038/s41467-021-23292-9.

Correspondence and requests for materials should be addressed to D.W.

Peer review information *Nature Communications* thanks the anonymous reviewer(s) for their contribution to the peer review of this work. Peer reviewer reports are available.

Reprints and permission information is available at http://www.nature.com/reprints

Publisher's note Springer Nature remains neutral with regard to jurisdictional claims in published maps and institutional affiliations.

Supplemental Material

Supplementary Information for
Network isolators inhibit failure spreading in complex networks

Franz Kaiser,[1,2] Vito Latora,[3,4,5,6] and Dirk Witthaut[1,2]

[1] *Forschungszentrum Jülich, Institute for Energy and Climate Research (IEK-STE), 52428 Jülich, Germany*
[2] *Institute for Theoretical Physics, University of Cologne, Köln, 50937, Germany*
[3] *School of Mathematical Sciences, Queen Mary University of London, London E1 4NS, UK*
[4] *Dipartimento di Fisica ed Astronomia, Università di Catania and INFN, 95123 Catania, Italy*
[5] *The Alan Turing Institute, The British Library, London NW1 2DB, UK*
[6] *Complexity Science Hub Vienna, 1080 Vienna, Austria*

(Dated: April 8, 2021)

This Supplementary Material contains four Supplementary Notes and twelve Supplementary Figures.

SUPPLEMENTARY FIGURES

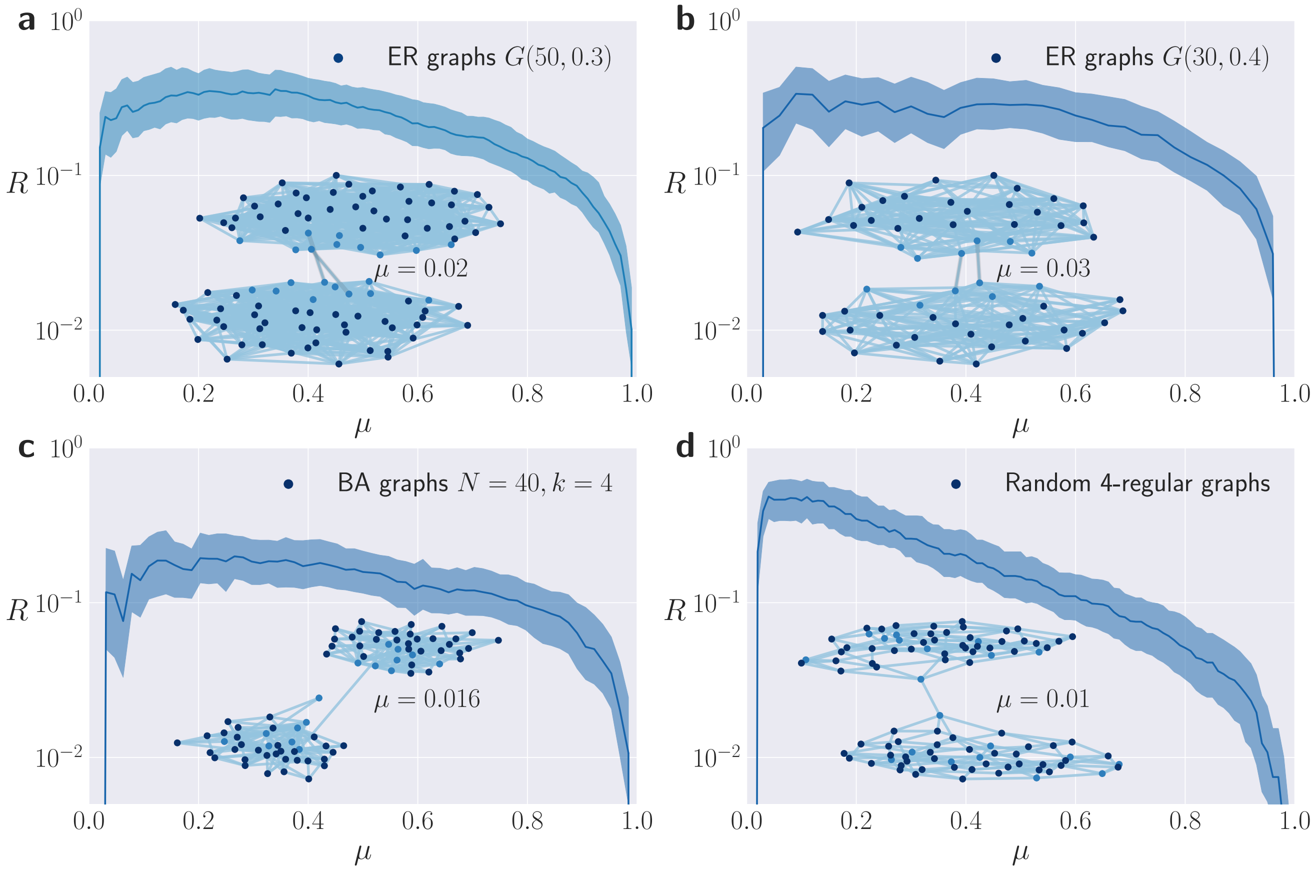

Supplementary Figure 1. **Averaged ratio of flow changes decays with high and low connectivity for different random graphs.** All panels show ratio of flow changes R averaged over all links and distances against connectivity parameter μ (see methods) along with corresponding graph for low values of the connectivity parameter. **a** Two ER graphs with parameters $N_i = 50, p_i = 0.3$ connected with probability $\mu = 0.02$ at a randomly chosen share of $c = 0.2$ their nodes. **b** Same as in (a), but with parameters $N_i = 30, p_i = 0.4, \mu = 0.03, c = 0.2$. **c** A similar scaling is observed if two BA random graphs with parameters $N_i = 40, k_i = 4$ are connected with probability $\mu = 0.016$ at a randomly chosen share of $c = 0.2$ their nodes. **d** The scaling is also preserved if two 4-regular, random graphs are connected with parameters $N = 50, \mu = 0.01, c = 0.2$. Blue line represents median value over all distances and shaded region indicates 0.25- and 0.75-quantiles for all graphs.

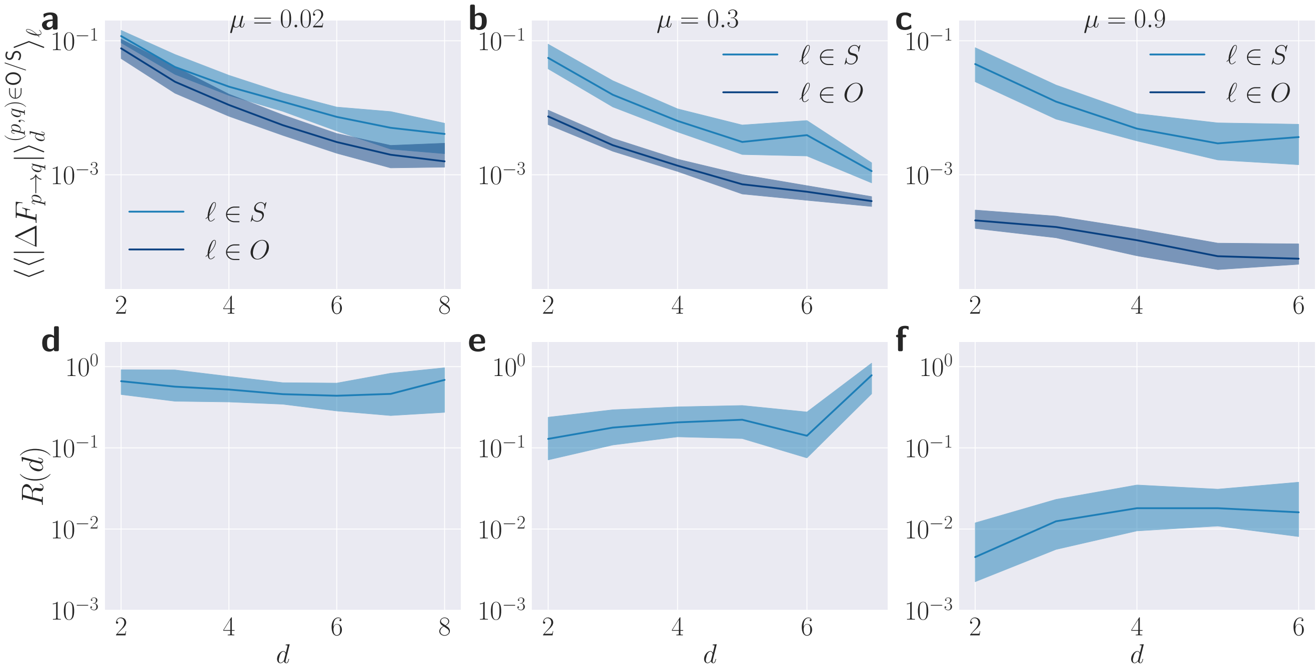

Supplementary Figure 2. **Ratio of flow changes depends weakly on distance.** We examine the scaling of link flow changes with distance for two ER random graphs $G(120, 0.02)$ that are connected at $c = 0.2$ nodes with changing probabilities $\mu = 0.02$ (left), $\mu = 0.3$ (centre) and $\mu = 0.9$ (right). We only consider the largest component from each of the two random graphs and remove all dead ends as they result in vanishing flow changes. **a** to **c** Normalised absolute flow changes decay with distance when averaging over all possible trigger links. We always assume a unit flow on the failing link before the failure. We distinguish flow changes in the same (blue, top) and the other (purple, bottom) module of the graph. Flow changes are consistently higher in the same module for all distances. **d** to **f** Ratio of flow changes averaged over all possible trigger links $R(d)$ reveals a weak dependence of the ratio on distance. Blue line represents median value over all distances and shaded region indicates 0.25- and 0.75-quantiles for all graphs.

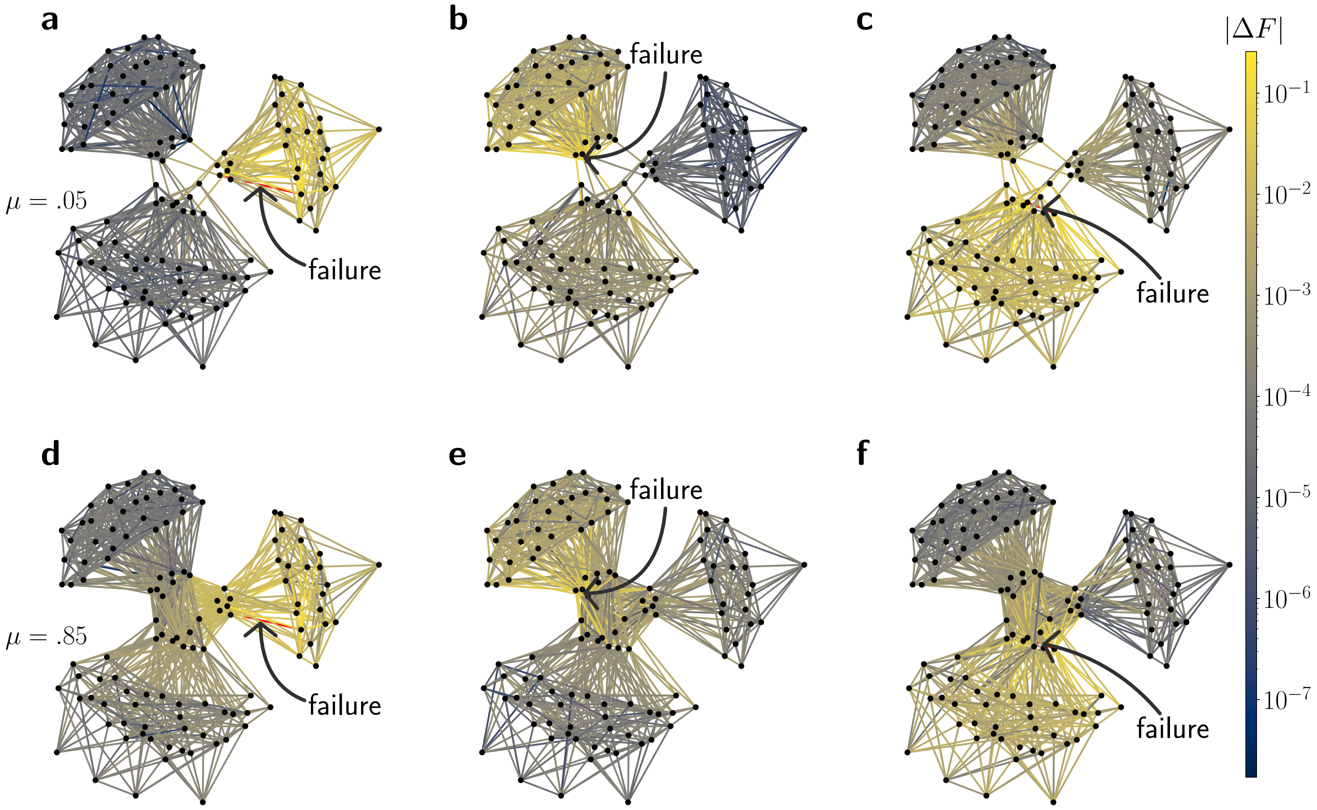

Supplementary Figure 3. **Increasing or decreasing connectivity between more than two modules reduces failure spreading equally well.** Here, we demonstrate a possible extension of the synthetic network model described in the Methods section to more than two modules. For each panel, we simulate a single link failure (red) that results in flow changes (colour coded). **a** to **c** Three ER random graphs $G(30, 0.3)$ (right), $G(50, 0.2)$ (bottom) and $G(40, 0.4)$ (top left) that are mutually interconnected with probability $\mu = 0.05$ at 20 percent, i.e., $c = 0.2$, thus resulting in three mutually weakly connected modules. **d** to **f** Connecting the same modules as shown in a to c with probability $\mu = 0.85$, thus resulting in strong inter-module connectivity, reduces failure spreading equally well.

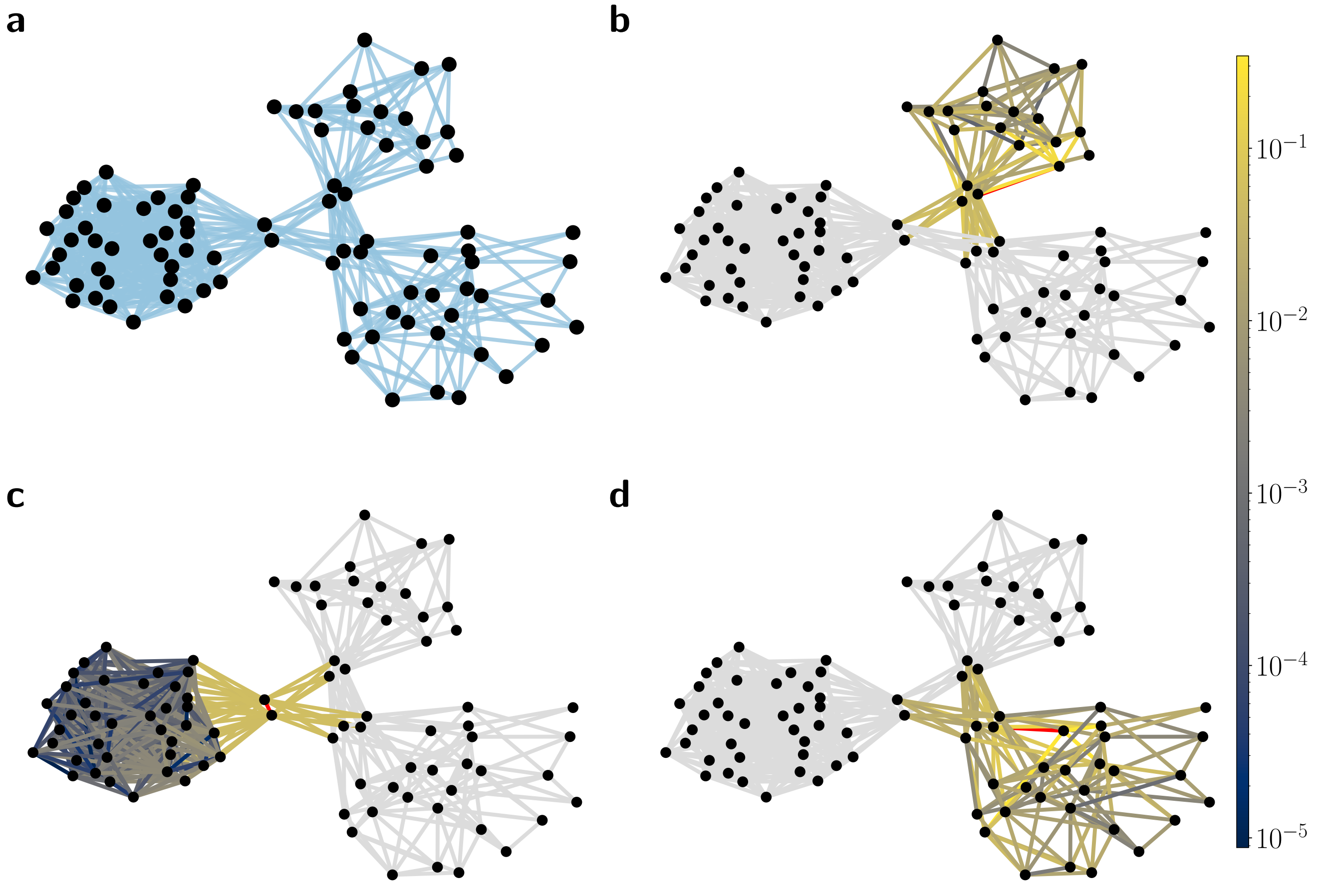

Supplementary Figure 4. **Networks isolators can be generalised to network consisting of more than two modules.** **a** Topology of a network consisting of three ER random graphs $G(40, 0.4)$ (left), $G(20, 0.3)$ (top) and $G(30, 0.2)$ (bottom right) that are mutually connected through network isolators. **b** to **d** Link failures in each of the individual subgraphs (red lines) do not change flows (colour code) in any of the other subgraphs.

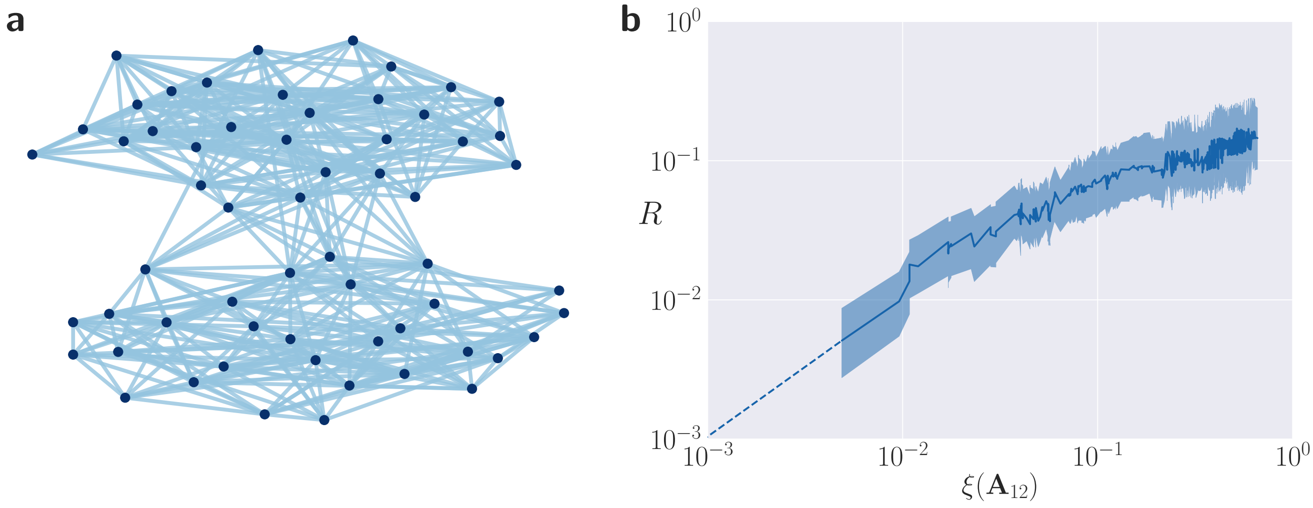

Supplementary Figure 5. **Robustness of network isolators shows the same scaling with perturbations for different graphs.** Robustness of network isolators measured by ratio of flow changes R averaged over all links against measure of perturbations to network isolators $\xi(\mathbf{A}_{1,2})$. **a** Graph created from the graph ensemble and shown in Fig. 1c was modified in such a way that it contains a network isolator connecting five nodes from one part to five nodes of the other part through a bipartite connectivity structure. Edge weights are drawn randomly from a normal distribution $\mathcal{N}(10, 1)$ except for the network isolator where the randomly chosen weights of five edges starting in the same node and connecting to all connecting nodes in the other part were chosen as basis weights for all other connections between the two parts. **b** The isolator robustness shows qualitatively the same scaling as for the 6-regular graph shown in Fig. 1c. Perturbations were applied in 1000 repetitions choosing a perturbation strength of $\alpha = 0.05$. Dotted line takes into account the fact that the curve goes through the point $\xi = R = 0$ for a perfect isolator.

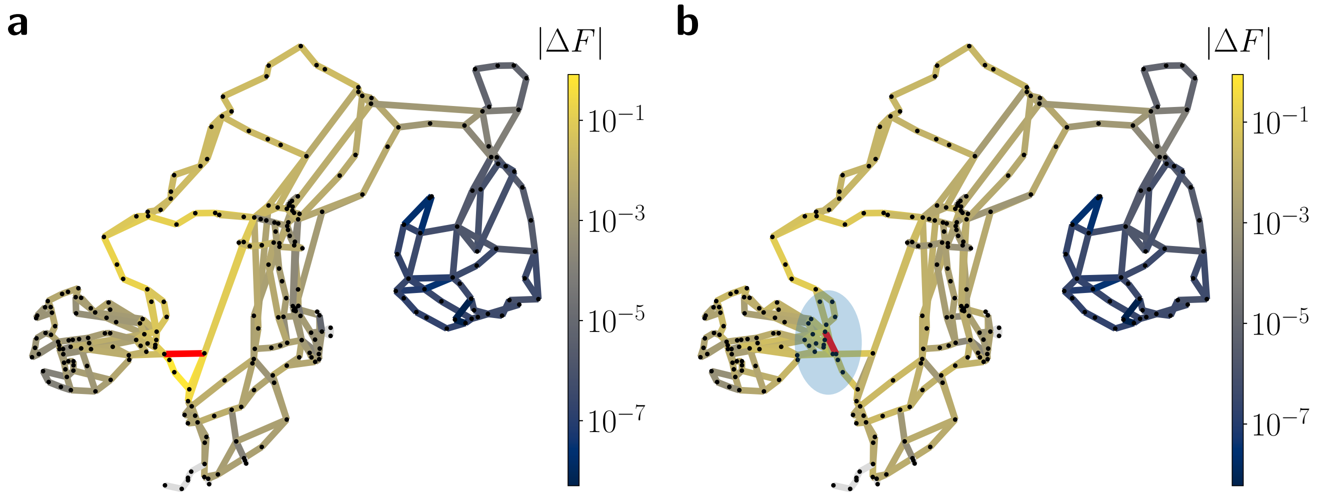

Supplementary Figure 6. **Network isolators do not generally increase grid vulnerability.** **a** Failure of a link with unit flow in the Scandinavian grid before the construction of the network isolator yields a strong response in terms of absolute flow changes $|\Delta F|$. **b** After adding two links to create a network isolator (blue shaded region, see Figure 3c), we simulate a failure of one of the links *in* the isolator. We observe that both, the failure within the isolator (panel b) as well as a failure in the initial grid in close proximity to the location where the isolator is constructed (panel a) yield a similar effect. In this case, the network's vulnerability is thus not increased by including the network isolator. However, a failure in the isolator may potentially affect the whole network.

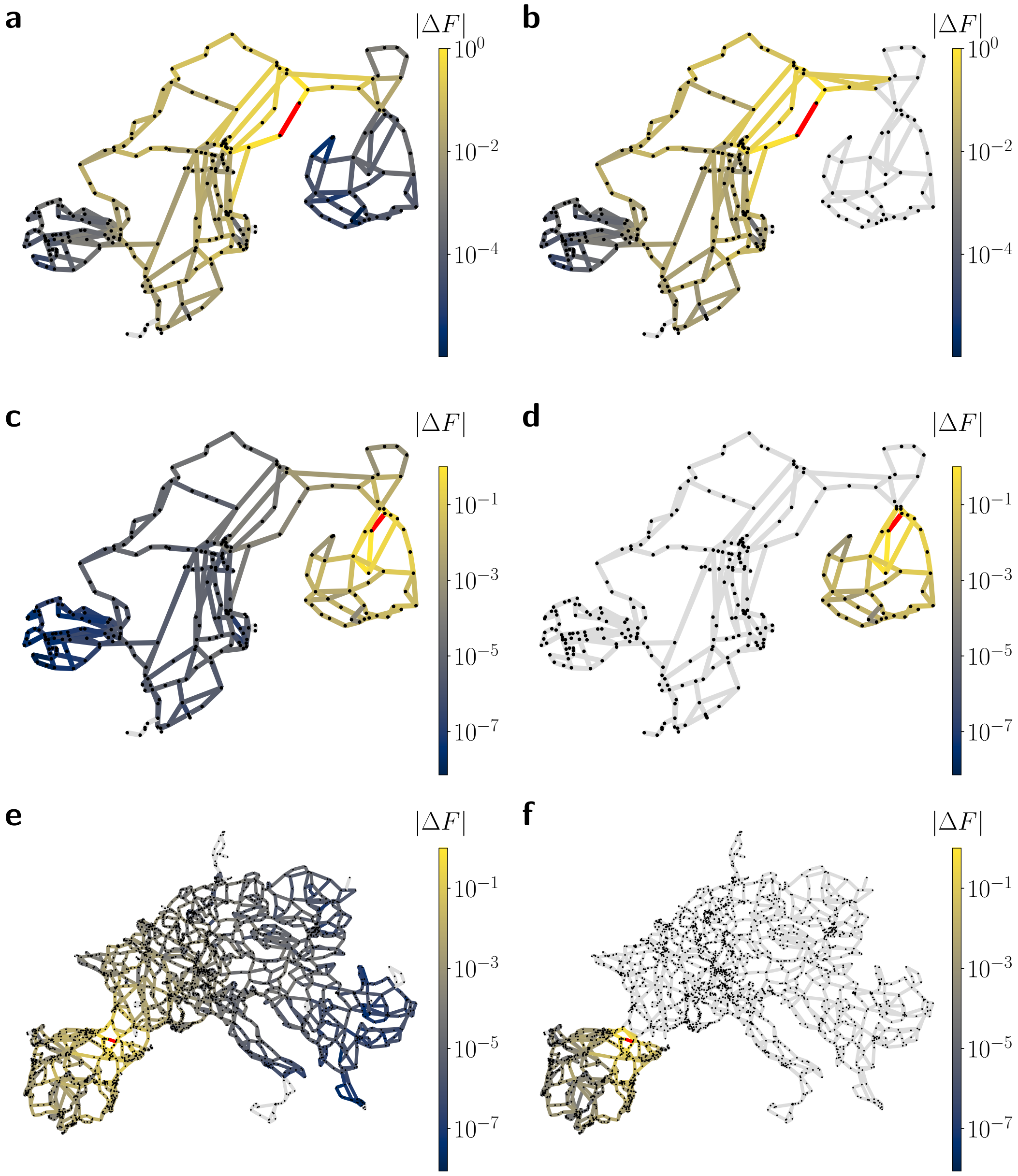

Supplementary Figure 7. **Network isolators may be realised in various real-world power grids.** All grid topologies and line susceptances were extracted from the open European energy system model PyPSA-Eur, which is fully available online[1]. **a,c,e** Initial failure of a link (red) with unit flow results in flow changes in the whole network for Scandinavia a,c as well as the central European grid e. **b,d,f** After introducing network isolators to the grids, failure spreading to other parts of the network is completely stopped. The construction of isolators follows the “recipes” illustrated in Figure 3.

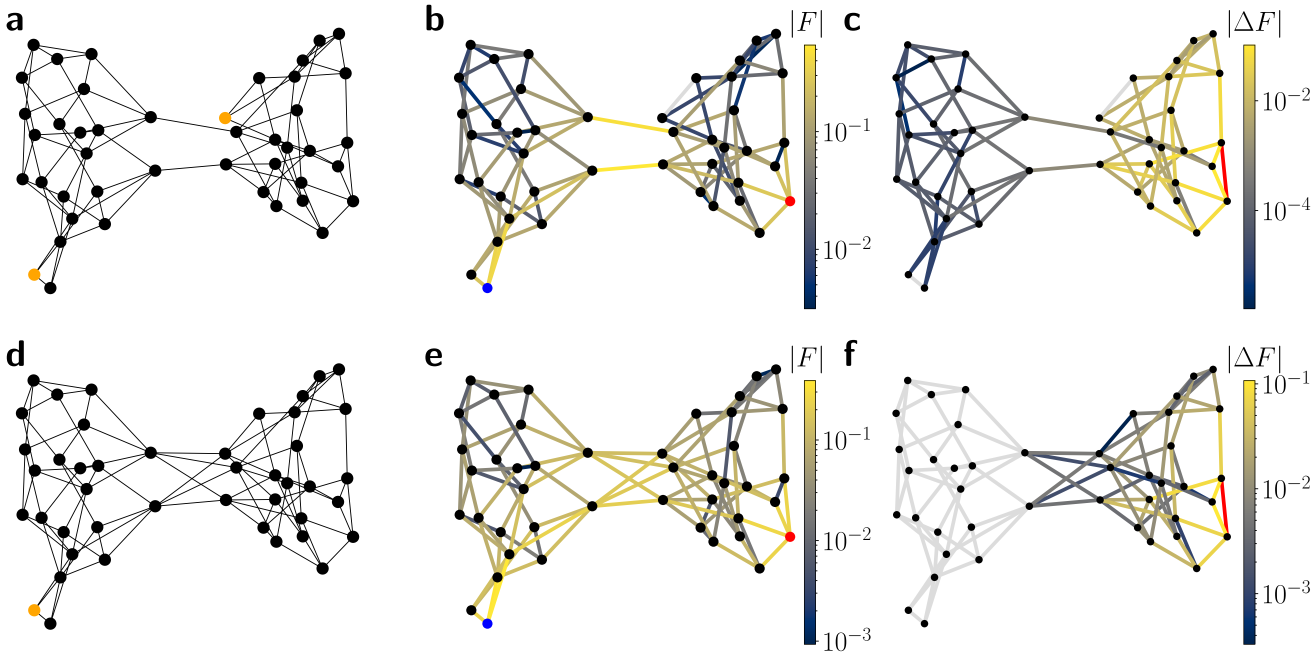

Supplementary Figure 8. **Isolators do not generally prevent the controllability of a network. a** An example of an undirected network with two weakly connected components that requires $N_D = 2$ driving nodes (in orange) to be controlled. This can be calculated from the graph adjacency matrix, which has, by construction, an eigenvalue $\lambda^M = -1$ with algebraic multiplicity $\delta(\lambda^M) = 2$ (See Eq. 20 and Ref. [2]). **d** After adding a few links to create a network isolator, we have $N_D = 1$ and only one node (colored orange) is necessary to control the entire network, i.e., the network isolator has in this case increased the controllability of the network. **b** We show the flows obtained by our linear flow model for a single source of power $P = 1$ at the node colored in red and a single sink with $P = -1$ at the node colored in blue. The resulting (absolute) flows are color-coded: The flow can easily reach from the red node to the blue node. **e** Adding the isolator, flow can still propagate freely from the source node (red) to the target node (blue) in the same way as in panel b. Hence, the isolator does not prevent the propagation of flows. **c** Simulating the failure of a single link (red), we observe that flows do also change in the other part of the network. **f** Conversely, the isolator does prevent propagation of flow changes caused by a link failure in the right part of the network to its left part.

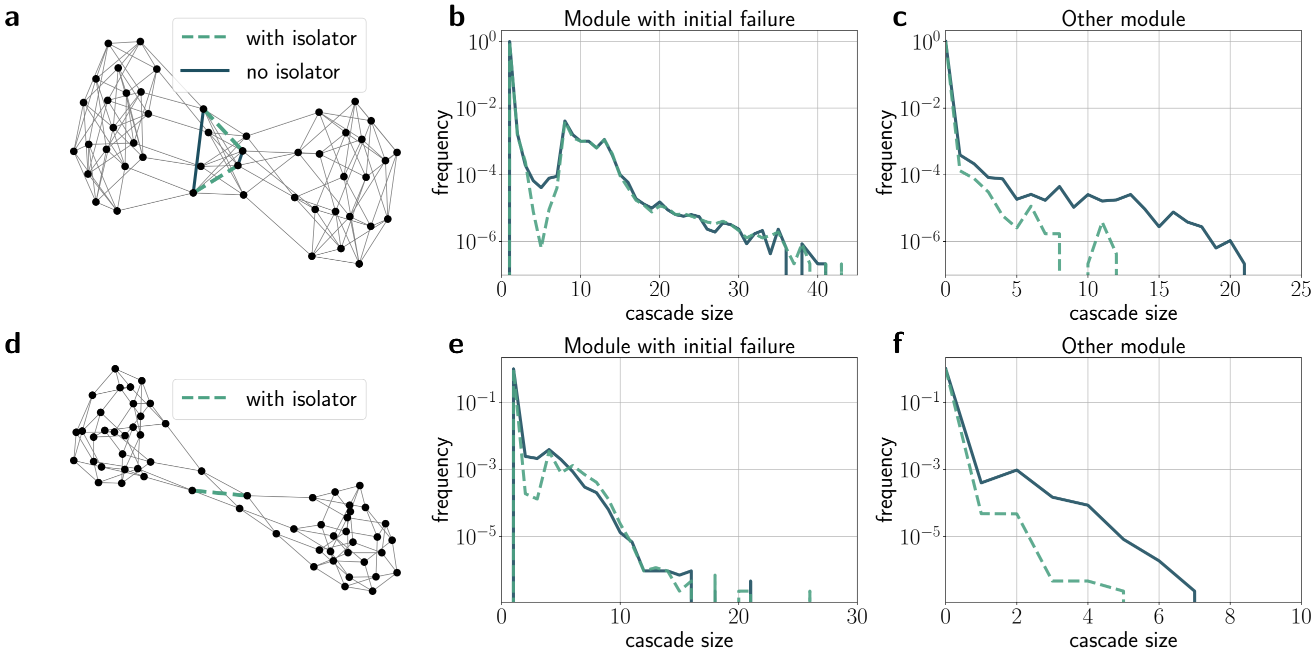

Supplementary Figure 9. **Cascade propagation is strongly suppressed in the presence of network isolators.** **a** We consider the six-regular graph shown in Figure 1c with unit edge weights and $7 \cdot 10^4$ different initial conditions where we randomly assign 25% of the nodes to be sources with $P_i = 2$ and the remaining ones to be sinks with $P_i = -\frac{2}{3}$. We then simulate the failure of any possible link in the left module of the network for each initial condition using the linear flow model and monitor the size of the resulting cascade of failures, setting the line limit to $F_{i\to j}^{\max} = 1.0$ (see Methods). We compare two different graphs: the six-regular graph containing a network isolator (light green, dotted) and a corresponding six-regular graph where to links have been rewired (dark green). **b,c** For both graphs, we compare the cascade sizes in the module where the failure was triggered (b) and the other module (c). As a result, cascade sizes are significantly smaller if the other module is shielded by a network isolator although the overall connectivity between the modules is higher in this case. **d-f** We perform the same set of simulations for the graph shown in panel d which conforms the result of reduced cacade sizes in the presence of network isolators. Parameters for panels d-f are given by $P_i = 0.9$ for sources and $P_i = -0.3$ for sinks.

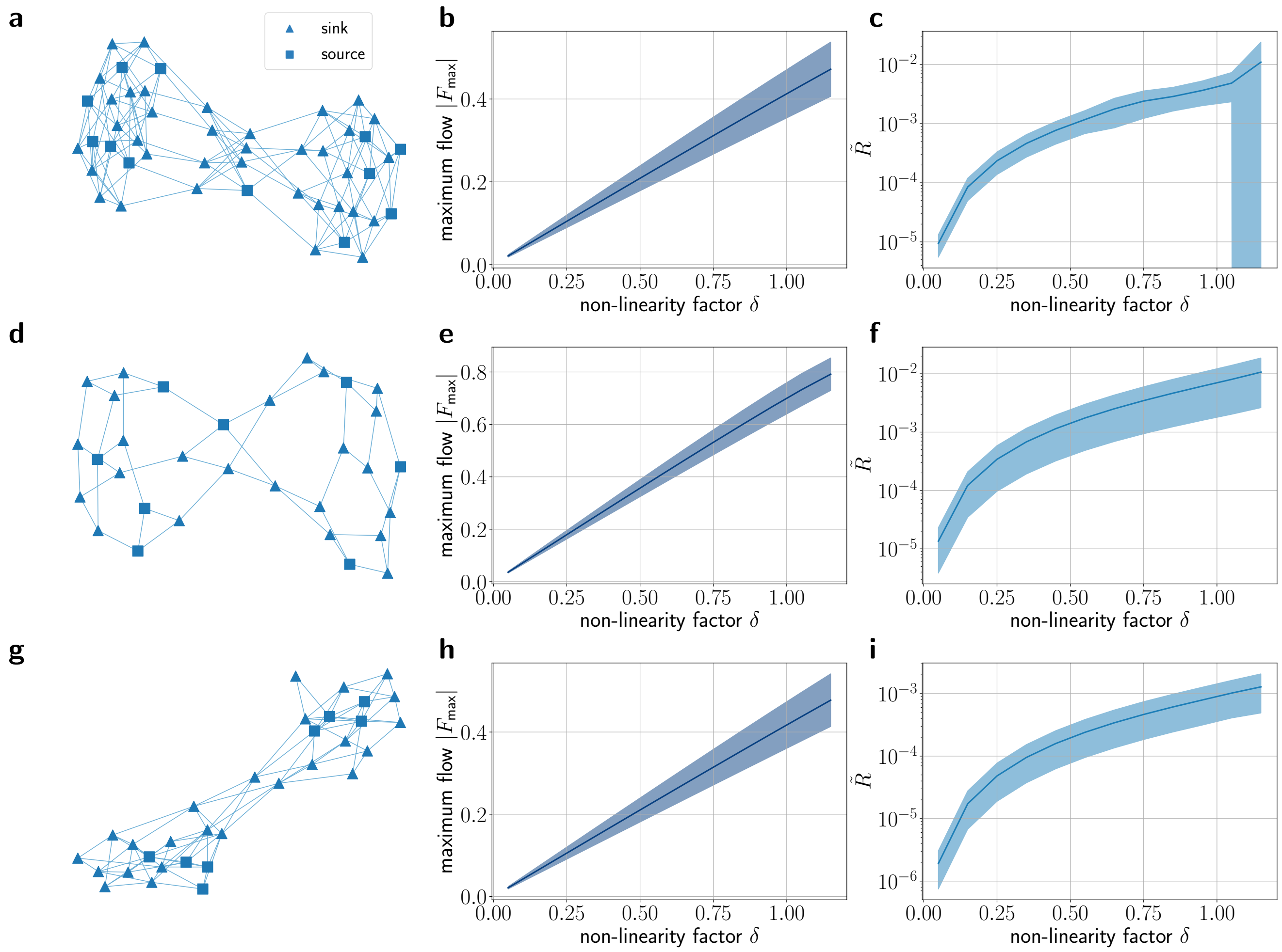

Supplementary Figure 10. **Network isolation effect persists for non-linear flows.** **a** We consider the six-regular graph shown in Figure 1c and simulate 50 different initial conditions where we randomly assign 25% of the nodes to be sources with $P_i = 0.9 \cdot \delta$ and the sinks correspondingly to balance the sources. Here, δ is a prefactor tuning the degree of non-linearity in the non-linear flows $\tilde{F}_{i\to j} = A_{i\to j} \cdot \sin(\vartheta_i - \vartheta_j)$. **b** For each initial condition, we analyse the maximum flow in the network $|F_{\max}|$ as an indicator of non-linearity for different degrees of non-linearity δ. **c** We then evaluate the ratio $\tilde{R}$ of non-linear flow changes which is obtained from Eq.(8) by replacing the flow changes ΔF by their non-linear counterpart and averaging over all distances and trigger links in the left module. To examine to what extent network isolators prevent perturbation spreading from the left module to the right module, we plot this ratio against the non-linearity factor. With increasing degree of non-linearity, there is no longer exact isolation, i.e. $R = 0$, but a strong shielding effect persists. **d-i** We perform the same type of analysis for two three-regular graphs (d) and two random graphs $G(16, 0.3)$ (g) connected via network isolators and observe a similar scaling of the ratio $\tilde{R}$ with the non-linearity factor. Shaded regions indicate half a standard deviation evaluated over all initial conditions for all plots.

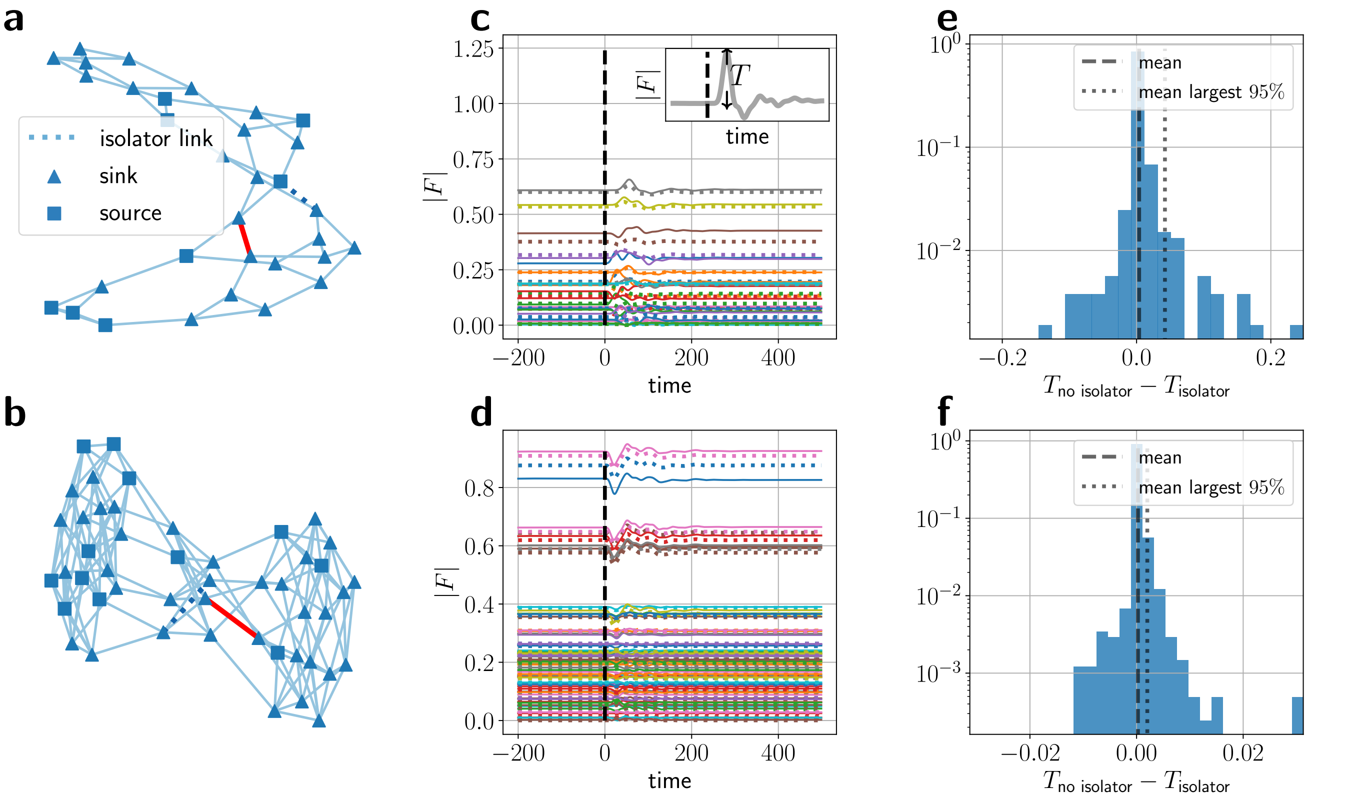

Supplementary Figure 11. **Transient amplitudes are slightly reduced in the presence of network isolators.** **a** We analyse a network consisting of two modules that are connected via three links and add a fourth link (dotted) to create a network isolator. We randomly assign 25% of the nodes to be generator nodes (squares) and the remaining ones to be load nodes (triangle). We then simulate the removal of a single link (red) and monitor the corresponding response in the dynamic nonlinear system described by the second order Kuramoto model (Eq. (10)). **c** Non-linear dynamics of the flows in the upper module after the failure of a single link at time zero (dotted, vertical line) in the network before (straight lines) and after the addition of the isolator link (dotted lines). We monitor the maximum Amplitude T of the transient dynamics comparing the fixed point before and after the failure (inset). **e** To analyse the impact of network isolators on transient overloads, we compare the transient amplitudes before ($T_{\text{no isolator}}$) and after (T_{isolator}) constructing the isolator in the upper module for all possible link failures in the lower module. In most cases, the transient amplitudes stay the same after introducing the network isolator as confired by the mean close to zero (black, dashed line). However, evaluating only the 95% changes in amplitudes with the largest changes in magnitudes (dotted line), we observe a significant shift towards positive values indicating a reduced risk of transient overloads when network isolators are present. **b,d,f** The result is confirmed by performing the same analysis for a different network containing a larger network isolator. Inertia constants are given by $M = 1$ and damping constants by $D = 0.3$ for all nodes and panels (see Eq. (10)).

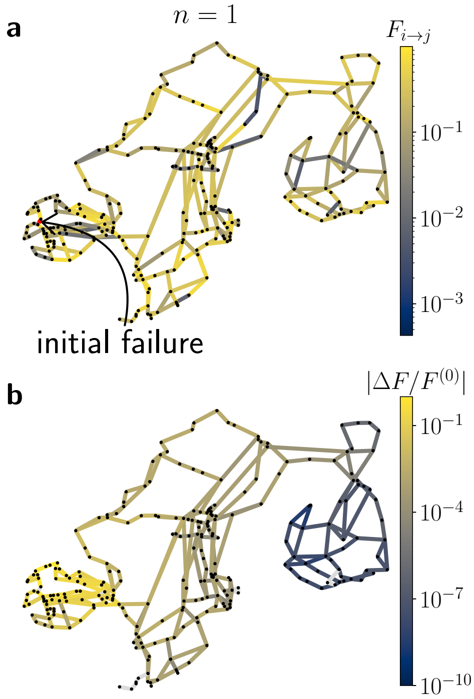

Supplementary Figure 12. **Non-locality of cascade propagation and decay of flow changes** We illustrate the first three steps of the cascade in the Scandinavian power grid for shown in Figure 4 in the main text for the grid without a network isolator. **a** Line loading in the Scandinavian grid prior to the initial failure with the initially failing link highlighted. Note that line loading is heterogeneously distributed within the network. **b** Relative flow changes $|\Delta F_\ell / F_{\text{fail}}^{(0)}|$ for any link ℓ as a result of the failure of the link shown in (a). Flow changes are normalized by the flow carried by the failing link $F_{\text{fail}}^{(0)}$ (a, arrow) before the failure, such that the maximum relative flow change is unity. The flow changes clearly decay with distance from the failing link. **c** Line loading after the initial failure: although flow changes decay with distance, the next failing link is relatively far apart from the initially failing link when considering the geographic or geodesic network distance. **d** Relative flow changes after the failure of the link shown in c, normalised again by the flow that the link shown in c carries before the failure. Again, the flow changes are localised. **e** Line loading after the failure of both links shown in panels a and c. The next failure is closer to the failing link shown in c, but even farther apart from the initially failing link, leading to an overall non-local cascade of failures. **f** Again, relative flow changes as a result of the link failure shown in panel e are strongly localised.

SUPPLEMENTARY NOTES

Supplementary Note 1: Flow networks

In this section, we briefly review the theory and applications of linear flow networks.

Mathematical description

In this work, the main model of interest is a linear flow network model which we introduce more formally in this section. Consider a connected graph $G = (E, V)$ consisting of $N = |V|$ nodes and $L = |E|$ edges. Assign to each node in the network a potential $\vartheta_n \in \mathbb{R},\ n \in V(G)$ and to each edge a weight $A_{ij} \in \mathbb{R}^+,\ \ell = (i, j) \in E(G)$. Now we assign a *flow* $F_{i\to j} \in \mathbb{R}$ to each link $\ell = (i, j) \in E(G)$ in the network that is assumed to be linear in the potential drop

$$F_{i\to j} = A_{ij} \cdot (\vartheta_i - \vartheta_j) = -F_{j\to i}. \tag{1}$$

Suppose that there are sources and sinks attached to the nodes of the networks $P_i \in \mathbb{R},\ i \in V(G)$. In this case, the in- and outflows at each node have to balance with the sources and sinks

$$P_i = \sum_{k=1}^{N} F_{i\to k}. \tag{2}$$

This equation is known as continuity equation or *Kirchhoff's current law.* If the sources and sinks P_i are given, Eqs. (2) and (1) completely determine the potentials in the network (up to a constant shift to all potentials). In a power grid, the sources and sinks are the power injections or withdrawals as a result of power production or consumption, respectively. When looking at the stable, operational fixed point of a power grid they are balanced such that $\sum_i P_i = 0$ – we therefore assume this to hold in the following sections. The theory of linear flow networks applies resistor networks, as well as AC power grids in the DC approximation, hydraulic networks and networks of limit cycle oscillators, which will be discussed in detail in this section.

Now we introduce a compact, vectorial notation which facilitates the analysis of perturbations or damages to the network. Note that the flow is a signed quantity that depends on the orientation of the edges that we arbitrarily fix for this purpose and say that the flow is directed from node i to node j in this case. We can write the flows in vectorial notation $\vec{F} = (F_1, ..., F_L)^\top \in \mathbb{R}^L$ as follows;

$$\vec{F} = \boldsymbol{K}\boldsymbol{I}^\top\vec{\vartheta}. \tag{3}$$

Here, $\boldsymbol{K} = \text{diag}(K_1, ..., K_L) \in \mathbb{R}^{L\times L}$ is the graph's weight matrix that collects the edge weights and $\boldsymbol{I}^\top$ is the transpose of the the graph's edge-node incidence matrix $\boldsymbol{I} \in \mathbb{Z}^{N\times L}$ that determines the orientation of the graph's edges by the following relationship

$$I_{j\ell} = \begin{cases} +1 & \text{if edge } \ell \,\hat{=}\, (j,k) \text{ starts at node } j, \\ -1 & \text{if edge } \ell \,\hat{=}\, (j,k) \text{ ends at node } j\ , \\ \ \ 0 & \text{otherwise.} \end{cases} \tag{4}$$

Furthermore, $\vec{\vartheta} = (\vartheta_1, ..., \vartheta_N)^\top \in \mathbb{R}^N$ is a vector of potentials or voltage phase angles. We can also define a vector of power injections $\vec{P} = (P_1, ..., P_N)^\top \in \mathbb{R}^N$ such that the continuity equation reads as

$$\vec{P} = \boldsymbol{I}\vec{F}. \tag{5}$$

In this expression, the correspondence between the power balance and *Kirchhoff's current law* becomes manifest: it states that the in- and outflows at each node have to balance the injections and withdrawals of power. Combining Eq.s (3) and (5), we may find a relationship between angles $\vec{\vartheta}$ and power injections $\vec{P}$, thus defining the graph's weighted *Laplacian matrix* $\boldsymbol{L} = \boldsymbol{I}\boldsymbol{K}\boldsymbol{I}^\top \in \mathbb{R}^{N\times N}$, by

$$\vec{P} = \boldsymbol{I}\boldsymbol{K}\boldsymbol{I}^\top\vec{\vartheta} = \boldsymbol{L}\vec{\vartheta}. \tag{6}$$

The weighted Laplacian matrix used here has the following entries

$$L_{ij} = \begin{cases} -A_\ell & \text{if } i \text{ is connected to } j \text{ via } \ell = (i,j), \\ \sum_{\ell=(i,k)\in E(G)} A_\ell & \text{if } i = j, \\ 0 & \text{otherwise.} \end{cases} \tag{7}$$

The Laplacian matrix plays an important role in graph theory [3]. If the underlying graph G is connected, it has one zero eigenvalue $\lambda_1 = 0$ with corresponding eigenvector $\vec{v}_1 = \vec{1}/\sqrt{N}$. Therefore, the matrix is not invertible. In many cases, it would nevertheless be desirable to invert the matrix, e.g. in order to find the phase variables given the power injections in Eq. (6). This problem is typically overcome by making use of the matrix's *Moore-Penrose pseudoinverse* $\boldsymbol{L}^\dagger$. It may be used to invert Eq. (6) in the same way as for the ordinary matrix inverse in the case of balanced power injections [4]. The Moore-Penrose pseudoinverse of the graph Laplacian $\boldsymbol{L}$ allows for the following representation: using $\boldsymbol{L}$'s eigenvalues sorted by magnitude $\lambda_1 = 0, \lambda_2 \leq ... \leq \lambda_N$ with corresponding eigenvectors $\vec{v}_1 = \vec{1}/\sqrt{N}, \vec{v}_2, ..., \vec{v}_N$, we can express its pseudoinverse $\boldsymbol{L}^\dagger$ as [5]

$$\boldsymbol{L}^\dagger = (\vec{v}_1, \vec{v}_2, ..., \vec{v}_N) \begin{pmatrix} 0 & 0 & ... & 0 \\ 0 & \lambda_2^{-1} & ... & 0 \\ ... & ... & ... & ... \\ ... & ... & ... & \lambda_N^{-1} \end{pmatrix} (\vec{v}_1, \vec{v}_2, ..., \vec{v}_N)^\top .$$

The second eigenvalue λ_2 is usually referred to as *Fiedler eigenvalue* or *algebraic connectivity* and is an indicator of the graph's overall connectivity. If we assume the overall graph to be connected, this eigenvalue is strictly greater than zero $\lambda_2 > 0$. Importantly, a large difference between second and third eigenvalue $\lambda_3 - \lambda_2$ implies a strong modularity in the graph and thus indicates the existence of a community structure [6–8].

Before we proceed, let us briefly fix the notation for the following sections: we will refer to an edge $\ell = (\ell_1, \ell_2) \in E(G)$ and its index ℓ in the ordered set of all edges interchangeably or refer to it by its terminal nodes ℓ_1 and ℓ_2. If we assume the edge space to be spanned by vectors in the two element field $GF(2)$, we may express the edge by a unit vector $\vec{l}_\ell = (0, ..., \underbrace{1}_{l}, ..0)^\top \in GF(2)^L$ which we refer to as the edge's indicator vector. The edge-node incidence matrix $\boldsymbol{I}$ then maps this unit vector to the corresponding unit vectors in the field of vertices $GF(2)^N$. We thus get the following result for the edge expressed in terms of its starting vertex ℓ_1 and terminal vertex ℓ_2:

$$\vec{\nu}_\ell = \boldsymbol{I} \cdot \vec{l}_\ell = \vec{e}_{\ell_1} - \vec{e}_{\ell_2} = \begin{pmatrix} 0 \\ ... \\ 1 \\ ... \\ -1 \\ ... \end{pmatrix} \begin{matrix} \\ \\ \}\ell_1 \\ \\ \}\ell_2 \\ \\ \end{matrix},$$

where $\vec{e}_{\ell_1}$ and $\vec{e}_{\ell_2}$ are basis vectors in $GF(2)^N$

$$\vec{e}_{\ell_1} = \begin{pmatrix} 0 \\ ... \\ 1 \\ ... \\ ... \\ 0 \end{pmatrix} \begin{matrix} \\ \\ \}\ell_1 \\ \\ \\ \\ \end{matrix}, \quad \vec{e}_{\ell_2} = \begin{pmatrix} 0 \\ ... \\ ... \\ 1 \\ ... \\ 0 \end{pmatrix} \begin{matrix} \\ \\ \\ \}\ell_2 \\ \\ \\ \end{matrix}.$$

This formulation allows us to easily switch between the edges expressed in edge space and the nodes corresponding to its terminal ends.

Applicability of linear flow models

The theoretical framework in the last section has many different applications. We will demonstrate its applicability to the following systems in this section:

1. Power grids [9, 10],

2. Resistor networks [11],

3. Hydraulic networks [12, 13],

4. Limit cycle oscillators [14].

Application to power grids

The power flow equations describing the steady state of a power system at an arbitrary node i are given by [9]

$$\begin{aligned} P_i &= \sum_{k=1}^{N} |V_i||V_k|(G_{ik}\cos(\vartheta_i-\vartheta_k)+B_{ik}\sin(\vartheta_i-\vartheta_k)), \\ Q_i &= \sum_{k=1}^{N} |V_i||V_k|(G_{ik}\sin(\vartheta_i-\vartheta_k)-B_{ik}\cos(\vartheta_i-\vartheta_k)). \end{aligned} \tag{8}$$

Here, P_i and Q_i are the real and reactive power generated or consumed at node or bus i, ϑ_i is the voltage angle at the same bus and $|V_i|$ is the voltage magnitude. The matrices $\boldsymbol{G} \in \mathbb{R}^{N\times N}$ and $\boldsymbol{B} \in \mathbb{R}^{N\times N}$ with elements G_{ij} and B_{ij}, respectively, are the real part and the complex part of the complex nodal admittance matrix $\boldsymbol{Y} = \boldsymbol{G} + i\boldsymbol{B} \in \mathbb{C}^{N\times N}$. Note that the matrices $\boldsymbol{B}$ and $\boldsymbol{G}$ are not actually matrices of susceptances and conductances, respectively. Instead, their entries read as follows

$$B_{ij} = \begin{cases} -b_{ij} & \text{if } (i,j)\in E(G),\ i\neq j, \\ b_i^{\text{shunt}} + \sum_{(i,k)\in E(G)} b_{ik} & \text{if } i=j, \\ 0 & \text{otherwise,} \end{cases}$$

where b_i^{shunt} denotes the shunt susceptance of node i and b_{ij} is the susceptance of the circuit connecting node i to node j. $\boldsymbol{G}$ has an analogous structure with elements

$$G_{ij} = \begin{cases} -g_{ij} & \text{if } (i,j)\in E(G),\ i\neq j, \\ g_i^{\text{shunt}} + \sum_{(i,k)\in E(G)} g_{ik} & \text{if } i=j, \\ 0 & \text{otherwise,} \end{cases}$$

where g_{ij} are the conductances of the circuit between nodes i and node j. The matrices $\boldsymbol{B}$ and $\boldsymbol{G}$ thus have the structure of a Laplacian matrix except for the diagonal entries which contain additional terms given by the shunt susceptances and conductances. The off-diagonal elements of the nodal admittance matrix thus read as

$$Y_{jk} = -y_{jk},\ \forall j\neq k; \quad y_{jk} = g_{jk} + ib_{jk} = \frac{1}{r_{jk}+ix_{jk}},$$

with the circuit's reactance x_{jk} and resistance r_{jk}. Note that line susceptances $b_\ell = \frac{-x}{r^2+x^2}$ are thus negative. The Eqs. (8) reduce to the lossless power flow equations in the case where the real part of the nodal admittance matrix is negligible $\boldsymbol{G} \approx \boldsymbol{0}$, i.e., lines are purely inductive.

We will focus on the so called *DC approximation* of this full AC power flow equations. This approximation is based on three assumptions [9]:

1. Voltages vary little, i.e., $|V_i| \approx \text{const},\ \forall i$ with respect to their base values,
2. Angular differences are small, i.e., $\sin(\vartheta_i-\vartheta_j) \approx \vartheta_i-\vartheta_j,\ \forall (i,j)\in E(G)$,
3. Transmission lines are purely inductive, i.e., $B_{ij} \gg G_{ij},\ \forall (i,j)\in E(G)$.

Typically, these assumptions are fulfilled for high voltage transmission grids if the line loading is not too large [15]. Using these approximations, Eq. (8) reduces to

$$P_i = \sum_{k=1}^{N} \underbrace{|V_i||V_k|B_{ik}}_{A_{ik}}(\vartheta_i-\vartheta_k),$$

thus revealing the analogy to Eq. (2).

Application to resistor networks

Resistor networks are another example which may be described using linear flow networks [16]. They have been studied for a long time leading to many fundamental results of graph theory [11]. We will briefly introduce the theory of resistor networks and use the symbol $\hat{=}$ to refer to the corresponding quantity in the mathematical framework of linear flow networks as introduced in section 1. For resistor networks, the flow along the graph's edges is a current flow $\vec{i} \in \mathbb{R}^L \hat{=} \vec{F}$ between nodes of different voltage $\vec{V} \in \mathbb{R}^N \hat{=} \vec{\vartheta}$. The line weights are given by the inverse resistances, i.e., the conductances, of the lines $\boldsymbol{G} \in \mathbb{R}^{L\times L} \hat{=} \boldsymbol{K}$ such that Eq. (3) reads in this case

$$\vec{i} = \boldsymbol{G}\boldsymbol{I}^\top \vec{V},$$

where $\boldsymbol{I}$ is again the node-edge incidence matrix. Along the same lines, Eq. (5) translates to

$$\vec{i}_{\text{in}} = \boldsymbol{I}\vec{i}.$$

Here, $\vec{i}_{\text{in}} \in \mathbb{R}^N \hat{=} \vec{P}$ is a vector of currents injected at the graph's nodes and the Equation is again a manifestation of Kirchhoff's current law. We may thus apply the same theoretical framework to resistor networks.

Applications to hydraulic networks

The same formalism can also be shown to apply to water transport networks that we refer to as hydraulic networks or pipe networks. Consider a hydraulic network consisting of pipes that connect to each other at junctions. Then we form the underlying graph by assigning a vertex to each of the junctions and put an edge between two vertices if they are connected via a pipe. The nodal quantity of interest in this case is the pressure $\vec{p} \in \mathbb{R}^N \hat{=} \vec{\vartheta}$. If we assume the pipes to be much longer than their radius $r \ll L$ and the flow across all pipes in the network to be laminar with a Newtonian, incompressible fluid flowing through it, we can approximate the fluid flow $\vec{Q} \in \mathbb{R}^L \hat{=} \vec{F}$ across a pipe $\ell = (i, j)$ by the *Hagen–Poiseuille equation*

$$Q_\ell = K_\ell \cdot (p_i - p_j).$$

Here, we collected different parameters describing the pipe and the fluid in the line parameter

$$K_\ell = \frac{\pi r_\ell^4}{8\mu L_\ell},$$

with the pipe radius r_ℓ, the pipe length L_ℓ and the fluid's dynamic viscosity μ. Conservation of mass then requires that inflows and outflows balance as in Eq. (2). Important applications of this framework are blood vessels in humans and animals [17], the vascular system of plants [13] or hydraulic networks [18]. For vascular networks, the system does not consist of pipes but rather of smaller vascular bundles such that the scaling of line parameter K with the radius r^4 does not necessarily exactly hold [19].

Applications to limit cycle oscillators

The linear flow model may be regarded as a linearisation of the *Kuramoto model* which naturally appears in many cases, in particular when approximating weakly coupled oscillator systems near a stable limit cycle [14].

Consider a connected, simple graph $G = (E, V)$. The Kuramoto model describes a set of weakly coupled oscillators with phase angles $\vec{\vartheta} \in \mathbb{R}^N$ attached to the graph's vertices that are coupled via the graph's edges through coupling constants $A_{ij}, (i, j) \in E(G)$, see e.g. Ref. [20]. The oscillators' tendency to synchronise through the coupling is counteracted by each oscillator's natural frequency ω_j that is written compactly as a vector $\vec{\omega} = (\omega_1, ..., \omega_N)^\top \in \mathbb{R}^N$. Then the dynamics of the phase angle ϑ_i attached to node i, where $i \in \{1, ..., N\}$, reads

$$\dot{\vartheta}_i = \omega_i - \sum_k A_{ik} \sin(\vartheta_i - \vartheta_k).$$

As before, we fix an orientation of the graph's edges and summarise the coupling coefficients for all edges $(i, j) \in E(G)$ in the diagonal coupling matrix $\boldsymbol{K} \in \mathbb{R}^{L\times L}$, such that the vectorised dynamics reads

$$\dot{\vec{\vartheta}} = \vec{\omega} - \boldsymbol{I}\boldsymbol{K} \sin(\boldsymbol{I}^\top \vec{\vartheta}). \tag{9}$$

Here, $\boldsymbol{I}$ is again the graph's node-edge incidence matrix (4) and the sine function is understood to be taken element-wise, i.e

$$\sin(\boldsymbol{I}^\top \vec{\vartheta}) = (\sin([\boldsymbol{I}^\top \vec{\vartheta}]_1), ..., \sin([\boldsymbol{I}^\top \vec{\vartheta}]_L))^\top.$$

Fixed points of the dynamics are defined by a vanishing time derivative $\dot{\vec{\vartheta}} = \vec{0}$. Therefore, the equation characterising the phase angles at the fixed point $\vec{\vartheta}^*$ reads

$$\vec{\omega} = \boldsymbol{I}\boldsymbol{K}\sin(\boldsymbol{I}^\top\vec{\vartheta}^*).$$

If the angular differences on all edges are small, we may reduce this to the linear equation $\sin(\boldsymbol{I}^\top\vec{\vartheta}) \approx \boldsymbol{I}^\top\vec{\vartheta}$, again retrieving an expression analogous to the discrete Poisson equation (6).

The second-order Kuramoto model

An extension of the Kuramoto model presented in Eq. (9) is given by the second-order Kuramoto model that is also frequently used in power systems analysis to describe synchronising generators [21–23], where it is also referred to as Kuramoto model with inertia. The model contains an additional second-order time derivative of phase angles representing the generators' inertia and reads as

$$\boldsymbol{M}\ddot{\vec{\vartheta}} = -\boldsymbol{D}\dot{\vec{\vartheta}} + \vec{\omega} - \boldsymbol{I}\boldsymbol{K}\sin(\boldsymbol{I}^\top\vec{\vartheta}). \tag{10}$$

Here, $\boldsymbol{M} = \mathrm{diag}(M_1, ..., M_N) \in \mathbb{R}^{N\times N}$ and $\boldsymbol{D} = \mathrm{diag}(D_1, ..., D_N) \in \mathbb{R}^{N\times N}$ are diagonal matrices incorporating the generators' inertia coefficients and damping coefficients, respectively [21] and the other quantities are defined the same way as for the first order Kuramoto model (9). The vector of frequencies in this model corresponds to the power injections $\vec{\omega} \in \mathbb{R}^N \hat{=} \vec{P}$. Fixed points of the second order model with phase angles $\vec{\vartheta}^*$ are characterized by both, first and second order time derivative vanishing $\ddot{\vec{\vartheta}} = \dot{\vec{\vartheta}} = \vec{0}$ resulting in the same equation as for the first order model

$$\vec{\omega} = \boldsymbol{I}\boldsymbol{K}\sin(\boldsymbol{I}^\top\vec{\vartheta}^*).$$

Again, this model reduces to the linear flow model if phase differences at the fixed point are small $\sin(\boldsymbol{I}^\top\vec{\vartheta}^*) \approx \boldsymbol{I}^\top\vec{\vartheta}^*$.

Supplementary Note 2: Description of link failures

In this section, we will briefly review the analysis of link failures within the linear flow theory setting. We will first demonstrate how the effects of a link failure may be approached on the nodal level [10]. Assume that a link $k = (r, s)$ with preoutage flow $\hat{F}_k$ fails, which does not disconnect the graph. This induces a change in the potentials

$$\vec{\vartheta}' = \vec{\vartheta} + \Delta\vec{\vartheta}$$

by virtue of the discrete Poisson equation (6). Here, we introduced the vector of potential changes $\Delta\vec{\vartheta} \in \mathbb{R}^N$ and a vector of potentials after the failure $\vec{\vartheta}' \in \mathbb{R}^N$. The corresponding equation for the new grid reads as

$$\vec{P} = (\boldsymbol{L} + \Delta\boldsymbol{L})(\vec{\vartheta} + \Delta\vec{\vartheta}).$$

Here, $\Delta\boldsymbol{L}$ is the change in the Laplacian matrix due to the removal of link k and takes the form $\Delta\boldsymbol{L} = K_k\boldsymbol{I}\vec{l}_k(\boldsymbol{I}\vec{l}_k)^\top$. If we subtract the discrete Poisson equation for the old grid before the failure of link k from this equation, we arrive at the expression

$$\Delta\vec{\vartheta} = -(\boldsymbol{L} + \Delta\boldsymbol{L})^\dagger\Delta\boldsymbol{L}\vec{\vartheta}.$$

Finally, we can use the Woodbury Matrix identity to rewrite the expression into the following form [10]

$$\boldsymbol{L}\Delta\vec{\vartheta} = q_k\vec{\nu}_k, \tag{11}$$

where

$$q_k = (1 - K_k(\boldsymbol{I}\cdot\vec{l}_k)^\top\boldsymbol{L}^\dagger\boldsymbol{I}\cdot\vec{l}_k)^{-1}\hat{F}_k$$

is a source term and $\vec{\nu}_k = \vec{e}_k - \vec{e}_j$. Similar expressions appear naturally when analysing resistor networks and have been studied, for example, in Refs. [4, 24]. After calculating the potential changes based on this equation, the flow changes on a link $\ell = (\ell_1, \ell_2)$ are given by the following equation

$$\Delta F_{\ell_1\to\ell_2} = K_\ell\cdot(\Delta\vartheta_{\ell_1} - \Delta\vartheta_{\ell_2}).$$

Supplementary Note 3: Network isolators inhibit failure spreading completely

In this section we formally establish the existence of network isolators. To this end we first fix some notation.

Fundamentals and notation

We consider a linear flow network consisting of two parts, i.e. its vertex set V is written as $V = V_1 \cup V_2$. We now label the nodes in V as follows without loss of generality

$1, \dots, m_1$:	nodes in V_1 that are connected to V_2
$m_1 + 1, \dots, n_1$:	nodes in V_1 that are not connected to V_2
$n_1 + 1, \dots, n_1 + m_2$:	nodes in V_2 that are connected to V_1
$n_1 + m_2 + 1, \dots, n_1 + n_2$:	nodes in V_2 that are not connected to V_1.

Then the weighted adjacency matrix of the network can be written as

$$\boldsymbol{A} = \begin{pmatrix} \boldsymbol{A}_1 & \boldsymbol{A}_{12} \\ \boldsymbol{A}_{12}^\top & \boldsymbol{A}_2 \end{pmatrix},$$
$$\boldsymbol{A}_{12} = \begin{pmatrix} \boldsymbol{a} & \boldsymbol{0} \\ \boldsymbol{0} & \boldsymbol{0} \end{pmatrix},$$

with $\boldsymbol{A}_1 \in \mathbb{R}^{n_1 \times n_1}$, $\boldsymbol{A}_2 \in \mathbb{R}^{n_2 \times n_2}$, $\boldsymbol{A}_{12} \in \mathbb{R}^{n_1 \times n_2}$ and $\boldsymbol{a} \in \mathbb{R}^{m_1 \times m_2}$. Furthermore, we define the degree matrices $\boldsymbol{D}_1$, $\boldsymbol{D}_2$ and $\boldsymbol{d}$ associated with the adjacency matrices $\boldsymbol{A}_1$, $\boldsymbol{A}_2$ and $\boldsymbol{a}$, that is

$$d_{kl} = \begin{cases} \sum_p a_{kp} & \text{for } \; k = l \\ 0 & \phantom{\text{for }} \; k \neq l \end{cases},$$

and the Laplacian matrices $\boldsymbol{L}_1 = \boldsymbol{D}_1 - \boldsymbol{A}_1$ of subnetwork 1, $\boldsymbol{L}_2 = \boldsymbol{D}_2 - \boldsymbol{A}_2$ of subnetwork 2 and $\boldsymbol{L}$ of the whole system.

Main theorem on network isolators

In this subsection, we proof the main Theorem 1 on network isolators. Consider the Theorem on network isolators.

Theorem 1. Consider a linear flow network composed of two modules 1,2 and let $\mathbf{A}_{12}$ denote the weighted adjacency matrix of the mutual connections. An edge failure in one module does not affect the flows in the other module if $\text{rank}(\mathbf{A}_{12}) = 1$. For unweighted networks this criterion is fulfilled if $\mathbf{A}_{12}$ describes a complete bipartite graph.

Proof. Assume that the adjacency matrix of the mutual connections has unit rank $\text{rank}(\boldsymbol{A}_{12}) = \text{rank}(\boldsymbol{a}) = 1$. We first proof that for any vector $\vec{y} \in \mathbb{R}^{n_1}$ the following statement holds

$$\vec{x} = \begin{pmatrix} \boldsymbol{d}^{-1}\boldsymbol{a} & \boldsymbol{0} \\ \boldsymbol{0} & \boldsymbol{0} \end{pmatrix} \vec{y} = c \begin{pmatrix} 1 \\ \vdots \\ 1 \\ 0 \\ \vdots \\ 0 \end{pmatrix}, \tag{12}$$

where $c \in \mathbb{R}$ is some real number. This result can be obtained by writing $\vec{x} \in \mathbb{R}^{n_2}$ in components. For all $j \in \{1, \dots, m_2\}$ we have

$$x_j = \frac{\sum_k a_{jk} y_k}{\sum_k a_{jk}}.$$

Since $\boldsymbol{a}$ has unit rank all its rows are linearly dependent such that we can write $a_{jk}/a_{1k} = a_{j1}/a_{11}$ for all $k \in \{1, \ldots, n_1\}$, such that $a_{jk} = a_{1k}a_{j1}/a_{11}$. Hence,

$$\begin{aligned} x_j &= \frac{a_{j1}/a_{11} \times \sum_k a_{1k}y_k}{a_{j1}/a_{11} \times \sum_k a_{1k}} \\ &= \frac{\sum_k a_{1k}y_k}{\sum_k a_{1k}} = x_1 =: c, \end{aligned}$$

and all elements of the vector are equal. The remaining $n_2 - m_2$ elements of the vector vanish, $x_j = 0$, $\forall j \in \{m_2 + 1, ..., n_2\}$, because the corresponding adjacency matrix $\boldsymbol{A}_{12}$ has only zero entries at the respective positions.

We now compute the impact of a failure of link k in $G(V_1)$ via the discrete Poisson equation (11)

$$\boldsymbol{L}\Delta\vec{\vartheta} = q_k\vec{\nu}_k.$$

We decompose this equation as well as the vectors $\Delta\vec{\vartheta}$ and $\vec{\nu}$ into two parts corresponding to the two parts of the network

$$\Delta\vec{\vartheta} = \begin{pmatrix} \Delta\vec{\vartheta}_1 \\ \Delta\vec{\vartheta}_2 \end{pmatrix}, \qquad \vec{\nu} = \begin{pmatrix} \vec{\nu}_1 \\ \vec{0} \end{pmatrix},$$

where $\Delta\vec{\vartheta}_1, \vec{\nu}_1 \in \mathbb{R}^{n_1}$ and $\Delta\vec{\vartheta}_2, \vec{\nu}_2 \in \mathbb{R}^{n_2}$. Then the lower part of Eq. (11) corresponding to the vertices $n_1+1, \ldots, n_1+n_2$ reads

$$\left[\boldsymbol{L}_2 + \begin{pmatrix} \boldsymbol{d} & \boldsymbol{0} \\ \boldsymbol{0} & \boldsymbol{0} \end{pmatrix}\right] \Delta\vec{\vartheta}_2 = \begin{pmatrix} \boldsymbol{a} & \boldsymbol{0} \\ \boldsymbol{0} & \boldsymbol{0} \end{pmatrix} \Delta\vec{\vartheta}_1, \tag{13}$$

using the notation established above. Using the prior result (12) and multiplying by the matrix

$$\begin{pmatrix} \boldsymbol{d}^{-1} & \boldsymbol{0} \\ \boldsymbol{0} & \boldsymbol{1} \end{pmatrix},$$

this equation can be rewritten as

$$\left[\begin{pmatrix} \boldsymbol{d}^{-1} & \boldsymbol{0} \\ \boldsymbol{0} & \boldsymbol{1} \end{pmatrix} \boldsymbol{L}_2 + \begin{pmatrix} \boldsymbol{1} & \boldsymbol{0} \\ \boldsymbol{0} & \boldsymbol{0} \end{pmatrix}\right] \Delta\vec{\vartheta}_2 = \begin{pmatrix} \boldsymbol{d}^{-1}\boldsymbol{a} & \boldsymbol{0} \\ \boldsymbol{0} & \boldsymbol{0} \end{pmatrix} \Delta\vec{\vartheta}_1 = c \begin{pmatrix} 1 \\ \vdots \\ 1 \\ 0 \\ \vdots \\ 0 \end{pmatrix}.$$

Now one can easily check via a direct calculation that

$$\Delta\vec{\vartheta}_2 = c \begin{pmatrix} 1 \\ \vdots \\ 1 \end{pmatrix}$$

is a solution to this equation. Furthermore, this solution is unique as the linear system of equation has full rank. This is most easily seen for Eq. (13), as the matrix on the left hand side is normal and positive definite.

We have thus shown that the nodal potentials in V_2 are shifted by the same constant c when a link in $G(V_1)$ fails. Hence the flow changes are given by

$$\Delta F_{\ell_1 \to \ell_2} = A_\ell(\Delta\vartheta_{\ell_1} - \Delta\vartheta_{\ell_2}) = 0 \quad \forall \ell_1, \ell_2 \in V_2.$$

□

Corollary 1 (Complete bipartite graphs are network isolators). Consider a linear flow network consisting of two modules with vertex sets V_1 and V_2 and assume that a single link in the induced subgraph $G(V_1)$ fails, i.e. a link (r, s) with $r, s \in V_1$. If the subgraph G' of mutual connections between the two modules is a complete bipartite graph with uniform edge weights $K = K_\ell = K_m,\ \forall \ell, m \in E(G')$, then the subgraph is a network isolator. If the whole graph is unweighted, G' always has uniform edge weights, thus a complete bipartite graph of mutual connections always is a network isolator for any unweighted network.

Proof. If the subgraph G' is complete and bipartite (ignoring all connections within both induced subgraphs $G(V_1)$ and $G(V_2)$), its adjacency matrix takes the form

$$\boldsymbol{A}' = K \cdot \begin{pmatrix} \boldsymbol{0} & \boldsymbol{1}_{m_1 \times m_2} \\ \boldsymbol{1}^\top_{m_1 \times m_2} & \boldsymbol{0} \end{pmatrix}.$$

We can immediately see that the matrix in the upper right corner, i.e. $\boldsymbol{A}'_{12} = K\boldsymbol{1}_{m_1 \times m_2}$ has unit rank, such that by theorem 1, G' is a network isolator. □

Network isolators in non-linear systems

We will now demonstrate how to extend the concepts of network isolators from linear systems to a certain class of non-linear networked systems

$$\vec{f}(\boldsymbol{L}\vec{x}) = (f_1([\boldsymbol{L}\vec{x}]_1), ..., f_N([\boldsymbol{L}\vec{x}]_N))^\top : \vec{x} \in \mathbb{R}^N \to \vec{f}(\boldsymbol{L}\vec{x}) \in \mathbb{R}^N$$

be a continuous function on the real numbers that depends on the product of Laplacian matrix $\boldsymbol{L}$ and vector $\vec{x}$. Here, $[\boldsymbol{L}\vec{x}]_j$ denotes the j-th row of the standard matrix-vector product $\boldsymbol{L}\vec{x}$. We assume that the underlying network topology is again separated into two subgraphs $G(V_1)$ and $G(V_2)$, see the beginning of this section. We further assume that

$$f_j(0) = 0, \ \forall j \in \{1, ...N\},$$

i.e., each of the functions vanishes at the origin. Note that the functions $f_j([\boldsymbol{L}\vec{x}]_j)$ can be different and non-linear, as long as they vanish at the origin. Consider a dynamical system of the form

$$\dot{\vec{x}} = \vec{f}(\boldsymbol{L}\vec{x}) \tag{14}$$

that admits a fixed point solution $\vec{x}^*$ with vanishing time derivative $\dot{\vec{x}} = \vec{0}$ that fulfils

$$\vec{0} = \vec{f}(\boldsymbol{L}\vec{x}^*). \tag{15}$$

Now add a perturbation vector

$$\Delta\vec{P} = \begin{pmatrix} \Delta\vec{P}_1 \\ \vec{0} \end{pmatrix} \tag{16}$$

to the system that has non-zero entries only at the nodes of the first induced subgraph $G(V_1)$ and assume that the dynamical system (14) relaxes to a new fixed point $\vec{x}'$ with

$$\Delta\vec{P} = \vec{f}(\boldsymbol{L}\vec{x}'). \tag{17}$$

Then the following corollary holds

Corollary 2 (Isolation in non-linear systems). Consider a non-linear dynamical networked system of the form (14) that consists of two modules with vertex sets V_1 and V_2 which are connected by a network isolator as of Theorem 1. Assume that the system admits a fixed point solution as given in Eq. (15). Assume that a perturbation as in Eq. (16) is applied to the nodes in the first induced subgraph $G(V_1)$ and that the system relaxes to a new fixed point as in Eq. (17). Then the new fixed point has the following form

$$\vec{x}' = \begin{pmatrix} \vec{x}'_1 \\ c\vec{1}_2 \end{pmatrix},$$

where $c \in \mathbb{R}$ is a constant.

The second module is thus isolated against perturbations in the first module and vice versa in the sense that a perturbation in one module results in a constant shift in the other module.

Proof. The proof is analogous to the proof of Theorem 1. Applying the function $\vec{f}$ to Eq. (13) describing the fixed point in the non-perturbed subgraph $G(V_2)$, we see that the system is still solved by

$$\vec{x}' = \begin{pmatrix} \Delta\vec{x}'_1 \\ c\vec{1}_2 \end{pmatrix}.$$

□

Even if not rigorously valid, we find that strong network isolation persists for an even larger class of non-linear systems that we will discuss in this section. Note that our analysis here closely follows a linear response theory analysis of Kuramoto oscillators that can be found in Ref. [14].
Consider a networked non-linear dynamical system of the form

$$\dot{\vec{x}}_i = \vec{f}(\vec{x}_i)_i + \sum_{k=1}^{N} A_{ik} g(x_i - x_k). \tag{18}$$

Here, $\vec{x} \in \mathbb{R}^N$ is a vector of nodal dynamical variables, $\vec{f}$ is a differentiable function of self-interactions of these variables and $\vec{g}(\vec{x})$ is a differentiable, odd function that depends only on the differences of nodal variables at neighbouring nodes. Odd functions are characterised by the property that $\vec{g}(-\vec{x}) = -\vec{g}(\vec{x})$ and this property results in a diffusive coupling between neighbouring nodes as is present for example in case of the sinusoidal coupling used in the Kuramoto model (see Eq. (9)). The strength of interactions is encoded in the graph's adjacency matrix $\boldsymbol{A}$. Assume that the system relaxes to a fixed point with $\dot{\vec{x}}_i = 0$ where $\vec{x}(t) = \vec{x}^*$. If we perturb the network locally at a node or an edge, we can compute the change in this fixed point using linear response theory [14]: to leading order, we obtain a linear system as above.
Assume that we perturb a single edge (n, m) by modifying its edge weight by a small number ΔA_{ij} such that

$$A_{ij} \to A'_{ij} = A_{ij} + \Delta A_{ij}$$
$$\Delta A_{ij} = \begin{cases} 0 & \text{if } (i,j) \neq (n,m) \\ \Delta A & \text{if } (i,j) = (n,m) \end{cases} .$$

Assume that this modification causes a change of the fixed point by

$$x_j^* \to x'_j = x_j^* + \Delta x_j, \quad \forall j \in \{1, ..., N\},$$

where Δx_j is the change in the fixed point that is assumed to be small such that the fixed points lie closed to each other. We can expand the dynamics to leading order in terms of the new fixed point

$$\frac{\partial f(x_j^*)}{\partial x_j} \Delta x_j + \sum_{k=1}^{N} A_{jk} \frac{\partial g(x_j^* - x_k^*)}{\partial x_j} (\Delta x_j - \Delta x_k) + s_j = 0.$$

Here, s_j is a source term that vanishes if node j is not part of the edge (n, m), $j \neq n, m$. The sum in this expression may be compactly written in terms of an effective Laplacian matrix $\tilde{\boldsymbol{L}}$

$$\sum_{k=1}^{N} A_{jk} \frac{\partial g(x_j^* - x_k^*)}{\partial x_j} (\Delta x_j - \Delta x_k) = [\tilde{\boldsymbol{L}} \Delta \vec{x}]_j,$$

where the Laplacian matrix has the off-diagonal entries

$$\tilde{\boldsymbol{L}}_{jk} = -A_{jk} \frac{\partial g(x_j^* - x_k^*)}{\partial x_j}.$$

Thus, if the underlying graph contains a network isolator, we can apply Theorem 1 to the system and see immediately that each component is (approximately) isolated against small perturbations in the other one. Note that this result is only valid if the change in the fixed point as well as the perturbation are small and relies on the fact that the system relaxes to a new fixed point after the perturbation. In particular, this description applies to Kuramoto oscillators (Eq. (9)) perturbed at a few nodes or edges and powergrids described by AC load flow equations 8 subject to a link failure. We can thus get approximate isolation in both models as shown in Figure 5 for the AC load flow model and Figures 4 and Supplementary Figure 10 for the Kuramoto model.

Supplementary Note 4: Linear controllability of complex networks

We now turn to a different theoretical concept in complex networks research: the controllability of a network. In this section, we briefly analyse the influence of network isolators on the controllabilty of complex systems with a linear

dynamics. In general, we find that introducing a network isolator to a complex network has no generic influence on its controllability.
Consider a linear dynamical system on a network with N nodes with a state vector $\vec{x} \in \mathbb{R}^N$ whose dynamics is given by [2]

$$\dot{\vec{x}} = \boldsymbol{A}\vec{x} + \boldsymbol{B}\vec{u}. \tag{19}$$

Here, $\boldsymbol{A} \in \mathbb{R}^{N\times N}$ denotes the graph's adjacency matrix, $\vec{u} \in \mathbb{R}^m$ is a (potentially time-varying) input vector that is supposed to achieve control of the network and $\boldsymbol{B} \in \mathbb{R}^{N\times m}$ is the control matrix. Then one definition of controllability is the following: Can we find a set of m driver nodes identified by the controllability matrix $\boldsymbol{B}$ such that the system may be driven from any initial state $\vec{x}_0$ to any final state $\vec{x}_f$ in finite time? If yes, the system is said to be *controllable* and a measure of its controllability is given by the minimum number of driving nodes $N_d \leq N$ necessary to achieve full controllability [2, 25, 26].
We identify this set of driver nodes necessary for exact controllability for a small sample network using a method due to Yuan et al. [2] who demonstrated that the minimum number of driver nodes N_d can be found by determining the multiplicity of the eigenvalues of the graph's adjacency matrix $\mathbf{A}$ [2]. Assume that the underlying network is undirected such that its adjacency matrix is symmetric as for the networks studied in this manuscript. In this case, we can calculate the algebraic multiplicity $\delta(\lambda_i)$ for all eigenvalues λ_i of this matrix to calculate the minimum number of driver nodes, N_D, necessary to control the network (cf. Eq.4, Ref. [2])

$$N_D = \max_i \left[\delta(\lambda_i)\right]. \tag{20}$$

This approach has the advantage that the driver nodes necessary to control the network, i.e., the controllability of a network, may immediately be identified, which is more complicated when using the classical Kalman rank condition [2].
In Figure 8, we illustrate a potential application of this formalism to network isolators. The adjacency matrix of the graph reported in panel (a) has the eigenvalue $\lambda_M = -1$ with multiplicity $\delta(\lambda^M) = 2$, while all other eigenvalues have multiplicity one. An eigenvalue $\lambda_M = -1$ in the adjacency matrix can easily be constructed by connecting two nodes to the other nodes in a network in exactly the same way [4]. Thus, by the criterion (20), only two nodes are required to control the network. These nodes have been determined using the method described in Ref. [2] and are highlighted in orange. After introducing the isolator into the system (panel (d)), the maximum multiplicity of any eigenvalue of the graph's adjacency matrix is one, i.e., $\delta(\lambda_i) = 1,\ \forall i$, which implies that the graph can be controlled by a single node (colored red). Therefore, in this case, the controllability of the network is increased after constructing the isolator. We emphasize that the network isolator prevents only flow changes, but not flows from passing as demonstrated in panels (b,c) and (e,f) .
For the remaining network isolators constructed in throughout this manuscript, we did not find any influence of the introduction of network isolators on the controllability of the underlying network and thus conclude that isolators do not generically influence network controllability.

SUPPLEMENTARY REFERENCES

[1] Hörsch, J., Hofmann, F., Schlachtberger, D. & Brown, T. PyPSA-eur: An open optimisation model of the european transmission system. *Energy Strategy Reviews* **22**, 207–215 (2018).
[2] Yuan, Z., Zhao, C., Di, Z., Wang, W.-X. & Lai, Y.-C. Exact controllability of complex networks. *Nature Communications* **4**, 2447 (2013).
[3] Newman, M. E. J. *Networks: An introduction* (Oxford University Press, 2010).
[4] Van Mieghem, P., Devriendt, K. & Cetinay, H. Pseudoinverse of the laplacian and best spreader node in a network. *Physical Review E* **96**, 032311 (2017).
[5] Dörfler, F., Simpson-Porco, J. W. & Bullo, F. Electrical networks and algebraic graph theory: Models, properties, and applications. *Proceedings of the IEEE* **106**, 977–1005 (2018).
[6] Radicchi, F., Castellano, C., Cecconi, F., Loreto, V. & Parisi, D. Defining and identifying communities in networks. *Proceedings of the National Academy of Sciences* **101**, 2658–2663 (2004).
[7] Girvan, M. & Newman, M. E. J. Community structure in social and biological networks. *Proceedings of the National Academy of Sciences* **99**, 7821–7826 (2002).
[8] Newman, M. E. J. Communities, modules and large-scale structure in networks. *Nature Physics* **8**, 25–31 (2012).
[9] Wood, A. J., Wollenberg, B. F. & Sheblé, G. B. *Power Generation, Operation and Control* (John Wiley & Sons, New York, 2014).
[10] Strake, J., Kaiser, F., Basiri, F., Ronellenfitsch, H. & Witthaut, D. Non-local impact of link failures in linear flow networks. *New Journal of Physics* **21**, 053009 (2019).
[11] Bollobás, B. *Modern graph theory*. No. 184 in Graduate texts in mathematics (Springer, 1998).

[12] Sack, L., Dietrich, E. M., Streeter, C. M., Sanchez-Gomez, D. & Holbrook, N. M. Leaf palmate venation and vascular redundancy confer tolerance of hydraulic disruption. *Proceedings of the National Academy of Sciences* **105**, 1567–1572 (2008).

[13] Katifori, E., Szöllősi, G. J. & Magnasco, M. O. Damage and fluctuations induce loops in optimal transport networks. *Physical Review Letters* **104**, 048704 (2010).

[14] Manik, D. *et al.* Network susceptibilities: Theory and applications. *Physical Review E* **95**, 012319 (2017).

[15] Purchala, K., Meeus, L., Dommelen, D. V. & Belmans, R. Usefulness of dc power flow for active power flow analysis. In *IEEE Power Engineering Society General Meeting*, 454–459 Vol. 1 (2005).

[16] Kaiser, F. & Witthaut, D. Topological theory of resilience and failure spreading in flow networks. *arXiv:2009.10349 [physics]* (2020). URL `http://arxiv.org/abs/2009.10349`. ArXiv: 2009.10349.

[17] Reichold, J. *et al.* Vascular graph model to simulate the cerebral blood flow in realistic vascular networks. *Journal of Cerebral Blood Flow & Metabolism* **29**, 1429–1443 (2009).

[18] Wurbs, R. A. & James, W. P. *Water Resources Engineering* (Pearson, 2001).

[19] Coomes, D. A., Heathcote, S., Godfrey, E. R., Shepherd, J. J. & Sack, L. Scaling of xylem vessels and veins within the leaves of oak species. *Biology Letters* **4**, 302–306 (2008).

[20] Rodrigues, F. A., Peron, T. K. D., Ji, P. & Kurths, J. The kuramoto model in complex networks. *Physics Reports* **610**, 1–98 (2016).

[21] Rohden, M., Sorge, A., Timme, M. & Witthaut, D. Self-organized synchronization in decentralized power grids. *Phys. Rev. Lett.* **109**, 064101 (2012).

[22] Nishikawa, T. & Motter, A. E. Comparative analysis of existing models for power-grid synchronization. *New Journal of Physics* **17**, 015012 (2015).

[23] Manik, D. *et al.* Supply networks: Instabilities without overload. *The European Physical Journal Special Topics* **223**, 2527–2547 (2014).

[24] Biggs, N. Algebraic potential theory on graphs. *Bulletin of the London Mathematical Society* **29**, 641–682 (1997).

[25] Gao, J., Liu, Y.-Y., D'Souza, R. M. & Barabási, A.-L. Target control of complex networks. *Nature Communications* **5**, 5415 (2014).

[26] Liu, Y.-Y., Slotine, J.-J. & Barabási, A.-L. Controllability of complex networks. *Nature* **473**, 167–173 (2011).

3.2. E) Topological theory of resilience and failure spreading in flow networks

[5] Kaiser, F. & Witthaut, D. Topological theory of resilience and failure spreading in flow networks. *Physical Review Research* **3,** 023161. doi:10.1103/PhysRevResearch.3.023161 (2021).

Topological theory of resilience and failure spreading in flow networks

Franz Kaiser * and Dirk Witthaut †

Forschungszentrum Jülich, Institute for Energy and Climate Research (IEK-STE), 52428 Jülich, Germany and Institute for Theoretical Physics, University of Cologne, 50937 Köln, Germany

(Received 11 September 2020; accepted 7 May 2021; published 1 June 2021)

Link failures in supply networks can have catastrophic consequences that can lead to a complete collapse of the network. Strategies to prevent failure spreading are thus heavily sought after. Here, we make use of a spanning tree formulation of link failures in linear flow networks to analyze topological structures that prevent failure spreading. In particular, we exploit a result obtained for resistor networks based on the *matrix tree theorem* to analyze failure spreading after link failures in power grids. Using a spanning tree formulation of link failures, we analyze three strategies based on the network topology that allow us to reduce the impact of single link failures. All our strategies either do not reduce the grid's ability to transport flow or do in fact improve it—in contrast to traditional containment strategies based on lowering network connectivity. Our results also explain why certain connectivity features completely suppress any failure spreading as reported in recent publications.

DOI: 10.1103/PhysRevResearch.3.023161

I. INTRODUCTION

The theory of linear flow networks provides a powerful framework, allowing one to study systems ranging from water supply networks [1,2] and biological networks, such as leaf venation networks [3–6], to resistor networks [7–9], or ac power grids [10,11]. Failures of transportation links in these networks can have catastrophic consequences up to a complete collapse of the network. As a result, link failures in linear flow networks and strategies to limit their consequences are a field of active study [12–19].

The study of linear flow networks is intimately related to graph theory since most phenomena can be analyzed on purely topological grounds [7]. This connection dates back to work by Kirchhoff [8], who analyzed resistor networks and introduced several major tools that are now the basis of the theory of complex networks, such as the matrix tree theorem [7,8,20]. These tools can now serve as a basis for the analysis of failure spreading in ac power grids, which can be modeled as linear flow networks based on the dc approximation [11]. A substantial part of security analysis in power grids is dedicated to the study of transmission line outages since they can lead to cascading outages in a series of failures [21–23].

The topological approach to failure spreading has been exploited to demonstrate that the strength of flow rerouting after link failures decays with distance to the failing link [12–15]. In particular, the so-called rerouting distance based on cycles in the network has been found to predict flow rerouting very well [12]. However, the analysis of flow rerouting still lacks a theoretical foundation. Here, we demonstrate that these observations made for flow rerouting may be understood based on a formalism originally developed to study current flows in resistor networks that uses spanning trees (STs) of the underlying graph. Moreover, the formalism explains recent results regarding the shielding against failure spreading in complex networks.

This paper is structured as follows. In Sec. II, we give an overview over the theory of linear flow networks and present an important lemma that relates the current flows in these networks to STs. In Sec. III, we demonstrate the analogy between such networks and ac power grids in the dc approximation and relate the ST formulation to line outages studied in power system security analysis. Finally, in Sec. IV we show how this formulation may be used to understand why certain connectivity features inhibit failure spreading extending on recent results [19].

II. FUNDAMENTALS OF RESISTOR NETWORKS

Resistor networks are a prime example of linear flow networks and have inspired research throughout centuries [7,8,24]. A resistor network can be described using a graph as follows. Let $G = (E, V)$ be a connected graph with vertex set $V = \{v_1, \dots, v_N\}$ and M edges in the edge set E. Then we assign a weight w_k to each edge $e_k = (a, b)$ in the graph given by the inverse resistance $w_k = R_k^{-1}$ between its terminal vertices a and b. If there is a potential difference $v_k = V_a - V_b$ between the terminal vertices of edge $e_k = (a, b)$, according to Ohm's law there is a current flow i_k between the two vertices given by

$$i_k = \frac{v_k}{R_k} = \frac{V_a - V_b}{R_k}. \tag{1}$$

*f.kaiser@fz-juelich.de

†d.witthaut@fz-juelich.de

In order to give a direction to the current flow, we assign an arbitrary orientation to each edge in the graph that is encoded by the graph's edge-node-incidence matrix $\mathbf{B} \in \mathbb{R}^{N\times M}$ defined as [7]

$$B_{n,\ell} = \begin{cases} 1 & \text{if line } \ell \text{ starts at node } n \\ -1 & \text{if line } \ell \text{ ends at node } n \\ 0 & \text{otherwise.} \end{cases} \tag{2}$$

The current flows and voltages are then subject to *Kirchhoff's circuit laws* [8]. The first of the laws, typically referred to as Kirchhoff's current law, at an arbitrary node $j \in V(G)$ reads as

$$\sum_{e_k\in\Lambda(j)}^{M} i_k = I_j.$$

Here, $I_j \in \mathbb{R}$ is the current injected into or withdrawn from node j, and $\Lambda(j) \subset E(G)$ is the set of all edges that connect to node j respecting their orientation. The current law may be regarded as a continuity equation and thus states that the inflows and outflows at each node in the network have to balance with the current injections at the respective node. It may be written more compactly making use of the node-edge-incidence matrix

$$\mathbf{Bi} = \mathbf{I}, \tag{3}$$

where $\mathbf{i} = (i_1,\dots,i_M)^\top \in \mathbb{R}^M$ is a vector of current flows and $\mathbf{I} = (I_1,\dots,I_N)^\top \in \mathbb{R}^N$ is a vector of current injections. On the other hand, we can also introduce a more compact notation for Ohm's law (1) by defining a vector of nodal voltage levels $\mathbf{V} = (V_1,\dots,V_N)^\top \in \mathbb{R}^N$ and a diagonal matrix of edge resistances $\mathbf{R} = \mathrm{diag}(R_1,\dots,R_M) \in \mathbb{R}^{M\times M}$ such that Ohm's law reads as

$$\mathbf{Ri} = \mathbf{B}^\top\mathbf{V}. \tag{4}$$

Combining Ohm's law with Kirchhoff's current law, we arrive at the following relationship between nodal voltages $\mathbf{V}$ and nodal current injections $\mathbf{I}$:

$$\mathbf{I} = \mathbf{BR}^{-1}\mathbf{B}^\top\mathbf{V}. \tag{5}$$

This Poisson-like equation has been analyzed in different contexts [7,12,25]. Note that Kirchhoff's voltage law is automatically satisfied by virtue of Eq. (3), because the resulting vector of potential differences $\mathbf{v} = \mathbf{B}^T\mathbf{V}$ vanishes along any closed cycle due to the duality between the graph's cycle space and its cut space [7,26]. In addition to that, the potential at one node may be chosen freely without affecting the result.

The matrix connecting the two quantities is referred to as a weighted graph Laplacian or Kirchhoff matrix $\mathbf{L} = \mathbf{BR}^{-1}\mathbf{B}^\top \in \mathbb{R}^{N\times N}$ and characterizes the underlying graph completely. It has the following entries [7]:

$$L_{mn} = \begin{cases} \sum_{\ell\in\Lambda(m)} w_\ell & \text{if } m = n \\ -w_\ell & \text{if } m \text{ is connected to } n \text{ by } \ell. \end{cases} \tag{6}$$

Here, the weight of an edge ℓ is again given by its inverse resistance $w_\ell = R_\ell^{-1}$. For a connected graph, this matrix has exactly one vanishing eigenvalue $\lambda_1 = 0$ with corresponding unit eigenvector $\mathbf{v}_1 = \mathbf{1}/\sqrt{N}$ such that $\mathbf{L1} = 0$. For this reason, the matrix is noninvertible. This is typically overcome by making use of the graph's Moore-Penrose-pseudoinverse $\mathbf{L}^\dagger$, which has properties similar to the actual inverse [27].

With this formalism at hand, we can in principle now determine the current on any edge given a particular injection pattern $\mathbf{I}$ and edge resistances $\mathbf{R}$. As a start, consider the situation where each edge has a unit resistance $\mathbf{R} = \mathrm{diag}(1)$ and a unit current is injected into a particular vertex s and withdrawn at another one t such that $\mathbf{I} = \mathbf{e}_s - \mathbf{e}_t$, where $\mathbf{e}_i = (0,\dots,\underbrace{1}_{i},\dots,0)^\top \in \{0,1\}^M$ are the unit vectors with entry one at position i and zero otherwise. In this situation, the current across any edge in the graph $\ell = (a, b)$ is given by the following lemma, which dates back to Kirchhoff [8,20] and has been popularized by Shapiro [7,28].

Lemma 1. Put a 1-A current between the vertices s and t of a connected, unweighted graph G such that $\mathbf{I} = \mathbf{e}_s - \mathbf{e}_t$. Then the current on any other edge (a, b) is given by

$$i_{ab} = \frac{\mathcal{N}(s, a\to b, t) - \mathcal{N}(s, b\to a, t)}{\mathcal{N}},$$

where $\mathcal{N}(s, a \to b, t)$ is the number of STs that contain a path from s to t of the form $s,\dots,a,b,\dots,t$ and $\mathcal{N}$ is the total number of STs of the graph.

Whereas this lemma only holds for graphs where all links have unit resistances, real-world resistor networks or other types of linear flow networks are typically weighted with non-homogeneous resistances. However, the extension to weighted networks is straightforward as summarized in the following corollary (see, e.g., Theorem II.2 in Ref. [7]).

Corollary 1. Put a 1-A current between the vertices s and t of a connected, weighted graph G such that $\mathbf{I} = \mathbf{e}_s - \mathbf{e}_t$. Then the current on any other edge (a, b) is given by

$$i_{ab} = \frac{\mathcal{N}^*(s, a\to b, t) - \mathcal{N}^*(s, b\to a, t)}{\mathcal{N}^*}, \tag{7}$$

where $\mathcal{N}^* = \sum_{T\in\mathcal{T}}\prod_{e\in T} w_e$ is the sum over the products of the weights w_e of all edges $e \in T$ that are part of the respective spanning tree T; $\mathcal{T}$ is the set of all STs in the graph. Similarly, $\mathcal{N}^*(s, a \to b, t)$ equals the sum over all STs that contain a path of the form $s,\dots,a,b,\dots,t$, where each ST is weighted with the product of the weight w_e of all edges that are part of it. We thus assign a weight to each ST given by the product of the weights of the edges on the ST and replace the unweighted STs in Lemma 1 by weighted STs.

We will demonstrate in the following sections how this lemma and corollary may be made use of to understand how failure spreading may be mitigated in linear flow networks such as ac power grids in the dc approximation.

III. ANALOGY BETWEEN RESISTOR NETWORKS AND POWER FLOW IN ELECTRICAL GRIDS

Importantly, the theoretical framework developed in the last section may be applied not only to resistor networks but also to power grids. In this section, we demonstrate how these results may be used to gain insight into the mitigation of failure spreading in power grids.

TABLE I. Analogy between resistor networks and ac power grids in the dc approximation.

dc approximation		Resistor network	
Quantity	Symbol	Quantity	Symbol
Power injections	$\mathbf{P}$	Nodal current	$\mathbf{I}$
Real power flow	$\mathbf{F}$	Current flow	$\mathbf{i}$
Nodal phase angles	ϑ	Nodal voltages	$\mathbf{V}$
Line susceptances	b_e	Inverse edge resistance	r_e^{-1}

A. Modeling power grids as linear flow networks

Most electric power transmission grids are made up of ac transmission lines and are, as such, governed by the nonlinear ac power flow equations [11]. However, the real power flow over transmission lines can be simplified to a linear flow model in what is referred to as the dc approximation of the ac power flow. This approximation is based on the following assumptions [29].

(i) Nodal voltage magnitudes vary little.

(ii) Transmission lines are purely inductive; that is, their resistance is negligible compared with their reactance $r_\ell \ll x_\ell,\ \forall \ell \in E(G)$.

(iii) Differences between nodal voltage angles ϑ_n, $n \in V(G)$, of neighboring nodes n, m are small $|\vartheta_n - \vartheta_m| \ll 1$.

Typically, these assumptions are met if the power grid is not heavily loaded and if the power grid is modeled at the transmission level where line resistances are small [29]. As a result, the real power flow F_ℓ along a transmission line $e_\ell = (n, m) \in E(G)$ in the dc approximation depends linearly on the nodal voltage phase angles ϑ_n of neighboring nodes

$$F_\ell = b_\ell(\vartheta_n - \vartheta_m). \tag{8}$$

Here, $b_\ell \approx x_\ell^{-1}$ is the line susceptance of line ℓ. Thus the vector of real power flow along the transmission lines in the power grid $\mathbf{F} = (F_1, \dots, F_M)^\top \in \mathbb{R}^M$ takes the role of current flow vector in the case of resistor networks. On the other hand, the nodal voltage phase angles $\boldsymbol{\vartheta} = (\vartheta_1, \dots, \vartheta_N)^\top \in \mathbb{R}^N$ take the role of the nodal voltages $\mathbf{V}$, and line weights are given by the line susceptances b_k of an edge e_k in correspondence with the inverse resistances R_k^{-1} in the case of resistor networks. Thus Ohm's law (4) translates to power grids as

$$\mathbf{F} = \mathbf{B}_d\mathbf{B}^\top\boldsymbol{\vartheta}.$$

Here, $\mathbf{B}_d = \mathrm{diag}(b_1, \dots, b_M) \in \mathbb{R}^{M\times M}$ is the diagonal matrix of line susceptances. Again, Kirchhoff's current law (3) holds, and we may express it using vector quantities as follows [11,12]:

$$\mathbf{BF} = \mathbf{P}.$$

Here, $\mathbf{P} = (P_1, \dots, P_N)^\top \in \mathbb{R}^N$ is the vector of nodal power injections, which thus takes the role of nodal current injections $\mathbf{I}$. We summarize these equivalences in Table I.

B. Sensitivity factors in power grid security analysis

In power grid security analysis, linear sensitivity factors are used to study and prevent line overloads which could cause disturbances to power system operation and result in power outages [11]. One of these factors is the *power transfer distribution factor* (PTDF). The $\mathrm{PTDF}_{s,t,k}$ then quantifies the change in flow ΔF_k on line $e_k \in E(G)$ if a power ΔP is injected at node r and withdrawn from node s. It is calculated as [11]

$$\mathrm{PTDF}_{r,s,k} = \frac{\Delta F_k}{\Delta P}. \tag{9}$$

Now assume that a single line e_m fails, for example, as a result of an overload, and is disconnected from the network. The change in power flow on a line e_k may then be calculated by using the *line outage distribution factor* (LODF) [11]

$$\mathrm{LODF}_{k,m} = \frac{\Delta F_k}{F_m^{(0)}}. \tag{10}$$

Here, $F_m^{(0)}$ is the flow on line e_m before the outage. Mathematically, we can map the flow changes after a failure to the flow changes after changes in the injection patterns by considering power injections that effectively compensate for the flow on the link that is assumed to fail (see Refs. [11,12]). As a result, the two quantities are related as follows if $e_m = (r, s)$ is the failing link [11]:

$$\mathrm{LODF}_{k,m} = \frac{\mathrm{PTDF}_{r,s,k}}{1 - \mathrm{PTDF}_{r,s,m}}. \tag{11}$$

Note that the description of link failures using LODFs relies on the dc approximation of the nonlinear ac power flow equations. However, extended descriptions have been proposed that incorporate nonlinear terms [31]. Furthermore, the dc approximation and thus the LODF-based description of link failures are commonly used to model cascading failures in power grids, where a single link triggers the failure of other links [23,32,33]. A comparison of the effect of link failures in linear and nonlinear models of power flows can, for example, be found in Ref. [34].

C. Spanning tree description of link failures

On the basis of the analogy between electrical grids and resistor networks developed in the last sections, we will now show how the ST formula presented in Corollary 1 may be used for power system security analysis. In the language of power grids, the lemma yields the $\mathrm{PTDF}_{s,t,m}$ for an edge $e_m = (a, b)$ if a unit power ΔP is injected at node r and withdrawn from node s. For this reason, the PTDF may be calculated as follows:

$$\mathrm{PTDF}_{s,t,m} = \frac{\mathcal{N}^*(s, a \to b, t) - \mathcal{N}^*(s, b \to a, t)}{\mathcal{N}^*}. \tag{12}$$

Based on Eq. (11), which yields the LODF expressed in terms of the PTDF, we can make use of this expression to derive an equivalent expression for the LODF. If $e_k = (r, s)$ is the failing link and $e_m = (a, b)$ is the link where the flow changes are monitored, the expression based on Eq. (12) reads as

$$\begin{aligned}\mathrm{LODF}_{m,k} &= \frac{\mathcal{N}^*(r, a \to b, s) - \mathcal{N}^*(r, b \to a, s)}{\mathcal{N}^* - [\mathcal{N}^*(r, r \to s, s) - \mathcal{N}^*(r, s \to r, s)]}\\ &= \frac{\mathcal{N}^*(r, a \to b, s) - \mathcal{N}^*(r, b \to a, s)}{\mathcal{N}^* - \mathcal{N}^*(r, r \to s, s)}\\ &= \frac{\mathcal{N}^*(r, a \to b, s) - \mathcal{N}^*(r, b \to a, s)}{\mathcal{N}^*_{\setminus\{k\}}}.\end{aligned} \tag{13}$$

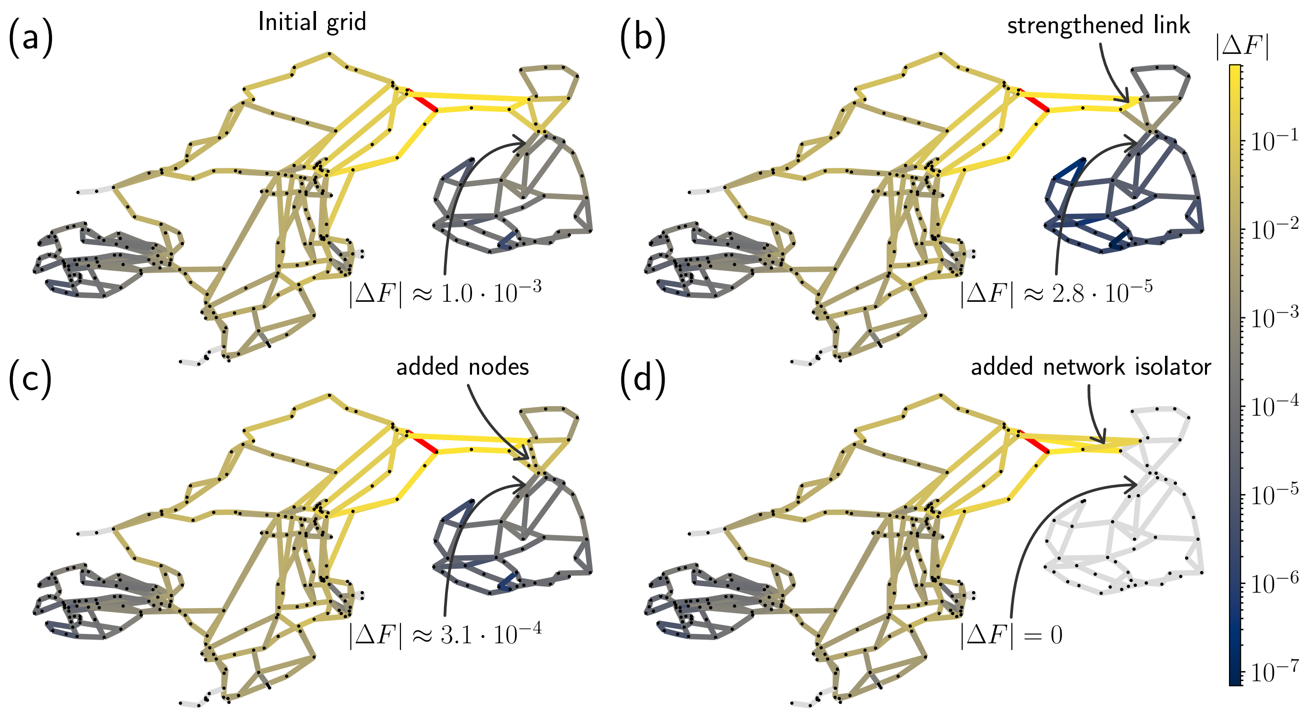

FIG. 1. Different methods for mitigating failure spreading in linear flow networks. (a) The failure of a single link (red) with unit flow results in flow changes ΔF (color scale) throughout the Scandinavian power grid. (b) Failure spreading to Finland may be reduced by strengthening a link that horizontally separates Sweden and Finland. (c) Adding nodes, thus increasing the length of the rerouting path, reduces failure spreading to Finland as well. (d) Adding two links to construct a network isolator results in a complete vanishing of flow changes in the other part of the grid. Grid topology was extracted from the open energy system model PyPSA-Eur [30].

Here, $\mathcal{N}^*_{\setminus\{k\}}$ denotes the weight of all STs in the graph evaluated *after* removing the edge e_k from the set of trees $\mathcal{T}$. We thus found an expression for the LODFs that is based purely on certain STs in the graph. This equation is the basis of our analysis of subgraphs inhibiting failure spreading which we will perform in the following sections. Note that a similar expression for the LODFs based on spanning 2-forests has recently been derived by Guo *et al.* [16].

IV. MITIGATING FAILURE SPREADING

We have seen in the last section that the spreading of failures is studied using LODFs in power system security analysis. To prevent large flow changes on other links after the failure of a link e_k which may potentially trigger dangerous cascades of failures, it is desirable for overall power system security to keep the LODFs small. A natural question to ask is thus the following: Can we design or alter the network topology in such a way that LODFs stay small? Based on Eq. (13) expressing the LODF in terms of STs, this question may be addressed in a purely topological manner. In particular, we deduce three strategies to reduce the effect of failure spreading.

(1) Fixing long paths between trigger link e_k and monitoring link e_l leaves only few degrees of freedom, which reduces the relative contribution of the numerator in Eq. (13).

(2) Fixing specific paths between trigger link e_k and monitoring link e_l can force links of large weights to be not contained in the numerator, thus reducing its relative contribution to Eq. (13).

(3) Introducing symmetric elements between parts of the network may lead to a complete balancing between the two contributions in the numerator of Eq. (13).

In Fig. 1 we illustrate three possible ways to realize these strategies to mitigate the impact of the failure of a single link (red) in a real power grid. All three strategies provide significant relief to the right module of the Scandinavian power grid, which represents Finland, after a link failure occurred in the left module. Remarkably, all these strategies are intimately related to the graph's topological properties as we will see in the following sections.

A. The role of the rerouting distance

With Eq. (13) expressing LODFs using STs at hand it is intuitively clear that certain paths in the network should play an important role in predicting the overall effect of line outages. In particular, we can see immediately that for a given failing link e_k, the numerator in Eq. (13) depends on the paths going through the link monitoring the flow changes e_l whereas the denominator does not. Therefore we expect the flow changes to be smaller on another link e_m that has a longer minimum path going through e_m and e_k compared with link e_l. This is due to the fact that reducing the number of possible paths in the sum over all STs $\mathcal{N}^*(r, a \rightarrow b, s)$ effectively reduces the number of STs by fixing a certain path.

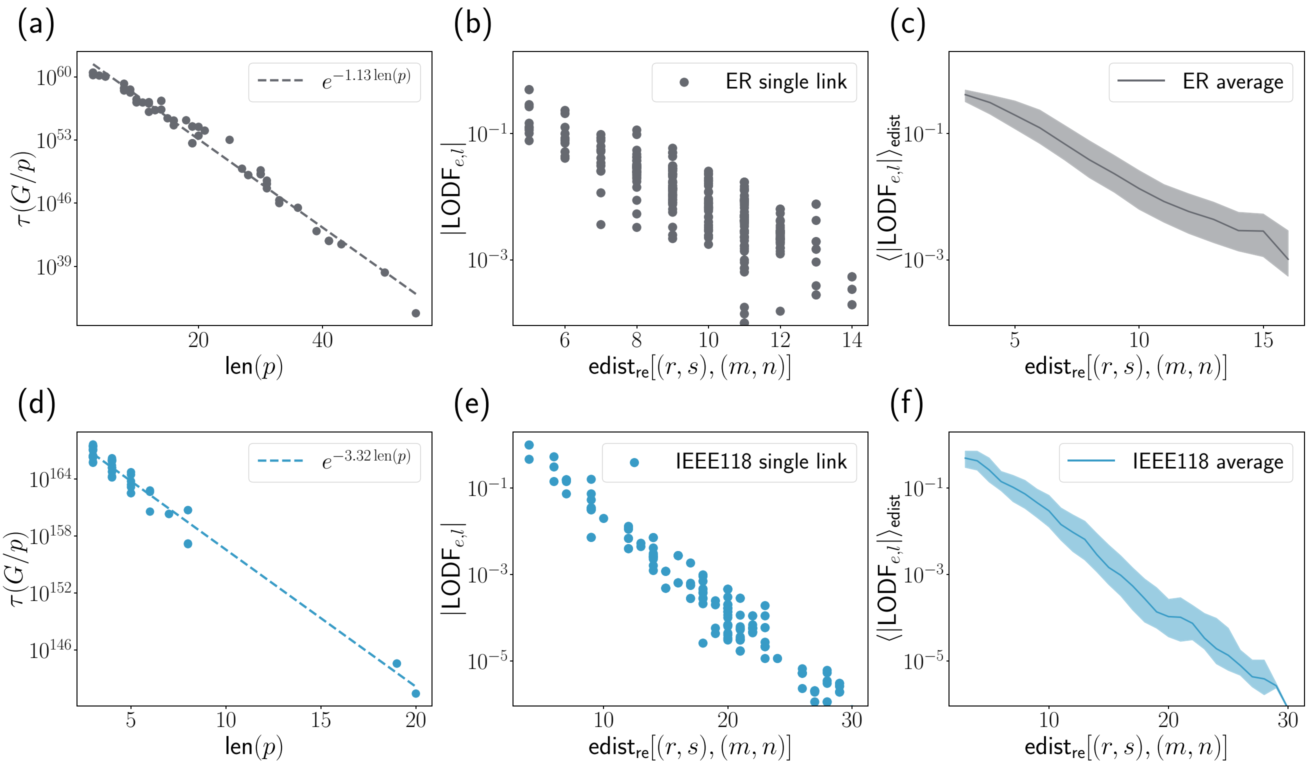

FIG. 2. Flow changes decay exponentially with cyclic paths in different networks. (a) and (d) Number of spanning trees (STs) $\tau(G/p)$ in an Erdős-Rényi (ER) random graph $G(200, 300)$ with 300 edges and 200 vertices (a) and in the power flow test case "IEEE 118" [35] (d) that contain a randomly chosen cyclic path p (y axis) plotted against the length of the path $\mathrm{len}(p)$ (x axis). The number of STs decays exponentially with the length of the path, thus appearing linear on a logarithmic y scale. (b) and (e) The rerouting distance scales exponentially with the LODF evaluated here for a single trigger for both grids. (c) and (f) The exponential scaling is preserved when averaging over all possible trigger links. Shading indicates 0.25 and 0.75 quantiles, a line represents the median. In Figs. 8 and 9 in the Appendix we demonstrate that the scaling robustly occurs for ER random graphs by analyzing 20 random realizations.

This intuitive idea is demonstrated to hold also quantitatively in Figs. 2(a) and 2(d): We illustrate that the number of STs $\tau(G/p)$ scales approximately exponentially with the length of the cyclic path contained in the STs for an unweighted Erdős-Rényi (ER) random graph $G(200, 300)$ with 300 edges and 200 vertices [36] [Fig. 2(a)] and the power flow test case "IEEE 118" [35,37] [Fig. 2(d)]. To study this scaling, we contract a cyclic path p between two arbitrarily chosen edges and quantify the number of STs using Kirchhoff's matrix tree theorem [8]. The theorem states that the number of STs in a graph may be calculated using the determinant of the graph's Laplacian matrix [7]

$$\tau(G) = \det(L_u).$$

Here, L_u is the matrix obtained from the Laplacian matrix L of G obtained by removing the row and column corresponding to an arbitrarily chosen vertex $u \in V(G)$. The number of STs $\tau(G/p)$ containing a path p may be calculated by contracting the path in the graph and the Laplacian matrix and then taking the determinant of the resulting Laplacian. Taking the difference in the numerator of Eq. (13) between the path and a reversed path will in general not affect the exponential scaling since the difference of two exponential functions with different exponents or different prefactors will again scale exponentially. In Fig. 8 in the Appendix, we show that the same scaling robustly occurs in ER random graphs by analyzing it for 20 different random realizations of ER graphs.

We may thus expect an exponential decay of LODFs with the length of fixed, cyclic paths. This result complements recent progress made in the understanding of the role played by distance for failure spreading in linear flow networks. In Ref. [12], it was shown that flow changes after a link failure are not captured well by the ordinary graph distance between the failing link and the link monitoring flow changes. Instead, a different distance measure referred to as rerouting distance captures this effect much better. It is defined as follows:

Definition 1. A *rerouting path* from vertex r to vertex s via the edge (m, n) is a path

$$(v_0 = r, v_1, \dots, v_i = m, v_{i+1} = n, v_{i+2}, \dots, v_k = s)$$

or

$$(v_0 = r, v_1, \dots, v_i = n, v_{i+1} = m, v_{i+2}, \dots, v_k = s)$$

where no vertex is visited twice. The *rerouting distance* between two edges (r, s) and (m, n) denoted by

$$\mathrm{edist}_{\mathrm{re}}[(r, s), (m, n)]$$

is the length of the shortest rerouting path from r to s via (m, n) plus the length of edge (r, s). Equivalently, it is the length of the shortest cycle crossing both edges (r, s) and

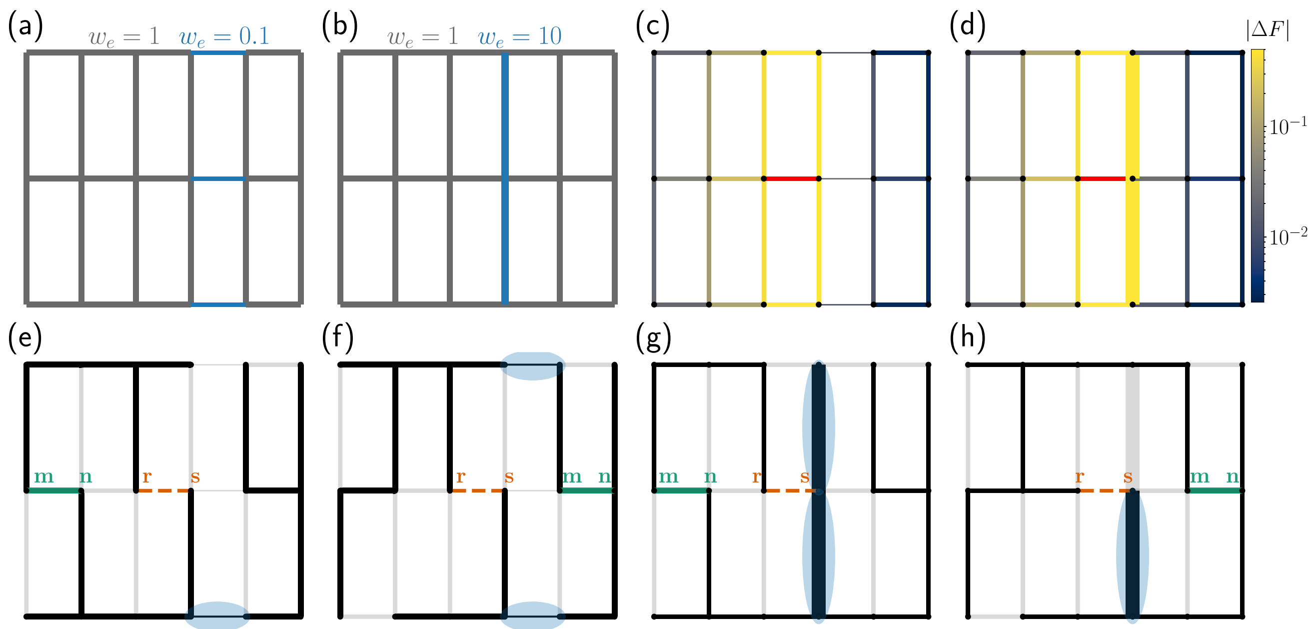

FIG. 3. Spanning trees (STs) may be used to explain the shielding effect of certain connectivity structures between different parts of a network. (a) and (b) A square grid is divided into two parts by either weakening the links connecting two parts [(a), blue, $w_e = 0.1$] or strengthening the links perpendicularly separating the two parts [(b), blue, $w_e = 10$]. (c) and (d) For both divisions, the failure of a single link with unit flow (red) significantly reduces failure spreading to the other part of the network. (e)–(h) Different STs (black) that contain specific paths of the form $(v_0 = r, v_1, \ldots, v_i = m, v_{i+1} = n, v_{i+2}, \ldots, v_k = s)$ used to calculate the flow changes on link (m, n) for a failure of link (r, s) by virtue of Eq. (7). (e) and (f) For the weakly connected network shown in (a) and (c), a monitoring link in the same part (e) may lead to STs that contain only one weak link (blue shading). Thus the contribution of this ST to the sum over all STs is much stronger than for a monitoring link in the other part, where STs have to contain at least two weak links [(f), blue shading]. (g) and (h) For the strongly connected network shown in (g) and (h), the STs with the highest contribution are the ones containing all edges with strong weights [(g), blue shading]. (h) If links (m, n) and (r, s) are in different parts, no ST may contain all edges with strong weights (blue shading), thus reducing failure spreading in this case.

(m, n). If no such path exists, the rerouting distance is defined to be ∞.

Note that we include the weight of the edge (r, s) to make sure the rerouting distance is symmetric. The rerouting distance defined this way is a proper distance metric as shown in Ref. [12]. With the arguments made before at hand it is intuitively clear why the rerouting distance performs very well in predicting the effects of line outages. Indeed, we observe an exponential scaling of the LODFs for a given trigger link in the ER random graph [Fig. 2(b)] and in the test case "IEEE 118" [Fig. 2(e)]. The same observation still holds if we average over all monitoring links located at a fixed rerouting distance to the possible trigger links over which we average thereafter [Figs. 2(c) and 2(f)]. In Fig. 9 we show that the observed scaling robustly appears by comparing it for 20 different realizations of ER random graphs.

B. The role of strong and weak network connectivity

Our second strategy to reduce failure spreading after link failures is based on fixing specific paths in the network in such a way that they cannot contain certain links with large weights. This way, the numerator in Eq. (13) does not contain the contribution of the links with large weights whereas the denominator does, thereby reducing the overall impact of the link failure. Note that in contrast to the last section, the fixed paths do not necessarily have to be long to prevent failure spreading. We will demonstrate this strategy for two cases: First, we use this reasoning to demonstrate that weakening the links between two parts of the network—thus effectively dividing it into communities—may reduce failure spreading between them. This is expected as weakly connected networks generally suppress failure spreading from one part to the other one, but this also limits the possibility of power flow between the parts. This is no longer true for the second strategy: We illustrate why also strengthening the links that separate two parts of the network perpendicularly to the community boundary reduces the impact of link failures.

The two strategies are illustrated for a simple 3×6 square grid in Fig. 3. We divide the square grid into two parts by either weakening the links that separate the parts [Fig. 3(a)] or strengthening the links perpendicular to these links [Fig. 3(b)]. We then monitor the flow changes (color scale) after the failure of a single link (red) in both cases [Figs. 3(c) and 3(d)]. For weak connectivity, the failure of link $e_k = (r, s)$ (dashed orange line) leads to a different contribution of the numerator in Eq. (13) if the monitoring link $e_\ell = (m, n)$ (green line) is contained in the same part [Fig. 3(e)] as compared with a different, weakly connected part [Fig. 3(f)] in an otherwise symmetrical situation. Note that the distance between monitoring link and trigger link is also the same in both Fig. 3(e) and Fig. 3(f). For a link in the same part, the numerator also

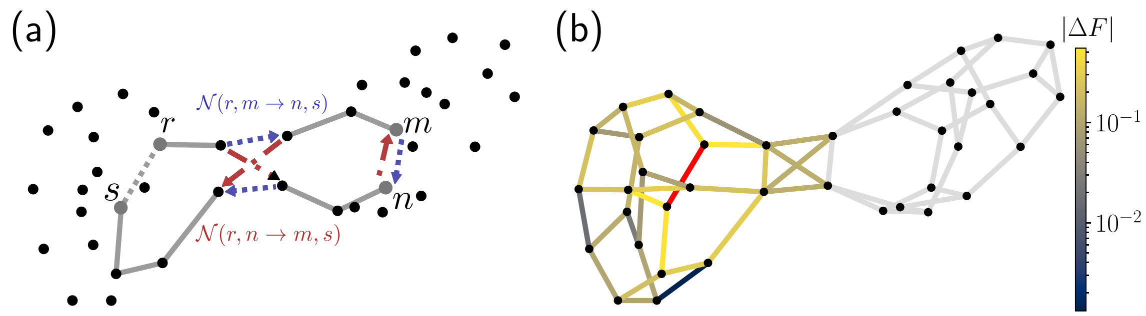

FIG. 4. Network isolators that lead to a complete vanishing of LODFs are created using certain symmetric paths in the network. (a) STs that contain a path starting at node r and terminating at node s and containing the edge (m, n) (blue) or (n, m) (red) have to cross the subgraph consisting of dotted, colored edges in the center. Since each path can contain each vertex and edge only once, each ST passing through the subgraph in one way (blue) has a counterpart passing through the subgraph in the other way (red). (b) Failure of a link (red) results in vanishing LODFs (color scale) in the part connected by a network isolator as predicted using the ST formulation of link failures.

contributes with STs containing only *one* weak link (thin line, blue shading). For a trigger link located in the other part, each ST connecting trigger link and monitoring link has to contain at least *two* weak links (shaded blue). Since the contribution in the numerator is proportional to the product of all weights along the ST and the situation is otherwise symmetric, we expect a weaker LODF and thus a shielding effect if the two links are contained in different, weakly connected parts.

A similar observation holds in the case of strong connectivity: If the monitoring link $e_\ell = (m, n)$ is contained in the same part of the network as the trigger link $e_k = (r, s)$ [Fig. 3(g)], now separated through strong connections, spanning trees connecting the two links may contain *two*—or generally, all—strong links. For a trigger link in the other part of the network, the spanning tree connecting them can contain maximally *one*—or generally, all minus one—strong links. Again, the term in the numerator scales with the link weights contained in the spanning trees. Therefore we expect the effect of link failures to be stronger for links located in the same part as compared with links contained in the other part, which is confirmed when simulating the failure of a single link in Fig. 3(d).

C. The role of symmetry

As a third strategy for reducing failure spreading, we suggest building networks in such a way that the terms in the numerator of Eq. (13) balance. In this case, failure spreading reduces to zero for the respective links. In order to balance the terms in the numerator of Eq. (13), we need the spanning trees passing through the monitoring link $e_\ell = (a, b)$ in both directions to have exactly the same weight

$$\mathcal{N}^*(r, m \to n, s) = \mathcal{N}^*(r, n \to m, s)$$
$$\Rightarrow \quad \sum_{T \in \mathcal{T}(r,m\to n,s)} \prod_{e \in T} w_e = \sum_{T \in \mathcal{T}(r,n\to m,s)} \prod_{e \in T} w_e.$$

Here, $\mathcal{T}(r, m \to n, s)$ is the set of all spanning trees containing a path of the form $(r, \ldots, m, n, \ldots, s)$. This equality is, for example, fulfilled if for each tree $T \in \mathcal{T}(r, m \to n, s)$ there is a counterpart $T \in \mathcal{T}(r, n \to m, s)$ of the same weight. This may be accomplished by introducing certain symmetric elements, referred to as *network isolators* [19], into the graph as demonstrated in Fig. 4: For each ST connecting trigger link $e_k = (r, s)$ and monitoring link $e_\ell = (m, n)$ and containing a path of the form $(r, \ldots, m, n, \ldots, s)$ (gray and blue lines) there is an ST containing a path of the form $(r, \ldots, n, m, \ldots, s)$ (gray and red lines). If we compare the product of weights for a single tree $T_0 \in \mathcal{T}(r, m \to n, s)$ and its counterpart $T_0^* \in \mathcal{T}(r, n \to m, s)$, such that both contain exactly the same edges except for the edges connecting the two parts, i.e., the links marked as blue and red arrows in Fig. 4(a), we can see that these products are equal except for the links r_1 and r_2 (red links) being contained only in T_0, and b_1 and b_2 (blue links) being contained only in T_0^*. We can thus conclude that the above equality is fulfilled, i.e., the product of weights is equal for both trees T_0 and T_0^*, if

$$b_1 \cdot b_2 = r_1 \cdot r_2.$$

In this case, a failure of link $e_k = (r, s)$ does not result in any flow changes on link $e_\ell = (m, n)$ at all. This reasoning has been generalized recently, where the concept was termed *network isolators* [19]. We also note that similar arguments were put forward by Guo *et al.* [16]. On general grounds, network isolators are defined as follows [19].

Lemma 2. Consider a linear flow network consisting of two parts with vertex sets V_1 and V_2 and assume that a single link in

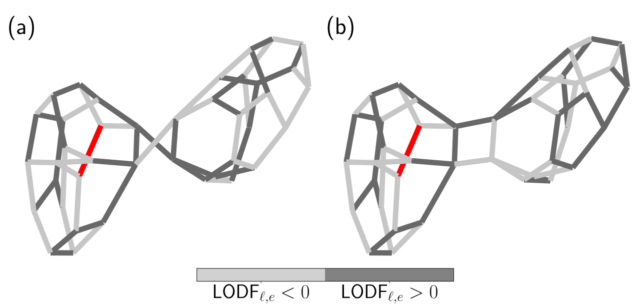

FIG. 5. Sign reversal of LODFs by symmetric subgraphs. (a) and (b) Modifying the subgraph connecting two graphs from the two parallel lines to the two crossing lines leads to a sign reversal of the LODFs in the connecting subgraphs (shades of gray). This is in line with the compensatory effect of the symmetric subgraphs used to create the network isolator in Fig. 4.

the induced subgraph $G(V_1)$ fails, i.e., a link (r, s) with $r, s \in V_1$. If the adjacency matrix of the mutual connections has unit rank rank$(\mathbf{A}_{12}) = 1$, then the flows on all links in the induced subgraph $G(V_2)$ are not affected by the failure; that is,

$$\Delta F_{m,n} \equiv 0 \quad \forall m, n \in V_2.$$

The subgraph corresponding to the mutual interactions is referred to as a *network isolator*.

Note that network isolators of arbitrary size may be understood using the same reasoning as presented above for a network isolator consisting of only four links.

1. Sign reversal of flow changes

Based on the symmetric elements—the network isolators—introduced in Sec. IV C, we can demonstrate yet another application of the ST formulation to link failures: We can modify the grid in such a way that the LODFs and thus the flow changes change their sign. This is again based on the symmetry of LODFs in terms of the paths $(r, \ldots, m, n, \ldots, s)$ and $(r, \ldots, n, m, \ldots, s)$. If we apply a symmetric modification such that paths of the first form are replaced by parts of the latter one, we can reverse the sign of the resulting flow changes in the other part. In particular, if we interchange the two terms appearing in the nominator of Eq. (13) for a subset of edges, we can change the sign of the LODF for these edges

$$\mathcal{N}^*(r, m \to n, s) \to \mathcal{N}^*(r, n \to m, s)$$
$$\mathcal{N}^*(r, n \to m, s) \to \mathcal{N}^*(r, m \to n, s)$$
$$\Rightarrow \mathrm{LODF}_{\ell,k} \to -\mathrm{LODF}_{\ell,k}.$$

This can be achieved using a modification similar to the one shown in Fig. 4(a): If the initial network contains the subgraph indicated by blue dashed arrows in the center, we can revert the sign of the $\mathrm{LODF}_{\ell,k}$ by changing this subgraph to the one indicated by red dashed arrows. This is demonstrated in Fig. 5: Changing the subgraph in the center connecting the two graphs from the “x”-shaped subgraph [Fig. 5(a)] to the “=”-shaped subgraph [Fig. 5(b)] leads to a sign reversal of the LODFs in the second graph (shades of gray), while the magnitude of LODFs is the same in both panels. This modification thus allows us to simultaneously change the sign of all LODFs in a subgraph, which may prevent overloads that are caused by flows going in a particular direction.

D. Comparison of strategies for mitigating failure spreading

Our theoretical analysis has led to three different strategies to mitigate failure spreading by optimizing the network topology. We will now quantify to what extent these modifications in topology improve the overall network resilience in terms of the impact of a single line failure.

To begin with, we quantify the suppression of failure spreading between two preselected parts of the network. As an indicator we use the ratio of the LODFs evaluated at a given distance d to the failing link m suggested in Ref. [19]

$$R(m, d) = \frac{\langle|\mathrm{LODF}_{k,m}|\rangle_d^{e_k \in O}}{\langle|\mathrm{LODF}_{k,m}|\rangle_d^{e_k \in S}}. \qquad (14)$$

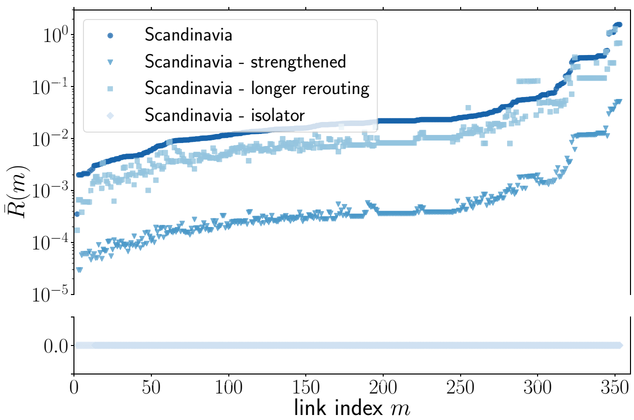

FIG. 6. Failure spreading between Finland and the rest of Scandinavia is suppressed for all three strategies. We evaluate the ratio of LODFs, $\bar{R}(m) := \langle R(m, d)\rangle_d$, averaged over distance d [Eq. (14)] between the right part of the grid, i.e., Finland, and its left part, i.e., the remainder of Scandinavia (see Fig. 1). We average the ratio over all distances d for a given trigger link m and sort the values by magnitude for the initial Scandinavian power grid (dark blue circles). We then analyze the ratio for the three strategies outlined in Sec. IV B and shown in Fig. 1. We observe that all strategies consistently yield reduced failure spreading between the two parts. Strengthening a specific link [blue triangles; cf. Fig. 1(b)] inhibits failure spreading more than increasing the length of the rerouting path [light blue squares; cf. Fig. 1(c)], while adding a network isolator [light blue diamonds; cf. Fig. 1(d)] completely suppresses failure spreading.

Here, O and S are the two preselected parts of the network that are supposed to be protected against each other in terms of failure spreading, $m \in S$ is the failing link located in part S, and d is the unweighted edge distance between trigger link m and monitoring link k. We average the absolute LODF over all links k located in the other (O, numerator) and the same (S, denominator) part located at the fixed distance d. The ratio assumes values between $R \approx 1$ if LODFs in both parts assume similar values and $R \approx 0$ if failure spreading to the other part O is suppressed completely.

In Fig. 6 we analyze to what extent the three strategies shown in Fig. 1 are able to reduce failure spreading between Finland and the remainder of Scandinavia. We analyze the LODF ratio for all possible trigger links m that are present in both the modified and the initial grid and compare the ratio for a given link by averaging the ratio over the distance d. Thereby, we are able to compare to what extent failure spreading caused by the failure of a given link is reduced in each grid modification scenario. We observe that all three strategies consistently suppress failure spreading to the other part as measured by a reduction in the LODF ratio. Whereas strengthening a single link [Fig. 1(b)] suppresses spreading more strongly than an increase in rerouting [Fig. 1(c)], adding a network isolator [Fig. 1(d)] provides the strongest reduction in failure spreading by setting the LODF ratio to zero.

While all three strategies suppress failure spreading *between* the two parts, we did not yet consider their overall impact on the entire network, i.e., including their impact on the same part where the trigger link is located. To quantify the

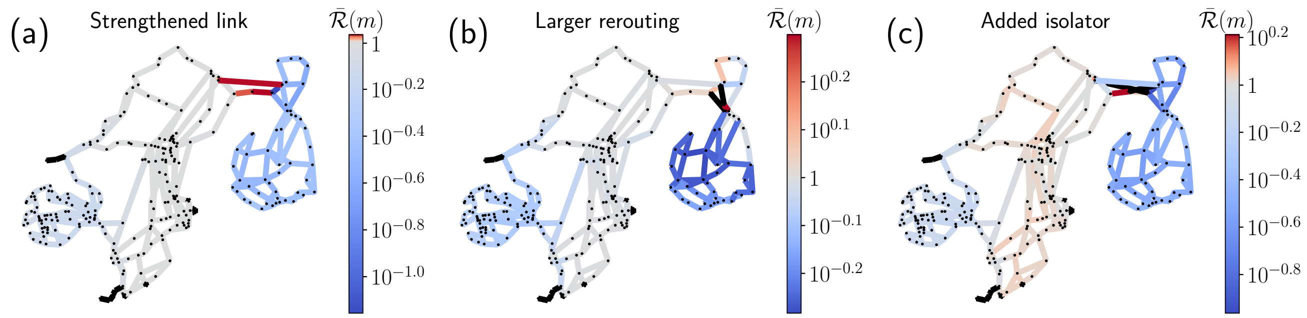

FIG. 7. Systematic analysis of the overall impact of a given strategy for mitigating failure spreading. We compare the impact of each of the strategies shown in Fig. 1 on the overall grid resilience measured by the LODF ratio $\bar{\mathcal{R}}(m) := \langle \mathcal{R}(m,d)\rangle_d$ averaged over distance d [Eq. (15)], which expresses to what extent the impact of the failure of a given link m on the network differs from its impact in the grid without the modification. We average the ratio over all distances to calculate a link-based measure of grid resilience. (a) We observe that strengthening a single link has an overall positive impact on grid resilience and reduces the LODF ratio up to tenfold (dark blue links), with only a few links showing an increase (red). (b) An increase in rerouting as shown in Fig. 1(c) improves resilience in most links as well; the effect is, however, less pronounced than in the previous case. (c) Adding a network isolator strongly improves resilience in Finland, while slightly weakening it in the rest of Scandinavia. Thus all three strategies consistently have a positive impact on link-based resilience in Finland.

overall impact, we now consider the ratio of LODFs *before and after* the grid modification

$$\mathcal{R}(m,d) = \frac{\langle|\mathrm{LODF}_{k,m}|\rangle_d^{e_k\in G'}}{\langle|\mathrm{LODF}_{k,m}|\rangle_d^{e_k\in G}}. \tag{15}$$

Here, G is the initial network, and G' is the network after the topology has been modified according to a chosen strategy. As before, m denotes the failing link, and the magnitudes of the LODFs are averaged over all links k at a given distance d to the trigger link m. Only links which are present in both G and G' are considered as trigger links. While being defined similarly to the ratio of LODFs in Eq. (14), the main difference between the two quantities is the following: The ratio considered here compares the impact of a link failure in two different networks, while the ratio in Eq. (14) compares the impact on two different parts of the same network. The ratio defined here thus quantifies whether a given modification leads to lower average LODFs in the entire grid or whether it increases the vulnerability of some links. It assumes values of unity, $\mathcal{R}(m,d) \approx 1$, if the impact of the failure on the entire grid is approximately the same in the initial and the modified grid and deviates from unity if the impact of a failure of the given link m on links at a distance d is reduced [$\mathcal{R}(m,d) < 1$] or increased [$\mathcal{R}(m,d) > 1$].

In Fig. 7, we analyze this ratio for the Scandinavian grid for each strategy and the resulting grid modification at the border between Finland and the remainder of Scandinavia shown in Fig. 1. To be precise, we evaluate the distance-averaged LODF ratio $\bar{\mathcal{R}}(m) := \langle \mathcal{R}(m,d)\rangle_d$ for all possible trigger links m. For all three strategies, we observe a reduction in failure spreading, i.e., $\bar{\mathcal{R}}(m) < 1$, if the trigger link m is located in the bulk of Finland or in western Norway. The benefits are strongest if a network isolator is added [Fig. 7(c)] and weakest if rerouting distance is increased [Fig. 7(b)]. For a trigger link m located in the central part of the grid, i.e., in Sweden, the addition of an isolator has a slightly negative effect such that $\bar{\mathcal{R}}(m) > 1$, which is, however, much weaker than the positive effects on the other parts of the grid. The two other strategies have a negligible impact if m is in this part of the grid. In all cases, the ratio indicates an increase in failure spreading for a few trigger links that are located in the vicinity of the topology modification. To conclude, we observe that the choice of a favorable strategy depends on the goal to be achieved. If trigger links in Sweden or in the vicinity of the border between Sweden and Finland have been identified as links that are likely to fail, none of the strategies will strongly increase grid resilience or will even deplete it. If, on the other hand, the goal is to protect the grid against likely link failures that emerge in Finland, all three strategies consistently provide a certain benefit to grid resilience which is also confirmed by the results in Fig. 6. In this case, adding a network isolator most likely provides the best results.

In total, the LODF ratios $R(m,d)$ and $\mathcal{R}(m,d)$ provide a complementary view on the different strategies by measuring the extent to which failures are suppressed between the two parts of a network, on the one hand, and the impact of a strategy on the network as a whole on the other one. For this reason, they can be used to balance the pros and cons of a grid modification and thus allow one to find which strategy performs best for the given grid or even allow one to study the impact of a combination of different strategies.

V. CONCLUSION

We demonstrated how a spanning tree formulation of link failures may be used to understand which topological patterns aid the mitigation of failure spreading in power grids and other types of linear flow networks. In particular, we derived and explained three strategies for reducing the effect of link failures in linear flow networks based on spanning trees. Our results offer an understanding of previous strategies used to inhibit failure spreading in power grids and may thus help to increase power grid security.

All strategies analyzed here for reducing failure spreading are based on extending—or at least not reducing—the network's ability to transport flows. This is in contrast to typical containment strategies in power grid security which are based

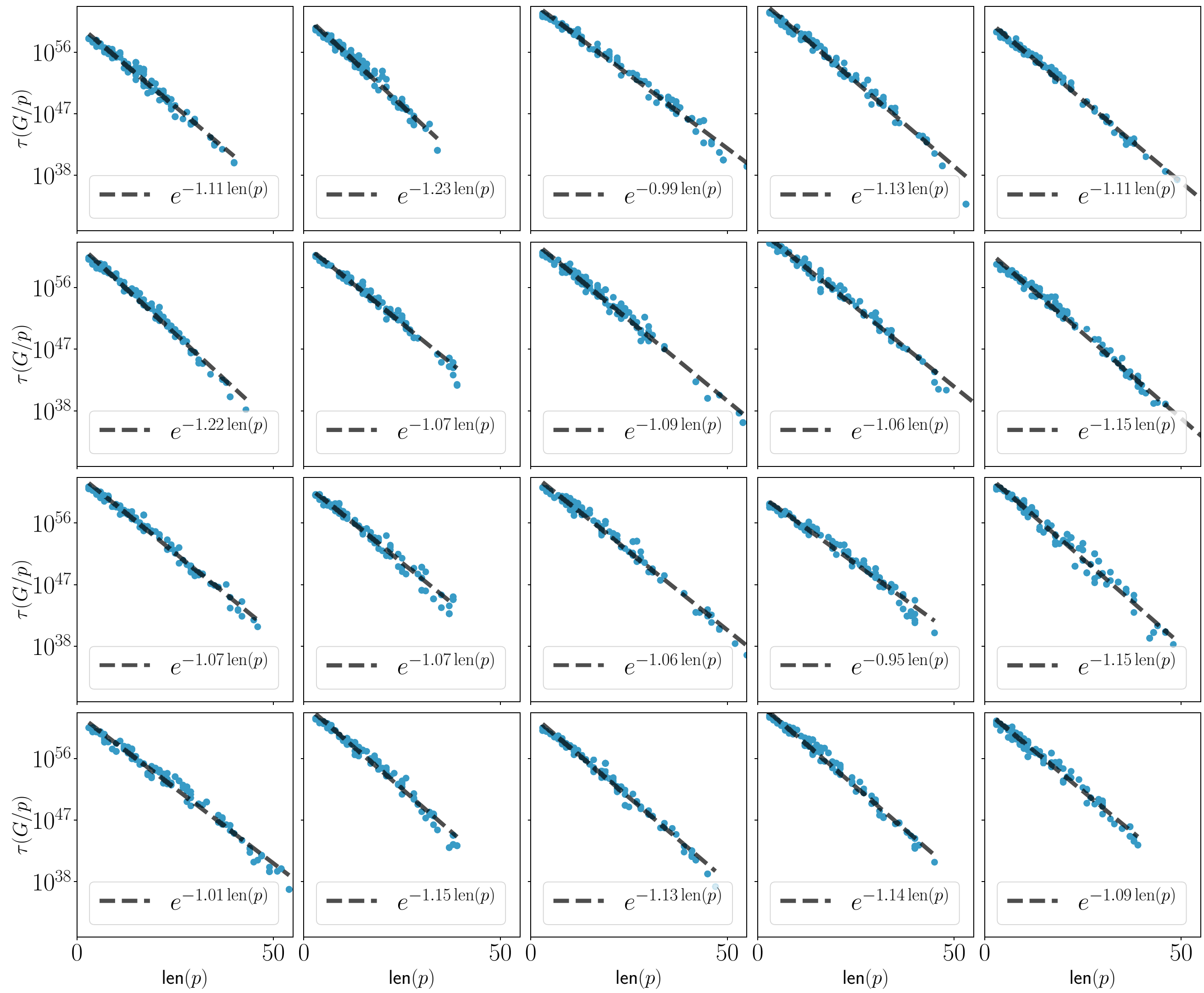

FIG. 8. Exponential decay of the number of spanning trees (STs) $\tau(G/p)$ in Erdős-Rényi (ER) random graphs, with length of randomly chosen cyclic path len(p), occurs robustly. Each panel shows the number of STs in a different, random realization of an ER graph $G(200, 300)$ with 300 edges and 200 vertices after collapsing a randomly chosen cyclic path. We analyze 200 randomly chosen cyclic paths for each ER graph (dots) and perform a least-squares fit of an exponential function on the semilog scale (dashed lines). The number of STs decays exponentially with the length of the path, thus appearing linear on a logarithmic y scale.

on islanding the power grid, i.e., reducing the connectivity for the sake of security. We illustrated how to exploit the intimate connection to graph theory to find and analyze subgraphs that allow for improving both power grid resilience and efficiency at the same time.

Our results offer a new understanding on a graph-theoretical level of network structures that have been found to inhibit or enhance failure spreading. We illustrated the fruitful approach of analyzing failure spreading in power grids by using spanning trees for several subgraphs but are confident that other subgraphs for enhancing or inhibiting failure spreading may be unveiled using this formalism.

Finally, the question arises regarding to what extent our theoretical results are relevant for the stability of real-world power grids, in particular, the stability to large-scale blackouts. In fact, a power grid blackout is typically triggered by the outage of a single transmission element, more rarely a single generation element [21]. When such a transmission line outage occurs, power flow is redistributed to parallel transmission paths, which may cause secondary overloads. Hence the scenario considered in this paper is of high practical relevance.

Our results have been derived for the linearized dc approximation; hence they will hold only approximately for scenarios where the dc approximation is no longer valid. In particular, there is no longer an exact analogy between resistor networks and ac power grids when flows are calculated nonlinearly using ac power flow models. However, the impact of line failures in high-voltage grids is typically well described by the linearized dc approximation [19,34]. Deviations occur mainly for high-loading scenarios, but even then the dc approximation usually gives a reasonable first-order estimate of the flow redistribution. It must be noted that the assumptions leading

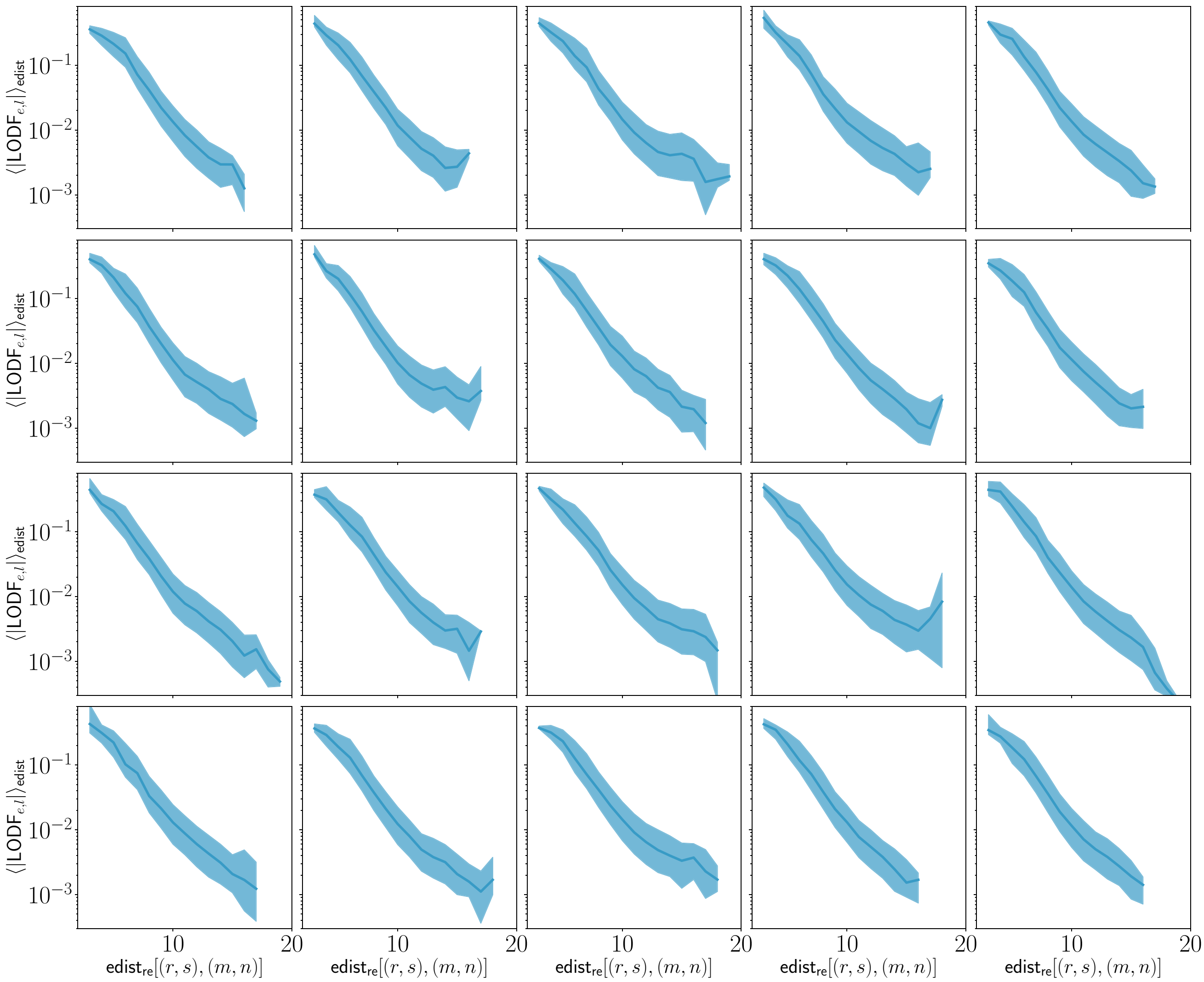

FIG. 9. Decay of averaged LODFs with rerouting distance to the trigger link is robust throughout 20 different realizations of Erdős-Rényi (ER) random graphs. Each panel shows the decay of LODFs for a different, random realization of an ER graph $G(200, 300)$ with 300 edges and 200 vertices. We observe an approximately exponential scaling of LODFs with rerouting distance when averaging over all possible links located at a fixed rerouting distance to the trigger link. Shading indicates 0.25 and 0.75 quantiles; a line represents the median.

to the dc approximation are not necessarily violated during the initial stages of a cascade. Secondary overloads occur when the current or real power flow exceeds a threshold. If the reactance x_ℓ is not too large, this will happen well before the angle difference becomes large. During the final stages of a cascade, nonlinear and dynamical effects must be taken into account.

Nevertheless, the focus of our study is on flow networks where flow distribution and redistribution after failures are governed by Kirchhoff's laws. Further studies are necessary to assess whether parts of our results may in some sense be transferred to topological models where flows are routed along shortest paths [38–40].

ACKNOWLEDGMENTS

We gratefully acknowledge support from the German Federal Ministry of Education and Research (Grant No. 03EK3055B) and the Helmholtz Association (via the joint initiative "Energy System 2050 – A Contribution of the Research Field Energy" and Grant No. VH-NG-1025).

APPENDIX

In this Appendix, we demonstrate that the scaling robustly occurs for ER random graphs by analyzing 20 random realizations (Figs. 8 and 9).

[1] N. Hwang and R. Houghtalen, *Fundamentals of Hydraulic Engineering Systems* (Prentice-Hall, Upper Saddle River, NJ, 1996).
[2] S. Díaz, J. González, and R. Mínguez, Observability analysis in water transport networks: Algebraic approach, J. Water Resour. Plann. Manage. **142**, 04015071 (2016).
[3] F. Corson, Fluctuations and Redundancy in Optimal Transport Networks, Phys. Rev. Lett. **104**, 048703 (2010).
[4] E. Katifori, G. J. Szöllősi, and M. O. Magnasco, Damage and Fluctuations Induce Loops in Optimal Transport Networks, Phys. Rev. Lett. **104**, 048704 (2010).
[5] D. Hu and D. Cai, Adaptation and Optimization of Biological Transport Networks, Phys. Rev. Lett. **111**, 138701 (2013).
[6] F. Kaiser, H. Ronellenfitsch, and D. Witthaut, Discontinuous transition to loop formation in optimal supply networks, Nat. Commun. **11**, 5796 (2020).
[7] B. Bollobás, *Modern Graph Theory*, Graduate Texts in Mathematics Vol. 184 (Springer, New York, 1998) .
[8] G. Kirchhoff, Ueber die Auflösung der Gleichungen, auf welche man bei der Untersuchung der linearen Vertheilung galvanischer Ströme geführt wird, Ann. Phys. (Berlin) **148**, 497 (1847).
[9] P. Van Mieghem, K. Devriendt, and H. Cetinay, Pseudoinverse of the Laplacian and best spreader node in a network, Phys. Rev. E **96**, 032311 (2017).
[10] D. Van Hertem, J. Verboomen, K. Purchala, R. Belmans, and W. Kling, Usefulness of DC power flow for active power flow analysis with flow controlling devices, in *The 8th IEE International Conference on AC and DC Power Transmission* (IEE, London, 2006), pp. 58–62.
[11] A. J. Wood, B. F. Wollenberg, and G. B. Sheblé, *Power Generation, Operation and Control* (John Wiley, New York, 2014).
[12] J. Strake, F. Kaiser, F. Basiri, H. Ronellenfitsch, and D. Witthaut, Non-local impact of link failures in linear flow networks, New J. Phys. **21**, 053009 (2019).
[13] F. Kaiser, J. Strake, and D. Witthaut, Collective effects of link failures in linear flow networks, New J. Phys. **22**, 013053 (2020).
[14] T. Gavrilchenko and E. Katifori, Resilience in hierarchical fluid flow networks, Phys. Rev. E **99**, 012321 (2019).
[15] H. Cetinay, F. A. Kuipers, and P. V. Mieghem, A topological investigation of power flow, IEEE Syst. J. **12**, 2524 (2018).
[16] L. Guo, C. Liang, and S. H. Low, Monotonicity properties and spectral characterization of power redistribution in cascading failures, in *2017 55th Annual Allerton Conference on Communication, Control, and Computing (Allerton)* (IEEE, Piscataway, NJ, 2017), pp. 918–925.
[17] L. Guo, C. Liang, A. Zocca, S. H. Low, and A. Wierman, Line failure localization of power networks Part II: Cut set outages in *IEEE Transactions on Power Systems* (IEEE, 2021).
[18] L. Guo, C. Liang, A. Zocca, S. H. Low, and A. Wierman, Line failure localization of power networks Part I: Non-cut outages, in *IEEE Transactions on Power Systems* (IEEE, 2021).
[19] F. Kaiser, V. Latora, and D. Witthaut, Network isolators inhibit failure spreading in complex networks, Nature Commun. **12**, 3143 (2021).
[20] J. C. Maxwell, *A Treatise on Electricity and Magnetism*, Cambridge Library Collection - Physical Sciences Vol. 2 (Cambridge University Press, Cambridge, 2010).
[21] P. Pourbeik, P. Kundur, and C. Taylor, The anatomy of a power grid blackout - Root causes and dynamics of recent major blackouts, IEEE Power Energy Mag. **4**, 22 (2006).
[22] D. Witthaut and M. Timme, Nonlocal effects and countermeasures in cascading failures, Phys. Rev. E **92**, 032809 (2015).
[23] Y. Yang, T. Nishikawa, and A. E. Motter, Small vulnerable sets determine large network cascades in power grids, Science **358**, eaan3184 (2017).
[24] V. Belevitch, Summary of the history of circuit theory, Proc. IRE **50**, 848 (1962).
[25] N. Biggs, Algebraic potential theory on graphs, Bull. London Math. Soc. **29**, 641 (1997).
[26] R. Diestel, *Graph Theory* (Springer, New York, 2010) .
[27] E. H. Moore, On the reciprocal of the general algebraic matrix, Bull. Am. Math. Soc. **26**, 394 (1920).
[28] L. W. Shapiro, An electrical lemma, Math. Mag. **60**, 36 (1987).
[29] K. Purchala, L. Meeus, D. V. Dommelen, and R. Belmans, Usefulness of DC power flow for active power flow analysis, in *IEEE Power Engineering Society General Meeting* (IEEE, Piscataway, NJ, 2005), Vol. 1, pp. 454–459.
[30] J. Hörsch, F. Hofmann, D. Schlachtberger, and T. Brown, PyPSA-Eur: An open optimisation model of the European transmission system, Energy Strategy Rev. **22**, 207 (2018).
[31] D. Manik, M. Rohden, H. Ronellenfitsch, X. Zhang, S. Hallerberg, D. Witthaut, and M. Timme, Network susceptibilities: Theory and applications, Phys. Rev. E **95**, 012319 (2017).
[32] M. Korkali, J. G. Veneman, B. F. Tivnan, J. P. Bagrow, and P. D. H. Hines, Reducing cascading failure risk by increasing infrastructure network interdependence, Sci. Rep. **7**, 44499 (2017).
[33] T. Nesti, F. Sloothaak, and B. Zwart, Emergence of Scale-Free Blackout Sizes in Power Grids, Phys. Rev. Lett. **125**, 058301 (2020).
[34] H. Cetinay, S. Soltan, F. A. Kuipers, G. Zussman, and P. V. Mieghem, Comparing the effects of failures in power grids under the AC and DC power flow models, IEEE Trans. Network Sci. Eng. **5**, 301 (2018).
[35] R. D. Zimmerman, C. E. Murillo-Sanchez, and R. J. Thomas, MATPOWER: Steady-state operations, planning and analysis tools for power systems research and education, IEEE Trans. Power Syst. **26**, 12 (2011).
[36] P. Erdős and A. Rényi, On the evolution of random graphs, Publ. Math. Inst. Hung. Acad. Sci. **5**, 17 (1960).
[37] C. Josz, S. Fliscounakis, J. Maeght, and P. Panciatici, AC power flow data in MATPOWER and QCQP format: iTesla, RTE snapshots, and PEGASE, arXiv:1603.01533 [math].
[38] O. Artime and M. D. Domenico, Abrupt transition due to non-local cascade propagation in multiplex systems, New J. Phys. **22**, 093035 (2020).
[39] A. E. Motter and Y.-C. Lai, Cascade-based attacks on complex networks, Phys. Rev. E **66**, 065102(R) (2002).
[40] P. Crucitti, V. Latora, and M. Marchiori, Model for cascading failures in complex networks, Phys. Rev. E **69**, 045104(R) (2004).

4. Designing optimal resilient supply networks

Now we turn from strategies to make a network resilient against failures to a more general perspective on network optimisation. To this end, we consider networks that are optimal in the sense that they minimise the dissipated energy. Again, this analysis relies on linear flow networks which allows us to draw an analogy to resistor networks: The dissipated energy is also known as Joule heating for resistor networks and manifests in resistive wires heating up and glowing as a result of a current flowing through the wire. A striking feature of power grids and other optimised supply networks is the presence of loops, i.e. redundant connection between pairs of nodes. But why do some networks display a large amount of loops while others do not show any? And what do loops tell us about network resilience?

In the first manuscript, we focus on the transition from non-loopy to loopy networks when varying costs for new connections or randomly damaging the network for a fluctuating supply. While previous work has shown *that* loops form in such optimised networks subject to fluctuations and damages, we analyse *how* they form. In fact, we demonstrate that loops arise via a discontinuous transition through what is, mathematically speaking, a *saddle-node* bifurcation: New minima of the network dissipation emerge separately instead of forming out of existing ones. Here, my contribution was as follows: I designed all figures, performed almost all numerical simulations – all except for the simulations on the edge-damage model – evaluated the results and wrote a major part of the text (see author contribution statement in the manuscript).

In the second publication, we focus on a different aspect of optimal networks and analyse their large scale structure. Again, we demonstrate that this large scale structure is shaped by fluctuations of supply and resilience to failures. Depending on the strength of fluctuations, optimal supply networks display either a primal community structure – a well-known type of communities where densely connected parts of a network are mutually weakly connected [74, 75] – or a novel type of community structure termed *dual communities* that are based on loops in the network. In the case of dual communities, the different parts of a network are exceptionally strongly connected. The transition to dual communities happens for dissipation-optimised networks as well as power transmission grids cost-optimised via the high-level open energy system model PyPSA-Eur [28]. In the latter case, an increase in fluctuations as a result of an increase in energy produced by variable renewable energy sources induces a transition to dual communities. In this project, I performed almost all numerical simulations – all except for generating the optimised power grids – designed all figures and wrote most of the paper. This manuscript has been submitted for publication.

4.1. F) Discontinuous transition to loop formation in optimal supply networks

[6] Kaiser, F., Ronellenfitsch, H. & Witthaut, D. Discontinuous transition to loop formation in optimal supply networks. *Nature Communications* **11,** 5796. doi:10.1038/s41467-020-19567-2 (2020).

nature COMMUNICATIONS

ARTICLE

https://doi.org/10.1038/s41467-020-19567-2 OPEN

Discontinuous transition to loop formation in optimal supply networks

Franz Kaiser [1,2]✉, Henrik Ronellenfitsch [3,4] & Dirk Witthaut [1,2]✉

The structure and design of optimal supply networks is an important topic in complex networks research. A fundamental trait of natural and man-made networks is the emergence of loops and the trade-off governing their formation: adding redundant edges to supply networks is costly, yet beneficial for resilience. Loops typically form when costs for new edges are small or inputs uncertain. Here, we shed further light on the transition to loop formation. We demonstrate that loops emerge discontinuously when decreasing the costs for new edges for both an edge-damage model and a fluctuating sink model. Mathematically, new loops are shown to form through a saddle-node bifurcation. Our analysis allows to heuristically predict the location and cost where the first loop emerges. Finally, we unveil an intimate relationship among betweenness measures and optimal tree networks. Our results can be used to understand the evolution of loop formation in real-world biological networks.

[1] Forschungszentrum Jülich, Institute for Energy and Climate Research (IEK-STE), 52428 Jülich, Germany. [2] Institute for Theoretical Physics, University of Cologne, 50937 Köln, Germany. [3] Department of Mathematics, Massachusetts Institute of Technology, Cambridge, MA 02139, USA. [4] Physics Department, Williams College, 33 Lab Campus Drive, Williamstown, MA 01267, USA. ✉email: f.kaiser@fz-juelich.de; d.witthaut@fz-juelich.de

The reliable function of supply networks is essential for biological as well as technical systems. Leaf venation networks supply plant leaves with water and nutrients[1] and vascular systems supply vertebrates with oxygen and nutrients[2]. On the other hand, society relies on man-made supply networks such as power grids[3] or hydraulic networks[4]. Finally, networks that formed over time such as drainage basins show a similar structure[5]. Understanding the design principles of such networks is a central challenge in network science[6].

The evolution or construction of supply and transportation networks is essentially determined by the trade-off between cost and resilience[7–9]. Cost limits the number of connections in the network, as resources are generally scarce. Resilience requires additional connections to cope with damages or perturbations. Many actual networks contain loops to establish a certain level of topological resilience, hence they stay connected and operational even if some elements fail[10]. The interplay of topology and resilience is analysed in various disciplines including traffic networks[8], communication networks[11] or dynamical networks[12]. Finally, a variety of results on structural resilience, that is the ability of a network to remain connected when a fraction of nodes or links fails, have been obtained in network science[13,14].

In this article, we focus on linear flow networks modelling power grids, hydraulic networks or vascular networks[3,4,15]. Different structural patterns are observed in nature, consisting of both networks with and without loops. For instance, leaf venation networks are loopy in general, except for a few old species such as *Ginkgo*. In electric power systems, large-scale transmission grids are strongly meshed, while local distribution grids are topological trees (Fig. 1). Optimal network structures balancing costs and resilience have been analysed via extensive numerical simulations in the setting where a single source supplies the remaining network, such as in plant leaves[15–17]. The optimal structure does not contain any loops if connections are reliable and perturbations are weak, for instance in distribution grids. Loops come into being when sources or sinks fluctuate strongly or connections are subject to damages, such as in transmission grids or newer leaf species. While some work has been done in the context of networks optimising transport time[18], the exact mechanism of loop formation in minimal-dissipation networks is still not fully understood.

Here, we analyse the transition to loop formation on a theoretical basis and derive several analytical results. We consider optimal network structures in the sense that function is optimised while costs are constrained or vice versa. Two aspects of resilience are studied in detail—damage to edges and fluctuations of supply and demand. In particular, we investigate the optimal structure as a function of the severity of damage and the strength of fluctuations. In contrast to prior work, we focus on the occurrence of the very first loop, which enables an analytical approach to loop formation and yields several rigorous results. We first establish this approach for an elementary sample network and then generalise it to networks of arbitrary size and compare analytic predictions and numerical results.

In particular, we demonstrate that the transition to loop formation is generally discontinuous in the sense that optimal edge-capacities jump discontinuously when fluctuations increase or costs decrease. Loopy network structures emerge as new local minima of the dissipation function that form via a saddle-node bifurcation, and not via a bifurcation of an already existing minimum. Hence, a large number of local minima may exist simultaneously and we establish a purely topological expression based on the edge betweenness to understand their structure. As a direct application of our analysis, we derive a simple criterion to predict the location of the first loop in the transition from a tree network.

Results

Modelling supply networks. We consider a simple supply network model which was previously used to study loop formation in generic distribution networks[15,16]. Mathematically, the supply network is constructed from a graph G with node set V and edge set E. At each node $n \in V$, there is an in- or outflow with a strength P_n, where $P_n > 0$ denotes a source and $P_n < 0$ a sink. The in- and outflows may either represent individual supply nodes or allocated demands associated with the node[19]. An edge in the network is either labelled by its index $e \in E$ or by its terminal

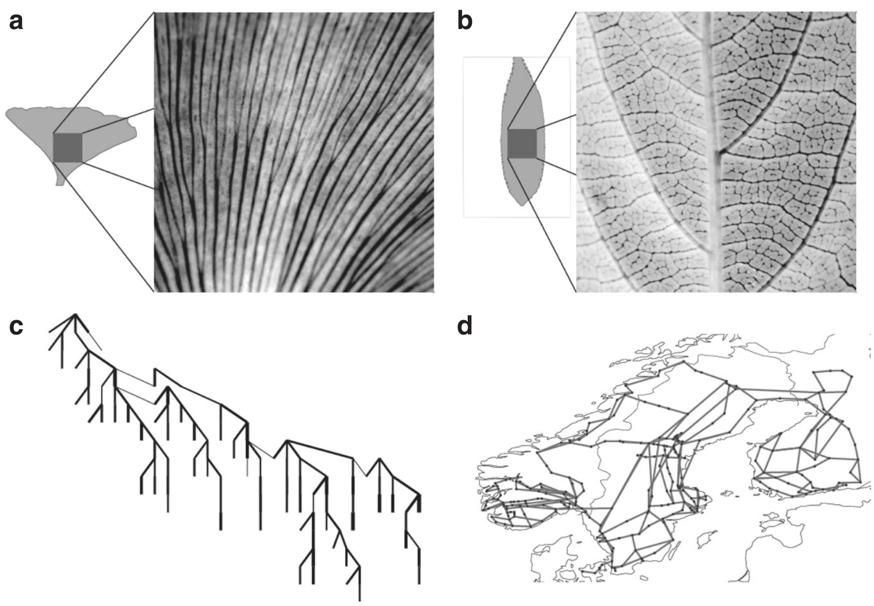

Fig. 1 Loopy and non-loopy real-world supply networks. a The leaves of *Ginkgo biloba* and **c** the distribution grid IEEE123 form loopless supply networks. **b** The venation network of *Prunus serrulata* and **d** the Scandinavian power grid on the transmission level form loopy supply networks. Leaf venation networks extracted from photographs, distribution grid taken from ref. [50] and transmission grid topology extracted from the open power system model PyPSA-Eur[49].

nodes $e = (n, m)$ which we use interchangeably. For each edge, we fix an orientation which is encoded in the node-edge incidence matrix $I \in \mathbb{R}^{|V| \times |E|}$ with elements

$$I_{n,e} = \begin{cases} 1 & \text{if edge } e \text{ starts at node } n, \\ -1 & \text{if edge } e \text{ ends at node } n, \\ 0 & \text{otherwise.} \end{cases} \quad (1)$$

Each edge is assigned a capacity $k_e \in \mathbb{R}_+$ and a flow whose strength or value is denoted as $F_e \in \mathbb{R}$. Fixing the orientation of an edge $e = (n, m)$ means that $F_e > 0$ describes a flow from node n to node m and $F_e < 0$ describes a flow from node m to node n. The flows satisfy the continuity equation or Kirchhoff's current law (KCL) at every node of the network,

$$\sum_{e \in E} I_{n,e} F_e = P_n, \quad \forall\, n \in V. \quad (2)$$

In addition to that, we assign a potential θ_n to each node in the network. In terms of physical quantities, this potential $\theta_n \in \mathbb{R}$ can represent the pressure at the nodes of a hydraulic network, the voltage in DC resistor networks or the nodal voltage phase angle in linearised AC power grids[4,15,20,21]. For these systems, the flow on a link $e = (n, m)$ scales linearly with the potential drop $\theta_n - \theta_m$ along the link and can be calculated as

$$F_e = k_e(\theta_n - \theta_m). \quad (3)$$

Together with the continuity equation (2), this linear set of equations determines the values of the potentials θ_n up to a global constant. The resulting flows automatically satisfy Kirchhoff's voltage law (KVL) which states that the flow around any closed loop expressed in terms of the edges $C = \{e_{c_1}, e_{c_2}, \ldots, e_{c_{\max}}\}$ vanishes [ref. [22], pp. 40]

$$\sum_{e \in C} z_e F_e = 0. \quad (4)$$

Here, the factor $z_e \in \{-1, 1\}$ is used to keep track of the orientation of an edge e with respect to the orientation of the edge in the loop C, i.e.

$$z_e = \begin{cases} 1 & \text{if edge } e = (e_1, e_2) \text{ is oriented from } e_1 \text{ to } e_2, \\ -1 & \text{if edge } e = (e_1, e_2) \text{ is oriented from } e_2 \text{ to } e_1. \end{cases}$$

Optimising supply networks: minimum dissipation topologies. We now illustrate how to determine the optimal supply network that is described by the above the set of equations. To this end, we want to find the edge capacities that determine the network structure that is optimal for performing a given task. Throughout this manuscript, we call the network structure optimal if the edge capacities are such that the overall network dissipation is minimised, as suggested for example in refs. [15–17]. The network dissipation may be calculated as

$$D = \sum_{e \in E} \frac{F_e^2}{k_e}. \quad (5)$$

In addition to that, we assume that the resources to build the network are limited. This resource constraint takes the form

$$\sum_{e \in E} k_e^\gamma = K^\gamma, \quad (6)$$

where the cost parameter $\gamma > 0$ depends on the type of problem under consideration. For instance, assuming Poiseuille flow through cylindrical pipes of fixed length and radius R_e, $k_e \sim R_e^4$, such that $\gamma = 1/2$ fixes total fluid volume and $\gamma = 1/4$ fixes total pipe mass[15–17,23,24]. The parameter K corresponds to the overall available budget. Note that different definitions of optimal networks arise in other applications, e.g. in hydraulic engineering where typically the cost is minimised while the dissipation is constrained[25]. In Supplementary Fig. 5 and Supplementary Note 5, we demonstrate that the same kind of discontinuous transition is observed when extending our analysis to this setup.

In general, it is neither useful nor meaningful to allow arbitrary connections between the nodes. Geometric constraints apply to a variety of networks. For instance, leaf vascular networks or river basins are naturally planar. To take into account such constraints and keep the problem feasible one typically fixes a set of potential edges $\mathcal{E}$ such that $E \subseteq \mathcal{E}$. These edges are often taken from a square grid[16], a triangular grid[15], or various types of disordered tessellations[7,26]. Note that while planarity of the network described by the set of potential edges $\mathcal{E}$ simplifies the theoretical analysis, our results are not limited to planar networks as we demonstrate for a simple, non-planar network in Supplementary Fig. 6.

We focus on two different models here: a model with fluctuating sources and sinks and a model of stochastic damage to the edges. Both models can be thought of as quantifying network resilience: We call a network resilient if it is able to function properly under the uncertainties induced by edge damage or fluctuating inputs. For both models, our main question will be the following: Under which conditions does the optimal network structure contain loops and how do these loops emerge?

Fluctuating sink model: First, we introduce the fluctuating sink model. In this model, we include fluctuations by treating the P_n as random variables. For each random realisation, the sources and sinks are balanced, i.e. they sum to zero,

$$\sum_{n \in V} P_n = 0. \quad (7)$$

Network structures are then optimised to have a minimum average dissipation

$$\langle D \rangle = \sum_{e \in E} \frac{\langle F_e^2 \rangle}{k_e}, \quad (8)$$

for a given set of resources. Here, the brackets $\langle \cdot \rangle$ denote the expected value taken over all realisations of the random variables P_n. Note that the fluctuations affect only the flows directly by virtue of Eq. (3), whereas the network topology is assumed to be fixed by the construction of the network such that the average is taken over the squared flows only. Equation (8) can be minimised analytically with respect to the k_e, where the resource constraint is taken into account via the method of Lagrange multipliers. Calculating the optimal edge capacities by extremising the Lagrange function yields[16] (Supplementary Note 1)

$$k_e = \frac{(\langle F_e^2 \rangle)^{\frac{1}{1+\gamma}}}{\left[\sum_{a \in E} (\langle F_a^2 \rangle)^{\frac{\gamma}{1+\gamma}}\right]^{1/\gamma}} K. \quad (9)$$

This expression depends on the second moments of the flows $\langle F_e^2 \rangle$, which in turn depend on the capacities k_e. Hence, Eq. (9) can be interpreted as a self-consistency condition which has to be solved together with Eq. (3).

Edge-damage model. A second class of dissipation-optimised networks that is relevant to biology and engineering seeks to find optimal networks subject to damage. For instance, leaf vasculature might be attacked by a herbivorous insect, or a power grid might lose a power line due to an outage. In the following, we generalise the broken-bond model considered in ref. [15] by allowing partial damage to the network capacities instead of complete removal of edges.

In this edge-damage model, the sources and sinks are still balanced but do not fluctuate stochastically. Instead, we assume

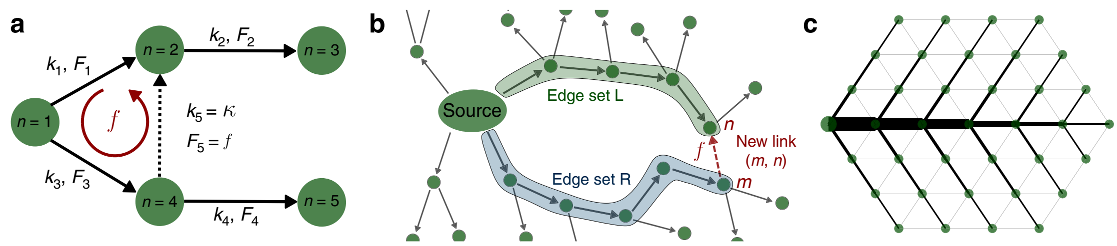

Fig. 2 Graph set up to analyse the transition from tree networks to loopy networks. a Elementary network to study spontaneous loop formation in optimum supply networks. The network consists of five nodes (green circles) where node $n = 1$ has an inflow of four, $P_1 = 4$, and all other nodes have an outflow of unity. These in and outputs determine the flows F_i, $i \in \{1, 2, 3, 4, 5\}$ along with the links with capacities k_i. The optimum topology for this set-up is a tree network. If the in- and outputs are fluctuating, an additional edge (dotted arrow) may be beneficial to reduce the average dissipation. This edge introduces a new degree of freedom expressed as a cycle flow f. **b** For a larger network, we generalise this setup as follows: we start from a tree network and then consider the impact of a new edge at an arbitrary position (n, m) (dotted, red arrow). We then collect the edge sets L (shaded green) and R (shaded blue) along the shortest path from the source to the newly formed edge. This edge induces a cycle flow f. **c** A network formed from a triangular grid with a set of potential edges $\mathcal{E}$ coloured in grey which we will analyse throughout the manuscript. Realised edges (black) correspond to a global minimum of the dissipation for the fluctuating sink model where a single, fluctuating source (large circle) supplies the remaining network.

that all nodes but one are sinks with $P_{j>1} = -\bar{P}$ supplied by a single node with $P_1 = (N-1)\bar{P}$, where N is the number of nodes.

To model partial damage of edge l, we modify the edge capacities according to

$$k_e \;\rightarrow\; (1-\Delta_e^{(l)})k_e, \tag{10}$$

with the damage fraction

$$\Delta_e^{(l)} = \begin{cases} 0 & \text{if } e \neq l, \\ \Delta \in (0,1] & \text{if } e = l. \end{cases} \tag{11}$$

Thus, a damage parameter $\Delta = 1$ corresponds to complete removal of the damaged edge. We now define the average over all possible damage scenarios. Specifically, if $g(k_e)$ is some function of the capacities k_e, we define

$$\langle g(k_e)\rangle' = \frac{1}{|E|}\sum_{l=1}^{|E|} g(\Delta_e^{(l)}k_e), \tag{12}$$

where $|E|$ is the number of edges in the network. Here and in the following, we use the notation $\langle\cdot\rangle'$ to distinguish the average over damage scenarios from the average over fluctuating sources and sinks.

As before, the central objective is to minimise the average dissipation of the network,

$$\langle D\rangle = \sum_e \left\langle \frac{F_e^2}{k_e}\right\rangle', \tag{13}$$

taken over all possible damaged edges under the resource constraint Eq. (6).

We now proceed to study loop formation in the two models outlined above in detail.

Discontinuous transition to loop formation in small network. As an illustrative example, let us consider an elementary network as sketched in Fig. 2a and analyse the transition to loop formation in both, the fluctuating sink model and the edge-damage model.

Disontinous transition in fluctuating sink model: The network consists of four variable sinks at nodes 2, 3, 4, 5 (circles) that are modelled as iid Gaussian random variables $P_{2,3,4,5} \sim \mathcal{N}(\mu, \sigma)$ and four edges (arrows) connecting them with capacities k_i and flows F_i, $i \in \{1, 2, 3, 4\}$. A fifth, potential edge is shown as a dotted arrow. If it exists, it carries flow $\tilde{F}_5$ and has capacity $k_5 = \kappa$ (Fig. 2a). The central question we will study for this setup is the following: When is the optimal network tree-like ($\kappa = 0$) and when is it loopy ($\kappa > 0$)—and how does κ behave at the transition point?

We first consider the case where the loop is not present, i.e. $\kappa = 0$. In this case, the network is a tree and we can calculate the second moments $\langle F_i^2\rangle$, $i \in \{1,2,3,4\}$ explicitly in terms of the capacities: they are determined by the statistics of the source and the sinks by virtue of the continuity equation (2). Using the optimal capacities for a tree network (6), we obtain an explicit equation for the optimal dissipation $\langle D_{\text{tree}}\rangle$ that only depends on the statistics of the sinks (Supplementary Note 4)

$$\langle D_{\text{tree}}\rangle = \frac{\left[2(\sigma^2+\mu^2)^{\frac{\gamma}{\gamma+1}} + 2(2\sigma^2+4\mu^2)^{\frac{\gamma}{\gamma+1}}\right]^{(\gamma+1)/\gamma}}{K}. \tag{14}$$

How does this result change if we allow closing the loop as illustrated in Fig. 2a, i.e. if we include the corresponding edge in the set of potential edges $\mathcal{E}$?

Let us assume that the loop carries a flow $\tilde{F}_5$ and has a non-zero capacity $k_5 = \kappa > 0$. In the following, we denote the flows and capacities in the loopy network with a tilde. In the presence of a loop, we can no longer determine the flows using the continuity equation (2) alone. Instead, we have an additional degree of freedom: a cycle flow f around the newly formed edge such that $\tilde{F}_1 = F_1 - f$, $\tilde{F}_3 = F_3 + f$ and $\tilde{F}_5 = f$. The strength of the cycle flow can be determined using the KVL (4)

$$\frac{f}{\kappa} + \frac{\tilde{F}_3}{\tilde{k}_1} - \frac{\tilde{F}_1}{\tilde{k}_1} = 0. \tag{15}$$

This approach allows us to eliminate the dependence on the cycle flow strength f, and we can evaluate the dissipation $\langle D_{\text{loopy}}\rangle$ of the loopy network by inserting the result into Eq. (8) (Supplementary Note 4). The new expression for the dissipation no longer contains the flows explicitly, which considerably simplifies finding the optimal topology: we no longer have to take care of the interdependence of flows and capacities, but can minimise $\langle D_{\text{loopy}}\rangle$ in terms of only the capacities $\tilde{k}_i$.

We proceed to evaluate the optimal network structure fixing the mean of fluctuations to $\mu = -1$ and the resource constraint to $K = 1$. To examine the effect of the two remaining parameters separately, we analyse the transition to loop formation for $\gamma = 0.9$ fixed while varying σ and for $\sigma = 3$ fixed with varying γ. We then compute the dissipation $\langle D_{\text{loopy}}\rangle$ as a function of the capacities κ and k_1 and compare it to the dissipation $\langle D_{\text{tree}}\rangle$ of the corresponding tree network. Note that the capacities in the optimum tree network are explicitly given by Eq. (9) such that $\langle D_{\text{tree}}\rangle$ is fixed. For the loopy network, we still need to determine the optimum structure, i.e. we compute the minima of $\langle D_{\text{loopy}}\rangle$ as

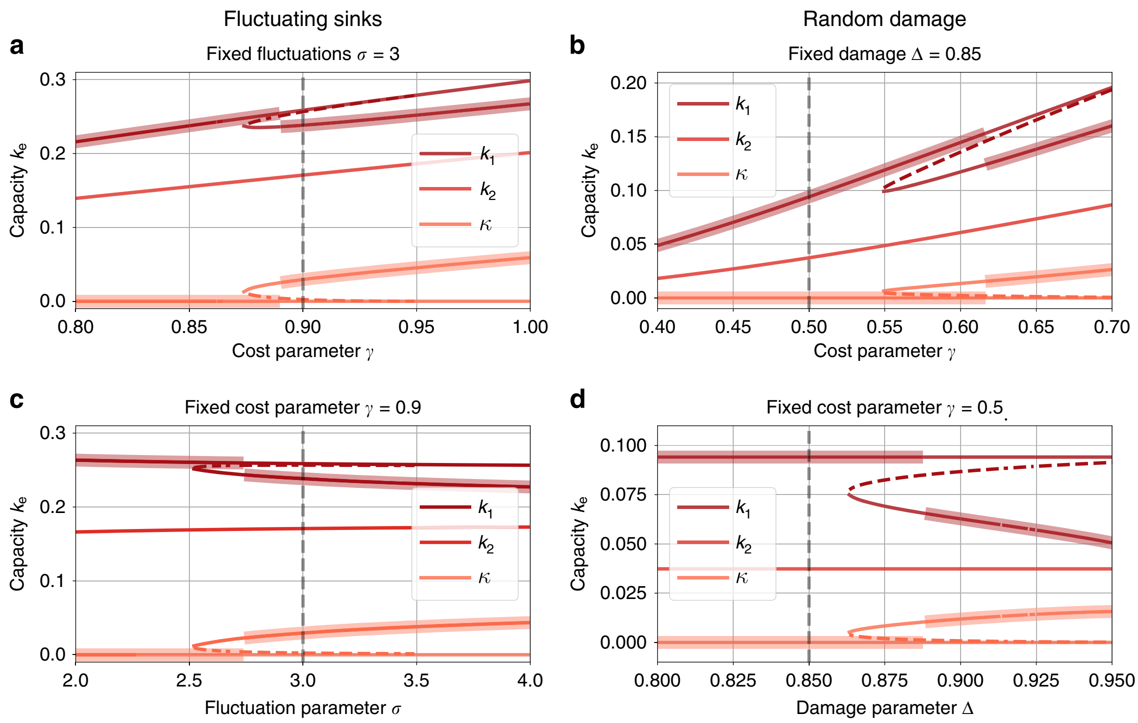

Fig. 3 Discontinuous transition in dissipation minimum appears throughout models and parameters. Capacities at the global minimum (thick lines) show a discontinuity for different models when analysing the topology shown in Fig. 2a. **a**, **c** We analyse the edge capacities k_e at the local minima (straight lines) and saddle (dotted lines) for varying cost parameter γ (**a**) and varying fluctuation parameter σ (**c**) for the fluctuating sink model with fluctuation mean $\mu = -1$ and total capacity $K = 1$. For both parameters, the capacity at the loop κ (light orange) undergoes a saddle-node bifurcation which causes a discontinuous transition in the global minima (thick lines) from non-loopy to loopy networks. **b**, **d** An analogous saddle-node bifurcation in the capacities k_e may be observed in the generalised damaged bond model in terms of both the cost parameter (**b**) and the damage parameter (**d**). For all four plots, dotted black lines denote the matching values in the other plot.

a function of κ and $\tilde{k}_1$ recalling that $\tilde{k}_3 = \tilde{k}_1$, $\tilde{k}_4 = \tilde{k}_2$ and $\tilde{k}_2$ is then fixed by the resource constraint Eq. (6).

For both varying fluctuations σ and varying costs γ, we find that the transition to loop formation is discontinuous: the loop starts to form with a non-zero capacity κ when analysing the globally optimal network structure (Fig. 3a, c, thick, orange line). Analogously, the capacity k_1 bifurcates (red line).

But what is the nature of this transition? In fact, we find that new minima emerge through a saddle-node bifurcation independently of the parameter we vary. Thus, new minima do not form from the existing tree minimum but instead emerge elsewhere in the energy landscape. To support this claim, we plot the capacity at the saddle in Fig. 3 (dotted, coloured lines) and analyse the dissipation landscape close to the bifurcation point (Supplementary Fig. 3). Using these results, we can also map out the parameter region where loop formation is beneficial (Supplementary Fig. 2). In Supplementary Fig. 7, we illustrate the nature of this transition for an even simpler network and find a closed-form solution for the region of the parameter space where loop formation is beneficial.

Discontinuous transition in edge-damage model: We now turn to the edge-damage model and analyse the optimal topology again for the graph shown in Fig. 2a. Most importantly, we find that the transition between a tree-like and a loopy optimal network is also discontinuous in the damage model in both the cost parameter γ and the damage parameter Δ, and new extrema appear again through saddle-node bifurcations (Fig. 3b, d). This demonstrates that despite the fact that in the damage model, the optima follow a different scaling law from those in the fluctuation model[15], the mechanism and type of the transition from tree-like to loopy optimum is generic.

Discontinuous transition persists beyond the first loop. Whereas the transition to the first loop that forms is important in many real-world supply networks, such as the *Gingko* leaf and the distribution grid shown in Fig. 1, other networks display several loops, such that their formation beyond the first loop becomes important. In particular, the tree has mainly theoretical importance in many applications such as hydraulic networks where spanning trees in loopy networks play an important role in modelling and optimisation[25,27–29]. Remarkably, we can demonstrate numerically that the discontinuous character of loop formation persists beyond the first loop.

In Fig. 4, we analyse this transition for the fluctuating sink model with cost parameter $\gamma = 0.5$ for a larger, globally optimal tree network which was formed from a set of potential edges $\mathcal{E}$ corresponding to a triangular grid as shown in Fig. 2c. We map out the order in which new loops form (colour code) when decreasing the cost for new edges and slightly perturbing the previous network structure. All new loops emerge discontinuously with a non-zero capacity from an existing loopy network topology (Fig. 4c). Note that in contrast to Fig. 3, the optimal capacities are obtained here using an iterative approach for finding local minima of the dissipation that is due to ref. [16] (see "Methods" section). In a Supplementary Fig. 8, we demonstrate that an analogous transition exists for varying fluctuation strength σ and fixed cost parameter γ.

Identifying optimal trees for networks of arbitrary size. We now generalise our reasoning to larger networks with an arbitrary number of nodes N. For this analysis, we focus on the fluctuating sink model. Again we assume that all nodes $j = 2, \ldots, N$ act as

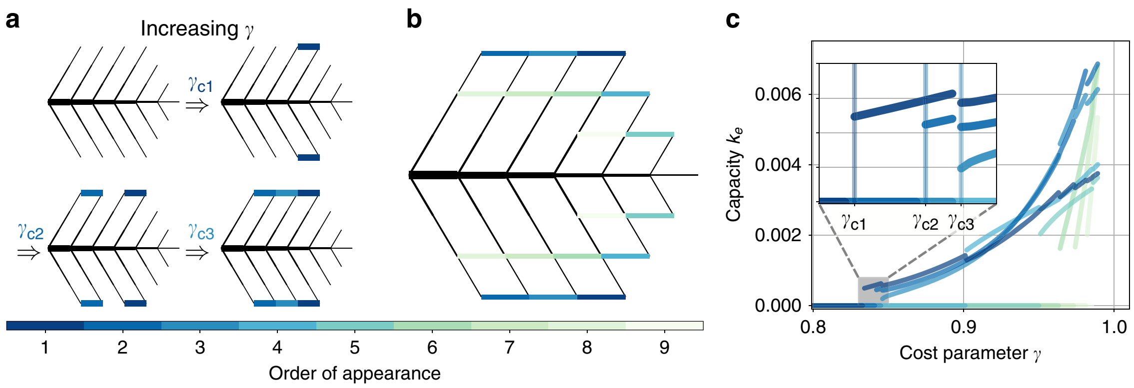

Fig. 4 Discontinuous transition to loop formation persists beyond the first loop. a, **b** We order the loops in a colour code according to their appearance with increasing cost parameter γ: the darker the edge colour, the earlier the edge appears. For the loop that appears as the i-th loop, we denote its critical cost parameter γ_{ci} where the loop starts to become beneficial for the dissipation-optimised network. **c** The transition to loop formation is discontinuous beyond the first loop: loops appearing at higher values of γ again appear with a non-zero capacity as shown in detail in the inset. Fluctuation strength is fixed to $\sigma = 0.5$ for all panels.

sinks with P_j being random variables and that the source $j = 1$ balances the sinks. We start from a tree network and analyse at what value of the cost parameter γ it becomes beneficial to add a single edge thus closing a single loop. This setup is sketched in Fig. 2b. We first demonstrate how to calculate the dissipation in such a setting and then illustrate the procedure to minimise it.

In an arbitrary tree network, the flows do not depend on the link capacities but only on the topology of the network as illustrated in the last section. This is due to the fact that for each node $j = 2, 3, \ldots$ there is only one path from the respective node to the root $j = 1$ of the tree. The flow F_e on an edge e is thus directly given by the KCL Eq. (2). Here, we fix the orientation of the flows such that they point away from the source as illustrated in Fig. 2b. Therefore, flows in tree networks are always positive.

To express the flows F_e in terms of the sources and sinks P_j, we introduce the tree matrix $\mathcal{T} \in \mathbb{R}^{|E|\times|E|}$ by

$$\mathcal{T}_{e,j} = \begin{cases} +1 & \text{if edge } e \text{ is on the path from node} \\ & j+1 \text{ to the root } j = 1 \\ 0 & \text{otherwise.} \end{cases} \tag{16}$$

This yields an explicit expression for the flows,

$$F_e = -\sum_{j=2}^{N} \mathcal{T}_{e,j-1} P_j \,. \tag{17}$$

We can insert this result into the network dissipation (Eq. (8)), which yields

$$\langle D_{\text{tree}} \rangle = \sum_{e\in T} \sum_{i,j=2}^{N} \mathcal{T}_{e,j-1} \mathcal{T}_{e,i-1} \langle P_i P_j \rangle k_e^{-1} \,, \tag{18}$$

where $T = E(G)$ is the set of all edges in the tree, i.e. before the addition of a loop.

From trees to loopy networks: optimising networks with a single loop. Remarkably, we can also find an explicit expression for the dissipation eliminating the flows in a near-tree network by exploiting the KVL to eliminate the new degrees of freedom, similar to the strategy in the previous section.

We consider a network that consists of a tree plus a single link $\ell = (m, n)$ with capacity κ as sketched in Fig. 2b. The edges on the paths from nodes n and m to the root node are summarised in the edge sets L and R, respectively, which we define as follows: Denote by $p(m)$ and $p(n)$ the set of all edges along the shortest path from the source node to the node m and n, respectively, oriented in the direction pointing away from the source. Note that these paths are unique in a tree network. Then define the following sets:

$$\begin{aligned} L &= p(n) \backslash (p(m) \cap p(n)), \\ R &= p(m) \backslash (p(m) \cap p(n)), \end{aligned} \tag{19}$$

such that the union of the edge set $L \cup R \cup \{(m, n)\}$ forms a cycle. As we will see in the following, this definition turns out to be useful when studying the dissipation in the presence of a single loop.

Due to the presence of the loop, we have a new degree of freedom, the cycle flow strength f. According to the KCL Eq. (2), the flows in the loopy network are given by

$$\tilde{F}_e = \begin{cases} f & \text{if } e = (m,n) \\ F_e + f & \text{if } e \in R(m) \\ F_e - f & \text{if } e \in L(n) \\ F_e & \text{otherwise.} \end{cases} \tag{20}$$

The value of f is fixed via the KVL:

$$\begin{aligned} &\sum_{e\in L} \frac{-F_e + f}{k_e} + \sum_{e\in R} \frac{F_e + f}{k_e} + \frac{f}{\kappa} = 0 \\ \Rightarrow \quad & f = \left(\kappa^{-1} + \sum_{e\in L\cup R} \tilde{k}_e^{-1}\right)^{-1} \left(\sum_{e\in L} \frac{F_e}{\tilde{k}_e} - \sum_{e\in R} \frac{F_e}{\tilde{k}_e}\right). \end{aligned} \tag{21}$$

We can now evaluate the dissipation Eq. (8) in the presence of the new edge (m, n) by plugging in the relations (20) and (21),

$$D_{\text{loopy}} = \sum_{e\in T} \frac{F_e^2}{\tilde{k}_e} - \frac{\kappa}{1 + \sum_{e\in L\cup R} \frac{\kappa}{\tilde{k}_e}} \left(\sum_{e\in L} \frac{F_e}{\tilde{k}_e} - \sum_{e\in R} \frac{F_e}{\tilde{k}_e}\right)^2 . \tag{22}$$

The average dissipation thus reads

$$\langle D_{\text{loopy}} \rangle = \sum_{e\in T} \frac{\langle F_e^2 \rangle}{\tilde{k}_e} - \frac{\kappa}{1 + C_{m,n}\kappa} B_{m,n}, \tag{23}$$

where we introduced the abbreviations

$$\begin{aligned} B_{m,n} &= \left\langle \left(\sum_{e\in L} \frac{F_e}{\tilde{k}_e} - \sum_{e\in R} \frac{F_e}{\tilde{k}_e}\right)^2 \right\rangle \\ C_{m,n} &= \sum_{e\in L\cup R} \tilde{k}_e^{-1}, \end{aligned} \tag{24}$$

which are functions only of the updated capacities $\tilde{k}_e$ along the sets of edges L and R. Importantly, the resulting expression no

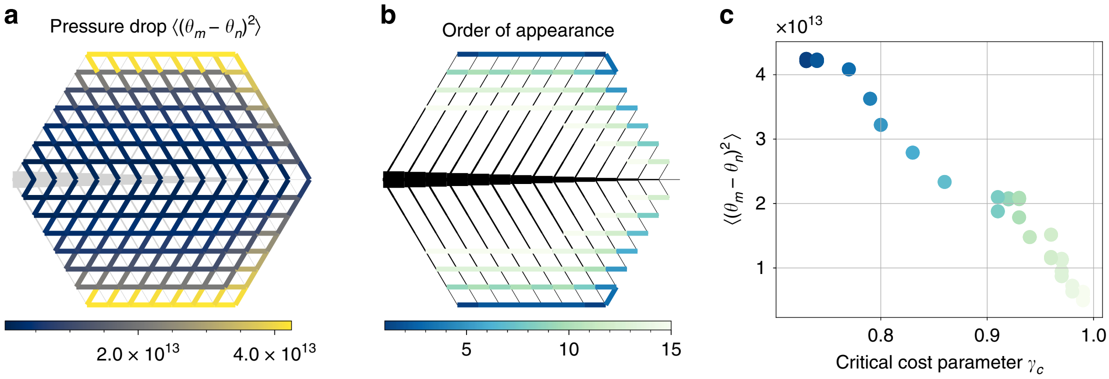

Fig. 5 Average pressure drop predicts the order of appearance of new loops as the cost parameter is varied. a The average squared pressure drop $\langle(\theta_m - \theta_n)^2\rangle$ (colour code, cf. Eq. (28)) calculated for the global tree optimum of dissipation allows predicting the location of the edges where loop formation first becomes beneficial. **b** Starting from a globally optimal tree network with cost parameter $\gamma = 0.4$, we slowly increase the cost parameter. We then determine in which order and at which critical value of the critical cost parameter γ_c new edges appear closing a loop. **c** The pressure drop is strongly correlated with the critical cost parameter γ_c where the given loop starts to form. Colour code corresponds to order of appearance of edges from dark (first) to light (last).

longer contains the updated flows $\tilde{F}_e$, but only the flows in the tree network F_e, which are determined by Eq. (17). This allows us to minimise the dissipation with respect to the updated capacities $\tilde{k}_e$ without having to take into account the interdependence of flows and capacities.

Now that we have derived an explicit equation for the dissipation in near-tree networks, we will demonstrate how to minimise the resulting expression. For tree networks, the minima of the dissipation may be calculated explicitly using the method of Lagrange multipliers (see Supplementary Note 2). In contrast to that, we have to take into account an inequality constraint $\kappa \geq 0$ for near-tree networks as local minima may exist also at the boundaries of the domain. This can be done using the Karush–Kuhn–Tucker (KKT) conditions with the new Lagrange type function

$$\begin{aligned}\tilde{\mathcal{L}}(\tilde{k}_e, \kappa) = &\sum_{e\in T} \frac{\langle F_e^2\rangle}{\tilde{k}_e} - \frac{\kappa}{1 + C_{m,n}\kappa} B_{m,n} \\ &- \tilde{\lambda}\left(K^\gamma - \sum_{e\in T} \tilde{k}^\gamma - \kappa^\gamma\right) - \mu\kappa,\end{aligned} \tag{25}$$

where $\tilde{\lambda}, \mu \in \mathbb{R}$ are KKT multipliers. The minimum is then determined by the KKT conditions (see "Methods" section).

This approach results in explicit equations for the optimal edge capacities $\tilde{k}_e$, κ in near-tree networks for which we could, however, not find a closed-form solution for arbitrary networks and values of γ (Supplementary Note 2). Still, we can make use of the resulting equations to gain insight into the process of loop formation. In particular, the KKT condition for the newly added edge (m, n) with capacity κ reads

$$B_{m,n} = (1 + C_{m,n}\kappa)^2 \kappa^{\gamma-1} \gamma \tilde{\lambda} \quad \vee \quad \kappa = 0, \tag{26}$$

i.e. the capacity of the new edge either vanishes ($\kappa = 0$) or has the non-zero value given above. Importantly, we can obtain insights into the process of loop formation even without explicitly solving these equations.

How do loops emerge? We now illustrate how to make use of Eq. (26) to understand the process of loop formation. In particular, we rigorously demonstrate that loops form discontinuously as illustrated for the small tree network. Furthermore, we show that the tree remains a local minimum of the average dissipation even after the formation of a loop. We summarise these results in the following.

Theorem 1 *(Tree remains KKT point) Consider a linear flow network subject to the resource constraint with $\gamma \in (0, 1)$. Then the following statements hold for the KKT points of the average dissipation $\langle D_{loopy}\rangle$:*

1. *There is always a KKT point at $\kappa = 0$, i.e. the tree is always a (potential) local minimum.*
2. *The KKT point at $\kappa = 0$ is isolated in the sense that we can find a real number $\varepsilon > 0$ such that there are no other KKT points for $\kappa \in (0, \varepsilon)$.*

The proof makes use of the fact that we can find lower and upper bounds for the functions $B_{m,n}$, $\tilde{\lambda}$ and $C_{m,n}$ even without explicitly solving Eq. (26) and can be found in Supplementary Note 3. We note that the fact that the tree remains a local minimum is well-known for deterministic sources[17,24].

We thus showed rigorously that for $\gamma < 1$, KKT points that characterise a loopy network cannot emerge through a bifurcation of the local optimum describing a tree network since the KKT point at $\kappa = 0$ is isolated. Instead, new local minima of the dissipation generally emerge elsewhere and the transition to loopy networks is discontinuous. Having understood the mechanism of loop formation, we now proceed to analyse which edges will form the first loops.

Where do loops emerge first? We now study the location of the first loop that appears in the globally optimal network as the parameters of the model are varied. We start from the regime where the global optimum is a topological tree. Consider the expression for the average loopy dissipation $\langle D_{\text{loopy}}\rangle$ to which a single edge (m, n) of capacity κ was added, as calculated in Eq. (23). We can find the location where loops form first by making the following approximation: assume that after the addition of the loop, the capacities of the edges e along the shortest path from the source to the loop, $e \in R \cup L$, change only by a constant factor $c(\gamma, e)$, i.e. $\tilde{k}_e = c(\gamma, e)\, k_e$, whereas the other edges remain unchanged such that $c(\gamma, e) = 1$ for these edges. Looking at Fig. 3a, we can see that this is a reasonable assumption for the small network considered there. Note that the prefactor can be expected to be close to unity $c(\gamma, e) \approx 1$ even for edges $e \in L \cup R$ if we assume that the network is very large because then the new edge will emerge with a very small capacity due to the resource

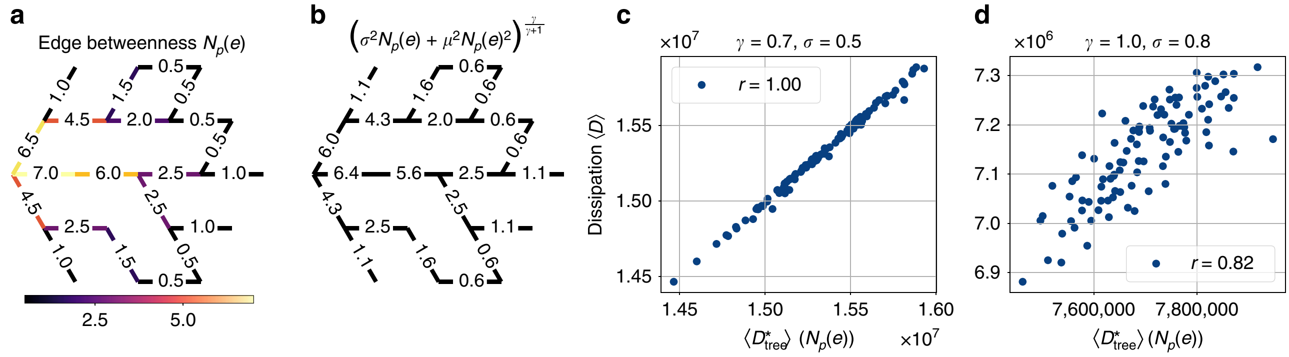

Fig. 6 Edge betweenness centrality determines the network dissipation at local minima in the fluctuating sink model. a Edge betweenness centrality $N_p(e)$ (numbers and colour code), determined with respect to a single source on the left, is closely related to the network dissipation. **b** The contribution $(N_p(e)\cdot\sigma^2 + N_p(e)^2\cdot\mu^2)^{\frac{\gamma}{\gamma+1}}$ of a single edge to the minimal network dissipation in a tree network $\langle D^*_{\mathrm{tree}}\rangle$ as given in Eq. (31) may be used to estimate the actual network dissipation at minima. Parameters used here are given by $\sigma = 0.5$, $\mu = 1$ and $\gamma = 0.9$. **c** The tree estimate $\langle D^*_{\mathrm{tree}}\rangle$ correlates strongly with the actual network dissipation at local minima $\langle D\rangle$ with high-cost $\gamma = 0.7$ and low fluctuations $\sigma = 0.5$ since on average only $\langle N_L\rangle = 1.44$ loops form for this set of parameters (Pearson correlation coefficient of $r = 1.0$). **d** Moving to networks containing many loops, $\langle N_L\rangle = 36.66$ on average, obtained by minimising the dissipation for lower cost $\gamma = 0.8$ and more fluctuations $\sigma = 1.0$, the tree estimate still strongly correlates with the dissipation at minima as measured by a Pearson correlation coefficient of $r = 0.82$. Results were obtained by applying the relaxation method 100 times for each set of parameters where the set of potential edges $\mathcal{E}$ forms a triangular network with $N = 169$ nodes as shown in Fig. 2c.

constraint $\sum_e \tilde{k}_e^\gamma + \kappa^\gamma = K^\gamma$. With this approximation, the loopy dissipation reads

$$\langle D_{\mathrm{loopy}}\rangle \approx \sum_{e\in T}\frac{\langle F_e^2\rangle}{c(\gamma,e)k_e} - \frac{\kappa}{c(\gamma,e)^2\left(1+\frac{C_{m,n}(k_e)\kappa}{c(\gamma,e)}\right)}B_{m,n}(k_e). \quad (27)$$

Here, we defined the quantities $B_{m,n}(k_e)$ and $C_{m,n}(k_e)$ which we obtain from $B_{m,n}$ and $C_{m,n}$ (Eq. (24)) by replacing the updated capacity $\tilde{k}_e$ by the tree capacity k_e. The last expression can then be simplified considerably by making use of Eq. (3),

$$\begin{aligned} B_{m,n}(k_e) &= \left\langle\left(\sum_{e\in L}\frac{F_e}{k_e} - \sum_{e\in R}\frac{F_e}{k_e}\right)^2\right\rangle \\ &= \left\langle(\theta_n-\theta_m)^2\right\rangle. \end{aligned} \quad (28)$$

Thus, the emergence of loops is essentially governed by the potential drop across neighbouring vessels. Similar to how cracks in brittle materials form to relieve high elastic stresses, loop formation is determined by the relief of large pressure drops. Our explicit prediction is consistent with the idea that the reduction of pressure drops may have driven the evolution of leaf venation[30]. From a developmental perspective, it connects to work explaining plant vein formation using models where mechanical stress relief is a crucial ingredient[31–33]. We confirm the 'stress relief' by loop formation in terms of the potential drop by analysing the pressure drop before and after the formation of the loop in Supplementary Fig. 1.

We now study the predictions made using Eq. (28) numerically (see "Methods" section for details). Starting from an optimal tree network, we first calculate the pressure drop (Fig. 5a). We then successively decrease the cost for new edges and monitor the order in which new loops form (Fig. 5b). Again, the transition to loop formation is discontinuous, such that loops emerge with a non-zero capacity at a critical value of the cost parameter γ_c, which is highly correlated to the pressure drop (Fig. 5c). We may thus predict the location and cost parameter where loops form based on the potential drop.

Edge betweenness determines network dissipation. As we have demonstrated, all trees are—and remain—locally optimal structures and loopy networks emerge via saddle-node bifurcations. Thus, there may be a multitude of different local minima for a given set of network parameters, so a natural question that arises is the following: How can we determine which of the local minima have less dissipation than others and how can we find an order of different topologies, e.g. to find the topology that globally minimises the dissipation? Remarkably, we can trace back the answer to a purely topological property: the edge betweenness centrality.

We start by simplifying the locally optimal dissipation of the tree networks. In Eq. (17), we expressed the flows F_e in a tree network using the tree matrix $\mathcal{T}$. If we plug this expression into the self-consistency equation for the capacities Eq. (9), set the overall available capacity to $K = 1$, and plug everything into the dissipation Eq. (8) we arrive at the locally optimal dissipation in tree networks

$$\langle D^*_{\mathrm{tree}}\rangle = \left[\sum_{e=1}^{N-1}\left(\sum_{i,j=2}^{N}\mathcal{T}_{e,j-1}\mathcal{T}_{e,i-1}\langle P_iP_j\rangle\right)^{\frac{\gamma}{\gamma+1}}\right]^{\frac{\gamma+1}{\gamma}}. \quad (29)$$

Importantly, the entries appearing in this expression only depend on the mixed moments of the sinks and their second moments. Since the sinks are i.i.d. Gaussian random variables, these moments are identical for different sinks and are given by

$$\begin{aligned} \langle P_i^2\rangle &= \mu^2+\sigma^2, \quad i>1 \\ \langle P_iP_j\rangle &= \mu^2, \quad i,j>1. \end{aligned} \quad (30)$$

Thus, the sum runs over identical entries and we can calculate the dissipation as

$$\langle D^*_{\mathrm{tree}}\rangle = \left[\sum_{e=1}^{N-1}\left(N_p(e)\cdot\sigma^2 + N_p(e)^2\cdot\mu^2\right)^{\frac{\gamma}{\gamma+1}}\right]^{\frac{\gamma+1}{\gamma}}. \quad (31)$$

Here, $N_p(e)$ is the sum over the column of the tree matrix $\mathcal{T}$ that corresponds to edge e. In fact, $N_p(e)$ has the following interpretation: it is the number of paths from the source s to any other node v that go through the edge e and may thus be identified as a measure of shortest-path edge betweenness[34,35] (see "Methods" section). What can we learn from this analysis for loopy networks?

To estimate the contribution of a single edge to the overall network dissipation in a loopy network, we first calculate its edge betweenness (Fig. 6a) and, based on this, the contribution it would have to the dissipation in a tree network (Fig. 6b). Adding up the resulting expressions, we arrive at the tree estimate of the dissipation in a loopy network $\langle D^*_{\mathrm{tree}}\rangle(N_p(e))$. For near-tree networks, the correlation between the estimate and the actual dissipation at local minima is almost perfect as predicted by Eq. (31) (Fig. 6c). Increasing the number of loops by tuning the noise parameter σ and the cost parameter γ, edge betweenness and dissipation remain correlated even when there is a significant number of loops present in the network (Fig. 6d). Thus, we can still understand the minimal dissipation in loopy networks based on this topological measure.

We further discuss the possibility of characterising the global tree minima of the network dissipation in Supplementary Note 6.

Discussion

In summary, we demonstrated that the transition to loop formation in optimal supply networks is discontinuous throughout different models and parameters. We explored this discontinuity in detail for a small example network and rigorously proved that the discontinuous nature of the transition persists for larger networks as well. We showed that loops emerge through a saddle-node bifurcation, explaining the discontinuous transition.

Our results shed light on recent advances in the study of optimal supply networks. While the emergence of loops through fluctuations or damage was discovered recently[15,16], the theoretical nature of this transition was until now not well understood. Here, we closed this gap by analysing the nature of the transition to loop formation in more detail. In particular, we obtained a measure of network stress that allowed us to predict the location and parameters where loops start to form. This opens a new pathway to the understanding of loop formation in natural networks such as leaves[10].

Our results offer a new understanding of the interplay between the structure and function of supply networks. By unveiling the relationship between the network's topological edge betweenness and its average dissipation, we established a new link between the form and function of networks. These results may aid in the understanding and design of globally optimal network structures such as biological vasculature, electrical grids, or neural networks. Our explicit prediction is consistent with the idea that the reduction of pressure drop variations may have been a factor in the evolution of leaf venation[30]. More generally, we show that globally optimal network structures may be obtained by following simple local rules for adding new links, in contrast to previous work based on pruning an existing network[26,36].

Let us finally discuss how our results derived for linear flow models relate to other types of networks and systems. The starting point of our analysis was the fundamental trade-off between cost and resilience, which determines the optimal structure of a network, and which extends far beyond the theory of supply networks. Resilience requires additional capacity or links which can take over the load in the presence of failures or fluctuations—but these are generally costly. From a practical view of network design, the fundamental question is thus: Where and how should new connections be added that increase resilience in an optimal way?

Firstly, we discuss the question where new links should be added. A large body of literature in network science approaches aspects of resilience from the viewpoint of percolation theory. The fundamental question in this purely structural treatment is: Given a network, how many nodes or links may fail before the network gets disconnected? It has been shown that a decisive quantity to assess the resilience to random failures is given by the ratio of the second and first moment of the degree distribution, $\langle k^2\rangle/\langle k^1\rangle$[37,38]. These fundamental results were then used to optimise network resilience with respect to both random failures and targeted attacks[13,14]. In the case of failures, it is beneficial to add links between nodes which already have a high degree to effectively increase $\langle k^2\rangle$. This result might appear very different from the findings of the present paper at first glance, but there are in fact common underlying principles. In supply network models, new links should be added where they will potentially attract a high flow. In percolation type models, new links should be added where they will potentially attract a high betweenness—a quantity which can also be interpreted as a flow[34,39]. As a result, one should pick nodes whose characteristic quantity, either potential θ_n or degree k, differs from their surrounding.

Secondly, we consider the question of how new links should be added. The main finding of our work is that new links emerge in a discontinuous way with a finite non-zero capacity. That is, to be beneficial for the network, new links must have a certain minimum connection strength. This result has no direct equivalence in percolation approaches to network resilience since the vast majority of studies in this field considers unweighted networks only. However, there is a strong interest in network formation processes, which induce discontinuities in macroscopic connectivity of the network—including competitive percolation models[40,41], as well as transportation network models[42]. In the context of network resilience, it has been shown that interdependencies and cascade effects can make the percolation transition discontinuous[43].

Methods

Numerical simulation of loop formation. When analysing the transition to loop formation such as in Figs. 4 and 5, we start from an optimal tree network T for given parameters μ, σ and γ corresponding to the dissipation minimum shown in Fig. 2c. As a next step, we add all non-tree edges from the underlying triangular grid with a very small capacity that corresponds to 1% of the minimum capacity in the optimal tree, $k_f = 0.01 \cdot \min_{e\in T}(k^*_e)$, and then renormalise all capacities to make sure the resource constraint (6) holds. Finally, we then apply the iterative method described in ref. [16] to let the new topology relax to a local minimum. If this minimum contains loops despite having started very close to the (global) tree minimum, and if its dissipation is lower than the one of the tree, we conclude that the given loopy topology is favourable.

To analyse the predictive power of the pressure drop in Fig. 5, we initially consider a large optimised tree network with $N = 169$ nodes and cost parameter $\gamma = 0.4$ for which we calculate the pressure drop (Fig. 5a) and then increase the cost parameter from $\gamma = 0.7$ to $\gamma = 0.99$, reoptimising the network for each value of gamma. Using the procedure outlined above, we compare the predicted positions of the first loops as indicated by the initial pressure drop $\langle(\theta_m - \theta_n)^2\rangle$ with the actual order in which they appear (Fig. 5b).

Evaluating edge betweenness. In Eq. (31), we derived an alternative expression for the network dissipation at local minima that is based on the edge betweenness $N_p(e)$. The edge betweenness is defined as[34,35,38]

$$N_p(e) = \sum_{t\in V} \frac{\sigma(s,t|e)}{\sigma(s,t)}. \qquad (32)$$

Here, $\sigma(s, t)$ is the number of shortest paths from node s to node t and $\sigma(s, t|e)$ is the number of these shortest paths that contain the edge e. In the given setting, we consider this measure with respect to a single source s that is identified as the source node of the network. Furthermore, when analysing tree networks, there is only one path from the source to every node $\sigma(s, t) = 1$ and thus $\sigma(s, t|e) = 1 \vee = 0$.

In the main text, the edge betweenness is calculated using a method implemented in PYTHON's NETWORKX library[44–46].

Finding minima of a function with inequality constraints using KKT conditions. Consider the function $D(\boldsymbol{k})$ of some real vector $\boldsymbol{k} = (k_1, \ldots, k_N)^\top \in \mathbb{R}^N$ that is subject to the equality constraint $h(\boldsymbol{k}) = 0$ and the inequality constraint $g(\boldsymbol{k}) \leq 0$ which we assume to be described by differentiable, real-valued functions $g, f: \mathbb{R}^N \to \mathbb{R}$. To identify potential maxima or minima of the function subject to the constraints, we can make use of the KKT conditions. To this end, we consider the Lagrange type function

$$\tilde{\mathcal{L}}(\boldsymbol{k}) = D(\boldsymbol{k}) + \tilde{\lambda} h(\boldsymbol{k}) + \mu g(\boldsymbol{k}), \qquad (33)$$

where $\tilde{\lambda}, \mu \in \mathbb{R}$ are called KKT multipliers. Then the following conditions, the KKT conditions, are a necessary condition for a point $\boldsymbol{k}^*$ being a minimum of $D(\boldsymbol{k})$[47,48]

$$\begin{aligned} \frac{\partial \tilde{\mathcal{L}}}{\partial k_i^*} &\overset{!}{=} 0, \quad \forall i \in \{1, \ldots N\}, \\ f(\boldsymbol{k}^*) &= 0, \\ g(\boldsymbol{k}^*) &\leq 0, \\ \mu &\geq 0, \\ \mu g(\boldsymbol{k}^*) &= 0. \end{aligned} \tag{34}$$

This formulation may be used to find out whether adding a single loop to a tree network may reduce its dissipation.

Data availability

Photographs of leaf venation networks in Fig. 1 are available upon request. The topology of the Scandinavian power grid has been extracted from the open European energy system model PyPSA-Eur[49], which is fully available online at https://doi.org/10.5281/zenodo.3886532. Distribution grid in Fig. 1c was extracted from ref. [50].

Code availability

Computer code will be made available at https://github.com/FNKaiser/Optimal_Supply_Networks upon publication.

Received: 23 June 2020; Accepted: 19 October 2020;
Published online: 16 November 2020

References

1. Sack, L. & Scoffoni, C. Leaf venation: structure, function, development, evolution, ecology and applications in the past, present and future. *N. Phytol.* **198**, 983–1000 (2013).
2. Pittman, R. N. *Regulation of Tissue Oxygenation* (Morgan & Claypool Life Sciences, San Rafael (CA), 2011).
3. Wood, A. J., Wollenberg, B. F. & Sheblé, G. B. *Power Generation, Operation and Control* (John Wiley & Sons, New York, 2014).
4. Hwang, N. & Houghtalen, R. *Fundamentals of Hydraulic Engineering Systems* (Prentice Hall, Upper Saddle River, NJ, 1996).
5. Rodríguez-Iturbe, I. & Rinaldo, A. *Fractal River Basins: Chance and Self-Organization* (Cambridge University Press, 2001).
6. Havlin, S. et al. Challenges in network science: applications to infrastructures, climate, social systems and economics. *Eur. Phys. J. Spec. Top.* **214**, 273–293 (2012).
7. Ronellenfitsch, H. & Katifori, E. Phenotypes of vascular flow networks. *Phys. Rev. Lett.* **123**, 248101 (2019).
8. Ganin, A. A. et al. Resilience and efficiency in transportation networks. *Sci. Adv.* **3**, e1701079 (2017).
9. Avena-Koenigsberger, A. et al. Path ensembles and a tradeoff between communication efficiency and resilience in the human connectome. *Brain Struct. Funct.* **222**, 603–618 (2017).
10. Katifori, E. & Magnasco, M. O. Quantifying loopy network architectures. *PLoS ONE* **7**, e37994 (2012).
11. Sterbenz, J. P. et al. Resilience and survivability in communication networks: Strategies, principles, and survey of disciplines. *Comput. Netw.* **54**, 1245–1265 (2010).
12. Gao, J., Barzel, B. & Barabási, A.-L. Universal resilience patterns in complex networks. *Nature* **530**, 307–312 (2016).
13. Shargel, B., Sayama, H., Epstein, I. R. & Bar-Yam, Y. Optimization of robustness and connectivity in complex networks. *Phys. Rev. Lett.* **90**, 068701 (2003).
14. Paul, G., Tanizawa, T., Havlin, S. & Stanley, H. E. Optimization of robustness of complex networks. *Eur. Phys. J. B* **38**, 187–191 (2004).
15. Katifori, E., Szöllősi, G. J. & Magnasco, M. O. Damage and fluctuations induce loops in optimal transport networks. *Phys. Rev. Lett.* **104**, 048704 (2010).
16. Corson, F. Fluctuations and redundancy in optimal transport networks. *Phys. Rev. Lett.* **104**, 048703 (2010).
17. Bohn, S. & Magnasco, M. O. Structure, scaling, and phase transition in the optimal transport network. *Phys. Rev. Lett.* **98**, 088702 (2007).
18. Kirkegaard, J. B. & Sneppen, K. Optimal transport flows for distributed production networks. *Phys. Rev. Lett.* **124**, 208101 (2020).
19. Farina, G., Creaco, E. & Franchini, M. Using EPANET for modelling water distribution systems with users along the pipes. *Civ. Eng. Environ. Syst.* **31**, 36–50 (2014).
20. Díaz, S., González, J. & Mínguez, R. Observability analysis in water transport networks: algebraic approach. *J. Water Resour. Plan. Manag.* **142**, 04015071 (2016).
21. Strake, J., Kaiser, F., Basiri, F., Ronellenfitsch, H. & Witthaut, D. Non-local impact of link failures in linear flow networks. *N. J. Phys.* **21**, 053009 (2019).
22. Bollobás, B. *Modern Graph Theory. No. 184 Graduate Texts in Mathematics* (Springer, New York, 1998).
23. Durand, M. Structure of optimal transport networks subject to a global constraint. *Phys. Rev. Lett.* **98**, 088701 (2007).
24. Banavar, J. R., Colaiori, F., Flammini, A., Maritan, A. & Rinaldo, A. Topology of the fittest transportation network. *Phys. Rev. Lett.* **84**, 4745–4748 (2000).
25. Creaco, E. & Franchini, M. Fast network multi-objective design algorithm combined with an a posteriori procedure for reliability evaluation under various operational scenarios. *Urban Water J.* **9**, 385–399 (2012).
26. Ronellenfitsch, H. & Katifori, E. Global optimization, local adaptation, and the role of growth in distribution networks. *Phys. Rev. Lett.* **117**, 138301 (2016).
27. Elhay, S., Simpson, A. R., Deuerlein, J., Alexander, B. & Schilders, W. H. A. Reformulated co-tree flows method competitive with the global gradient algorithm for solving water distribution system equations. *J. Water Resour. Plan. Manag.* **140**, 04014040 (2014).
28. Creaco, E. & Franchini, M. Comparison of Newton-Raphson global and loop algorithms for water distribution network resolution. *J. Hydraul. Eng.* **140**, 313–321 (2014).
29. Ciaponi, C., Creaco, E., Franchioli, L. & Papiri, S. The importance of the minimum path criterion in the design of water distribution networks. *Water Supply* **17**, 1558–1567 (2017).
30. Roth-Nebelsick, A., Uhl, D., Mosbrugger, V. & Kerp, H. Evolution and function of leaf venation architecture: a review. *Ann. Bot.* **87**, 553–566 (2001).
31. Laguna, M. F., Bohn, S. & Jagla, E. A. The role of elastic stresses on leaf venation morphogenesis. *PLoS Comput. Biol.* **4**, e1000055 (2008).
32. Couder, Y., Pauchard, L., Allain, C., Adda-Bedia, M. & Douady, S. The leaf venation as formed in a tensorial field. *Eur. Phys. J. B* **28**, 135–138 (2002).
33. Bar-Sinai, Y. et al. Mechanical stress induces remodeling of vascular networks in growing leaves. *PLoS Comput. Biol.* **12**, e1004819 (2016).
34. Anthonisse, J. M. *The Rush in a Directed Graph*. Technical Report (Stichting Mathematisch Centrum, Centrum Wiskunde & Informatica, 1971).
35. Newman, M. E. J. & Girvan, M. Finding and evaluating community structure in networks. *Phys. Rev. E* **69**, 026113 (2004).
36. Hu, D. & Cai, D. Adaptation and optimization of biological transport networks. *Phys. Rev. Lett.* **111**, 138701 (2013).
37. Callaway, D. S., Newman, M. E., Strogatz, S. H. & Watts, D. J. Network robustness and fragility: Percolation on random graphs. *Phys. Rev. Lett.* **85**, 5468 (2000).
38. Newman, M. *Networks: An Introduction* (Oxford University Press, Oxford, 2018).
39. Newman, M. E. A measure of betweenness centrality based on random walks. *Soc. Netw.* **27**, 39–54 (2005).
40. Achlioptas, D., D'Souza, R. M. & Spencer, J. Explosive percolation in random networks. *Science* **323**, 1453–1455 (2009).
41. D'Souza, R. M. & Nagler, J. Anomalous critical and supercritical phenomena in explosive percolation. *Nat. Phys.* **11**, 531–538 (2015).
42. Schröder, M., Nagler, J., Timme, M. & Witthaut, D. Hysteretic percolation from locally optimal individual decisions. *Phys. Rev. Lett.* **120**, 248302 (2018).
43. Buldyrev, S. V., Parshani, R., Paul, G., Stanley, H. E. & Havlin, S. Catastrophic cascade of failures in interdependent networks. *Nature* **464**, 1025–1028 (2010).
44. Hagberg, A. A., Schult, D. A. & Swart, P. J. *Proc. 7th Python in Science Conference* (eds Varoquaux, G., Vaught, T. & Millman, J.) 11–15 (Pasadena, CA USA, 2008).
45. Brandes, U. A faster algorithm for betweenness centrality. *J. Math. Sociol.* **25**, 163–177 (2001).
46. Brandes, U. On variants of shortest-path betweenness centrality and their generic computation. *Soc. Netw.* **30**, 136–145 (2008).
47. Boyd, S. P. & Vandenberghe, L. *Convex Optimization* (Cambridge University Press, Cambridge, UK; New York, 2004).
48. Kuhn, H. W. & Tucker, A. W. *Proc. Second Berkeley Symposium on Mathematical Statistics and Probability* 481–492 (University of California Press, Berkeley, Calif., 1951).
49. Hörsch, J., Hofmann, F., Schlachtberger, D. & Brown, T. PyPSA-eur: an open optimisation model of the european transmission system. *Energy Strat. Rev.* **22**, 207–215 (2018).
50. Kersting, W. H. *2001 IEEE Power Engineering Society Winter Meeting. Conference Proceedings (Cat. No. 01CH37194)* Vol. 2, 908–912 (2001).

Acknowledgements

We thank Eleni Katifori for valuable discussions. We gratefully acknowledge support from the Federal Ministry of Education and Research (BMBF Grant No. 03EK3055B D.W.), the Helmholtz Association (via the joint initiative 'Energy System 2050 – a Contribution of the Research Field Energy' and Grant No. VH-NG-1025 to D.W.).

Author contributions
D.W. conceived research and acquired funding. F.K. and D.W. designed research. F.K. and H.R. carried out numerical simulations. F.K. evaluated the results and designed all figures. All authors contributed to discussing the results and writing the manuscript.

Funding
Open Access funding enabled and organized by Projekt DEAL.

Competing interests
The authors declare no competing interests.

Additional information
Supplementary information is available for this paper at https://doi.org/10.1038/s41467-020-19567-2.

Correspondence and requests for materials should be addressed to F.K. or D.W.

Peer review information *Nature Communications* thanks the anonymous reviewers for their contribution to the peer review of this work. Peer reviewer reports are available.

Supplemental Material

Supplementary Information for "Discontinuous transition to loop formation in optimal supply networks"

Franz Kaiser,[1,2,*] Henrik Ronellenfitsch,[3,4] and Dirk Witthaut[1,2,†]

[1] *Forschungszentrum Jülich, Institute for Energy and Climate Research (IEK-STE), 52428 Jülich, Germany*
[2] *Institute for Theoretical Physics, University of Cologne, Köln, 50937, Germany*
[3] *Department of Mathematics, Massachusetts Institute of Technology, Cambridge, MA 02139, U.S.A.*
[4] *Physics Department, Williams College, 33 Lab Campus Drive, Williamstown, MA 01267, U.S.A.*

This Supplementary Material contains six Supplementary Notes and eight Supplementary Figures.

* f.kaiser@fz-juelich.de

† d.witthaut@fz-juelich.de

SUPPLEMENTARY FIGURES

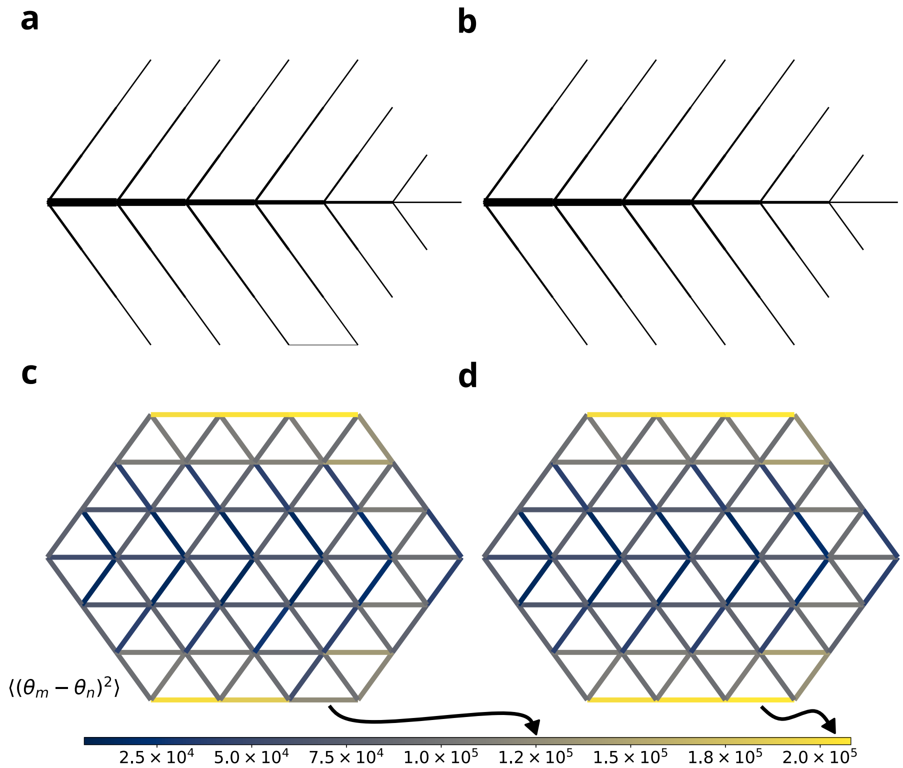

Supplementary Figure 1. **Adding a new loop significantly reduces the average squared potential drop along the corresponding vein. a,b** We allow for a loop to be added to a tree network whose capacities are optimised for the fluctuating sink model with cost parameter $\gamma = 0.84$, mean $\mu = -1$ and standard deviation $\sigma = 0.5$. **c,d** The loop formation significantly reduces the average squared potential drop along the corresponding edge (marked by arrows). The reduction is by approximately 42% of the original potential drop and thus provides significant stress relief for the network.

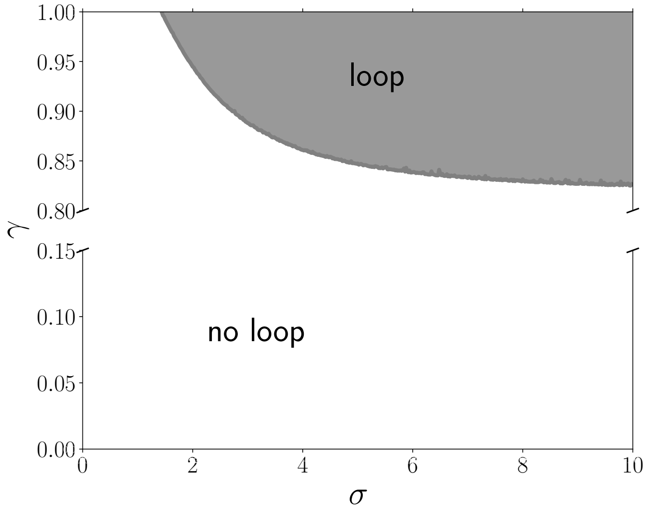

Supplementary Figure 2. **Phase diagram of the globally optimal network structure for the small five node network shown in Figure 2.** In the grey region in the upper right corner, loop formation is beneficial for the network dissipation. Interestingly, loop formation starts to be beneficial at a nonzero value of the fluctuation strength σ for any value of the cost parameter γ. Sinks have mean $\mu = -1$ in this setting.

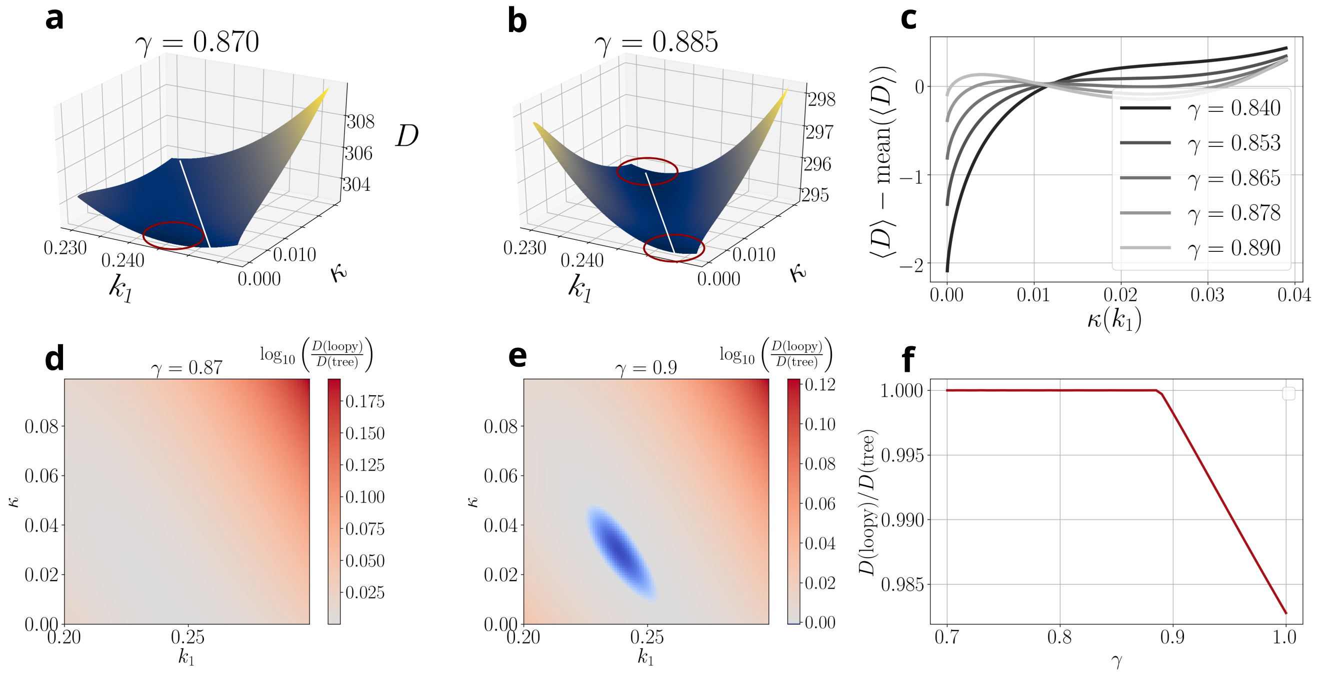

Supplementary Figure 3. **Emergence of loops for the five node network shown in Figure 2**. The landscape of dissipation for the loopy network has a single minimum for $\gamma = 0.87$ **a** as marked by a red circle. However, increasing the cost parameter to $\gamma = 0.885$, a second, local minimum emerges through a saddle node bifurcation **b**. Note that the second minimum is a local one for this set of parameters which turns into a global one for $\gamma > \gamma_c \approx 0.888$. **c** Moving along the white line indicated in panels (a) and (b) for varying values of γ, the emergence of a second, local minimum becomes visible. **d,e** We plot $\log_{10}(D_{\text{loopy}}/D_{\text{tree}})$ as a function of the edge capacities k_1 and $k_5 = \kappa$ in the loopy network. For $\gamma = 0.87$ we have $D_{\text{loopy}} > D_{\text{tree}}$ for all values of k_1 and κ. Hence the optimum network is a tree. (e) For $\gamma = 0.9$ there is a global minimum of D_{loopy} with $D_{\text{loopy}} < D_{\text{tree}}$ (blue). Hence, the optimum network is loopy. **f** The ratio of dissipations $D_{\text{loopy}}/D_{\text{tree}}$ for the optimum loopy and optimum tree networks as a function of the scaling exponent γ. This plot was produced for parameters $\sigma = 3$, $\mu = -1$ and $K = 1$.

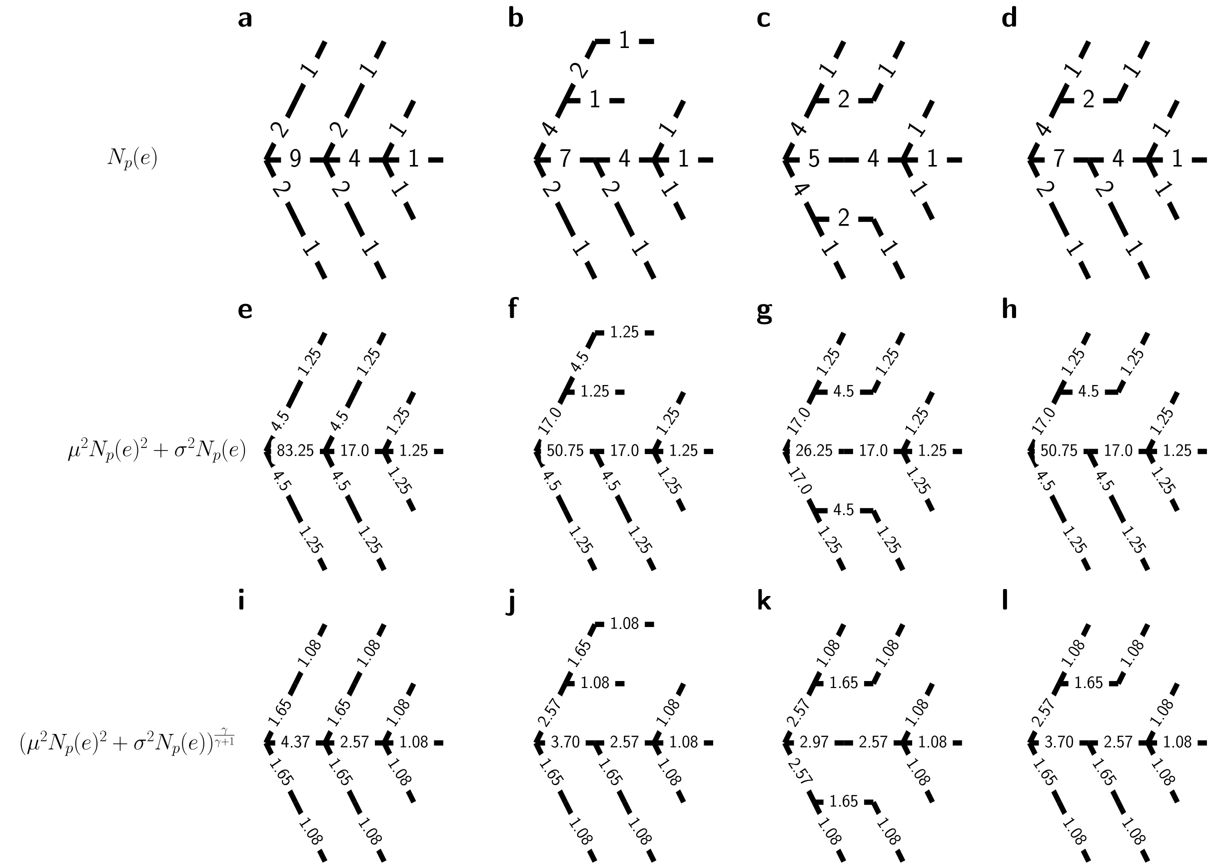

Supplementary Figure 4. **Edge betweenness may be used to identify the global minima of dissipation. a-d** Numbers on edges give the value of edge betweenness for different exemplary spanning trees on small triangular networks. **e-h** Measure of edge betweenness $N_p(e)\sigma^2 + N_p(e)^2\mu^2$ for mean of fluctuations $\mu = 1$ and standard deviation $\sigma = 0.5$. **i-l** Taking the measure of edge betweenness to the power of $\gamma/(\gamma+1)$ where here $\gamma = 0.5$ to calculate the contribution of an edge to the tree network dissipation, we can identify the globally minimising topology: we can conclude that the network shown in panels a and e is the globally optimal network, since it minimises the sum over all edges. This is due to the fact that the quasi-norm has a concave structure such that the minima are located at the boundaries of the domain: the network in panels (a,e,i) maximises the spread between the individual values of edge betweenness, accumulating as much flow as possible on as few edges as possible and thus minimises the dissipation.

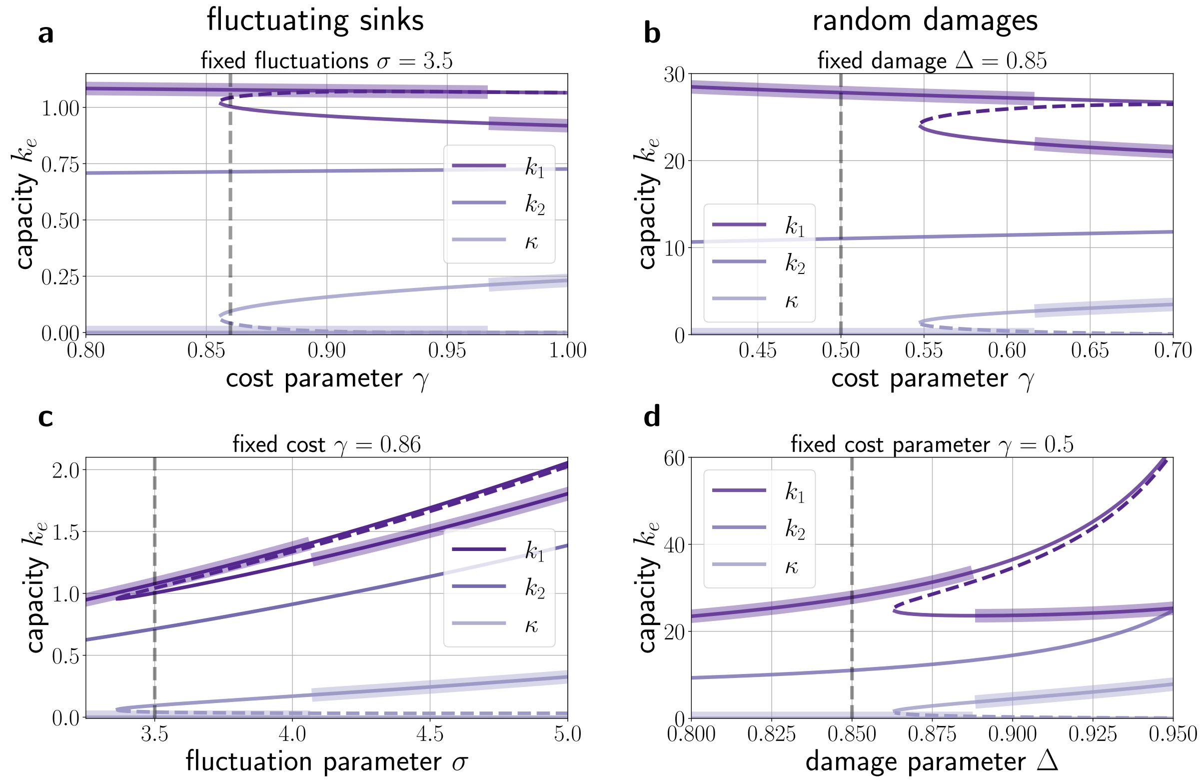

Supplementary Figure 5. **Discontinuous transition for minimum cost topologies** Capacities at the global minimum (thick lines) show a discontinuous transition to loop formation for different models for the five node network shown in Figure 2: Here, we minimise the cost while keeping the average network dissipation fixed at a given value D. **a,c** We analyse the edge capacities k_e at the local minima (straight lines) and saddle (dotted lines) for varying cost parameter γ (a) and varying fluctuation parameter σ (c) for the fluctuating sink model with fluctuation mean $\mu = -1$. For both parameters, the capacity at the loop κ (light purple) undergoes a saddle node bifurcation which causes a discontinuous transition in the global minima (thick lines) from non-loopy to loopy networks. **b,d** An analogous saddle-node bifurcation in the capacities k_e may be observed in the generalised damaged bond model in terms of both the cost parameter (b) and the damage parameter (d). The dissipation is fixed to $D = 90$ in panels (a) and (c) and to $D = 1$ in panels (b) and (d).

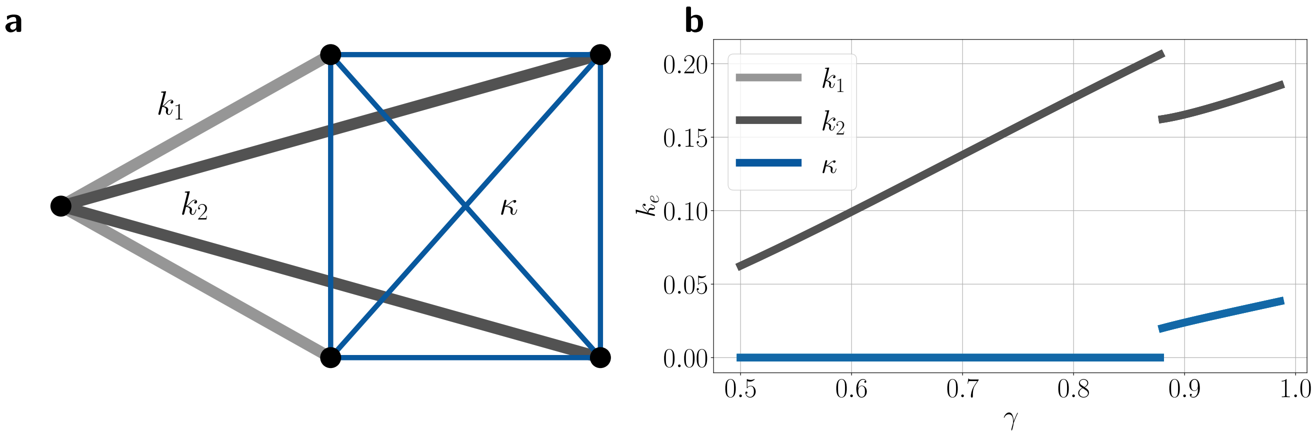

Supplementary Figure 6. **Discontinuous transition to loop formation in non-planar network a** To analyse the transition to loop formation in the simplest non-planar graph, the set of potential edges $\mathcal{E}$ is chosen as the edge set of the complete graph on five nodes K_5. Similar to the network setup shown in Figure 2a, we choose the node on the left as the node supplying the entire network and start from the tree network indicated by grey edges. **b** We then increase the cost parameter γ and perturb the edge capacities according to the procedure described in the methods section to monitor when new edges form. Again, we observe a discontinuous transition to loop formation. Due to the high degree of symmetry in the network, we observe that all potential loops form simultaneously with a non-zero capacity κ.

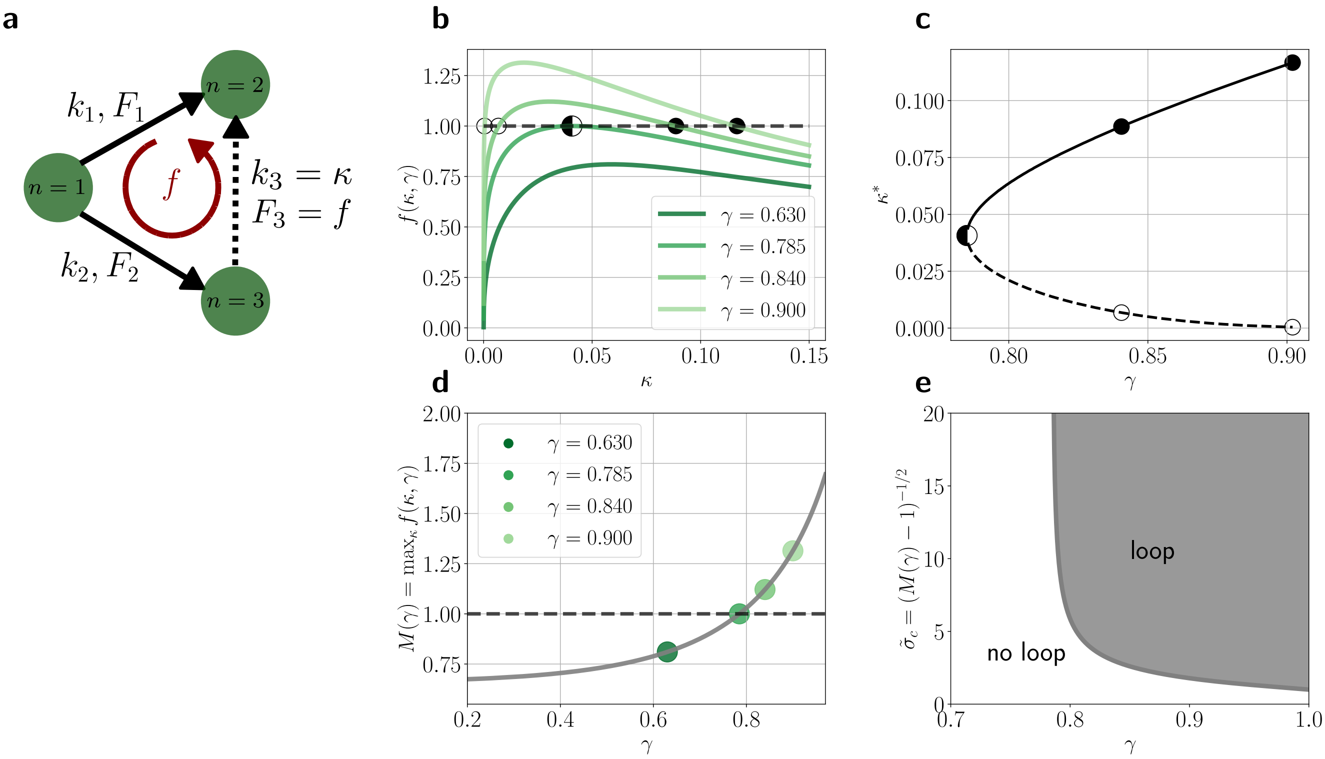

Supplementary Figure 7. **Three node network to analyse the transition to loop formation.** **a** Elementary network to study spontaneous loop formation in optimum supply networks. The network consists of three nodes (green circles) where node $n = 1$ has an inflow of two, $P_1 = 2$, and all other nodes have an outflow of unity. These in and outputs determine the flows $F_i, i \in \{1, 2, 3\}$ along the links with capacities k_i. The optimum topology for this set-up is a tree network. If the in- and outputs are fluctuating, however, an additional edge (dotted arrow) may be beneficial to reduce the average dissipation. This edge introduced a new degree of freedom expressed as a cycle flow f. **b** The points where the function $f(\kappa, \gamma)$ as defined in Eq. (6) crosses the dotted, black line at unity determine determine potential KKT points κ^*, where the loop in panel a is closed. The single peak crossing the dotted line clearly illustrates the saddle-node character of the bifurcation. **c** There are two potential KKT points κ^* which can be determined by finding the points where $f(\kappa, \gamma)$ is unity. One represents the saddle (empty circle) and the other one a minimum (filled circle). **d** Since the function shown in panel a has a single peak $M(\gamma)$ for these values of the cost parameter γ, the critical value γ_c where the loop starts to form can be determined by determining the value of γ for which this maximum reaches unity. **e** As a result of Eq. (7), we can find the critical value of the effective fluctuation strength $\sigma_c^2 = \sigma^2/\mu^2$ in dependence of the cost parameter γ by using the maximum $M(\gamma)$ and thus identify the region of the parameter space, where loop formation becomes beneficial.

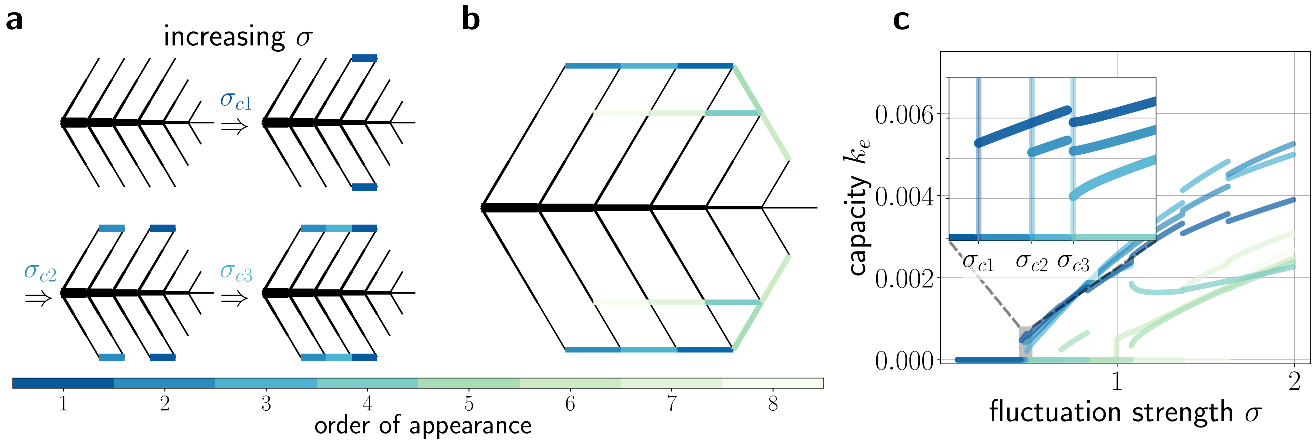

Supplementary Figure 8. **Discontinuous transition beyond the first loop for varying fluctuation strength σ a,b** We order the loops in a colour code according to their appearance with increasing fluctuation strength σ: the darker the edge colour, the earlier the edge appears. For the loop that appears as the i-th loop, we denote its fluctuation strength σ_c where the loop starts to become beneficial for the dissipation-optimised network. **c** The transition to loop formation is discontinuous beyond the first loop: loops appearing at higher values of σ again appear with a non-zero capacity as shown in detail in the inset. Cost parameter is fixed to $\gamma = 0.85$ for all panels.

SUPPLEMENTARY NOTES

Supplementary Note 1: Minimising dissipation using Lagrange's method

In this section, we illustrate how to minimise the dissipation with an equality constraint for a tree network using the method of Lagrange multipliers. The minimisation problem thus reads

$$\text{Minimise } \langle D_{\text{tree}} \rangle = \sum_{e \in E} \frac{\langle F_e^2 \rangle}{k_e}$$
$$\text{subject to}$$
$$\sum_{e \in T} k_e^\gamma = K^\gamma.$$

This can be solved by minimising the Lagrange function

$$\mathcal{L}(k_e) = \sum_{e \in E} \frac{\langle F_e^2 \rangle}{k_e} - \lambda \left(K^\gamma - \sum_{e \in E} k_e^\gamma \right).$$

The optimum edge weights are then found by taking the derivative and setting it to zero;

$$\frac{\partial \mathcal{L}}{\partial k_e} = -\frac{\langle F_e^2 \rangle}{k_e^2} + \lambda \gamma k_e^{\gamma - 1} \stackrel{!}{=} 0,$$
$$\Rightarrow k_e^* = \left(\frac{\langle F_e^2 \rangle}{\lambda \gamma} \right)^{\frac{1}{1+\gamma}}.$$

Substituting this result into the capacity constraint yields the value of the Lagrange multiplier λ

$$\lambda = \frac{1}{\gamma} \left[\frac{\sum_{a \in E} (\langle F_a^2 \rangle^{\frac{\gamma}{1+\gamma}}}{K^\gamma} \right]^{\frac{\gamma+1}{\gamma}}.$$

Then we finally obtain

$$k_e^* = \frac{(\langle F_e^2 \rangle)^{\frac{1}{1+\gamma}}}{\left[\sum_{a \in E} (\langle F_a^2 \rangle)^{\frac{\gamma}{1+\gamma}} \right]^{1/\gamma}} K.$$

This yields the minimised average dissipation

$$\langle D_{\text{tree}}^* \rangle = \frac{\left[\sum_{a=1}^{N-1} (\langle F_a^2 \rangle)^{\frac{\gamma}{\gamma+1}} \right]^{(\gamma+1)/\gamma}}{K}.$$

Supplementary Note 2: Minimising dissipation using Karush-Kuhn-Tucker conditions

When minimising the dissipation in the tree network with a single additional edge, we have to take into account an inequality constraint $\kappa \geq 0$ for the newly added edge (m, n). We have the optimisation problem

$$\begin{aligned} &\text{Minimise } \langle D_{\text{loopy}} \rangle = \sum_{e \in T} \frac{\langle F_e^2 \rangle}{\tilde{k}_e} - \frac{\kappa}{1 + C_{m,n} \kappa} B_{m,n} \\ &\text{subject to} \\ &\sum_{e \in T} \tilde{k}_e^\gamma = K^\gamma - \kappa^\gamma, \\ &\kappa \geq 0. \end{aligned} \tag{1}$$

This problem can be solved by using a generalisation of the method of Lagrange multipliers due to Karush, Kuhn and Tucker [1]. We first define the following Lagrange-type function

$$\begin{aligned}\tilde{\mathcal{L}}(\tilde{k}_e, \kappa) = &\sum_{e\in T} \frac{\langle F_e^2\rangle}{\tilde{k}_e} - \frac{\kappa}{1+C_{m,n}\kappa} B_{m,n} \\ &- \tilde{\lambda}\left(K^\gamma - \sum_{e\in T} \tilde{k}^\gamma - \kappa^\gamma\right) - \mu\kappa.\end{aligned}$$

Now we can proceed constructing the KKT conditions, whose solutions are potential local minima of the problem under the constraint and referred to as *KKT points*

$$\begin{aligned}&\frac{\partial \tilde{\mathcal{L}}}{\partial \tilde{k}_e} \overset{!}{=} 0, \quad \forall e \in T \cup \{\ell\} \\ &K^\gamma = \sum_{e\in T} \tilde{k}^\gamma + \kappa^\gamma, \\ -&\kappa \leq 0 \\ &\mu \geq 0, \\ &\mu\kappa^* = 0.\end{aligned}$$

We first compute the derivatives of the Lagrange function $\tilde{\mathcal{L}}$. In order to do so, we distinguish two types of edges: the ones that lie on the shortest path from the source to the new edge ℓ, i.e. where $e \in L \cup R$, and the other ones as sketched in Figure 2,b. For all edges $e \notin L, R$ that are not on the path we find

$$\begin{aligned}\frac{\partial \tilde{\mathcal{L}}}{\partial \tilde{k}_e} &= -\frac{\langle F_e^2\rangle}{\tilde{k}_e^2} + \tilde{\lambda}\gamma\tilde{k}_e^{\gamma-1} \overset{!}{=} 0, \\ \Rightarrow \tilde{k}_e &= \left(\frac{\langle F_e^2\rangle}{\tilde{\lambda}\gamma}\right)^{\frac{1}{1+\gamma}}.\end{aligned} \tag{2}$$

That is, we have the same result as in the tree except for a different normalisation factor $\tilde{\lambda}$. To get rid of the dependence of $\tilde{\lambda}$ on the edges not on the path $e \notin R, L$, we make use of the equality constraint

$$\frac{\partial \tilde{\mathcal{L}}}{\partial \tilde{\lambda}} \overset{!}{=} 0 \Rightarrow K^\gamma = \sum_{e\in T} \tilde{k}^\gamma + \kappa^\gamma.$$

Now summing over all edges that are not located on the path, we get

$$\begin{aligned}K^\gamma - \sum_{e\in L\cup R} \tilde{k}_e^\gamma - \kappa^\gamma &= \sum_{e\notin L\cup R} \tilde{k}_e^\gamma \\ &= \sum_{e\notin L\cup R} \left(\frac{\langle F_e^2\rangle}{\tilde{\lambda}\gamma}\right)^{\frac{\gamma}{1+\gamma}}, \\ \Rightarrow \tilde{\lambda} &= \frac{1}{\gamma}\left[\frac{\sum_{e\notin L\cup R}(\langle F_e^2\rangle)^{\gamma/(\gamma+1)}}{K^\gamma - \sum_{e\in L\cup R}\tilde{k}_e^\gamma - \kappa^\gamma}\right]^{(\gamma+1)/\gamma},\end{aligned} \tag{3}$$

thus eliminating the entire dependence of $\tilde{\lambda}$ on $\tilde{k}_e, e \notin L \cup R$. For all edges on the path, $e \in L \cup R$, we find

$$\begin{aligned}&\frac{\partial \tilde{\mathcal{L}}}{\partial \tilde{k}_e} \overset{!}{=} 0 \\ \Rightarrow &\frac{\langle F_e^2\rangle}{\tilde{k}_e^2} = -\frac{\kappa}{1+C_{m,n}\kappa}\frac{\partial B_{m,n}}{\partial \tilde{k}_e} \\ &\qquad + \frac{\kappa^2 B_{m,n}}{(1+C_{m,n}\kappa)^2}\frac{\partial C_{m,n}}{\partial \tilde{k}_e} + \tilde{\lambda}\gamma\tilde{k}_e^{\gamma-1}.\end{aligned}$$

The derivatives appearing here can be readily calculated letting the edge $e \in L$, wlog;

$$\begin{aligned}\frac{\partial C_{m,n}}{\partial \tilde{k}_e} &= -\frac{1}{\tilde{k}_e^2},\\ \frac{\partial B_{m,n}}{\partial \tilde{k}_e} &= -2\frac{\langle F_e^2\rangle}{\tilde{k}_e^3}\\ &\quad - \frac{1}{\tilde{k}_e^2}\sum_{a\in L, a\neq e}\frac{\langle F_e F_a\rangle}{\tilde{k}_a} + \frac{2}{\tilde{k}_e^2}\sum_{a\in R}\frac{\langle F_e F_a\rangle}{\tilde{k}_a}.\end{aligned}$$

For the new edge $\ell = (m,n)$ we obtain

$$\begin{aligned}\frac{\partial \tilde{\mathcal{L}}}{\partial \kappa} &= -\frac{B_{m,n}}{(1+C_{m,n}\kappa)^2} + \tilde{\lambda}\gamma\kappa^{\gamma-1} - \mu \overset{!}{=} 0,\\ \Rightarrow \mu &= -\frac{B_{m,n}}{(1+C_{m,n}\kappa)^2} + \tilde{\lambda}\gamma\kappa^{\gamma-1}.\end{aligned}$$

The last KKT condition, the complementary slackness, thus yields

$$\begin{aligned}\mu\kappa = 0 \;\Rightarrow & -\frac{\kappa B_{m,n}}{(1+C_{m,n}\kappa)^2} + \tilde{\lambda}\gamma\kappa^{\gamma} \overset{!}{=} 0,\\ &\Rightarrow B_{m,n} = (1+C_{m,n}\kappa)^2\kappa^{\gamma-1}\gamma\tilde{\lambda} \;\vee\; \kappa = 0.\end{aligned}$$

Note that $B_{m,n}$, $C_{m,n}$ and $\tilde{\lambda}$ depend on the updated capacities $\tilde{k}_e$. In general, i.e. for arbitrary network topologies and arbitrary parameters γ, σ and μ, the resulting set of equations does not have an analytical solution. However, it may be used to gain insight into the general structure of the minima as we will see in the next section.

Supplementary Note 3: Proof of Theorem 1

In this section we prove Theorem 1.

Proof. To prove this, we will make use of the last KKT condition, the complementary slackness in Eq. (19) in the main text

$$B_{m,n} = (1+C_{m,n}\kappa)^2\kappa^{\gamma-1}\gamma\tilde{\lambda}. \tag{4}$$

Now let $1 \gg \varepsilon > 0$ be a small positive number and let the loop capacity be $\kappa = \varepsilon$. We will now demonstrate that this capacity cannot be arbitrarily close to zero, i.e. that

$$\exists\; C \in \mathbb{R}^{>0} \text{ s.t. } \kappa = \varepsilon \geq C.$$

Let $\tilde{k}_{\min} = \min_{e\in L\cup R}\tilde{k}_e > 0$ be the minimum optimal capacity after the addition of the loop with capacity $\kappa = \varepsilon$ which can be obtained by solving the KKT problem resulting from Eq. (1). Now we can bound $B_{m,n}$ from above by

$$\begin{aligned}\infty > B_{m,n}^{\max} &= \tilde{k}_{\min}^{-2}\left\langle\left(\sum_{e\in L}F_e - \sum_{e\in R}F_e\right)^2\right\rangle\\ \geq B_{m,n} &= \left\langle\left(\sum_{e\in L}\frac{F_e}{\tilde{k}_e} - \sum_{e\in R}\frac{F_e}{\tilde{k}_e}\right)^2\right\rangle.\end{aligned}$$

On the other hand, we know that the first term on the right-hand side of Eq. (4) is larger than one $(1+C_{m,n}\kappa)^2 > 1$ since both expressions are positive, $C_{m,n} > 0$ and $\kappa > 0$, such that we can bound the entire right-hand side from below by

$$\kappa^{\gamma-1}\tilde{\lambda}\gamma < \kappa^{\gamma-1}\tilde{\lambda}\gamma(1+C_{m,n}\kappa)^2.$$

Finally, we can also upper bound the Lagrange multiplier $\tilde{\lambda}$. To achieve this, we make use of the expression in Eq. (2) and Eq. (3) which relate the multiplier to the capacity of an edge $e \notin R \cup L$ that is not located on the shortest path connecting source and added edge. First we note that all edges have to have capacities smaller than the overall capacity $\tilde{k}_e < K$ by virtue of the capacity constraint. Thus we find

$$\begin{aligned}
\tilde{\lambda} &= \frac{1}{\gamma}\left[\frac{\sum_{e\notin L\cup R}(\langle F_e^2\rangle)^{\gamma/(\gamma+1)}}{\sum_{e\notin L\cup R}\tilde{k}_e^{\gamma}}\right]^{(\gamma+1)/\gamma}, \\
>\tilde{\lambda}^{\min} &= \frac{1}{\gamma K^{\gamma+1}}\left[\sum_{e\notin L\cup R}\langle F_e^2\rangle^{\gamma/(\gamma+1)}\right]^{(\gamma+1)/\gamma}, \\
\Rightarrow \frac{1}{\tilde{\lambda}} &< \frac{1}{\tilde{\lambda}^{\min}}.
\end{aligned}$$

Thus, upper bounding the left-hand side and lower bounding the right-hand side of Equation 4, we arrive at

$$\begin{aligned}
\kappa^{\gamma-1}\tilde{\lambda} &< \frac{B_{m,n}^{\max}}{\gamma}, \\
\Rightarrow \kappa^{\gamma-1} &< \frac{B_{m,n}^{\max}}{\gamma\tilde{\lambda}^{\min}}, \\
\Rightarrow \kappa &> \left(\frac{B_{m,n}^{\max}}{\gamma\tilde{\lambda}^{\min}}\right)^{1/(\gamma-1)} := C.
\end{aligned}$$

The last step holds due to the fact that $\gamma \in (0,1)$ such that the last manipulation results in the reciprocal on both sides of the inequality. Therefore we demonstrated that the optimal capacity of the loop κ has to be larger than the threshold parameter C if it is non-vanishing. □

Supplementary Note 4: Minimising the dissipation explicitly for the five- and three node network

Set of equations for five node network

Tree network Here, we explicitly derive the optima topology for the network shown in Figure 2,a. The network consists of four variable sinks at nodes $2, 3, 4, 5$ (circles) and four edges (arrows) connecting them with capacities k_i and flows $F_i, i \in \{1, 2, 3, 4\}$. A fifth, potential edge is shown as dotted arrow. If it exists, it carries flow $\tilde{F}_5$ and has capacity κ. We first consider the case of a tree network, i.e. $\kappa = 0$.

In the fluctuating sink model, we describe the sinks as i.i.d. Gaussian random variables,

$$P_{2,3,4,5} \sim \mathcal{N}(\mu, \sigma).$$

The source at node 1 balances the sinks

$$P_1 = -\sum_{j=2}^{5} P_j.$$

While generic local minima with asymmetric capacities k_e exist, networks close to the global minimum generally show a high degree of symmetry [2, 3]. Therefore, in the following we consider symmetric optimal networks with capacities $k_3 = k_1$ and $k_4 = k_2$. If there is no loop ($\kappa = 0$), the flows may be calculated directly using the continuity equation (2)

$$\begin{aligned}
F_1 &= -(P_2 + P_4), \qquad & F_2 &= -P_4, \\
F_3 &= -(P_3 + P_5), \qquad & F_4 &= -P_5,
\end{aligned}$$

which results in the following expressions for the second moments of flows

$$\begin{aligned}
&\langle F_1^2\rangle = \langle F_3^2\rangle = 4\mu^2 + 2\sigma^2, \quad \langle F_2^2\rangle = \langle F_4^2\rangle = \mu^2 + \sigma^2, \\
&\langle F_1 F_3\rangle = 4\mu^2,\ \langle F_2 F_4\rangle = \mu^2, \\
&\langle F_1 F_2\rangle = \langle F_3 F_4\rangle = 2\mu^2 + \sigma^2.
\end{aligned}$$

Using the optimal capacities and this set of equations, we can deduce explicit equations for the optimal capacities and thus the dissipation (see first section of this SI)

$$\langle D_{\text{tree}} \rangle = \frac{\left[2(\sigma^2 + \mu^2)^{\frac{\gamma}{\gamma+1}} + 2(2\sigma^2 + 4\mu^2)^{\frac{\gamma}{\gamma+1}}\right]^{(\gamma+1)/\gamma}}{K}.$$

Loopy network How does this result change if we allow to close the loop as illustrated in Figure 2a, i.e., if we include the corresponding edge in the set of potential edges $\mathcal{E}$?

Let us assume a non-zero capacity $k_5 = \kappa > 0$ with flow $\tilde{F}_5$. In the following, we denote the flows and capacities in the loopy network with a tilde. In the presence of a loop, we can no longer determine the flows using the continuity equation alone.We can exploit Kirchhoff's voltage law Eq. (5)to eliminate the additional degree of freedom: it is given by a cycle flow f around the newly formed edge such that

$$\begin{aligned}
\tilde{F}_1 &= F_1 - f, \qquad & \tilde{F}_2 &= F_2, \\
\tilde{F}_3 &= F_3 + f, \qquad & \tilde{F}_4 &= F_4, \\
\tilde{F}_5 &= f
\end{aligned}$$

Using Kirchhoff's voltage law (Eq. (5)) we can express the cycle flow in terms of the remaining flows as

$$\begin{aligned}
& \frac{f}{\kappa} + \frac{\tilde{F}_3}{\tilde{k}_1} - \frac{\tilde{F}_1}{\tilde{k}_1} = 0, \\
\Leftrightarrow \quad & f = \left(2 + \frac{\tilde{k}_1}{\kappa}\right)^{-1} \times (F_1 - F_3).
\end{aligned}$$

Finally, we can use this result to calculate the second moments of the flows as

$$\begin{aligned}
\langle \tilde{F}_1^2 \rangle &= \langle \tilde{F}_3^2 \rangle = 4\mu^2 + 2\sigma^2 \left[1 - \frac{2\kappa}{2\kappa + \tilde{k}_1} + \frac{2\kappa^2}{(2\kappa + \tilde{k}_1)^2}\right] \\
\langle \tilde{F}_2^2 \rangle &= \langle \tilde{F}_4^2 \rangle = \mu^2 + \sigma^2, \\
\langle \tilde{F}_5^2 \rangle &= \langle f^2 \rangle = 4\sigma^2 \left(2 + \frac{\tilde{k}_1}{\kappa}\right)^{-2}.
\end{aligned}$$

Using the KKT conditions, we can derive a closed-form solution for the loopy capacity κ. For the five node network, the dissipation of the loopy network reads

$$\langle D_{\text{loopy}} \rangle = \frac{2(\sigma^2 + \mu^2)}{\tilde{k}_2} + \frac{2(4\mu^2 + 2\sigma^2)}{\tilde{k}_1} - \frac{4\sigma^2\kappa}{\tilde{k}_1^2 + 2\kappa\tilde{k}_1}.$$

Here, we made use of the symmetries in the network such that $\tilde{k}_1 = \tilde{k}_3$ and $\tilde{k}_2 = \tilde{k}_4$ and we used that in the situation at hand the two constants appearing in the expression are given by $B_{m,n} = \frac{4\sigma^2}{\tilde{k}_1^2}$ and $C_{m,n} = 2/\tilde{k}_1$. Taking the derivatives of the Lagrange function and setting them to zero, we arrive at the following set of equations

$$\begin{aligned}
& \tilde{k}_1 = \tilde{k}_3, \\
& \tilde{k}_2 = \tilde{k}_4 = \left(\frac{\mu^2 + \sigma^2}{\tilde{\lambda}\gamma}\right)^{1/(1+\gamma)}, \\
\Rightarrow & \tilde{\lambda} = \frac{(\mu^2 + \sigma^2)}{\gamma}\left[\frac{2}{K^\gamma - 2\tilde{k}_1^\gamma - \kappa^\gamma}\right]^{\frac{\gamma+1}{\gamma}}, \\
& \frac{4\sigma^2}{\tilde{k}_1^2} = (1 + 2\kappa/\tilde{k}_1)^2 \kappa^{\gamma-1}\gamma\tilde{\lambda} \vee \kappa = 0, \\
& \gamma\tilde{\lambda}\tilde{k}_1^{\gamma+1} = (4\mu^2 + 2\sigma^2) - \frac{4\sigma^2\kappa(\kappa + \tilde{k}_1)}{(\tilde{k}_1 + 2\kappa)^2}.
\end{aligned}$$

From this expression, we can also immediately read off the Lagrange multiplier representing the inequality constraint in the case where $\kappa \neq 0$;

$$\mu = \frac{4\sigma^2}{\tilde{k}_1^2} - (1 + 2\kappa/\tilde{k}_1)^2 \kappa^{\gamma-1} \left[\frac{2(\mu^2+\sigma^2)^{\frac{\gamma}{\gamma+1}}}{K^\gamma - 2\tilde{k}_1^\gamma - \kappa^\gamma} \right]^{\frac{\gamma+1}{\gamma}}. \tag{5}$$

Inserting the expression for the Lagrange multiplier $\tilde{\lambda}$ into the last two equations, we arrive at the following set of equations for the two variables κ and $\tilde{k}_1$;

$$\begin{aligned}
&(1 + 2\kappa/\tilde{k}_1)^2 \kappa^{\gamma-1} (\mu^2+\sigma^2) \left[\frac{2}{K^\gamma - 2\tilde{k}_1^\gamma - \kappa^\gamma} \right]^{(\gamma+1)/\gamma} \\
&= \frac{4\sigma^2}{\tilde{k}_1^2} \vee \kappa = 0, \\
&(\mu^2+\sigma^2) \left[\frac{2}{K^\gamma - 2\tilde{k}_1^\gamma - \kappa^\gamma} \right]^{\frac{\gamma+1}{\gamma}} \tilde{k}_1^{\gamma+1} \\
&= (4\mu^2 + 2\sigma^2) - \frac{8\sigma^2\kappa}{\tilde{k}_1 + 2\kappa} + \frac{4\sigma^2\kappa^2}{(\tilde{k}_1+2\kappa)^2}.
\end{aligned}$$

However, these equations are still hard to solve analytically for arbitrary parameters μ, γ and σ.

Set of equations for three node network

We now turn to an even simpler network to shed further light on the transition to loop formation. In Figure 7a, we present a simple three node network with a potential loop with capacity κ and cycle flow $\tilde{F}_3 = f$.
The average dissipation in the presence of the loop can be readily calculated using the expression in Eq. 1 and is given by

$$\langle D_{\text{loopy}} \rangle = 2\frac{\sigma^2+\mu^2}{\tilde{k}_1} - \frac{2\kappa\sigma^2}{\tilde{k}_1^2 + 2\kappa\tilde{k}_1}$$

The KKT conditions for this problem thus read

$$\begin{aligned}
2\lambda\gamma\tilde{k}_1^{\gamma+1} &= 2(\sigma^2+\mu^2) - \frac{4\sigma^2\kappa(\kappa+\tilde{k}_1)}{(\tilde{k}_1+2\kappa)^2} \\
1 &= 2\tilde{k}_1^\gamma + \kappa^\gamma \\
\lambda\gamma\kappa^{\gamma-1}(2\kappa+\tilde{k}_1)^2 &= 2\sigma^2 \vee \kappa = 0
\end{aligned}$$

Putting everything together, we arrive at the following self-consistent equation for the loopy capacity κ

$$1 + \frac{\mu^2}{\sigma^2} = \frac{2\kappa\left(\kappa + \left(\frac{1}{2}(1-\kappa^\gamma)\right)^{1/\gamma}\right)}{\left(2\kappa + \left(\frac{1}{2}(1-\kappa^\gamma)\right)^{1/\gamma}\right)^2} + \frac{2\left(\frac{1}{2}(1-\kappa^\gamma)\right)^{(\gamma+1)/\gamma}\kappa^{1-\gamma}}{\left(2\kappa + \left(\frac{1}{2}(1-\kappa^\gamma)\right)^{1/\gamma}\right)^2}.$$

Note that the critical value of γ saturates for high values of σ^2 as shown in Figure 2. We can thus try to calculate this critical, saturated value γ_c by setting $\mu = -1$, w.l.o.g., and letting $\sigma^2 \to \infty$ to arrive at a self-consistent equation involving only γ and κ

$$1 = \frac{2\kappa\left(\kappa + \left(\frac{1}{2}(1-\kappa^\gamma)\right)^{1/\gamma}\right) + 2\left(\frac{1}{2}(1-\kappa^\gamma)\right)^{(\gamma+1)/\gamma}\kappa^{1-\gamma}}{\left(2\kappa + \left(\frac{1}{2}(1-\kappa^\gamma)\right)^{1/\gamma}\right)^2}$$

Now we want to find for which value of γ there is a $\kappa > 0$ that solves the above equation. To this end, we define the function

$$f(\kappa,\gamma) = \frac{2\kappa\left(\kappa + \left(\frac{1}{2}(1-\kappa^\gamma)\right)^{1/\gamma}\right) + 2\left(\frac{1}{2}(1-\kappa^\gamma)\right)^{1+1/\gamma}\kappa^{1-\gamma}}{\left(2\kappa + \left(\frac{1}{2}(1-\kappa^\gamma)\right)^{1/\gamma}\right)^2} \tag{6}$$

and plot it for different values of κ and γ in Figure 7,b. Thus, the critical value of the cost parameter where the loop starts to form, γ_c, can be calculated by finding the minimum value of the function where it approaches unity

$$\gamma_c = \min\left(\{\gamma \in (0,1) | \exists \kappa \in (0,1) \text{ s.t. } f(\kappa,\gamma) = 1\}\right).$$

Looking at the graph of $f(\kappa,\gamma)$ in Figure 7,b, we see that the function has a single maximum in terms of κ for a given value of γ. We can thus calculate the critical value γ_c by determining, for which value this maximum reaches unity for the first time. Denote by $M(\gamma) = \max_{\kappa\in(0,1)} f(\kappa,\gamma=\gamma)$ the maximum of the function for a given value of γ. Then we can also find the critical value γ_c as

$$M(\gamma_c) = 1.$$

We now turn back to non-infinite values of the fluctuation strength to map out the relationship between the critical fluctuation amplitude σ_c and the critical value of the cost parameter γ_c, similar to the phase diagram shown in Figure 2. For non-infinite values of the fluctuation strength σ, the above equation becomes

$$\begin{aligned} M(\gamma) &= 1 + \frac{\mu^2}{\sigma^2} \\ \Rightarrow \tilde{\sigma}_c &= \frac{1}{\sqrt{(M(\gamma)-1)}} \end{aligned} \tag{7}$$

where we defined the rescaled fluctuation strength $\tilde{\sigma} = \sigma/\mu$. Finally, we can also calculate the minimum rescaled fluctuation strength necessary for a loop to exist. To this end, we calculate $\lim_{\gamma\to 1} M(\gamma)$ which may be calculated analytically and note that the maximum $M(\gamma)$ strictly increases with the cost parameter γ

$$\begin{aligned} \lim_{\gamma\to 1} M(\gamma) = \max_{\kappa\in(0,1)} \lim_{\gamma\to 1} f(\kappa,\gamma) &= \max_{\kappa\in(0,1)} \left[\frac{6\kappa^2+2}{(3\kappa+1)^2}\right] \\ \Rightarrow \frac{\partial f(\kappa,\gamma=1)}{\partial\kappa} &= \frac{12(\kappa-1)}{(1+3\kappa)^3} < 0 \quad \forall\kappa \in (0,1). \end{aligned}$$

The derivative is strictly decreasing for the given interval, the maximum thus occurs at the boundary of the domain. The value at $\lim_{\kappa\to 0} f(\kappa,\gamma=1)$ is given by $M(\gamma) = 2$. We can thus determine the minimum necessary fluctuation strength for the loop to exist as

$$\sigma_{c,\min} = \frac{1}{\sqrt{2-1}} = 1.$$

Supplementary Note 5: Minimising cost using Karush-Kuhn-Tucker conditions

Instead of finding the capacities that minimise the dissipation for a given system cost, we can consider a dual problem: Minimising the system cost while fixing the average dissipation. Again, we want to find out when the first loop emerges. So denote by D the fixed, average dissipation and by C the cost. Formulating the KKT conditions for this related problem, we are thus left with the following optimisation problem

$$\begin{aligned} &\text{Minimise } C = \sum_{e\in T} \tilde{k}_e^\gamma + \kappa^\gamma \sum_{e\in T} \tilde{k}_e^\gamma \\ &\text{subject to} \\ &D = \frac{\langle F_e^2\rangle}{\tilde{k}_e} - \frac{\kappa}{1+C_{m,n}\kappa} B_{m,n} \\ &\kappa \geq 0. \end{aligned} \tag{8}$$

We again define the following Lagrange-type function

$$
\begin{aligned}
\tilde{\mathcal{L}}(\tilde{k}_e, \kappa) &= \sum_{e \in T} \tilde{k}_e^{\gamma} + \kappa^{\gamma} \\
&- \tilde{\lambda} \left(\sum_{e \in T} \frac{\langle F_e^2 \rangle}{\tilde{k}_e} - \frac{\kappa}{1 + C_{m,n}\kappa} B_{m,n} - D \right) - \mu \kappa .
\end{aligned}
$$

Similarly, we can now identify the *KKT points* via the following set of equations

$$
\begin{aligned}
&\frac{\partial \tilde{\mathcal{L}}}{\partial \tilde{k}_e} \stackrel{!}{=} 0, \quad \forall e \in T \cup \{\ell\} \\
&D = \sum_{e \in T} \frac{\langle F_e^2 \rangle}{\tilde{k}_e} - \frac{\kappa}{1 + C_{m,n}\kappa} B_{m,n}, \\
&-\kappa \leq 0 \\
&\mu \geq 0, \\
&\mu \kappa^* = 0.
\end{aligned}
$$

Supplementary Note 6: Identification of global minima of dissipation for tree networks using edge betweennees

Suppose we assign a vector $\boldsymbol{v}(T) \in \mathbb{R}^{|\mathcal{E}|}$ to each tree T, where the entry at position i of edge e corresponds to the measure of edge betweenness $N_p(e)\sigma^2 + N_p(e)^2\mu^2$. These vectors will in general contain mainly zero entries for tree networks. In this case, finding the globally optimal tree network corresponds to finding the vector $\boldsymbol{v}(T)$ that is globally minimal with respect to the quasi-norm induced by $\frac{\gamma}{\gamma+1} \in [0, 0.5]$, i.e. the tree T^* for which $\|\boldsymbol{v}(T^*)\|_{\frac{\gamma}{\gamma+1}}$ is minimal. Note that the ratio of cost parameters $\frac{\gamma}{\gamma+1} < 1$ is smaller than one, such that it does not induce a proper L^p-norm.

For the topology used throughout this paper, i.e. the network constructed by cutting out edges and nodes of a triangular grid such that it corresponds to the shape of a leaf (see Figure 2c), we can demonstrate how to find the global minimum. In Figure 4, we show different realizations of spanning trees for a small sample network and the according edge betweenness as numbers on the edges which can then be used to form the vectors $\boldsymbol{v}(T)$. In panels (e-h), we compare the entries of this vector for the spanning trees. Notably, the network shown in panels (a,e) displays the highest allocation of edge betweenness on as few links as possible and thus the highest imbalance in the vectors $\boldsymbol{v}(T)$. Indeed, taking the entries to the power of $\gamma/(\gamma+1)$ in order to calculate each edge's contribution to the dissipation (panels i-l), we observe that the tree with the highest allocation has the minimum dissipation. This can easily be seen by adding up the values on the three edges connected to the source in the four panels and noting that the other values remain the same, even if distributed among the edges differently.

We also numerically tested this argument by randomly sampling the local tree minima, but also the shortest path trees for larger networks and did not find any network with less dissipation.

SUPPLEMENTARY REFERENCES

[1] Kuhn, H. W. & Tucker, A. W. Nonlinear programming. In *Proceedings of the Second Berkeley Symposium on Mathematical Statistics and Probability*, 481–492 (University of California Press, Berkeley, Calif., 1951).

[2] Katifori, E., Szöllősi, G. J. & Magnasco, M. O. Damage and fluctuations induce loops in optimal transport networks. *Phys. Rev. Lett.* **104**, 048704 (2010).

[3] Ronellenfitsch, H. & Katifori, E. Global Optimization, Local Adaptation, and the Role of Growth in Distribution Networks. *Phys. Rev. Lett.* **117**, 138301 (2016).

4.2. G) Resilience and fluctuations shape primal and dual communities in spatial networks

[7] Kaiser, F., Ronellenfitsch, H., Latora, V. & Witthaut, D. Resilience and fluctuations shape primal and dual communities in spatial networks. *arXiv:2105.06687 [physics]*. arXiv: 2105.06687 (2021).

Resilience and fluctuations shape primal and dual communities in spatial networks

Franz Kaiser,[1,2] Henrik Ronellenfitsch,[3,4] Vito Latora,[5,6,7,8] and Dirk Witthaut[1,2]

[1] *Forschungszentrum Jülich, Institute for Energy and Climate Research (IEK-STE), 52428 Jülich, Germany*

[2] *Institute for Theoretical Physics, University of Cologne, Köln, 50937, Germany*

[3] *Physics Department, Williams College, 33 Lab Campus Drive, Williamstown, MA 01267, U.S.A.*

[4] *Department of Mathematics, Massachusetts Institute of Technology, Cambridge, MA 02139, U.S.A.*

[5] *School of Mathematical Sciences, Queen Mary University of London, London E1 4NS, UK*

[6] *Dipartimento di Fisica ed Astronomia, Università di Catania and INFN, 95123 Catania, Italy*

[7] *The Alan Turing Institute, The British Library, London NW1 2DB, UK*

[8] *Complexity Science Hub Vienna, 1080 Vienna, Austria*

(Dated: May 17, 2021)

Abstract

Both human-made and natural supply networks are built to operate reliably in changing conditions full of external stimuli. Many of these spatial networks exhibit community structures. Here, we show the existence of a second class of communities. These dual communities are based on an exceptionally strong mutual connectivity and can be found for example in leaf venation networks. We demonstrate that traditional and dual communities emerge naturally as two different phases of optimised network structures that are shaped by fluctuations and that they suppress failure spreading, which underlines their importance in understanding the shape of real-world supply networks.

Community structures are a fundamental trait of complex networks and have found numerous applications in systems from social networks [1] to biological networks [2, 3] and critical infrastructures [4]. Typically, communities are defined by a strong connectivity within each community compared to a relatively weak connectivity between them [1, 5, 6]. Intuitively, community structures play an important role for failure spreading, i.e. small perturbations stay within the community, which is both predicted by theory [7, 8] as well as observed in experiments [9].

Many human-made and biological networks are spatially embedded and planar [10–13]. For planar graphs, it is possible to define a *dual graph*. Every node of the dual graph corresponds to a facet of the original graph's planar drawing (see Fig. 1a). If two facets share an edge, their corresponding dual nodes are connected by a dual edge. Dual graphs turn out to be useful not only when analysing resistor networks, power grids or natural gas networks [14–17], but also to study fixed points in coupled oscillator systems [18, 19].

Remarkably, the analysis of dual graphs allows to reveal patterns in the network structure that are hidden in the primal graph, such as *dual communities*. We show that not only a relatively *weak* connectivity, but also a relatively *strong* connectivity between parts of the network may be used to define community structures. This is due to the fact that strong connections in the primal graph translate into weak connections in the dual graph.

Consider a weighted, simple graph $G(V, E, W)$ with vertex set V containing $N = |V|$ vertices and edge set E of $M = |E|$ edges. Spectral bisection is a commonly used method to determine the community structure of a graph that dates back to Fiedler [20] and makes use of the graph Laplacian $\boldsymbol{L}$. This an $N \times N$ matrix defined as [21]

$$L_{ij} = \begin{cases} -w_{ij} & \text{if } i \text{ is connected to } j, \\ \sum_{(i,k)\in E} w_{ik} & \text{if } i = j, \\ 0 & \text{otherwise.} \end{cases} \tag{1}$$

Here, $w_{ij} > 0$ is the weight of an edge (i, j). Let us label the graph's edges as $\ell = 1, 2, \ldots, M$ and fix an orientation for each edge. Based on this orientation, we can define the graph's weighted incidence matrix $\boldsymbol{I} \in \mathbb{R}^{M\times N}$ as

$$I_{\ell n} = \begin{cases} \sqrt{w_\ell} & \text{if line } \ell \text{ starts at node } n, \\ -\sqrt{w_\ell} & \text{if line } \ell \text{ ends at node } n, \\ 0 & \text{otherwise.} \end{cases} \tag{2}$$

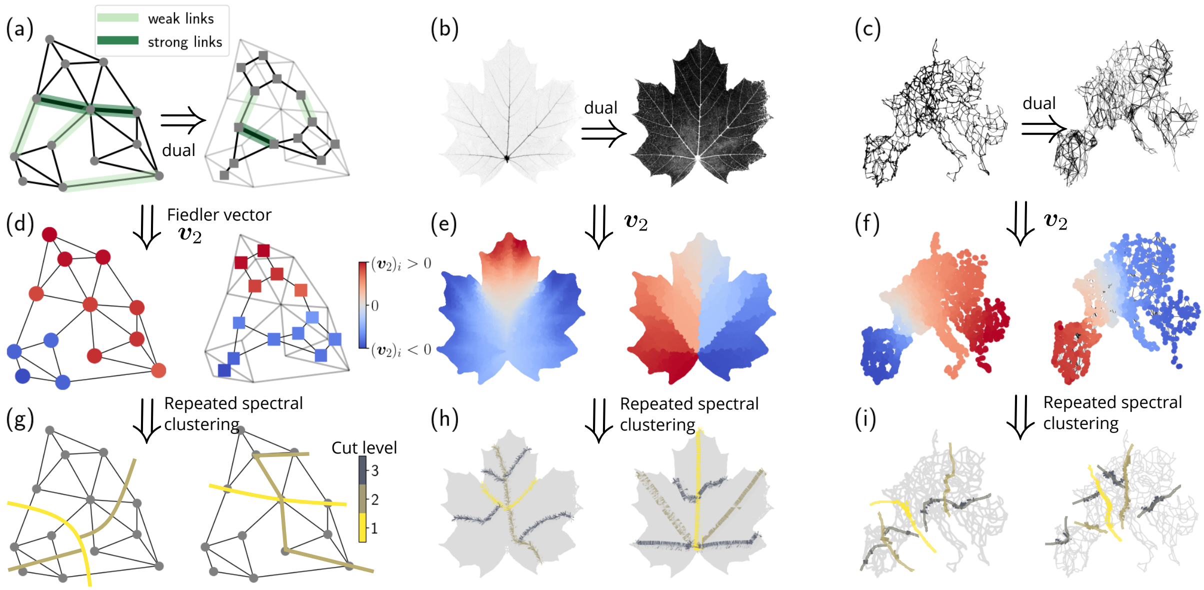

Figure 1. Communities and hierarchies in spatial networks. (a) A planar graph with edges characterised by either large (dark green), small (light green) or intermediate edge weights, and its dual graph. To construct the dual, each face is transformed into a dual node and a dual edge is added if two faces share an edge, where an edge with large weight is transformed into a weak link in the dual (see Eq. (4)). (d) Spectral clustering by means of the Fiedler vector $\boldsymbol{v}_2$ reveals the community structure in both the graph (left) and its dual (right). (g) Based on repeated spectral clustering, the graphs are further decomposed into a hierarchy of smaller subunits which is different in the graph (left) and its (dual). (b,e,h) If we perform the same analysis on the venation network of a leaf of *Acer platanoides*, the resulting hierarchies in the original graph do not provide useful information ((h),left). The hierarchies in the dual graph, however, correspond to the functional components ((e),(h),right). (c-i) For the Continental European power grid ((i),left) and its dual (right) both primal and dual hierarchies provide different, but equally useful information about the network structure.

The Laplacian can be rewritten in terms of the incidence matrix as $\boldsymbol{L} = \boldsymbol{I}^\top \boldsymbol{I} \in \mathbb{R}^{N\times N}$, where '$\top$' denotes the matrix transpose.

We now construct the dual graph G^*. The concept of dual graphs is based on the duality between a graph's cut space and its cycle space [22]. This duality may be expressed more formally by making use of the fact that the fundamental cycles of a graph form the kernel of the weighted incidence matrix. This relationship can be written compactly introducing the weighted edge-cycle incidence matrix $\boldsymbol{C} \in \mathbb{R}^{M \times N^*}$ as

$$\boldsymbol{I}^\top \boldsymbol{C} = 0, \tag{3}$$

where $N^* = M - N + 1$ is the number of independent cycles in the graph [22]. Thus, the elements of $\boldsymbol{C}$ are given by

$$C_{\ell c} = \begin{cases} 1/\sqrt{w_\ell} & \text{if edge } \ell \text{ is part of cycle } c, \\ -1/\sqrt{w_\ell} & \text{if reversed edge } \ell \text{ is part of cycle } c, \\ 0 & \text{otherwise.} \end{cases}$$

Finally, we can then define the Laplacian matrix of the dual graph as

$$\boldsymbol{L}^* = \boldsymbol{C}^\top \boldsymbol{C} \in \ \mathbb{R}^{N^* \times N^*}. \tag{4}$$

Thus, edges in the dual graph are weighted with the inverse of edge weights in the primal graph.

Dual communities can be extracted by means of any community detection algorithm applied to the dual graph, see e.g. Ref. [23]. We focus on spectral graph bisection to unveil the graph's community structure because it is immediately obtained from the graph Laplacian. Spectral graph bisection methods rely on the fact that the community structure is encoded in the second smallest eigenvalue of the graph Laplacian $\lambda_2 \geq 0$, known as the *algebraic connectivity* or *Fiedler value*, which vanishes if the graph consists of two disconnected components and increases with increasing connectivity between them. The graph's nodes are then assigned to one of two communities based on the corresponding eigenvector $\boldsymbol{v}_2^*$, the (dual) *Fiedler vector* [5]: two dual vertices j^* and i^* are in the same community if they share the same sign of the dual Fiedler vector, $\text{sign}((\boldsymbol{v}_2^*)_i - m) = \text{sign}((\boldsymbol{v}_2^*)_j - m)$, where $m \in \mathbb{R}$ is a threshold parameter. Here, we choose $m = 0$. As we demonstrate in Fig. 1b,e, dual communities appear naturally in real-world networks such as the vascular networks of leaves. Instead of weakly connected components, the two communities are separated by a strong vein with large edge weights [24].

Dual communities reveal hierarchical organisation of supply networks. The spectral clustering method for community detection can be applied to both the primal and the dual graph, revealing different structural information about the network (Fig. 1d). Furthermore,

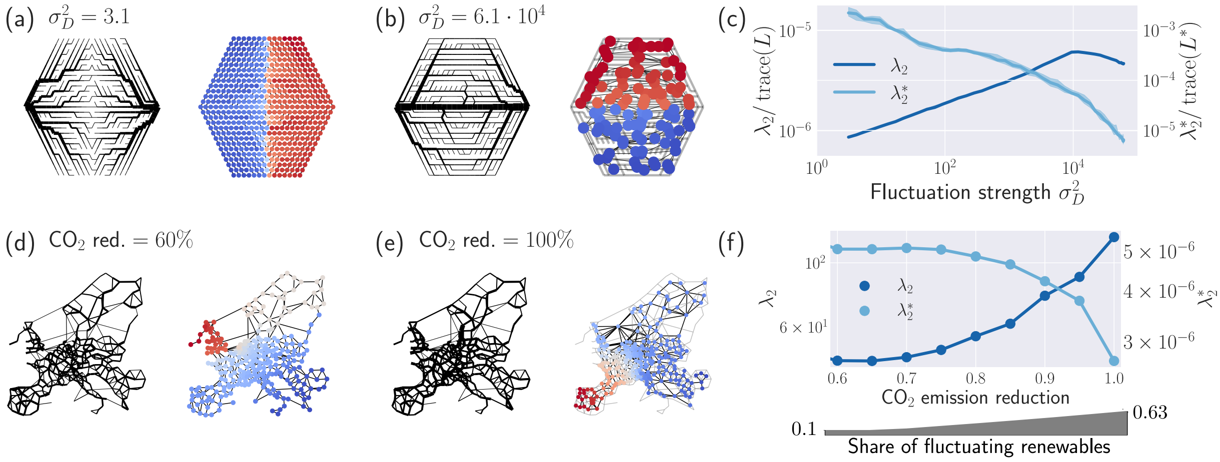

Figure 2. Primal and dual communities emerge naturally in optimal supply networks. (a-c) We consider a triangular supply network with two fluctuating sources located at the leftmost and the rightmost node and Gaussian sinks attached to all other nodes. We impose additional weak (a) and strong (b) fluctuations with variance σ_D^2 on the sources and optimise the edge weights to minimise the average dissipation. We observe a transition from primal to dual communities measured by the Fiedler vectors (coulour code) of (a) the primal or (b) dual graph and (c) scaling of the corresponding primal (λ_2, circles) and dual (λ_2^*, crosses) Fiedler value. (d-f) Similarly, the European power grid experiences a transition from (d) primal to (e) dual communities when transmission line capacities are optimised for different carbon-dioxide (CO_2) emission reduction levels. (f) Again, the result is confirmed by the scaling of primal and dual Fiedler values for increasing emission reduction which corresponds to an increasing share of fluctuating renewables (lower axis). The grids were obtained using the high-resolution European energy system model 'PyPSA-EUR' [25] to minimise the cost for transmission expansion [26]. Cost parameter for (a,b) is $\gamma = 0.9$.

we can use this approach to extract a network's hierarchical organisation as follows. Starting from the initial network, we compute the Fiedler vector, identify the communities and then split the network into two parts at the resulting boundary by removing all edges between the communities. Then we iterate the procedure starting from the subgraphs obtained in the previous step. Repeated application of this procedure reveals different boundaries and thus different hierarchies in the primal graph and its dual (Fig. 1g).

Consider the venation network of a leaf as shown in Fig. 1b and provided by the authors of Ref. [27]. Such a supply network consists of two clearly visible parts separated by a central vein that can be identified as *dual* communities, whereas the same structural pattern is not visible in the primal community structure (Fig. 1e). Remarkably, we can use the hierarchical decomposition to reveal that this central organisational pattern repeats in a hierarchical order: dual communities are split by secondary veins in a repeated manner (Fig. 1h) while the same decomposition in the primal graph does not provide useful information. Thus, leaf venation networks clearly display a dual community structure.

We now turn to another type of supply networks: power grids. Fig. 1c shows the European power transmission grid and its dual graph. Again, a hierarchical decomposition reveals different levels of hierarchies in the grid that correspond to its functional components. These components may also be interpreted geographically: the mountain ranges such as the Pyrenees or the Alps as well as the former Iron Curtain are clearly visible in the decomposition. Remarkably, both primal and dual decompositions provide useful structural information here. In particular, there is a dual community boundary at cut level three that closely corresponds to a system split in Eastern Europe that occurred on January, 8th, 2021, where the European power grid was split into two parts along this boundary.

Although mathematically similar [24, 28, 29], the two types of networks we studied display different structural hierarchies and communities. Whereas leaf venation networks are evolutionarily optimised, the structure of power grids depends strongly on historical aspects and their ongoing transition to include a higher share of renewable energy sources. This transition aspect also manifests in their community structure as we will see in the next section.

Fluctuations shape community structures in optimal flow networks. Understanding how the structure of optimal supply networks emerges is an important part of complex networks research [30–33]. For networks where a single source supplies the entire network, it is well established that fluctuations in the supply can cause a transition from a tree-like to loopy network [29–31]. We extend this result by studying how does the increase in fluctuations influences the optimal network structure in supply networks with multiple strongly fluctuating sources and weakly fluctuating sinks.

To interpolate between strongly fluctuating sources and weakly fluctuating ones, we use a similar setup as in Ref. [31]. We consider a linear flow network consisting of a triangular lattice with N nodes of which N_s are sources and with sinks whose outflows are fluctuating iid Gaussian random variables. Additionally, we add fluctuations only to the sources of the networks that can be tuned by the additional variance of fluctuations σ_D^2 without affecting the statistics of the sinks. We then tune the edge weights w_ℓ such that they minimize the average network dissipation $\langle D \rangle = \mathrm{trace}\left(\boldsymbol{P}^\top \boldsymbol{L}^\dagger \boldsymbol{P}\right)$ while fixing the overall cost $\sum_{\ell=1}^{N} w_\ell^\gamma$ to build the network. Here $\boldsymbol{L}^\dagger$ is the Moore-Penrose pseudoinverse of the Laplacian, $\boldsymbol{P} = (P_1, ..., P_N)^\top \in \mathbb{R}^N$ is the vector of sources and sinks attached to the nodes $1, ..., N$ of the network, and $\gamma \in \mathbb{R}$ is a cost parameter [26].

Whereas the optimal network structure shows primal communities for weakly fluctuating sources, $\sigma_D^2 \approx 1$, it undergoes a transition to a dual community structure for strong fluctuations, $\sigma_D^2 \gg 1$ (see Fig. 2). We can capture this transition in terms of the primal and dual Fiedler values (Fig. 2c). Thus, optimal supply networks have a community structure – whether it is primal or dual depends on the degree of fluctuations.

Strikingly, an analogous transition is observed for actual power transmission grids when optimising the network structure for different levels of fluctuating renewable energy sources. We consider the European power transmission grid and optimise its network structure for different carbon dioxide (CO_2) emission reduction targets compared to the year 1990 ranging from 60% to 100% reduction using the open energy system model 'PyPSA-Eur' [25]. We then obtain the network structure by setting the edge weight to the overall transmission capacity. With increasing penetration of fluctuating renewables, we observe a decrease in the dual Fiedler value λ_2^* and an increase in the primal Fiedler value λ_2 and thus a transition from primal to dual communities. Note that the generation mix in the optimised power system changes for different emission scenarios from conventionally-dominated grids to highly-renewable grids [26].

Dual communities determine robustness of supply networks. To study the robustness of a linear flow network with respect to small perturbations, we make use of a sensitivity factor. We add an inflow ΔP at a node e_1 and an outflow of the same amount at another node e_2 and study how much this will change the flow ΔF_ℓ on a link ℓ. Here, we focus on the case where e_1 and e_2 are the terminal nodes of an edge $e = (e_1, e_2)$ and treat the more general case of inflows at two arbitrary nodes in the SI [26]. The sensitivity factor $\eta_{e_1,e_2,\ell} = \frac{\Delta F_\ell}{\Delta P}$ that relates the flow changes to the inflow is given by [26, 34, 35]

$$\eta_{e_1,e_2,\ell} = \sqrt{\frac{w_\ell}{w_e}} \boldsymbol{l}_\ell^\top \boldsymbol{I} \boldsymbol{L}^\dagger \boldsymbol{I}^\top \boldsymbol{l}_e, \tag{5}$$

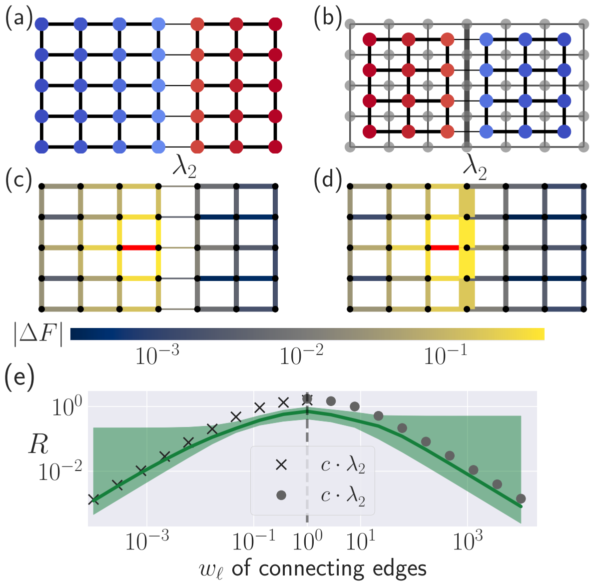

Figure 3. Primal and dual communities inhibit failure spreading. A square grid is divided into (a) two primal communities by weakening the links connecting two parts of the network or (b) into two dual communities by strengthening the links horizontally separating the two parts. The Fiedler vector (colour code) reveals the community structure. (c,d) Both primal and dual communities inhibit flow changes $|\Delta F|$ (colour coded) in the other community after the failure of a single link (red) with unit flow. (e) We interpolate between primal and dual communities in a square grid of size 21×10 by tuning the weight w_e of the horizontal edges or vertical edges (see a,b). The flow ratio R reveals that failure spreading to the other community is largest for $w_\ell = 1$. It decays for either type of community as measured by primal and dual Fiedler values λ_2 (crosses) and λ_2^* (circles), respectively. The green line represents the median value and the shaded regions indicate the 25% and 75% quantiles.

where $\boldsymbol{l}_e \in \mathbb{Z}^M$ is the indicator vector of edge e which is equal to one at the positions indicated by the subscript and zero otherwise. Importantly, the sensitivity factor may also be used to simulate the failure of a link $e = (e_1, e_2)$ by choosing the inflow ΔP accordingly [26] and is well-known in the context of power system security analysis, where it is referred to as *power transfer distribution factor* [34].

Sensitivity to changes in the flow patterns is determined by the primal community structure of a linear flow network measured by the Fiedler value λ_2 [7, 26, 28, 36]. Remarkably, we can find an analogous description in the dual graph [15]

$$\eta_{e_1,e_2,\ell} = -\sqrt{\frac{w_\ell}{w_e}} \boldsymbol{l}_\ell^\top \boldsymbol{C} (\boldsymbol{L}^*)^\dagger \boldsymbol{C}^\top \boldsymbol{l}_e. \tag{6}$$

The dual Laplacian $\boldsymbol{L}^*$ contributes to the sensitivity factor $\eta_{e_1,e_2,\ell}$ in the same way as the primal Laplacian. Hence, primal and dual community structures determine network flows in an equivalent manner: if a network admits a dual community structure and λ_2^* is small, then changes in one community will only weakly affect the other one.

Consider an inflow and simultaneous outflow ΔP at two nodes ℓ_1 and ℓ_2, respectively, that are connected via an edge $\ell = (\ell_1, \ell_2)$. We compare the resulting flow changes in the same (S) and the other (O) community as the given edge by evaluating their ratio $R(\ell, d)$ at a given distance d to the link [28]

$$R(\ell, d) = \frac{\langle |\Delta F_k| \rangle_d^{k \in \mathrm{O}}}{\langle |\Delta F_r| \rangle_d^{r \in \mathrm{S}}} = \frac{\langle |\eta_{\ell_1,\ell_2,k}| \rangle_d^{k \in \mathrm{O}}}{\langle |\eta_{\ell_1,\ell_2,r}| \rangle_d^{r \in \mathrm{S}}}.$$

We then average over all possible trigger links and distances to arrive at the mean flow ratio $R = \langle R(\ell, d) \rangle_{\ell,d}$. The mean flow ratio ranges from $R \approx 0$ if the other module is weakly affected, i.e. there is a strong community effect, to $R \approx 1$ if there is no noticeable effect. We note that R describes flow changes after perturbations in the in- and outflows as well as flow changes as a result of the complete failure of links [26].

Fig 3 illustrates that both primal and dual communities suppress flow changes in the other community. The flow ratio R decays for either community structure and the decay is well-captured by the Fiedler value of the primal (λ_2) and the dual (λ_2^*) graph (see SI [26]).

Discussion and Conclusion. We have introduced a new way to define and identify community structures in planar graphs that we refer to as *dual communities*. We demonstrated that both primal and dual community structures emerge as different phases of optimized networks – whether the one or the other is realised in a given optimal network depends on the degree of fluctuations. In addition to that, both types of communities have the ability to suppress failure spreading – they are thus optimised to limit the effect of link failures or other perturbations.

An important difference between primal and dual communities is the fact that the former are based on a weak connectivity, while dual communities require a strong connectivity. This has important consequences for supply networks such as power grids. While preventing failure spreading, dual communities will not affect the network's ability to transport energy between them, or may even increase the supply capabilities. This is in stark contrast to primal communities that limit failure spreading from one community to the other one, but also supply. Thus, the construction of dual communities may also serve as a strategy against failure spreading, in line with other ideas brought forward recently [28].

We thank Torsten Eckstein for providing some of the digitized leaf networks, Tom Brown and Fabian Neumann for providing us with the optimised power grids and Eleni Katifori for helpful discussions. We gratefully acknowledge support from the Federal Ministry of Education and Research (BMBF grant no. 03EK3055B to D.W.) and the Helmholtz Association (via the joint initiative "Energy System 2050 – a Contribution of the Research Field Energy").

[1] F. Radicchi, C. Castellano, F. Cecconi, V. Loreto, and D. Parisi, Proceedings of the National Academy of Sciences **101**, 2658 (2004).

[2] M. Girvan and M. E. J. Newman, Proceedings of the National Academy of Sciences **99**, 7821 (2002).

[3] R. J. Fletcher, A. Revell, B. E. Reichert, W. M. Kitchens, J. D. Dixon, and J. D. Austin, Nature Communications **4**, 2572 (2013).

[4] L. M. Shekhtman, S. Shai, and S. Havlin, New Journal of Physics **17**, 123007 (2015).

[5] M. E. J. Newman, Proceedings of the National Academy of Sciences of the United States of America **103**, 8577 (2006).

[6] M. E. J. Newman, Nature Physics **8**, 25 (2012).

[7] D. Manik, M. Rohden, H. Ronellenfitsch, X. Zhang, S. Hallerberg, D. Witthaut, and M. Timme, Physical Review E **95** (2017), 10.1103/PhysRevE.95.012319.

[8] R. M. May, Nature **238**, 413 (1972).

[9] L. J. Gilarranz, B. Rayfield, G. Liñán-Cembrano, J. Bascompte, and A. Gonzalez, Science **357**, 199 (2017).

[10] M. P. Viana, E. Strano, P. Bordin, and M. Barthelemy, Scientific Reports **3**, 3495 (2013).

[11] M. Barthélemy, Physics Reports **499**, 1 (2011).

[12] M. Barthelemy, *Morphogenesis of Spatial Networks* (Springer International Publishing, 2018).

[13] M. Barthelemy, *The Structure and Dynamics of Cities: Urban Data Analysis and Theoretical*

Modeling (Cambridge University Press, Cambridge, 2016).

[14] B. Bollobás, *Modern graph theory*, Graduate texts in mathematics No. 184 (Springer, 1998).

[15] H. Ronellenfitsch, M. Timme, and D. Witthaut, IEEE Transactions on Power Systems **32**, 1007 (2017).

[16] H. Ronellenfitsch, D. Manik, J. Hörsch, T. Brown, and D. Witthaut, IEEE Transactions on Power Systems **32**, 4060 (2017).

[17] D. Brkić, Applied energy **86**, 1290 (2009).

[18] D. Manik, M. Timme, and D. Witthaut, Chaos: An Interdisciplinary Journal of Nonlinear Science **27**, 083123 (2017).

[19] F. Dörfler, M. Chertkov, and F. Bullo, Proceedings of the National Academy of Sciences **110**, 2005 (2013).

[20] M. Fiedler, Czechoslovak mathematical journal **23**, 298 (1973).

[21] M. E. J. Newman, *Networks: an introduction* (Oxford University Press, 2010).

[22] R. Diestel, *Graph Theory* (Springer, New York, 2010).

[23] S. Fortunato, Physics Reports **486**, 75 (2010).

[24] T. Gavrilchenko and E. Katifori, Physical Review E **99**, 012321 (2019).

[25] J. Hörsch, F. Hofmann, D. Schlachtberger, and T. Brown, Energy Strategy Reviews **22**, 207 (2018).

[26] See SI for further examples of dual communities in leaf venation networks, additional figures on the open energy system models and extended methods describing linear flow networks, link failures and the fluctuating sink model in detail, which includes Refs. [35, 37–50].

[27] H. Ronellenfitsch, J. Lasser, D. C. Daly, and E. Katifori, PLOS Computational Biology **11**, e1004680 (2015).

[28] F. Kaiser, V. Latora, and D. Witthaut, arXiv:2009.02910 (2020).

[29] F. Kaiser, H. Ronellenfitsch, and D. Witthaut, Nature Communications **11**, 5796 (2020).

[30] E. Katifori, G. J. Szöllősi, and M. O. Magnasco, Phys. Rev. Lett. **104**, 048704 (2010).

[31] F. Corson, Physical Review Letters **104**, 048703 (2010).

[32] S. Bohn and M. O. Magnasco, Physical Review Letters **98**, 088702 (2007).

[33] P. S. Dodds, Physical review letters **104**, 048702 (2010).

[34] A. J. Wood, B. F. Wollenberg, and G. B. Sheblé, *Power Generation, Operation and Control* (John Wiley & Sons, New York, 2014).

[35] J. Strake, F. Kaiser, F. Basiri, H. Ronellenfitsch, and D. Witthaut, New Journal of Physics **21**, 053009 (2019).

[36] F. Kaiser, J. Strake, and D. Witthaut, New Journal of Physics **22**, 013053 (2020).

[37] K. Purchala, L. Meeus, D. V. Dommelen, and R. Belmans, in *IEEE Power Engineering Society General Meeting* (2005) pp. 454–459 Vol. 1.

[38] D. Van Hertem, J. Verboomen, K. Purchala, R. Belmans, and W. Kling, in *The 8th IEEE International Conference on AC and DC Power Transmission* (2006) pp. 58–62.

[39] F. Dörfler, J. W. Simpson-Porco, and F. Bullo, Proceedings of the IEEE **106**, 977 (2018).

[40] G. Kirchhoff, Annalen der Physik **148**, 497 (1847).

[41] N. Hwang and R. Houghtalen, *Fundamentals of Hydraulic Engineering Systems* (Prentice Hall, Upper Saddle River, NJ, 1996).

[42] S. Díaz, J. González, and R. Mínguez, Journal of Water Resources Planning and Management **142**, 04015071 (2016).

[43] E. H. Moore, Bull. Amer. Math. Soc. **26**, 394 (1920).

[44] D. Witthaut, M. Rohden, X. Zhang, S. Hallerberg, and M. Timme, Phys. Rev. Lett. **116**, 138701 (2016).

[45] L. E. Ballentine, *Quantum Mechanics – A Modern Development* (World Scientific, Singapore, 1998).

[46] A. Ben-Israel and T. N. E. Greville, *Generalized inverses: theory and applications*, 2nd ed., CMS books in mathematics No. 15 (Springer, New York, 2003).

[47] U. Miekkala, BIT **33**, 485 (1993).

[48] S. Kettemann, Physical Review E **94** (2015), 10.1103/PhysRevE.94.062311.

[49] D. Labavic, R. Suciu, H. Meyer-Ortmanns, and S. Kettemann, The European Physical Journal Special Topics **223**, 2517 (2014).

[50] D. Jung and S. Kettemann, Physical Review E **94**, 012307 (2016).

Supplemental Material

Supplementary Information for Resilience and fluctuations shape primal and dual communities in spatial networks

Franz Kaiser,[1,2] Henrik Ronellenfitsch,[3,4] Vito Latora,[5,6,7,8] and Dirk Witthaut[1,2]

[1]*Forschungszentrum Jülich, Institute for Energy and Climate Research (IEK-STE), 52428 Jülich, Germany*

[2]*Institute for Theoretical Physics, University of Cologne, Köln, 50937, Germany*

[3]*Physics Department, Williams College, 33 Lab Campus Drive, Williamstown, MA 01267, U.S.A.*

[4]*Department of Mathematics, Massachusetts Institute of Technology, Cambridge, MA 02139, U.S.A.*

[5]*School of Mathematical Sciences, Queen Mary University of London, London E1 4NS, UK*

[6]*Dipartimento di Fisica ed Astronomia, Università di Catania and INFN, 95123 Catania, Italy*

[7]*The Alan Turing Institute, The British Library, London NW1 2DB, UK*

[8]*Complexity Science Hub Vienna, 1080 Vienna, Austria*

(Dated: April 7, 2021)

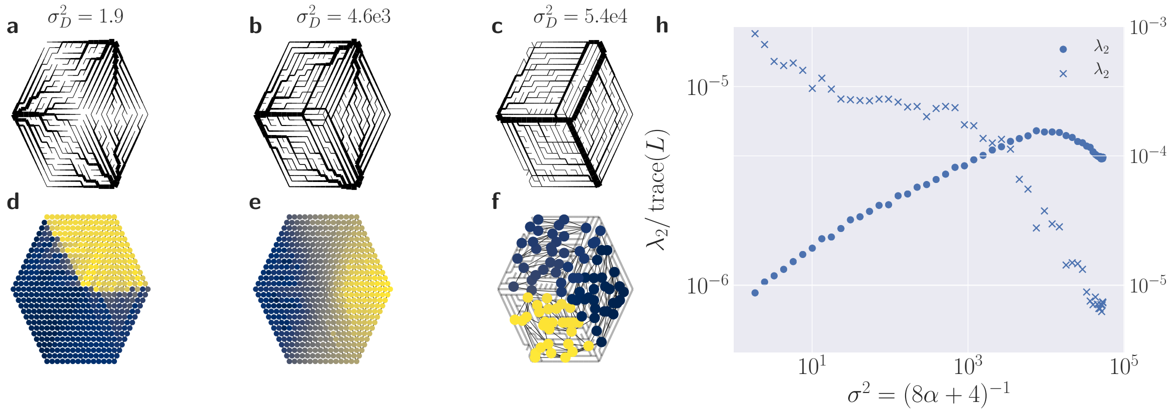

Supplementary Figure S1. **Primal and dual communities emerge naturally in optimal supply networks.** (a-c) We consider a supply network consisting of three fluctuating sources on the left and the right of every network and iid Gaussian sinks attached to all other nodes in a triangular grid. We then optimize the capacities of every edge using the model used in Refs. [1] and [2] with a constrained, overall capacity with parameter $\gamma = 0.5$. We impose additional fluctuations on the sources through additive dirichlet variables whose variance can be tuned by a parameter $\alpha \in [0, \infty]$ interpolating between weak (a, $\alpha \gg 1$) to strong (c, $\alpha \ll 1$) fluctuations. The resulting network has either a primal (a) or dual (c) community structure which we demonstrate by color-coding the Fiedler vectors of the primal (d,e) or dual network (f). (h) The Fiedler of both primal (λ_2, circles) and dual (λ_2^*, crosses) graph scale reversely with the variance of the additive dirichlet noise imposed on the sources indicating that the minimum dissipation network has a primal community structure for small fluctuations and a dual one for strong fluctuations.

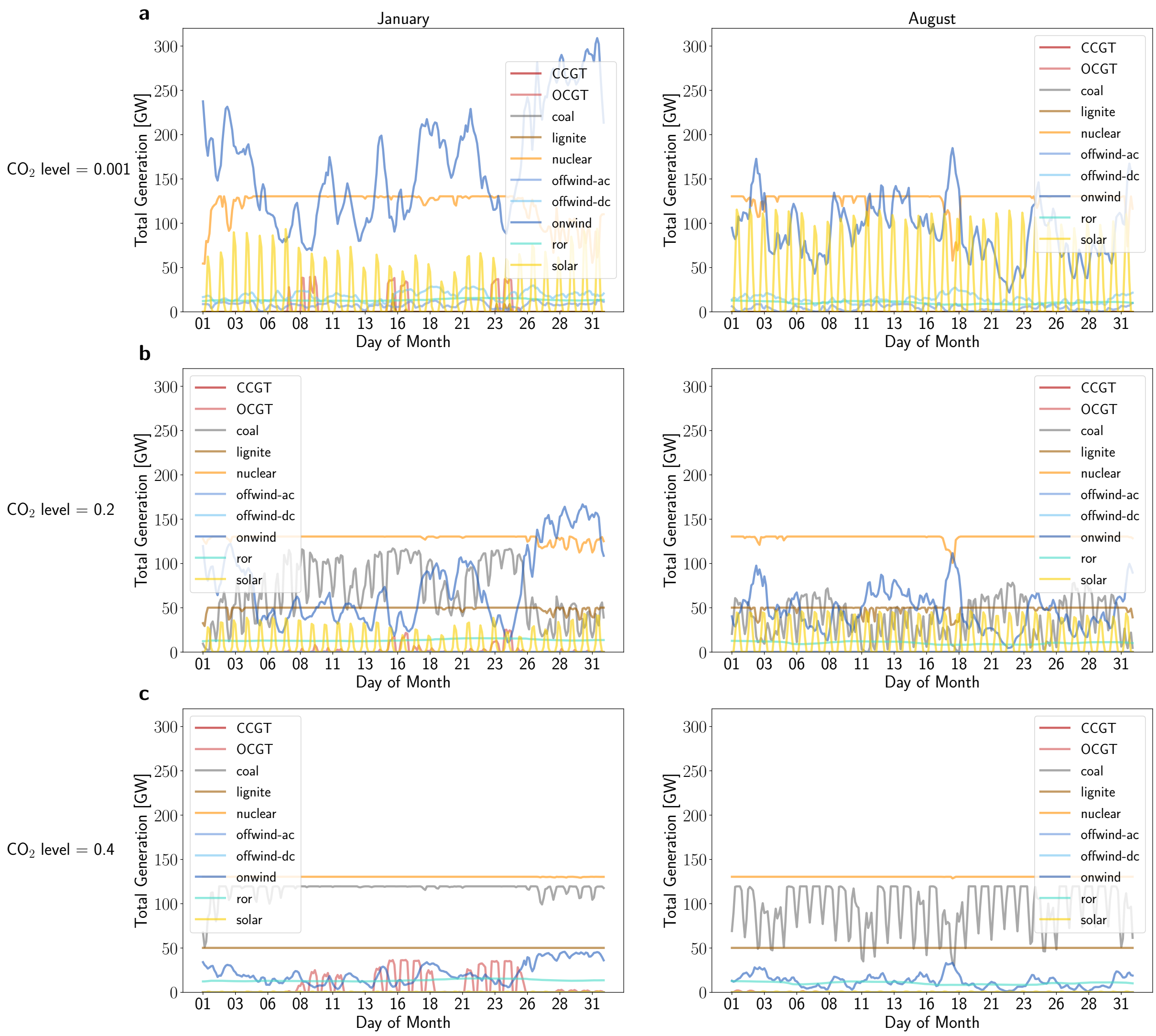

Supplementary Figure S2. **Total power generation in open energy system model by generator type for two exemplary months and different emission reduction levels.** (a) Total generation for January (left) and August (right) over time for the entire European grid obtained via transmission system optimisation using the open energy system model 'PyPSA-Eur' (see Methods). (b-c) We analyse different carbon-dioxide (CO_2) emission levels as compared to the emissions in the year 1990 where a CO_2 level of 0.4 corresponds to 40% of the emissions in 1990. With decreasing levels of CO_2 we observe an increased generation of renewable energy sources. In Figure S3 we show the corresponding aggregated generation on the network level.

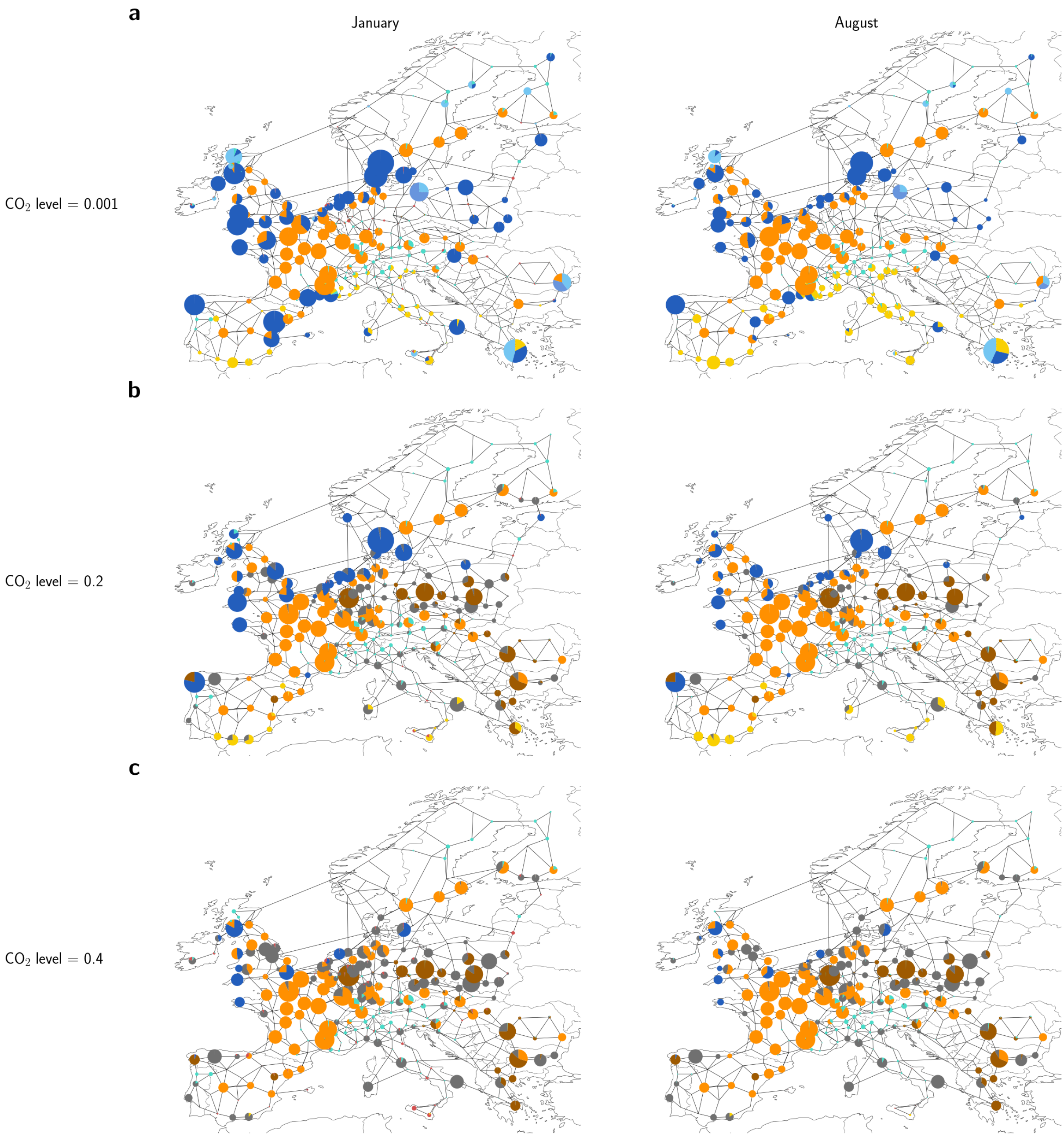

Supplementary Figure S3. **Total aggregated generation on the network level by generator type for two exemplary months and different emission reduction levels.** (a) Total aggregated generation for January (left) and August (right) for the entire European grid obtained via transmission system optimisation using the open energy system model 'PyPSA-Eur' (see Methods). (b-c) We analyse different carbon-dioxide (CO_2) emission levels as compared to the emissions in the year 1990 where a CO_2 level of 0.4 corresponds to 40% of the emissions in 1990. With decreasing levels of CO_2 we observe an increased generation of renewable energy sources. Colour code corresponds to the colour code in Figure S2.

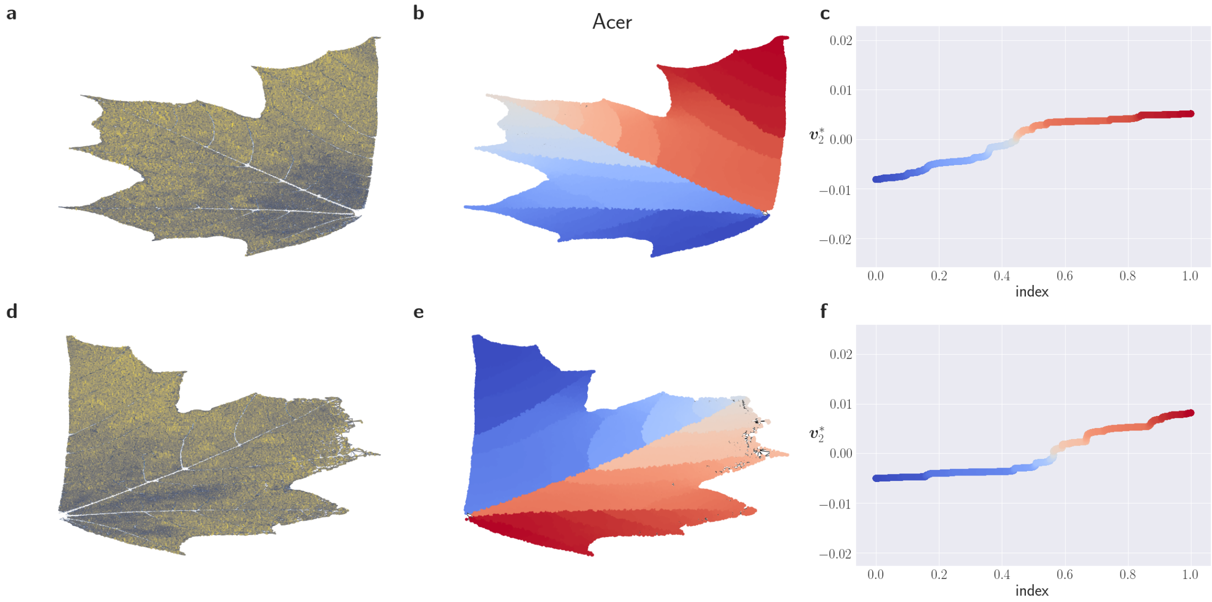

Supplementary Figure S4. **Dual community structure of an *Acer platanoides* leaf.** The leaf is divided into two dual communities using the method shown in Figure 1. (a,d) The two dual communities clearly show the venation network when plotting the dual graph with edge width proportional to the thickness of the dual veins. (b,e) Fiedler vector of the two communities reveals the finer network structure. (c.f) The resulting sorted dual Fiedler $\boldsymbol{v}_2^*$ vectors may be used to classify and distinguish leaves of different genera.

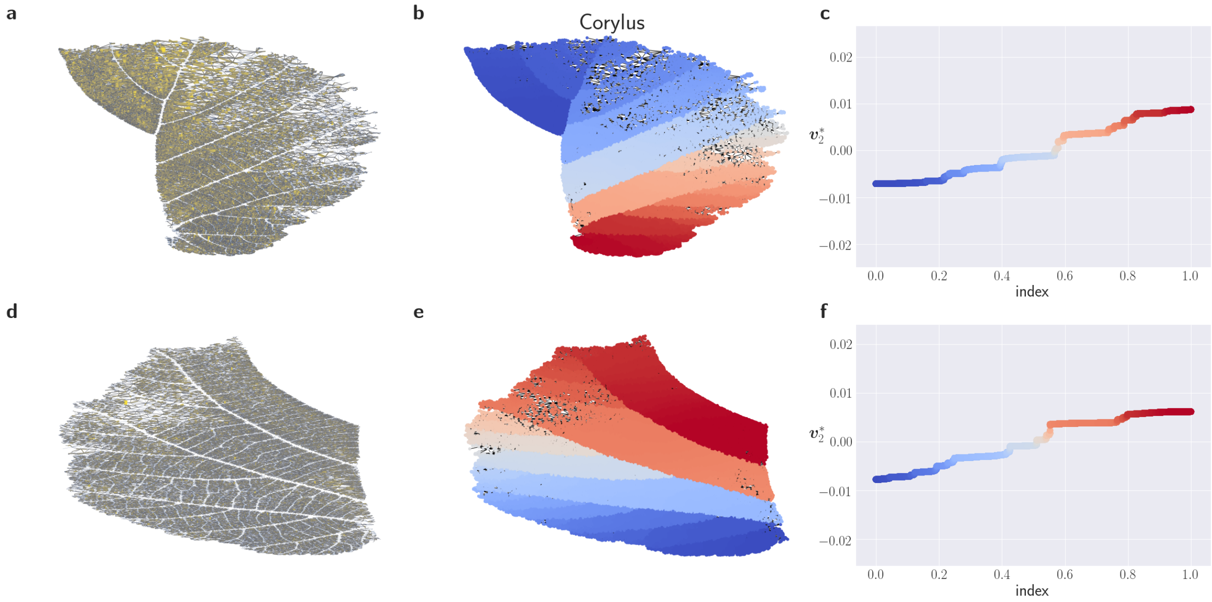

Supplementary Figure S5. **Dual community structure of an *Corylus avellana* leaf.** The leaf is divided into two dual communities using the method shown in Figure 1. (a,d) The two dual communities clearly show the venation network when plotting the dual graph with edge width proportional to the thickness of the dual veins. (b,e) Fiedler vector of the two communities reveals the finer network structure. (c.f) The resulting sorted dual Fiedler $\boldsymbol{v}_2^*$ vectors may be used to classify and distinguish leaves of different genera.

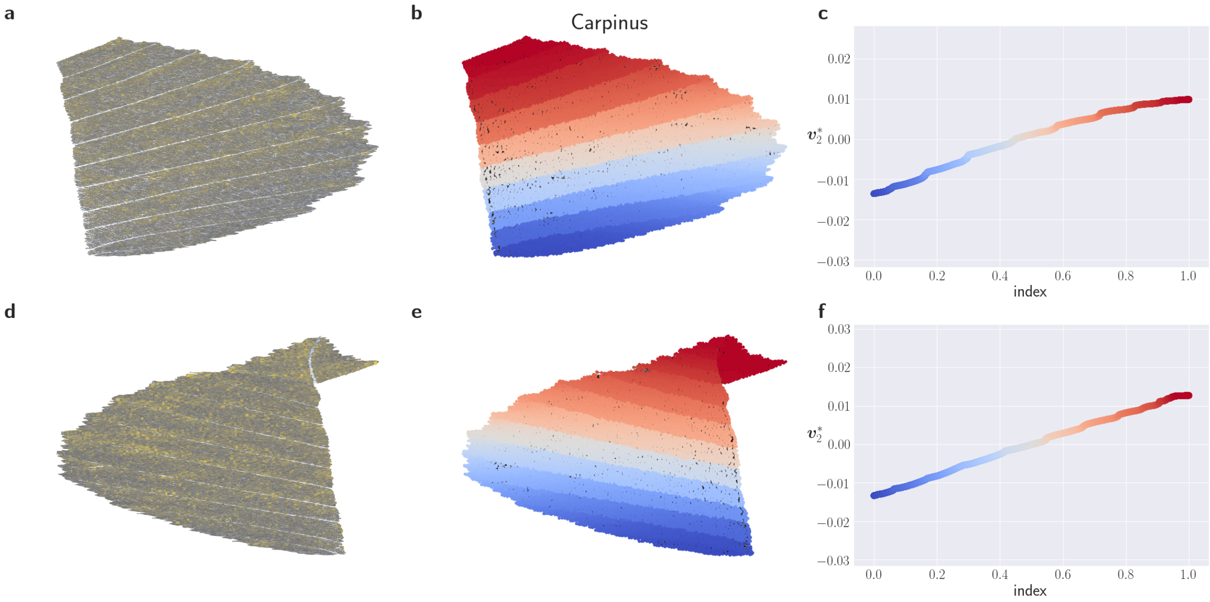

Supplementary Figure S6. **Dual community structure of an *Carpinus betulus* leaf.** The leaf is divided into two dual communities using the method shown in Figure 1. (a,d) The two dual communities clearly show the venation network when plotting the dual graph with edge width proportional to the thickness of the dual veins. (b,e) Fiedler vector of the two communities reveals the finer network structure. (c.f) The resulting sorted dual Fiedler $\boldsymbol{v}_2^*$ vectors may be used to classify and distinguish leaves of different genera.

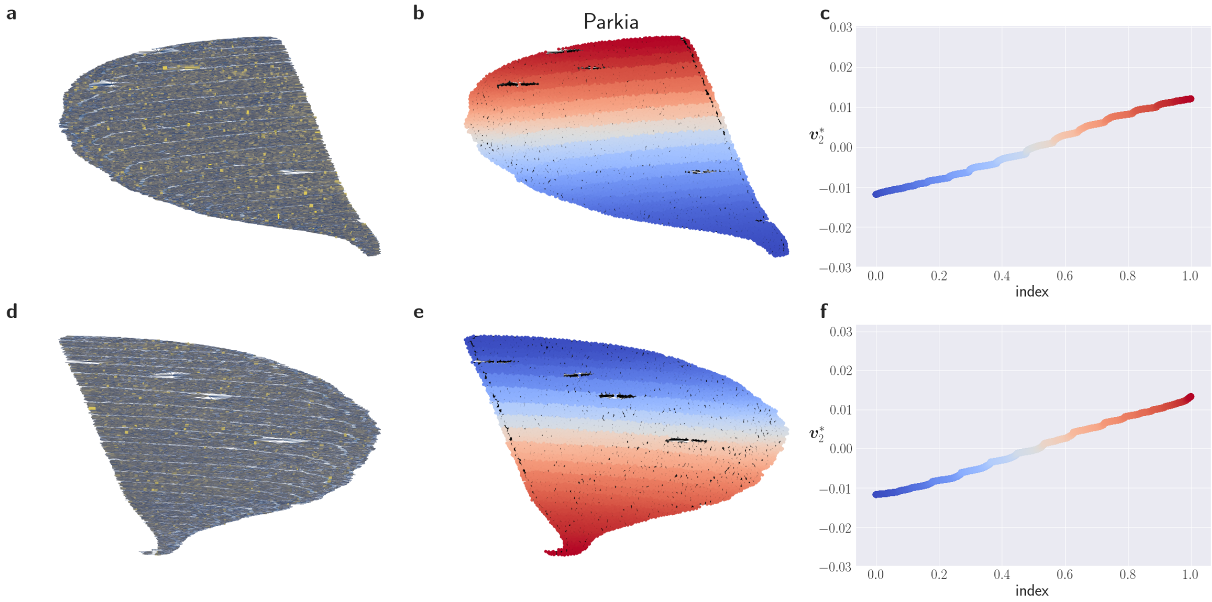

Supplementary Figure S7. **Dual community structure of an *Parkia nitida* leaf.** The leaf is divided into two dual communities using the method shown in Figure 1. (a,d) The two dual communities clearly show the venation network when plotting the dual graph with edge width proportional to the thickness of the dual veins. (b,e) Fiedler vector of the two communities reveals the finer network structure. (c.f) The resulting sorted dual Fiedler $\boldsymbol{v}_2^*$ vectors may be used to classify and distinguish leaves of different genera.

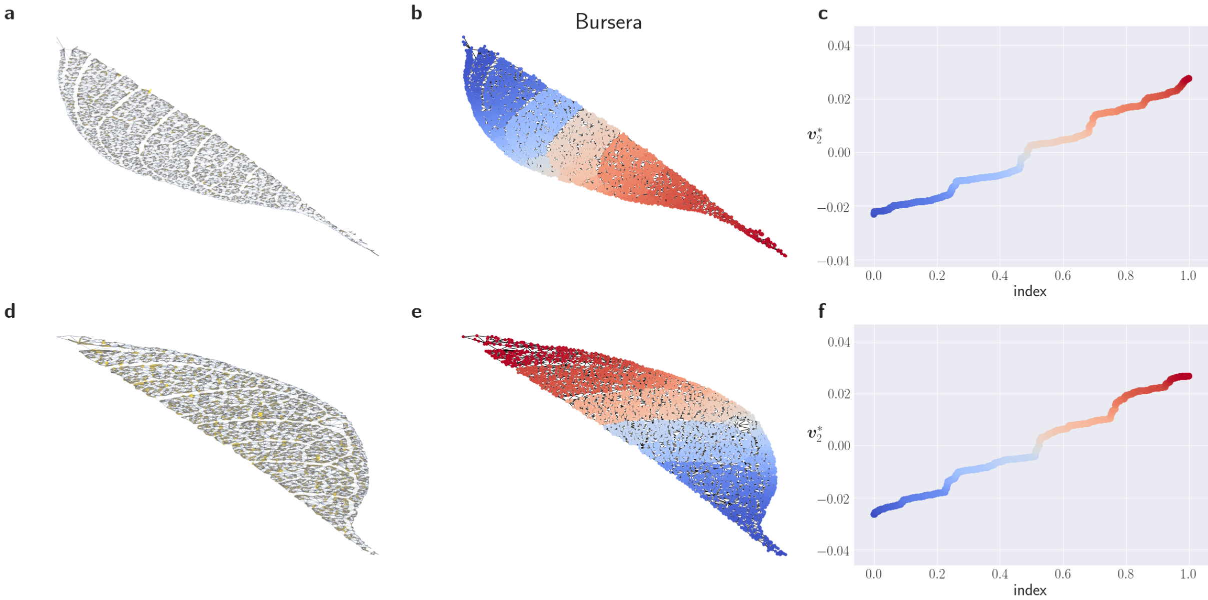

Supplementary Figure S8. **Dual community structure of an *Bursera simaruba* leaf.** The leaf is divided into two dual communities using the method shown in Figure 1. (a,d) The two dual communities clearly show the venation network when plotting the dual graph with edge width proportional to the thickness of the dual veins. (b,e) Fiedler vector of the two communities reveals the finer network structure. (c.f) The resulting sorted dual Fiedler $\boldsymbol{v}_2^*$ vectors may be used to classify and distinguish leaves of different genera.

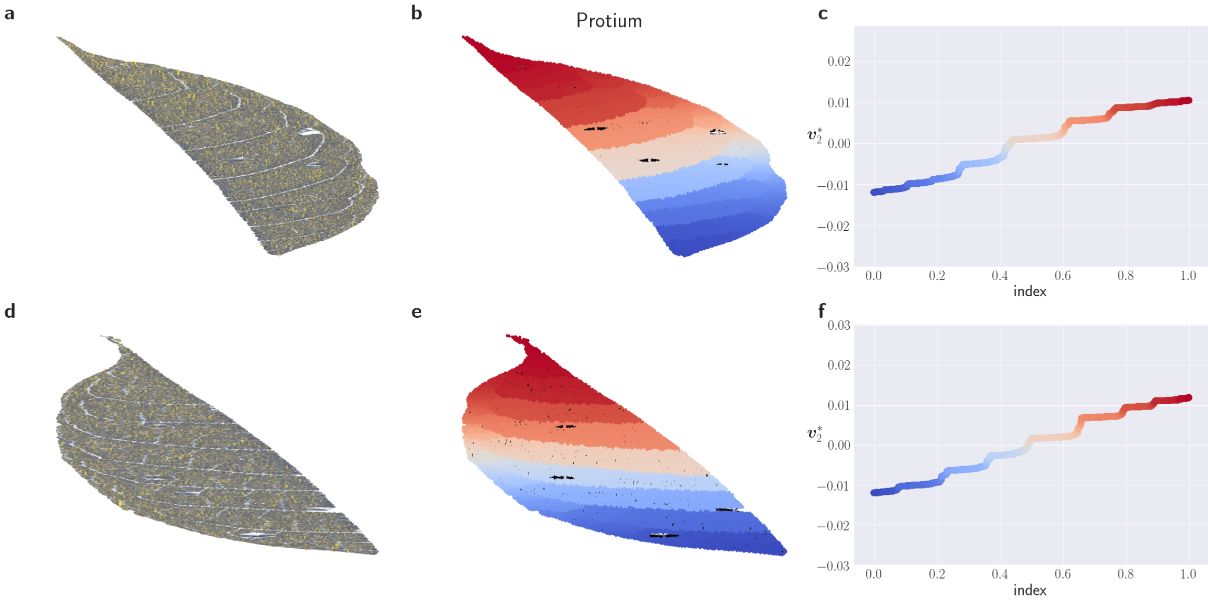

Supplementary Figure S9. **Dual community structure of an *Protium sp. nov. 8* leaf.** The leaf is divided into two dual communities using the method shown in Figure 1. (a,d) The two dual communities clearly show the venation network when plotting the dual graph with edge width proportional to the thickness of the dual veins. (b,e) Fiedler vector of the two communities reveals the finer network structure. (c.f) The resulting sorted dual Fiedler $\boldsymbol{v}_2^*$ vectors may be used to classify and distinguish leaves of different genera.

SUPPLEMENTARY METHODS

Linear flow networks

Linear flow networks describe a generic model for many types of supply networks including AC power grids [3–5], DC electric circuits [6–8], hydraulic networks [9, 10], and vascular networks of plants [1]. Assume that the underlying network is given by a simple graph $G = (E, V)$ with $N = |V|$ nodes and $M = |E|$ edges. Then we assign a potential $\theta_n \in \mathbb{R}$ to each node $n \in V$. This potential has the following interpretation: In AC power grids in the DC approximation, it denotes the voltage phase angle whereas in DC electric circuits, it refers to the voltage level at node n. Finally, in hydraulic or vascular networks, θ_n denotes the pressure at node n. Then the flow F_ℓ along a link $\ell = (m, n)$ is given by

$$F_\ell = w_\ell(\theta_m - \theta_n). \tag{1}$$

Here, w_ℓ is the weight of the link ℓ. In AC power grids, w_ℓ is proportional to the link's susceptance, in resistor networks it is given by the link's conductance and in a hydraulic or vascular network it depends on the geometry of the pipe or vein. Note that we assume that the weights are independent of the orientation of the link, i.e. $w_{\ell=(\ell_1,\ell_2)} = w_{\ell=(\ell_2,\ell_1)}$. Since this equation involves only phase differences, the potentials θ_n are only determined up to a constant phase shift applied to all nodes. This problem may be solved by assigning a reference potential to a preselected node n, e.g. setting $\theta_n := 0$.

Now assume that there is an inflow P_m at every node m. P_m is positive if a current, power, or fluid is injected to the node and negative if it is withdrawn from the node. The flows F_ℓ along the edges $\ell \in E$ may then determined using Kirchhoff's current law, the continuity equation,

$$\sum_{\ell \in E} \tilde{I}_{\ell,n} F_\ell = P_n, \qquad \forall\, n \in V. \tag{2}$$

Here, $\tilde{I}_{\ell,n}$ are the entries of the graph's unweighted edge-node incidence matrix which we use to assign an orientation to the graph's edges. The entries are given by [11]

$$\tilde{I}_{\ell,n} = \begin{cases} 1 & \text{if edge } \ell \text{ starts at node } n, \\ -1 & \text{if edge } \ell \text{ ends at node } n, \\ 0 & \text{otherwise.} \end{cases}$$

Note that in contrast to the definition of the weighted node-edge incidence matrix in Equation (2) in the main text, this definition does not explicitly include the weights of the edges. The potentials θ_n which fulfil the continuity equation (2) and the equation for the flows (1) automatically satisfy Kirchhoff's voltage law which states that the potential drop around any closed loop $\mathcal{C}$ needs to vanish

$$\sum_{(n,m) \in \mathcal{C}} \theta_n - \theta_m = 0. \tag{3}$$

Defining a vector of flows $\boldsymbol{F} = (F_1, .., F_L)^\top \in \mathbb{R}^M$, a vector of potentials $\boldsymbol{\theta} = (\theta_1, ..., \theta_N)^\top \in \mathbb{R}^N$ and a vector of inflows $\boldsymbol{P} = (P_1, ..., P_N)^\top \in \mathbb{R}^N$, we can write these relationships more compactly. Kirchhoff's current law (2) in vectorized form reads as

$$\tilde{\boldsymbol{I}}^\top \boldsymbol{F} = \boldsymbol{P}.$$

Here and in the following, we assume that the in- and outflows sum to zero, $\sum_i^N P_i = 0$, and call them 'balanced'. In addition to that, we can write the relationship between flows and potentials in vectorized form,

$$\boldsymbol{F} = \boldsymbol{W}\tilde{\boldsymbol{I}}\boldsymbol{\theta}. \tag{4}$$

Here, $\boldsymbol{W} = \mathrm{diag}(w_1, ..., w_L) \in \mathbb{R}^{M\times M}$ is a diagonal matrix summarising the edge weights. Now we can put together the last two Equations to arrive at a discrete Poisson equation for the nodal potentials

$$\boldsymbol{L}\boldsymbol{\theta} = \boldsymbol{P}. \tag{5}$$

Here, $\boldsymbol{L}$ is the Laplacian matrix (see Eq. (1)).

Quantifying the impact of perturbations - primal graph

We now use the notation developed in the last section to study the effect of links failures. In particular, we derive the expression for the sensitivity factor $\eta_{i,k,\ell}$ given in Equation (6) in the main text. Assume that we have an inflow ΔP at one node i and an outflow of the same amount at another node k. Then we can write the vector of changes in the inflows as

$$\boldsymbol{\Delta P} = \Delta P(\boldsymbol{e}_i - \boldsymbol{e}_k).$$

This causes a change in the nodal potentials $\boldsymbol{\theta}' = \boldsymbol{\theta} + \boldsymbol{\Delta\theta}$, where $\boldsymbol{\theta}'$ denotes the potentials after the change in inflows. The new potentials have to fulfill the Poisson equation (5), so we can subtract the Poisson equation in the for the potentials before and after the change in inflows to arrive at an explicit equation for the change in nodal potentials

$$\boldsymbol{L}\boldsymbol{\Delta\theta} = \Delta P(\boldsymbol{e}_i - \boldsymbol{e}_k).$$

Note that the Laplacian matrix of a connected graph always has one zero eigenvalue ([11]). Thus, we cannot simply invert this equation to calculate the change in the nodal potentials $\boldsymbol{\Delta\theta}$. This problem is typically solved by making use of the Moore-Penrose pseudoinverse of the Laplacian matrix $\boldsymbol{L}^\dagger$ which has properties similar to the matrix inverse [12].

Now we can use Kirchhoff's current law (2) to calculate the resulting changes in the flows

$$\boldsymbol{\Delta F} = \boldsymbol{W}\tilde{\boldsymbol{I}}\boldsymbol{L}^\dagger(\boldsymbol{e}_i - \boldsymbol{e}_k)\Delta P.$$

Finally, we can read off the change of the flow on line ℓ

$$\Delta F_\ell = \boldsymbol{l}_\ell^\top \boldsymbol{\Delta F} = w_\ell \boldsymbol{l}_\ell^\top \tilde{\boldsymbol{I}} \boldsymbol{L}^\dagger (\boldsymbol{e}_i - \boldsymbol{e}_k)\Delta P = \sqrt{w_\ell}\boldsymbol{l}_\ell^\top \boldsymbol{I} \boldsymbol{L}^\dagger (\boldsymbol{e}_i - \boldsymbol{e}_k)\Delta P := \eta_{i,k,\ell}\Delta P,$$
$$\Rightarrow \eta_{i,k,\ell} = \frac{\Delta F_\ell}{\Delta P} \tag{6}$$

where we inserted the weighted incidence matrix $\tilde{\boldsymbol{I}}$. Note that the sensitivity factor is purely topological, i.e. it may be calculated only based on the network topology and weights and does *not* depend on the in- and outflows. If the two nodes i and k are the terminal nodes of an edge $p = (i, k)$, we can identify

$$\boldsymbol{e}_i - \boldsymbol{e}_k = \tilde{\boldsymbol{I}}^\top \boldsymbol{l}_p,$$

where $\boldsymbol{l}_p$ is again the indicator vector of edge p, such that the above expression reduces to the expression appearing in the main text.

Quantifying the impact of perturbations - dual graph

The discussion of perturbations in the in- and outflows developed in the last section was recently extended to the dual graph [13, 14]. We will briefly cover this here and derive the dual expression for the sensitivity factor η. To this end, assume again that there is an inflow ΔP at one node i and an outflow of the same amount at another node k which results in a vector of inflows $\boldsymbol{\Delta P} = \Delta P(\boldsymbol{e}_i - \boldsymbol{e}_k)$. By subtracting Kirchhoff's current law (2) for the situation before and after the change in inflow, we arrive at

$$\tilde{\boldsymbol{I}}^\top \boldsymbol{\Delta F} = \Delta P(\boldsymbol{e}_i - \boldsymbol{e}_k),$$

which leaves us with is an underdetermined system of equations: We have $M - N + 1$ unknown flow changes ΔF_ℓ, but only N equations. We can solve this problem by using the duality relationship (4) in the main text. The kernel of the node-edge incidence matrix is spanned by the cycle-edge incidence matrix

$$\tilde{\boldsymbol{I}}^\top \tilde{\boldsymbol{C}} = 0,$$

where we defined the unweighted cycle-edge incidence matrix

$$\tilde{C}_{\ell c} = \begin{cases} 1 & \text{if edge } \ell \text{ is part of cycle } c, \\ -1 & \text{if reversed edge } \ell \text{ is part of cycle } c, \\ 0 & \text{otherwise.} \end{cases}$$

Thus, we can decompose the flow changes into a particular solution $\boldsymbol{\Delta F}_{\mathrm{part}} \in \mathbb{R}^M$ and a vector of cycle flows $\boldsymbol{f} \in \mathbb{R}^{M-N+1}$ - one for each cycle - such that

$$\boldsymbol{\Delta F} = \boldsymbol{\Delta F}_{\mathrm{part}} + \tilde{\boldsymbol{C}}\boldsymbol{f}. \tag{7}$$

Thus, there is an additional degree of freedom given by the cycle flows. To determine the cycle flows, we make use of Kirchhoff's voltage law (Eq. 3), which may be written compactly as

$$\begin{aligned} \tilde{\boldsymbol{C}}^\top \boldsymbol{I} \boldsymbol{\Delta\theta} &\stackrel{!}{=} 0, \\ \Leftrightarrow \quad \tilde{\boldsymbol{C}}^\top \boldsymbol{W}^{-1} \boldsymbol{\Delta F} &\stackrel{!}{=} 0, \\ \Rightarrow \quad \tilde{\boldsymbol{C}}^\top \boldsymbol{W}^{-1} \tilde{\boldsymbol{C}} \boldsymbol{f} &= -\tilde{\boldsymbol{C}}^\top \boldsymbol{W}^{-1} \boldsymbol{\Delta F}_{\mathrm{part}}, \\ \Leftrightarrow \quad \boldsymbol{L}^* \boldsymbol{f} &= -\tilde{\boldsymbol{C}}^\top \boldsymbol{W}^{-1} \boldsymbol{\Delta F}_{\mathrm{part}}, \end{aligned}$$

where we inserted the relationship (4) between potential changes $\boldsymbol{\Delta\theta}$ and flow changes in the second step and the definition of the dual Laplacian in the last step. We thus found a discrete Poisson equation for the cycle flows with the dual Laplacian $\boldsymbol{L}^*$ in direct correspondence to its primal counterpart (5). We can now proceed as for the primal graph: Inverting the discrete Poisson equation for the cycle flows and plugging the result into Eq. (7), we thus arrive at

$$\boldsymbol{\Delta F} = (\boldsymbol{1}_M - \tilde{\boldsymbol{C}} (\boldsymbol{L}^*)^\dagger \tilde{\boldsymbol{C}}^\top \boldsymbol{W}^{-1}) \boldsymbol{\Delta F}_{\mathrm{part}}.$$

Here, $\boldsymbol{1}_M$ denotes the identity matrix of dimensions $M \times M$. As a last step, we need to determine a particular solution $\boldsymbol{\Delta F}_{\mathrm{part}}$. This can be accomplished as follows [14]: Let $\mathcal{T}^{ik} \in \mathbb{R}^M$ be a vector determining an (arbitrary) path between the node i with inflow ΔP and node k with the same outflow. The entries of $\mathcal{T}^{ik}$ are given as follows

$$\mathcal{T}_e^{ik} = \begin{cases} 1 & \text{if edge } e \text{ is element of the path } i \to k, \\ -1 & \text{if reversed edge } e \text{ is element of the path } i \to k, \\ 0 & \text{otherwise.} \end{cases}$$

Then a particular solution is given by $\boldsymbol{\Delta F}_{\mathrm{part}} = \mathcal{T}^{ik} \Delta P$ and we can plug this into the above equation

$$\begin{aligned} \boldsymbol{\Delta F} &= (\boldsymbol{1}_M - \tilde{\boldsymbol{C}} (\boldsymbol{L}^*)^\dagger \tilde{\boldsymbol{C}}^\top \boldsymbol{W}^{-1}) \mathcal{T}^{ik} \Delta P, \\ \Rightarrow \Delta F_\ell = \boldsymbol{l}_\ell^\top \boldsymbol{\Delta F} &= \left(\boldsymbol{l}_\ell^\top \mathcal{T}^{ik} - \boldsymbol{l}_\ell^\top \tilde{\boldsymbol{C}} (\boldsymbol{L}^*)^\dagger \tilde{\boldsymbol{C}}^\top \boldsymbol{W}^{-1} \mathcal{T}^{ik} \right) \Delta P. \end{aligned}$$

If nodes i and k are the two terminal ends of an edge $e = (i, k) \neq \ell$, the path vector may be identified with the edge's indicator vector, $\mathcal{T}^{ik} = \mathbf{l}_e$. In this case, the above expression reads

$$\Delta F_\ell = -w_p^{-1} \boldsymbol{l}_\ell^\top \tilde{\boldsymbol{C}} (\boldsymbol{L}^*)^\dagger \tilde{\boldsymbol{C}}^\top \boldsymbol{l}_e \Delta P,$$

where the first expression vanishes since $\boldsymbol{l}_\ell^\top \boldsymbol{l}_e = \delta_{\ell e}$. Thus, we can identify the sensitivity factor $\eta_{i,k,\ell}$ as

$$\eta_{i,k,\ell} = -w_e^{-1} \boldsymbol{l}_\ell^\top \boldsymbol{C} (\boldsymbol{L}^*)^\dagger \boldsymbol{C}^\top \boldsymbol{l}_e = -\sqrt{\frac{w_\ell}{w_e}} \boldsymbol{l}_\ell^\top \boldsymbol{C} (\boldsymbol{L}^*)^\dagger \boldsymbol{C}^\top \boldsymbol{l}_e$$

Modelling link failures

The sensitivity factor $\eta_{i,k,\ell}$ may also be used to describe the failure of links. Assume that a link e fails, thus loosing its ability to carry flow and setting the weight to zero, $w_e = 0$. Instead of removing the link from the network, we can find an analogous description based on the sensitivity factor [3, 15].

Assume that the link $e = (e_1, e_2)$ carries a flow F_e before the outage. Now we model the removal of the link by an in- and outflow at the two ends of the link: To this end, we assume that the line was disconnected from the network and consider a fictious flow $\hat{F}_e$ which is the result of a (fictious) inflow $\Delta P = \hat{F}_e$ at the starting node e_1 and an outflow of the same amount at the terminal node e_2 of link e. On the other hand, we can also calculate the flow $\hat{F}_e$ flowing on line e after the injection by a self-consistency argument: It can be calculated using the sensitivity factor

$$\begin{aligned} \hat{F}_e &= F_e + \eta_{e_1,e_2,e}\Delta P = F_e + \eta_{e_1,e_2,e}\hat{F}_e \\ \Rightarrow \Delta P &= \hat{F}_e = F_e(1 - \eta_{e_1,e_2,e})^{-1}. \end{aligned}$$

Now we can calculate the change in the flow on another link ℓ due to the failure of link e as

$$\Delta F_\ell = \eta_{e_1,e_2,\ell}\Delta P = \frac{\eta_{e_1,e_2,\ell}}{1 - \eta_{e_1,e_2,e}} F_e.$$

We can thus calculate the flow change ΔF_ℓ on any link ℓ due to the failure of another link e based on the initial flow on link e and the sensitivity factor η. The fraction appearing here $\eta_{e_1,e_2,\ell}(1 - \eta_{e_1,e_2,e})^{-1}$ is known as *Line Outage Distribution Factor* in power system security analysis [3].

Thus both, link failures and changes in the inflows can be captured by the sensitivity factor. To quantify the effect of (dual) communities on network robustness in linear flow networks we defined the ratio of flow changes in the main text (see Ref. [16]),

$$R(\ell, d) = \frac{\langle |\Delta F_k| \rangle_d^{k \in \mathrm{O}}}{\langle |\Delta F_r| \rangle_d^{r \in \mathrm{S}}}.$$

Importantly, the ratio can be used to quantify both, the community effect on changes in the inflow patterns and the community effect on failure spreading. For an inflow and outflow of ΔP at the two terminal ends of the link ℓ, ℓ_1 and ℓ_2, respectively, the ratio is calculated as

$$R(\ell, d) = \frac{\langle |\Delta F_k| \rangle_d^{k \in \mathrm{O}}}{\langle |\Delta F_r| \rangle_d^{r \in \mathrm{S}}} = \frac{\langle |\eta_{\ell_1,\ell_2,k}\Delta P| \rangle_d^{k \in \mathrm{O}}}{\langle |\eta_{\ell_1,\ell_2,r}\Delta P| \rangle_d^{r \in \mathrm{S}}} = \frac{\langle |\eta_{\ell_1,\ell_2,k}| \rangle_d^{k \in \mathrm{O}}}{\langle |\eta_{\ell_1,\ell_2,r}| \rangle_d^{r \in \mathrm{S}}}.$$

On the other hand, if we instead calculate the ratio for the failure of a link ℓ with initial flow F_ℓ, we arrive at

$$R(\ell, d) = \frac{\langle |\Delta F_k| \rangle_d^{k \in \mathrm{O}}}{\langle |\Delta F_r| \rangle_d^{r \in \mathrm{S}}} = \frac{\langle |\eta_{\ell_1,\ell_2,k}(1 - \eta_{\ell_1,\ell_2,\ell})^{-1} F_\ell| \rangle_d^{k \in \mathrm{O}}}{\langle |\eta_{\ell_1,\ell_2,r}(1 - \eta_{\ell_1,\ell_2,\ell})^{-1} F_\ell| \rangle_d^{r \in \mathrm{S}}} = \frac{\langle |\eta_{\ell_1,\ell_2,k}| \rangle_d^{k \in \mathrm{O}}}{\langle |\eta_{\ell_1,\ell_2,r}| \rangle_d^{r \in \mathrm{S}}}. \tag{8}$$

Thus, in both cases, the ratio is determined by the sensitivity factor η which is in turn governed by the Pseudo-inverse of the Laplacian matrix $\boldsymbol{L}^\dagger$ or the Pseudo-inverse of the dual Laplacian $(\boldsymbol{L}^*)^\dagger$ when formulating the problem in the dual graph.

Connectivity structure determines network response to link failures

In this section, we will demonstrate why a weak connection between two components of a network limits the flow changes in one component when a link in the other one fails. Our analysis follows the approach towards perturbation spreading used in Manik et al. [17, 18] that is based on Rayleigh-Schrödinger perturbation theory [19].

Perturbation theory reveals scaling of flow changes after failures with connectivity

Consider a connected graph $G = (E, V)$ with N nodes and L edges consisting of two subgraphs $G_1 = (E_1, V_1)$ and $G_2 = (E_2, V_2)$ with n_1 nodes and $n_2 = N - n_1$ nodes, respectively, that are mutually weakly connected. Here, a weak connection between the two subgraphs may either be realised through a (relatively) weak number of links in case of an unweighted graph or the overall weight of the connections between the two subgraphs being small [20]. We then sort the graph's vertices V in such a way that the first n_1 vertices belong to the first subgraph G_1 and the other n_2 vertices belong to the second one G_2. We may regard the weak connections between the to subgraphs as a perturbation to the graph in which the two subgraphs are disconnected. In terms of the graph Laplacian $\boldsymbol{L}$, we thus write

$$\boldsymbol{L} = \boldsymbol{L}_0 + \tilde{\boldsymbol{L}} = \begin{pmatrix} \boldsymbol{L}_1 & \mathbf{0}_{n_1 \times n_2} \\ \mathbf{0}_{n_2 \times n_1} & \boldsymbol{L}_2 \end{pmatrix} + \begin{pmatrix} \boldsymbol{D}_{12} & -\boldsymbol{A}_{12} \\ -\boldsymbol{A}_{12}^\top & \boldsymbol{D}_{21} \end{pmatrix}.$$

Here, $\boldsymbol{L}_0$ is the graph Laplacian for the graph when disconnecting the two subgraphs, expressed in terms of their Laplacian matrices $\boldsymbol{L}_1 \in \mathbb{R}^{n_1 \times n_1}$ and $\boldsymbol{L}_2 \in \mathbb{R}^{n_2 \times n_2}$ and $\tilde{\boldsymbol{L}}$ is the perturbation matrix with the diagonal degree matrices $\boldsymbol{D}_{12}$ and $\boldsymbol{D}_{21}$ denoting the degree for the graph connecting the two subgraphs. $\boldsymbol{A}_{12}$ is the adjacency matrix for this graph that is assumed to be relatively sparse, thus indicating the weak inter-subgraph connections.

To examine the effect of link failures, we need to study the pseudoinverse of this matrix. Therefore, we denote by $\boldsymbol{X} = \boldsymbol{L}^\dagger$ the Moore-Penrose pseudoinverse of the overall graph Laplacian and by $\boldsymbol{X}_1 = \boldsymbol{L}_1^\dagger$ and $\boldsymbol{X}_2 = \boldsymbol{L}_2^\dagger$ the Moore-Penrose pseudoinverses of the subgraphs' Laplacian matrices $\boldsymbol{L}_1$ and $\boldsymbol{L}_2$, respectively. For the inverse $\boldsymbol{X}_0$ of the unperturbed Laplacian $\boldsymbol{L}_0$, we then get

$$\boldsymbol{X}_0 = \begin{pmatrix} \boldsymbol{X}_1 & \mathbf{0}_{n_1 \times n_2} \\ \mathbf{0}_{n_2 \times n_1} & \boldsymbol{X}_2 \end{pmatrix}.$$

In order to calculate the matrix inverse $\boldsymbol{X}$, we can expand this matrix using the Neumann series (see e.g. Ref. [21]) [22]

$$\begin{aligned}\boldsymbol{X} &= (\boldsymbol{L}_0 + \tilde{\boldsymbol{L}})^\dagger = \left[\boldsymbol{L}_0\left(\boldsymbol{1} + \boldsymbol{X}_0\tilde{\boldsymbol{L}}\right)\right]^\dagger = \left[\left(\boldsymbol{1} + \tilde{\boldsymbol{L}}\boldsymbol{X}_0\right)\boldsymbol{L}_0\right]^\dagger \\ &= \boldsymbol{X}_0\left[\left(\boldsymbol{1} - (-\boldsymbol{X}_0\tilde{\boldsymbol{L}})\right)\right]^\dagger = \boldsymbol{X}_0\sum_{k=1}^{\infty}(-1)^k(\tilde{\boldsymbol{L}}\boldsymbol{X}_0)^k,\end{aligned}$$

where we inserted the Neumann series in the last step. We can thus approximate the matrix inverse of the graph Laplacian as

$$\boldsymbol{X} = \boldsymbol{X}_0 - \boldsymbol{X}_0\tilde{\boldsymbol{L}}\boldsymbol{X}_0 + \mathcal{O}(\tilde{\boldsymbol{L}}^2),$$

where $\mathcal{O}(\tilde{\boldsymbol{L}}^2)$ denotes terms of at least order two in the perturbation matrix $\tilde{\boldsymbol{L}}$.

Now we can use these expressions to calculate a first order approximation for the sensitivity factor $\eta_{i,k,\ell}$ in the weakly connected limit. Assume we are monitoring the flow changes on line l with indicator vector $\vec{\nu}_\ell = \boldsymbol{I}\cdot\vec{l}_\ell = \vec{e}_{\ell_1} - \vec{e}_{\ell_2}$ as a result of a power transfer along line $k = (k_1, k_2)$ with indicator vector $\vec{\nu}_k$. We can then calculate the sensitivity factor as

$$\eta_{k_1,k_2,\ell} = w_\ell\vec{\nu}_\ell^\top\boldsymbol{X}\vec{\nu}_k.$$

Now we distinguish two cases; First assume that ℓ and k are contained in the same subgraph, say G_1. In this case, we can write with slight abuse of notation $\vec{\nu}_\ell = (\hat{\vec{\nu}}_\ell, \vec{0}_{n_2})^\top$ and $\vec{\nu}_k = (\hat{\vec{\nu}}_k, \vec{0}_{n_2})^\top$, where $\hat{\vec{\nu}}_l$ denotes the projection of the vector onto the subspace of vertices the first subgraph G_1 and the whole vector $\vec{\nu}_\ell$ is still understood as a vector in $GF(2)^N$. In this case, we may write the sensitivity factor as

$$\eta_{k_1,k_2,\ell} = w_\ell(\hat{\vec{\nu}}_\ell^\top, \vec{0}_{n_2}^\top)\boldsymbol{X}\begin{pmatrix}\hat{\vec{\nu}}_k \\ \vec{0}_{n_2}\end{pmatrix} = w_\ell\hat{\vec{\nu}}_\ell^\top\boldsymbol{X}_1\hat{\vec{\nu}}_k + \mathcal{O}(\tilde{\boldsymbol{L}}). \tag{9}$$

Now consider the case where ℓ and k are contained in different modules of the network. In this case, we may write $\vec{\nu}_\ell = (\hat{\vec{\nu}}_\ell, \vec{0}_{n_2})^\top$ and $\vec{\nu}_k = (\vec{0}_{n_1}, \hat{\vec{\nu}}_k)^\top$ and calculate the sensitivity factor as

$$\begin{aligned}\eta_{k_1,k_2,\ell} &= w_\ell(\hat{\vec{\nu}}_\ell^\top, \vec{0}_{n_2}^\top)\boldsymbol{X}\begin{pmatrix}\vec{0}_{n_1} \\ \hat{\vec{\nu}}_k\end{pmatrix} \\ &= w_\ell(\hat{\vec{\nu}}_\ell^\top, \vec{0}_{n_2}^\top)\left[\boldsymbol{X}_0 + \boldsymbol{X}_0\tilde{\boldsymbol{L}}\boldsymbol{X}_0\right]\begin{pmatrix}\vec{0}_{n_1} \\ \hat{\vec{\nu}}_k\end{pmatrix} + \mathcal{O}(\tilde{\boldsymbol{L}}^2) \\ &= w_\ell\left[0 + (\hat{\vec{\nu}}_\ell^\top\boldsymbol{X}_1, \vec{0}_{n_2}^\top)\tilde{\boldsymbol{L}}\begin{pmatrix}\vec{0}_{n_1} \\ \boldsymbol{X}_2\hat{\vec{\nu}}_k\end{pmatrix}\right] + \mathcal{O}(\tilde{\boldsymbol{L}}^2).\end{aligned}$$

We thus observe that the leading order contribution of the perturbation matrix to the sensitivity factor is $\tilde{\boldsymbol{L}}^0$ if both links are contained in the same module and $\tilde{\boldsymbol{L}}^1$ if they are contained in different modules.

Now we compare this to the scaling of Laplacian eigenvalues with the perturbation matrix. The first eigenvector of $\boldsymbol{L}_0$ is given by the constant shift $\vec{v}_1 = N^{-1/2}\vec{1}_N$ and has eigenalue $\lambda_1 = 0$. In the weakly connected limit considering only $\boldsymbol{L}_0$, the Fiedler eigenvalue vanishes as well $\lambda_2^{(0)} = 0$, and has an associated eigenvector [17]

$$\vec{v}_2^{(0)} = N^{-1/2}(\underbrace{\sqrt{n_2/n_1}, ..., \sqrt{n_2/n_1}}_{n_1 \text{ times}}, \underbrace{-\sqrt{n_1/n_2}, ..., -\sqrt{n_1/n_2}}_{n_2 \text{ times}})^\top.$$

Here, we use the superscript (0) to denote the eigenvector and eigenvalue in the unberturbed case. A first order estimate for the Fiedler value may thus be calculated by using Rayleigh Schrödinger perturbation theory as

$$\lambda_2^{(1)} = (\vec{v}_2^{(0)})^\top \tilde{\boldsymbol{L}} \vec{v}_2^{(0)} + \mathcal{O}(\tilde{\boldsymbol{L}}^2). \tag{10}$$

For weakly connected graphs, we thus expect the sensitivity factor $\eta_{\ell_1,\ell_2,k}$ to scale with the connectivity of the graph in the same way as the Fiedler value of the graph if l and k lie in different communities due to the fact that $\lambda_2^{(1)} \propto \tilde{\boldsymbol{L}}$ and expect it to be to leading order independent of the Fiedler value if l and k are in the same community.

Flow ratio scales with increasing connectivity between weakly connected modules

In the main part of the manuscript, we consider the ratio $R(\ell, d)$ between the flow changes within the other community ΔF^{O} and the flow changes in the same community ΔF^{S} after a link failure. It is well established that the flow changes typically decay with distance to the failing link [15, 23–25]. To be able to neglect this effect on the flow changes, we take the average absolute flow changes at a fixed distance d denoted by $\langle |\Delta F_{i\to j}|\rangle_d^{(i,j)\in \mathrm{S}}$ for the same community and $\langle |\Delta F_{i\to j}|\rangle_d^{(i,j)\in \mathrm{O}}$ for the other community where we average over all edges $\ell = (i, j)$ within the respective community that are located at an unweighted edge distance of d to the failing link. With this formalism at hand, we can now estimate the scaling of this ratio with the strength of the perturbation. Suppose that link $k = (r, s)$ is failing. Then the flow ratio reads (cf. Eq. (8))

$$R(\ell, d) = \frac{\langle |\eta_{\ell_1,\ell_2,k}|\rangle_d^{k\in \mathrm{O}}}{\langle |\eta_{\ell_1,\ell_2,r}|\rangle_d^{r\in \mathrm{S}}}.$$

Now we can make use of our results on the scaling of the sensitivity factors with increasing connectivity between the subnetworks. From Eqs. (9) and, (10) we see that this ratio scales with the first order of the perturbation

$$
\begin{aligned}
R(\ell, d) &= \frac{\left\langle \left| w_\ell (\hat{\vec{\nu}}_\ell^\top \boldsymbol{X}_1, \vec{0}_{n_2}^\top) \tilde{\boldsymbol{L}} \begin{pmatrix} \vec{0}_{n_1} \\ \boldsymbol{X}_2 \hat{\vec{\nu}}_k \end{pmatrix} \right| \right\rangle_d^{k=(i,j)\in \mathrm{O}} + \mathcal{O}(\tilde{\boldsymbol{L}}^2)}{\left\langle \left| w_\ell \hat{\vec{\nu}}_\ell^\top \boldsymbol{X}_1 \hat{\vec{\nu}}_r \right| \right\rangle_d^{r=(p,q)\in \mathrm{S}} + \mathcal{O}(\tilde{\boldsymbol{L}})} \\
\Rightarrow & R \propto \tilde{\boldsymbol{L}} + \mathcal{O}(\tilde{\boldsymbol{L}}^2)
\end{aligned}
$$

in the weakly connected limit assuming without loss of generality that the failing link is located in the first subgraph G_1, $\ell \in E(G_1)$. Since we deduced in Eq. (10) that the Fiedler value scales with the perturbation in the first order as well, we expect the two quantities to show a similar scaling with the perturbation matrix $\tilde{\boldsymbol{L}}$.

Note that the derivation works exactly the same way for the dual graph G^* and dual Fiedler value λ_2^*: We simply have to replace the sensitivity factor $\eta_{\ell_1,\ell_2,k}$ by its dual representation.

Fluctuating sink model with additive Dirichlet noise

We will first briefly cover the fluctuating sink model and then explain our modification to it. We will use the model analysed by Corson [2]. Consider a linear flow network on a graph G with N nodes and M edges summarized in the node set V and edge set E. Then we choose one vertex to be the source of the network while all the others are sinks and order all nodes such that the source node has the first index w.l.o.g. We assume the sinks to be uncorrelated, iid Gaussian variables $P_i \sim \mathcal{N}(\mu, \sigma),\ i \in \{2, ..., N\}$ which fluctuate in time and that sources and sinks have to balance at any point in time such that

$$\sum_{i=1}^{N} P_i = 0. \tag{11}$$

This equation immediately yields the statistical properties of the source as a consequence of the statistics of the sinks

$$\langle P_1 \rangle = -(N-1)\mu,$$

where $\langle \cdot \rangle$ denotes the mean over different realisations of the Gaussian variables.

For a given topology, we then seeks to find the link weights w_ℓ that minimise the average dissipation

$$\langle D \rangle = \sum_{\ell=1}^{M} \frac{\langle F_\ell^2 \rangle}{w_\ell}.$$

Here, $\langle F_\ell^2 \rangle$ is the second moment of the flows which are determined by the statistics of the sources and sinks by virtue of the continuity equation (2). However, we assume that our budget for constructing or strengthening edges is limited: there is a resource constraint which limits the overall available edge weights and needs to be taken into account when minimsing the dissipation

$$\sum_{\ell \in E} w_\ell^\gamma = 1.$$

Here, γ is a cost parameter that controls how expensive it is to increase the weight of an edge. The main challenge when performing the minimisation is the interdependence between link weights and flows which cannot be varied independently. Corson [2] and Katifori et al [1] independently came up with a procedure to identify edge weights that locally minimise the network dissipation by using the method of Lagrange multipliers. Starting from random edge weights that satisfy the resource constraint, the optimal edge weights have to satisfy

$$w_\ell = \frac{\langle F_\ell^2 \rangle^{1/(1+\gamma)}}{\left(\sum_{e \in E} \langle F_e^2 \rangle^{\gamma/(1+\gamma)}\right)^{1/\gamma}}.$$

Then, the locally minimal edge weights can be found by iteratively updating the edge weights based on this formula and then the flows they result in until no further changes occur.

Now we extend this set-up to a network with multiple sources. Assume that we again label the nodes such that the first N_s nodes are sources and the remaining $N - N_s$ nodes sinks, which are still uncorrelated, iid Gaussian variables. However, when considering more than one source, $N_s > 1$, the distribution of the sources is not completely determined by Equation (11), but has additional degrees of freedom - in contrast to the case of a single source. We use this degree of freedom to put additive Dirichlet noise $X_i \sim \mathrm{Dir}(\alpha)$ on the sources. Since in- and outflow match at any point in time, we have

$$\sum_{i=1}^{N_s} P_i = -\sum_{j=N_s+1}^{N} P_j. \tag{12}$$

We thus have the following set of equations:

$$\sum_{i=1}^{N_s} \mu_{s_i} = (N - N_s)\mu$$

and

$$\begin{aligned}
\sum_{i=1}^{N_s} \langle P_i P_j \rangle &= -\sum_{i=N_s+1}^{N} \langle P_i P_j \rangle \\
&= -(N - N_s)\mu^2 - \sigma^2, \quad \text{if } j > N_s, \\
\sum_{i=1}^{N_s} \langle P_i P_j \rangle &= -\sum_{i=N_s+1}^{N} \langle P_i P_j \rangle \quad \text{if } j \leq N_s,
\end{aligned}$$

where the equalities follow from Eq. 12 and the fact that the variables are uncorrelated. Now assume that we model the sources as iid Gaussian variables $P_{s_i} \sim \mathcal{N}(\mu_s, \sigma_s)$, as above, but now add Dirichlet noise with identical parameter α

$$P_{s_i} = -\frac{1}{N_s} \sum_{i=N_s+1}^{N} P_i + K\left(\frac{1}{N_s} - X_i\right), \quad X_i \sim \mathrm{Dir}(\alpha).$$

Here, $K \in \mathbb{R}$ is a scaling parameter. Then we can calculate the mean and variance of the Gaussian distribution governing the sources as

$$\mu_s = \frac{N - N_s}{N_s}\mu, \quad \sigma_s^2 = \frac{N - N_s}{N_s}\sigma^2,$$

as follows from plugging the expression for P_{s_i} into the above equations. Importantly, the Dirichlet variables sum to unity $\sum_{i=1}^{N_s} X_i = 1$ at any point in time. Therefore, they have the mean

$$\langle X_i \rangle = \frac{1}{N_s}$$

and second moment

$$\langle X_i^2 \rangle = \frac{(N_s - 1)}{N_s^2(N_s\alpha + 1)} + \frac{1}{N_s^2}$$

and are correlated with the following correlation

$$\langle X_i X_j \rangle = -\frac{1}{N_s^2(N_s\alpha + 1)} + \frac{1}{N_s^2}.$$

Note that this results in a vanishing sum over the second moments

$$\sum_{i=1}^{N_s} \langle X_i X_j \rangle = 0,$$

by virtue of the definition of the Dirichlet parameter and the first equation. Now we can shift to new random variables $Y_i = K\left(\frac{1}{N_s} - X_i\right)$ with zero mean, $\langle Y_i \rangle = 0$, and the following second moments

$$\begin{aligned}
\langle Y_i Y_j \rangle &= K^2 \left\langle \left(\frac{1}{N_s} - X_i\right)\left(\frac{1}{N_s} - X_j\right) \right\rangle \\
&= K^2 \left(-\frac{1}{N_s^2} + \langle X_i X_j \rangle\right) \\
&= -K^2 \frac{1}{N_s^2(N_s\alpha + 1)}, \quad i \neq j, \\
\langle Y_i^2 \rangle &= K^2 \left\langle \left(\frac{1}{N_s} - X_i\right)^2 \right\rangle = K^2 \frac{(N_s - 1)}{N_s^2(N_s\alpha + 1)}
\end{aligned}$$

such that the sum over the second moment still vanishes $\sum_{i=1}^{N_s} \langle Y_i Y_j \rangle = 0$.

Thus, using the Dirichlet noise, we can tune the variance of the sources without affecting the statistics of the sinks or the fact that the sources and sinks have to balance at any point in time (Eq. (11)).

[1] E. Katifori, G. J. Szöllősi, and M. O. Magnasco, Damage and fluctuations induce loops in optimal transport networks, Phys. Rev. Lett. **104**, 048704 (2010).

[2] F. Corson, Fluctuations and Redundancy in Optimal Transport Networks, Physical Review Letters **104**, 048703 (2010).

[3] A. J. Wood, B. F. Wollenberg, and G. B. Sheblé, *Power Generation, Operation and Control* (John Wiley & Sons, New York, 2014).

[4] K. Purchala, L. Meeus, D. V. Dommelen, and R. Belmans, Usefulness of dc power flow for active power flow analysis, in *IEEE Power Engineering Society General Meeting* (2005) pp. 454–459 Vol. 1.

[5] D. Van Hertem, J. Verboomen, K. Purchala, R. Belmans, and W. Kling, Usefulness of dc power flow for active power flow analysis with flow controlling devices, in *The 8th IEEE International Conference on AC and DC Power Transmission* (2006) pp. 58–62.

[6] B. Bollobás, *Modern graph theory*, Graduate texts in mathematics No. 184 (Springer, 1998).

[7] F. Dörfler, J. W. Simpson-Porco, and F. Bullo, Electrical networks and algebraic graph theory: Models, properties, and applications, Proceedings of the IEEE **106**, 977 (2018).

[8] G. Kirchhoff, Ueber die Auflösung der Gleichungen, auf welche man bei der Untersuchung der linearen Vertheilung galvanischer Ströme geführt wird, Annalen der Physik **148**, 497 (1847).

[9] N. Hwang and R. Houghtalen, *Fundamentals of Hydraulic Engineering Systems* (Prentice Hall, Upper Saddle River, NJ, 1996).

[10] S. Díaz, J. González, and R. Mínguez, Observability analysis in water transport networks: Algebraic approach, Journal of Water Resources Planning and Management **142**, 04015071 (2016).

[11] M. E. J. Newman, *Networks: an introduction* (Oxford University Press, 2010).

[12] E. H. Moore, On the reciprocal of the general algebraic matrix, Bull. Amer. Math. Soc. **26**, 394 (1920).

[13] H. Ronellenfitsch, D. Manik, J. Hörsch, T. Brown, and D. Witthaut, Dual theory of transmission line outages, IEEE Transactions on Power Systems **32**, 4060 (2017).

[14] H. Ronellenfitsch, M. Timme, and D. Witthaut, A dual method for computing power transfer distribution factors, IEEE Transactions on Power Systems **32**, 1007 (2017).

[15] J. Strake, F. Kaiser, F. Basiri, H. Ronellenfitsch, and D. Witthaut, Non-local impact of link failures in linear flow networks, New Journal of Physics **21**, 053009 (2019).

[16] F. Kaiser, V. Latora, and D. Witthaut, Inhibiting failure spreading in complex networks, arXiv:2009.02910 (2020).

[17] D. Manik, M. Rohden, H. Ronellenfitsch, X. Zhang, S. Hallerberg, D. Witthaut, and M. Timme, Network susceptibilities: Theory and applications, Physical Review E **95**, 10.1103/PhysRevE.95.012319 (2017).

[18] D. Witthaut, M. Rohden, X. Zhang, S. Hallerberg, and M. Timme, Critical links and nonlocal rerouting in complex supply networks, Phys. Rev. Lett. **116**, 138701 (2016).

[19] L. E. Ballentine, *Quantum Mechanics – A Modern Development* (World Scientific, Singapore, 1998).

[20] R. Diestel, *Graph Theory* (Springer, New York, 2010).

[21] A. Ben-Israel and T. N. E. Greville, *Generalized inverses: theory and applications*, 2nd ed., CMS books in mathematics No. 15 (Springer, New York, 2003).

[22] We note that some problems may arise in this perturbative treatement and the series expansion, as the Moore-Penrose pseudo-inverse is not continuous in general. However, these problems do not apply here. We can easily circumenvent the formal problems by fixing the phase of an arbitrarily chosen slack node n as $\theta_n \equiv 0$ and removing the n-th row from the linear set of equations. The resulting set of equations is of full rank and admits a unique solution. The corresponding matrices are called Grounded Laplacians [26] and are invertible. The matrix inverse is continuous and admits a series expansion as in Equation (9). For the sake of notational simplicity and coherence, we will however stick to the ordinary Laplacians.

[23] S. Kettemann, Delocalization of disturbances and the stability of ac electricity grids, Physical Review E **94**, 10.1103/PhysRevE.94.062311 (2015).

[24] D. Labavic, R. Suciu, H. Meyer-Ortmanns, and S. Kettemann, Long-range response to transmission line disturbances in DC electricity grids, The European Physical Journal Special Topics **223**, 2517 (2014).

[25] D. Jung and S. Kettemann, Long-range response in ac electricity grids, Physical Review E **94**, 012307 (2016).

[26] U. Miekkala, Graph properties for splitting with grounded Laplacian matrices, BIT **33**, 485 (1993).

5. Understanding which conditions shape network vulnerability: cascading failures and system splits

Finally, we turn to a different aspect of network vulnerability. We consider once again networks that are economically optimised using the open energy system model PyPSA-EUR [28], but focus on the risk of system splits. In Section 1.4, we discussed the system split in Europe in 2006 which demonstrates that cascading failures, and in particular system splits, pose a critical threat to power system stability. A more recent example is given by the system split in Europe in January 2021, even if the consequences were much less severe in this case [76]. But how do these dangerous splits emerge?

Understanding which factors favour or even cause such splits is essential for power system security. Importantly, the essential mechanism governing cascading failures that lead to system split – the iterative pattern of flow rerouting and subsequent line overloads – is well-captured by linear flow networks and thus by the cascading mechanisms discussed in previous sections. Therefore, we can profit from the knowledge about link failures developed throughout this thesis in understanding which conditions favour dangerous system splits.

In this manuscript draft, we analyse and classify possible system splits in the German power transmission system. We consider networks optimised using the open energy system model PyPSA-EUR and presented in Ref. [55]. We evaluate different possible system splits in the German power grid using different network topologies and weather scenarios representing the years 2013-2018. To this end, we consider an economic dispatch representing the load and generation for the entire historic German transmission grid in hourly resolution and simulate the failure of every possible transmission line. We then monitor whether a system split occurs and estimate the resulting frequency response that characterises the severity of the given split. Here, my contribution was the following: I wrote most of the source code to analyse the optimised PyPSA-Eur networks, performed the evaluation, wrote most of the paper and designed all figures. This manuscript is not yet published and has not been submitted.

5.1. H) Identifying critical infrastructures and predicting cascading failures in future power systems

Identifying critical infrastructures and predicting cascading failures in future power systems

Franz Kaiser [1,2,*] Philipp C. Böttcher [1,2,†] Martha Frysztacki,[3] Tom Brown,[3] and Dirk Witthaut [1,2,‡]

[1] *Forschungszentrum Jülich, Institute for Energy and Climate Research (IEK-STE), 52428 Jülich, Germany*

[2] *Institute for Theoretical Physics, University of Cologne, Köln, 50937, Germany*

[3] *Institute for Automation and Applied Informatics, Karlsruhe Institute of Technology, 76344 Eggenstein-Leopoldshafen, Germany*

(Dated: June 16, 2021)

The world's power systems are undergoing a rapid transformation, shifting away from centralised, carbon-intensive power generation to a decentralised generation based on variable renewable energy (VRE). As a result, there is a growing importance of long-distance transport of electrical power and the power transmission system will have to be able to deal with increasing line loadings. A major threat to present and future transmission systems is given by cascading outages where an initial failure triggers a subsequent cascade of failures and eventually results in a system split that disconnect parts of the grid. Here, we analyse to what extent the risk of dangerous system splits increases with a growing share of renewable power production. We systematically analyse and quantify the risk of system splits for different carbon emission reduction scenarios that we generate using high-level energy system models of the European grid. To this end, we identify potential vulnerabilities of a given grid using statistical analyses and identify the most likely splits for a given scenario. Finally, we examine to what extent the increase in VRE corresponds to higher frequency responses as a result of system splits.

I. INTRODUCTION

Mitigating the impact of climate change is one of the biggest challenges in the upcoming decades [1, 2]. In the Paris Agreement, most of the world's countries have committed to reducing their carbon footprint to work towards this goal [3]. While the overall reduction target can only be met by a wide range of measures in different sectors [2], a major share of carbon emissions is generated directly or indirectly by the production of electrical energy [4].

As a result, a shift from fossil fuel-based energy production to a production based on renewable energy resources is essential. This ongoing transition requires a fundamental transformation of nowadays power system which has immediate consequences for the security and reliability of the energy supply: Energy production shifts from centralised, easily controllable generating facilities to a decentral, more volatile power production which is subject to varying weather conditions[5, 6]. The consequences are manifold and not necessarily intuitive and thus not easily compensated: While energy production will not be limited to a few centralised production facilities, localised weather patterns and different potential yield of different production sites can lead to more long-ranged transport of electricity [7]. In addition to that, changing weather patterns make it harder to predict congestion, which causes the need to resolve the bottlenecks using costly congestion management measures such as redispatch and curtailment[8, 9]. Finally, conventional generators provide inertia to the power system by their large rotating masses, while the most prominent renewable resources, i.e. wind and solar, are typically connected to the grid via power electronics which do not naturally provide inertia [10, 11].

The changes resulting from this transformation might critically deteriorate power system security. On the one hand, at present, the most common strategies to stabilise the power grid after unforeseen events such as power outages are based on power system inertia [11, 12]. Replacing a large amount of inertia-providing conventional generation with inverter-based, non-inertia generation facilities might thus endanger the stable operation of future power systems [10, 13]. Increased line loading and longer range transport, on the other hand, increase the likelihood of a line exceeding its transmission capacity and tripping, which can lead to a cascade of failing transmission elements [14, 15]. In the worst case, a cascade of failures can disconnect parts of the grid, i.e. a system split occurs, which has severe consequences for the electricity supply as recent examples demonstrate [16, 17]. For example, the Western European power outage in 2006, where millions of households had to be disconnected from the electricity grid in one of the components, resulted from a cascade of failures that caused a system split [18–20]. While both phenomena on their own threaten power system security, a combination of both can be fatal for power system security: An increased risk of large scale cascades in combination with a decrease in system inertia might result in more frequent system splits in which one of the split components has a significant lack of inertia. In such cases, the transmission system operators (TSOs) are left with very few drastic containment strategies such as load shedding, where consumers are cut-off from the

* f.kaiser@fz-juelich.de

† p.boettcher@fz-juelich.de

‡ d.witthaut@fz-juelich.de

electricity supply [21, 22]. It is therefore of utmost importance to understand which conditions favour system splits, which splits are the most dangerous ones and how these can be prevented.

In this work, we evaluate the likelihood of system splits occurring under different conditions and classify situations that are exceptionally harmful to the power system. To this end, we make use of the open energy system model PyPSA to calculate the power generation for different weather scenarios using an economic dispatch [23]. The underlying topology represents the transmission grid of Germany throughout the different years. We then simulate link failures to identify situations where system splits occur and classify them by how dangerous they are. This enables us to identify transmission elements that are either responsible for a dangerous system split or are often involved in a subsequent cascade. Knowledge of the elements that are involved in system splits allows to expand the transmission capacities of these elements or modify the system to increase the resilience of their power system.

II. METHODS

A. AC power grids in the DC approximation

We describe the power grid using a simple graph $G(V, E)$, where individual nodes $i \in V(G)$ correspond to buses in the power grids and collect all loads, storages and generators attached to the bus and transmission lines are described by weighted edges $\ell \in E(G)$. We assume that the grid has $N = |V(G)|$ nodes and $M = |E(G)|$ edges. The power flow in the network may then be calculated using the AC load flow equations. The AC load flow equations relate the injections of real power P_i and reactive power Q_i at a given node $i \in V(G)$ to the power flows through the network. They are calculated as [24]

$$\begin{aligned} P_i &= \sum_{k=1}^{N} |V_i||V_k|(G_{ik}\cos(\vartheta_i - \vartheta_k) + B_{ik}\sin(\vartheta_i - \vartheta_k)), \\ Q_i &= \sum_{k=1}^{N} |V_i||V_k|(G_{ik}\sin(\vartheta_i - \vartheta_k) - B_{ik}\cos(\vartheta_i - \vartheta_k)). \end{aligned} \tag{1}$$

Here, V_i and ϑ_i is the voltage magnitude and voltage phase angle, respectively, at node i and G_{ik} and B_{ik} are the elements of the network's nodal conductance and susceptance matrices, respectively. Here, we focus on the DC approximation of the AC power flow equations. This approximation is based on the following assumptions

- Magnitudes of nodal voltages are constant in the p.u. system, i.e. $|V_i| \approx 1, \; \forall i \in V(G)$.
- Transmission lines are purely inductive, i.e. their resistance vanishes when compared to the reactance $r_\ell \ll x_\ell, \; \forall \ell \in E(G)$.
- Differences between nodal voltage angles $\vartheta_n, \; n \in V(G)$ of neighbouring nodes n, m are small $|\vartheta_n - \vartheta_m| \ll 1$.

Typically, this approximates the real power flows well for power grids on the transmission level if line loadings are not too high [25]. As a result, the flow of real power $f_{m\to n}$ along a transmission line $e_\ell = (m, n) \in E(G)$ that connects two nodes m and n is approximated by the linear drop in the voltage phase angles ϑ_m

$$f_{m\to n} = b_\ell(\vartheta_m - \vartheta_n). \tag{2}$$

Here, b_ℓ is the inverse line reactance $b_\ell = 1/x_\ell$ of the transmission line ℓ, i.e. it corresponds to the elements of the susceptance matrix $b_\ell = -B_{mn}$. The power flows are determined by the effective power injections or withdrawal p_n at a node n by virtue of Kirchhoff's current law

$$p_n = \sum_{e\in\Gamma(n)} f_e, \quad \forall n \in V, \tag{3}$$

where $\Gamma(n)$ denotes the set of all edges connected to node n. In the following, we assume that the power injections in the grid are balanced at any point in time, i.e. that the injections sum to zero,

$$\sum_{n\in V(G)} p_n = 0. \tag{4}$$

Together, Eqs. (3) and (2) fully determine the power flows in the network up to a constant shift applied to all voltage phase angles once the power injections p_n at any node $n \in V(G)$ is known.

In addition to Kirchhoff's voltage law (3) and Kirchhoff's current law (2), the power flow problem, i.e. the solution to the above equations, may be subject to additional constraints. Each transmission line $\ell \in E(G)$ has a maximal loading

$$|f_\ell| \leq f_{\ell,\max}$$

that, if violated, leads to a shutdown of the corresponding line. Here we assume that the maximal loading is the same independent of the direction of the flow.

To ensure a stable power supply in the case of unforeseen events, most power grids are operated in $N-1$ security which means that power system stability is not threatened even in case of the failure of a single transmission or generation element. Here, we incorporate $N-1$ security via a 'rule of thumb' which we refer to as the '70%-rule' that simplifies the underlying optimisation problem considerably. It states that $N-1$ security is approximately satisfied if no transmission element is loaded more heavily than 70% of its maximal loading and is commonly used for power flow calculations [5, 26, 27].

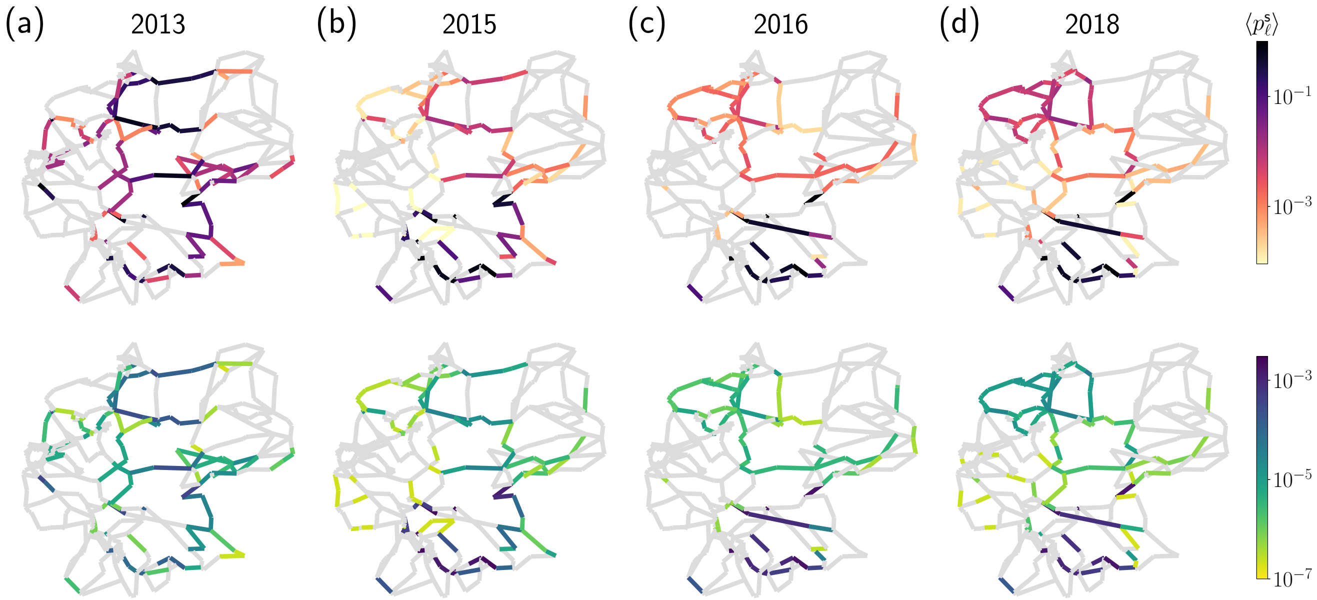

FIG. 1. Links that fail: Likely system splits in the German transmission grid for different dispatch and transmission grid scenarios representing the years 2013, 2015, 2016 and 2018 (a-d). Top row: empirical probability $\langle p_\ell \rangle$ that a given link will fail during a system split that results in at least two large connected components. Note that this probability is evaluated based only on the events resulting in large connected components, i.e. it gives the probability that an edge will fail provided that a split resulting in large components happens at all. Bottom row: Probability that a given link will fail during a cascade that results in at least two large components evaluated over an entire year and provided that a single link failed. We observe that the pattern of links that are likely to fail changes: Whereas the links connecting Eastern and Western Germany in are the most likely to fail in 2013, the most likely failures in later years occur between Eastern Germany and South-Eastern Germany, on the one hand, and South-Eastern and South-Western Germany on the other one. This is likely due to a transmission expansion in the region connecting Eastern Germany with South-Eastern Germany ("Thüringer Strombrücke").

B. Energy system models

All networks analysed in this study were optimised using the open energy system model PyPSA-Eur [23]. We focus on the German power grid at the transmission level as presented in Ref. [28] at a resolution of $N = 306$ nodes with $M = 403$ edges in the year 2013 up to $M = 407$ edges in the year 2018 due to transmission expansion, counting multiple circuit lines only once. The assumptions underlying the optimisation procedure can be found in detail in Ref. [28]. We briefly summarise these in the following paragraph.

The power system data used for the analysis is based on an economic dispatch of the generator and storage fleet of the respective year. The overall generation has to match the corresponding historical demand data that is disaggregated from a country-based to a nodal level using a predefined heuristic. Finally, the transmission grid is based on the transmission map provided by the ENTSO-E and the line capacities and building status are based on information provided by the transmission system operators.

C. Cascading failures and system splits

Algorithm 1 Algorithm for cascading failures.

```
for All scenarios and target years do
  for all hours in the respective year do
    Determine the dispatch
    for all pre-specified trigger events do
      Remove the trigger transmission elements
      Simulate cascade of failures
      if a system split occurred then
        Store key variables:
        – Load imbalance ΔP in each connected component
        – Inertia estimate in components
      end if
    end for
  end for
end for
```

To study the probability of a system splits and to identify to what extent a given system split threatens power system security, we study the scenario outlined in Section II B in depth. To this end, we simulate the failure of each non-bridge link for each possible hour in a given

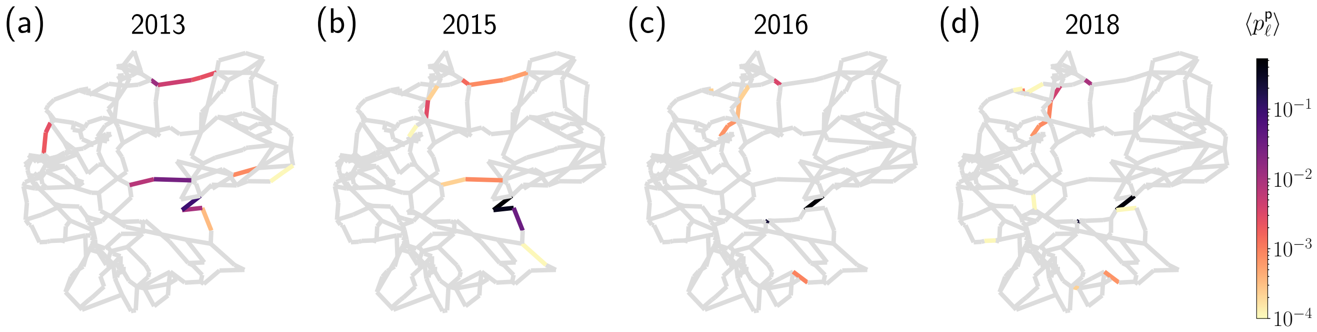

FIG. 2. Links that cause failures: Probability of primary failures in the German transmission grid for different dispatch and transmission grid scenarios representing the years 2013, 2015, 2016 and 2018 (a-d). We analyse the probability of primary failures which a given link causes a system split that results in large split components evaluated over each hour in the year. To obtain the probability, we simulate the failure of the link for each hour in the year and monitor the (potential) system split that it causes.

scenario as we outline in the following, schematic algorithm:

D. Identifying critical system splits

After identifying all possible system splits, we now turn to the impact of a given split on power system security. The severity of a split is characterised by the response in the grid frequency: If the grid frequency in a given disconnected part drops slowly, primary control may be able to balance the mismatch that causes the drop and restore the grid frequency. A system split may, however, result in a very fast drop of the grid frequency, such that the grid operators are left with no other option than performing emergency load shedding where parts of the consumers are disconnected from the power supply. Whether the frequency drops or increases fast is characterised using the *Rate of Change of Frequency (RoCoF)* [29]. The RoCoF measures the instantaneous frequency response of the grid with respect to the grid frequency ω_0 immediately after a change in the power injections by an amount ΔP, e.g. through the loss of a generating unit. It is calculated as

$$\mathrm{RoCoF} = \frac{\omega_0 \Delta P}{2\sum_{i=1}^{M} H_i S_{\max,i}}. \tag{5}$$

Here, $S_{\max,i}$ and H_i are the apparent power rating, i.e. the maximal power output, and inertia constant, respectively, of the synchronous machine with index i. The higher the RoCoF, the larger the frequency response after the perturbation and thus the more dangerous the given failure is. In particular, a system split can lead to a mismatch in load and generation which causes potentially large frequency excursions – depending on the available inertia remaining in each of the split components.

Here we assume that a certain class of conventional generators and storages participate in power system inertia generation (see Table I). For simplicity, we assume that all generators and storages have the same inertia constant $H = 6$s which is in the typical range of inertia constants for conventional generators [30, Table 16.1]. As a result, we approximate the RoCoF after a system split that results in a load imbalance of $\pm\Delta P$ in the resulting component C

$$\mathrm{RoCoF}' = \frac{50}{2\cdot 6}\frac{\Delta P}{\sum_{i\in C} S_{\max,i}}\mathrm{Hz}\cdot\mathrm{s}^{-1}. \tag{6}$$

E. Classifying system splits

To classify the system splits on the network level, we suggest two metrics that relate the probability of a given split to the network structure. Similar to Ref. [31], we evaluate the empirical probability that a given edge will fail during a cascade. However, since we are mostly concerned with cascades that result in a system split, we condition this probability on the fact that the cascade resulted in at least two individual connected components consisting of m nodes each. Here and in the following, we set $m = 10$. Furthermore, we do not distinguish between edges that trigger the cascade or edges that fail at some point during the cascade at this point. We thus calculate the probability

$$\langle p_\ell^{\mathrm{s}}(m)\rangle_T = \frac{1}{|T|}\sum_{t\in T} p_\ell^{\mathrm{s}}(m,t) \tag{7}$$

where $p_\ell^{\mathrm{s}}(m,t)$ is the probability that link ℓ was involved in a cascade at time t that lead to a division of the network into two or more connected components of which two or more consist of at least m nodes and T is the set of points in time under consideration. In the following, we will omit the argument (m) since we fix $m = 10$ and simply write $\langle p_\ell^{\mathrm{s}}\rangle := \langle p_\ell^{\mathrm{s}}(m=10)\rangle_T$.

The probability that a given link fails during a system split provides a detailed perspective on how the cascades

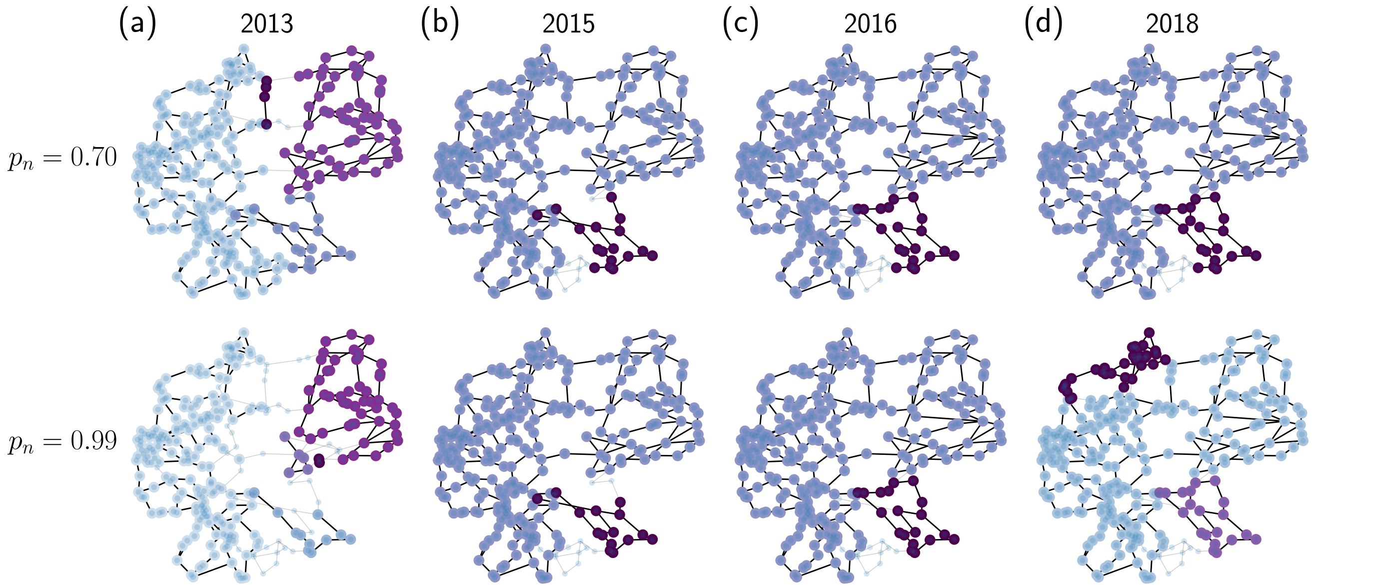

FIG. 3. Likely system splits in the German transmission grid evaluated on the level of nodes for different dispatch and transmission grid scenarios representing the years 2013, 2015, 2016 and 2018 (a-d). We analyse the components of the German transmission grid that are likely to remain connected after a large system split happened. Top: We set the nodal probability to $p_n = 0.7$ and thus group nodes together (colours from purple to blue) that are contained in the same component after a system split in 70% of all analysed cases. Bottom: Same as top but evaluated for $p_n = 0.99$. Notably, there is no strong difference between the components evaluated in the top row and the bottom one, which means that even in 99% of all splits, the corresponding nodes end up in the same component. A major difference between the top and the bottom row is a new component that emerges in the North-Western part of Germany and contains a large share of wind power production.

propagate in the grid and allows to compactly visualise the system splits on a network level. However, it does not provide information about likely causes of dangerous splits. This is accomplished by the probability of a primary failure

$$\langle p_\ell^{\mathrm{p}} \rangle = \frac{1}{|T|} \sum_{t \in T} p_\ell^{\mathrm{p}}(t) \tag{8}$$

which measures the probability that a given link ℓ causes such a system split if it fails [31]. Here, we calculate this probability again for a split that results in at least two components with size $m = 10$.

To understand which parts of the grid are likely to remain connected after a split, we consider a node-based metric: we evaluate the nodal probability $p_n^{(m)}$ that a given set of nodes is contained in the same subgraph after a split. Again, we condition this probability on the set of all splits that results in at least two connected subgraphs of which two have at least m nodes. Since we evaluate this probability again for $m = 10$ nodes, we will simply denote it by $p_n = p_n^{(10)}$. By increasing the value of p_n, we can thus visualise smaller and smaller subgraphs after a split and thereby identify splits of smaller and smaller sizes. Thus, nodes that are assigned to the same component for a value of e.g. $p_n = 0.9$ remain connected after 90% of the splits that were evaluated.

III. RESULTS

A. Identifying likely splits in the German transmission grid

We first analyse the results with regard to the probability of certain system splits and components of the network that likely remain connected. In Figure 2, we encode the empirical probability of secondary failures $\langle p_\ell^{\mathrm{s}} \rangle$ (Eq. (7)) for the German transmission grid for the four different scenario years 2013, 2015, 2016 and 2018 (a-d) corresponding to historical transmission expansion, and load and generation patterns. We calculate the probability conditioned on two different events: Firstly, we consider the probability that a given line fails during a system split, provided that a system split happens at all (top). Secondly, we analyse probability that such a failure happens provided that a single transmission line fails, evaluated over the dispatch of an entire year. In the year 2013, we observe that transmission lines connecting Eastern Germany and Western Germany are the most likely ones to fail during a split, reaching values of around $\langle p_\ell^{\mathrm{s}} \rangle \approx 3 \cdot 10^{-3}$ for the empirical probability conditioned on the failure of any transmission line. In the year 2015, we observe that the probability of failure for these lines is slightly reduced, with the most likely failures occurring now on the transmission lines connecting South-Eastern

generator type	CCGT	OCGT	coal	lignite	nuclear	oil	ror	biomass
storage type	pumped hydro							

TABLE I. Generator types and storage types assumed to participate in inertia generation.

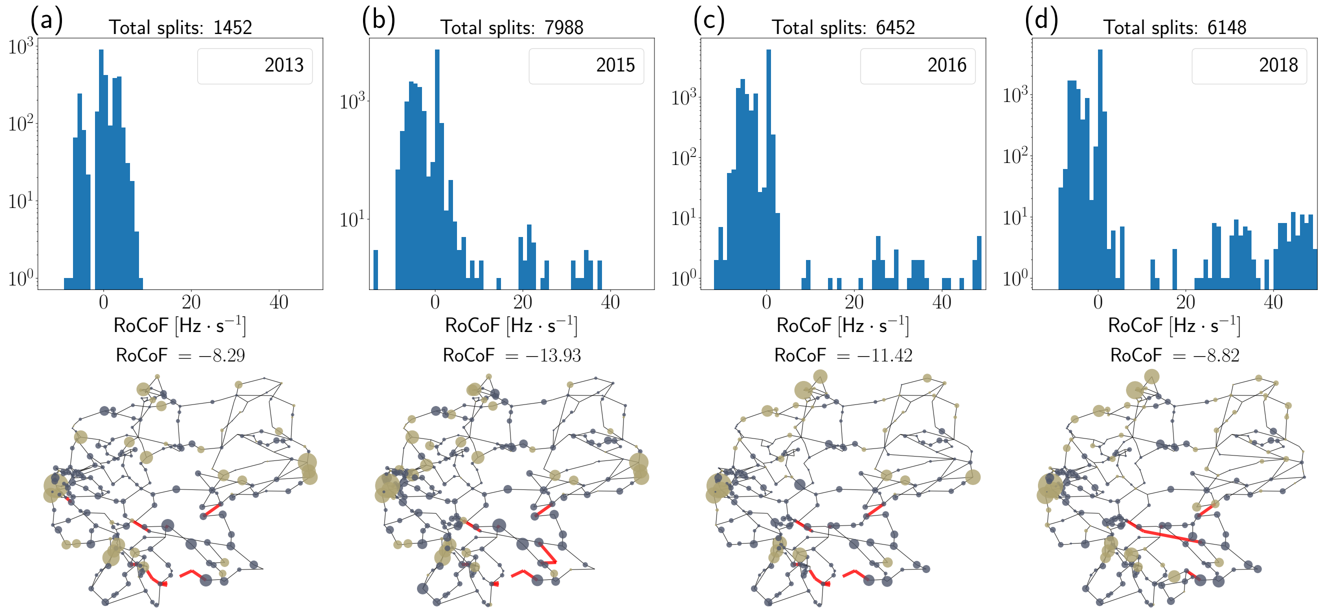

FIG. 4. RoCoF estimate (see Eq. (6)) evaluated for the system splits in the German power transmission system for different dispatch and transmission grid scenarios representing the years 2013, 2015, 2016 and 2018 (a-d). We present a histogram that gives the number of splits and associated RoCoF estimate on a logarithmic scale (top). We then show the transmission grid for the worst case negative RoCoF that occurred and encode the corresponding distribution of effective generation (yellow) and load (grey) at each bus with the size being proportional to the absolute power attached to the corresponding node and highlight the links that failed during the split (red). For all years, the worst case negative RoCoF appears for a split separating South-Eastern Germany and the remainder.

Germany with the remainder. After the completion of parts of the "Thüringer Strombrücke" in the year 2016 that extends the transmission capacities between Eastern Germany and Southern Germany, we observe that for both years 2016 and 2018, the connections between Western and Eastern Germany are much less likely to fail, while the risk for the lines connecting South-Eastern Germany with the remainder is increased. In addition to that, we observe a gradual increase in the secondary failure probability for a set of transmission lines located in North-Western Germany over the years, which is likely connected to an increase in power being produced by wind turbines in that region. In total, we observe that the transmission expansion likely reduces the risk of system splits that separate Eastern Germany and Western Germany while potentially increasing the risk for splits that separate South-Eastern Germany from the rest.

But what causes the secondary failures that result in these cascades? To understand how the failure cascades propagate through the grid and to identify potential causes, we now turn to the empirical probability of primary failures $\langle p_\ell^{\mathrm{p}} \rangle$ (Eq. (7)). This measure evaluates how likely a system split with two components of size at least $m = 10$ occurred in the simulations after the line ℓ failed. We present this probability in Figure 2 for the same data set. Again we observe a similar effect of the transmission expansion on system security: The probability of primary failures for transmission lines connecting Eastern Germany and Western Germany decreased throughout the years until it vanished for the years 2016 and 2018. Remarkably, a single transmission line seems to be responsible for the majority of failures throughout all years analysed here. It connects Eastern Germany and South-Eastern Germany, namely the substations of Remptendorf and Redwitz, which is a known bottleneck in the German power transmission grid [32]. In the years 2015, 2016 and 2018, the empirical probability of primary failure for this transmission line is around $\langle p_\ell^{\mathrm{p}} \rangle = 0.5$, i.e. its failure caused a system split in almost 50% of all hours analysed.

Finally, we want to adopt a different perspective to study which components of the grid are likely to remain connected in case of system splits. To this end, we consider the nodal probability p_n (see Sec. II E) and evaluate it for the German transmission grid for each of the scenario years. For a nodal probability of $p_n = 0.7$ (top row), i.e. when considering nodes that end up in the same component with 70% empirical probability, we observe very similar results for the years 2015, 2016 and 2018 (b-d) whereas the resulting components differ slightly for the dataset of 2013 (a). In the former ones, only splits separating South-East Germany from the remainder are visible (coloured nodes) while the resulting components for the year 2013 also include a separated component that corresponds to Eastern Germany for this value of p_n. When increasing the probability to $p_n = 0.99$ (bottom row), we observe similar components. For the year 2013, smaller components appear, which indicates that the splits do not always propagate along the same set of edges when separating Eastern Germany from the rest of the grid. The components for the other years strongly coincide with the components obtained for $p_n = 0.7$. In the year 2018, however, a new component becomes visible (dark purple, bottom right) that separates the coastlines in North-Western Germany from the rest of the grid. This might indicate high power flows from the offshore wind facilities located in this region to the remainder of the grid for this year.

B. Evaluating the risk of a given split for the German transmission grid

Finally, we focus on the analysis of the risk that a given system split poses to system security. To this end, we consider the effective RoCoF' as calculated using Eq. (6) to quantify how severely a given split will affect the grid frequency. We focus mainly on negative values of the RoCoF' for the following reason: Negative values of the RoCoF correspond to an underproduction of power in the component where they occur, i.e. the generation is smaller than the consumption. Typically, this power mismatch will result in load shedding where consumers have to be disconnected from the grid and are no longer supplied with electrical power. This is due to the fact that system splits typically happen within a few seconds, such that the available generators typically cannot ramp up power production fast enough to account for the missing power. In contrast to that, a positive mismatch is typically easier to balance by curtailing power and, as a result, has less severe consequences.

In Figure 4, we show the statistics of the effective RoCoF' for the four sample years considered here and all system splits that result in large connected components. We analyse the frequency of occurrence of RoCoF' values throughout the years (a-d, top). For every year, we then present the transmission grid for the single split with the most negative value of the RoCoF' along with the effective consumption or generation at every node and the failing lines (bottom). While the number of splits is much higher for the years 2015, 2016 and 2018 than it is for the year 2013, this seems to lead mainly to more positive RoCoF values. The worst case negative RoCoFs are comparable for all years, ranging from $\mathrm{RoCoF}' \approx -8.3\mathrm{Hz}\cdot\mathrm{s}^{-1}$ for the year 2013 to $\mathrm{RoCoF}' \approx -13.9\mathrm{Hz}\cdot\mathrm{s}^{-1}$ for the year 2015.

In all cases, the worst case split separates South-Eastern Germany from the rest of the grid and the split results in the failure of a similar set of links for all years. In addition to that, the generation and consumption patterns (yellow and grey circles with size proportional to magnitude) are similar for all four worst-case splits: After the split, around 6GW of generation are missing in South-Eastern Germany where relatively large consumers of power are located for all four scenarios. A major difference between the splits in the years 2013 and 2015, on the one hand, and the ones in 2016 and 2018 on the other one, is the amount of power being generated by the lignite power plants in Eastern Germany. For the former splits, these are among the largest generators and are visible in the map by eye whereas for the latter ones, there is less power production in Eastern Germany, but a higher share of wind power production in the North-Western coastal area. This fact does, however, not seem to strongly influence the worst case split since the RoCoF' is comparable in all four splits.

Note that the values observed here for the positive value of the effective RoCoF' are orders of magnitude larger than typical values observed in the operation of real-world power grids of $1-2\mathrm{Hz}\cdot\mathrm{s}^{-1}$ as tolerable values for a stable operation to around $6\mathrm{Hz}\cdot\mathrm{s}^{-1}$ in extreme situations such as blackouts [33, 34]. We will discuss the shortcomings of our approach that might have driven these high values in the next section.

IV. DISCUSSION AND CONCLUSION

In this manuscript, we analysed and classified system splits in the German power system at the transmission level using scenarios from the years 2013 to 2018. We found that the transmission expansion between Eastern Germany and South-Eastern Germany ("Thüringer Strombrücke") likely changed the way disturbances propagate through the grid: While Eastern Germany and Western Germany are likely disconnected in system splits before 2015, splits after 2015 are more likely to result in South-Eastern Germany being disconnected from the remaining grid. Finally, we found that system splits pose increasingly larger threats to system stability as measured by the Rate of Change of Frequency, which increases slightly over the years, and by the increase in the number of system splits.

Our results confirm the observations that with an increasing share of inverter-based renewable energy sources, the risk of incurring situations where one of the components after a system split has a very high RoCoFs increases [17]. Thus, low inertia power systems will have to rely on different strategies and observables other than the frequency to ensure a stable power supply even in the case of contingencies [10]. On the other hand, inverters connected to renewable energy sources may be designed such that they provide virtual inertia to the system – an approach not considered in the present work.

Even though our approach allows gaining insight into likely splits and provides a solid basis for further studies, there are some shortcomings in the methodology used here that could trigger unusually high values of the RoCoF and might result in an overestimation of the number of splits that occur. Firstly, we consider the German transmission grid effectively in island mode, i.e. disregarding its interconnection with the Central-European grid. As a result, the components resulting from each split are comparably small islands and cases where a large share of the renewable energy sources is contained in one of the islands occur frequently. Secondly, the scenarios analysed here incorporate $N-1$ security via the 70% rule and – as a result – the risk of system splits is likely to be overestimated. With a reduced risk of system splits, we also expect fewer events with an unusually high RoCoF. Thirdly, we neglect the ability of renewable energy sources connected to grid-forming inverters that may contribute to system inertia [35–37] – again potentially overestimating the RoCoF. Finally, the scenario analysed here displays unusually high levels of congestion for the high spatial resolution considered here due to load being allocated to the wrong nodes in some cases (see Ref. [28]). Therefore, we expect that this unusually high line loading leads to yet another increase in the frequency of occurrence of large scale blackouts and thus system splits.

ACKNOWLEDGEMENTS

We thank Mark Thiele and colleagues at TenneT for fruitful discussions. We gratefully acknowledge support from the German Federal Ministry of Education and Research (BMBF grant no. 03EK3055B), the Helmholtz Association (via the joint initiative "Energy System 2050 – A Contribution of the Research Field Energy", the grant no. VH-NG-1025 to D.W. and support from the "HIDA Trainee Network" to F.K.).

---

[1] Fawzy, S., Osman, A. I., Doran, J. & Rooney, D. W. Strategies for mitigation of climate change: a review. *Environmental Chemistry Letters* **18**, 2069–2094 (2020).

[2] IPCC. *Summary for Policymakers*, book section SPM, 1–30 (In Press, 2018).

[3] Paris agreement. URL `https://treaties.un.org/pages/ViewDetails.aspx?src=TREATY&mtdsg_no=XXVII-7-d&chapter=27&clang=_en`. Adopted on 12 December 2015.

[4] Gielen, D. *et al.* The role of renewable energy in the global energy transformation. *Energy Strategy Reviews* **24**, 38–50 (2019).

[5] Schlachtberger, D. P., Brown, T., Schramm, S. & Greiner, M. The Benefits of Cooperation in a Highly Renewable European Electricity Network. *Energy* **134**, 469–481 (2017). ArXiv: 1704.05492.

[6] Tröndle, T., Lilliestam, J., Marelli, S. & Pfenninger, S. Trade-Offs between Geographic Scale, Cost, and Infrastructure Requirements for Fully Renewable Electricity in Europe. *Joule* **4**, 1929–1948 (2020).

[7] Huber, M., Dimkova, D. & Hamacher, T. Integration of wind and solar power in Europe: Assessment of flexibility requirements. *Energy* **69**, 236–246 (2014).

[8] Ackermann, T. *et al.* Integrating Variable Renewables in Europe : Current Status and Recent Extreme Events. *IEEE Power and Energy Magazine* **13**, 67–77 (2015).

[9] Bird, L. *et al.* Wind and solar energy curtailment: A review of international experience. *Renewable and Sustainable Energy Reviews* **65**, 577–586 (2016).

[10] Milano, F., Dörfler, F., Hug, G., Hill, D. J. & Verbič, G. Foundations and Challenges of Low-Inertia Systems (Invited Paper). In *2018 Power Systems Computation Conference (PSCC)*, 1–25 (2018).

[11] Machowski, J., Bialek, J. W. & Bumby, J. R. *Power system dynamics: stability and control* (Wiley, Chichester, U.K, 2008), 2nd ed edn.

[12] Tielens, P. & Van Hertem, D. The relevance of inertia in power systems. *Renewable and Sustainable Energy Reviews* **55**, 999–1009 (2016).

[13] Homan, S., Mac Dowell, N. & Brown, S. Grid frequency volatility in future low inertia scenarios: Challenges and mitigation options. *Applied Energy* **290**, 116723 (2021).

[14] Kaiser, F. & Witthaut, D. Universal Statistics of Redistribution Factors and Large Scale Cascades in Power Grids. *IEEE Access* **9**, 67364–67378 (2021).

[15] Kaiser, F., Latora, V. & Witthaut, D. Network isolators inhibit failure spreading in complex networks. *Nature Communications* **12**, 3143 (2021).

[16] Ippolito, M. G., Musca, R. & Zizzo, G. Analysis and Simulations of the Primary Frequency Control during a System Split in Continental Europe Power System. *Energies* **14**, 1456 (2021).

[17] Kannan, A., Nuschke, M., Dobrin, B.-P. & Strauß-Mincu, D. Frequency stability analysis for inverter dominated grids during system split. *Electric Power Systems Research* **188**, 106550 (2020).

[18] van der Vleuten, E. & Lagendijk, V. Transnational infrastructure vulnerability: The historical shaping of the 2006 European "Blackout". *Energy Policy* **38**, 2042–2052 (2010).

[19] Union for the Coordination of Transmission of Electricity. Final report on the system disturbance on 4 november 2006. URL `https://www.entsoe.eu/fileadmin/user_upload/_library/publications/ce/otherreports/Final-Report-20070130.pdf`.

[20] Bialek, J. W. Why has it happened again? comparison between the ucte blackout in 2006 and the blackouts of 2003. In *2007 IEEE Lausanne Power Tech*, 51–56 (IEEE, 2007).

[21] De Boeck, S. *et al.* Review of Defence Plans in Europe: Current Status, Strenghts and Opportunities. *CIGRE Science & Engineering* **5**, 6–16 (2016). Publisher: CIGRE International Council on Large Electric Systems.

[22] ENTSOE. P5 – policy 5: Emergency operations (2015). URL `https://eepublicdownloads.entsoe.eu/clean-documents/Publications/SOC/Continental_Europe/oh/20150916_Policy_5_Approved_by_ENTSO-E_RG_CE_Plenary.pdf`.

[23] Hörsch, J., Hofmann, F., Schlachtberger, D. & Brown, T. Pypsa-eur: An open optimisation model of the european transmission system. *Energy strategy reviews* **22**, 207–215 (2018).

[24] Wood, A. J., Wollenberg, B. F. & Sheblé, G. B. *Power Generation, Operation and Control* (John Wiley & Sons, New York, 2014).

[25] Purchala, K., Meeus, L., Dommelen, D. V. & Belmans, R. Usefulness of dc power flow for active power flow analysis. In *IEEE Power Engineering Society General Meeting*, 454–459 Vol. 1 (2005).

[26] Gathmann, M. World's first dynamic control center in germany automates load balancing and outage prevention. `https://new.siemens.com/global/en/company/stories/infrastructure/2019/dynamic-power-grid.html` (2019).

[27] Ackermann, T., Tröster, E., Schierhorn, P.-P. & Brown, T. Optimising the European transmission system for 77% renewable electricity by 2030. *IET Renewable Power Generation* **10**, 3–9 (2016).

[28] Frysztacki, M. & Brown, T. Modeling Curtailment in Germany: How Spatial Resolution Impacts Line Congestion. In *2020 17th International Conference on the European Energy Market (EEM)*, 1–7 (2020).

[29] Broderick, C. Rate of Change of Frequency (ROCOF) withstand capability (2017). URL `https://eepublicdownloads.entsoe.eu/clean-documents/Networkcodesdocuments/Implementation/CNC/IGD-RoCoF_withstand_capability.pdf`.

[30] Grainger, J. J., Stevenson, W. D. & Stevenson, W. D. *Power system analysis*. McGraw-Hill series in electrical and computer engineering (McGraw-Hill, New York, 1994).

[31] Yang, Y., Nishikawa, T. & Motter, A. E. Small vulnerable sets determine large network cascades in power grids. *Science* **358**, eaan3184 (2017).

[32] Pesch, T., Allelein, H.-J. & Hake, J.-F. Impacts of the transformation of the German energy system on the transmission grid. *The European Physical Journal Special Topics* **223**, 2561–2575 (2014).

[33] Mehigan, L. *et al.* Renewables in the European power system and the impact on system rotational inertia. *Energy* **203**, 117776 (2020).

[34] Yan, R., Masood, N., Saha, T. K., Bai, F. & Gu, H. The Anatomy of the 2016 South Australia Blackout: A Catastrophic Event in a High Renewable Network. *IEEE Transactions on Power Systems* **33**, 5374–5388 (2018). Conference Name: IEEE Transactions on Power Systems.

[35] Lasseter, R. H., Chen, Z. & Pattabiraman, D. Grid-Forming Inverters: A Critical Asset for the Power Grid. *IEEE Journal of Emerging and Selected Topics in Power Electronics* **8**, 925–935 (2020).

[36] Pattabiraman, D., Lasseter, R. H. & Jahns, T. M. Comparison of Grid Following and Grid Forming Control for a High Inverter Penetration Power System. In *2018 IEEE Power Energy Society General Meeting (PESGM)*, 1–5 (2018). ISSN: 1944-9933.

[37] Kroposki, B. *et al.* Achieving a 100% Renewable Grid: Operating Electric Power Systems with Extremely High Levels of Variable Renewable Energy. *IEEE Power and Energy Magazine* **15**, 61–73 (2017).

6. Discussion and Conclusion

In this thesis, I have analysed how the structure of a supply network determines its resilience against failure spreading. I have focused mainly on power grids, but have extended some results also to other supply networks that are well-described by linear flow networks, such as leaf venation networks. Using the direct mathematical connection between network topology and flow rerouting after failures, I have unveiled fundamental mechanisms of failure spreading and have introduced novel containment strategies that are based on results from graph theory. These strategies were found to be very effective in reducing, or even inhibiting failure spreading completely, thereby greatly improving a supply network's resilience against cascading failures. Finally, I have demonstrated how different types of optimal networks are shaped by fluctuations and damages, pinpointing to potential impacts of the energy transition on the structure of the underlying network. These findings could aid transmission expansion scenarios that aim to build reliable future power systems: They allow to combine the ability of the grid to transport more power over long distances while increasing the overall power system security. While my results improve the understanding of power system stability and security for power transmission grids under most circumstances, there are different possible ways to extend the present work, some of which I will discuss in the following sections.

6.1. Power flows beyond linear flow models

Whereas the present thesis focuses mainly on linear models of power flows, the load flow equations that describe the transport of apparent power in AC power grids are in fact highly nonlinear. A first, natural extension of the linear model can be obtained by replacing the linear difference of potentials by a sinusoidal interaction, which reduces to the linear model for small arguments $\sin(x) \approx x, x \ll \pi/2$. Different studies compare the two models and suggest under which circumstances to extend the linear model with its non-linear counterpart, see e.g. Refs. [66, 77]. Physically, the non-linear extension captures power flows over transmission lines that are more heavily loaded such that the linear model may no longer be exactly valid. It has been demonstrated that the two models differ in some aspects. In particular, the non-linear model results in additional stable states for the power grid where the (power) flows are no longer uniquely determined by the (power) injections: The system is multistable [78, 79]. We have analysed how this extended model affects our results on failure spreading in parts in Ref. [4] and also in Ref. [9] that is not part of this thesis. Nevertheless, additional studies could shed further light on how to extend the present results to these non-linear models.

While both the linear analysis and its extension are suitable for high-voltage transmission grids where resistive losses are typically negligible, resistive losses play an important role in distribution grids or other medium- to low-voltage grids [80]. In the resulting model, an additional term is included into the balance between flows and injections that corresponds to the losses. Recent works of ours [8] and others [81] have demonstrated that losses induce yet additional possible stable states. Again, the flows are no longer uniquely determined by the power injections in that case, but the mechanism underlying this non-uniqueness is different compared to the model featuring only sinusoidal interactions: Different levels of losses need to be compensated for by different levels of power generation. Since losses are highly relevant for medium voltage and distribution grids, extending my results on failure spreading to these types of power grids will require models that include losses.

Finally, the results presented in this thesis and the extensions discussed so far focus entirely on real power flows. However, complex power flows also include an imaginary part which is known as reactive power flow. We have focused on real power flows due to the fact that many phenomena relevant for power system security, such as transmission line overloads as a result of overheating, are governed by real power flows and these are typically orders of magnitude larger than the reactive ones, in particular in the case of the linear approximation under consideration. In addition to that, power grid analyses in the physics community have focused mainly on the real power flow, due to its formal similarity to synchronisation models [82, 83]. Nevertheless, there are approaches that combine the assumption of lossless transmission lines with reactive power flow analyses [84]. Furthermore, reactive power flows are intimately related to voltage related stability issues such as voltage collapse [85, 86]. In the future, the results on failure spreading presented in this thesis should be extended to include power system failures related to reactive power flow.

6.2. Dynamic stability of power grids

Until now, we have focused on static models of power systems. However, given that energy production and consumption patterns clearly vary over time and unforeseen events such as failures result in changes of power flows, the variables describing the state of the power system evolve dynamically over time. Whereas the static perspective on power systems approximates many crucial aspects of power system stability very well, others can only be understood from a point of view of dynamical systems.

The dynamical analysis of power system stability gives rise to additional phenomena that are not present in the static model. A networked dynamical system can respond in manifold ways to a perturbation, such as a link failure. For example, a new *unstable* state may exist, such that a naive static analysis might conclude that the system is in a new state which it will, in fact, never reach. In the simplest case, power grids are modelled by Kuramoto-type models, where consumers and producers of power form a network of diffusively coupled phase-oscillators that describe rotating motors. For this setup, the only dynamical variables, that describe the time evolution of each motor, are the voltage phase angle and the motor's frequency of rotation [36, 82, 87, 88].

Recently, two types of behaviour have been analysed in these dynamical models that are not easily captured by static models. First, the power flow limits of transmission lines might be exceeded during the transient phase where the system moves dynamically from one state to the other one, although they are *not* exceeded in the final state described by the static analysis. In this case, static theory would predict a new state, although the dynamical overloads might result in a transmission line failure, and eventually in a cascade of failures, before the new state is reached [89, 90]. Secondly, the generators in the power system might actually desynchronise as a result of the failure and thus never reach the new state predicted by static theory [91, 92]. The latter phenomenon is well-known in the context of transient analysis of power system stability [93].

In Refs. [4, 9], we performed a first analysis on which results on the inhibition of failure spreading may be applied to non-linear dynamical models of power flows, with a particular focus on network isolators. We found that isolators can reduce the risk of transient cascading failures and decrease the control effort necessary to keep the power system at its nominal frequency in the presence of fluctuations. However, further research would be beneficial to examine how the proposed strategies may be adapted to reduce failure spreading or prevent desynchronisation in dynamical models.

Already for the simplest dynamical models of power grids where networks of Kuramoto oscillators are considered, there are different ways of representing the consumers and generators that may affect how the system reacts to perturbations [94, 95]. Actual exact models of synchronous machines involve nine or more dynamical variables per machine, thus making a network based analysis of an entire grid very challenging [43]. If we extend Kuramoto-type models by considering a third dynamical variable – the voltage level at every motor – a novel type of instability emerges known as voltage collapse [86, 96, 97]. Such voltage-induced instabilities can play an important role in cascading failures [51]. Further research is necessary to assess to which extent the presented methods may also be used to prevent voltage-induced cascading failures and how they can be extended to be able to prevent failure spreading in this case.

6.3. Power grid stability and the energy transition

The power system is undergoing a rapid transformation from fossil-fuel based to carbon-free energy production that poses new challenges to its stability, as discussed in the introduction. We will conclude the discussion about power grids by analysing how the results presented in this thesis can help to ensure the stable operation of future power systems.

Whereas traditional power production is typically centralised and easily scheduled ahead of dispatch, potentials for variable renewable energy sources (VRES) are more decentralised and their power production varies stronger over time due to weather dependencies. On the other hand, potentials for some VRES such as offshore wind are strongly localised at the coastlines, which at present leads to highly loaded transmission grids [98] and causes high costs via redispatch [99, 100] or even significant curtailment at peak generation times [101, 102]. For this reason, long-range transport of electrical power becomes increasingly important to smooth localised weather patterns and to be able to transport all the power generated by VRES to the consumers even at peak times [21–23]. In this thesis, I addressed this problem by proposing strategies to limit failure spreading and cascade propagation that rely on building additional transmission lines while at the same time increasing power grid security.

Additionally, the energy transition poses new challenges to the dynamical stability of power grids. VRES are typically connected to the power grid via power electronics such as inverters which – unlike traditional power generators that are typically based on large rotating masses – do not naturally provide inertia to the power systems [45] and whose behaviour depends on their design [103–106]. However, traditional control mechanisms to dynamically stabilise the grid rely on inertia [45, 46]. Thus, the question of how low-inertia or zero-inertia power systems can be operated stably is under investigation [45, 46, 107]. In particular, cascading failures that lead to system splits can become even more critical in low-inertia systems if power in one of the split components is produced mainly by VRES [108]. We have laid a first foundation for quantifying the effect of decreased system inertia on the risk of dangerous system splits in Section 5. However, further analyses are necessary, in particular to predict and counteract the most critical splits in a constantly changing energy mix.

6.4. Network structure and flow networks beyond power grids

Linear flow networks do not only describe power grids, but can also be used to describe a variety of other systems. In this section, I would like to broaden the perspective again to extend the discussion to other types of supply networks.

As we have seen in Chapter 4, there is a surprising degree of similarity between the optimal structures of different types of supply networks. I have focused on comparing optimal structures of leaf venation networks, dissipation-optimised networks and power grids due to the similarity in their mathematical description and due to data availability. Nevertheless, other spatial networks such as hydraulic networks [62] or resistor networks [65] are described by the same model and the question of optimal network design plays an important role also in water distribution system research [109, 110]. Finally, similar models also emerge in transportation networks [111, 112]. Thus, it would be interesting to see if the presented approach to loop formation and optimal networks can be extended to other types of networks and flow models. In addition to that, topological analyses play an important role also in purely structural, i.e. non-model-based approaches, for spatial [42, 113] and non-spatial networks [74, 114, 115] throughout disciplines. The dual community approach that we used to describe optimal networks shaped by fluctuations and damages [7] could be applied to unveil structural information also for other types of networks.

In addition to optimal network structure, network resilience against failures, the other central topic of this thesis, also plays an important role for other types of networks. In this thesis, I focused on link failures and perturbations in flow models ruled by Kirchhoff's laws, which results in flows being rerouted along different parallel paths in a network. Other network-based models incorporate different failure or cascading mechanisms, such as shortest path routing of flows [116–118], redistribution to neighbouring nodes or edges [119–122] or contagion between topological neighbours [123].

However, the insight gained about cascading failures from topological models may differ considerably from power flow models [69, 124]. In particular, depending on the type of model, different conclusions can be drawn about strategies to limit cascading failures and failure spreading. In line with experimental observations [125, 126], different models identify that a reduction in connectivity between different parts of a network limits the spreading of failures or cascades between them [122, 127–129]. Many recent approaches that analyse cascading failures using power flow models come to the similar conclusion that limiting connectivity between different parts of the network or even islanding it, i.e. cutting all connections between the parts, is a promising strategy to mitigate failure spreading [72, 73, 130, 131]. Our approaches presented in Refs. [4, 5] complement these approaches by presenting a strategy against failure spreading that is based on a targeted increase in connectivity by adding or strengthening selected links between different parts of the networks. Further research is necessary to determine if our results may be transferred to other cascading and failure spreading models.

6.5. Outlook: recent developments related to the manuscripts

In the final part of this thesis, I would like to comment on recent studies that appeared after or during the completion of the manuscripts that form the basis for this thesis. I will discuss the manuscripts presented in each of the chapters separately.

6.5.1. Recent work on link failures and linear flow models (Chapter 2)

I will start with recent developments regarding the impact of single link failures and collective effects of multiple failures in linear flow networks.

Notably, inverse square laws, such as the one we have identified as a characteristic of the decay of flow changes with distance in regular grids in Ref. [1], seem to emerge more generally in linear flow networks. A recent publication has found an inverse square law for the change in permeability in homogeneous spatial networks upon removal of a single link in linear flow networks [132]. The main difference of the approach used in this reference compared to the one that we used is the following: While in power grid-inspired linear flow models, the nodal power injections are typically fixed for all nodes and the power flows and nodal potentials can be directly calculated from these, the setup used in Ref. [132] is applied to biologically inspired networks, where a fixed pressure difference between a set of nodes is often considered. This corresponds to fixing nodal voltage angles or nodal potentials for a set of nodes in the power grid context, which is not typically the case for power systems. It would be interesting to see whether the findings on power laws may be connected, or whether similar scaling laws can be identified in other setups.

Regarding the aspect of multiple link failures that we studied in Ref. [2], the resulting generalised Line Outage Distribution Factors (GLODFs) were analysed recently in Ref. [133] where the generalised formula for addressing the impact of multiple failing links was considered. The authors focus on bridge-block decompositions and demonstrate that not only the LODFs, but also the GLODFs vanish between for links that are contained in different blocks using a spectral representation of GLODFs.

6.5.2. Recent work on reducing the impact of link failures (Chapter 3)

Now we turn to recent publications that relate to our work on suppressing the impact of link failures. A recent series of papers [131, 133, 134] examines strategies to limit failure spreading based on a spectral representation of Line Outage Distribution Factors (LODFs).

This approach is similar to our work presented in Ref. [5] since both approaches derive strategies to limit failure spreading based on a spanning tree formulation of LODFs. However, the focus of our work and the aforementioned publications is slightly different: While the latter focus mainly on identifying possible bridge-block decompositions, i.e. regions of a network with a particularly low connectivity, and suggest an algorithm to achieve this in the most efficient way in Ref. [133], our work focuses on network isolators and other network structures that limit failure spreading while increasing connectivity. Nevertheless, further research may allow to combine the approaches, e.g. via extending the algorithm proposed in Ref. [133] by allowing to include other network structures such as network isolators.

6.5.3. Recent work on optimal network design (Chapter 4)

The analysis of optimal supply networks is a field of very active and broad research. A recent manuscript examines loop formation in multi-commodity networks [135] with a set-up similar to the one used in our work [5]. The authors analyse how loop formation is altered in the presence of multiple commodities that each fulfil the conservation laws we fix for a single commodity and that share the same network infrastructure. They find that including multiple commodities changes the parameter space where optimal networks contain loops compared to the single commodity case. It would be interesting to see which results about discontinuous transitions that we found for the single commodity case may be translated to optimised networks of multiple commodities.

In Ref. [136], the authors consider three-dimensional, intertwined linear flow networks inspired by real-world biological examples such as liver or kidney networks. Again, the networks are locally optimised to minimise the dissipation, but there is an additional term that accounts for the distance between the two different networks expressed in terms of the tube radii. Again, a transition to loop formation is observed that occurs robustly throughout different parameters and a unified description of this transition independent of the parameters is identified. Interestingly, the transition to loop formation appears to be continuous in this case even though the approaches are formally similar. Further research is necessary to determine whether a discontinuous transition can also be identified in this setting.

Bibliography

1. Strake, J., Kaiser, F., Basiri, F., Ronellenfitsch, H. & Witthaut, D. Non-local impact of link failures in linear flow networks. *New Journal of Physics* **21,** 053009. doi:10.1088/1367-2630/ab13ba (2019).
2. Kaiser, F., Strake, J. & Witthaut, D. Collective effects of link failures in linear flow networks. *New Journal of Physics* **22,** 013053. doi:10.1088/1367-2630/ab6793 (2020).
3. Kaiser, F. & Witthaut, D. Universal Statistics of Redistribution Factors and Large Scale Cascades in Power Grids. *IEEE Access* **9,** 67364–67378. doi:10.1109/ACCESS.2021.3076892 (2021).
4. Kaiser, F., Latora, V. & Witthaut, D. Network isolators inhibit failure spreading in complex networks. *Nature Communications* **12,** 3143. doi:10.1038/s41467-021-23292-9 (2021).
5. Kaiser, F. & Witthaut, D. Topological theory of resilience and failure spreading in flow networks. *Physical Review Research* **3,** 023161. doi:10.1103/PhysRevResearch.3.023161 (2021).
6. Kaiser, F., Ronellenfitsch, H. & Witthaut, D. Discontinuous transition to loop formation in optimal supply networks. *Nature Communications* **11,** 5796. doi:10.1038/s41467-020-19567-2 (2020).
7. Kaiser, F., Ronellenfitsch, H., Latora, V. & Witthaut, D. Resilience and fluctuations shape primal and dual communities in spatial networks. *arXiv:2105.06687 [physics].* arXiv: 2105.06687 (2021).
8. Balestra, C., Kaiser, F., Manik, D. & Witthaut, D. Multistability in lossy power grids and oscillator networks. *Chaos: An Interdisciplinary Journal of Nonlinear Science* **29,** 123119. doi:10.1063/1.5122739 (2019).
9. Wassmer, J., Witthaut, D. & Kaiser, F. Targeted suppression of failure spreading in multistable oscillator networks. *Journal of Physics: Complexity* **2,** 035003. doi:10.1088/2632-072X/abf090 (2021).
10. Kaiser, F. & Alim, K. Order parameter allows classification of planar graphs based on balanced fixed points in the Kuramoto model. *Physical Review E* **99,** 052308. doi:10.1103/PhysRevE.99.052308 (2019).

11. *Paris Agreement* adopted on 12 December 2015. United Nations Treaty Collection, Chapter XXVII 7. d. `https://treaties.un.org/pages/ViewDetails.aspx?src=TREATY&mtdsg_no=XXVII-7-d&chapter=27&clang=_en` (14th June 2021).
12. IPCC. in *Global Warming of 1.5°C. An IPCC Special Report on the impacts of global warming of 1.5°C above pre-industrial levels and related global greenhouse gas emission pathways, in the context of strengthening the global response to the threat of climate change, sustainable development, and efforts to eradicate poverty* (eds Masson-Delmotte, V. *et al.*) 1–30 (In Press, 2018).
13. Roelfsema, M. *et al.* Taking stock of national climate policies to evaluate implementation of the Paris Agreement. *Nature Communications* **11,** 2096. doi:`10.1038/s41467-020-15414-6` (2020).
14. Rogelj, J. *et al.* Paris Agreement climate proposals need a boost to keep warming well below 2 °C. *Nature* **534,** 631–639. doi:`10.1038/nature18307` (2016).
15. *Warming Projections Global Update December 2020* Climate Action Tracker. `https://climateactiontracker.org/documents/829/CAT_2020-12-01_Briefing_GlobalUpdate_Paris5Years_Dec2020.pdf` (14th June 2021).
16. *Bundes-Klimaschutzgesetz* German Environment Agency. `https://www.bmu.de/gesetz/bundes-klimaschutzgesetz/` (14th June 2021).
17. *National Inventory Reports for the German Greenhouse Gas Inventory 1990 to 2019 (as of 12/2020)* German Environment Agency. `https://www.umweltbundesamt.de/en/indicator-greenhouse-gas-emissions` (14th June 2021).
18. Dyke, K. J., Schofield, N. & Barnes, M. The impact of transport electrification on electrical networks. *IEEE Transactions on Industrial Electronics* **57,** 3917–3926. doi:`10.1109/TIE.2010.2040563` (2010).
19. Lechtenböhmer, S., Nilsson, L. J., Åhman, M. & Schneider, C. Decarbonising the energy intensive basic materials industry through electrification – Implications for future EU electricity demand. *Energy* **115,** 1623–1631. doi:`10.1016/j.energy.2016.07.110` (2016).
20. Schiffer, Z. J. & Manthiram, K. Electrification and Decarbonization of the Chemical Industry. *Joule* **1,** 10–14. doi:`10.1016/j.joule.2017.07.008` (2017).
21. Stetz, T. *et al.* Twilight of the Grids: The Impact of Distributed Solar on Germany?s Energy Transition. *IEEE Power and Energy Magazine* **13.** Conference Name: IEEE Power and Energy Magazine, 50–61. doi:`10.1109/MPE.2014.2379971` (2015).

22. Becker, S., Rodriguez, R. A., Andresen, G. B., Schramm, S. & Greiner, M. Transmission grid extensions during the build-up of a fully renewable pan-European electricity supply. *Energy* **64,** 404–418. doi:10.1016/j.energy.2013.10.010 (2014).

23. Tröndle, T., Lilliestam, J., Marelli, S. & Pfenninger, S. Trade-Offs between Geographic Scale, Cost, and Infrastructure Requirements for Fully Renewable Electricity in Europe. *Joule* **4,** 1929–1948. doi:10.1016/j.joule.2020.07.018 (2020).

24. *Net Zero by 2050 - A Roadmap for the Global Energy Sector* Paris. International Energy Agency (IEA). https://www.iea.org/reports/net-zero-by-2050 (14th June 2021).

25. Brown, T., Schierhorn, P.-P., Tröster, E. & Ackermann, T. Optimising the European transmission system for 77% renewable electricity by 2030. *IET Renewable Power Generation* **10,** 3–9. doi:https://doi.org/10.1049/iet-rpg.2015.0135 (2016).

26. Schlachtberger, D. P., Brown, T., Schramm, S. & Greiner, M. The benefits of cooperation in a highly renewable European electricity network. *Energy* **134,** 469–481. doi:10.1016/j.energy.2017.06.004 (2017).

27. Huber, M., Dimkova, D. & Hamacher, T. Integration of wind and solar power in Europe: Assessment of flexibility requirements. *Energy* **69,** 236–246. doi:10.1016/j.energy.2014.02.109 (2014).

28. Hörsch, J., Hofmann, F., Schlachtberger, D. & Brown, T. PyPSA-Eur: An Open Optimisation Model of the European Transmission System. *Energy Strategy Reviews* **22,** 207–215. doi:10.1016/j.esr.2018.08.012 (2018).

29. Hörsch, J., Neumann, F., Hofmann, F., Schlachtberger, D. & Brown, T. *PyPSA-Eur: An Open Optimisation Model of the European Transmission System (Dataset)* version v0.3.0 (Zenodo, 2020). doi:10.5281/zenodo.4307930.

30. Dörfler, F., Simpson-Porco, J. W. & Bullo, F. Electrical Networks and Algebraic Graph Theory: Models, Properties, and Applications. *Proceedings of the IEEE* **106,** 977–1005. doi:10.1109/JPROC.2018.2821924 (2018).

31. Bollobás, B. *Modern graph theory Graduate texts in mathematics* **184** (Springer, New York, 1998).

32. Motter, A. E., Myers, S. A., Anghel, M. & Nishikawa, T. Spontaneous synchrony in power-grid networks. *Nature Physics* **9,** 191–197. doi:10.1038/nphys2535 (2013).

33. Menck, P. J., Heitzig, J., Kurths, J. & Joachim Schellnhuber, H. How dead ends undermine power grid stability. *Nature Communications* **5,** 3969. doi:10.1038/ncomms4969 (2014).

34. Pagani, G. A. & Aiello, M. The Power Grid as a complex network: A survey. *Physica A: Statistical Mechanics and its Applications* **392,** 2688–2700. doi:10.1016/j.physa.2013.01.023 (2013).

35. Ke Sun. *Complex Networks Theory: A New Method of Research in Power Grid* in *2005 IEEE/PES Transmission Distribution Conference Exposition: Asia and Pacific* (2005), 1–6. doi:10.1109/TDC.2005.1547099.

36. Rohden, M., Sorge, A., Timme, M. & Witthaut, D. Self-Organized Synchronization in Decentralized Power Grids. *Physical Review Letters* **109,** 064101. doi:10.1103/PhysRevLett.109.064101 (2012).

37. Albert, R., Albert, I. & Nakarado, G. L. Structural vulnerability of the North American power grid. *Physical Review E* **69,** 025103. doi:10.1103/PhysRevE.69.025103 (2004).

38. Soltan, S. & Zussman, G. *Generation of synthetic spatially embedded power grid networks* in *2016 IEEE Power and Energy Society General Meeting (PESGM)* (2016), 1–5. doi:10.1109/PESGM.2016.7741383.

39. Schultz, P., Heitzig, J. & Kurths, J. A random growth model for power grids and other spatially embedded infrastructure networks. *The European Physical Journal Special Topics* **223,** 2593–2610. doi:10.1140/epjst/e2014-02279-6 (2014).

40. Espejo, R., Lumbreras, S. & Ramos, A. A Complex-Network Approach to the Generation of Synthetic Power Transmission Networks. *IEEE Systems Journal* **13,** 3050–3058. doi:10.1109/JSYST.2018.2865104 (2019).

41. Wang, Z., Thomas, R. J. & Scaglione, A. *Generating Random Topology Power Grids* in *Proceedings of the 41st Annual Hawaii International Conference on System Sciences (HICSS 2008)* (IEEE, Waikoloa, HI, 2008), 183–183. doi:10.1109/HICSS.2008.182.

42. Barthélemy, M. Spatial networks. *Physics Reports* **499,** 1–101. doi:10.1016/j.physrep.2010.11.002 (2011).

43. Sauer, P. W. & Pai, M. A. *Power system dynamics and stability* (Wiley Online Library, 1998).

44. *Article 127, Commission Regulation (EU) 2017/1485 of 2 August 2017 establishing a guideline on electricity transmission system operation* adopted on 2 August 2017. the European Commission. https://eur-lex.europa.eu/eli/reg/2017/1485/oj (14th June 2021).

45. Milano, F., Dörfler, F., Hug, G., Hill, D. J. & Verbič, G. *Foundations and Challenges of Low-Inertia Systems (Invited Paper)* in *2018 Power Systems Computation Conference (PSCC)* (2018), 1–25. doi:10.23919/PSCC.2018.8450880.

46. Tielens, P. & Van Hertem, D. The relevance of inertia in power systems. *Renewable and Sustainable Energy Reviews* **55,** 999–1009. doi:10.1016/j.rser.2015.11.016 (2016).

47. Pourbeik, P., Kundur, P. & Taylor, C. The anatomy of a power grid blackout - Root causes and dynamics of recent major blackouts. *IEEE Power and Energy Magazine* **4,** 22–29. doi:10.1109/MPAE.2006.1687814 (2006).

48. Hines, P., Balasubramaniam, K. & Sanchez, E. Cascading failures in power grids. *IEEE Potentials* **28,** 24–30. doi:10.1109/MPOT.2009.933498 (2009).

49. Union for the Coordination of Transmission of Electricity. *Final report on the system disturbance on 4 November 2006* provided by the successor organization of the UCTE, the European Network of Transmission System Operators for Electricity (ENTSO-E). https://www.entsoe.eu/fileadmin/user_upload/_library/publications/ce/otherreports/Final-Report-20070130.pdf (14th June 2021).

50. Union for the Coordination of Transmission of Electricity. *FINAL REPORT of the Investigation Committee on the 28 September 2003 Blackout in Italy* provided by the successor organization of the UCTE, the European Network of Transmission System Operators for Electricity (ENTSO-E). https://eepublicdownloads.entsoe.eu/clean-documents/pre2015/publications/ce/otherreports/20040427_UCTE_IC_Final_report.pdf (14th June 2021).

51. Venkatasubramanian, V. & Li, Y. Analysis of 1996 Western American electric blackouts. *Bulk Power System Dynamics and Control-VI, Cortina d'Ampezzo, Italy,* 22–27 (2004).

52. De Boeck, S. *et al.* Review of Defence Plans in Europe: Current Status, Strenghts and Opportunities. *CIGRE Science & Engineering* **5,** 6–16 (2016).

53. Victoria, M., Zhu, K., Brown, T., Andresen, G. B. & Greiner, M. Early decarbonisation of the European energy system pays off. *Nature Communications* **11,** 6223. doi:10.1038/s41467-020-20015-4 (2020).

54. Hitaj, C. Location matters: The impact of renewable power on transmission congestion and emissions. *Energy Policy* **86,** 1–16. doi:10.1016/j.enpol.2015.06.019 (2015).

55. Frysztacki, M. & Brown, T. *Modeling Curtailment in Germany: How Spatial Resolution Impacts Line Congestion* in *2020 17th International Conference on the European Energy Market (EEM)* (2020), 1–7. doi:10.1109/EEM49802.2020.9221886.

56. Schermeyer, H., Vergara, C. & Fichtner, W. Renewable energy curtailment: A case study on today's and tomorrow's congestion management. *Energy Policy* **112,** 427–436. doi:10.1016/j.enpol.2017.10.037 (2018).

57. Kunz, F. Improving Congestion Management: How to Facilitate the Integration of Renewable Generation in Germany. *The Energy Journal* **34,** 55–78. doi:10.5547/01956574.34.4.4 (2013).

58. Hines, P. D. H., Dobson, I. & Rezaei, P. Cascading Power Outages Propagate Locally in an Influence Graph That is Not the Actual Grid Topology. *IEEE Transactions on Power Systems* **32,** 958–967. doi:10.1109/TPWRS.2016.2578259 (2017).

59. Everhart, K. & Molnar, G. *Severe power cuts in Texas highlight energy security risks related to extreme weather events* International Energy Agency. https://www.iea.org/commentaries/severe-power-cuts-in-texas-highlight-energy-security-risks-related-to-extreme-weather-events (14th June 2021).

60. Chunyan Li, Yuanzhang Sun & Xiangyi Chen. *Analysis of the blackout in Europe on November 4, 2006* in *2007 International Power Engineering Conference (IPEC 2007)* (2007), 939–944.

61. Dörfler, F., Simpson-Porco, J. W. & Bullo, F. Electrical Networks and Algebraic Graph Theory: Models, Properties, and Applications. *Proceedings of the IEEE* **106,** 977–1005. doi:10.1109/JPROC.2018.2821924 (2018).

62. Hwang, N. & Houghtalen, R. *Fundamentals of Hydraulic Engineering Systems* (Prentice Hall, Upper Saddle River, NJ, 1996).

63. Katifori, E., Szöllősi, G. J. & Magnasco, M. O. Damage and Fluctuations Induce Loops in Optimal Transport Networks. *Physical Review Letters* **104,** 048704. doi:10.1103/PhysRevLett.104.048704 (2010).

64. Gavrilchenko, T. & Katifori, E. Resilience in hierarchical fluid flow networks. *Physical Review E* **99,** 012321. doi:10.1103/PhysRevE.99.012321 (2019).

65. Kirchhoff, G. Ueber die Auflösung der Gleichungen, auf welche man bei der Untersuchung der linearen Vertheilung galvanischer Ströme geführt wird. *Annalen der Physik* **148,** 497–508. doi:10.1002/andp.18471481202 (1847).

66. Purchala, K., Meeus, L., Dommelen, D. V. & Belmans, R. *Usefulness of DC power flow for active power flow analysis* in *IEEE Power Engineering Society General Meeting* (2005), 454–459 Vol. 1. doi:10.1109/PES.2005.1489581.

67. Dobson, I., Carreras, B. A., Lynch, V. E. & Newman, D. E. Complex systems analysis of series of blackouts: Cascading failure, critical points, and self-organization. *Chaos: An Interdisciplinary Journal of Nonlinear Science* **17,** 026103. doi:10.1063/1.2737822 (2007).

68. Andrey, B., Daniel, B., David, H., Meric, U. & Gil, Z. Sensitivity analysis of the power grid vulnerability to large-scale cascading failures. *ACM SIGMETRICS Performance Evaluation Review.* doi:10.1145/2425248.2425256 (2012).

69. Korkali, M., Veneman, J. G., Tivnan, B. F., Bagrow, J. P. & Hines, P. D. H. Reducing Cascading Failure Risk by Increasing Infrastructure Network Interdependence. *Scientific Reports* **7,** 44499. doi:10.1038/srep44499 (2017).

70. Yang, Y., Nishikawa, T. & Motter, A. E. Small vulnerable sets determine large network cascades in power grids. *Science* **358,** eaan3184. doi:10.1126/science.aan3184 (2017).

71. Braess, D. Über ein Paradoxon aus der Verkehrsplanung. *Unternehmensforschung Operations Research* **12,** 258–268. doi:10.1007/BF01918335 (1969).

72. Mureddu, M., Caldarelli, G., Damiano, A., Scala, A. & Meyer-Ortmanns, H. Islanding the power grid on the transmission level: less connections for more security. *Scientific Reports* **6,** 34797. doi:10.1038/srep34797 (2016).

73. Pahwa, S., Youssef, M., Schumm, P., Scoglio, C. & Schulz, N. Optimal intentional islanding to enhance the robustness of power grid networks. *Physica A: Statistical Mechanics and its Applications* **392,** 3741–3754. doi:10.1016/j.physa.2013.03.029 (2013).

74. Girvan, M. & Newman, M. E. J. Community structure in social and biological networks. *Proceedings of the National Academy of Sciences* **99,** 7821–7826. doi:10.1073/pnas.122653799 (2002).

75. Newman, M. E. J. Modularity and community structure in networks. *Proceedings of the National Academy of Sciences of the United States of America* **103,** 8577–8582. doi:10.1073/pnas.0601602103 (2006).

76. European Network of Transmission System Operators for Electricity (ENTSO-E). https://www.entsoe.eu/news/2021/01/26/system-separation-in-the-continental-europe-synchronous-area-on-8-january-2021-2nd-update/ (14th June 2021).

77. Dörfler, F. & Bullo, F. *Novel insights into lossless AC and DC power flow* in *2013 IEEE Power Energy Society General Meeting* (2013), 1–5. doi:10.1109/PESMG.2013.6672260.

78. Manik, D. *et al.* Network susceptibilities: Theory and applications. *Physical Review E* **95,** 012319. doi:10.1103/PhysRevE.95.012319 (2017).

79. Delabays, R., Coletta, T. & Jacquod, P. Multistability of phase-locking in equal-frequency Kuramoto models on planar graphs. *Journal of Mathematical Physics* **58,** 032703. doi:10.1063/1.4978697 (2017).

80. Oeding, D. & Oswald, B. R. *Elektrische Kraftwerke und Netze: mit 140 Tabellen* (Springer, Berlin, 2011).

81. Hellmann, F. *et al.* Network-induced multistability through lossy coupling and exotic solitary states. *Nature Communications* **11,** 592. doi:10.1038/s41467-020-14417-7 (2020).

82. Filatrella, G., Nielsen, A. H. & Pedersen, N. F. Analysis of a power grid using a Kuramoto-like model. *The European Physical Journal B* **61,** 485–491. doi:10.1140/epjb/e2008-00098-8 (2008).

83. Rodrigues, F. A., Peron, T. K. D., Ji, P. & Kurths, J. The Kuramoto model in complex networks. *Physics Reports* **610,** 1–98. doi:10.1016/j.physrep.2015.10.008 (2016).

84. Simpson-Porco, J. W. A Theory of Solvability for Lossless Power Flow Equations—Part I: Fixed-Point Power Flow. *IEEE Transactions on Control of Network Systems* **5,** 1361–1372. doi:10.1109/TCNS.2017.2711433 (2018).

85. Zhang, W., Li, F. & Tolbert, L. M. Review of Reactive Power Planning: Objectives, Constraints, and Algorithms. *IEEE Transactions on Power Systems* **22,** 2177–2186. doi:10.1109/TPWRS.2007.907452 (2007).

86. Simpson-Porco, J. W., Dörfler, F. & Bullo, F. Voltage collapse in complex power grids. *Nature Communications* **7,** 10790. doi:10.1038/ncomms10790 (2016).

87. Dörfler, F. & Bullo, F. Synchronization in complex networks of phase oscillators: A survey. *Automatica* **50,** 1539–1564. doi:10.1016/j.automatica.2014.04.012 (2014).

88. Dörfler, F. & Bullo, F. Synchronization and Transient Stability in Power Networks and Nonuniform Kuramoto Oscillators. *SIAM Journal on Control and Optimization* **50,** 1616–1642. doi:10.1137/110851584 (2012).

89. Hellmann, F., Schultz, P., Grabow, C., Heitzig, J. & Kurths, J. Survivability of Deterministic Dynamical Systems. *Scientific Reports* **6,** 29654. doi:10.1038/srep29654 (2016).

90. Schäfer, B., Witthaut, D., Timme, M. & Latora, V. Dynamically induced cascading failures in power grids. *Nature Communications* **9,** 1975. doi:10.1038/s41467-018-04287-5 (2018).

91. Witthaut, D., Rohden, M., Zhang, X., Hallerberg, S. & Timme, M. Critical Links and Nonlocal Rerouting in Complex Supply Networks. *Physical Review Letters* **116,** 138701. doi:10.1103/PhysRevLett.116.138701 (2016).

92. Manik, D. *et al.* Supply networks: Instabilities without overload. *The European Physical Journal Special Topics* **223,** 2527–2547. doi:10.1140/epjst/e2014-02274-y (2014).

93. Kundur, P. *Power system stability and control* (McGraw-Hill, New York, 1994).

94. Nishikawa, T. & Motter, A. E. Comparative analysis of existing models for power-grid synchronization. *New Journal of Physics* **17,** 015012. doi:10.1088/1367-2630/17/1/015012 (2015).

95. Wolff, M. F., Lind, P. G. & Maass, P. Power grid stability under perturbation of single nodes: Effects of heterogeneity and internal nodes. *Chaos: An Interdisciplinary Journal of Nonlinear Science* **28,** 103120. doi:10.1063/1.5040689 (2018).

96. Sharafutdinov, K., Rydin Gorjão, L., Matthiae, M., Faulwasser, T. & Witthaut, D. Rotor-angle versus voltage instability in the third-order model for synchronous generators. *Chaos: An Interdisciplinary Journal of Nonlinear Science* **28,** 033117. doi:10.1063/1.5002889 (2018).

97. Schmietendorf, K., Peinke, J., Friedrich, R. & Kamps, O. Self-Organized Synchronization and Voltage Stability in Networks of Synchronous Machines. *The European Physical Journal Special Topics* **223,** 2577–2592. doi:10.1140/epjst/e2014-02209-8 (2014).

98. Pesch, T., Allelein, H.-J. & Hake, J.-F. Impacts of the transformation of the German energy system on the transmission grid. *Eur. Phys. J. Special Topics* **223,** 2561. doi:10.1140/epjst/e2014-02214-y (2014).

99. Marinescu, B., Coulondre, J., Tsamasphyrou, P. & Bourmaud, J.-Y. *Improving TSO's coordination for cross-border redispatch: a discussion of possible approaches in the European context* in *CIGRE/IEEE PES, 2005 International Symposium* (2005), 378–385. doi:10.1109/CIGRE.2005.1532766.

100. Wohland, J., Reyers, M., Märker, C. & Witthaut, D. Natural wind variability triggered drop in German redispatch volume and costs from 2015 to 2016. *PLOS ONE* **13,** e0190707. doi:10.1371/journal.pone.0190707 (2018).

101. Bird, L. *et al.* Wind and solar energy curtailment: A review of international experience. *Renewable and Sustainable Energy Reviews* **65,** 577–586. doi:10.1016/j.rser.2016.06.082 (2016).

102. Ackermann, T. *et al.* Integrating Variable Renewables in Europe : Current Status and Recent Extreme Events. *IEEE Power and Energy Magazine* **13,** 67–77. doi:10.1109/MPE.2015.2461333 (2015).

103. Lasseter, R. H., Chen, Z. & Pattabiraman, D. Grid-Forming Inverters: A Critical Asset for the Power Grid. *IEEE Journal of Emerging and Selected Topics in Power Electronics* **8,** 925–935. doi:10.1109/JESTPE.2019.2959271 (2020).

104. Schiffer, J., Ortega, R., Astolfi, A., Raisch, J. & Sezi, T. Conditions for stability of droop-controlled inverter-based microgrids. *Automatica* **50,** 2457–2469. doi:10.1016/j.automatica.2014.08.009 (2014).

105. Beck, H. & Hesse, R. *Virtual synchronous machine* in *2007 9th International Conference on Electrical Power Quality and Utilisation* (2007), 1–6. doi:10.1109/EPQU.2007.4424220.

106. Kroposki, B. *et al.* Achieving a 100% Renewable Grid: Operating Electric Power Systems with Extremely High Levels of Variable Renewable Energy. *IEEE Power and Energy Magazine* **15,** 61–73. doi:10.1109/MPE.2016.2637122 (2017).

107. Homan, S., Mac Dowell, N. & Brown, S. Grid frequency volatility in future low inertia scenarios: Challenges and mitigation options. *Applied Energy* **290,** 116723. doi:10.1016/j.apenergy.2021.116723 (2021).

108. Kannan, A., Nuschke, M., Dobrin, B.-P. & Strauß-Mincu, D. Frequency stability analysis for inverter dominated grids during system split. *Electric Power Systems Research* **188,** 106550. doi:10.1016/j.epsr.2020.106550 (2020).

109. Eiger, G., Shamir, U. & Ben-Tal, A. Optimal design of water distribution networks. *Water Resources Research* **30,** 2637–2646. doi:https://doi.org/10.1029/94WR00623 (1994).

110. Singh, M. K. & Kekatos, V. Optimal Scheduling of Water Distribution Systems. *IEEE Transactions on Control of Network Systems* **7,** 711–723. doi:10.1109/TCNS.2019.2939651 (2020).

111. Nagurney, A. & Qiang, Q. Robustness of transportation networks subject to degradable links. *Europhysics Letters (EPL)* **80,** 68001. doi:10.1209/0295-5075/80/68001 (2007).

112. Maerivoet, S. & De Moor, B. Transportation Planning and Traffic Flow Models. *arXiv:physics/0507127* (2005).

113. Alim, K., Amselem, G., Peaudecerf, F., Brenner, M. P. & Pringle, A. Random network peristalsis in Physarum polycephalum organizes fluid flows across an individual. *Proceedings of the National Academy of Sciences* **110,** 13306–13311. doi:`10.1073/pnas.1305049110` (2013).

114. Newman, M. E. J. *Networks: An introduction* (Oxford University Press, Oxford; New York, 2010).

115. Newman, M. E. J. Communities, modules and large-scale structure in networks. *Nature Physics* **8,** 25–31. doi:`10.1038/nphys2162` (2012).

116. Motter, A. E. & Lai, Y.-C. Cascade-based attacks on complex networks. *Physical Review E* **66,** 065102. doi:`10.1103/PhysRevE.66.065102` (2002).

117. Crucitti, P., Latora, V. & Marchiori, M. Model for cascading failures in complex networks. *Physical Review E* **69,** 045104. doi:`10.1103/PhysRevE.69.045104` (2004).

118. Crucitti, P., Latora, V. & Marchiori, M. A topological analysis of the Italian electric power grid. *Physica A: Statistical Mechanics and its Applications* **338,** 92–97. doi:`10.1016/j.physa.2004.02.029` (2004).

119. Wang, J.-W. & Rong, L.-L. Cascade-based attack vulnerability on the US power grid. *Safety Science* **47,** 1332–1336. doi:`10.1016/j.ssci.2009.02.002` (2009).

120. Bak, P., Tang, C. & Wiesenfeld, K. Self-organized criticality: An explanation of the 1/f noise. *Physical Review Letters* **59,** 381–384. doi:`10.1103/PhysRevLett.59.381` (1987).

121. Goh, K.-I., Lee, D.-S., Kahng, B. & Kim, D. Sandpile on Scale-Free Networks. *Physical Review Letters* **91,** 148701. doi:`10.1103/PhysRevLett.91.148701` (2003).

122. Brummitt, C. D., D'Souza, R. M. & Leicht, E. A. Suppressing cascades of load in interdependent networks. *Proceedings of the National Academy of Sciences* **109,** E680–E689. doi:`10.1073/pnas.1110586109` (2012).

123. Watts, D. J. A simple model of global cascades on random networks. *Proceedings of the National Academy of Sciences* **99,** 5766–5771. doi:`10.1073/pnas.082090499` (2002).

124. Hines, P., Cotilla-Sanchez, E. & Blumsack, S. Do topological models provide good information about electricity infrastructure vulnerability? *Chaos: An Interdisciplinary Journal of Nonlinear Science* **20,** 033122. doi:`10.1063/1.3489887` (2010).

125. Stouffer, D. B. & Bascompte, J. Compartmentalization increases food-web persistence. *Proceedings of the National Academy of Sciences* **108,** 3648–3652. doi:10.1073/pnas.1014353108 (2011).

126. Gilarranz, L. J., Rayfield, B., Liñán-Cembrano, G., Bascompte, J. & Gonzalez, A. Effects of network modularity on the spread of perturbation impact in experimental metapopulations. *Science* **357,** 199–201. doi:10.1126/science.aal4122 (2017).

127. Nematzadeh, A., Ferrara, E., Flammini, A. & Ahn, Y.-Y. Optimal Network Modularity for Information Diffusion. *Physical Review Letters* **113.** doi:10.1103/PhysRevLett.113.088701 (2014).

128. Wu, J.-j., Gao, Z.-y. & Sun, H.-j. Cascade and breakdown in scale-free networks with community structure. *Physical Review E* **74,** 066111. doi:10.1103/PhysRevE.74.066111 (2006).

129. Ash, J. & Newth, D. Optimizing complex networks for resilience against cascading failure. *Physica A: Statistical Mechanics and its Applications* **380,** 673–683. doi:10.1016/j.physa.2006.12.058 (2007).

130. Esmaeilian, A. & Kezunovic, M. Prevention of Power Grid Blackouts Using Intentional Islanding Scheme. *IEEE Transactions on Industry Applications* **53,** 622–629. doi:10.1109/TIA.2016.2614772 (2017).

131. Guo, L., Liang, C., Zocca, A., Low, S. & Wierman, A. Line Failure Localization of Power Networks Part I: Non-cut outages. *IEEE Transactions on Power Systems,* 1–1. doi:10.1109/TPWRS.2021.3066336 (2021).

132. Lange, S. & Friedrich, B. M. Network permeability changes according to a quadratic power law upon removal of a single edge. *arXiv:2007.10130 [cond-mat, physics:physics, q-bio]* (2020).

133. Zocca, A., Liang, C., Guo, L., Low, S. H. & Wierman, A. A Spectral Representation of Power Systems with Applications to Adaptive Grid Partitioning and Cascading Failure Localization. *arXiv:2105.05234 [physics].* arXiv: 2105.05234 (2021).

134. Guo, L., Liang, C., Zocca, A., Low, S. H. & Wierman, A. Line Failure Localization of Power Networks Part II: Cut Set Outages. *IEEE Transactions on Power Systems,* 1–1. doi:10.1109/TPWRS.2021.3068048 (2021).

135. Lonardi, A., Facca, E., Putti, M. & De Bacco, C. Optimal transport for multicommodity routing on networks. *arXiv:2010.14377 [nlin, physics:physics].* arXiv: 2010.14377 (2020).

136. Kramer, F. & Modes, C. D. How to pare a pair: Topology control and pruning in intertwined complex networks. *Physical Review Research* **2,** 043171. doi:10.1103/PhysRevResearch.2.043171 (2020).

A. Appendix

A.1. Erklärung zur Dissertation

gemäß der Promotionsordnung vom 12. März 2020

Hiermit versichere ich an Eides statt, dass ich die vorliegende Dissertation selbstständig und ohne die Benutzung anderer als der angegebenen Hilfsmittel und Literatur angefertigt habe. Alle Stellen, die wörtlich oder sinngemäß aus veröffentlichten und nicht veröffentlichten Werken dem Wortlaut oder dem Sinn nach entnommen wurden, sind als solche kenntlich gemacht.
Ich versichere an Eides statt,

- dass diese Dissertation noch keiner anderen Fakultät oder Universität zur Prüfung vorgelegen hat;
- dass sie - abgesehen von unten angegebenen Teilpublikationen und eingebundenen Artikeln und Manuskripten - noch nicht veröffentlicht worden ist sowie,
- dass ich eine Veröffentlichung der Dissertation vor Abschluss der Promotion nicht ohne Genehmigung des Promotionsausschusses vornehmen werde.

Die Bestimmungen dieser Ordnung sind mir bekannt. Darüber hinaus erkläre ich hiermit, dass ich die Ordnung zur Sicherung guter wissenschaftlicher Praxis und zum Umgang mit wissenschaftlichem Fehlverhalten der Universität zu Köln gelesen und sie bei der Durchführung der Dissertation zugrundeliegenden Arbeiten und der schriftlich verfassten Dissertation beachtet habe und verpflichte mich hiermit, die dort genannten Vorgaben bei allen wissenschaftlichen Tätigkeiten zu beachten und umzusetzen.
Ich versichere, dass die eingereichte elektronische Fassung der eingereichten Druckfassung vollständig entspricht.

Teilpublikationen

A) Strake, J., Kaiser, F., Basiri, F., Ronellenfitsch, H. & Witthaut, D. Non-local impact of link failures in linear flow networks. *New Journal of Physics* **21,** 053009. doi:`10.1088/1367-2630/ab13ba` (2019). (Section 2.1)

B) Kaiser, F., Strake, J. & Witthaut, D. Collective effects of link failures in linear flow networks. Englisch. *New Journal of Physics* **22,** 013053. doi:`10.1088/1367-2630/ab6793` (2020). (Section 2.2)

C) Kaiser, F. & Witthaut, D. Universal Statistics of Redistribution Factors and Large Scale Cascades in Power Grids. *IEEE Access* **9,** 67364–67378. doi:`10.1109/ACCESS.2021.3076892` (2021). (Section 2.3)

D) Kaiser, F., Latora, V. & Witthaut, D. Network isolators inhibit failure spreading in complex networks. *Nature Communications* **12,** 3143. doi:`10.1038/s41467-021-23292-9` (2021). (Section 3.1)

E) Kaiser, F. & Witthaut, D. Topological theory of resilience and failure spreading in flow networks. *Physical Review Research* **3,** 023161. doi:`10.1103/PhysRevResearch.3.023161` (2021). (Section 3.2)

F) Kaiser, F., Ronellenfitsch, H. & Witthaut, D. Discontinuous transition to loop formation in optimal supply networks. *Nature Communications* **11,** 5796. doi:`10.1038/s41467-020-19567-2` (2020). (Section 4.1)

G) Kaiser, F., Ronellenfitsch, H., Latora, V. & Witthaut, D. Resilience and fluctuations shape primal and dual communities in spatial networks. *arXiv:2105.06687 [physics].* arXiv: 2105.06687 (2021). (Section 4.2)

Ein weiteres Manuskript (Section 5.1) wurde noch nicht zur Veröffentlichung eingereicht.

29. Juni 2021, Franz Kaiser